

Communication: Overtone (2NH) spectroscopy of NH₃-Ar

K. Didriche,^{a)} T. Földes, T. Vanfleteren, and M. Herman

Laboratoire de Chimie quantique et Photophysique, CP160/09, Faculté des Sciences,
 Université Libre de Bruxelles, 50 ave. Roosevelt, B-1050 Brussels, Belgium

(Received 2 April 2013; accepted 23 April 2013; published online 8 May 2013)

The $\Pi(1_1) \leftarrow \Sigma(0_0)$ 2NH ($\nu_1 + \nu_3$) band of the NH₃-Ar van der Waals complex formed in a supersonic jet expansion, with origin at 6628 cm⁻¹ was recorded at high-resolution using cavity ring down spectroscopy. The analysis leads to upper state rotational constants and J -dependent predissociation lifetimes estimated from linewidth analysis, with a mean value about 0.6 ns. © 2013 AIP Publishing LLC. [<http://dx.doi.org/10.1063/1.4804421>]

Near infrared (NIR), high-resolution overtone spectroscopy of van der Waals molecules is most challenging. The usual weakness of overtone transitions combined to the production of weakly bound molecular complexes in limited concentration, usually in supersonic expansions, must be compensated by additional, ultra-high sensitivity in the detection means. Moreover, the vibration-rotation energy pattern in overtone ranges is typically very dense and not precisely understood, in some cases even for the monomer species supporting the overtone excitation. Finally, existing potential energy surfaces (PES) fully based on *ab initio* calculations or merging only ground vibrational state experimental information are hardly of any use to deal with the detailed rotational structure in highly excited, overtone states.

Among the few molecular complexes experimentally investigated in the NIR range under high-resolution spectral conditions, one can cite those containing HF,¹ C₂H₂,² and various water isotopologues,^{3,4} only quoting here selected references. The most recent of these NIR studies were performed using a cavity ring down spectrometer (CRDS) probing a powerful supersonic expansion. This setup was developed over the years at ULB-Brussels⁵ and is named FANTASIO+ (for “Fourier trANSform, Tunable diode and quadrupole mAss spectrometers interfaced to a Supersonic expansIOn,” with the + standing for various updates since the initial report in 2007). We were successful in investigating acetylene and water molecules complexed to various other species, including rare gas atoms, diatomic and polyatomic molecules (see previous references). In the present Communication, we report on the use of FANTASIO+ to investigate ammonia (NH₃)-containing complexes in the range of the 2NH, $\nu_1 + \nu_3$ monomer absorption band. This is actually the first literature report on NIR spectroscopy of ammonia-containing molecular complexes. The carrier of the presently single reported band could be identified to NH₃-Ar.

The ground and the intermolecular vibrational states of NH₃-Ar were extensively investigated in earlier far infrared and *ab initio* studies (e.g., Refs. 6–9), leading to determine an intermolecular PES,¹⁰ as well as in an infrared literature paper.¹¹ A structure with Ar linked to the center of gravity of

NH₃ was demonstrated, with various possible orientations of ammonia relative to this intermolecular, van der Waals bonding axis, depending whether the internal angular momentum j , i.e., of the almost freely rotating NH₃ unit, is roughly directed along (Π) or perpendicular (Σ) to this axis.⁸ The usual j, k quantum numbers of the NH₃ unit, defining the monomer level to which the dimer ones correlate, are conventionally used for labeling energy levels in the dimer, as well as J , corresponding to the end-over-end rotation of the complex.

Details about FANTASIO+ have been provided in the literature⁵ and only major or recent features are highlighted here. We used a single distributed feedback (DFB) diode for this first report, scanning from 6623 to 6638 cm⁻¹ (Sumitomo, SLT5411-CB-S850, centered at 1.510 μm ; 1 MHz linewidth). The cavity was made of two concave mirrors (Layertec 106767, radius = 1000 mm; reflectivity = 99.9985%), separated by about 540 mm, ensuring some 72 000 passes, i.e., about 725 m effective absorption path length below the 1 cm long slit, thus in the jet-cooled molecules. To increase the ring-down event rate, a newly built tracking circuit was used,¹² typically allowing some 200 ringdowns per spectral point to be recorded in less than 0.3 s, yielding a noise level $\alpha_{\text{min}} = 5 \times 10^{-10}$ cm⁻¹ (considering the full length of the cavity as effective absorption path length), with α the absorption coefficient as defined in Ref. 5. Line positions were calibrated to better than 0.001 cm⁻¹ using a 10 cm long ¹²C₂H₂ reference cell.¹³ The gas mixture was prepared by on-line mixing Ar (Air liquide) with a premixed sample (10% NH₃/90% Ar; Air liquide) resulting in a 1% NH₃/Ar mixture which was injected at a flow rate of 4460 sccm (where sccm denotes cubic centimeter per minute at standard conditions for temperature and pressure). The reservoir (p_0) and residual (p_∞) pressures were kept constant at 53 kPa and 2 Pa, respectively.

The recorded band is presented in Fig. 1. It shows P/R and Q branches and is therefore of perpendicular-type. The R/P ground state combination differences nicely compare to the FIR values of the $\Sigma(0_0)$ sub-state, from Ref. 7, therefore confirming this assignment for the lower state in the overtone transition. The upper level must thus correspond to the $\Pi(1_1)$ state of the 2NH ($\nu_1 + \nu_3$) state of the complex.¹⁴ We fitted the various J -lines to a linear-type $\Pi - \Sigma^+$ band structure using the PGOPHER software.¹⁵ The P/R and Q branches, reaching different sets of upper states, were fitted

^{a)} Author to whom correspondence should be addressed. Electronic mail: kdidrich@ulb.ac.be. FNRS postdoctoral fellow.

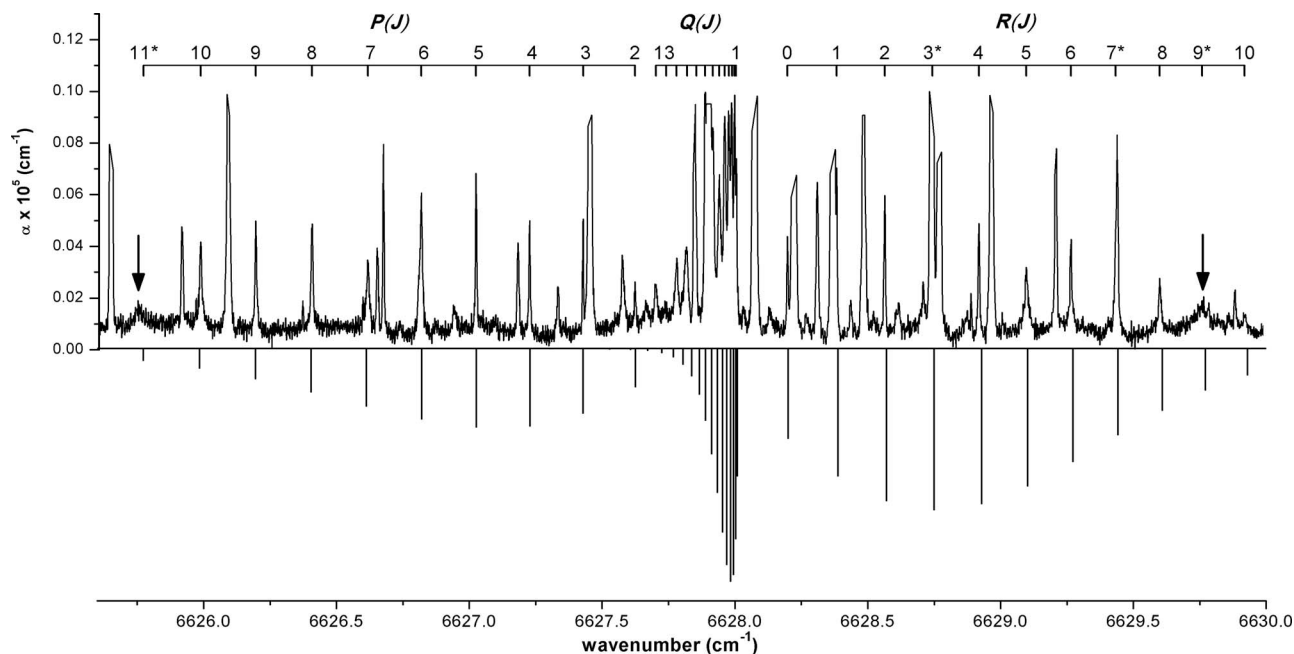


FIG. 1. Observed (top) and simulated (bottom) spectrum of the $\Pi(1_1) \leftarrow \Sigma(0_0)$ 2NH ($\nu_1 + \nu_3$) absorption band of the $\text{NH}_3\text{-Ar}$ van der Waals complex. Experimental conditions are detailed in the text. The simulation is performed using the vibration-rotation constants from Table I and $T_{\text{rot}} = 8$ K. The arrows point anomalously large line broadenings discussed in the text. The signs * point out the lines not included in the fitting procedure.

separately. Line assignments are detailed in Fig. 1. The resulting rotational constants are listed in Table I and the list of assigned lines is provided in the supplementary material,¹⁶ as well as the calculated positions of $R(3)$, $R(7)$, $Q(9)$, and $Q(12)$ which were not observed due to overlapping by monomer transitions.

The analysis of the upper state vibrational and rotational constants relative to the ground state and the monomer constants is made difficult because of a very complex pattern of vibration-rotation interactions evidenced in the 2NH range of the monomer, actually not fully modeled, yet.¹⁴ The weakly bound Ar atom could furthermore affect this pattern. A more detailed analysis of the constants was therefore not attempted, yet.

The rotational temperature, $T_{\text{rot}} = 8$ K, was retrieved from the comparison between observed and simulated spectra. We performed a line shape analysis for the strongest and less overlapped lines. They were fitted to a Voigt profile, imposing the Doppler FWHM corresponding to the estimated

TABLE I. Spectroscopic constants and standard deviation on the line positions (σ) from the analysis of the $\Pi(1_1) \leftarrow \Sigma(0_0)$ 2NH ($\nu_1 + \nu_3$) absorption band of the $\text{NH}_3\text{-Ar}$ van der Waals complex (cm^{-1}). Errors in parentheses concern the last mentioned digit and correspond to one standard deviation.

	Ground state ^a	2NH- Q branch	2NH- P/R branches
B	0.09596128(7)	0.094552(49)	0.094543(37)
D	$2.94(9) \times 10^{-6}$	$7.67(68) \times 10^{-6}$	$2.59(30) \times 10^{-6}$
H	$-2.9(0) \times 10^{-9}$	$1.49(25) \times 10^{-8}$...
$\bar{\nu}_0$...	6628.01014(82)	6628.01169(85)
# lines	...	11	17
Σ	...	1.1×10^{-3}	1.8×10^{-3}

^aFrom Schmuttenmaer *et al.*⁷

value of T_{rot} . The retrieved Lorentzian FWHM is shown in Fig. 2 together with their uncertainties estimated from the line shape fitting procedure. Values from R and P lines agree reasonably well for the same J' upper state. Values from Q lines concern different upper states but remain consistent with R/P ones. It can be seen in Fig. 2 that the Lorentzian FWHM decrease with J' , with lifetimes thus evolving oppositely, as can be expected. The mean Lorentzian FWHM is 320 MHz, corresponding to a mean predissociation lifetime of 0.6 ns for the $\Pi(1_1)$ 2NH ($\nu_1 + \nu_3$) state, using the procedure detailed in Ref. 2. This value is lower than the 7.5 ns and 3.5 ns similarly extracted for the overtone states in the previously

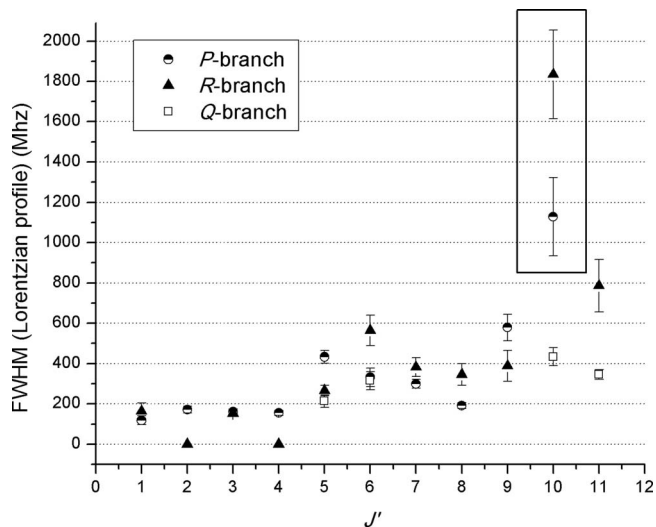


FIG. 2. Lorentzian FWHM of the $\Pi(1_1)$ 2NH ($\nu_1 + \nu_3$) levels of the $\text{NH}_3\text{-Ar}$ van der Waals complex: Black triangles, half-blackened circles, and empty squares are for R , P , and Q lines, respectively. The box points out two anomalously broadened lines.

NIR observed argon-containing complexes, i.e., C_2H_2-Ar ¹⁷ and HDO/D_2O-Ar ,⁴ respectively. There seems not to be any other value in ammonia-Ar to compare with. It is interesting to point out that the $R(9)$ and $P(11)$ lines (see arrows in Fig. 1) show a much larger broadening (as also highlighted in Fig. 2), resulting in a lifetime about 3 times larger, indicating a local, probably Coriolis-type perturbation at $J' = 10$. These lines were not included in the fit to determine the rotational constants. Their calculated positions are listed in the supplementary material.¹⁶

The experimental search for more bands in NH_3-Ar is under way, that might lead to a more complete picture of the upper, and possibly lower state energy patterns. We plan to attempt further extending this series of investigation to more ammonia partners, as we successfully achieved with acetylene and water, possibly stimulating challenging theoretical and *ab initio* investigations to complete the overall bonding picture in these species.^{9,18}

This work was sponsored by the Fonds National de la Recherche Scientifique (FNRS), the « Action de Recherches Concertées de la Communauté française de Belgique », the “Wiener-Anspach” foundation (ACME project), the Brussels-Capital Region within the program Prospective Research for Brussels (Innoviris) and the Belgian Federal Science Policy Office (Contract No. SD/CS/07A, Advanced Exploitation of Ground-Based Measurements for Atmospheric Chemistry and Climate applications – II).

¹Z. Yu, C. Chuang, P. Medley, T. A. Stone, and W. Klemperer, *J. Chem. Phys.* **120**, 6922 (2004); Z. Yu, E. Hammam, and W. Klemperer, *ibid.* **122**, 194318 (2005); P. Medley, Z. Yu, B. Connors, W. Klemperer, S. N. Tsang, and C. Chuang, *ibid.* **124**, 214314 (2006); M. Hippler, L. Oeltjen, and M. Quack, *J. Phys. Chem. A* **111**, 12659 (2007).

²K. Didriche, T. Földes, C. Lauzin, D. Golebiowski, J. Liévin, and M. Herman, *Mol. Phys.* **110**, 2781 (2012).

³M. P. Ziemkiewicz, C. Pluetzer, D. J. Nesbitt, Y. Scribano, A. Faure, and A. van der Avoird, *J. Chem. Phys.* **137**, 084301 (2012).

⁴K. Didriche and T. Földes, *J. Chem. Phys.* **138**, 104307 (2013); *Mol. Phys.* **111**, 355 (2013).

⁵M. Herman, K. Didriche, D. Hurtmans, B. Kizil, P. Macko, A. Rizopoulos, and P. Van Poucke, *Mol. Phys.* **105**, 815 (2007); K. Didriche, C. Lauzin, T. Földes, X. de Ghellinck D’Elseghem Vaernewijck, and M. Herman, *ibid.* **108**, 2155 (2010).

⁶D.-H. Gwo, M. Havenith, K. L. Busarow, R. C. Cohen, C. A. Schmuttenmaer, and R. J. Saykally, *Mol. Phys.* **71**, 453 (1990); J. W. I. Van Bladel, A. Van der Avoird, and P. E. S. Wormer, *J. Chem. Phys.* **94**, 501 (1991); G. C. M. van der Sanden, P. E. S. Wormer, A. van der Avoird, C. A. Schmuttenmaer, and R. J. Saykally, *Chem. Phys. Lett.* **226**, 22 (1994).

⁷C. A. Schmuttenmaer, R. C. Cohen, J. G. Loeser, and R. J. Saykally, *J. Chem. Phys.* **95**, 9 (1991).

⁸E. Zwart, H. Linnartz, W. Leo Meerts, G. T. Fraser, D. D. Nelson, and W. Klemperer, *J. Chem. Phys.* **95**, 793 (1991); C. A. Schmuttenmaer, J. G. Loeser, and R. J. Saykally, *ibid.* **101**, 139 (1994).

⁹G. Bistoni, L. Belpassi, F. Tarantelli, F. Pirani, and D. Cappelletti, *J. Phys. Chem. A* **115**, 14657 (2011).

¹⁰C. A. Schmuttenmaer, R. C. Cohen, and R. J. Saykally, *J. Chem. Phys.* **101**, 146 (1994).

¹¹Y. Matsumoto, B. J. Howard, and M. Takami, *Reza Kagaku Kenkyu* **12**, 1 (1990).

¹²T. Földes, *Rev. Sci. Instrum.* **84**, 016102 (2013).

¹³K. Nakagawa, T. Katsuda, A. S. Shelkovich, M. de Labachellerie, and M. Ohtsu, *Opt. Commun.* **107**, 369 (1994); Q. Kou, G. Guelachvili, M. A. Tamsamani, and M. Herman, *Can. J. Phys.* **72**, 1241 (1994).

¹⁴K. Sung, L. R. Brown, X. Huang, D. W. Schwenke, T. J. Lee, S. L. Coy, and K. K. Lehmann, *J. Quant. Spectrosc. Radiat. Transfer* **113**, 1066 (2012); P. Cacciani, P. Cermak, J. Cosléou, M. Khelkhal, P. Jeseck, and X. Michaut, *ibid.* **113**, 1084 (2012).

¹⁵C. M. Western, PGOPHER, a program for simulating rotational structure, University of Bristol, UK, see <http://pgopher.chm.bris.ac.uk>.

¹⁶See supplementary material at <http://dx.doi.org/10.1063/1.4804421> for the list of assigned transitions in NH_3-Ar .

¹⁷C. Lauzin, K. Didriche, P. Macko, J. Demaison, J. Liévin, and M. Herman, *J. Phys. Chem. A* **113**, 2359 (2009).

¹⁸D. D. Nelson, Jr., G. T. Fraser, and W. Klemperer, *Science* **238**, 1670 (1987); J. G. Loeser, C. A. Schmuttenmaer, R. C. Cohen, M. J. Elrod, D. W. Steyert, R. J. Saykally, R. E. Bumgarner, and G. A. Blake, *J. Chem. Phys.* **97**, 4727 (1992).

High resolution spectroscopy of the Ar-D₂O and Ar-HDO molecular complexes in the near-infrared range

K. Didriche^{a)} and T. Földes^{b)}

Laboratoire de Chimie quantique et Photophysique, CP160/09, Faculté des Sciences, Université libre de Bruxelles (U.L.B.), Ave. Roosevelt, 50, B-1050 Brussels, Belgium

(Received 5 January 2013; accepted 20 February 2013; published online 11 March 2013)

Three rovibrational bands of Ar-D₂O and two rovibrational bands of Ar-HDO were observed in the 1.5 μm range by continuous wave cavity ringdown spectroscopy. Their analyses led to the determination of rotational constants for the upper states and vibrational shifts indicating that the potential energy surface is only slightly affected by the vibrational excitation. Some Coriolis couplings were identified. The observed lines were fitted to retrieve a 3.5 ns lifetime of the upper state, showing that even with a triple or double excitation quanta in the water subunit, the Ar-D₂O and Ar-HDO complexes are long-lived species. © 2013 American Institute of Physics. [<http://dx.doi.org/10.1063/1.4794161>]

I. INTRODUCTION

The water molecule is known to interact with atoms and molecules, leading to a variety of phenomena studied in physics, chemistry, and biology. These phenomena are governed, on the microscopic level, by the structure and the dynamics of binary van der Waals molecular complexes consisting of a single water molecule bonded to a solute particle. One of these simplest complexes, thought to play an important role in the photophysics of the atmosphere,¹ is the model system formed by a water molecule and an argon atom, to which a large number of experimental and theoretical studies have been devoted.

Indeed, in 1988, Cohen *et al.*² carried out the first study of argon-water van der Waals complexes at high resolution, probing vibration-rotation tunneling (VRT) states of Ar-H₂O in the far infrared region. Later, they extended their observations to the van der Waals stretching vibration³ and other VRT states.⁴ The first microwave spectrum of Ar-H₂O was recorded by Fraser *et al.*⁵ in 1990, along with the spectra of the other isotopologues Ar-HDO and Ar-D₂O. This work was later extended to higher resolution by Germann and Gutowsky,⁶ leading to the observation of some hyperfine structures. The first VRT spectra of deuterated species came in 1991 by Suzuki *et al.*,⁷ followed by additional observations made by Zwart and Meerts.⁸ At the same time, the Nesbitt's group⁹ investigated argon-water complexes in the OH stretch region, well above their dissociation energy, leading to the determination of predissociation dynamics.¹⁰ Later, they extended their work to the water bending region¹¹ and to the first and second OH overtones.^{12,13} The first observation of Ar-D₂O above its dissociation limit was reported by Stewart *et al.*¹⁴ in 2011 but was never published. An analysis of a new spectrum was later carried out by Li *et al.*¹⁵ Argon-water complexes have also been studied in helium nanodroplets¹⁶

and plasma beams.¹⁷ Also noteworthy is that argon-water aggregates from dimer to pentamer have been observed, with low resolution, in the OH stretch range by Moudens *et al.*¹⁸

The binding energy of the Ar-H₂O complex is estimated to be around 140 cm^{-1} from *ab initio* calculations¹⁹ and semi-empirical potential energy surface (PES) fitted to experimental data.²⁰ The bottom of the potential surface is relatively flat and the barriers to internal rotation in the complex are comparable to the rotational constants of water, leading to a nearly free internal rotor behavior of the water subunit. Due to this nearly free internal rotation, the overall rotation and intermolecular stretching degrees of freedom can be approximately described in a pseudo-diatom context.⁵ As explained by Weida and Nesbitt,¹¹ the argon atom can be viewed as a perturbation on the free water rotational levels that lifts the spatial degeneracy of \mathbf{j} , i.e., the angular momentum of the water subunit. The energy states of the complex are thus denoted according to the corresponding free monomer energy states. As an example, in the $\Sigma(0_{00})$ level, Σ reflects the vanishing projection of \mathbf{j} on the intermolecular axis, and 0_{00} is the corresponding free monomer j_{kac} asymmetric top rotation state.

In this paper, we present the first observations of the Ar-HDO and Ar-D₂O complexes in the 1.5 μm range, corresponding to 2 and 3 excitation quanta in the HDO and D₂O subunits, respectively. This investigation is part of an extensive study of D₂O and HDO complexes, starting by the observation of the C₂H₂-D₂O complex.²¹

II. EXPERIMENTAL PROCEDURE

The high resolution spectra of the Ar-D₂O and the Ar-HDO complexes were recorded using Continuous Wave Cavity Ringdown Spectroscopy (CW-CRDS) in a supersonic expansion of Ar and D₂O/HDO using the FANTASIO+ setup.²² D₂O was added to the Ar flow (4460 sccm, where sccm denotes cubic centimeter per minute at standard conditions for temperature and pressure) by bubbling part of the gas stream through a water reservoir. HDO was prepared by mixing D₂O

^{a)} Author to whom correspondence should be addressed. Electronic mail: kdidrich@ulb.ac.be. F.R.S.-FNRS postdoctoral researcher.

^{b)} AGACC postdoctoral researcher.

and H₂O in equal amounts. The setup consisted of a vacuum chamber in which the continuous supersonic expansion was produced using two large Leybold MAG W3200 CT teflon coated turbomolecular pumps, which were backed by an Alcatel ADS 860 HII group. The reservoir (p_0) and residual (p_∞) pressures were measured using MKS Baratron gauges (1000 and 1 Torr full scale, respectively) and were kept constant at 53 kPa and 2 Pa, respectively. The CW-CRDS used laser diodes emitting in the 1.5 μm range (DFB, ILX light-wave, 1 MHz linewidth). The frequency was continuously tuned by sweeping the laser temperature using a home-made proportional-integral-derivative (PID) controller. The cavity was made of two concave mirrors (radius = 1000 mm; reflectivity = 99.9985%), separated by about 540 mm. Each ringdown transient was fitted by an exponential curve using a nonlinear Levenberg–Marquardt procedure. Typically, some 200 ringdowns per spectral point were fitted and their mean characteristic decay time (τ) recorded, directly providing the absorption coefficient α , which can be calculated using

$$\alpha = \left(\frac{1}{\tau} - \frac{1}{\tau_0} \right) \frac{L}{cl}. \quad (1)$$

τ_0 is the ringdown time of the empty cavity (typically 130 μs); L (540 mm) and l (10 mm) are the lengths of the cavity and of the absorption path in the medium, respectively, the latter assumed to be identical to the slit length in the given geometrical arrangement; c is the speed of light. The 130 μs ringdown time corresponds to some 72 000 passes, i.e., about 725 m effective absorption pathlength in the jet-cooled molecules when using a 1 cm long slit nozzle. This nozzle is about 30 μm wide. The line positions were calibrated using a procedure presented in Ref. 22, leading to a position accuracy of $\pm 10^{-3} \text{ cm}^{-1}$.

III. Ar-D₂O

Three rovibrational bands of Ar-D₂O were observed in the 1.5 μm range. This region corresponds to the $\nu_1 + \nu_2 + \nu_3$ combination band region of D₂O, centered around 6533 cm^{-1} .²³ These bands can be attributed unambiguously to Ar-D₂O by comparisons with ground state combination differences.⁵ The ortho/para nuclear spin classification of the D₂O subunit is preserved in the Ar-D₂O complex and bands arising from both species are observed. A diagram of the energy levels involved in the observed transitions is shown in Figure 1, along with the corresponding states of the D₂O subunit from which they originate. The energy levels of the observed rovibrational transitions for each internal-rotor state can be fitted to a pseudo-diatomic Hamiltonian⁵

$$E(J) = \nu_0 + B J(J + 1) - D [J(J + 1)]^2, \quad (2)$$

where ν_0 , B , and D are the origin of the band, the rotational constant, and the centrifugal distortion constant, respectively.

A. Analysis of the ortho Ar-D₂O bands

The first and most intense band observed is centered around 6536 cm^{-1} , as shown in Figure 2. By comparison of the combination differences, the lower level of this transition

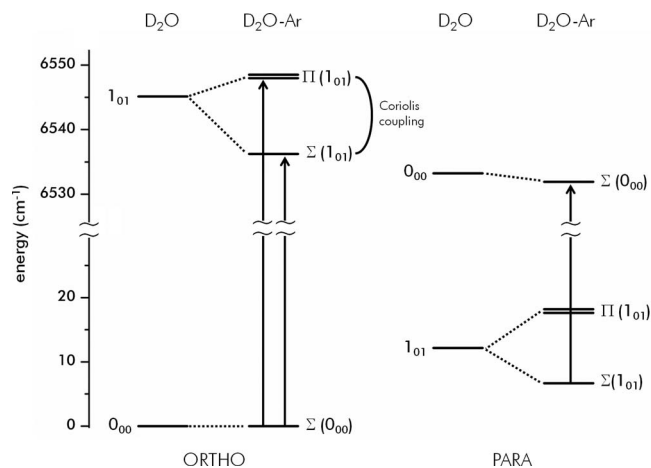


FIG. 1. Energy levels of D₂O-Ar in the excited $\nu_1 + \nu_2 + \nu_3$ state of the D₂O subunit. The corresponding states of the D₂O subunit from which they originate are also shown by dotted lines. Π states are degenerate (as indicated by double lines). The observed D₂O-Ar bands are indicated by arrows. The observed Coriolis coupling is also indicated.

can be attributed to the $\Sigma(0_{00})$ state of the ortho Ar-D₂O.^{5,15} As the only D₂O transition arising from the 0_{00} state in this range is $1_{01} \leftarrow 0_{00}$,²³ the upper level must correspond to the 1_{01} state of the free D₂O. Furthermore, as no Q branch is observed, the upper level must be a Σ state, leading to its assignment to $\Sigma(1_{01})$.

Another band, less intense, was observed around 6548 cm^{-1} , as shown in Figure 3. By combination differences comparison, the lower level of this transition can also be attributed to the $\Sigma(0_{00})$ state of the ortho Ar-D₂O.^{5,15} As a strong Q branch is observed and the $P(1)$ line is missing, the upper level must be a Π state, leading to its logical assignment to $\Pi(1_{01})$. Fitting the transitions, the rotational constant B was found to be significantly different for the Q branch and the P/R branches, i.e., 0.09057 cm^{-1} and 0.09263 cm^{-1} , respectively. This difference is likely to arise from a Coriolis coupling between the $\Pi(1_{01})$ state and another state. This type of interaction couples states with the same monomer $j_k a_k c_k$ state, same overall J , same parity, and K differing by ± 1 .¹¹ Therefore, the state coupled to $\Pi(1_{01})$ state must be $\Sigma(1_{01})$. The difference in the B constant between the Q branch and the P/R branches comes from that, taking into account the above selection rules, only the e levels of the $\Pi(1_{01})$ state (accessed by the P/R branches) are perturbed by the levels of the $\Sigma(1_{01})$ state, leaving the f levels (accessed by the Q branch) unperturbed. The larger B rotational constant for the P and R branch indicates that the $\Pi(1_{01})$ e parity levels become increasingly higher in energy with respect to the f parity levels for increasing J . This in turn suggests that the Coriolis coupling with the $\Pi(1_{01})$ level arises from a state lower in energy. This is consistent with the picture of $\Sigma(1_{01})$ being the state interacting with the $\Pi(1_{01})$ e parity levels through a Coriolis coupling.

The two bands $\Sigma(1_{01}) \leftarrow \Sigma(0_{00})$ and $\Pi(1_{01}) \leftarrow \Sigma(0_{00})$ were fitted together thanks to the PGOPHER program,²⁴ the ground state constants being fixed to the literature data.⁶ Because of the interaction between the $\Sigma(1_{01})$ and $\Pi(1_{01})$ states, a Coriolis coupling model was added to the model presented

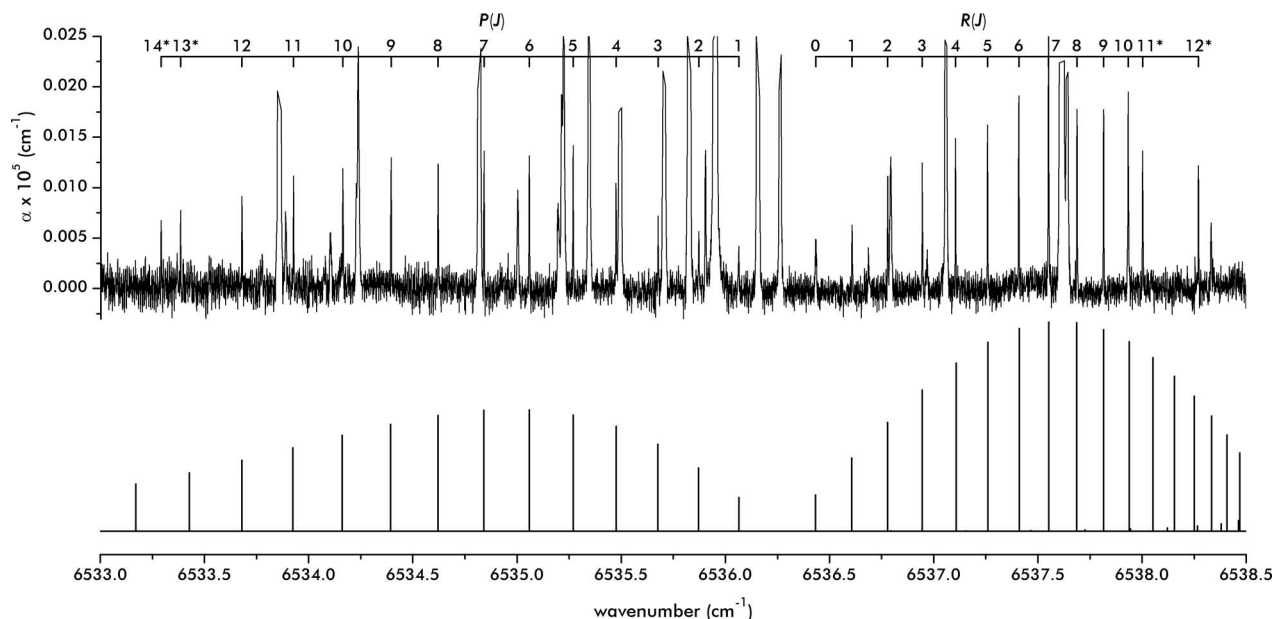


FIG. 2. (Top) Observed spectrum of the $\Sigma(1_{01}) \leftarrow \Sigma(0_{00})$ band of the ortho Ar-D₂O complex. Experimental conditions are detailed in the text. (Bottom) Simulated spectrum based on the rotational constants from Table I, using $T_{\text{rot}} = 15$ K. *transitions involving a perturbed level and not included in the fit.

in Eq. (2), as already presented in Ref. 25. The Coriolis interaction was modeled using the PGOPHER “L uncouple” operator, whose value in terms of parameters defined in Ref. 26, is equal to $(\beta/2)^{1/2}$,²⁵ where β is the strength of the Coriolis interaction. All together, 51 lines were identified for the ortho Ar-D₂O bands but due to perturbations, only 42 lines were included in the fit (see below). The retrieved rotational and coupling constants are listed in Table I. The standard deviation (σ) of the fit is 1×10^{-3} cm⁻¹ and each of the 42 transitions is reproduced within 3σ . Using the rotational constants from Table I, simulations were made, as shown in Figures 2 and 3, showing excellent agreements between observed (top)

and simulated (bottom) spectra. The calculated intensities are found to compare better to the experimental ones when the simulation is performed using 15 K rotational temperature. All the identified lines are listed in the supplementary material (Table A),²⁷ with their assignments, and their calculated and observed frequencies.

The value of β was found to be 0.028 cm⁻². Theory gives β as $2B^2 J^*(J^*+1)$, where J^* is an effective J -value which approaches 1 in the free rotor limit.²⁸ Indeed, by taking the B value for the $\Pi(1_{01})$ state, we can find that $J^* = 0.9$, confirming the free rotor approximation of the Ar-D₂O system, even in this excited state.

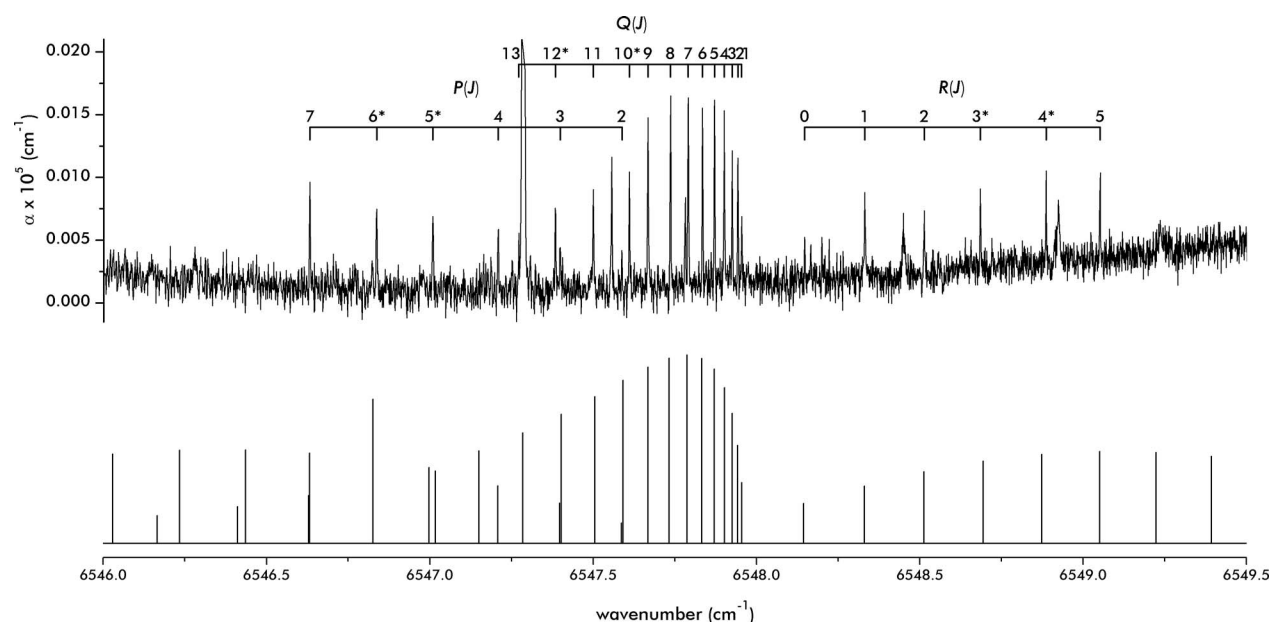


FIG. 3. (Top) Observed spectrum of the $\Pi(1_{01}) \leftarrow \Sigma(0_{00})$ band of the ortho Ar-D₂O complex. Experimental conditions are detailed in the text. (Bottom) Simulated spectrum based on the rotational constants from Table I, using $T_{\text{rot}} = 15$ K. *transitions involving a perturbed level and not included in the fit.

TABLE I. Spectroscopic constants from the analysis of the ortho Ar-D₂O van der Waals complex bands (values are in cm⁻¹).

	$\Sigma(0_{00})^a$	$\Sigma(1_{01})$	$\Pi(1_{01})$
B	0.093258423	0.093140(31)	0.090543(18)
$D \times 10^6$	2.568	3.78(17)	8.41(11)
$\bar{\nu}_0$	0	6536.25045(50)	6547.95870(46)
β	...	0.028	
# lines	...	23	19
σ	...	1×10^{-3}	

^aValues from Ref. 6.

Interestingly enough, it can be seen in Figure 2 that the $P(13)$ and $R(11)$, and $P(14)$ and $R(12)$ lines are shifted by the same amount but in opposite directions, meaning that the $J = 12$ and $J = 13$ levels of the $\Sigma(1_{01})$ state are shifted to a lower and higher energy, respectively. It is likely that this perturbation arises from an avoided crossing with a dark state. The same effect is observed for e parity of $J = 4$ and $J = 5$ levels of the $\Pi(1_{01})$ state, as shown in Figure 3. Furthermore, lines accessing the $\Pi(1_{01})$ e parity levels with $J > 6$ are not observed on the spectra, despite the relatively high signal-to-noise ratio (S/N) of the other transitions. Unfortunately, the identification of these interacting states is made difficult by the lack of information about the layout of the energy levels in the observed range. Indeed, at least three vibrational bands of D₂O are present around 1.5 μm : $2\nu_1 + \nu_2$, $\nu_1 + \nu_2 + \nu_3$, and $\nu_2 + 2\nu_3$,²³ each with its own rotational levels, everyone of them leading to one or more rovibrational states of Ar-D₂O.

B. Analysis of the para Ar-D₂O band

A third band, weaker than the two previous ones, was observed around 6525 cm⁻¹, as shown in Figure 4. By comparison of the combination differences, the lower level of this transition can also be attributed to the $\Sigma(1_{01})$ state of

TABLE II. Spectroscopic constants from the analysis of the para Ar-D₂O van der Waals complex band (values are in cm⁻¹).

	$\Sigma(1_{01})^a$	$\Sigma(0_{00})$
B	0.091033524	0.092778(37)
$D \times 10^6$	1.771	3.42(25)
$\bar{\nu}_0$	0	6525.25487(81)
# lines	...	13
σ	...	2×10^{-3}

^aValues from Ref. 6.

the para Ar-D₂O.^{5,15} The corresponding transition in D₂O is $0_{00} \leftarrow 1_{01}$, as it is the only one arising from the 1_{01} state in this range.²³ Furthermore, as no Q branch is observed, the upper level must be a Σ state, leading to its assignment to $\Sigma(0_{00})$.

The line positions were fitted thanks to the PGOPHER program²⁴ with the ground state constants fixed to at the literature values.⁶ All together, 23 lines were identified for the $\Sigma(0_{00}) \leftarrow \Sigma(1_{01})$ para Ar-D₂O band but due to perturbations, only 13 lines were included in the fit (see below). The retrieved rotational and coupling constants are listed in Table II. The standard deviation (σ) of the fit is 2×10^{-3} cm⁻¹ and each of the 13 transitions is reproduced within 3σ . Using the rotational constants from Table II, simulations were made, as shown in Figure 4, showing excellent agreements between the observed (top trace) and the simulated (bottom trace) spectra. The calculated intensities are found to compare better to the experimental ones when the simulation is performed using 15 K rotational temperature. All the identified lines are listed in the supplementary material (Table B),²⁷ with their assignments, and their simulated and observed energies. The differences in position between the observed and calculated lines are shown in Figure 5. The trend is the same for the P and R branches, clearly showing that the perturbation is due to an avoided crossing with another state around $J = 5$. Unfortunately, the identification of this state is again made difficult by

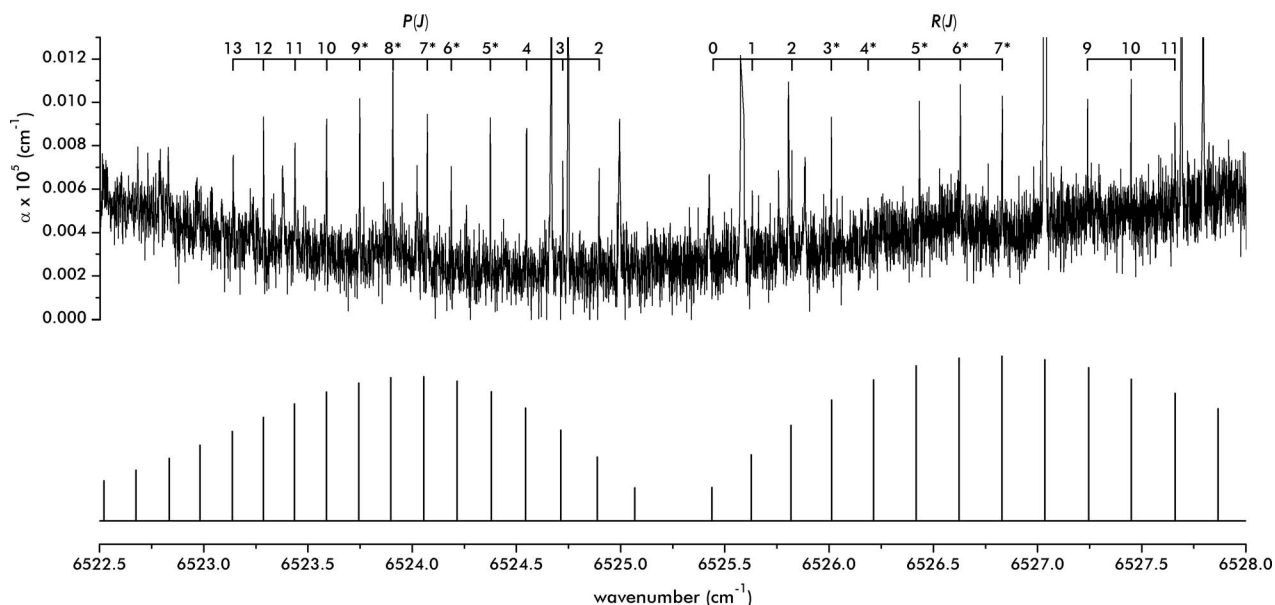


FIG. 4. (Top) Observed spectrum of the $\Sigma(0_{00}) \leftarrow \Sigma(1_{01})$ band of the para Ar-D₂O complex. Experimental conditions are detailed in the text. (Bottom) Simulated spectrum based on the rotational constants from Table II, using $T_{\text{rot}} = 15$ K. *transitions involving a perturbed level and not included in the fit.

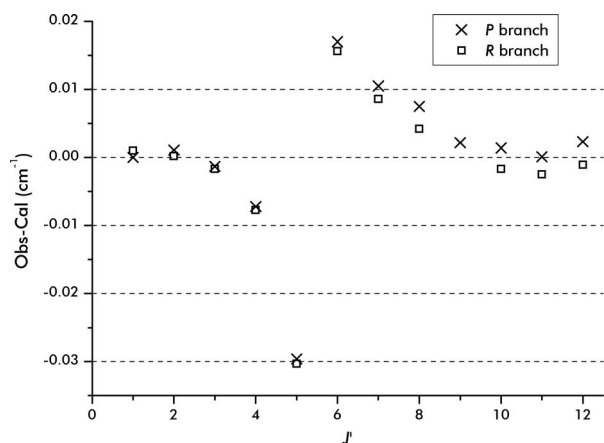


FIG. 5. Differences between the observed and calculated lines positions of the para Ar-D₂O $\Sigma(0_{00}) \leftarrow \Sigma(1_{01})$ band.

the lack of information about the layout of the energy levels in the observed range.

IV. Ar-HDO

Two rovibrational bands of Ar-HDO were observed in the 1.5 μm range. This region corresponds to the $\nu_1 + \nu_3$ combination band region of HDO, centered around 6423 cm^{-1} .²⁹ Compared to D₂O or H₂O, there is no ortho/para nuclear spin classification in HDO, allowing, at low temperature, the relaxation of population in the lowest rotational level 0_{00} . Therefore, the strongest transitions in Ar-HDO should arise from the $\Sigma(0_{00})$ state.

The first band, shown in Figure 6 centered near 6442.3 cm^{-1} can be attributed unambiguously to Ar-HDO by comparisons with combination differences from the ground state, identifying the lower level as $\Sigma(0_{00})$.⁷ The identification of the upper level is less evident. As a Q branch is

observed, the upper level must be a Π state, which is consistent with the two HDO transitions originating from the 0_{00} state present in the observed range: $1_{01} \leftarrow 0_{00}$ and $1_{11} \leftarrow 0_{00}$, at 6430.6585 and 6444.61046 cm^{-1} , respectively.³⁰

The intensity of the transitions in Ar-HDO arises from the water subunit and therefore the relative transition intensity in HDO should be conserved in the molecular complex. As only one $\Pi \leftarrow \Sigma(0_{00})$ band is observed in the spectrum, it should arise from the strongest corresponding monomer line: $1_{11} \leftarrow 0_{00}$. Therefore, the observed band is attributed to $\Pi(1_{11}) \leftarrow \Sigma(0_{00})$. Fitting the transitions, the rotational constant B was found to be significantly different for the Q branch and the P/R branches, i.e., 0.09580 cm^{-1} and 0.1015 cm^{-1} , respectively. As for Ar-D₂O, this difference is likely to arise from a Coriolis coupling between the $\Pi(1_{11})$ state and the $\Sigma(1_{11})$ state. The larger B rotational constant for the P and R branches indicates that the $\Pi(1_{11})$ e parity levels become increasingly higher in energy with respect to the f parity levels for increasing J . This in turn suggests that the Coriolis coupling with the $\Pi(1_{11})$ level arises from a state lower in energy. This is consistent with the other band observed, around 6439 cm^{-1} , as shown in Figure 6. This band consists only of a R branch, and despite its reasonable intensity, no Q branch is observed, probably meaning that the transition connects Σ states, logically corresponding to the $\Sigma(1_{11}) \leftarrow \Sigma(0_{00})$ band. This is consistent with the picture of $\Sigma(1_{11})$ being the state interacting with the $\Pi(1_{11})$ e parity levels through a Coriolis coupling. Unfortunately, no P branch is observed and no combination differences could be obtained, leaving the assignments unclear. For the same reason, the origin of this band could not be determined exactly but is estimated to be around 6439.5 cm^{-1} . Simulations for the $\Sigma(1_{11}) \leftarrow \Sigma(0_{00})$ band were tested extensively, never resulting in good agreements. No definitive assignments were possible. It is likely that the $\Sigma(1_{11})$ state is highly perturbed and its

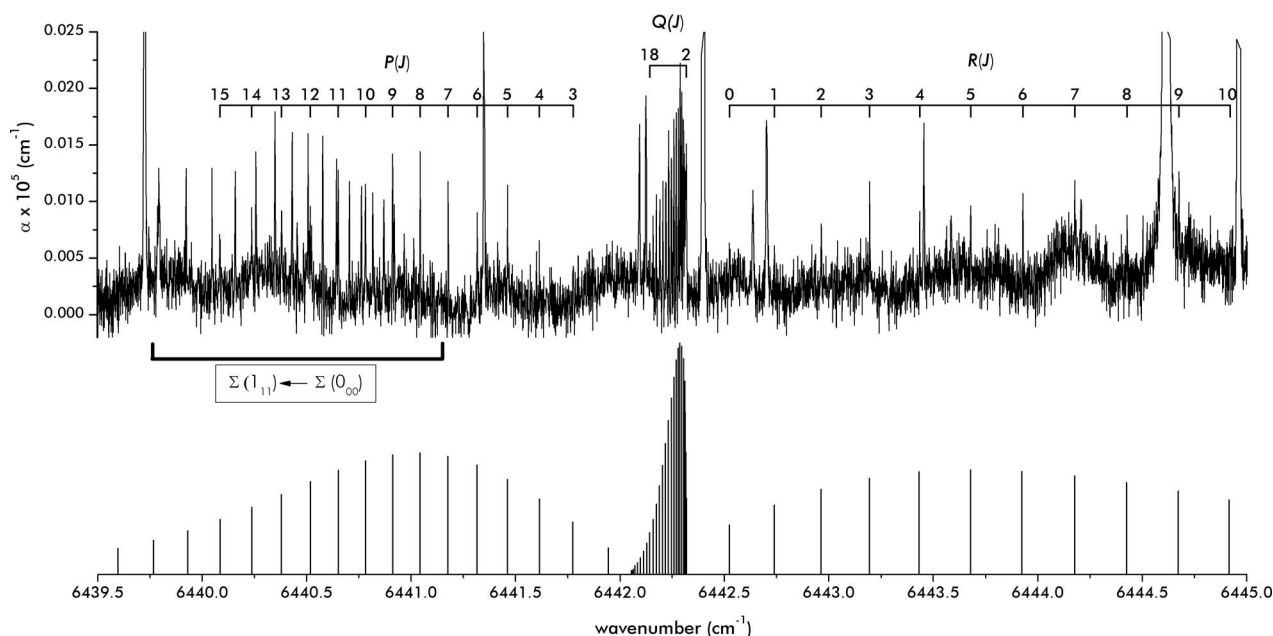


FIG. 6. (Top) Observed spectrum of the $\Pi(1_{11}) \leftarrow \Sigma(0_{00})$ band of the Ar-HDO complex. Experimental conditions are detailed in the text. (Bottom) Simulated spectrum based on the rotational constants from Table III, using $T_{\text{rot}} = 15$ K. The position of the probable $\Sigma(1_{11}) \leftarrow \Sigma(0_{00})$ band is highlighted.

TABLE III. Spectroscopic constants from the analysis of the Ar-HDO van der Waals complex bands (values are in cm^{-1}).

	$\Sigma(0_{00})^a$	$\Pi(1_{11})$	$\Sigma(1_{11})^b$
B	0.09639732	0.0958121(48)	(0.0945)
$D \times 10^6$	2.9127	2.826(15)	(26)
$H \times 10^{10}$	-2.9
$\bar{\nu}_0$	0	6442.32043(27)	(6439.5)
β	...	(0.017)	...
# lines	...	41	...
σ	...	5×10^{-4}	...

^aValues from Ref. 7.^bEmpirical constants (see text for details).

retrieved rotational constants are purely empirical and have no physical value. In the ground state, Lascola and Nesbitt⁹ predicted that the $\Sigma(1_{11})$ state lies 1 cm^{-1} above the $\Pi(1_{11})$ state. In the double stretch excitation vibrational state, this energy scheme is modified, probably by some angular-radial coupling with other rotational states. Further research with improved S/N will be necessary to reveal the corresponding P branch and unequivocally assign the lines.

Finally, the P/R and Q branches of the $\Pi(1_{11}) \leftarrow \Sigma(0_{00})$ band were fitted together thanks to the PGOPHER program,²⁴ the ground state constants being fixed to the literature values.⁷ A Coriolis coupling model was added to the model presented in Eq. (2) coupling the $\Sigma(1_{11})$ and $\Pi(1_{11})$ states, the origin of the $\Sigma(1_{11})$ state being fixed at 6439.5 cm^{-1} and its rotational constants B and D having been let free, as no line assignment was possible. The retrieved rotational constants of the $\Sigma(1_{11})$ are thus purely empirical and have no physical value. All together, 41 lines were fitted. The retrieved rotational and coupling constants are listed in Table III. The standard deviation (σ) of the fit is $7 \times 10^{-4} \text{ cm}^{-1}$ and each of the 41 transitions is reproduced within 2σ . Using the rotational constants from Table III, simulations were made, as shown in Figure 6, showing excellent agreements between observed (top) and simulated (bottom) spectra. The calculated intensities are found to compare better to the experimental ones when the simulation is performed using 15 K rotational temperature. All the identified lines are listed in the supplementary material (Table C),²⁷ with their assignments, and their calculated and observed frequencies.

A diagram of the energy levels involved in the observed transitions is shown in Figure 7, along with the corresponding states of the HDO subunit from which they originate.

V. LIFETIME

As shown in Figures 2–4 and 6, the lines arising from Ar-D₂O or Ar-HDO are very sharp. Their line shapes were fitted with a Voigt profile based on a Doppler FWHM fixed to 60 MHz, corresponding to a 15 K distribution, and their Lorentzian FWHM ($\Delta\nu_{FWHM}^L$) were retrieved. As the translational temperature should be lower than the rotational temperature, the 60 MHz Doppler FWHM corresponds to an upper-limit value, leading to the retrieval of a lower-limit Lorentzian FWHM. The average value of $\Delta\nu_{FWHM}^L$ was found to be around 45 MHz. No difference between Ar-D₂O

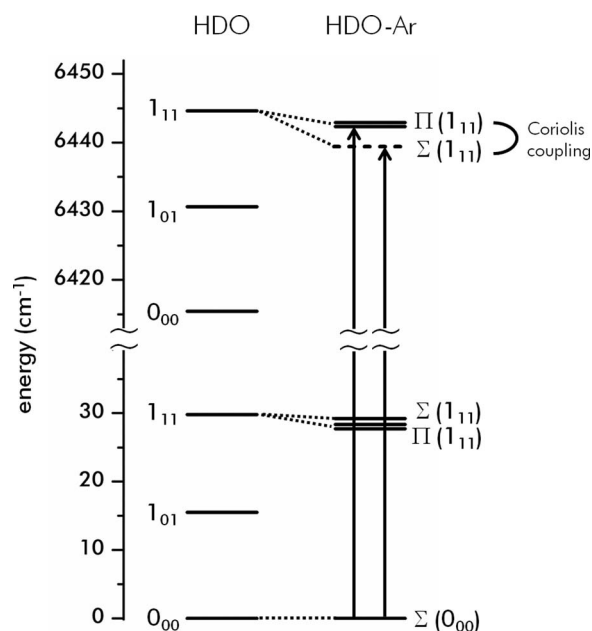


FIG. 7. Energy levels of HDO-Ar in the excited $\nu_1 + \nu_3$ state of the HDO subunit. The corresponding states of the HDO subunit from which they originate are also shown by dotted lines. Π states are degenerate (as indicated by double lines). The observed HDO-Ar bands are indicated by arrows. The observed Coriolis coupling is also indicated. The $\Sigma(1_{11})$ state is indicated by a dashed line due to the uncertainty of its position (see text for details).

and Ar-HDO was noticed, despite the extra bending motion excitation in the corresponding Ar-D₂O transitions. As previously said, the value of 45 MHz is a lower-limit. Furthermore, the general weakness of the bands allows only a few experimental points per line (typically 3–5), making the fit of the Voigt profile imprecise. An estimation of the upper state molecular lifetime could anyway be extracted using

$$\Delta\nu_{FWHM}^L = \frac{1}{2\pi} \left(\frac{1}{\tau_0} + \frac{1}{\tau_1} \right). \quad (3)$$

In this expression, $\tau_{0/1}$ is the mean lifetime in the ground/excited vibrational state, with τ_0 taken as ∞ . The upper state predissociation half-lifetime was found to be around 3.5 ns. This value can be compared with the 0.28 ns determined for D₂O-C₂H₂ in the same excitation state²¹ and the 7.2 ns determined for Ar-H₂O in the ν_2 bend range of H₂O,¹¹ showing that the water molecule is less perturbed by the argon atom than by the C₂H₂ molecule. The strong interaction between water and acetylene is also observable on the “C₂H₂ side” by comparing linewidth of C₂H₂-Ar and C₂H₂-H₂O or C₂H₂-D₂O transitions.²²

VI. DISCUSSION

In a general way, one can see that the vibrational properties of the water molecule D₂O or HDO is only slightly affected by the presence of the Ar atom. Indeed, the water subunit can rotate freely in the complex and as schematized in Figures 1 and 7, the water vibrational constants slightly differ by its complexation with the Ar atom. In Ar-D₂O, the energy of the vibrational state corresponding to the symmetric

+ the antisymmetric O-D stretches + the bending can be deduced by adding the predicted energy of the $\Sigma(1_{01})$ in the ground state⁹ to the observed $\Sigma(0_{00}) \leftarrow \Sigma(1_{01})$ para Ar-D₂O transition energy. The result is 6531.1 cm⁻¹, about 2.1 cm⁻¹ redshifted compared to the $\nu_1 + \nu_2 + \nu_3$ band origin of D₂O. This is very small, considering that 3 quanta of vibration are present in the molecular complex. The redshift value is consistent with the value determined for the bending¹⁵ (0.97 cm⁻¹). One can deduce that the redshift due to the symmetric or antisymmetric O-D stretches should be quite small, probably about 0.5 cm⁻¹. In Ar-HDO, the energy of the vibrational state corresponding to the symmetric and the antisymmetric O-D stretch can be estimated by subtracting the predicted energy of the $\Pi(1_{11})$ in the ground state⁹ to the observed $\Pi(1_{11}) \leftarrow \Sigma(0_{00})$ transition energy. The result is 6413.9 cm⁻¹, about 9.1 cm⁻¹ redshifted compared to the $\nu_1 + \nu_3$ band origin of HDO. This value, larger than the redshift value determined to be 3.35 cm⁻¹ in the double overtone of the OD stretch,¹³ must be taken with care as it does not correspond to difference in energy of the $\Sigma(0_{00})$ states. The observation of a small redshift upon complexation for Ar-D₂O and Ar-HDO, consistent with previous observations in the Ar-H₂O complex,^{9–11,16} reflects also a small variation of the potential energy surface upon vibrational excitation. This effect can also be observed by comparing the ground state and the excited states rotational constants in Tables I–III. Indeed, it seems that the water-argon complex geometry, and therefore the potential energy surface, is only slightly affected by the vibrational excitation, resulting in small changes of the rotational constants upon excitation: 0.5% and 2% for the Ar-D₂O $\Sigma(0_{00})$ and $\Sigma(1_{01})$ states, respectively, and 0.5% for the Ar-HDO $\Pi(1_{11})$ state. This small variation of the potential energy surface upon vibrational excitation is more striking by examining the splitting of the water subunit internal rotational levels. Indeed, the splitting between the $\Sigma(1_{01})$ and $\Pi(1_{01})$ states of Ar-D₂O increases only from 10.2 to 11.7 cm⁻¹ upon excitation, based on predicted ground state values,⁹ suggesting that there is only a small change in the angular anisotropy of the potential in the excited state.

VII. CONCLUSION

Three rovibrational bands of Ar-D₂O and two rovibrational bands of Ar-HDO were observed in the 1.5 μm range. Their analyses led to the determination of rotational constants for the upper states and vibrational shifts showing that the potential energy surface to be only slightly affected by the vibrational excitation. Coriolis couplings were observed and the identification of the perturbing states was made difficult by the lack of information on the layout of the energy levels in the observed range. The observed lines were fitted to retrieve a 3.5 ns lifetime of the upper state, showing that even with a triple or double excitation quanta in the water subunit, the Ar-D₂O and Ar-HDO complexes are long-lived species.

ACKNOWLEDGMENTS

This work was sponsored by the Fonds National de la Recherche Scientifique (FNRS), the « Action de Recherches Concertées de la Communauté française de Belgique » and the Belgian Federal Science Policy Office (Contract No. SD/CS/07A, Advanced Exploitation of Ground-Based Measurements for Atmospheric Chemistry and Climate applications-II).

- ¹H. G. Kjaergaard, T. W. Robinson, D. L. Howard, J. S. Daniel, J. E. Headrick, and V. Vaida, *J. Phys. Chem. A* **107**, 10680 (2003).
- ²R. C. Cohen, K. L. Busarow, K. B. Laughlin, G. A. Blake, M. Havenith, Y. T. Lee, and R. J. Saykally, *J. Chem. Phys.* **89**, 4494 (1988).
- ³R. C. Cohen, K. L. Busarow, Y. T. Lee, and R. J. Saykally, *J. Chem. Phys.* **92**, 169 (1990).
- ⁴R. C. Cohen and R. J. Saykally, *J. Chem. Phys.* **95**, 7891 (1991).
- ⁵G. T. Fraser, F. J. Lovas, R. D. Suenram, and K. Matsumura, *J. Mol. Spectrosc.* **144**, 97–112 (1990).
- ⁶T. C. Germann and H. S. Gutowsky, *J. Chem. Phys.* **98**, 5235–5238 (1993).
- ⁷S. Suzuki, R. E. Bumgarner, P. A. Stockman, P. G. Green, and G. A. Blake, *J. Chem. Phys.* **94**, 824 (1991).
- ⁸E. Zwart and W. L. Meerts, *Chem. Phys.* **151**, 407–418 (1991).
- ⁹R. Lascola and D. J. Nesbitt, *J. Chem. Phys.* **95**, 7917 (1991).
- ¹⁰D. J. Nesbitt and R. Lascola, *J. Chem. Phys.* **97**, 8096 (1992).
- ¹¹M. J. Weida and D. J. Nesbitt, *J. Chem. Phys.* **106**, 3078–3089 (1997).
- ¹²S. A. Nizkorodov, M. Ziemkiewicz, D. J. Nesbitt, and A. E. Knight, *J. Chem. Phys.* **122**, 194316 (2005).
- ¹³O. Votava, S. R. MacKenzie, and D. J. Nesbitt, *J. Chem. Phys.* **120**, 8443–8452 (2004).
- ¹⁴J. T. Stewart, B. E. Brumfield, and B. J. McCall, “High-resolution mid-infrared spectroscopy of deuterated water clusters using a quantum cascade laser-based cavity ringdown spectrometer,” in *Proceedings of the TA03, the 66th International Symposium on Molecular Spectroscopy*, Ohio State University, Columbus, OH, 2011.
- ¹⁵S. Li, R. Zheng, Y. Zhu, and C. Duan, *J. Mol. Spectrosc.* **272**, 27–31 (2012).
- ¹⁶S. Kuma, M. Slipchenko, T. Momose, and A. F. Vilesov, *J. Phys. Chem. A* **114**, 9022–9027 (2010).
- ¹⁷D. Verdes and H. Linnartz, *Chem. Phys. Lett.* **355**, 538–542 (2002).
- ¹⁸A. Moudens, R. Georges, M. Goubet, J. Makarewicz, S. E. Lokshantov, and A. A. Vigin, *J. Chem. Phys.* **131**, 204312 (2009).
- ¹⁹J. Makarewicz, *J. Chem. Phys.* **129**, 184310 (2008).
- ²⁰R. C. Cohen and R. J. Saykally, *J. Chem. Phys.* **98**, 6007 (1993).
- ²¹K. Didriche and T. Földes, “High-resolution overtone spectra of molecular complexes,” *Mol. Phys.* (in press).
- ²²K. Didriche, T. Földes, C. Lauzin, D. Golebiowski, J. Liévin, and M. Herman, *Mol. Phys.* **110**, 2781–2796 (2012).
- ²³P. S. Ormsby, K. N. Rao, M. Winnewisser, B. P. Winnewisser, O. V. Naumenko, A. D. Bykov, and L. N. Sinita, *J. Mol. Spectrosc.* **158**, 109–130 (1993).
- ²⁴C. M. Western, PGOPHER, a program for simulating rotational structure, University of Bristol, UK, see <http://pgopher.chm.bris.ac.uk>.
- ²⁵M. Rezaei, N. Moazzen-Ahmadi, A. R. W. McKellar, B. Fernandez, and D. Farrelly, *Mol. Phys.* **110**, 2743–2750 (2012).
- ²⁶M. Wangler, D. A. Roth, G. Winnewisser, I. Pak, and A. R. W. McKellar, *Can. J. Phys.* **79**, 423–434 (2001).
- ²⁷See supplementary material at <http://dx.doi.org/10.1063/1.4794161> for the list of assigned transitions of the (a) ortho Ar-D₂O van der Waals complex bands, (b) para Ar-D₂O van der Waals complex band, and (c) Ar-HDO van der Waals complex bands.
- ²⁸M. D. Brookes, D. J. Hughes, and B. J. Howard, *J. Chem. Phys.* **104**, 5391–5405 (1996).
- ²⁹O. N. Ulenikov, S.-M. Hu, E. S. Bekhtereva, G. A. Onopenko, X.-H. Wang, S.-G. He, J.-J. Zheng, and Q.-S. Zhu, *J. Mol. Spectrosc.* **208**, 224–235 (2001).
- ³⁰R. A. Toth, *J. Mol. Spectrosc.* **186**, 66–89 (1997).

1997–2007 CO trend at the high Alpine site Jungfraujoch: a comparison between NDIR surface in situ and FTIR remote sensing observations

B. Dils¹, J. Cui², S. Henne³, E. Mahieu⁴, M. Steinbacher³, and M. De Mazière¹

¹Belgian Institute for Space Aeronomy, Brussels, Belgium

²Institute for Atmospheric and Climate Science, ETH Zürich, Switzerland

³Empa, Swiss Federal Laboratories for Materials Science and Technology, Dübendorf, Switzerland

⁴Institute of Astrophysics and Geophysics, University of Liège, Liège, Belgium

Received: 4 March 2011 – Published in Atmos. Chem. Phys. Discuss.: 16 March 2011

Revised: 11 June 2011 – Accepted: 29 June 2011 – Published: 13 July 2011

Abstract. Within the atmospheric research community, there is a strong interest in integrated datasets, combining data from several instrumentations. This integration is complicated by the different characteristics of the datasets, inherent to the measurement techniques. Here we have compared two carbon monoxide time series (1997 till 2007) acquired at the high-Alpine research station Jungfraujoch (3580 m above sea level), with two well-established measurement techniques, namely in situ surface concentration measurements using Non-Dispersive Infrared Absorption technology (NDIR), and ground-based remote sensing measurements using solar absorption Fourier Transform Infrared spectrometry (FTIR). The profile information available in the FTIR signal allowed us to extract an independent layer with a top height of 7.18 km above sea level, appropriate for comparison with our in situ measurements. We show that, even if both techniques are able to measure free troposphere CO concentrations, the datasets exhibit marked differences in their overall trends (-3.21 ± 0.03 ppb year⁻¹ for NDIR vs. -0.8 ± 0.4 ppb year⁻¹ for FTIR). Removing measurements that are polluted by uprising boundary layer air has a strong impact on the NDIR trend (now -2.62 ± 0.03 ppb year⁻¹), but its difference with FTIR remains significant. Using the LAGRANTO trajectory model, we show that both measurement techniques are influenced by different source regions and therefore are likely subject to exhibit significant differences in their overall trend behaviour. However the observation that the NDIR-FTIR trend difference is as significant before as after 2001 is at odds with available emission databases which claim a significant Asian CO increase after 2001 only.

1 Introduction

Carbon monoxide (CO) is mainly produced by incomplete combustion of carbon-containing materials (fossil fuels or biomass) and plays an important role in tropospheric chemistry. Its reaction with the hydroxyl radical (OH) is widely considered as its most important sink, and at the same time it is also the dominant reaction partner for OH (barring strongly polluted or forested areas) (Logan et al., 1981). As such, CO has a strong indirect impact on the growth rates of many important greenhouse gases such as CH₄ and O₃ (Daniel and Solomon, 1998; Wild and Prather, 2000; Levy et al., 1997). It also has a direct influence on CO₂ through its oxidation.

Therefore accurate long-term measurements of tropospheric CO concentrations are important as they improve our understanding of the earth's past, present and future atmosphere. While the usage of space-borne instruments such as MOPITT, SCIAMACHY and IASI have become increasingly important for measuring the atmospheric composition on a global scale, their use for long-term trend analysis is often hampered by system degradation and drifts (Deeter et al., 2010). Thus ground-based measurements are vital for providing very accurate and consistent data with high temporal resolution over extended periods of time, ideally suited for satellite validation and trend analysis purposes. The downside of in situ measurements is their limited spatial coverage. The size of the area for which a station is representative depends on a multitude of parameters such as the site's location and lifetime of the target species in question (Henne et al., 2010; Folini et al., 2009). CO is particularly interesting in this respect as its global average lifetime is about two months, although the range is considerable: 10–15 days in summer over continents and up to a year in winter at high



Correspondence to: B. Dils
(bart.dils@bira-iasb.be)

latitudes (Holloway et al., 2000). This implies that it can be transported over long intercontinental distances, while at the same time its lifetime is too short for it being well mixed throughout the troposphere in both hemispheres. These properties make CO an ideal element in tracer studies, but they also potentially make the observed CO concentrations particularly sensitive to the measurement location. Indeed Zellweger et al. (2009) compared surface in situ CO measurements from several Swiss stations and noticed a clear dependence of the long-term CO trend on the altitude of the station. Barret et al. (2003) already performed a comparison between CO measurements from solar absorption Fourier transform Infrared Spectrometry (FTIR), MOPITT and Non-Dispersive Infrared Absorption technology (NDIR) at Jungfraujoch for the period between 1997 and 2000. For this limited time period they found a good correlation and no significant bias between NDIR and “surface” FTIR, defined as the 3.58–6.5 km layer.

With 11 years of data available now, we will revisit this comparison, focusing on the observed FTIR and NDIR long-term trends between 1997 and 2007 and assess whether two different measurement techniques at the same site could also harbour strong inherent differences, due to the above mentioned properties of CO.

2 Study site Jungfraujoch

The high-Alpine research station Jungfraujoch (JFJ, 46.5° N, 8° E, 3580 m above sea level) is situated on a mountain saddle between the Jungfrau (4158 m a.s.l.) and Mönch (4099 m a.s.l.) peaks, on the northern edge of the Swiss Alps. Due to its unique location, the year-round accessibility, and the excellent infrastructure, the Jungfraujoch research station is well suited for long-term ground-based monitoring of trace gas mixing ratio trends in the free troposphere. However, the site is also intermittently influenced by polluted boundary layer air (Zellweger et al., 2003) reaching the site during föhn or thermally-induced vertical transport conditions (Henne et al., 2004). The area influencing JFJ was recently compared with other European background monitoring sites and the site was categorized as “mostly remote” (Henne et al., 2010). Continuous ground-based in situ trace gas measurements are performed as part of the Swiss National Air Pollution Monitoring Network (NABEL). The long-term ground-based remote sensing observations are conducted as part of the Network for the Detection of Atmospheric Composition Change (NDACC), formerly the Network for the Detection of Stratospheric Change (NDSC). Meteorological parameters are measured by the Swiss Federal Office of Meteorology and Climatology (MeteoSwiss). The station is one of the 27 global stations of the Global Atmosphere Watch (GAW) of the World Meteorological Organization (WMO).

3 Experimental systems

3.1 NDIR measurements at Jungfraujoch

Continuous ground-based in situ CO measurements have been performed by the Swiss Federal Laboratories for Materials Science and Technology (Empa) as part of the NABEL network since April 1996. These measurements have been performed with a commercial instrument (Horiba APMA-360, Kyoto, Japan) using Cross Flow Modulated Non-Dispersive Infrared Absorption technology. Sample gas and reference gas are injected alternately (1 Hz frequency) into the measurement cell using solenoid valve modulation. Sample air is taken to generate CO-free reference gas by using a catalyst to oxidize CO to CO₂. Since the same gas is used for both the sample gas and the reference gas, zero drifts and interference effects are minimized. The sample air is dried using an additional Nafion drier to reduce potential water vapour interferences.

A zero check of the instrument is performed every 49 h using externally generated zero air by means of a CO/CO₂ converter, molecular sieve 3 Å and metal catalysts to convert CO (SOFNOCAT). Calibration of the instrument is performed twice a month using CO standards in the low-ppm range that are calibrated against NIST (National Institute of Standards and Technology, USA) and NMI (Nederlands Meetinstituut, The Netherlands) standards. The detection limit (zero + 3σ of the zero signal) is about 30 ppbv. A complete service check is performed once per year by the Swiss Horiba sales and service company (Deltatech, Switzerland).

Data are routinely recorded as 10 min averages. The overall measurement uncertainty for these values is estimated to be <10 % below 100 ppbv and <5 % above 100 ppbv.

3.2 FTIR observations at Jungfraujoch

Pioneering ground-based infrared measurements have been performed at the Jungfraujoch by the University of Liège (ULg) in the early 1950s (Zander et al., 1989, 2008). Regular FTIR measurements started in 1984 using a homemade instrument, backed since 1990 by a commercial Bruker IFS-120HR spectrometer. We considered here the Bruker time series of CO vertical profile data covering the 1997–2007 time period; it is part of the 1989–2010 dataset publicly available in the database of the Network for the Detection of Atmospheric Composition Change (NDACC) (see <http://www.ndacc.org>).

For the retrieval, the SFIT2 (v3.91) algorithm was used; it is based on the Optimal Estimation Method (OEM) as described by Rodgers (1976). The spectroscopic parameters of the absorption lines have been taken from the HITRAN2004 database (Rothman et al., 2003), including all the August 2006 updates (<http://www.hitran.com>). Three microwindows were simultaneously fitted, with limits ranging from 2057.7 to 2058 cm⁻¹, 2069.56 to 2069.76 cm⁻¹ and

2157.3 to 2159.15 cm^{-1} , respectively. Interferences by the solar spectrum and by telluric absorptions of N_2O , O_3 , H_2O and CO_2 were accounted for. The sole CO a priori profile and associated statistics used for all retrievals have been constructed using averaged volume mixing ratio (vmr) from the WACCM model (the Whole Atmosphere Community Climate Model; <http://waccm.acd.ucar.edu>) and from ACE-FTS occultation measurements (version 2.2 of the Atmospheric Chemistry Experiment Fourier Transform Spectrometer; see Clerbaux et al., 2008), in the 15.4–100 km and 6.5–15.4 km altitude ranges, respectively. This profile was extrapolated further down and set to 137 ppb for the first layer, considering the slope shown by the ACE-FTS averaged profile in the mid troposphere. Pressure and temperature data are taken from the National Center for Environmental Prediction (NCEP). The CO concentrations are retrieved in 39 layers from the ground (3.58 km) up to 100 km. The first retrieval layer extends from 3.58 to 4.23 km, the following tropospheric layers go up to 4.91, 5.63, 6.39, 7.18, 8.01, 8.88, 9.78, 10.72 and 11.7 km, the latter being close to the mean tropopause height above Jungfraujoch (11.3 km over the last decade). The retrieved profiles are characterized by the so-called averaging kernels, as described by Rodgers (1990, 2000). The retrieved volume mixing ratio profile x_r is thus related to the true profile x and to the a priori profile x_a by

$$x_r = x_a + \mathbf{A}(x - x_a) + (\text{errors}) \quad (1)$$

in which \mathbf{A} is the matrix whose rows are the averaging kernels. Equation (1) shows that for each layer, the retrieved vmr is a weighted mean of the vmr values at all altitudes, with weights given by the corresponding averaging kernel elements. In the ideal case, the averaging kernels are delta-functions (\mathbf{A} is the unit matrix). In reality they are bell-shaped functions since no layer can be truly independent from its neighbours. The amplitudes of these functions give an indication of the sensitivity of the retrieval to the true profile in each layer, and their widths of the vertical resolution for that layer. The trace of the averaging kernel matrix \mathbf{A} gives the Degrees Of Freedom for Signal (DOFS). On average the retrievals contain 2.23 DOFS for CO. Thus the signal can be separated into two independent layers. To obtain a layer with at least one degree of freedom the first 5 layers need to be combined (from 3.58 till 7.18 km), as confirmed by the analysis of the eigenvectors and eigenvalues which are similar to those in Fig. 2 of Barret et al. (2003). While independent, the combined 3.58–7.18 km layer, harbours still, as per Eq. (1), information from the a priori, nor is this layer free from the influence of CO variability above this combined layer. The second eigenvalue is equal on average to 0.92, indicating that 8% from the information retrieved in this layer is conveyed by the a priori. Regular HBr Cell measurements are performed and analyzed with linefit v9 (Hase et al., 1999) to characterize the instrumental function of the Bruker IFS-120HR instrument, nor is there any indication of

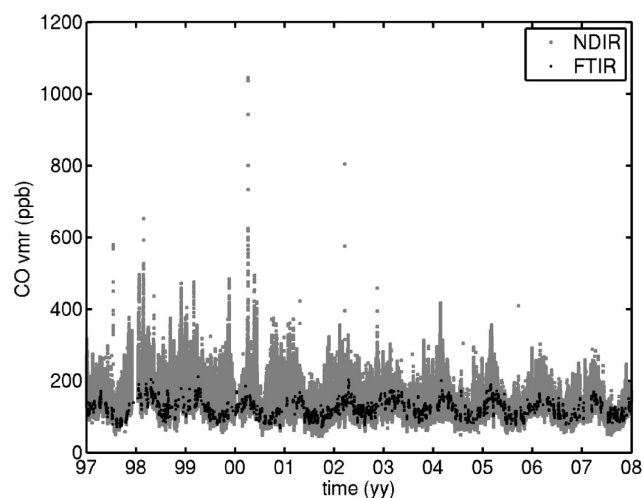


Fig. 1. CO concentrations (in ppb) as a function of time (year). All individual NDIR (grey) and FTIR data (black) prior to any selection/correction criteria.

quality change (such as a shift or drop in the observed DOFS) over time.

The FTIR retrieval data used by Barret et al. (2003), used slightly different input parameters (spectroscopic parameters from HITRAN2000, an a priori profile identical to the one used in the MOPITT version 3 retrieval (Deeter et al., 2003)) and vertical resolution (29 layers between 3.58 and 100 km). They also used a smaller 3.58–6.5 km layer in their comparison study. This has of course the advantage, when comparing with in situ measurements, that the difference in sampled air-mass is smaller. However since we would like to minimize the impact of the averaging kernel on the long-term trend evolution we deemed a 3.58–7.18 layer more suited for our purposes.

4 Data and data treatment

4.1 Raw datasets

It is obvious in Fig. 1 (showing the original data prior to any manipulation) that the NDIR dataset exhibits far larger peak values (especially prior to 2003) than the FTIR measurements. This can be attributed to the larger integrated air mass sampled by the FTIR instrument (and thus vertical and horizontal averaging). The FTIR data are less sensitive to “local” events such as thermally-induced vertical transport of CO from the valleys (Henne et al., 2004). Also clear sky conditions are needed to perform the FTIR measurements whereas 2 to 6% of NDIR CO measurements are associated with (cloudy) South Föhn events (Zellweger et al., 2003). Such events are capable of transporting polluted air masses from the highly industrialized Po Basin in Northern Italy to the Jungfraujoch (Reimann et al., 2008). Indeed, in

situ CO concentrations at JFJ are on average highest during south-easterly advection (Gilge et al., 2010). Other meteorological situations associated with elevated CO, are synoptic lifting and thermally-induced vertical transport (Zellweger et al., 2003).

The second striking feature is the different temporal evolution of the FTIR and NDIR datasets. While the overall CO trend of the FTIR data is only slightly negative (-0.8 ± 0.4 ppb year $^{-1}$), the NDIR data exhibit a far stronger negative trend (-3.21 ± 0.03 ppb year $^{-1}$). The trends were obtained by a simple robust linear fit, using bisquare weights. The uncertainty on the slope corresponds to the 2σ standard error. The trend for the in situ measurements agrees well with the observed CO trend at the Zugspitze summit (2962 m a.s.l. in the German Alps) of -3.16 ± 0.4 ppb year $^{-1}$ for the 1995 to 2002 period (Gilge et al., 2010). Next we will explore possible reasons for the trend difference observed at JFJ.

4.2 Humidity correction

Since the NDIR instrument removes H₂O prior to the detection of CO, it effectively measures the dry air volume mixing ratios. FTIR does not and thus measures moist air vmrs. Using meteorological data, in casu relative humidity (RH), temperature (T) and total pressure (p_{moist}), from MeteoSwiss, we have converted the dry air NDIR measurements to moist air volume mixing ratios by using the following approach:

We can derive the partial pressure of H₂O ($p_{\text{H}_2\text{O}}$) from the relative humidity and temperature using:

$$\text{RH} = \frac{p_{\text{H}_2\text{O}}}{p_{\text{H}_2\text{O},\text{sat}}} \times 100 \% \quad (2)$$

And the saturated water vapour pressure above water as given by:

$$p_{\text{H}_2\text{O},\text{sat}} = 6.112 \exp\left(\frac{17.62 T}{243.12 + T}\right) \quad (3)$$

(T in °C, p in hPa, taken from the guide to Meteorological Instruments and Methods of Observation (CIMO Guide) (World Meteorological Organisation, 2008)).

Then the ratio of moist air CO vmr over dry air CO vmr is given by

$$\frac{\text{CO}_{\text{moist}}}{\text{CO}_{\text{dry}}} = \frac{(p_{\text{moist}} - p_{\text{H}_2\text{O}})/M_{\text{dry air}}}{((p_{\text{moist}} - p_{\text{H}_2\text{O}})/M_{\text{dry air}} + p_{\text{H}_2\text{O}}/M_{\text{H}_2\text{O}})} \quad (4)$$

with

$$M_{\text{dry air}} = 28.96 \text{ g mol}^{-1} \quad \text{and} \quad M_{\text{H}_2\text{O}} = 18.015 \text{ g mol}^{-1}$$

The correction factor ranges between 0.978 and 0.9998, with a mean value of 0.993. The impact on the slope and general appearance of the dataset is negligible, with the NDIR trend for moist air volume mixing ratio equal to -3.20 ± 0.03 ppb year $^{-1}$. Note that this correction does not take into

account the variability of the humidity as a function of altitude. However, given the negligible impact of the implemented correction on the overall trend, we can safely state that a further correction or inversely, the conversion of the FTIR data into dry air columns would not explain the observed trend differences.

4.3 Selection of data representative of free troposphere air

It is obvious that there is a substantial difference between both techniques with regard to the actual air sampled. As mentioned in Sect. 2, NDIR essentially samples the CO concentration in the surface air at the Jungfraujoch site. The FTIR instrument, on the other hand, samples the CO content in the air along a slant column between the station and the sun. Pressure broadening of the spectroscopic lines allows the retrieval of a CO vertical distribution although it is characterized by a low vertical resolution. Therefore, the 3.58–7.18 km layer air mass used here is far larger than the in situ sampled air mass. Also note that at high solar zenith angles the horizontal extent above the Jungfraujoch reaches up to 20 km.

While air measured in situ at the Jungfraujoch site can mostly be regarded as representative of the free troposphere, given the site's altitude, influence from the boundary layer cannot be completely discarded. While the convective boundary layer (CBL) above the Alps might not reach the station altitude it is not necessarily identical with the mixing height of surface pollutants (De Wekker et al., 2004). A so called injection (or aerosol) layer can form above the CBL top which intermittently receives CBL air (Henne et al., 2004). It has been shown from airborne Lidar observations (Nyeki et al., 2000) and model studies (De Wekker et al., 2004) that JFJ can be situated well within the injection layer during summer, day-time, fair-weather conditions. It is clear from Fig. 1, that the NDIR data are often influenced by high CO events, probably associated with atmospheric boundary layer (ABL) air reaching the Jungfraujoch observatory. As mentioned above, regional pollution from the Po Basin is likely to be occasionally measured at JFJ during south-easterly advection. Since the European emissions declined significantly during the considered years (see Fig. 13), the negative in situ CO trends at JFJ are indeed more pronounced for south-easterly (-2.0 % year $^{-1}$) than for north-westerly advection (-1.6 % year $^{-1}$) (Gilge et al., 2010).

It is therefore crucial to somehow filter out these events, separating the background free tropospheric measurements from the disturbed ones (Zellweger et al., 2003). There are several methods to perform this filtering. One is to analyze and take into account various meteorological parameters (Forrer et al., 2000; Zellweger et al., 2003). Other methods use the determination of air mass origin (Derwent et al., 1998) or statistical filtering techniques such as the one described by Novelli et al. (1998); O'Doherty et al. (2001); or Ruckstuhl et al. (2010).

Statistical methods do not require auxiliary data, but exist in several forms and shapes. The one used in this article is the one developed by Ruckstuhl et al. (2010). In this so-called REBS technique (Robust Extraction of Background Signal), like in other statistical techniques, one tries to identify measurements that deviate significantly from the best fit to the dataset. One assumes that background data have a normal distribution around this fit. Typically a polynomial function is fitted through the data after which only the negative residual values are used to determine the shape of the normal distribution (Novelli et al., 1998; O’Doherty et al., 2001). REBS differs from the above in that it does not fit a polynomial, but uses robust local regression (Cleveland, 1979) to determine the optimal fit. This implies that no a priori assumptions on the shape of the fit are made. A bandwidth of 3 months is used such that the majority of the data falling within this band is likely to have a normal distribution (a prerequisite for the technique to work properly) while at the same time an appropriate mapping of the seasonality is still feasible.

Note that the technique does not offer a disturbed/background flag for each individual measurement. Instead it calculates a smooth curve fit, representative for the background free troposphere signal. Background air is thus defined as those measurements which fall within the Gaussian distribution around this curve fit. By the way it is calculated, the negative NDIR-REBS fit residuals are well represented by this Gaussian fit, but it is harder to draw a line for the positive residuals. One could define that all data with residuals that exceed 3σ are polluted as per Ruckstuhl et al. (2010), but this leaves a significant number of disturbed measurements that fall below this 3σ threshold, which in turn results in an overrepresentation of data points with a positive residual towards the REBS curve fit.

Therefore we calculate the residuals towards the REBS robust curve fit and plot a histogram of these residuals using 1 ppb size bins. A Gaussian curve is fitted through the histogram using only the negative residuals (which are mirrored onto the positive side to obtain a true Gaussian shape). For all data points that have a residual larger than 1σ , as determined from the Gaussian fit, the following method is applied. For each individual histogram bin, the difference between the total number of data points and the Gaussian histogram fit, determines the number of data that need to be rejected. For each point within the bin, the summed NDIR-REBS fit residual of its 2 neighbouring (in time) data points, was calculated. Data points which are taken shortly before or after measurements which have a high excess CO value (and are thus probably disturbed by boundary air), are more likely affected themselves. All data within the bin are ranked according to this combined neighbour residual (CNR) and those with the highest CNR are primarily rejected until the number of data points to be rejected is reached. 12.5 % of the NDIR data is thus removed from the dataset with the REBS-CNR routine.

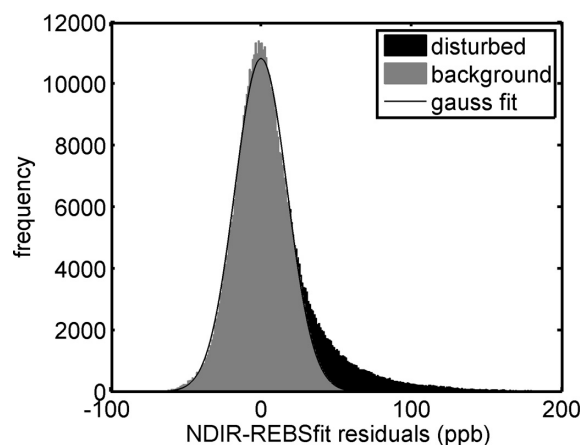


Fig. 2. Histograms of filtered (grey) and rejected (black) NDIR-REBS residuals data using REBS filtering.

A histogram of the whole NDIR dataset and the background data is shown in Fig. 2. Using a robust linear fit we calculate a slope of $-2.62 \pm 0.03 \text{ ppb year}^{-1}$ of the REBS-CNR filtered free troposphere dataset. Also note that the slope is somewhat lower than one would obtain by fitting the REBS curve fit itself or by using purely random selection criteria on the entire gauss curve, instead of the CNR method, namely $-2.66 \text{ ppb year}^{-1}$. In any case it is clear that the derived slope depends somewhat upon the selection method used and that the actual uncertainty on the trend exceeds the reported 2σ standard error. For instance, a completely different more crude filtering method in which we merely take the lowest 68 % of the CO data points for autumn (September to November) and winter (December till February) or 40 % for the spring–summer seasons, as based on Zellweger et al. (2003), yields an overall NDIR CO trend of $-2.74 \pm 0.03 \text{ ppb year}^{-1}$. But even taking an enlarged uncertainty into account, the FTIR and NDIR trends remain significantly different.

While the FTIR data are far less affected by local pollution, a similar filtering mechanism (but using 2 ppb bin widths to obtain a more regular Gaussian histogram shape) was applied for consistency’s sake. The resulting residual histogram is shown in Fig. 4. The FTIR residual data hardly show a distinct tail. Still 9.4 % of the data was filtered out. The obtained histogram also shows a smaller standard deviation (12 ppb) than the NDIR data (17 ppb), which is probably due to the larger integrated airmass sampled.

While the filtering has a significant impact on the NDIR timeseries (see Fig. 3), its overall trend changing from -3.20 to $-2.62 \pm 0.03 \text{ ppb year}^{-1}$, its impact on the FTIR timeseries is minimal as can be seen in Fig. 5 (trend changing from -0.8 to $-0.7 \pm 0.3 \text{ ppb year}^{-1}$). The difference between FTIR and NDIR trend remains substantial and can therefore not be explained by the impact of boundary layer influence alone.

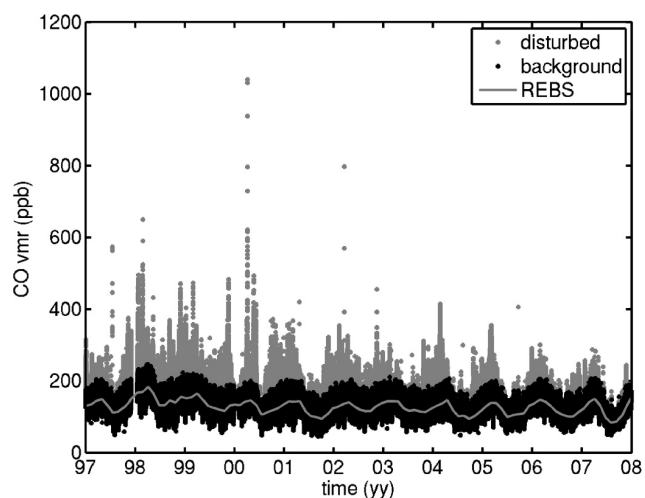


Fig. 3. Time series of NDIR CO concentrations (in ppb) at Jungfraujoch: the complete dataset before filtering (grey) and the dataset after REBS-CNR filtering (black; the grey curve is the REBS-CNR fit).

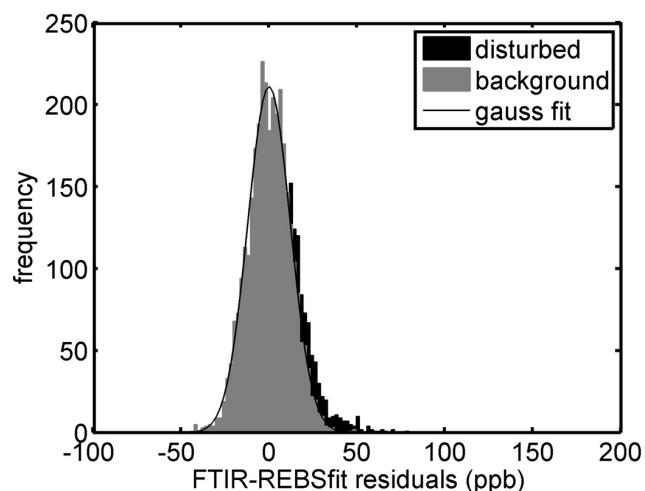


Fig. 4. Histogram of filtered background (grey) and rejected disturbed (black) FTIR-REBS residual data using REBS-CNR filtering.

4.4 Temporal overlap issues

NDIR measurements are taken 24 h a day, regardless of meteorological conditions. FTIR measurements however are only possible during daytime and they require strict cloud-free conditions. Therefore we looked at NDIR and FTIR data which have been taken in close temporal (± 10 min) proximity of each other.

We also wanted to look at the correlation between the overlapping NDIR and FTIR data. For each individual FTIR measurement, a corresponding NDIR data point was constructed by taking the average of all NDIR measurements within a

Table 1. NDIR and FTIR CO trend in ppb year^{-1} and number of data points (#) for the original raw data (Original), after humidity correction (Hum corrected), after humidity correction and REBS-CNR filtering (REBS-CNR) and after all the above and using either ± 10 min, ± 3 h or ± 2 day overlap times.

	NDIR trend	NDIR #	FTIR trend	FTIR #
Original	-3.21 ± 0.03	538 789	-0.8 ± 0.4	2687
Hum corrected	-3.20 ± 0.03	538 789	-0.8 ± 0.4	2687
REBS-CNR	-2.62 ± 0.03	471 365	-0.7 ± 0.3	2456
10 min	-2.7 ± 0.3	2273	-0.8 ± 0.3	2273
3 h	-2.7 ± 0.3	2372	-0.7 ± 0.3	2372
2 day	-2.7 ± 0.3	2427	-0.7 ± 0.3	2427

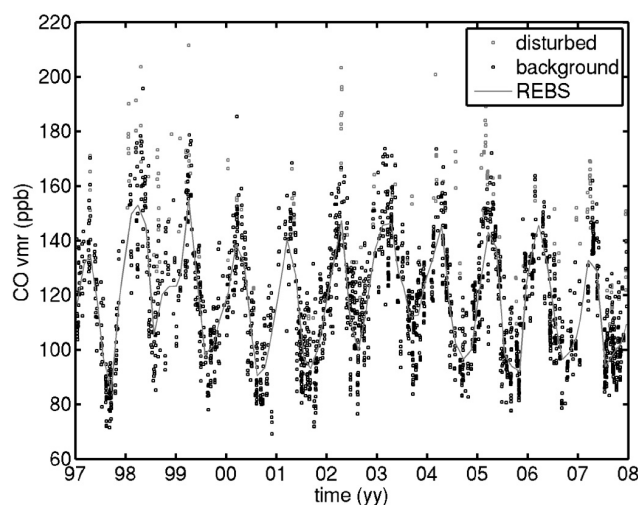


Fig. 5. Time series of FTIR CO concentrations (in ppb) at Jungfraujoch. Background data determined by REBS-CNR filtering are shown in black. The curve of the REBS-CNR fit is shown in grey.

certain overlap time of the FTIR measurement. Note that an individual FTIR measurement takes on average approximately 10 min. We also wanted to explore how wide this overlap time needed to be taken to obtain the best correlation. Therefore we varied the temporal overlap width between ± 10 min and ± 1000 h, again averaging all NDIR data that fall within the temporal overlap bounds of each FTIR measurement.

The correlation coefficient (R) reaches a maximum of 0.76 when averaging the NDIR data within 30 h of each FTIR measurement. Only after the overlap time increases over ± 60 h, does the correlation start to decline again. Given that the large correlation is probably largely due to the seasonal cycle (hence the large 30 h integration time), we also wanted to verify if there is a significant correlation between FTIR and NDIR CO on even shorter timescales. Therefore we also looked at the correlation between the NDIR and

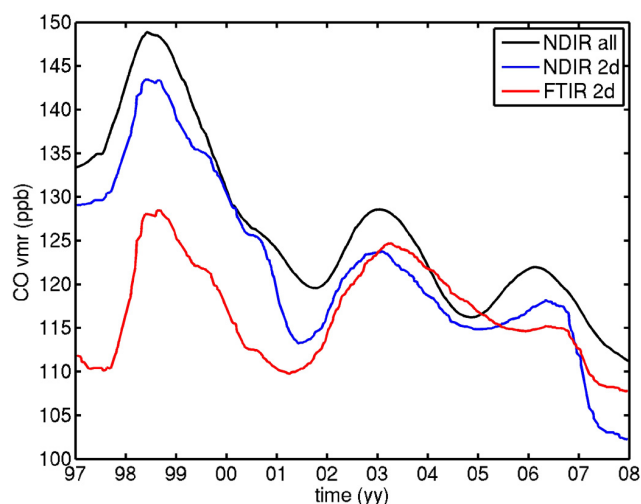


Fig. 6. Time series of NDIR (black and blue curves) and FTIR (red curve) data for CO vmr smoothed with KZ(365,3). For the black curve, all NDIR data were considered; for the blue curve, NDIR data were selected according to a temporal overlap criterium with the FTIR data of ± 2 days.

FTIR CO-REBS fit residuals. This removes the seasonal and long-term variability from the dataset. The correlation is far weaker for the residual values (0.48) and reaches a maximum between ± 3 and ± 8 h overlap time. These results show that the correlation between NDIR and FTIR is significant even with regard to short-term CO fluctuations. However, as with the REBS-CNR filtering routine, the choice of temporal collocation criteria does not have a significant impact on the NDIR and FTIR trend. Table 1 lists all the linear robust fit results for the original raw data, after humidity correction, after REBS-CNR filtering and using ± 10 min, ± 2 days and ± 3 h overlap times.

All the above indicates that both NDIR and FTIR are to a large degree influenced by the same CO fluctuations, yielding significantly high correlation coefficients, but at the same time are sufficiently diverse for such significant discrepancies in trends to arise.

4.5 Kolmogorov-Zurbenko filtered data

Given that a simple linear fit is rather simplistic as a trend marker, a Kolmogorov-Zurbenko filter (or KZ filters in short) (Zurbenko, 1986) was applied to the original REBS filtered and 2-day overlapping NDIR-FTIR datasets. The KZ(m, k) filter is a low pass filter described by k repetitions of a moving average of m data points ($-i$ to i), which smoothes the time series to a selected cut-off frequency:

$$Y_k = \frac{1}{m} \sum_{j=-i}^i X_{k,j} \quad (5)$$

The resulting time series becomes the input data for the second pass and so on until the number of passes is equal to

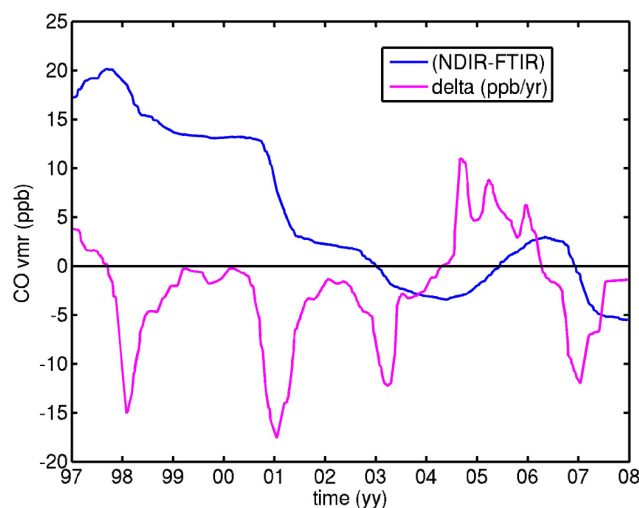


Fig. 7. Blue curve: Time series of the difference between NDIR and FTIR data. NDIR data have been defined according to a temporal overlap criterium with the FTIR data of ± 2 days. Magenta curve: KZ(74,5) smoothed gradient of the NDIR-FTIR difference as a function of time.

k . The benefit of this filter technique is that it is capable of averaging over sections of missing data without the need for restoration. Selected cut-off frequencies are defined by the m and k values of the moving average. The characteristic filter values that achieve the cut-off frequencies can be used to interpret an effective filter width (N_{eff}):

$$N_{\text{eff}} = m \cdot k^{1/2} \quad (6)$$

This width defines the effective separation value between frequencies allowed to pass through the filter and those that are not. Imposing separation at several frequencies, allows for separation of multiple timescales.

Here we have applied a $m = 365$ days or 12 months and $k = 3$ filter ($N_{\text{eff}} = 1.7$ years), typically noted as KZ(365,3), to determine the long-term trend. Likewise the KZ(74,5) combination is often used to determine the seasonal pattern. Figure 6 shows the time series of the KZ filtered NDIR data and the 2 day overlapping NDIR and FTIR data. The NDIR signal clearly shows three distinct episodes of CO increases. The first 1998 peak is attributed to an increase of biomass burning emission on a global scale (Simmonds et al., 2005). 2003 featured extremely high Central European summer temperatures and accompanying forest fires in Portugal which could explain the observed increase, either directly or via increased vertical upward transport (Luterbacher et al., 2004; Tressol et al., 2008; Yurganov et al., 2004, 2005). According to van der Werf et al. (2010), also 2005–2006 did not feature any increase of CO emissions on a global scale; however regional fires could be substantial. Fires in Mexico and Central America for instance were particularly intense during this period (as they were in 2003) (see GFEDv3 database, van der Werf et al., 2010).

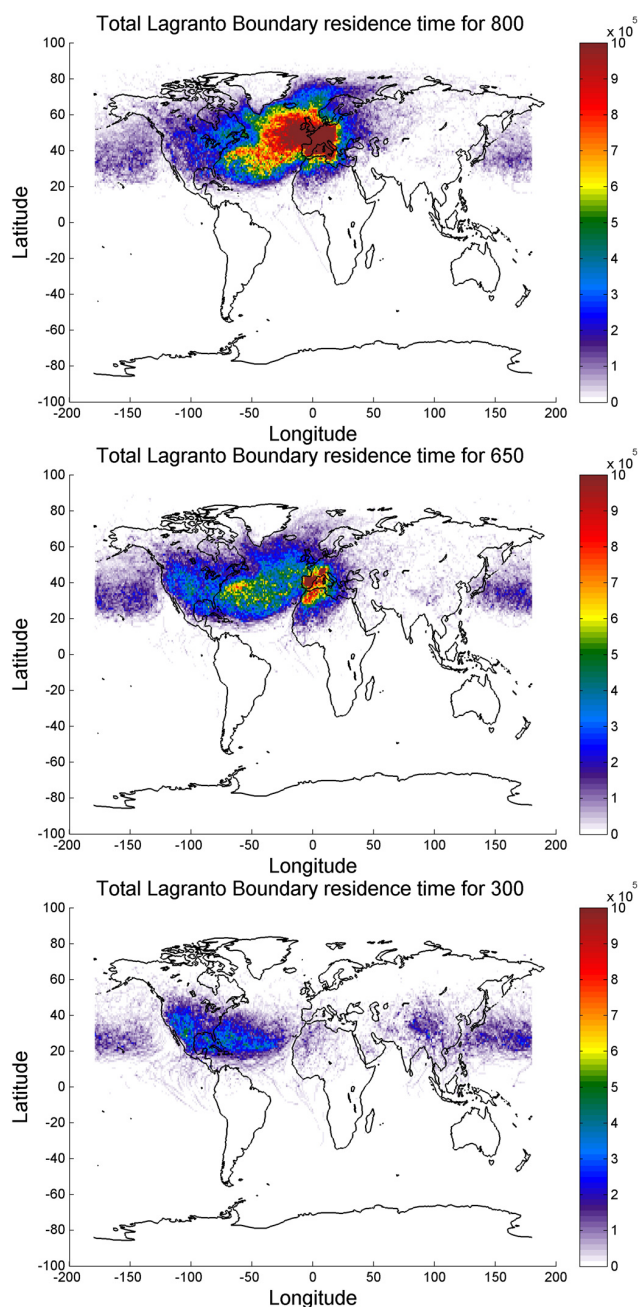


Fig. 8. Total boundary residence time (in seconds) for air masses arriving at Jungfraujoch at 800 (top), 650 (middle) and 300 hPa (bottom) averaged over the 1997–2007 period, as simulated by Lagranto. Scale is from 0 to 10×10^5 s (~ 12 days).

All these features are also present in the FTIR data, although the 2006 peak is much less prominent. This lower FTIR sensitivity to the 2005–2006 episode, also causes the only strong reversal in the overall negative NDIR-FTIR difference gradient (see Fig. 7). The strongest contrast with NDIR observations is that after each increased episode the FTIR data return to the same ~ 110 ppb base value (see

Fig. 6). In case of the NDIR time series, the minima in the inter-annual trend line are consistently getting lower. If we look at the NDIR-FTIR difference (Fig. 7), we see an almost stepwise pattern and indeed if we plot this trend line as well as its gradient (smoothed with the KZ(74,5) filter to eliminate short-term noise), we see that between mid 1997 and mid 2004, the trend is almost consistently negative, with strong peak increases in the NDIR-FTIR difference during winter 1997–1998, 2000–2001 and spring 2003. Such stepwise decreases could point to temporary problems with the instrumentation. Here we have to note that these steps are visible in the NDIR-FTIR difference only and do not occur in the individual NDIR or FTIR dataset. Furthermore, it is clear from Sect. 3.1 that the NDIR data are routinely calibrated against a NIST reference and that any perpetuating drift is extremely unlikely, nor is there any indication of quality change in the FTIR dataset (see Sect. 3.2). A more reasonable explanation is that a quasi constant NDIR-FTIR bias shift is periodically influenced by episodes of elevated CO emissions which have a higher impact on NDIR CO. However, it is also clear that due to the limited number of overlapping NDIR FTIR data the KZ smoothing function might level out otherwise visible features such as the 2004 decrease (see Fig. 6) which is much less prominent in the NDIR 2d (using a ± 2 day temporal overlap window with FTIR, see Sect. 4.4) dataset than in the full NDIR dataset.

5 Identification of source regions

In order to account for the different long-term CO trends in the FTIR and NDIR data we turn our attention to the difference in the vertical airmass sampled and the implied possible difference in the source regions that influence the CO content in both measurement types. Indeed, Zellweger et al. (2009) explained their observed difference between surface in situ CO measurements from several Swiss stations, on the influence of different source regions on each individual station, especially as a function of altitude.

Thus the Lagranto (Wernli and Davies, 1997) Lagrangian trajectory model was used to calculate transport pathways towards the Jungfraujoch site, based on European Centre for Medium-Range Weather Forecasts Re-Analysis (ECMWF ERA) Interim windfields from 1990 to end of 2007. Starting points ranged from 850 to 100 hPa. Back trajectories were calculated every 6 h going 20 days backwards in time. This brings them well beyond the synoptic period and thus individual trajectories can be considered unreliable due to the poor simulation of fronts and convective processes which occur along their path. Using ensembles of trajectories mediates this problem to a certain degree but systematic errors on the long range pathways (especially towards Asia) cannot be completely ruled out. Also the model uses $1 \times 1^\circ$ wind fields and thus the orography of the Alps is not optimally represented. The model sets the ground level at Jungfraujoch at

1500 m (~ 850 hPa) instead of the actual 3580 m (~ 650 hPa). Therefore the actual contributions to the JFJ station might contain some sub 650 hPa altitude information as well.

From these trajectories, the time an air mass had spent within the atmospheric boundary layers (ABL) over Europe, North America, Asia, etc. was calculated by comparing the trajectory altitude with boundary layer heights as taken from ERA Interim re-analysis.

It can be seen in Fig. 8 that the CO concentration observed above Jungfraujoch has a different source region depending on the altitude above the surface, in agreement with Pfister et al. (2004), who used the MOZART-2 chemistry transport model to simulate the CO budget over Europe. The lowest arrival height features a strong influence of Western Central Europe and the Eastern Atlantic, whereas the 650 hPa arrival level covers most parts of the United States, the Atlantic and South-western Europe. For the highest arrival height, the European influence is negligible but the air masses had been in contact with the boundary layer over the Western Atlantic, the United States, the Pacific and Asia.

We did not observe any significant long-term trend in the source regions over the years (not shown), although a year to year variability is present (Cui et al., 2011). Also a seasonal difference was clearly noticeable. Figure 9 shows an Asian influence during winter, while the European influence is strongest during the summer. The seasonality of the North American pathways exhibit a smaller seasonal cycle at low altitudes. At higher altitudes, the European influence becomes ever smaller and North America and Asia become the dominant contributors. The shown uncertainties have been derived by using yearly ensembles of the data. It therefore contains real year to year variability, but also contains a large fraction of actual uncertainty of the ensemble method.

Given this seasonality we calculated the trends using all REBS-CNR filtered NDIR and FTIR data for winter (DJF) and summer (JJA) (not shown). For the NDIR data, we see a difference in the summer and winter trend. While the overall trend was -2.62 ± 0.03 ppb year $^{-1}$ (see Table 1), the winter NDIR was only -1.57 ± 0.05 ppb year $^{-1}$ while the summer data was -2.72 ± 0.04 ppb year $^{-1}$. This is in line with what can be expected, if there is an increased impact of growing Asian emissions in winter. The FTIR data on the other hand, having fewer data points and thus substantially larger uncertainty, showed a reverse, but insignificant trend: -0.7 ± 0.3 ppb year $^{-1}$ (overall, see Table 1), -0.2 ± 0.5 ppb year $^{-1}$ (winter) and -0.1 ± 0.4 ppb year $^{-1}$ (summer).

Single trajectory models such as LAGRANTO are not suited for the quantitative determination of the CO concentrations above Jungfraujoch, as they do not account for dispersion processes. However, using an ensemble of single LAGRANTO trajectories does allow for a qualitative assessment when combined with emission inventories. Combining all calculated trajectories at a certain pressure level gives a good indication of the overall source area. Since

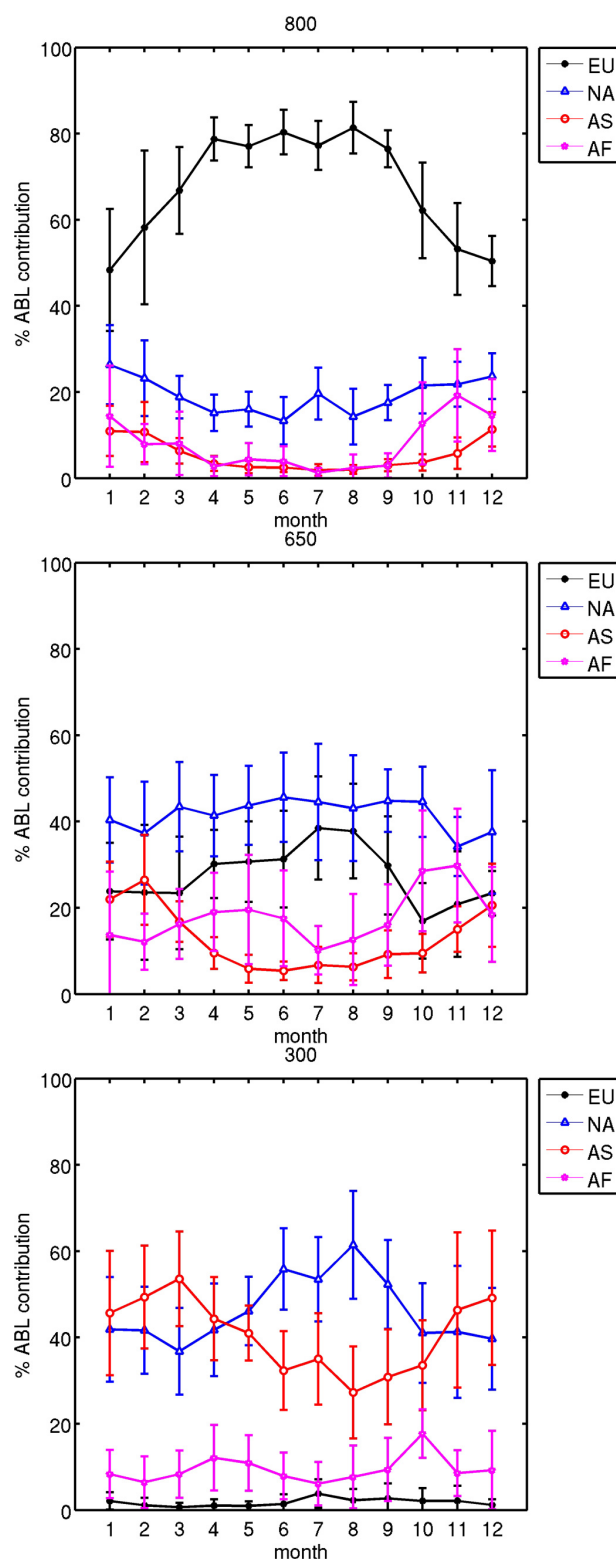


Fig. 9. Average monthly residence time in the Atmospheric Boundary Layer (ABL) per region (EU: Europe, NA: North America, AS: Asia, AF: Africa) relative to the total ABL residence time arriving at Jungfraujoch at 800 (top), 650 (middle) and 300 hPa (bottom plot). The error bars correspond to the 1σ standard deviation, derived from analysing the yearly contributions separately.

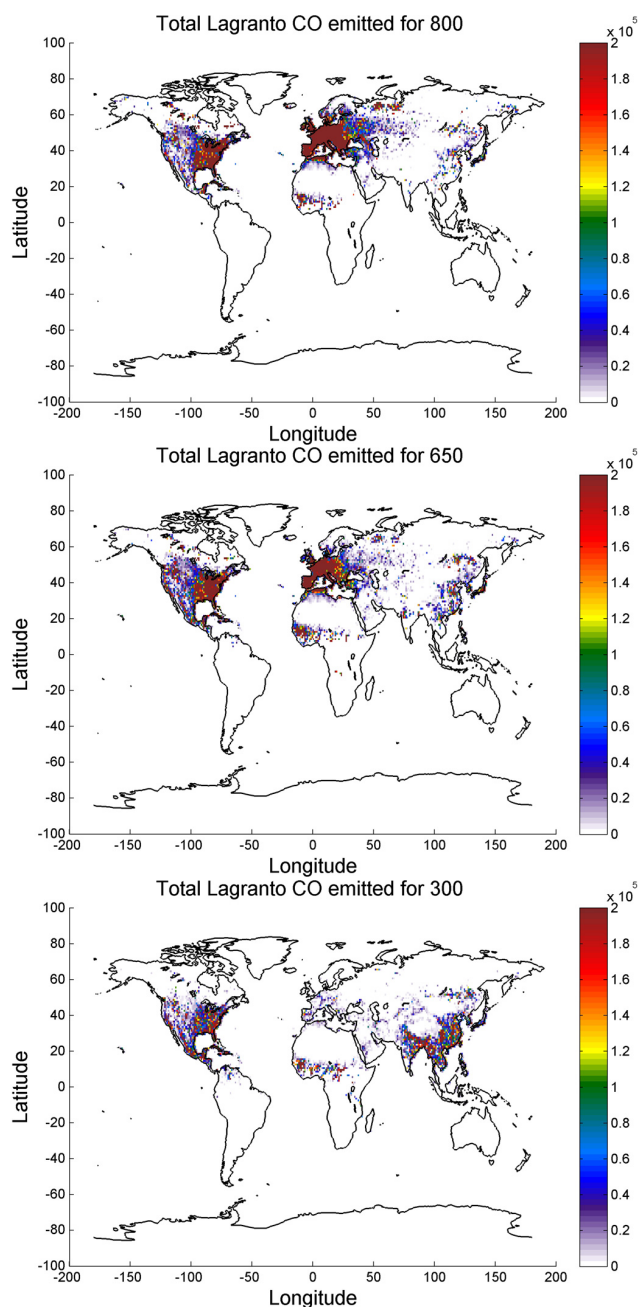


Fig. 10. Total CO emitted and transported towards Jungfraujoch at 800 (top), 650 (middle) and 300 hPa (bottom) for the year 2000, using total 1997–2007 residence times, as simulated by Lagranto and EDGAR v4.1 and GFED v3 emissions. Scale ranges between 0 and 2×10^5 kg.

we did not see any noticeable trend in this source area distribution over the years, we started with the summed total residence time over the entire 1997–2007 period. This ignores the inter-annual variability in the source regions. Using yearly summed residence times, instead of the entire 1997–2007 period, yielded ensembles which still showed clear in-

dividual trajectories instead of a more uniform source region area. The only inter-annual variability thus might come from changes in emissions. For biomass burning we have used the GFEDv3 CO emissions (van der Werf et al., 2010). For the anthropogenic emissions we used the EDGAR emission database (European Commission, Joint Research Centre (JRC)/Netherlands Environmental Assessment Agency (PBL). Emission Database for Global Atmospheric Research (EDGAR), release version 4.1, <http://edgar.jrc.ec.europa.eu>, 2009).

The yearly gridded EDGAR data consist of 2000–2005 data only. The 2006 and 2007 data were constructed by extrapolating the 2004–2005 trend. The 1997 till 1999 data were constructed from the linear interpolation of the 1995 (present in the database) and 2000 gridded data. The monthly GFED data was summed to yearly values, to comply with EDGAR.

Multiplying the total residence time (in s) with the emission strength for a given year at each grid box (in kg s^{-1}) yields the mass that gets fed into that grid box and ends up being transported towards the Jungfraujoch at a particular pressure level. In order to account for the different air-mass densities at different pressure levels, one needs to convert the emitted CO mass to mass mixing ratios at the emission source and back again to mass values at the Jungfraujoch site. This was done by using the International Standard Atmosphere (International Organization for Standardization, Standard Atmosphere, ISO 2533:1975, 1975.) air density values (thus air mass density variability in time and emission source location is not taken into account, nor is the variability of the boundary layer height, which is arbitrarily set to 1 m).

For the REBS-CNR filtered NDIR dataset we looked at the 650 hPa level which more or less corresponds to the Jungfraujoch station altitude. To map the above discussed LAGRANTO output (Lg), shown in Fig. 10, which (given the use of the constructed ensemble residence time output) is in arbitrary kg units but proportional to the CO vmr values, onto the NDIR data, one needs to find the corresponding factor f for which

$$f \times \text{Lg} = \text{CO} \quad (7)$$

With Lg in kg, CO in ppb and f in ppb kg^{-1} .

Since the LAGRANTO run and emissions do not take any (photo)chemical production (and removal) of CO into account, these background contributions should be taken into account into the equation, thus

$$(f \times \text{Lg}) + \text{CO}_{\text{background}} = \text{CO}_{\text{observed}} \quad (8)$$

While the background CO level is unknown, by assuming that it is constant over time, f can still be determined by fitting Eq. (8). The optimal conversion factor f turned out to be $(7.3 \pm 1.4) \times 10^{-8}$ (ppb kg^{-1}), while the background CO value equalled 46.6 ± 15 ppb. This is in line with the contribution to the total CO signal of 35–48 ppb due to the oxidation of CH_4 and non-methane hydrocarbons as reported by

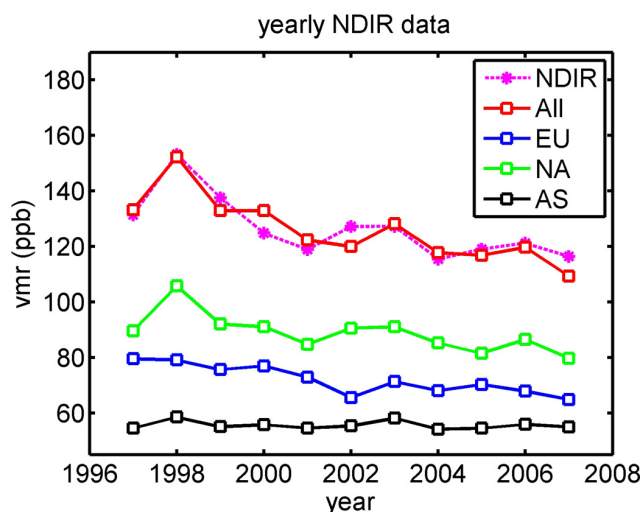


Fig. 11. Yearly mean ground-based in situ CO data (NDIR) as well as model simulated CO mixing ratios above the Jungfraujoch. All, corresponds to the global model simulations, while EU, NA and AS are the model contributions from Europe, North America and Asia, respectively. The fitted 46.6 ppb background has been added to all model output (also the regional ones).

Zellweger et al. (2009). The yearly mean measured and modelled (using the $7.3 \times 10^{-8} \cdot \text{Lg} + 46.6$ ppb formula) NDIR CO evolution is plotted in Fig. 11.

For the REBS-CNR filtered FTIR remote sensing dataset, we need to combine the modelled output from several pressure levels, taking into account the averaging kernel information (see Eq. 1). The latter is important as the FTIR data still contain some a priori information, which remains constant over time (as discussed in Sect. 3.2). This contribution dampens any potential FTIR trend and therefore this effect needs to be equally applied to the model data. Since we only have a qualitative idea of the real partial column information we've built the "real" partial column (x) from the a priori (x_a), corrected by the LAGRANTO CO mass mixing ratio (in kg kg^{-1} air but holding no quantitative information) towards 1997 as in

$$x(\text{yr}) = x_a \cdot \text{Lg}(\text{yr}) / \text{Lg}(1997). \quad (9)$$

The LAGRANTO CO mass mixing ratios needed to be mapped onto the FTIR vertical retrieval grid first (this is also the reason we did not use absolute mass values as these depend on grid size). The averaging kernel smoothing is then applied (as per Eq. 1) onto the thus obtained partial column x , resulting in the observed partial column x_r . Merging the bottom 5 layers of x_r , yields our model generated 3.58–7.18 km layer.

Here, using the same routine as with the NDIR data (fitting Eq. 8), yields an optimal background signal of 43 ± 17 ppb. This is similar to the one found for NDIR. Figure 12 also reveals the declining impact of European emissions and a slight

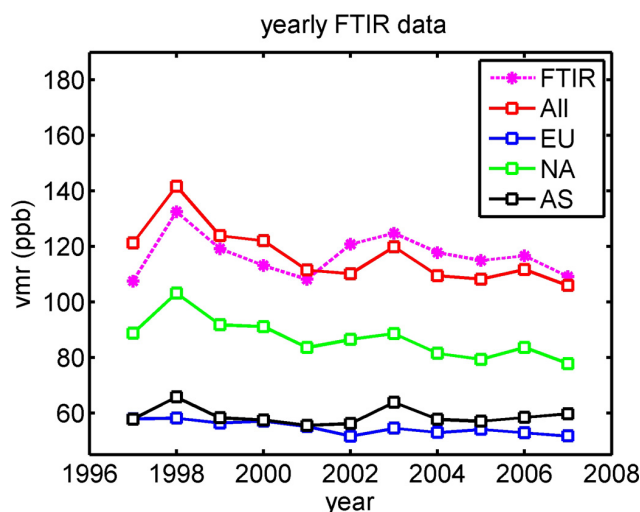


Fig. 12. Yearly mean FTIR data as well as model simulated CO concentrations above the Jungfraujoch. All, corresponds to the global model simulations, while EU, NA and AS are the model contributions from Europe, North America and Asia respectively. Again the fitted 43 ppb background has been added to all model output (also the regional ones).

increase in the importance of Asian emissions compared to the NDIR run (Fig. 11).

When we look at the year to year variability of both NDIR and FTIR simulations, we clearly see the 1998, 2003 and 2006 peaks. These are mostly driven by the North American (for NDIR) and Asian emissions. Both model runs seem to underestimate the 2002 emissions, while overestimating the 2000 values. Note that the NDIR and FTIR data used are the REBS-CNR filtered data and the year 2000 saw some of the highest in situ CO concentrations, which all have been filtered out. The overall temporal evolution of the CO concentrations is very well reproduced by the model in the NDIR case, but less so in the FTIR simulation. A crude linear fit through the modelled FTIR data yields a slope of -3.7 ± 0.6 ppb year^{-1} . Disregarding the averaging kernel smoothing (Eq. 1), the slope would have been -3.6 ± 0.6 ppb year^{-1} . Therefore the impact of the constant a priori content on the FTIR signal is minimal.

6 Discussion

The observed overall decline of NDIR CO concentrations can mainly be attributed to the steady reduction of European and North American emission sources. The EDGAR emission database shows a decrease from 50.5 Gt to 32 Gt between 1997 and 2005 for Central and OECD (Organisation for Economic Co-operation and Development) Europe (tagged as EU in Fig. 13). Likewise the combined US-Mexican emissions (tagged as NA in Fig. 13) dropped from 103 Gt to 69.6 Gt over the, same time frame.

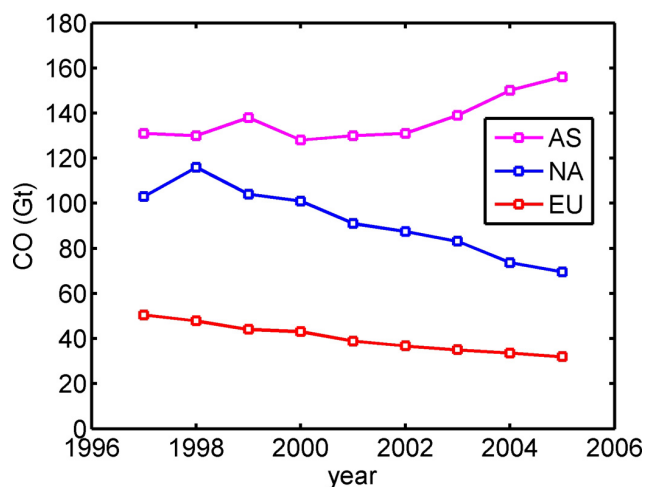


Fig. 13. CO emissions over time for AS (India+China), EU (OECD and Central Europe) and NA (USA+Mexico). Source: EC-JRC/PBL. EDGAR version 4.1. <http://edgar.jrc.ec.europa.eu/>, 2010.

Both EU and NA emissions decreased at a fairly constant pace, by 36.6% and 32.4% respectively, over the period 1997–2005. The combined anthropogenic emissions from India and China (the dominant Asian contributors according to Pfister et al., 2004), increased from 131 Gt to 156 Gt or 19% over the same time period.

However, as mentioned before, the increase in the NDIR-FTIR difference looks rather gradual throughout 1998 till 2004. At least the 1997 to 2001 decrease is just as, if not more, significant as the 2001–2004 decrease. To account for the small negative FTIR trend and the influence of decreasing European and North American emissions in the FTIR signal, the Asian emissions should likewise show a gradual increase. Indeed, there is strong evidence that particularly Chinese CO emissions increased between 2001 and 2005. The EDGAR database shows a 78.4 to 103.6 Gt (32%) increase between 2001 and 2005, while the REAS (Regional Emission Inventory in Asia) database (Ohara et al., 2007) displays a 17 Gt increase of Chinese emissions between 2000 and 2003. However, both EDGAR and REAS show no significant increase for the 1997 to 2001 period, but a 3–4 Gt decrease. Therefore, the increase can hardly be called gradual and one would expect a much stronger evolution of the NDIR-FTIR difference after 2001. This is also reproduced in our FTIR model simulation. While the 2001–2007 period shows no significant trend for the model (in agreement with the FTIR data), the 1997 to 2001 period features a stronger trend than observed. Particularly the 1997–1998 modelled values are significantly higher than those measured by FTIR. Sure enough there is considerable uncertainty in the CO baseline from oxidation, as well as the exact contribution of certain source regions to the overall signal but any shift regarding these parameters will deteriorate the quality of the post 2001 fit or

vice versa. Given the quality of the NDIR model fit, which adds credibility to our method, and the significant contributions from North American and European emissions sources on the NDIR signal, an overestimation of the pre-2001 Asian data (or underestimation of its positive trend) is the most likely culprit.

However, other factors might come into play as well. Given that the FTIR dataset is sparser than the NDIR dataset, it is more likely that the FTIR measurements become influenced by year to year variabilities in the average source region, which is taken as a constant in the model run. Combined with the large impact of the 1998 fires on the 1997–2001 CO evolution, this could potentially lead to significant over- and underestimations. However, the above would likely have a random impact, not a systematic pre- and post 2001 feature.

7 Concluding remarks

In this paper, we have looked into the 1997–2007 CO measurements made at the Jungfraujoch research station, using two different ground-based measurement techniques, namely NDIR in situ sampling and FTIR remote sensing. The substantial differences in sampled air masses, combined with the fact that the atmospheric life time of CO (~ 2 months) is too short for it to be well mixed throughout the free troposphere but yet is long enough to feel the influence of far away source regions (both qualities which makes CO an ideal component for tracer studies), makes that substantial differences between NDIR and FTIR can arise, especially with regards to the overall trend.

The impact of background air selection methods and temporal overlap criteria has been discussed. The latter clearly showed that both techniques are still to a significant degree influenced by the same CO variability, as is indicated by their correlations, even on a day to day variability scale.

Kolmogorov-Zurbenko smoothing revealed the strong inter-annual variability and impact of biomass burning events on the overall trend. Both NDIR and FTIR instruments exhibited the same features although the respective impact of the episodes on the measurement signal could differ. It is also clear that underneath these features, the overall NDIR trend was significantly negative, while the FTIR signal always reverted back to its ~ 110 ppb background. The gradient of the NDIR-FTIR difference proved to be consistently negative apart from the year 2005–2006.

We have also shown that, for FTIR, the influence from Asian emissions is indeed much larger than for NDIR. LAGRANTO-EDGAR-GFED simulations yield excellent agreement with the NDIR measurements and also show a tempered trend in the 2001–2007 FTIR data. However, the evolution of the pre-2001 FTIR trend is less well captured by the model. Emission databases typically indicate an Asian CO increase after 2001 only. Thus, since the NDIR-FTIR

trend difference propagates over the entire 1997–2004 period, it cannot be explained by the impact of Asian emissions alone. Whether the increasing Asian CO emission trend has been underestimated for the pre-2001 period, or that hitherto unknown factors play a role remains to be investigated.

Acknowledgements. We would like to thank the International Foundation High Altitude Research Stations Jungfraujoch and Gornergrat (HFSJG, Bern) for supporting the facilities needed to perform the observations. The Swiss National Air Pollution Monitoring Network is run by Empa in joint collaboration with the Swiss Federal Office for the Environment (FOEN). Work at University of Liège and BIRA-IASB was supported by the Belgian Science Policy Office (PRODEX and SSD programs) as well as by the European Commission through the GEOMon (Global Earth Observation and Monitoring) Integrated Project under the 6th Framework Program (contract number FP6-2005-Global-4-036677). We are grateful to the many Belgian colleagues who contributed to the FTIR data acquisition.

We thank MeteoSwiss for the provision of meteorological data. The NDIR and FTIR datasets are available from the WMO GAW World Data Centre for Greenhouse Gases (<http://gaw.kishou.go.jp/wdcgg/>) and the NDACC (<ftp://ftp.cpc.ncep.noaa.gov/ndacc/station/>) database, respectively.

Edited by: N. M. Donahue

References

- Barret, B., De Mazière, M., and Mahieu, E.: Ground-based FTIR measurements of CO from the Jungfraujoch: characterisation and comparison with in situ surface and MOPITT data, *Atmos. Chem. Phys.*, 3, 2217–2223, doi:10.5194/acp-3-2217-2003, 2003.
- Clerbaux, C., George, M., Turquety, S., Walker, K. A., Barret, B., Bernath, P., Boone, C., Borsdorff, T., Cammas, J. P., Catoire, V., Coffey, M., Coheur, P.-F., Deeter, M., De Mazière, M., Drummond, J., Duchatelet, P., Dupuy, E., de Zafra, R., Eddounia, F., Edwards, D. P., Emmons, L., Funke, B., Gille, J., Griffith, D. W. T., Hannigan, J., Hase, F., Höpfner, M., Jones, N., Kagawa, A., Kasai, Y., Kramer, I., Le Flochmoën, E., Livesey, N. J., López-Puertas, M., Luo, M., Mahieu, E., Murtagh, D., Nédélec, P., Pazmino, A., Pumphrey, H., Ricaud, P., Rinsland, C. P., Robert, C., Schneider, M., Senten, C., Stiller, G., Strandberg, A., Strong, K., Sussmann, R., Thouret, V., Urban, J., and Wiacek, A.: CO measurements from the ACE-FTS satellite instrument: data analysis and validation using ground-based, airborne and spaceborne observations, *Atmos. Chem. Phys.*, 8, 2569–2594, doi:10.5194/acp-8-2569-2008, 2008.
- Cleveland, W. S.: Robust Locally Weighted Regression and Smoothing Scatterplots, *J. Am. Stat. Assoc.*, 74, 829–836, 1979.
- Cui, J., Pandey Deolal, S., Sprenger, M., Henne, S., Staehelin, J., Steinbacher, M., and Nédélec, P.: Free tropospheric ozone changes over Europe as observed at Jungfraujoch (1990–2008): An analysis based on backward trajectories, *J. Geophys. Res.*, 116, D10304, doi:10.1029/2010JD015154, 2011.
- Daniel, J. S. and Solomon, S.: On the climate forcing of carbon monoxide, *J. Geophys. Res. Atmos.*, 103, 13249–13260, 1998.
- Deeter, M. N., Emmons, L. K., Francis, G. L., Edwards, D. P., Gille, J. C., Warner, J. X., Khattatov, B., Ziskin, D., Lamarque, J.-F., Ho, S.-P., Yudin, V., Attie, J.-L., Packman, D., Chen, J., Mao, D., and Drummond, J. R.: Operational carbon monoxide retrieval algorithm and selected results for the MOPITT instrument, *J. Geophys. Res.*, 108, 4399, doi:10.1029/2002JD003186, 2003.
- Deeter, M. N., Edwards, D. P., Gille, J. C., Emmons, L. K., Francis, G., Ho, S. P., Mao, D., Masters, D., Worden, H., Drummond, J. R., and Novelli, P. C.: The MOPITT version 4 CO product: Algorithm enhancements, validation, and long-term stability, *J. Geophys. Res. Atmos.*, 115, D07306, doi:10.1029/2009JD013005, 2010.
- Derwent, R., Simmonds, P., O'Doherty, S., Ciais, P., and Ryall, D.: European source strengths and northern hemisphere baseline concentrations of radiatively active trace gases at Mace Head, Ireland, *Atmos. Environ.*, 32, 3703–3715, 1998.
- De Wekker, S. F. J., Steyn, D. G., and Nyeki, S.: A comparison of aerosol layer and convective boundary layer structure over a mountain range during 97, *Bound.-Layer Meteor.*, 113, 249–271, 2004.
- Folini, D., Kaufmann, P., Ubl, S., and Henne, S.: Region of influence of 13 remote European measurement sites based on modeled carbon monoxide mixing ratios, *J. Geophys. Res. Atmos.*, 114, D08307, doi:10.1029/2008JD011125, 2009.
- Forrer, J., Ruttimann, R., Schneiter, D., Fischer, A., Buchmann, B., and Hofer, P.: Variability of trace gases at the high-Alpine site Jungfraujoch caused by meteorological transport processes, *J. Geophys. Res. Atmos.*, 105, 12241–12251, 2000.
- Gilge, S., Plass-Duelmer, C., Fricke, W., Kaiser, A., Ries, L., Buchmann, B., and Steinbacher, M.: Ozone, carbon monoxide and nitrogen oxides time series at four alpine GAW mountain stations in central Europe, *Atmos. Chem. Phys.*, 10, 12295–12316, doi:10.5194/acp-10-12295-2010, 2010.
- Hase, F., Blumenstock, T., and Paton-Walsh, C.: Analysis of the instrumental line shape of high-resolution Fourier transform IR spectrometers with gas cell measurements and new retrieval software, *Appl. Optics*, 38, 3417–3422, 1999.
- Henne, S., Furger, M., Nyeki, S., Steinbacher, M., Neininger, B., de Wekker, S. F. J., Dommen, J., Spichtinger, N., Stohl, A., and Prévôt, A. S. H.: Quantification of topographic venting of boundary layer air to the free troposphere, *Atmos. Chem. Phys.*, 4, 497–509, doi:10.5194/acp-4-497-2004, 2004.
- Henne, S., Brunner, D., Folini, D., Solberg, S., Klausen, J., and Buchmann, B.: Assessment of parameters describing representativeness of air quality in-situ measurement sites, *Atmos. Chem. Phys.*, 10, 3561–3581, doi:10.5194/acp-10-3561-2010, 2010.
- Holloway, T., Levy, H., and Kasibhatla, P.: Global distribution of carbon monoxide, *J. Geophys. Res. Atmos.*, 105, 12123–12147, 2000.
- Levy, H., Kasibhatla, P. S., Moxim, W. J., Klonecki, A. A., Hirsch, A. I., Oltmans, S. J., and Chameides, W. L.: The global impact of human activity on tropospheric ozone, *Geophys. Res. Lett.*, 24, 791–794, 1997.
- Logan, J. A., Prather, M. J., Wofsy, S. C., and McElroy, M. B.: Tropospheric Chemistry – a Global Perspective, *J. Geophys. Res.-Oceans and Atmospheres*, 86, 7210–7254, 1981.
- Luterbacher, J., Dietrich, D., Xoplaki, E., Grosjean, M., and Wanner, H.: European seasonal and annual temperature variability, trends, and extremes since 1500, *Science*, 303, 1499–1503, 2004.

- Novelli, P. C., Masarie, K. A., and Lang, P. M.: Distributions and recent changes of carbon monoxide in the lower troposphere, *J. Geophys. Res. Atmos.*, 103, 19015–19033, 1998.
- Nyeki, S., Kalberer, M., Colbeck, I., De Wekker, S., Furger, M., Gäggeler, H.W., Kossmann, M., Lugauer, M., Steyn, D., Weingartner, E., Wirth, M., and Baltensperger, U.: Convective Boundary Layer Evolution to 4 km als over High-Alpine Terrain: Airborne Lidar Observations in the Alps, *Geophys. Res. Lett.*, 27, 689–692, 2000.
- O'Doherty, S., Simmonds, P., Cunnold, D., Wang, H., Sturrock, G., Fraser, P., Ryall, D., Derwent, R., Weiss, R., Salameh, P., Miller, B., and Prinn, R.: In situ chloroform measurements at Advanced-Global Atmospheric Gases Experiment atmospheric research stations from 1994 to 1998, *J. Geophys. Res.*, 106, 20429–20444, 2001.
- Ohara, T., Akimoto, H., Kurokawa, J., Horii, N., Yamaji, K., Yan, X., and Hayasaka, T.: An Asian emission inventory of anthropogenic emission sources for the period 1980–2020, *Atmos. Chem. Phys.*, 7, 4419–4444, doi:10.5194/acp-7-4419-2007, 2007.
- Pfister, G., Petron, G., Emmons, L. K., Gille, J. C., Edwards, D. P., Lamarque, J. F., Attie, J. L., Granier, C., and Novelli, P. C.: Evaluation of CO simulations and the analysis of the CO budget for Europe, *J. Geophys. Res. Atmos.*, 109, D19304, doi:10.1029/2004JD004691, 2004.
- Reimann, S., Vollmer, M. K., Folini, D., Steinbacher, M., Hill, M., Buchmann, B., Zander, R., and Mahieu, E.: Observations of Anthropogenic Halocarbons at the High-Alpine site of Jungfraujoch for assessment of trends and European sources, *Sci. Tot. Environ.*, 391, 224–231, 2008.
- Rodgers, C. D.: Retrieval of atmospheric temperature and composition from remote measurements of thermal radiation, *Rev. Geophys. Space Phys.*, 14(4), 609–624, 1976.
- Rodgers, C. D.: Characterisation and error analysis of profiles retrieved from remote sounding measurements, *J. Geophys. Res.*, 95, 5587–5595, 1990.
- Rodgers, C. D.: Inverse methods for atmospheric sounding: Theory and Practice, Series on Atmospheric, Oceanic and Planetary Physics – Vol. 2, World Scientific, 2000.
- Rothman, L. S., Barbe, A., Benner, D. C., Brown, L. R., Camy-Peyret, C., Carleer, M. R., Chance, K., Clerbaux, C., Dana, V., Devi, V. M., Fayt, A., Flaud, J.-M., Gamache, R. R., Goldman, A., Jacquemart, D., Jucks, K. W., Lafferty, W. J., Mandin, J.-Y., Massie, S. T., Nemtchinov, V., Newnham, D. A., Perrin, A., Rinsland, C. P., Schroeder, J., Smith, K. M., Smith, M. A. H., Tang, K., Toth, R. A., Vander Auwera, J., Varanasi, P., and Yoshino, K.: The HITRAN Molecular Spectroscopic Database: Edition 2000 including Updates through 2001, *J. Quant. Spectrosc. Radiat. Transfer*, 82, 5–44, 2003.
- Ruckstuhl, A. F., Henne, S., Reimann, S., Steinbacher, M., Buchmann, B., and Hueglin, C.: Robust extraction of baseline signal of atmospheric trace species using local regression, *Atmos. Meas. Tech. Discuss.*, 3, 5589–5612, doi:10.5194/amtd-3-5589-2010, 2010.
- Simmonds, P. G., Manning, A. J., Derwent, R. G., Ciais, P., Ramonet, M., Kazan, V., and Ryall, D.: A burning question. Can recent growth rate anomalies in greenhouse gases be attributed to large-scale biomass burning events?, *Atmos. Environ.*, 39, 2513–2517, 2005.
- Tressol, M., Ordonez, C., Zbinden, R., Brioude, J., Thouret, V., Mari, C., Nedelec, P., Cammas, J.-P., Smit, H., Patz, H.-W., and Volz-Thomas, A.: Air pollution during the 2003 European heat wave as seen by MOZAIC airliners, *Atmos. Chem. Phys.*, 8, 2133–2150, doi:10.5194/acp-8-2133-2008, 2008.
- van der Werf, G. R., Randerson, J. T., Giglio, L., Collatz, G. J., Mu, M., Kasibhatla, P. S., Morton, D. C., DeFries, R. S., Jin, Y., and van Leeuwen, T. T.: Global fire emissions and the contribution of deforestation, savanna, forest, agricultural, and peat fires (1997–2009), *Atmos. Chem. Phys.*, 10, 11707–11735, doi:10.5194/acp-10-11707-2010, 2010.
- Wernli, H. and Davies, H. C.: A Lagrangian-based analysis of extratropical cyclones. I: The method and some applications., *Q. J. Roy. Meteorol. Soc.*, 123, 467–489, 1997.
- Wild, O. and Prather, M. J.: Excitation of the primary tropospheric chemical mode in a global three-dimensional model, *J. Geophys. Res. Atmos.*, 105, 24647–24660, 2000.
- World Meteorological Organisation: Guide to Meteorological Instruments and Methods of Observations, WMO-No. 8 (Seventh edition), 2008.
- Yurganov, L. N., Blumenstock, T., Grechko, E. I., Hase, F., Hyer, E. J., Kasischke, E. S., Koike, M., Kondo, Y., Kramer, I., Leung, F.-Y., Mahieu, E., Mellqvist, J., Notholt, J., Novelli, P. C., Rinsland, C. P., Scheel, H. E., Shultz, A., Strandberg, A., Sussmann, R., Tanimoto, H., Velazco, V., Zander, R., and Zhao, Y.: A Quantitative Assessment of the 1998 Carbon Monoxide Emission Anomaly in the Northern Hemisphere Based on Total Column and Surface Concentration Measurements, *J. Geophys. Res.*, 109(D15), D15305, doi:10.1029/2004JD004559, 2004.
- Yurganov, L. N., Duchatelet, P., Dzhola, A. V., Edwards, D. P., Hase, F., Kramer, I., Mahieu, E., Mellqvist, J., Notholt, J., Novelli, P. C., Rockmann, A., Scheel, H. E., Schneider, M., Schulz, A., Strandberg, A., Sussmann, R., Tanimoto, H., Velazco, V., Drummond, J. R., and Gille, J. C.: Increased Northern Hemispheric carbon monoxide burden in the troposphere in 2002 and 2003 detected from the ground and from space, *Atmos. Chem. Phys.*, 5, 563–573, doi:10.5194/acp-5-563-2005, 2005.
- Zander, R., Demoulin, P., Ehhalt, D. H., Schmidt, U., and Rinsland, C. P.: Secular Increase of the Total Vertical Column Abundance of Carbon-Monoxide above Central-Europe since 1950, *J. Geophys. Res. Atmos.*, 94, 11021–11028, 1989.
- Zander, R., Mahieu, E., Demoulin, P., Duchatelet, P., Roland, G., Servais, C., Maziere, M. D., Reimann, S., and Rinsland, C. P.: Our changing atmosphere: Evidence based on long-term infrared solar observations at the Jungfraujoch since 1950, *Sci. Total Environ.*, 391, 184–195, 2008.
- Zellweger, C., Forrer, J., Hofer, P., Nyeki, S., Schwarzenbach, B., Weingartner, E., Ammann, M., and Baltensperger, U.: Partitioning of reactive nitrogen (NO_y) and dependence on meteorological conditions in the lower free troposphere, *Atmos. Chem. Phys.*, 3, 779–796, doi:10.5194/acp-3-779-2003, 2003.
- Zellweger, C., Hüglin, C., Klausen, J., Steinbacher, M., Vollmer, M., and Buchmann, B.: Inter-comparison of four different carbon monoxide measurement techniques and evaluation of the long-term carbon monoxide time series of Jungfraujoch, *Atmos. Chem. Phys.*, 9, 3491–3503, doi:10.5194/acp-9-3491-2009, 2009.
- Zurbenko, I. G.: The Spectral Analysis of Time Series. North-Holland, 248 pp., 1986.

Université
de Liège



Faculty of Sciences
Institute of Astrophysics and Geophysics

**Fluorine in the atmosphere:
Inorganic fluorine budget and long-term trends
based on FTIR measurements at Jungfraujoch**

A dissertation presented by Pierre Duchatelet
in fulfillment of the thesis requirement for the degree of
Doctor of Philosophy in Sciences

2011

The oral defense of this dissertation took place at the University of Liège on May 3rd, 2011. The thesis committee was composed of the following members:

Prof. Jean-Claude Gérard, University of Liège, Promoter
Prof. Pierre Magain, University of Liège, Chairman
Dr. Emmanuel Mahieu, University of Liège, Advisor

Dr. Martine de Mazière, BIRA-IASB, External examiner
Prof. Bertrand Calpini, MeteoSwiss, External examiner
Dr. Claude Camy-Peyret, Pierre and Marie Curie University, External examiner

Acknowledgements

First, I wish to thank Prof. Jean-Claude Gérard, Head of Unit of the Infrared Group of Atmospheric and Solar Physics of the University of Liège, to have accepted to be the promoter of this thesis.

I am also grateful to my thesis advisor, Dr. Emmanuel Mahieu, whose crucial guidance and support from the initial to the final level enabled me to develop an understanding of the subject and to definitely improve the scientific quality of this research. I am thankful for his time spent to read this thesis and to always give constructive critical comments.

I additionally benefited from the constructive contribution and from the long scientific experience of Dr. Rodolphe Zander, whose valuable advices and fruitful comments were very much appreciated.

Many thanks further go to past and current colleagues of my research team (Jacqueline Bosseloirs, Dr. Luc Delbouille, Philippe Demoulin, Olivier Flock, Bernard Lejeune, Dr. Ginette Roland, Dr. Christian Servais, Vincent Vandeweerd and Diane Zander) for collecting FTIR data at Jungfraujoch over the years, for crucial developing work of FTIR instrumentation or for technical support.

Thanks are also extended to all collaborators (including colleagues from the Royal Observatory of Belgium and from the Belgian Institute for Space Aeronomy) who contributed to FTIR data acquisition at Jungfraujoch and to the whole staff of the Jungfraujoch station.

I am also very grateful to Dr. Martine de Mazière (Belgian Institute for Space Aeronomy), Prof. Bertrand Calpini (Meteoswiss) and Dr. Claude Camy-Peyret (Pierre and Marie Curie University) who have spontaneously agreed to join my thesis committee. Prof. Pierre Magain (University of Liège) is further acknowledged for accepting to be the chairman of my jury.

I would like to thank scientific members of the ACE-FTS team (Prof. Peter Bernath, Dr. Chris Boone and Dr. Kaley Walker), of the KASIMA team (Dr. Roland Ruhnke), of the SLIMCAT team (Prof. Martyn Chipperfield and Dr. Wuhu Feng) and of the AGAGE network (Dr. Jens Mühle) for providing data and for productive collaboration during the last years.

I am grateful to Dr. Frank Hase and Dr. Matthias Schneider (Institute for Meteorology and Climate Research, Karlsruhe Institute of Technology, Germany) for their strong support during my learning phase with the PROFFIT code as well as to all members of the same research unit for their welcome during my stay in Karlsruhe.

Finally, I would like to thank my family for the support they provided me through my entire life. In particular, I must acknowledge my wife, Aline, whose love and persistent confidence in me were essential. My thoughts are also going to my son, Matthias, whose birth gave another meaning to my life.

Abstract

High resolution solar spectra are routinely recorded since more than two decades by the University of Liège at the International Scientific Station of the Jungfraujoch (Swiss Alps, 46.5°N, 8.0°E, 3580 m asl) with Fourier Transform Infrared (FTIR) spectrometers. Over the last years, major improvements have been implemented in the algorithms used to retrieve the abundances of atmospheric constituents accessible to the FTIR technique. Now, in addition to total column, information on the vertical distribution of the target gas is often available, allowing producing partial column data sets. We take advantage of these improvements to generate and characterize long-term total and partial columns time series of some important inorganic fluorinated trace gases deduced from FTIR measurements performed at Jungfraujoch.

First, our investigations on hydrogen fluoride (HF) indicate that the adoption of a Galatry line shape model for this species significantly improves the fitting quality of the retrievals. The sensitivity of our FTIR measurements to HF inversions in three distinct regions that range from the low to the high stratosphere is confirmed thanks to products derived from two satellites and from two numerical models. We further demonstrate that the HF seasonal variations that occur in the low stratosphere are mainly responsible for the seasonal cycle observed in our HF total column time series.

We have also developed an original multi-spectrum multi-window retrieval strategy allowing to derive, for the first time, some information on the vertical distribution of carbonyl fluoride (COF₂) from ground-based FTIR measurements. After comparison with model data, our COF₂ and HF FTIR datasets are combined to assess the atmospheric inorganic fluorine burden F_y .

A trend analysis of our HF, COF₂ and F_y time series is then performed for four different time periods spanning the 1985-2010 time interval. While we observe a recent stabilization for HF, corresponding COF₂ data show a significant rise, after a period of significant reduction in its accumulation rate. This is probably ascribable to the combination of the decrease of its main source gas CFC-12 with the increase of the substitute product HCFC-22. However, this increase in the COF₂ rate of change does not significantly impact the F_y trend, which is essentially driven by the change in HF. In addition, we show that the partitioning between the two major fluorine reservoirs HF and COF₂ has not changed since the beginning of this century. Together, they account for around 95% of total inorganic fluorine in the atmosphere.

Finally, we study the long-term evolution of carbon tetrafluoride (CF₄), for the first time from ground-based FTIR measurements. The trend analysis of our time series indicates a slowing, initiated during the nineties, in the CF₄ growth rate despite the fact that the absolute loading of this compound is still increasing. Our linear accumulation rates are consistent with those deduced from space or surface measurements.

Résumé

Des spectres d'absorption solaire à haute résolution sont enregistrés de façon régulière depuis plus de vingt ans par l'Université de Liège à la Station Scientifique Internationale du Jungfraujoch (Alpes suisses, 46.5°N, 8.0°E, 3580 m) à l'aide de spectromètres par transformée de Fourier opérant dans l'infrarouge (FTIR). Au cours des dernières années, d'importantes améliorations ont été apportées aux algorithmes d'inversion des observations FTIR. Il est maintenant possible de déduire de l'information sur la distribution verticale du gaz cible et de générer des ensembles de données de colonnes partielles en plus des colonnes totales. Nous tirons profit de ces améliorations pour produire et caractériser les séries temporelles à long terme de colonnes totale ou partielle de quelques principaux gaz en trace inorganiques fluorés, au départ des données FTIR enregistrées au Jungfraujoch.

Tout d'abord, nos investigations menées sur le fluorure d'hydrogène (HF) indiquent que l'adoption pour ce gaz d'un modèle de raie de Galatry aide à minimiser de façon significative les résidus systématiques des inversions. La sensibilité de nos mesures FTIR aux inversions de HF dans trois régions de la basse à la haute stratosphère est confirmée à l'aide des produits correspondant issus de deux satellites et de deux modèles numériques. Nous démontrons en outre que ce sont les variations saisonnières de HF ayant lieu dans la basse stratosphère qui dictent le cycle saisonnier observé dans notre série des colonnes totales de HF.

Nous avons également développé une stratégie d'inversion originale qui combine plusieurs spectres FTIR et plusieurs micro-fenêtres spectrales afin d'obtenir, pour la première fois, de l'information sur la distribution verticale de l'oxyfluorure de carbone (COF_2) à partir de mesures FTIR sol. Après comparaison avec des données issues de modèles, nos abondances FTIR de COF_2 sont combinées à celles de HF afin de déterminer et de caractériser la charge atmosphérique en fluor inorganique F_y .

Une analyse de tendance de nos séries temporelles de HF, COF_2 et F_y est ensuite réalisée pour quatre périodes différentes entre 1985 et 2010. Tandis qu'une stabilisation dans le taux de croissance de HF est observée, le taux d'accumulation de COF_2 ré-augmente de manière significative après une période de croissance moins soutenue. Cela résulte probablement des effets combinés de la diminution de son principal gaz source CFC-12 et de l'augmentation du produit de substitution HCFC-22. Toutefois, cette augmentation du taux de croissance de COF_2 n'influence pas significativement le taux de croissance de F_y qui demeure assez stable au cours des dix dernières années. En outre, le partitionnement entre les deux principaux réservoirs de fluor HF et COF_2 n'a pas évolué depuis le début du XXI^e siècle. Ensemble, ils représentent environ 95% de la charge totale de fluor inorganique présent dans l'atmosphère.

Finalement, nous étudions l'évolution à long terme du tétrafluorure de carbone (CF_4), pour la première fois à partir de mesures FTIR sol. L'analyse de notre série temporelle indique un ralentissement, initié dans les années 1990, du taux d'accumulation de ce composé, même si sa charge atmosphérique absolue augmente toujours. Les taux linéaires d'accumulation que nous avons déduits sont cohérents avec ceux obtenus à partir de mesures spatiales ou de surface.

Table of Contents

Introduction

Chapter 1 – Halogenated compounds in the Earth’s atmosphere.....	1.1
1.1. Overview of the Earth’s atmosphere.....	1.2
1.1.1. Chemical composition.....	1.2
1.1.2. Vertical structure.....	1.3
1.1.3. Atmospheric dynamic and transport.....	1.4
1.2. Halogenated compounds in the Earth’s atmosphere.....	1.10
1.2.1. Inventory, sources and sinks.....	1.10
1.2.2. Controlling the harmful effects of halogens on the atmosphere.....	1.18
1.2.3. Recent trends and potential future evolution of CFCs, HCFCs and HFCs..	1.23
References.....	1.27
Chapter 2 – FTIR measurements at Jungfraujoch.....	2.1
2.1. Basics of the FTIR technique.....	2.2
2.2. FTIR observations at the Jungfraujoch.....	2.5
2.3. Inversion and characterization of FTIR products.....	2.8
2.4. The problematic of the instrumental line shape.....	2.16
References.....	2.19
Chapter 3 – Long-term FTIR time series of hydrogen fluoride.....	3.1
3.1. Introduction.....	3.3
3.2. HF observational database and retrieval strategy.....	3.4
3.2.1. A priori information.....	3.5
3.2.2. Fitting algorithm.....	3.6
3.2.3. Choice of line shape model.....	3.7
3.2.4. Information content and error budget.....	3.9
3.3. FTIR HF time series at Jungfraujoch and intercomparison.....	3.11
3.3.1. FTIR versus space data.....	3.12
3.3.2. FTIR versus model data.....	3.15
3.4. Summary and conclusions.....	3.24
Appendix A.....	3.25
A.1. Additional FTIR database statistics.....	3.25
A.2. Retrieval input parameters.....	3.26
A.3. HF information content analysis.....	3.26
A.4. HF total and partial columns error budget.....	3.28
A.5. Latitudinal effect on the HF seasonal cycle based on HALOE climatology...	3.30
References.....	3.32
Chapter 4 – FTIR multi-spectrum multi-window fitting of carbonyl fluoride	4.1
4.1. Introduction.....	4.3
4.2. Retrieval strategy.....	4.4

4.3. Information content and error budget.....	4.7
4.4. Discussion of line parameters and retrieval approach.....	4.12
4.5. Comparisons with model data.....	4.16
4.6. Conclusions and perspectives.....	4.21
References.....	4.22
Chapter 5 – The inorganic fluorine budget above Jungfraujoch.....	5.1
5.1. Overview of previous fluorine inventories.....	5.2
5.2. Databases and method for determining inorganic fluorine above Jungfraujoch.....	5.4
5.3. Results and discussion.....	5.10
5.3.1. Inorganic fluorine trend analysis and partitioning.....	5.10
5.3.2. Hypothesis for trends explanation.....	5.19
References.....	5.22
Chapter 6 – FTIR monitoring of carbon tetrafluoride.....	6.1
6.1. Introduction.....	6.1
6.2. FTIR measurements of CF ₄ at Jungfraujoch.....	6.6
6.2.1. Introduction.....	6.7
6.2.2. FTIR measurements and retrieval strategy.....	6.8
6.2.3. Results and discussion.....	6.11
6.2.4. Summary and conclusions.....	6.15
References.....	6.16
General conclusions and perspectives	
Appendix A – The bootstrap resampling method	
Appendix B – List of acronyms	
Appendix C – List of publications	

List of Figures

Chapter 1

Figure 1.1: Relative abundances of the main constituents of the Earth's atmosphere.....	1.2
Figure 1.2: Typical mid-latitude atmospheric temperature profile.....	1.4
Figure 1.3: The global circulation of the Earth's atmosphere.....	1.5
Figure 1.4: General configuration and cross section of the polar and subtropical jet streams.....	1.7
Figure 1.5: Connection between Rossby waves with the formation of depressions and anticyclones in the northern hemisphere.....	1.9
Figure 1.6: Schematic representation of the Brewer Dobson circulation.....	1.9
Figure 1.7: Schematic representation of the formation of major stratospheric fluorine reservoirs.....	1.16
Figure 1.8: Example of average northern mid-latitudes profiles for some fluorinated sources and reservoirs recorded by ACE-FTS.....	1.17
Figure 1.9: Global annual anthropogenic production of the main halogenated source gases between 1980 and 2007.....	1.20
Figure 1.10: Global greenhouse gases emissions derived from six different IPCC emission scenarios and global averages of surface warming.....	1.23
Figure 1.11: Time series of CFC-12, CFC-11 and HCFC-22 derived from FTIR observations above Jungfraujoch.....	1.24
Figure 1.12: Annual global mean mole fraction of HCFC-141b, HCFC-142b and HFC-134a derived from the AGAGE and the NOAA/ESRL networks.....	1.25
Figure 1.13: Temporal evolution of the atmospheric content of the most abundant CFCs and HCFCs until the middle of this century.....	1.27

Chapter 2

Figure 2.1: Optical configuration of a Michelson interferometer.....	2.2
Figure 2.2: The convolution product of a spectrum composed by Dirac delta function with the Fourier transform of a boxcar function.....	2.4
Figure 2.3: The International Scientific Station of the Jungfraujoch.....	2.5
Figure 2.4: The Bruker IFS-120HR Fourier transform spectrometer in operation at Jungfraujoch.....	2.7
Figure 2.5: Experimental spectra recorded with the Bruker 120HR spectrometer for the six most frequently used bandpass filters at Jungfraujoch.....	2.8
Figure 2.6: Simplified representation of the inverse problem.....	2.9
Figure 2.7: Columns of the COF ₂ VMR-altitude correlation matrix versus the altitude.....	2.13
Figure 2.8: Time evolution of the EAP characterizing the Bruker spectrometer in station at Jungfraujoch.....	2.17
Figure 2.9: Deseasonalized time series of EAP derived from atmospheric O ₃ observations above Jungfraujoch.....	2.18
Figure 2.10: Example of HF retrieved profiles with PROFFIT derived before the Bruker realignment when EAP correction is applied.....	2.18

Chapter 3

Figure 3.1: A priori HF VMR profile and corresponding variability profile adopted for our FTIR HF retrievals.....	3.6
Figure 3.2: Impact of the adoption of a Voigt or a Galatry line shape model on HF retrieved profiles and on the fitting residuals.....	3.9
Figure 3.3: HF error budget for different systematic and statistical error sources..	3.11
Figure 3.4: HF partial columns as observed at Jungfraujoch by FTIR technique and by space occultations (HALOE and ACE-FTS).....	3.13
Figure 3.5: HF total and partial column time series derived from FTIR measurements and from SLIMCAT and KASIMA CTMs.....	3.17
Figure 3.6: HF seasonal cycles derived from FTIR and model time series.....	3.19
Figure 3.7: Typical example of individual HF retrieved profiles when different tropopause heights are observed.....	3.22
Figure 3.8: Typical individual and merged HF averaging kernels and corresponding three first eigenvectors.....	3.27
Figure 3.9: HF monthly mean concentrations derived from the HALOE climatology at three different equivalent latitudes and pressure levels.....	3.31

Chapter 4

Figure 4.1: A priori information used for our COF ₂ profile inversions.....	4.6
Figure 4.2: Typical information content for COF ₂ retrievals from ISSJ spectra....	4.9
Figure 4.3: Selection of microwindows for COF ₂ profile inversions.....	4.10
Figure 4.4: Example of COF ₂ vertical profiles derived by applying the multi-spectrum approach to FTIR ground-based observations at Jungfraujoch...	4.13
Figure 4.5: Relative mean differences between COF ₂ vertical profiles, total and partial columns retrieved from InSb and MCT spectra ranges.....	4.14
Figure 4.6: COF ₂ partial columns time series as observed by FTIR technique at Jungfraujoch and as computed by KASIMA and SLIMCAT CTMs.....	4.17
Figure 4.7: COCIF partial columns time series as observed by ACE-FTS and as computed by KASIMA and SLIMCAT CTMs.....	4.20

Chapter 5

Figure 5.1: Stratospheric fluorine inventory derived from ACE-FTS in five different latitude belts.....	5.3
Figure 5.2: COCIF absorption features used by ACE-FTS for its COCIF retrievals.....	5.5
Figure 5.3: Time series of monthly mean total columns of 2 x COF ₂ , HF and F _y [*] derived from FTIR measurements at Jungfraujoch.....	5.10
Figure 5.4: Time series of FTIR monthly mean total columns of 2 x COF ₂ , HF and F _y [*] compared with corresponding modeled data from KASIMA and SLIMCAT.....	5.11
Figure 5.5: Mean atmospheric COF ₂ , HF and F _y [*] growth rates computed from FTIR, model and space data over four successive time periods.....	5.14
Figure 5.6: Global temporal evolution of organic fluorine at the Earth's surface and in the stratosphere, according to A1 emission scenario.....	5.20

Chapter 6

Figure 6.1: CF ₄ emissions by major source categories in the EDGAR v4.0 datasets.....	6.1
Figure 6.2: Electrolytic bath used for the production of primary aluminum.....	6.2
Figure 6.3: Percentage change in primary aluminum production and total direct greenhouse gas emissions from all primary aluminum production processes.....	6.3
Figure 6.4: Global CF ₄ emissions from several experimental datasets, numerical model inversions or estimates derived from surveys.....	6.4
Figure 6.5: CF ₄ microwindow used for our FTIR retrievals and typical example of the adjustment with the SFIT-2 code of an FTIR spectrum.....	6.10
Figure 6.6: FTIR time series of CF ₄ total columns above the Jungfraujoch.....	6.12
Figure 6.7: FTIR, AGAGE and satellite CF ₄ VMR monthly time series and corresponding linear trend fits.....	6.13

List of Tables

Chapter 1

Table 1.1: Recent typical global concentrations of some atmospheric gases.....	1.3
Table 1.2: Mean abundances and lifetimes of the main halogenated source gases	1.11
Table 1.3: Major organic degradation products of some HCFCs and HFCs.....	1.14
Table 1.4: ODP and GWP for 100-yr time horizon of the most abundant atmospheric fluorine source gases.....	1.19
Table 1.5: Phase out schedule of depleting ozone substances adopted by non-developing countries during the Montreal Protocol.....	1.21
Table 1.6: Recent growth rates of the most abundant CFCs, HCFCs and HFCs....	1.26

Chapter 2

Table 2.1: Main characteristics of the six most frequently used bandpass filters at Jungfraujoch.....	2.8
---	-----

Chapter 3

Table 3.1: HF microwindow used for our FTIR retrievals.....	3.5
Table 3.2: Error sources taken into account in our HF error budget with PROFFIT 9.5.....	3.10
Table 3.3: Statistics of the relative differences between the HF daily mean partial columns derived from FTIR measurements and coincident satellite observations.....	3.13
Table 3.4: Statistics of the relative differences between the HF daily mean partial columns derived from FTIR measurements and coincident model calculations.....	3.18
Table 3.5: HF main seasonal cycle characteristics.....	3.20
Table 3.6: Correlation coefficients between HF partial/total columns derived from FTIR measurements or model runs and corresponding tropopause heights.....	3.23
Table 3.7: Main characteristics of FTIR spectra analyzed in the present study.....	3.25
Table 3.8: Main regularization parameters and ancillary inputs adopted for our final HF inversions with PROFFIT 9.5.....	3.26
Table 3.9: Main systematic and statistical errors for HF total and partial columns at Jungfraujoch for a Galatry and for a Voigt line shape model.....	3.29
Table 3.10: Main characteristics of the FTIR spectra selected for our HF error budget evaluation.....	3.30

Chapter 4

Table 4.1: Microwindows selected for COF ₂ profile inversions.....	4.5
Table 4.2: Typical information content of microwindows sets selected for COF ₂ profile inversions.....	4.7
Table 4.3: Major random and systematic error sources and resulting relative uncertainties affecting COF ₂ total and partial columns.....	4.12

Table 4.4: Number of COF ₂ lines in each microwindow, as listed in the HITRAN 1996 and HITRAN 2004 spectroscopic line lists.....	4.15
Table 4.5: COF ₂ main seasonal cycle characteristics.....	4.18

Chapter 5

Table 5.1: Some characteristics of the five datasets involved in our inorganic fluorine inventory.....	5.4
Table 5.2: HF, COF ₂ and COCIF production and destruction reactions assumed by the KASIMA model.....	5.7
Table 5.3: HF, COF ₂ and COCIF production and destruction reactions assumed by the SLIMCAT model.....	5.8
Table 5.4: COF ₂ , HF and F _y [*] linear trends computed from FTIR and model data for four successive time periods.....	5.13
Table 5.5: COF ₂ , HF and F _y [*] linear trends computed from ACE-FTS and HALOE data.....	5.16
Table 5.6: Partitioning between HF, COF ₂ and COCIF derived from FTIR, model and space data.....	5.18

Chapter 6

Table 6.1: Impact of major sources of random and systematic errors on typical individual CF ₄ total column retrievals above the Jungfraujoch.....	6.11
Table 6.2: CF ₄ linear growth rates for the 1990-2010 time period.....	6.14

Introduction

Many of the well-known changes that have affected or still influence the chemical composition of the Earth's atmosphere on a global scale are of human origin. It is widely accepted that the increase in the magnitude of such anthropogenic perturbations starts with the agricultural and industrial revolutions around 1850 and has potentially important consequences on our future climate, with numerous potential impacts on the biosphere. The discovery of the formation of an ozone hole over Antarctica during the eighties, the increasing trends in the atmospheric abundance of most of the long-lived greenhouse gases as well as in the tropospheric concentration of air pollutants constitute some examples of important changes observed during the last decades.

In that context, the atmospheric chemistry community is now devoting a large amount of its efforts to the study of the global change. In particular, to well understand the physical and chemical processes that control the Earth's atmosphere, as well as the interactions that exist between its different regions, it is necessary to know in details the spatial distribution and the temporal behavior of the atmospheric trace gases. A better knowledge of the chemical composition of our atmosphere is also essential to establish the current state of our environment, to explain its past and present changes and to predict its future evolution. Such improved understanding of our atmosphere is also indispensable to provide a solid scientific basis to the political decisions internationally adopted to regulate the anthropogenic emissions of trace gases that have been identified as efficient stratospheric ozone depleting substances or as strong greenhouse gases.

Among the list of gases whose anthropogenic emissions are directly targeted by the Montreal or the Kyoto Protocols, we find several fluorine-containing species. In particular, the photodecomposition in the lower stratosphere of the man-made halogenated source gases, i.e. the ozone depleting chlorofluorocarbons (CFCs) and their substitute products the hydrochlorofluorocarbons (HCFCs) and the hydrofluorocarbons (HFCs), that are all strong greenhouse gases, notably releases fluorine atoms in the atmosphere and thus widely feeds the two most abundant stratospheric inorganic fluorine reservoirs that are hydrogen fluoride (HF) and carbonyl fluoride (COF_2). Even if fluorine is not significantly involved in the depletion of stratospheric ozone, measurements of individual atmospheric fluorine-bearing species remain important as they indirectly reflect the amount of the above-mentioned source gases – that also often contain chlorine atoms, precursors of the ozone layer destruction – injected in the atmosphere by human activities. Moreover, such measurements also provide an insight into the partitioning between major

fluorine sources and reservoirs and allow to establish a global inventory of inorganic (F_y), organic (CF_y) and total (F_{TOT}) fluorine. When monitored as a function of time, these inventories reflect the man-made changes in the emissions of anthropogenic halogenated source gases regulated by the Montreal and the Kyoto Protocols and therefore provide an opportunity to check the effectiveness of such Protocols. The Chapter 1 of the present study is largely devoted to atmospheric fluorine: we notably describe the chemical reactions that lead to the formation of inorganic fluorine compounds from halogenated source gases and we explain how the emissions of these later species have been regulated in order to control their detrimental effects on the Earth's atmosphere.

Obviously, to derive precisely the trends in the atmospheric amounts of trace gases, long-term series are necessary. At northern mid-latitudes, such historical ground-based observations are collected by the University of Liège since more than two decades at the International Scientific Station of the Jungfraujoch (Swiss Alps, 46.5°N, 8.0°E, 3580 m asl) by using two state-of-the-art Fourier transform spectrometers (FTS) that operate at high resolution in the infrared (IR). The systematic monitoring of the chemical composition of the Earth's atmosphere from such FTIR observations at Jungfraujoch has started in 1984, in the continuity of grating spectrometer measurements that have already gone on for about ten years.

The spectroscopic data so collected at Jungfraujoch by the University of Liège have already proved to be extremely useful for the study of the variability and the long-term trend of various atmospheric species. Combined with its unequalled length, the high quality of the FTIR database of the Jungfraujoch definitely justify why this scientific station has been selected in 1989 as one of the primary component of the Network for the Detection of Atmospheric Composition Change (NDACC), a worldwide network historically created in support of the 1985 Vienna Convention for the Protection of the Ozone Layer and whose primary objectives are: (1) the detection of trends in overall atmospheric composition and the understanding of their impacts on both the stratosphere and the troposphere, and (2) the establishment of links between the global climate change and the atmospheric chemical composition.

The databases gathered at Jungfraujoch over the years are usually expressed in terms of vertical total columns and are derived with a retrieval algorithm (SFIT-1) that exploits the temperature dependence of the absorption lines encompassed in the FTIR spectra. However, since the beginning of this century, new retrieval algorithms based on a statistical approach that combines the FTIR measurement with the best a priori information available additionally allow to derive information on the vertical distribution of the target gas as well as partial column values. Moreover, the products retrieved with these codes can also be fully characterized in terms of information content and error budget. Currently, the SFIT-2 and the PROFFIT algorithms are the two reference retrieval codes adopted within the FTIR community. While the first part of Chapter 2 is dedicated to the description of the FTIR technique and of the FTIR instrumentation in operation at the Jungfraujoch station since the mid-eighties, its second part essentially describes the mathematical aspects on which the two above-mentioned retrieval codes are based.

The goals of the present study are multiple. First of all, we will take advantage of the recent and numerous possibilities proposed by the SFIT-2 and PROFFIT codes to

produce, from long-term FTIR measurements at Jungfraujoch, updated time series of HF and COF₂ to be archived at NDACC. These updated, and sometimes innovative for some aspects, retrieval strategies are fully described in Chapters 3 and 4, respectively. In addition, in order to validate our FTIR time series, Chapters 3 and 4 also include several comparisons with satellite measurements or with data derived from numerical model runs. All results presented in Chapters 3 and 4 are part of two scientific papers published in 2010 and 2009, respectively.

Based on these FTIR datasets, a complete reassessment of the inorganic fluorine burden F_y (for which HF and COF₂ contribute for the largest part in the stratosphere) for the northern mid-latitudes is then performed (Chapter 5). The discussion notably includes comparisons with satellite and model data. For all HF, COF₂ and F_y time series, we further present a trend analysis for four different successive time periods between 1985 and 2010. This especially allows characterizing the changes that have occurred in the atmospheric abundances of the major stratospheric fluorine reservoirs during the last 25 years. These observed changes are discussed in the context of past and current emissions of halogenated source gases and are compared with the trends derived from space instrument and model run data. Both satellite and model data also help us to reassess the partitioning between major inorganic fluorine reservoirs. The original results presented in Chapter 5 are part of a scientific publication to be submitted this year.

Finally, to complement our studies concerning the inorganic fluorine described in Chapters 3-5, the Chapter 6 focuses on the possibilities to derive, from ground-based FTIR observations and with the SFIT-2 code, the atmospheric abundance of another fluorinated compound, carbon tetrafluoride (CF₄ or PFC-14). The importance of monitoring the atmospheric burden of this gas is mainly double. First of all, with an atmospheric lifetime of several thousands of years and with a high global warming potential, CF₄ figures among the various greenhouse gases targeted by the Kyoto Protocol. Secondly, due to lacking or incomplete CF₄ emissions factor from inventories performed in industrial fields, it is difficult to precisely quantify the real magnitude of CF₄ emissions coming from human activities. The present contribution is innovative in the sense that to our knowledge, no CF₄ time series derived from ground-based FTIR measurements have been published to date. Without a shadow of a doubt, the ability to monitor CF₄ from FTIR measurements at Jungfraujoch is mainly ascribable to the exceptional observation conditions offered by this high-altitude site. Again, the original results presented in Chapter 6 are part of a scientific publication to be submitted this year.

Chapter 1

Halogenated compounds in the Earth's atmosphere

Interest in the study of halogenated compounds in the atmosphere mainly resulted from the proposal in the early seventies that the chemistry of chlorine in the stratosphere could lead to the destruction of the ozone layer and that man-made chlorofluorocarbons (CFCs) could be a significant source of stratospheric chlorine [Stolarski and Cicerone 1974; Molina and Rowland, 1974]. Although the CFCs constitute the largest fraction of halogen burden in the atmosphere, a significant number of additional halogenated compounds, like Halons, hydrochlorofluorocarbons (HCFCs) and hydrofluorocarbons (HFCs) have to be considered to establish a complete atmospheric halogen budget. Altogether, these trace gases are very often referred to as halogenated source gases.

In the stratosphere, the photodissociation of the halogenated source gases frees fluorine, chlorine and bromine atoms. It is now well established that both chlorine and bromine are subsequently involved in catalytic destruction cycles of stratospheric ozone. In most cases, given the combination of long lifetimes with strong absorption features in the infrared, the halogenated source gases are also significant contributors to the Earth's global warming. As a result, anthropogenic emissions of halogenated compounds are regulated by the Montreal Protocol (1989) or by the Kyoto Protocol (1997). The effectiveness of such Protocols could be notably evaluated by monitoring the evolution with time of the loading of the main stratospheric fluorine reservoirs.

The main objective of this Chapter is to present the principal characteristics of the atmospheric halogenated compounds. Then we discuss their sources and sinks, with a special attention on the chemical reactions that lead to the release of halogen atoms in the atmosphere. After a description of the practical decisions adopted by the international authorities to limit the accumulation of halogenated compounds in the Earth's atmosphere, we evaluate the consequences of these decisions by providing an inventory of recent growth rates of the most abundant CFCs, HCFCs and HFCs. For CFCs and HCFCs, a perspective of future trends is also given. But before, this Chapter provides a short overview of the Earth's atmosphere, with an emphasis on atmospheric dynamics and transport, that both play an important role in the vertical and latitudinal distributions of halogenated gases.

1.1. Overview of the Earth's atmosphere

1.1.1. Chemical composition

The Earth's atmosphere is the thin gaseous layer that surrounds our planet. Despite its very weak thickness in comparison with the Earth's radius, our atmosphere plays a crucial role in the filtering process of solar radiations that is essential for the life on Earth. The Earth's atmosphere is made (in volume) of about 78% nitrogen (N_2) and of about 21% oxygen (O_2), the remaining $\sim 1\%$ being mainly attributed to Argon (Ar). These three gases are deservedly called the major constituents (Figure 1.1). The many remaining constituents, that altogether account for less than 1% in volume of the chemical composition of our atmosphere, can be classified into two different categories. The first category, called minor constituents, includes water vapor (H_2O), whose concentration is extremely variable in the atmosphere, methane (CH_4), hydrogen (H_2), nitrous oxide (N_2O), carbon monoxide (CO) and ozone (O_3). The second category includes a large number of constituents, the trace gases, whose impact on the Earth's radiative budget or on its atmospheric chemical composition could be significant, despite the fact that atmospheric concentrations of these trace gases are very low. Among trace gases, one can cite carbon compounds (C_2H_6 , C_2H_2 , H_2CO , etc.), sulfur compounds (SO_2 , OCS , etc.) and halogenated gases (such as chlorofluorocarbons or CFCs), that bear one or several halogens (i.e. fluorine, chlorine, bromine or iodine atoms) and that are closely related to the problematic of the ozone layer depletion (see section 1.2).

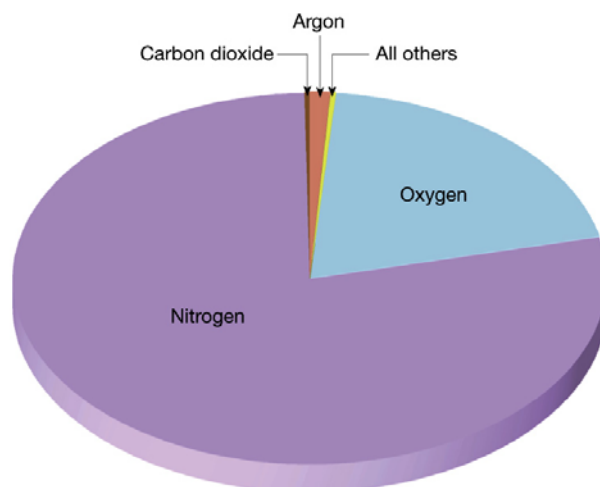


Fig. 1.1. Relative abundances of the main constituents of the Earth's atmosphere (Figure extracted from Lutgens and Tarbuck, 2001).

The abundance of atmospheric gases is often expressed in terms of volume mixing ratio (VMR), which represents the ratio between the volume occupied by the considered gas and the corresponding volume of dry air. Units frequently used are part per million by volume (ppmv, 10^{-6}), part per billion by volume (ppbv, 10^{-9}) and part per trillion by volume (pptv, 10^{-12}). Table 1.1 provides actual typical global concentrations of some of the atmospheric gases evoked above. The large seasonal and latitudinal variability characterizing tropospheric formaldehyde is linked to its relatively short atmospheric lifetime, of a few hours.

	Gas	Concentration (in dry air)
Major components	Nitrogen (N ₂)	780840 ppmv ^a
	Oxygen (O ₂)	209460 ppmv ^a
	Argon (Ar)	9340 ppmv ^a
Minor components	Carbon dioxide (CO ₂)	385 ppmv ^b
	Stratospheric ozone (O ₃)	1-10 ppmv ^c
	Methane (CH ₄)	1797 ppbv ^b
	Hydrogen (H ₂)	550 ppbv ^a
	Nitrous oxide (N ₂ O)	322 ppbv ^b
Trace gases	CFC-12 (CCl ₂ F ₂)	544 pptv ^c
	CFC-11 (CCl ₃ F)	253 pptv ^c
	Upper tropospheric formaldehyde (H ₂ CO)	10-170 pptv ^d
	Halon-1211 (CBrClF ₂)	4 pptv ³

^a According to Lutgens and Tarbuck, 2001.

^c According to WMO, 2007.

^b According to WMO, 2009.

^d Above Europe, according to Dufour et al., 2009.

Table 1.1. Recent typical global concentrations of some atmospheric gases.

1.1.2. Vertical structure

Along the vertical direction, the Earth's atmosphere is mainly subject to the gravity that is responsible for the exponential decrease of the pressure with altitude. In addition, as a result of different heating and cooling mechanisms, the atmosphere is not isotherm and can be divided in different layers, based on the successive minima and maxima observed in the temperature vertical distribution (Figure 1.2).

Starting from the ground, the first layer is the troposphere that extends up to the tropopause. In the troposphere, the temperature decreases regularly with altitude (with a typical gradient of $-5^{\circ}\text{C}/\text{km}$), since the main source of heating is the infrared radiation emitted by the ground. This negative gradient makes the troposphere dynamically instable and convective. As a consequence, it is in the troposphere that occur most of the meteorological phenomena that define the weather conditions observed at the ground level. It is also in the troposphere that all anthropogenic gases are directly emitted. A first minimum in the temperature profile is reached at the tropopause. The altitude of the tropopause varies significantly, mainly according to the latitude and to the season. On average, the tropopause is close to 8 km in the polar regions and close to 18 km near the equator.

Above the tropopause, we find the stratosphere, where the temperature gradient increases with altitude due to the heat production caused by the absorption of solar ultraviolet radiation (i.e. UV-C, whose wavelengths λ are lower than 280 nm) by ozone. Indeed, the ozone vertical distribution peaks at its maximum in the stratosphere, near 35 km (i.e. the stratospheric ozone layer). This increase of temperature with altitude makes the stratosphere dynamically stable: the convection is weak and most of the air masses displacements are horizontal, leading to a stratified structure of this layer. The maximum heating of the stratosphere is reached at the stratopause, at an altitude close to 50 km.

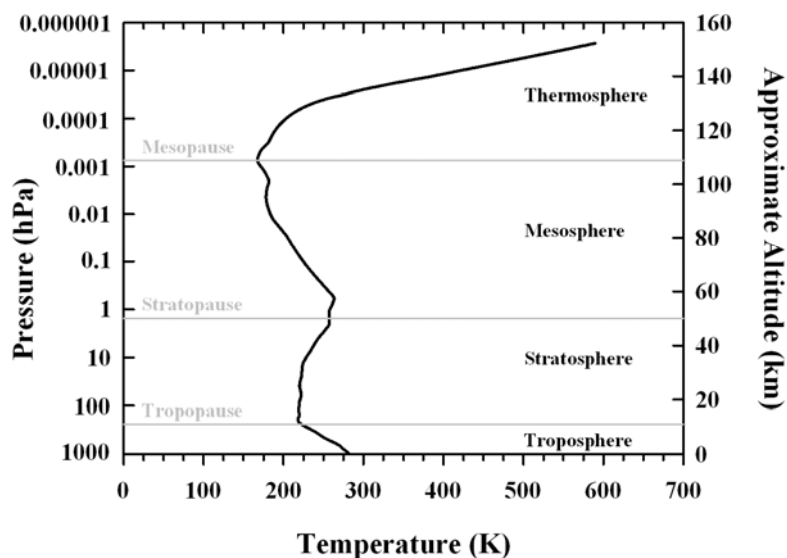


Fig. 1.2. Typical midlatitude atmospheric temperature profile. The major regions of the atmosphere as well as temperature inversion points are indicated in black and grey, respectively.

The layer above the stratopause is the mesosphere, where temperature decreases again with altitude, due to infrared emissions by atomic oxygen, NO and CO₂. A new minimum in the temperature profile is reached at the mesopause. Above the mesopause, the temperature increase again with altitude in the thermosphere, as a consequence of the absorption of the solar far UV radiation (i.e. $\lambda < 200$ nm) by molecular oxygen and despite the fact that the density becomes very low above 100 km. High temperatures that are reached in the thermosphere widely depend on the solar activity. Due to the gravity, lightest gases (such as hydrogen and helium) are the most abundant with increasing altitude. Ionization phenomena (like aurora) are linked to the interactions between the Earth's magnetic field and the solar flux and occur near the top of the Earth's atmosphere.

It is important to notice that altitudes of boundaries given here are representative, but they are subject to significant variations with latitude and season. In the next chapters, more precise definitions of these layers or boundaries will be given, when necessary.

1.1.3. Atmospheric dynamics and transport

The dynamics also plays an important role in the vertical and latitudinal distribution of trace gases. Indeed, all gases characterized by relative long atmospheric lifetimes see their distributions governed not only by chemical processes but also by motions associated to air masses. At this stage, it is important to distinguish between *dynamics* and *transport*. Atmospheric dynamics (or atmospheric circulation) refers to the fluid physical phenomena that occur in the Earth's atmosphere and to the physical laws that govern them. By regulating the direction and the time scales of atmospheric motions, the dynamics strongly constrains transport processes, which results in air motions carrying physical or chemical properties from one region of the atmosphere to another one. Transport notably enables different chemical species, with different local sources, to interact. That is also through transport processes that human activities at

the Earth's surface impact higher regions of the Earth's atmosphere. Transport also determines source and sink regions of most atmospheric species.

Our atmosphere is, like the Earth, in rotation around the Earth's axis. As a consequence, each air particle is subject, for an observer located in a terrestrial frame of reference, to the Coriolis forces. At a synoptic scale, the Coriolis forces play an important role on the motions of air masses. Indeed, in meteorology, these are the Coriolis forces that explain the direction of rotation of cyclones and anticyclones. As illustrated by light blue arrows on Figure 1.3, the Coriolis forces deviate air masses of the Northern Hemisphere towards the East, while air masses of the Southern Hemisphere are deviated towards the West. This effect is also more important with decreasing latitude.

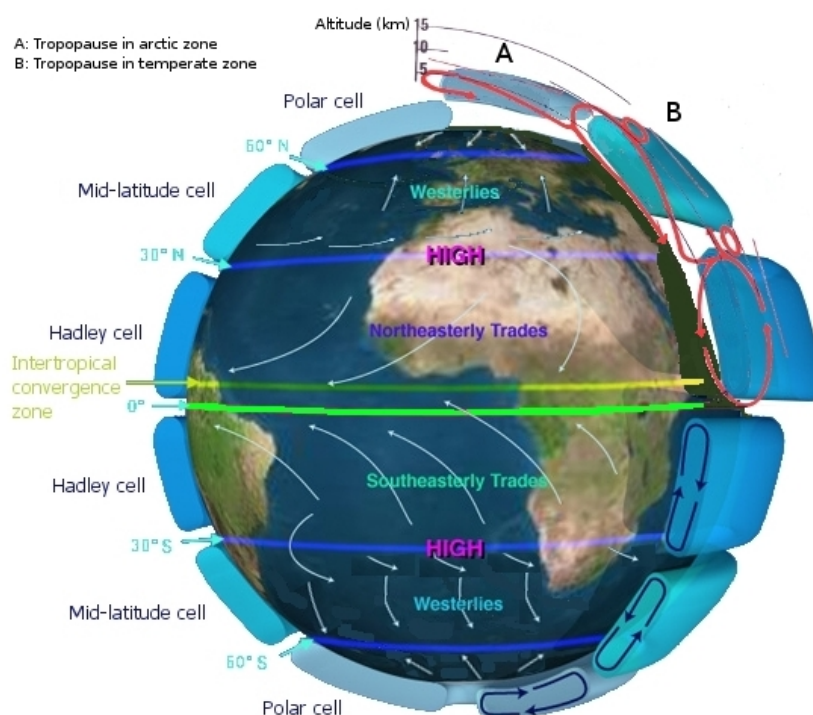


Fig. 1.3. The global circulation of the Earth's atmosphere (Courtesy of NASA/JPL-Caltech).

However, the Coriolis forces are not at the origin of the motion of air masses, these motions being rather notably ascribable to the heat quantity received by air masses. As already evoked above, the decrease of temperature with altitude observed in the troposphere makes this layer unstable and favorable to thermal convection: while low pressure zones are associated to the convective ascension of hot air masses, high pressure zones occur in subsidence zones of cold air masses, where these air masses get compressed due to their convective descent movement. The convection phenomena thus play a crucial role in the global tropospheric circulation that is based on the so-called convective cells. Basically, air masses heated by the solar radiation at the equator rise up and an equatorial low pressure zone grows. During this ascent motion, these air masses, enriched in water vapor due to their passing over oceans or over wet areas, cool, leading to the condensation of water vapor that generates strong precipitations. Dried air then goes down above the Tropics, at around 30° in latitude.

These dried air masses explain the presence of major desert areas at these latitudes, such as the Sahara, the Gobi or the Kalahari deserts. Finally, these air masses join the equator again, ending a complete cycle that forms the so-called Hadley cells [Hadley, 1735] (see Figure 1.3; one cell in each hemisphere near the Equator). At the ground level, the motion of air masses towards the Equator is deviated by the Coriolis forces, as already evoked above. In both hemispheres, these eastern dominant winds are called the trade winds. Trade winds join in a zone called the Inter-Tropical Convergence Zone (ITCZ, see the yellow line on Figure 1.3). In one year, Hadley cells mix a volume of air equivalent to the volume of the whole troposphere.

As illustrated on Figure 1.3, two additional cells complete the Hadley cells in both hemispheres: the Mid-latitude cells (also known as the Ferrel cells) and the Polar cells. These cells are due to the existence of successive low and high pressure zones. Low pressures occur near 60° in latitude, at the limit between Ferrel and polar cells, forming the so-called polar fronts (see dark blue lines on Figure 1.3). High pressure zones occur above the poles, where temperatures are low. Ascent motions of Ferrel and polar cells are alimented by low pressures of the polar fronts. Air masses then move towards tropical and polar subsidence zones. Near the surface, as a consequence of the Coriolis forces, dominant winds at mid-latitudes are westerly winds while dominant winds in polar regions are easterly winds (see Figure 1.3). Since there is less landmass to slow them down, westerly winds of the southern mid-latitudes blow quite strongly. Between 40° and 50°S (resp. 50° and 60°S), these violent winds are known as the Roaring Forties (resp. the Furious Fifties). In the Northern Hemisphere, the alternation between mountainous and oceanic areas breaks this symmetry, leading to a system of four pressure zones. During the winter, two anticyclones are centered on Siberia and on Canada, and two depressions are centered on oceans (above Iceland and Aleutian Islands). During the summer, the contrary is observed, with two high pressure zones observed above oceanic areas (the Azores High and the Hawaiian High) and with two low pressure zones centered on American and Asiatic continents.

That is the tropospheric circulation, such as described in the two last paragraphs, that governs the transport of atmospheric gases in the troposphere. The transport of gases emitted at the surface is firstly zonal, followed by a mixing in the whole troposphere. This provides a mechanism whereby species with sources at the Earth's surface and characterized by rather short chemical lifetimes (i.e. too short to reach the tropopause by diffusion) can interact at ground level. Components with medium lifetimes and produced in industrial areas (e.g. ozone, nitrogen dioxide) can be transported above oceans by the same mechanism. Moreover, components with longer lifetimes (e.g. methane, CFCs) see their VMR profiles uniformly distributed throughout the troposphere.

In addition, the tropospheric circulation also influences the vertical distribution of some gases in the lower stratosphere, via the tropopause height. Indeed, the tropopause height is notably dependent on the low and high pressure systems. The tropopause can thus act as a cover that pushes a gas downwards or upwards and consequently distorts its vertical distribution. In the same way, at the local scale, transitions between low and high pressure zones lead to variations in the tropopause height. For example, during the passing of a cold occlusion, the rapid variation of pressure can generate subsidence, i.e. the injection of stratospheric air (eventually enriched in a given atmospheric gas) into the troposphere. An example of interaction

that can exist between the tropopause height and the amount of an atmospheric gas in different regions of the atmosphere will be given in Chapter 3.

The stratospheric circulation is mainly controlled by zonal winds that tend to homogenize the zonal distribution of atmospheric compounds. In particular, the stratospheric circulation is dominated by howling winds: the jet streams. Jet streams are fast flowing, narrow air currents that can be considered as real “rivers of air”. These “rivers” typically extend over several thousands of kilometers in length, over several hundreds of kilometers in width and over a few kilometers in thickness. Inside the jet streams, winds blow from West to the East (in the direction of the Earth's rotation) and reach speeds ranging from 200km/h to 300km/h. In both hemispheres, there are two principal jet streams: the polar jet (located near 60° in latitude) and the subtropical jet (located near 30° in latitude; see top panel of Figure 1.4). In particular, the polar jet usually affects the weather in North America, in Europe and in Asia. The subtropical jet stream is commonly used during flights between North America and Europe, in order to reduce the travel time.

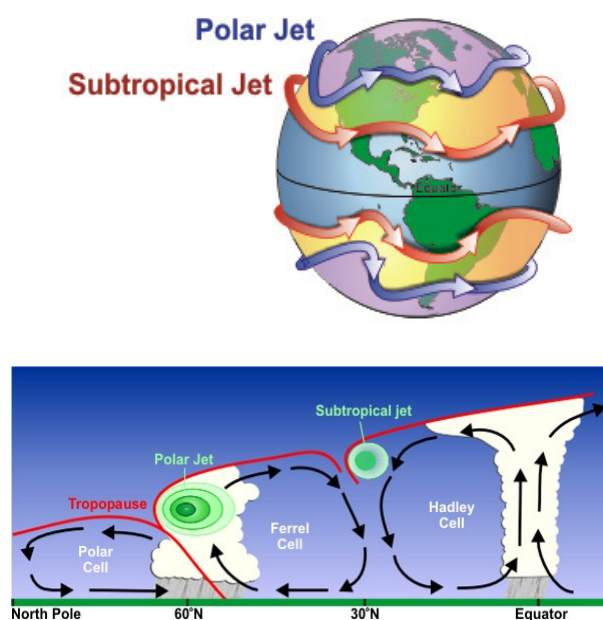


Fig. 1.4. Top panel: general configuration of the polar and subtropical jet streams. Bottom panel: cross section of the subtropical and polar jet streams, by latitude. (Photos credit: <http://meteorology.lyndonstate.edu> and <http://www.srh.noaa.gov>).

Polar jets form at the boundaries between cold air masses coming from the poles and warmer air coming from the tropics. The subtropical jet develops at the top of converging air where the Hadley and Ferrel cells meet (see bottom panel of Figure 1.4). The strong thermal contrast constrains the air to flow horizontally and, since the Earth is in rotation around its axis, this air in motion gathers speed to finally produce a jet stream. Jet streams consequently mark the boundary between cold air masses (north of the jet) and warm air masses (south of the jet). Strongest jet streams also usually occur during winter months, when the difference in temperatures between air masses coming from low and high latitudes is important. This leads to the formation, each winter, in polar regions, of the polar night jet stream (or polar vortex). Indeed, during the polar night, air masses located above the winter pole get strongly colder. Following the same mechanism evoked above, a pronounced circumpolar wind field

is then established, known as the polar vortex. The polar vortex is a real fence that isolates, over a lengthy period, polar air from mid-latitudes air masses, avoiding any chemical or physical exchanges. Over Antarctica, due to the circular symmetry of the South Polar Ocean, the polar vortex is very stable and more intense than in the Arctic regions. This serves the formation of the so-called Polar Stratospheric Clouds (PSC), precursors of a severe destruction of the stratospheric ozone over Antarctica during the austral summer and known as the Antarctic ozone hole (see section 1.2.1). Over Arctic regions, the alternation between lands and water surfaces avoid the formation of a stable vortex that is also less intense and that loses its shape more easily. The Arctic polar air is therefore not completely confined and remains warmer. This explains why we do not systematically observe a stable ozone hole over the Arctic during the spring in the Northern Hemisphere.

Atmospheric waves also play a major role in the transport of trace gases in the stratosphere. Basically, there are two types of atmospheric waves: the gravity waves and the Rossby waves (or planetary waves). In the manner of material waves that propagate at the surface of oceans, gravity waves are vertical oscillations that disturb the laminated structure of the stratosphere. They are generated by disturbances like the passing of frontal systems or by airflow over mountains. Gravity waves then propagate upwards to reach the mesosphere where they generate a tridimensional mix of atmospheric components. They therefore constitute a key element for exchanges between the troposphere and the upper atmospheric layers. Typical wavelengths that characterize gravity waves range from 10 to 100km, with a period of a few ten-minutes to a few hours.

Rosby waves [Rosby, 1939] are due to the variation in the Coriolis forces with latitude and are typically characterized by wavelengths of around 2000 km. They arise in the troposphere, when the air reaches an obstacle (like mountains). The air then has to flow in a thinner atmospheric layer, accelerating the rotation in the flux ζ . To conserve the total flux (given by the sum of the rotation in the flux ζ and the rotation related to the Coriolis forces f), the airflow deviates towards the Equator, in order to decrease the contribution associated to f . When the airflow goes past the obstacle, it deviates towards polar latitudes for the inverse reason, generating undulations in the atmospheric circulation. As illustrated on Figure 1.5, the formation of Rossby waves is also intimately connected with the formation of depressions and anticyclones in the middle latitudes of the Northern Hemisphere. Indeed, each time the airflow slows down, it causes a convergence zone just ahead of the ridge which follows. This convergence zone generates a downwards flow and consequently, a high pressure system at ground level. Similarly, when the airflow accelerates, a divergence zone is created, leading to an upwards flux that causes low pressures systems at ground level.

When Rossby waves reach the stratosphere, they horizontally break towards the poles in a zone called the *surf zone* [McIntyre and Palmer, 1983]. This essentially occurs in winter [Chen and Robison, 1992]. Mixing of chemical constituents by breaking Rossby waves constitutes an efficient transport mechanism in the stratospheric surf zone. This could notably increase the observed intra-day variability in the concentration of some stratospheric trace gases. Since the orography is more contrasted in the Northern Hemisphere, Rossby waves are more pronounced than in the Southern Hemisphere. That also explains why the polar vortex is less stable in the Arctic regions, because Rossby waves can interact with the polar vortex by deforming

and eroding it. The interaction between Rossby waves and the polar vortex is indeed at the origin of the split in two parts of the ozone hole over Antarctica, as observed in September 2002.

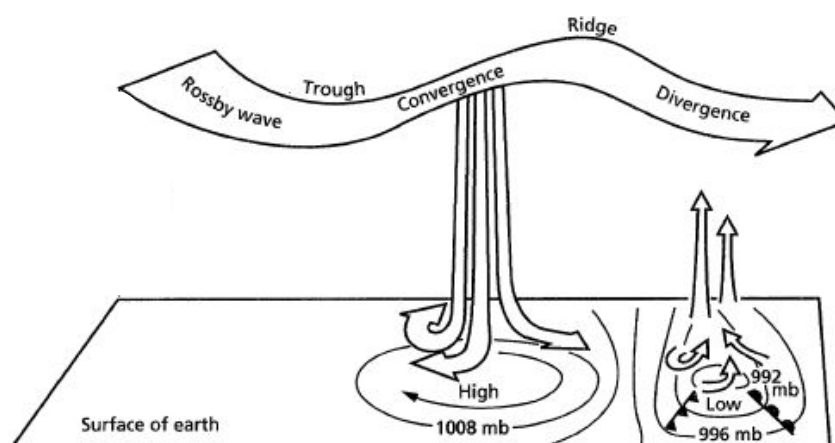


Fig. 1.5. Connection between Rosby waves with the formation of depressions and anticyclones in the Northern Hemisphere (Photo credit: <http://www.answers.com>)

Finally, it is clear that exchanges of mass that can occur between the troposphere and the stratosphere also play an important role for the chemistry of these two regions of the atmosphere. Indeed, these exchanges allow to bring chemical species with sources located in the troposphere (like CFCs) into the stratosphere, and vice-versa. Despite the fact that the positive gradient of temperature in the stratosphere strongly limits vertical transport by convection and that the high static stability of the stratosphere isolates it from the troposphere, there exists a stratospheric transport cell at large scale, described by the so-called Brewer-Dobson circulation [Brewer, 1949]. The Brewer-Dobson model describes how the air is redistributed between the troposphere and the stratosphere in the winter hemisphere: it consists in a single cell characterized by a uniform rising motion across the tropical tropopause, a slow stratospheric drift towards the middle and high latitudes, a descent motion at mid-latitudes and through the polar vortex, and a tropospheric return flow in the extra-tropics (Figure 1.6).

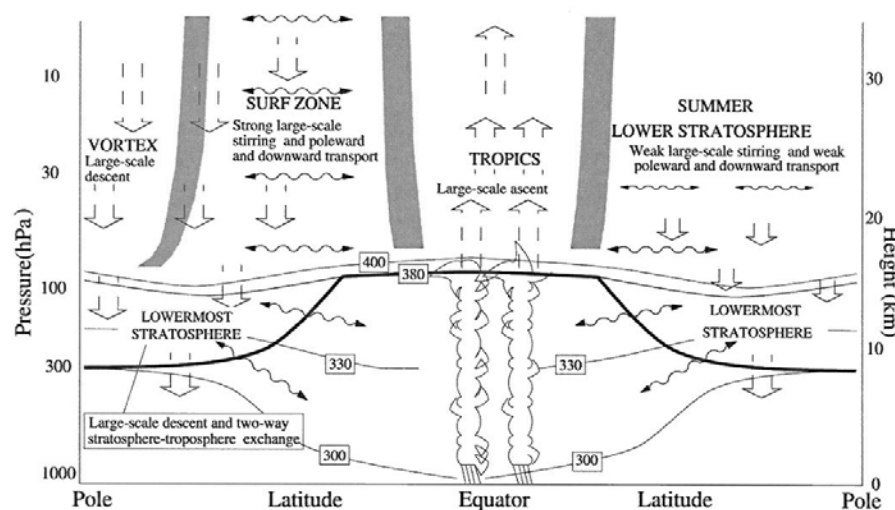


Fig. 1.6. Schematic representation of the Brewer-Dobson circulation (Courtesy of NASA).

Although this model is relatively simple and does not provide a complete description of the tropospheric-stratospheric exchanges, it is believed to be substantially correct. It notably explains why tropical air has less ozone than polar air, even though the tropical stratosphere is where most of the atmospheric ozone is produced. The origin of the Brewer-Dobson cell is totally different from tropospheric convective cells evoked above, as the Brewer-Dobson circulation is now known to be primarily wave driven: in winter, the circulation is generated by the break of Rossby waves in the surf zone, what is pushing air masses towards the pole. At equinoxes, the circulation towards one pole changes to flow towards the other pole.

The Brewer-Dobson circulation is much slower than motions associated to tropospheric convective cells. According to Austin and Li [2006], the intensity of the Brewer-Dobson circulation can be estimated on basis of measurements of mean age of stratospheric air, i.e. the average over the distribution of transport time of an air parcel travelling from the tropopause to a certain location in the stratosphere. An example of such mean age of air measurements is given in Stiller et al. [2008]. Recent model predictions foresee an intensification of the Brewer-Dobson circulation as a direct consequence of climate change [Butchart et al., 2006; Austin et al., 2006].

1.2. Halogenated compounds in the Earth's atmosphere

1.2.1. Inventory, sources and sinks

The presence of halogen atoms (i.e. fluorine, chlorine, bromine or iodine atom) in our atmosphere is mainly ascribable to the decomposition of organic halogenated compounds. These compounds, that bear one or several halogens, are principally manufactured by human activities and are therefore principally emitted from the surface. That explains why they are generally referred to as source gases. The halogenated source gases can be grouped in several categories. Table 1.2 provides some properties of the most abundant halogenated source gases, per category.

Destruction of the source gases will result in the release of the halogens in the atmosphere. They are subsequently partitioned among a number of inorganic forms through various chemical reactions. Major forms of inorganic halogenated compounds are as follows: X, XO, HX, HOX and XONO₂, where X designates an halogen atom. Some of these inorganic halogens are very reactive species, with very limited atmospheric lifetime. However, for some of them, their strong chemical stability allows them to accumulate in the atmosphere, to form atmospheric reservoirs.

It is clear from Table 1.2 that the most abundant halogenated source compounds are CFCs, and in particular CFC-12 and CFC-11. Chlorofluorocarbons offer interesting physical and thermodynamical properties: non toxic, nonflammable, stable and odourless, they have consequently been adopted for several industrial and domestic applications after the fifties. Large amounts of man-made CFC-12, CFC-11, CFC-113, CFC-114 and CFC-115 have therefore been emitted during the last decades. The two first above-mentioned gases have been notably widely used as propellants in aerosol bombs, as refrigerants, in air-conditioning systems or as foam-blowing agents. Among applications involving CFC-113 one can cite the cleaning of electronic components during their assemblage.

Common or industrial name	Chemical formula	2004 annual mean abundance ^a [ppt]	Lifetime ^b [years]
Chlorofluorocarbons (CFCs)			
CFC-12	CCl ₂ F ₂	543.8	100
CFC-11	CCl ₃ F	253.1	45
CFC-113	CCl ₂ FCClF ₂	78.7	85
CFC-114	CClF ₂ CClF ₂	17.31	300
CFC-115	CClF ₂ CF ₃	8.34	1700
Halons			
Halon-1211	CBrClF ₂	4.33	16
Halon-1301	CBrF ₃	3.14	65
Hydrochlorofluorocarbons (HCFCs)			
HCFC-22	CHClF ₂	163.9	12
HCFC-141b	CH ₃ CCl ₂ F	17.42	9.3
HCFC-142b	CH ₃ CClF ₂	15.38	17.9
HCFC-124	CHClF ₂ CF ₃	1.64	5.8
Hydrofluorocarbons (HFCs)			
HFC-134a	CH ₂ FCF ₃	31.5 ^c	14
HFC-23	CHF ₃	18 ^d	270
HFC-152a	CH ₃ CHF ₂	5 ^e	1.4
HFC-125	CHF ₂ CF ₃	4.1 ^e	29
Perfluorocarbons (PFCs)			
PFC-14	CF ₄	78 ^f	50000
PFC-116	C ₂ F ₆	4.1 ^f	10000
PFC-218	C ₃ F ₈	0.53 ^f	2600

^a Except when indicated, values are in situ data collected by the AGAGE (Advanced Global Atmospheric Gases Experiment) network and published in WMO, 2007.

^b Values are those published in WMO, 2007.

^c AGAGE annual mean for the year 2005.

^d Monthly mean values recorded by UEA (University of East Anglia, Cape Grim, Tasmania) at the end of 2004.

^e Monthly mean values recorded by AGAGE at Mace Head, Ireland, at the end of 2004.

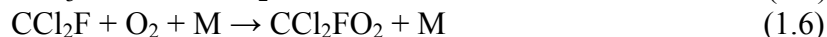
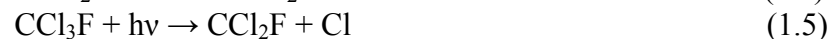
^f According to Figures published in Mühle et al., 2010.

Table 1.2. Mean abundances and lifetimes of the main halogenated source gases.

One of the properties that led to the development of the CFCs as major industrial products was their chemical inertness. However, that is precisely this property that also leads to their harmful effects on the environment. Indeed, once emitted from the surface, chlorofluorocarbons mix into the troposphere, where there exists no mechanism for their destruction or removal. Their long tropospheric lifetimes allow them to be transported to the stratosphere, where they are destroyed by photochemical processes. The altitude at which a given CFC will be destroyed directly depends on its chemical composition. Basically, the more chlorine atoms are present in the molecule, the more its UV absorption spectrum is shifted towards longer wavelengths, allowing photolysis to occur at lower altitudes and resulting in a decrease in the atmospheric lifetime of the compound.

The photochemical destruction of CFCs mainly results in the release of chlorine atoms in the stratosphere. For example, destruction reactions of CFC-12 and CFC-11

are given below (M designates a third body and $h\nu$ a solar radiation of appropriate wavelength):



Photochemical processes are however not the only destruction path of CFCs, as some of them are destroyed by reaction with $\text{O}(^1\text{D})$, an excited electronic state of oxygen that is produced during the short-wavelength photolysis of ozone (i.e. for wavelength lower than 320 nm). Reaction of CFCs with $\text{O}(^1\text{D})$ can occur via different ways, as illustrated here for CFC-12:



With a probability close to 60%, the reaction (1.10) is dominant. Reactions (1.10) to (1.13) also become more effective as the altitude increases, since the $\text{O}(^1\text{D})$ concentration rapidly grows with altitude. However, photochemical processes remain the principal destruction path of CFCs, since, for example, destruction by $\text{O}(^1\text{D})$ only contributes to ~1% and ~30% to the total loss of CFC-11 and CFC-12, respectively.

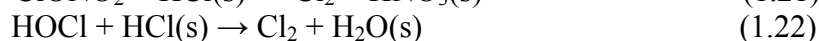
The release of free chlorine atoms in the stratosphere by the destruction of CFCs is the main issue, since it allows chlorine atoms to be involved in a catalytic destruction cycle of stratospheric ozone, following the reactions:



These catalytic cycles, involving chlorine as precursor of the ozone destruction, were identified for the first time in 1974, simultaneously by Stolarski and Cicerone [1974], and by Molina and Rowland [1974]. Reactions (1.15) and (1.18) indicate that each chlorine atom involved in a catalytic cycle is released in the atmosphere. Each chlorine atom can therefore participate to several successive catalytic cycles and contribute to the destruction of many thousands of ozone molecules. As a

consequence, if reactions (1.14) to (1.20) were the only chemical cycles involving Cl and ClO in the stratosphere, it is clear that stratospheric ozone levels would be highly diminished. Fortunately, by reacting with CH₄, H₂, HO₂, H₂O₂ and NO₂, Cl and ClO can be converted to the two inactive reservoir species HCl and ClONO₂. In the lower stratosphere, typical lifetimes of these two reservoir species are about one month and a few hours, respectively [Brasseur, 1999]. While HCl is returned to active Cl mainly via reaction with OH, ClONO₂ is principally destroyed by photolysis or by reaction with O atoms.

However, the catalytic cycles evoked above do not allow to explain the formation of an ozone hole during the polar spring over Antarctica. During the polar night, and due to the isolation of the Antarctic stratosphere from other air masses by the polar vortex (see section 1.1.3), very low temperatures are reached. So-called Polar Stratospheric Clouds (PSC) are then formed in the polar stratosphere from nucleation sites: nitric acid (HNO₃) and water condense on preexisting sulfur-containing particles producing solid and liquid PSC particles that become large and numerous enough to form clouds [Steele et al., 1983; Toon et al., 1986]. PSC act as real heterogeneous catalysts. The following reactions that occur at the surface of PSC, convert the inactive chlorine reservoirs into chlorine molecules [Solomon et al., 1986; McElroy et al., 1986; Crutzen and Arnold, 1986]:



When the sunlight comes back over Antarctica at the end of the polar night, these chlorine molecules are quickly photodissociated and free chlorine atoms that can then participate to the catalytic ozone destruction cycles described above. The subsequent massive destruction of ozone leads to the formation of the Antarctic ozone hole. This ozone hole is generally observed from the end of August until the end of December. When the polar summer is approaching, the Antarctic stratosphere warms and the polar vortex becomes less active, allowing a mix between polar and lower latitudes air masses that fills in the hole. In the Northern Hemisphere, the higher variability of the dynamics (see section 1.1.3) avoids the formation of a stable ozone depletion, even if some studies have demonstrated that ozone losses within a same air mass can reach 55% during cold winters [Schoeberl et al., 2002].

Chlorofluorocarbons are not the only halogenated gases that deplete ozone. Indeed, the bromine atoms liberated during the dissociation of Halons in the stratosphere is also at the origin of a bromine catalytic cycle that destroys stratospheric ozone. Halons are halogenated species that have been widely used in the past as fire-extinguishers. As they do not contain any C-H bonds, their quite long lifetime (10 years and more; see Table 1.2) allows them to reach the stratosphere where they are photodissociated. Similarly to the CFCs, the photolysis is indeed the main destruction pathway of Halons. However, Halons generally photolyze faster than CFCs (and have thus shorter lifetimes; see Table 1.2) since the presence of bromine in these molecules shifts the absorption spectrum to longer wavelengths and consequently allows the photolysis of the Halons to occur at lower altitudes than for CFCs. Although the

chemistry of bromine in the stratosphere is not as well understood as that of chlorine, it is however quite clear that the potential for ozone destruction by bromine is significantly larger than for an equivalent amount of chlorine (probably by a factor of about 60 [WMO, 2007; Sinnhuber et al., 2009]). The principal reason for this is that the two main bromine reservoir species (HBr and BrONO₂) are less stable than their chlorine counterparts (typical lifetimes in the lower stratosphere for these two gases are a couple of days and about 10 minutes, respectively). Fortunately, this higher efficiency for ozone depletion by bromine species is balanced by their stratospheric abundances that are significantly lower than chlorine.

Due to their intense and wide absorption bands in the infrared, chlorofluorocarbons and Halons are also strong greenhouse gases. The combination of this latter property with their high ozone destruction potential is at the origin of the progressive reduction and banishment of anthropogenic CFCs and Halons emissions from the surface (see next section). One of the first consequences of this banishment was the necessity to develop new compounds that offer similar industrial properties as CFCs and Halons, that are economically profitable, and that have minor impact on the environment. In such context, the rationale behind the development of such substitute products was to find compounds that possess significant tropospheric removal processes. The guideline adopted was to develop molecules that contain hydrogen atoms, susceptible to react with tropospheric OH: the fraction of molecules able to reach the stratosphere would therefore be reduced. In addition, these new molecules would also contain no (or fewer) chlorine atoms (than CFCs). In fine, these industrial researches have led to the synthesis of hydrochlorofluorocarbons HCFCs and hydrofluorocarbons HFCs.

Concretely, the mechanism of the photo-oxidation of HCFCs and HFCs by the OH radical is quite complex. These destruction processes result in the production of a number of partially oxidized compounds, some of which still contain halogen atoms. Table 1.3 lists the major halogen-containing products obtained from OH attack on most of HCFCs and HFCs reported in Table 1.2 [Wallington et al., 1994; Tuazon and Atkinson, 1993].

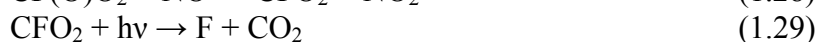
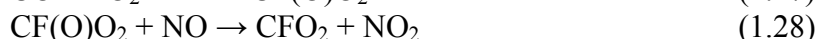
Compound	Major organic degradation products
Hydrochlorofluorocarbons (HCFCs)	
HCFC-22	COF ₂
HCFC-141b	COClF, CCl ₂ FCHO, CO, CO ₂
HCFC-142b	COF ₂ , CClF ₂ CHO, CO, CO ₂
HCFC-124	CF ₃ COF
Hydrofluorocarbons (HFCs)	
HFC-134a	COF ₂ , CF ₃ CHO, CF ₃ OH, CO ₂
HFC-152a	COF ₂ , CH ₂ O, CO
HFC-125	COF ₂ , CF ₃ OH

Table 1.3. Major organic degradation products of some HCFCs and HFCs.

Since OH is present throughout the atmosphere, destruction of HCFCs and HFCs first occurs in the troposphere. The rate at which these partially hydrogenated compounds are removed in the troposphere is therefore controlled by the rate of their reaction with OH. In many cases, the rate coefficients are rather small, leading to sufficiently

long tropospheric lifetimes (a few months to a couple of years) such that a significant fraction of these compounds can be transported to the stratosphere. Once in the stratosphere, reaction with OH, photolysis and reaction with O(¹D) lead to the continued removal of HCFCs and HFCs. Note that for compounds whose dominant loss process is reaction with OH in both the troposphere and the stratosphere, the stratospheric lifetime is considerably longer than the tropospheric lifetime, owing to the rather large temperature dependence of the rate coefficients for reaction with OH.

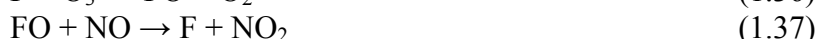
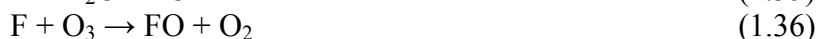
Table 1.3 notably shows that the photo-oxidation of HCFCs and HFCs by OH leads to the formation of two fluorinated carbonyl compounds: carbonyl fluoride (COF₂) and carbonyl chlorofluoride (COCIF). In the troposphere, the lifetime of these two compounds is quite limited (from 5 to 10 days for COF₂, from 5 to 20 days for COCIF), since they are mainly destroyed by heterogeneous uptake into clouds [Wallington et al., 1994]. However, if the degradation of HCFCs and HFCs occur in the stratosphere, the atmospheric lifetimes of these two carbonyl compounds increase significantly: according to Chipperfield et al. [1997], their lower stratospheric lifetimes are of the order of months. Nevertheless, regarding their current atmospheric abundances (see Table 1.2), the major sources of stratospheric COF₂ and COCIF remain CFC-12 and CFC-11 (Eq. (1.1)-(1.4) and (1.5)-(1.8)). In the stratosphere, COF₂ and COCIF are then themselves photolyzed, releasing free fluorine:



As evoked above for CFCs, COF₂ and COCIF can also be destroyed by reaction with O(¹D), but the photolysis remains the main destruction pathway. The free fluorine atoms so liberated mostly react with O₂ in the following null cycle (i.e. the fluorine atom F is preserved at the end of the cycle):



The fluorine atoms can also eventually react with CH₄, H₂, H₂O and O₃ [Stolarski and Rundel, 1975; Brasseur, 1999]:



where Eq. (1.33) and (1.34) constitute the two principal pathways [Kompa and Wanner, 1972; DeMore *et al.*, 1997]. The formation of hydrogen fluoride (HF) by Eq. (1.33)-(1.35) is significant since HF is a very stable species. Indeed, due to its strong bond, HF cannot react with OH (this reaction is endothermic) and the effectiveness of

its photolysis at 213 nm remains poor in the stratosphere. The main sink of HF would be its slow diffusion down to the troposphere, where it is eliminated by acid rainouts. In addition, fluorine atoms liberated by Eq. (1.38) will also rapidly be converted to HF. All this makes HF the main fluorine reservoir in the stratosphere, before COF_2 and COCIF [Nassar et al., 2006]. A simplified schematic of the formation of major stratospheric fluorine reservoirs is reproduced on Figure 1.7.

The extreme stability of HF makes this species very often used as a dynamical tracer, for example to follow the vertical motions in the stratosphere [Chipperfield et al., 1997]. This extreme stability also ensures that almost no fluorine is present in the form of F or FO, and consequently prevents fluorine to significantly participate to the ozone layer destruction. Moreover, Stolarski and Rundel [1975] have quantified to what extent fluorine is involved in the erosion process of stratospheric ozone layer: it has been demonstrated by these authors that, between 25 and 50 km, fluorine is 10000 to 50000 less effective than chlorine to destruct ozone. In addition, since almost all atmospheric fluorine released by halogenated source compounds is converted into HF, measurements of its atmospheric abundance already provide a good estimate of the amplitude of halogenated compounds emissions from the surface as well as of their decomposition in the stratosphere. In that context, Chapter 3 of the present study is devoted to the production of long-term HF total and partial vertical abundances time series above Jungfraujoch from FTIR measurements (see Chapter 2 for details concerning the FTIR technique and the scientific station of the Jungfraujoch). In particular, partial amounts cover three distinct regions of the stratosphere, for which comparisons with satellite and model data are notably presented.

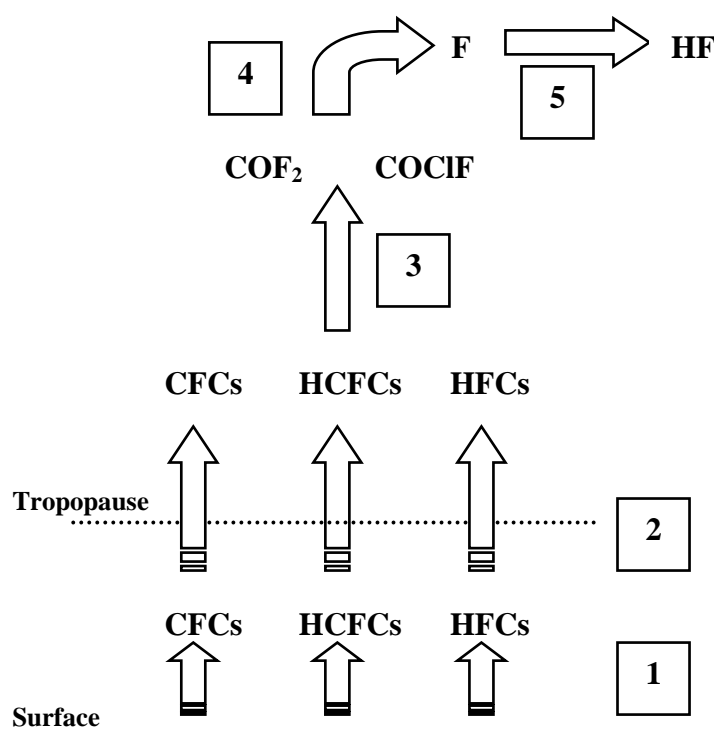


Fig. 1.7. Schematic representation of the formation of major stratospheric fluorine reservoirs: (1) Anthropogenic emissions of CFCs, HCFCs and HFCs from the surface; (2) Transport of CFCs, HCFCs and HFCs through the tropopause; (3) CFCs, HCFCs and HFCs produce the two temporary stratospheric reservoir species COF_2 and COCIF by photodissociation or by reaction with OH or $\text{O}(^1\text{D})$; (4) COF_2 and COCIF are photodissociated to produce fluorine atoms; (5) fluorine atoms are quickly converted to form the extreme stable stratospheric reservoir HF.

As already evoked, carbonyl fluoride is the second most abundant fluorine reservoir in the stratosphere. At mid-latitude, the vertical distribution of COF_2 peaks at around 30 km (Figure 1.8). Above this altitude, its vertical distribution decreases quite rapidly, as a consequence of its destruction by photodissociation. In addition, it has also been shown by Zander et al. [1994], on basis of space data, that the maximum observed in the COF_2 vertical distribution is located at higher altitudes when moving from mid-latitudes towards the tropics. Studies dealing with ground-based measurements of COF_2 vertical distribution are quite sparse. Chapter 4 of the present study deals with the possibility to derive such kind of information from FTIR observations operated from the ground. In addition, our COF_2 results will be combined with those obtained for HF in order to more precisely evaluate (i.e. with respect to the consideration of HF or COF_2 data only) the temporal evolution of the total inorganic fluorine budget (see Chapter 5).

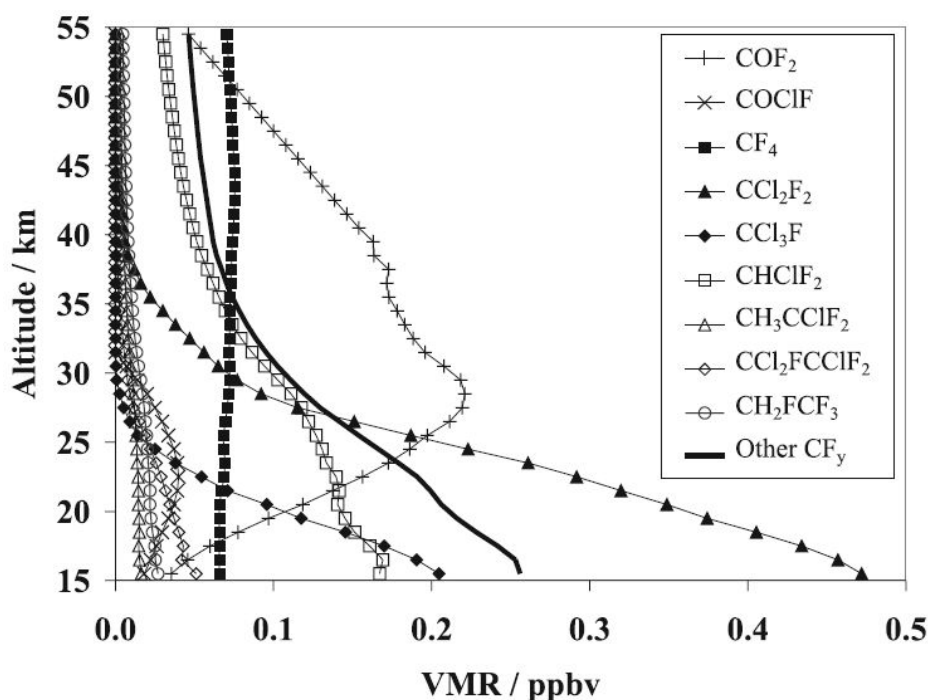


Fig. 1.8. Example of average northern mid-latitudes (30° - 60° N) profiles for some fluorinated sources and reservoirs recorded by the Atmospheric Chemistry Experiment – Fourier Transform Spectrometer (ACE-FTS) space instrument. HF is not shown as its vertical profile is mostly above 0.5 ppbv (for comparison, a typical example of mean HF profile is shown on Figure 1 of Chapter 3). Figure extracted from Nassar et al. [2006].

Since COCIF mainly results from the breakdown of CFC-11 (that contain three chlorine atoms and that is consequently photodissociated at lower altitudes than CFC-12 that only contains two chlorine atoms; see above), it has a peak in the lower to middle stratosphere (Figure 1.8). As for COF_2 , the vertical distribution of COCIF rapidly decreases above its maximum, due to its photolysis. Carbonyl chlorofluoride is besides the fluorine reservoir whose photolysis is the more effective. The contribution to the total atmospheric fluorine burden of this third fluorine reservoir is however limited, compared to HF and COF_2 , since COCIF profiles do not exceed 0.05 ppbv at Northern mid-latitudes (Figure 1.8). Since the detection of COCIF is not possible by ground-based FTIR technique (mainly due to strong interferences by water vapor) its contribution to the inorganic fluorine budget will be evaluated in Chapter 5 on the basis of model data.

We close this inventory of atmospheric halogenated compounds with perfluorocarbons (PFCs). Perfluorocarbons are compounds derived from hydrocarbons (like methane CH_4 , ethane C_2H_6 or propane C_3H_8) by replacement of all hydrogen atoms by fluorine atoms. Due to the strength of their carbon-fluoride bonds, PFCs are characterized by a strong chemical inertness and stability. These gases have several medical applications (medical imaging, eye surgery, etc.) and non-medical applications (refrigerating units as substitute products of CFCs, fire extinguishers, plasma cleaning of silicon wafers, etc.). Among the different perfluorocarbon gases, carbon tetrafluoride (CF_4) is by far the most abundant (see Table 1.2). In addition, its very long lifetime of around 50000 years, which is highly greater than typical transport time scales, allows CF_4 to present a quasi constant vertical distribution throughout the entire atmosphere (see Figure 1.8). In a more general way, the long lifetimes of PFCs are explained by the fact that they do not react with OH or $\text{O}(^1\text{D})$ but are only photolyzed very slowly, even if other additional loss mechanisms exist such as reaction with hydrogen atoms, uptake by oceans and soils or reactions with electrons and ions at the top of the atmosphere. The combination of these long lifetimes with their high warming potential make PFCs extremely potent greenhouse gases, whose emissions are therefore regulated by the Kyoto Protocol (see next section). Chapter 6 will be devoted to CF_4 measurements and trends.

1.2.2. Controlling the harmful effects of halogens on the atmosphere

In the context of the search for CFC substitutes, criteria allowing to characterize their environmental acceptability have been developed, leading to the concepts of the Ozone Depletion Potential (ODP) and Global Warming Potential (GWP). These two parameters are essentially determined through the use of numerical models: a known amount of a given gas is added in the model atmosphere and its effects both on total stratospheric ozone and on the radiative forcing are determined. These effects are then compared to the effects generated by a reference gas. Reference gases for the ODP and GWP computations are CFC-11 and CO_2 , respectively.

Table 1.4 compares GWP and ODP (when applicable) for all halogenated compounds listed in Table 1.2. GWP values provided in Table 1.4 are those computed for a 100-yr time horizon. This latter value simply expresses the time horizon over which the numerical computation is performed. The comparison of OPD characterizing CFCs and Halons with OPD of their substitute products clearly highlights the fact that these latter compounds are indeed less ozone depleting substances than chlorofluorocarbons and Halons. Except for HFC-23, these substitute products also always systematically present lower GWP than CFCs. The lower GWP values of CFCs replacements, combined with their shorter atmospheric lifetimes (see Table 1.2), consequently limit the forcing by these gases on the Earth's radiative budget. These GWP values are however important with respect to other most abundant but shorter-lived greenhouse gases, like CO_2 , CH_4 and N_2O (GWP of 1, 23 and 300, respectively, with atmospheric lifetimes that do not exceed 115 years [WMO, 2003]). Emissions of some of these substitute products have therefore been deservedly regulated in the frame of important international decisions adopted to limit the Earth's global warming (see below).

Common or industrial name	Chemical formula	ODP	GWP [100-yrs time horizon]
Chlorofluorocarbons (CFCs)			
CFC-12	CCl ₂ F ₂	1.0	10720
CFC-11	CCl ₃ F	1.0	4680
CFC-113	CCl ₂ FCClF ₂	0.8	6030
CFC-114	CClF ₂ CClF ₂	1.0	9880
CFC-115	CClF ₂ CF ₃	0.6	7250
Halons			
Halon-1211	CBrClF ₂	3.0	1860
Halon-1301	CBrF ₃	10.0	7030
Hydrochlorofluorocarbons (HCFCs)			
HCFC-22	CHClF ₂	0.055	1780
HCFC-141b	CH ₃ CCl ₂ F	0.11	713
HCFC-142b	CH ₃ CClF ₂	0.065	2270
HCFC-124	CHClF ₂ CF ₃	0.022	599
Hydrofluorocarbons (HFCs)			
HFC-134a	CH ₂ FCF ₃	< 1.5 10 ⁻⁵	1320
HFC-23	CHF ₃	< 4.0 10 ⁻⁴	12240
HFC-152a	CH ₃ CHF ₂	NA	122
HFC-125	CHF ₂ CF ₃	< 3.0 10 ⁻⁵	3450
Perfluorocarbons (PFCs)			
PFC-14	CF ₄	NA	5820
PFC-116	C ₂ F ₆	NA	12010
PFC-218	C ₃ F ₈	NA	8690

Table 1.4. Ozone Depletion Potential (ODP) and Global Warming Potential (GWP) for 100-yrs time horizon of the most abundant atmospheric fluorine source gases [values are from WMO, 2003.]

That is however the first observational evidence of the occurrence of an ozone hole over Antarctica by Farman et al. [1985] that has definitely urged the international authorities to adopt measures concerning the protection of the stratospheric ozone layer. It started in March 1985 with the Vienna Convention for the Protection of the Ozone Layer, even if this convention does not include any constraining measures for signatory countries but rather foresees that specific protocols could be subsequently added. This happened two years later with the Montreal Protocol on Substances that Deplete the Ozone Layer. Signed in September 1987 by 46 countries, the Montreal Protocol has been effective the 1st January 1989: all countries that have ratified the Protocol have thus accepted to complete short- and long-term objectives concerning their production and consumption of main CFCs and Halons. These first objectives were a two-steps procedure: firstly, maintain CFCs and Halons production and consumption levels to the levels of the year 1986, and then reduce these levels by 50% within 10 years.

The Montreal Protocol is complex, but its most important characteristic is its dynamics: scientific evaluations have to take place each four years and constitute the basis of new decisions concerning the reduction of substances eroding the ozone layer (i.e. to decide or not to accelerate the phase out rates of target gases). In addition, this

dynamics has also allowed to include in the Protocol additional compounds that were not initially targeted. This has led to several successive Amendments and Adjustments of the original Montreal Protocol. That was the case in London in 1990, in Copenhagen in 1992, in Vienna in 1995, in Montreal in 1997 and in Beijing in 1999. Table 1.5 on next page provides the corresponding final phase out schedule applicable by all non-developing countries that have ratified the Protocol. The integral text of the Montreal Protocol as well as of its Amendments and Adjustments is available on the United Nations Environment Program (UNEP) web pages (<http://www.unep.ch/>). The Montreal Protocol is currently ratified by more than 180 countries.

In support of the Montreal Protocol, the Alternative Fluorocarbons Environmental Acceptability Study (AFEAS) publishes annual global production of the main halogenated source compounds. Figure 1.9 published on their website¹ shows total production of the main CFCs, HCFCs and HFCs between 1980 and 2007. Figure 1.9 clearly highlights the spectacular decrease of CFCs production as a direct consequence of the limitations imposed by the Montreal Protocol since 1989. On the other hand, this decrease is balanced by the rapid increase of CFCs replacements. Even if a decrease is however observed for HCFCs since the beginning of this century, HFCs production is still increasing, as they do not contribute to the erosion of the ozone layer (HFCs do not contain any chlorine or bromine atoms) and are consequently not included in the list of substances regulated by the Montreal Protocol. Due to their high GWP, HFCs emissions are however regulated by the Kyoto Protocol.

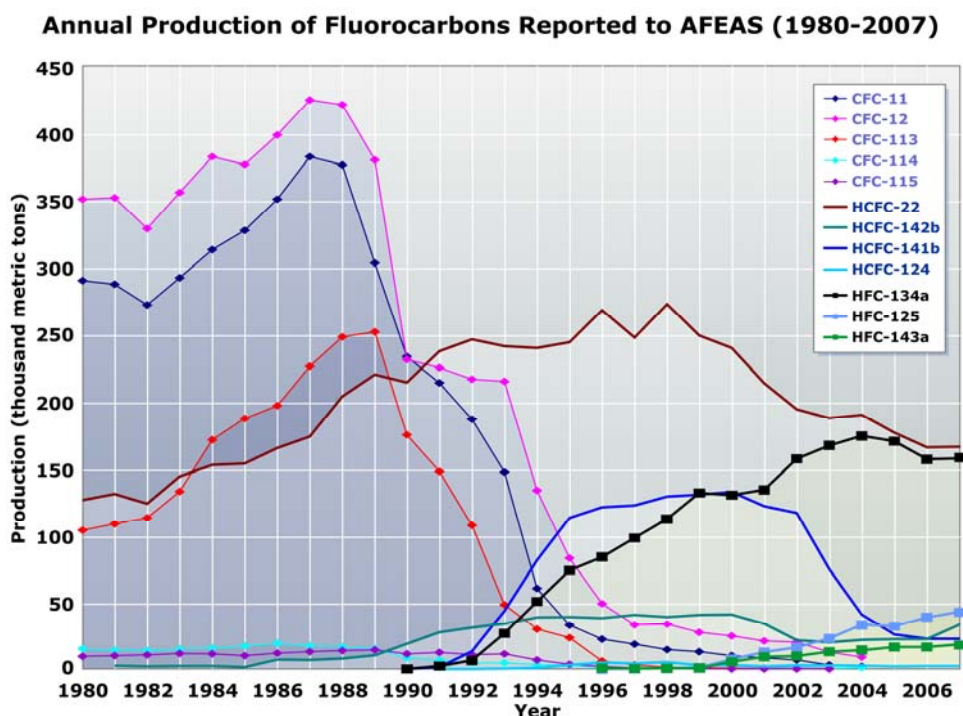


Fig. 1.9. Global annual anthropogenic production of the main halogenated source gases between 1980 and 2007 (source: <http://www.afeas.org/>).

¹ <http://www.afeas.org/>

Substance	Phase out schedule
CFC-11, -12, -113, -114, -115	Freeze at 1986 level by 1989 75% reduction of 1986 level by 1994 Total phase out by 1996
Halon-1211, -1301, -2402	Freeze at 1986 level by 1992 Total phase out by 1994
CFC-13, -111, -112, 211, -212, -213, -214, -215, -216, -217	20% reduction of 1989 level by 1993 75% reduction of 1989 level by 1994 Total phase out by 1996
Carbon tetrachloride	85% reduction of 1989 level by 1995 Total phase out by 1996
Methyl chloroform	Freeze at 1989 level by 1993 50% reduction of 1989 level by 1994 Total phase out by 1996
HCFC	Freeze at the standard level ^a by 1996 35% reduction of the standard level by 2004 65% reduction of the standard level by 2010 90% reduction of the standard level by 2015 99.5% reduction of the standard level by 2020 Total phase out by 2030
HBFC ^b	Total phase out by 1996
Methyl bromide	Freeze at 1991 level by 1995 (except the amounts used for quarantine and pre-shipment applications)

^a The standard level = 1989 calculated consumption level of HCFC
+ 1989 calculated consumption level of CFC x 0.031

^b Hydrobromofluorocarbons

Table 1.5. Phase out schedule of depleting ozone substances adopted by non-developing countries during the Montreal Protocol and its successive Amendments and Adjustments (source: <http://www.unep.ch/ozone/index.shtml>).

Ten years after the Montreal Protocol, the United Nations have established in December 1997 the Kyoto Protocol that aims at fighting the global warming of the Earth's atmosphere. The Kyoto Protocol aims at controlling and limiting the anthropogenic emissions of four greenhouse gases (CO₂, CH₄, N₂O and SF₆) as well as of two groups of halogenated gases (HFCs and PFCs). Under the Kyoto Protocol,

the so-called Annex I countries¹ agree to reduce their collective aggregated greenhouse gas emissions by at least 5% (with respect to the 1991 level) from 2008 to 2012, individual objectives of each signatory country depending on their own initiatives and situations.

To come into force, the Kyoto Protocol needed the signature of at least 55 countries, whose greenhouse gas emissions represent at least 55% of the global emissions. With the ratification of the Kyoto Protocol by Russia in November 2004, this latter condition was satisfied, leading to the entry into force of the Protocol in February 2005. As of November 2009, the European Community and 187 additional countries have ratified the Kyoto Protocol. Probably the most notable non-party to the Protocol are the United States of America, who occupied in 2005 the second position in the world ranking of the largest emitters of greenhouse gases, just after China. Thus far, BRIC² representatives like China, India and Brazil, who are also important emitters of greenhouse gases given their rapid economic development, are still in the non-Annex I group³, meaning that they have ratified the Kyoto Protocol but that they do not have accepted the emission reductions specified above.

In support to the Kyoto Protocol, an Intergovernmental Panel on Climate Change (IPCC) has also been co-jointly established in 1988 by two organizations of the United Nations (namely, the World Meteorological Organization (WMO) and the United Nations Environment Program (UNEP)) in order to ease the political decisions making by providing information relevant for the understanding of the risk of human-induced climate change. This information is provided to decision makers in the form of assessments summarizing results from the published and peer-reviewed scientific literature. Political decisions are effectively often complicated by financial and economical interests as well as by some aspects of the Protocol itself. Indeed, the Protocol approves several flexible mechanisms, such as emissions trading, that allow to any country to purchase greenhouse gases emission credits from elsewhere, through financial exchanges or projects that reduce emissions in another Annex I country, in a non-Annex I country or in an Annex I country with an excessive emissions allowance. The IPCC consequently produces a range of projections of, for example, what the future increase in global mean temperature, which is directly linked to the massive injection of greenhouse gases in the atmosphere, might be. In that context and according to IPCC [2007], there is high agreement and much evidence that with the current policies on climate change and all related sustainable development practices, global greenhouse gases will continue to grow over the next few decades (see left panel of Figure 1.10). As a direct consequence, it has also been established that for the next two decades, a global warming of about 0.2°C/decade is projected (see right panel of Figure 1.10).

Moreover, even if the concentrations of all greenhouse gases are kept constant to their 2000 levels, a warming of about 0.1°C/decade would be expected in the future. Predictions for farther decades depend on specific emissions scenarios. The scenarios

¹ Annex-I countries include industrialized nations, members of the Organization for Economic Cooperation and Development (OECD) in 1992, and countries with economies in transition (i.e. principally countries from Central and Eastern Europe). See <http://unfccc.int> for a complete list of the Annex-I countries.

² Acronym commonly used for the four fastest emerging economies, Brazil, Russia, India and China.

³ Non Annex-I countries mostly group developing countries. See <http://unfccc.int> for a complete list of the non-Annex-I countries.

used by the IPCC are complex emissions scenarios taking into account several demographic, social, political and economic factors. They are grouped in four scenarios families (A1, A2, B1 and B2) that are fully described in IPCC [2000].

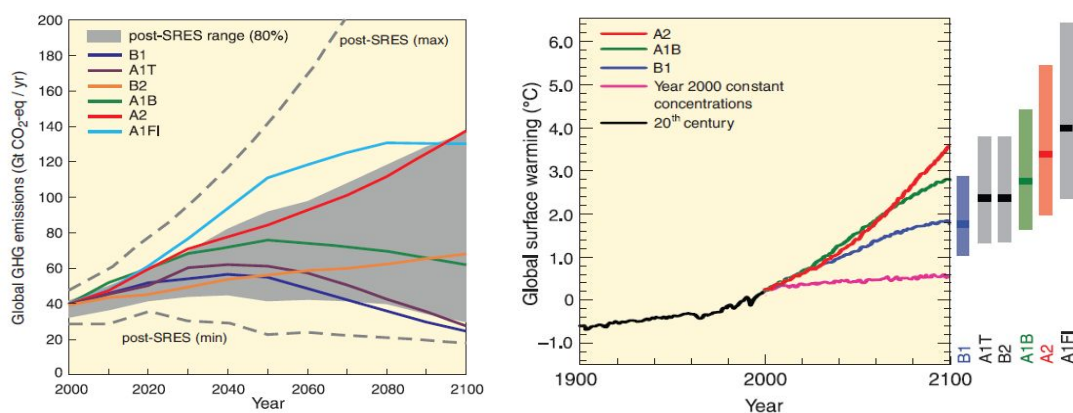


Fig. 1.10. Left panel: global greenhouse gases emissions in the absence of additional climate policies and derived from six different IPCC emissions scenarios (solid colored lines). The corresponding 80% level confidence is illustrated with the grey shaded area. The two grey dashed lines reproduce the full range of all IPCC scenarios. Right panel: colored solid lines are global averages of surface warming (relative to the 1980-1999 time period) derived from the three IPCC scenarios mentioned in the legend and as continuations of the 20th century simulations (black solid line). The pink solid line corresponds to the case where concentrations of greenhouse gases are held at their year 2000 levels. The bars at the right part of the figure indicate the uncertainty range of each scenario, with solid lines within each bar indicating the best estimate.

1.2.3. Recent trends and potential future evolution of CFCs, HCFCs and HFCs

Concretely, the Montreal Protocol leads first to slow down, and then to the inversion of the atmospheric increase of main ozone depleting compounds. A clear evidence of this success is the change observed in the atmospheric total inorganic chlorine burden Cl_y . A good proxy of Cl_y can be obtained by summing the contributions of the two main chlorine reservoirs (namely HCl and $ClONO_2$), since they represent more than 90% of total inorganic chlorine at mid-latitudes [Zander et al., 1996]. Very recently, Mahieu et al. [2010] have derived the annual change for inorganic chlorine over the 1996-2009 time period. Based on FTIR HCl and $ClONO_2$ time series recorded at the high altitude mid-latitude scientific station of the Jungfraujoch, these authors have obtained for Cl_y a trend equals to $-0.93 \pm 0.14\%/yr$ (when considering the year 1996 as the year of reference in the trend computation), in strong contrast with positive rates larger than $3\%/yr$ observed before 1996. This decrease is mainly ascribable to the significant decrease observed in the atmospheric loading of the source gases CFC-11, carbon tetrachloride (CCl_4) (see Table 2 of Mahieu et al., 2010) and methyl chloroform (CH_3CCl_3).

In addition, the FTIR time series of CFC-12 above Jungfraujoch shows a significant slowdown since the second half of the nineties, after a rapid increase during the eighties and the first half of the nineties (Figure 1.11). After a period of stabilization observed at the beginning of this century, the current rate of growth of CFC-12, computed over the 2001-2010 time period, equals $-0.15 \pm 0.04\%/yr$ [Mahieu et al., 2010]. For the same time period, the annual change of CFC-11 (whose time series is

also reproduced on Figure 1.11) equals $-0.83 \pm 0.06\%/yr$. The decrease observed from the nineties in the time series of CFC-11 is linked to its atmospheric lifetime, shorter than the one of CFC-12 (see Table 1.2). Waple et al. [2002] have also determined that the atmospheric abundances of CFC-11 and CFC-12 should reach their “pre-ozone hole over Antarctica” levels by 50 to 100 years. The decline currently observed in the atmospheric abundance of these two source gases is obviously a good omen for the recovery of the stratospheric ozone layer. A recent simulation by Newman et al. [2009] besides predicts the destruction of the majority of the stratospheric ozone layer (i.e. global annual average losses of ozone greater than 60%) by 2065, if the Montreal Protocol had never existed and if the production of ozone-depleting substances had continued to grow at an annual rate of 3%.

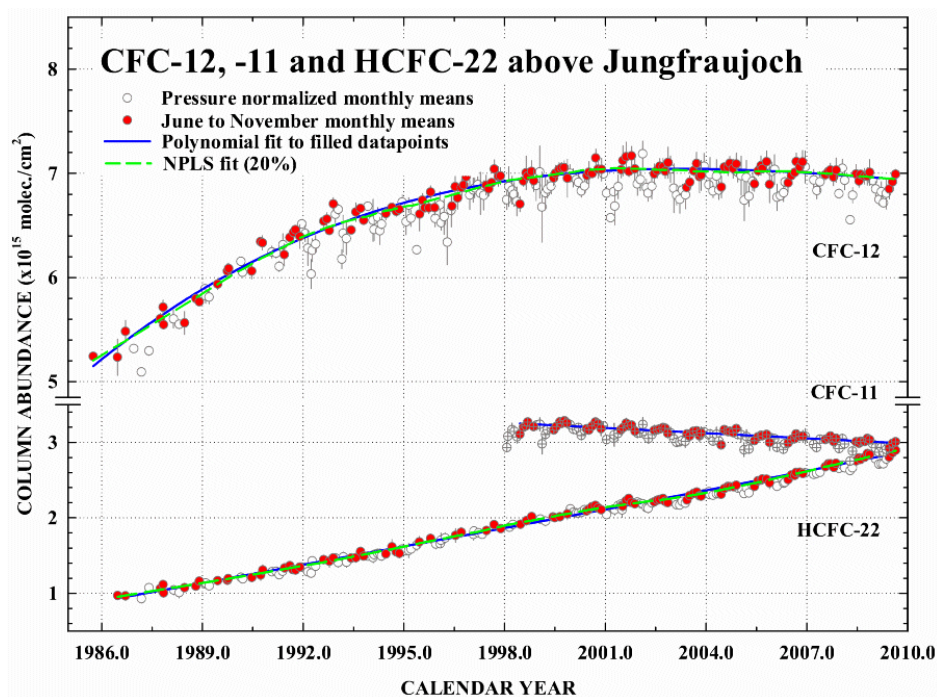


Fig. 1.11. Time series of CFC-12, CFC-11 and HCFC-22 derived from FTIR observations above Jungfraujoch. Data points are monthly mean values. Only June to November monthly means (corresponding to the quietest months in terms of dynamics; see red dots) have been used for the fitting of each time series (blue and green lines). Note the break in the vertical scale.

Since the Montreal Protocol plans the total phase out of CFCs substitute products by 2030 for the non-developing countries (see Table 1.5) and by 2040 for developing countries, their current atmospheric concentrations are still increasing (see Figure 1.11 for HCFC-22 and left and middle panels of Figure 1.12 for HCFC-141b and -142b). With a value close to 4%/yr, the growth rate of HCFC-22 is rather constant over the last decade [Mahieu et al., 2010]. This latter value is further in good agreement with the HCFC-22 stratospheric rate of $3.5 \pm 0.4\%/yr$ derived for mid-latitudes between 1994 and 2003 by Moore and Remedios [2008] and with the $3.9 \pm 2.1\%/yr$ rate obtained for the year 2004 by Rinsland et al. [2005]. Both HCFC-141b and HCFC-142b have however seen their accumulation rate significantly slowed since the end of the nineties, as their 2000-2004 rates of growth (7.6%/yr and 4.5%/yr, respectively) represent half the rates observed for these two gases for the 1996-2000 time period [WMO, 2007]. Figure 1.12 additionally shows that these slowdowns were not

predicted by model projections (see black curves on left and middle panels of Figure 1.12). For HCFC-142b, Rinsland et al. [2009] have derived from space data and for northern mid-latitudes a linear increase of $4.9 \pm 1.5\%/yr$ over the 2004-2008 time period.

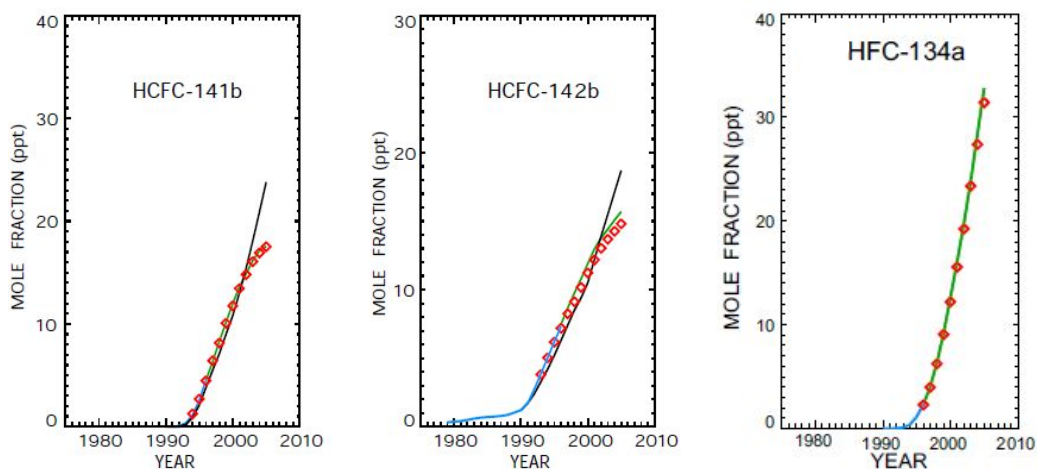


Fig. 1.12. Annual global mean mole fraction of HCFC-141b (left panel), HCFC-142b (middle panel) and HFC-134a (right panel) derived from the AGAGE (green solid lines) and from the National Oceanic and Atmospheric Administration/Earth System Research Laboratory (NOAA/ESRL, red diamonds) ground-based networks. For each panel, blue lines before 1995 are based on analysis of air archived in Australia [Oram et al., 1995]. Also shown in black on left and middle panels are tropospheric annual values from 1990 to 2005 derived from emissions scenario described in WMO [2003]. Figures extracted from WMO [2007].

It also appears that the recent atmospheric abundances of all measured HFCs are still increasing, despite efforts in latest years to limit their emissions through the Kyoto Protocol. In particular, the most abundant HFC-134a (right panel of Figure 1.12), that has widely replaced CFC-12 in several refrigeration and air-conditioning applications, has seen its growth rate reach 13%/yr in 2004, while the globally averaged concentrations of the two less abundant HFC-125 and HFC-152a were characterized, during the same year, by increases of 23%/yr and 17%/yr, respectively [WMO, 2007]. As it is principally emitted as a byproduct of HCFC-22 production, HFC-23 has increased at a similar mean rate as HCFC-22. According to WMO [2007], this rate equals 4%/yr for the 2001-2004 time period. Additional details concerning the response of HFC-23 emissions to HCFC-22 production can be found, for example, in Miller et al. [2010]. Table 1.6 provides an overview of all recent trends characterizing the atmospheric growths of CFCs, HCFCs and HFCs that have been mentioned in this section.

Based upon the objectives of the Montreal Protocol and its subsequent Amendments and Adjustments and upon the past and recent trends in halogenated source gases, the potential future mixing ratio of most of these source gases, as well as their impact on the stratospheric ozone layer, can be simulated from chemistry-climate models (CCMs). In that context, Eyring et al. [2010] have very recently analyzed projections of stratospheric ozone until the year 2100, derived from 17 CCMs characterized by different horizontal resolutions. Eyring et al. [2010] so conclude that for Northern mid-latitudes, the date of return of the mean annual total abundance of ozone to its 1980 level is around 2020 (with an uncertainty close to 7 years). Over the Antarctica, the return of the mean austral spring total abundance of ozone to its 1980 level is

predicted to occur around the middle of this century (see Table 3 of Eyring et al., 2010).

Common or industrial name	Linear trend ^a [%/yr]	References for details
Chlorofluorocarbons (CFCs)		
CFC-12	-0.15±0.04 [2001-2010]	Mahieu et al. [2010]
CFC-11	-0.83±0.06 [2001-2010]	Mahieu et al. [2010]
Hydrochlorofluorocarbons (HCFCs)		
HCFC-22	+4.22±0.07 [2001-2010]	Mahieu et al. [2010]
	+3.5±0.4 [1994-2003]	Moore and Remedios [2008]
	+3.9±2.1 [2004]	Rinsland et al. [2005]
HCFC-141b	+7.6 [2000-2004]	WMO [2007]
HCFC-142b	+4.5 [2000-2004]	WMO [2007]
	+4.9±1.5 [2004-2008]	Rinsland et al. [2009]
Hydrofluorocarbons (HFCs)		
HFC-134a	+13 [2004]	WMO [2007]
HFC-23	+4 [2001-2004]	WMO [2007]
HFC-152a	+17 [2004]	WMO [2007]
HFC-125	+23 [2004]	WMO [2007]

^a The corresponding uncertainty is also given, when available. Values between brackets specify the year or the time period for which the linear trend has been computed.

Table 1.6. Recent growth rates of the most abundant CFCs, HCFCs and HFCs.

The simulations (REF-B2 runs) performed in the study by Eyring et al. [2010] are based on assumptions made by the emission scenario A1B of IPCC [2000] for greenhouse gases (i.e. CH₄, CO₂ and N₂O; see also left panel of Figure 1.10 for the corresponding emission curve) and on a slightly adjusted version of the halogen scenario A1 of WMO [2007] for halogenated source gases emissions [Eyring et al., 2008]. The adjustment mainly consists in an accelerated phase out of HCFCs, as decided at the 2007 Meeting of the Parties to the Montreal Protocol (i.e. reduction of 75% of HCFCs emissions by 2010, instead of a reduction of 65%, the other objectives remaining unchanged). The simulations by Eyring et al. [2010] also only include the anthropogenic forcing, and not the natural contribution due, for example, to volcanic eruptions or solar variability, since they can not be known in advance.

Figure 1.13 reproduces the predicted mixing ratios of main CFCs (solid lines) and HCFCs (dashed lines) until 2050 that are based on the original A1 emission scenario of WMO [2007]. The vertical grey dashed line symbolizes the come into force of the Montreal Protocol. This Figure highlights the decrease of the atmospheric content of most of CFCs, typically less than 10 years after the Montreal Protocol. For CFC-12, the decrease is however postponed around 2005, after a period of stabilization initiated at the beginning of this century. These simulations reproduce qualitatively well what it has been experimentally observed above the Jungfraujoch station since the mid-eighties (see Figure 1.11). According to the simulated curve of HCFC-22, its atmospheric content should start to decrease within the next two years.

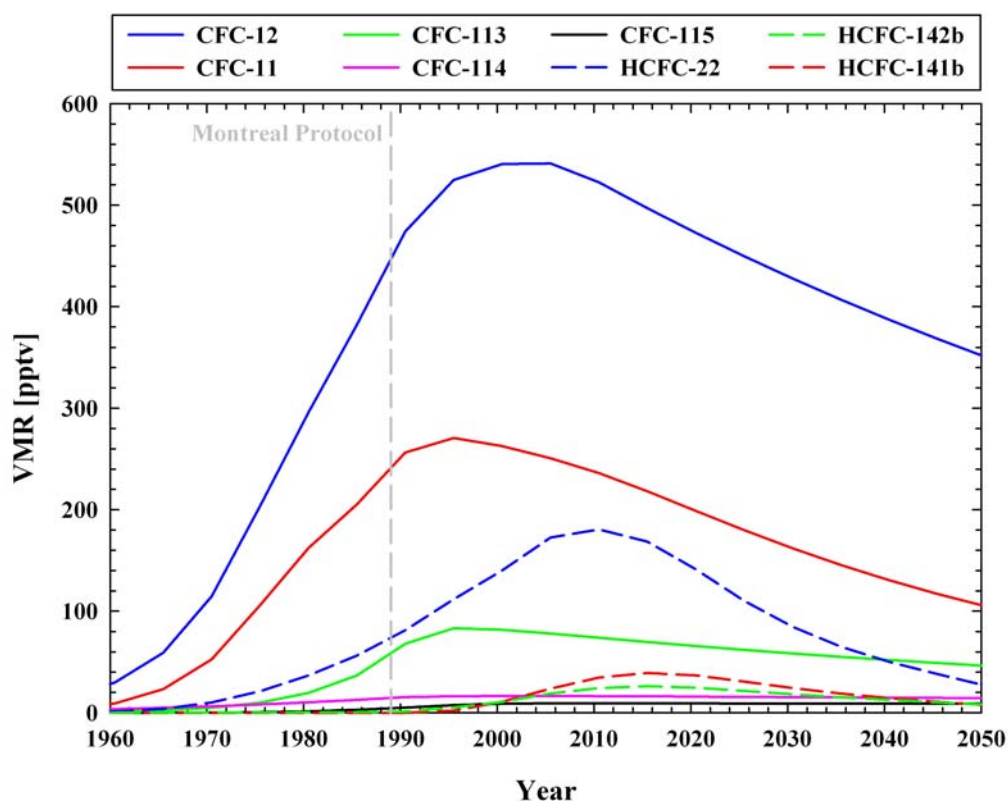


Fig. 1.13. Temporal evolution of the atmospheric content of the most abundant CFCs (solid curves) and HCFCs (dashed curves) until the middle of this century. These simulated curves have been obtained under the assumptions of the emission scenario A1 of WMO [2007] for halogenated source gases. The grey dashed vertical line refers to the come into force of the Montreal Protocol.

In Chapter 5, we will refer to such simulations of atmospheric mixing ratios of CFCs and HCFCs to notably explain the trends that characterize the evolution of the two main stratospheric fluorine reservoirs HF and COF_2 over the last decades. The monitoring of such reservoirs is obviously important since, as already evoked, their respective evolution with time notably allows to estimate the amount of relevant anthropogenic ozone-depleting substances or greenhouse gases injected in the atmosphere and therefore, to quantify the impact of human activities on the stratospheric ozone layer and on the global climate change, respectively.

References

Austin, J. and F. Li, On the relationship between the strength of the Brewer-Dobson circulation and the age of stratospheric air, *Geophys. Res. Lett.*, 33, L17807, 2006.

Brasseur, G. P., J. J. Orlando and G. S. Tyndall, *Atmospheric chemistry and global change*, Oxford University Press, 1999.

Brewer, A., Evidence for a world circulation provided by the measurements of helium and water vapour distribution in the stratosphere, *Quart. J. R. Meteorol. Soc.*, 75, 351-363, 1949.

Butchart, N., A. A. Scaife, M. Bourqui, et al., Simulations of anthropogenic change in the strength of the Brewer-Dobson circulation, *Clim. Dyn.*, 27, 727–741, 2006.

Chen, P., and W. A. Robison, Propagation of planetary waves between the troposphere and stratosphere, *J. Atmos. Sci.*, 49, 2533-2545, 1992.

Chipperfield, M. P., M. Burton, W. Bell, et al., On the use of HF as a reference for the comparison of stratospheric observations and models, *J. Geophys. Res.* 102, 12901-12919, 1997.

Also available at <http://orbi.ulg.ac.be/handle/2268/14547>

Crutzen, P. J., and F. Arnold, Nitric acid cloud formation in the cold Antarctic stratosphere: a major cause for the springtime "ozone hole", *Nature*, 324, 651–655, 1986.

DeMore, W. B., S. P. Sander, D. M. Golden, et al., Chemical kinetics and photochemical data for use in stratospheric modeling, Jet Propulsion Laboratory, California Institute of Technology, Evaluation No. 12, JPL Publ. 97-4, 1997.

Dufour, G., S. Szopa, M. P. Barkley, et al., Global upper-tropospheric formaldehyde : seasonal cycles observed by the ACE-FTS satellite instrument, *Atmos. Chem. Phys.*, 9, 3893-3910, 2009.

Eyring, V., M. P. Chipperfield, M. A. Giorgetta, et al., Overview of the New CCMVal Reference and Sensitivity Simulations in Support of Upcoming Ozone and Climate Assessments and the Planned SPARC CCMVal Report, SPARC Newsletter No. 30, 20–26, 2008.

Eyring, V., I. Cionni, G. E. Bodeker, et al., Multi-model assessment of stratospheric ozone return dates and ozone recovery in CCMVal-2models, *Atmos. Chem. Phys.*, 10, 9451-9472, 2010.

Farman, J., B. Gardner, and J. Shanklin, Large losses of total ozone in Antarctica reveal seasonal ClO_x/NO_x interaction, *Nature*, 315, 207–210, 1985.

Hadley, G., Concerning the cause of the general trade winds, *Philosophical Transactions*, 39, 58-62, 1753.

IPCC, Special report on emissions scenarios, Tech. rep., Intergovernmental Panel on Climate Change, IPCC/WMO/UNEP, 2000.

IPCC, Climate change 2007: The scientific basis, Tech. rep., Intergovernmental Panel on Climate Change, IPCC/WMO/UNEP, 2007.

Kompa, K. L., and J. Wanner, Study of some fluorine atom reactions using a chemical laser method, *Chem. Phys. Lett.*, 12, 560, 1972.

Lutgens, F. K. and Tarback, E. J., *The Atmosphere: An Introduction to Meteorology*, Prentice Hall, Upper Saddle River, New Jersey 07458, 8th edition, 2001.

Mahieu, E., C. P. Rinsland, T. Gardiner, et al., Recent trends of inorganic and halogenated source gases above the Jungfraujoch and Kitt Peak stations derived from high-resolution FTIR solar observations, poster presented at the EGU 2010 General Assembly, 2-7 May 2010, Vienna, Austria, 2010.

Also available at <http://orbi.ulg.ac.be/handle/2268/35065>

McElroy, M. B., R. J. Salawitch, S. C. Wofsy, and J. A. Logan, Reductions of Antarctic ozone due to synergistic interactions of chlorine and bromine, *Nature*, 321, 759–762, 1986.

McIntyre, M., and T. Palmer, Breaking planetary waves in the stratosphere, *Nature*, 305, 598-600, 1983.

Miller, B. R., M. Rigby, L. J. M. Kuijpers, et al., HFC-23 (CHF₃) emission trends response to HCFC-22 (CHClF₂) production and recent HFC-23 emission abatement measures, *Atm. Chem. Phys.*, 10, 7875-7890, 2010.

Molina, M., and F. Rowland, Stratospheric sink for chlorofluoromethanes: chlorine atom-catalysed destruction of ozone, *Nature*, 249, 810–2, 1974.

Mühle, J., A. L. Ganesan, B. R. Miller, et al., Perfluorocarbons in the global atmosphere: tetrafluoromethane, hexafluoroethane, and octafluoropropane, *Atmos. Chem. Phys.*, 10, 5145-5164, 2010.

Moore, D. P., and J. J. Remedios, Growth rates of stratospheric HCFC-22, *Atmos. Chem. Phys.*, 8, 73-82, 2008.

Nassar, R., P. F. Bernath, C. D. Boone, et al., A global inventory of stratospheric fluorine in 2004 on Atmospheric Chemistry Experiment Fourier transform spectrometer (ACE-FTS) measurements, *J. Geophys. Res.*, 111, 2006.

Also available at <http://orbi.ulg.ac.be/handle/2268/4285>

Newman, P. A., L. D. Oman, A. R. Douglass, et al., What would have happened to the ozone layer if chlorofluorocarbons (CFCs) had not been regulated?, *Atmos. Chem. Phys.*, 9, 2113-2128, 2009.

Oram, D. E., C. E. Reeves, S. A. Penkett, and P. J. Fraser, Measurements of HCFC-124b and HCFC-141b in the Cape Grim air archive: 1978-1993, *Geophys. Res. Lett.*, 22, 2741-2744, 1995.

Rinsland, C. P., C. Boone, R. Nassar, et al., Trends of HF, HCl, CCl₂F₂, CCl₃F, CHClF₂ (HCFC-22), and SF₆ in the lower stratosphere from Atmospheric Chemistry Experiment (ACE) and Atmospheric Trace Molecule Spectroscopy (ATMOS) measurements near 30°N latitude, *Geophys. Res. Lett.*, 32, 2005.

Also available at <http://orbi.ulg.ac.be/handle/2268/2400>

Rinsland, C. P., L. Chiou, C. Boone, et al., First measurements of the HCFC-142b trend from atmospheric chemistry experiment (ACE) solar occultation spectra, *J. Quant. Spec. and Rad. Transf.*, 110, 2127-2134, 2009.

Also available at <http://orbi.ulg.ac.be/handle/2268/27956>

Rosby, C.-G., Relation between variations in the intensity of the zonal circulation of the atmosphere and the displacements of the semi-permanent centers of action, *J. Marine Research*, 38-55, 1939.

Schoeberl, M. R., P. A. Newman, L. R. Lait, et al., An assessment of the ozone loss during the 1999-2000 SOLVE/THESEO 2000 Arctic campaign, *J. Geophys. Res.*, 107, 4334, 2002.

Sinnhuber, B.-M., N. Sheode, M. Sinnhuber, M. P. Chipperfield, and W. Feng, The contribution of anthropogenic bromine emissions to past stratospheric ozone trends: a modeling study, *Atmos. Chem. Phys.*, 9, 2863-2871, 2009.

Solomon, S., R. R. Garcia, F. S. Rowland, and D. J. Wuebbles, On the depletion of Antarctic ozone, *Nature*, 321, 755–758, 1986.

Steele, H. M., P. Hamill, M. P. McCormick, and T. J. Swisler, The formation of polar stratospheric clouds, *J. Atmos. Sci.*, 40, 2055–2067, 1983.

Stiller, G. P., T. von Clarman, M. Höpfner, et al., Global distribution of mean age of stratospheric air from MIPAS SF₆ measurements, *Atmos. Chem. Phys.*, 8, 677-695, 2008.

Stolarski, R., and R. J. Cicerone, Stratospheric chlorine: a possible sink for ozone, *Can. J. Chem.*, 52, 1610–1615, 1974.

Stolarski, R. S. and R. D. Rundel, Fluorine photochemistry in the stratosphere, *Geophys. Res. Lett.* 2, 433-434, 1975.

Toon, O. B., P. Hamill, R. P. Turco, and J. Pinto, Condensation of nitric acid and hydrochloric acid in the winter polar stratospheres, *Geophys. Res. Lett.*, 13, 1284–1287, 1986.

Tuazon, E. C., and R. Atkinson, Tropospheric transformation products of a series of hydrofluorocarbons and hydrochlorofluorocarbons, *J. Atm. Chem.*, 17, 1993.

Wallington, T. J., W. F. Schneider, D. R. Worsnop, et al., The environmental impact of CFC replacements – HFCs and HCFCs, *Env. Sci. Technol.*, 28, 320A, 1994.

Waple, A.M., J. H. Lawrimore, M. S. Halpert, et al., Climate Assessment for 2001, *Bulletin of the American Meteorological Society* 83, 2002.

World Meteorological Organization, WMO Report No. 47: Scientific Assessment of Ozone Depletion: 2002, P.O. Box 2300, Geneva 2, CH 1211, Switzerland, 2003.

World Meteorological Organization, WMO Report No. 50: Scientific Assessment of Ozone Depletion: 2006, P.O. Box 2300, Geneva 2, CH 1211, Switzerland, 2007.

World Meteorological Organization, Greenhouse Gas Bulletin: The State of Greenhouse Gases in the Atmosphere Using Global Observations through 2008, *Bulletin n°5*, November 2009.

Zander, R., C. P. Rinsland, E. Mahieu, et al., Increase of carbonyl fluoride (COF₂) in the stratosphere and its contribution to the 1992 budget of inorganic fluorine in the upper stratosphere, *J. Geophys. Res.* 99, 16737-16743, 1994.

Also available at <http://orbi.ulg.ac.be/handle/2268/14537>

Zander R., E. Mahieu, M. R. Gunson, et al., The 1994 northern midlatitude budget of stratospheric chlorine derived from ATMOS/ATLAS-3 observations, *Geophys. Res. Lett.*, 23, 2357-2360, 1996.

Also available at <http://orbi.ulg.ac.be/handle/2268/14566>

Chapter 2

FTIR measurements at Jungfraujoch

During the last three decades, environmental research at the International Scientific Station of the Jungfraujoch (hereinafter ISSJ; Swiss Alps, 46.5°N, 8.0°E, 3580 m asl) has been increasingly focused on the Earth's atmosphere. The suite of instruments operated at this research facility allows collecting many atmospheric parameters, such as trace gases and aerosols concentrations, meteorological data as well as solar and cosmic radiations. These measurements are derived by using several techniques, including infrared, microwave and UV spectroscopy, GPS receivers, multi-wavelength LIDAR system, mass spectrometry, and many others. Grouping, at the same place, such different scientific experiments, all devoted to the study of the Earth's atmosphere, is remarkable. One reason that explains this is the exceptional observational conditions that offer the Jungfraujoch site. As a direct consequence, all the geophysical data gathered by this multitude of instruments – most of which operated on the long-term - provides a precise and wide overview of the global state of our atmosphere, as well as an accurate idea of its temporal evolution.

The Solar and Atmospheric Physics Laboratory of the University of Liège is one of the pioneering experience devoted to the study of the Earth's atmosphere from the Jungfraujoch site, with first observations carried out in the early fifties. In 1974, this lab installs its first Fourier Transform Infrared (FTIR) spectrometer at ISSJ, progressively backed onwards by more modern spectrometers, allowing many thousands of FTIR spectra to be recorded. Regular operations have allowed over the years to constitute an outstanding observational high-resolution infrared time series, i.e. the longest FTIR database available worldwide.

In this Chapter, we firstly briefly explain the elemental physical and mathematical principles on which the FTIR technique is based. We then describe in details the configuration of the FTIR system currently in operation at the Jungfraujoch station. After having reviewed the fundamentals concerning the numerical analysis and characterization of FTIR products, we finally discuss on the possibilities to determine the instrumental line shape of a FTIR spectrometer from experimental data sets.

2.1. Basics of the FTIR technique

The mid-infrared region (wavelengths between 2 and 15 μm or wavenumbers between about 650 and 5000 cm^{-1}) encompasses the spectral signature of rotational or vibrational transitions of numerous atmospheric gases. Most modern atmospheric infrared measurements are performed with Fourier Transform Spectrometers (FTS) in order to obtain high signal-to-noise ratio in combination with high spectral resolution. When operating in the mid-infrared region, these spectrometers (i.e. FTIR spectrometers) record wide spectral intervals, allowing to derive the abundance of several dozens of atmospheric compounds.

The basic principle of a FTIR spectrometer is the same than for a Michelson interferometer. In such an interferometer (see Figure 2.1), the incident light falls on a semi-reflector beam-splitter (BS) that transmits half of the incident light, the other half being reflected. This latter part hits a fixed mirror (M1), while the transmitted component is reflected back by a moving mirror (M2). Both beams are then redirected on the beam-splitter, where they recombine. The starting position of the moving mirror is called the “Zero Path Difference” (ZPD) and corresponds to equal optical path lengths for both the transmitted and reflected beams. The Optical Path Difference (OPD) is defined as x if $x/2$ designates the displacement of the moving mirror. The maximum OPD is $2L$ if L is the maximum displacement of the moving mirror. The light beams that leaves the interferometer is then focused, by a collimating lens (CL), on the detector. The signal recorded by the detector is the light intensity of the combined beams versus the optical path difference x . Such signal is called an interferogram $I(x)$. At ZPD, all wavelengths have constructive interference and the interferogram is maximum.

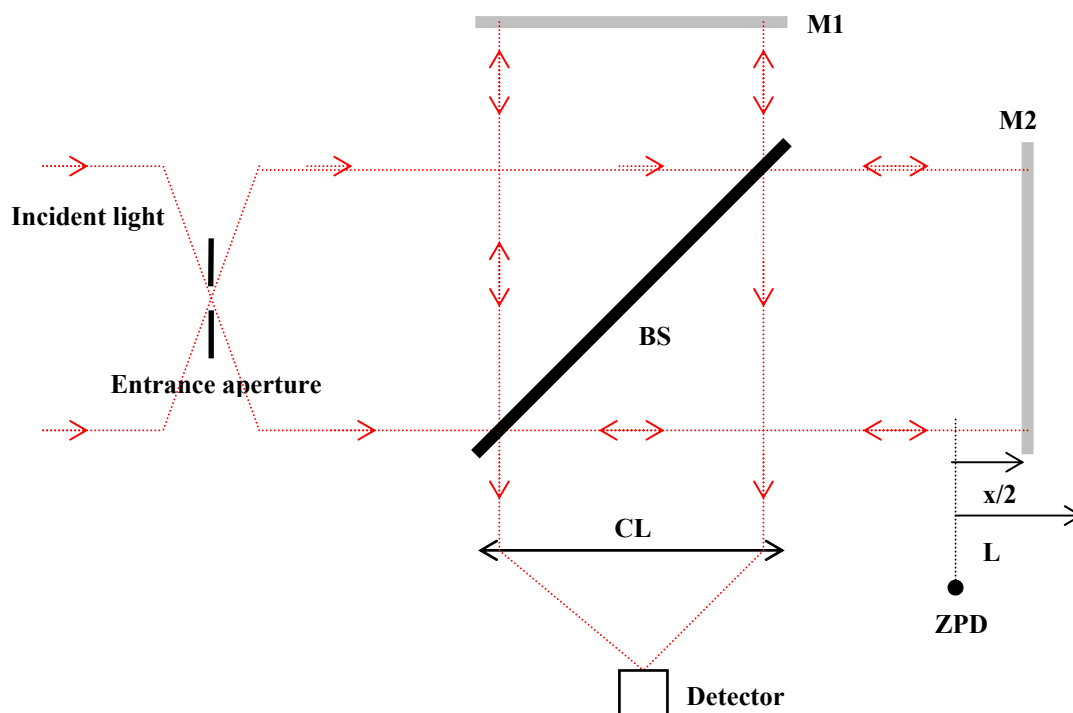


Fig. 2.1. Optical configuration of a Michelson interferometer (see text for acronyms definition).

For any displacement of M2, a light interference phenomenon occurs between the two beams which have not covered the same distance in each arm of the interferometer: the interferogram decreases to zero after showing successive maxima and minima, corresponding to constructive or destructive interferences, respectively. For a monochromatic light source, the interferogram $I(x)$ is given by:

$$I(x) = \frac{I}{2} \left(1 + \cos \left(\frac{2\pi x}{\lambda} \right) \right) \quad (2.1)$$

where I is the intensity of the light source and λ , its wavelength. As a consequence, a constructive interference is recorded by the detector (i.e. the signal $I(x)$ is maximum) each time the OPD is a round multiple of λ . If the OPD is an odd multiple of the half-wavelength $\lambda/2$, the interference is destructive and $I(x)$ equals zero. In practice, the interference fringes generated by a He-Ne laser are used by the spectrometer to control the position of the moving mirror. The infrared interferogram is also sampled each time the laser interferogram equals zero.

For a polychromatic light source (e.g. the light of the sun), characterized by a spectral distribution $S(\sigma)$, the interferogram $I(x)$ is given by the sum of the contributions of each spectral component $d\sigma$, that is:

$$I(x) = \int_0^{+\infty} S(\sigma) \cos(2\pi\sigma x) d\sigma \quad (2.2)$$

with $\sigma = 1/\lambda$ the wavenumber associated to each spectral component. This latter equation can be rewritten in complex notations, if we define, for $x > 0$, the physical, real and even function $S_e(\sigma) = [S(\sigma) + S(-\sigma)]/2$:

$$I(x) = \int_{-\infty}^{+\infty} S_e(\sigma) e^{2i\pi\sigma x} d\sigma \quad (2.3)$$

The interferogram is therefore given by the Fourier transform of the spectral signature of the light source. A high resolution spectrum of the source, modulated by the instrumental function (i.e. the ILS, for “Instrumental Line Shape”, see below) could consequently be obtained by taking the inverse Fourier transform of the interferogram, that is:

$$S_e(\sigma) = \int_{-\infty}^{+\infty} I(x) e^{-2i\pi\sigma x} dx \quad (2.4)$$

In Eq. (2.4), the integration interval is $]-\infty; +\infty[$, meaning that the moving mirror can be displaced on an infinite distance. Observed lines would therefore be Dirac delta functions (see top left panel of Figure 2.2). That is obviously not the case in practice. In reality, the maximum OPD is $2L$ and then, Eq. (2.4) becomes:

$$S_e(\sigma) = 2 \int_0^L I(x) e^{-2i\pi\sigma x} dx \quad (2.5)$$

or

$$S_e(\sigma) = \int_{-\infty}^{+\infty} I(x) D(x) e^{-2i\pi\sigma x} dx \quad (2.6)$$

where $D(x)$ is a rectangle function (or “boxcar” function) whose width is $2L$. Because the Fourier transform of a product of two functions is equivalent to the convolution product¹ of the Fourier transforms, Eq. (2.6) becomes:

$$S_e(\sigma) = \int_{-\infty}^{+\infty} D(x) e^{-2i\pi\sigma x} dx \otimes \int_{-\infty}^{+\infty} I(x) e^{-2i\pi\sigma x} dx \quad (2.7)$$

In Eq. (2.7), the Fourier transform of the boxcar function is a sinc function $\text{sinc}(x)$ and physically corresponds to the ILS of the spectrometer. Such $\text{sinc}(x)$ function has the propriety to present a maximum centered on $x=0$ and to have successive positive and negative lobes whose areas decrease as far as x becomes different from zero (see top right panel of Figure 2.2). Starting from the center of the $\text{sinc}(x)$ function, the distance that separates the two first cancellation points located on both sides of the center is $L/2$. This leads to one definition of the resolution that characterizes an FTIR spectrum: the resolution R is given by the inverse of the distance between two cancellation points of the $\text{sinc}(x)$ function, that is $R = 1/L$. According to Eq. (2.7), the observed FTIR lines are therefore deformed by the ILS (see bottom left panel of Figure 2.2).

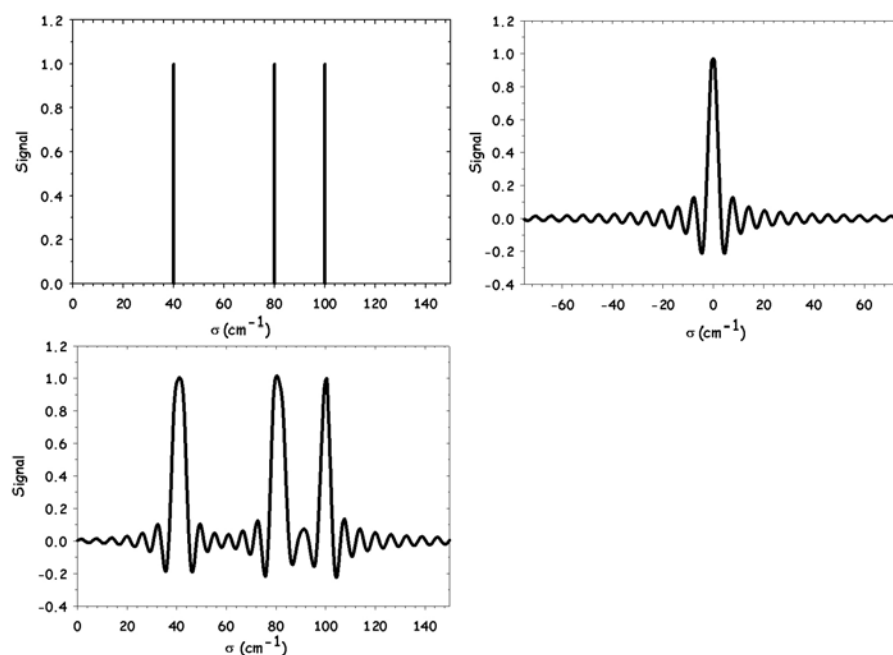


Fig. 2.2. The convolution product of a spectrum composed by Dirac delta functions (top left panel) with the Fourier transform of a boxcar function (top right panel) provides distorted spectral lines (bottom left panel).

To limit this effect, it is possible to apply special functions to the FTIR spectrum, or directly to its corresponding interferogram. Such functions are the so-called apodization functions. The positive and negative lobes of the $\text{sinc}(x)$ function are due to the abrupt decrease of the boxcar function. An apodization function is therefore a function equals to 1 when the OPD equals 0, and that slightly decreases to 0 as far as the moving mirror reaches the maximum OPD. Examples of apodization functions are triangles functions or Norton-Beer functions. One effect of the apodization functions is to increase the full width at half-maximum of the lines and thus, to decrease the

¹ The notation adopted here to designate such convolution product is \otimes .

spectral resolution. No apodization operation has been applied to the FTIR spectra analyzed in this work.

2.2. FTIR observations at the Jungfraujoch

All spectra that have led to the FTIR products presented in the four forthcoming chapters have been recorded at the International Scientific Station of the Jungfraujoch (Figure 2.3). As already evoked at the beginning of this chapter, the excellent observation conditions prevailing at this site have led the University of Liège to install and develop a specific instrumentation devoted to the recording of solar spectra, allowing the study of a wide number of atmospheric gases.



Fig. 2.3. The International Scientific Station of the Jungfraujoch. The Solar and Atmospheric Physics Laboratory of the University of Liège is based in the Sphinx observatory, at 3580 m asl (grey building on top of the picture).

The story starts in 1950, when M. Migeotte records his first solar infrared observations at Jungfraujoch. The air dryness (the water vapor abundance at Jungfraujoch is generally at least 20 times lower than at sea level) as well as the almost total absence of local pollution (no major industries for 20 km around) mainly explain the choice of a such high-altitude site (3580 m asl). The first spectrometer installed at Jungfraujoch by the University of Liège was a grating spectrometer with a focal length of 1 m. Corresponding ²spectral resolutions range from 0.12 to 0.40 cm⁻¹. However, these resolutions were already sufficient to record some absorption bands of carbon monoxide (CO) and methane (CH₄) [Migeotte and Neven, 1950; Nielsen and Migeotte, 1952].

Height years later, L. Delbouille and G. Roland install a more efficient grating spectrometer, whose focal length reaches 7.3 m. This instrument, fed by the solar light collected by an outdoor heliostat, has been mainly used to publish two atlases of the

solar spectrum in the near-infrared, in the visible and in the near-UV [Delbouille and Roland, 1963; Delbouille et al., 1973]. Most of the abundances of solar constituents that are still currently used by the scientific community are coming from these observations.

After the detection of HF in the Earth's atmosphere by R. Zander in 1975 [Zander, 1975] and after several studies related to the destruction of the stratospheric ozone layer [Crutzen, 1970; Johnston, 1971; Farman et al., 1985], observations at Jungfraujoch will mainly focus again on the chemical composition of the Earth's atmosphere. Total vertical abundances of gases such as HCl, HF, CH₄ and C₂H₆ will be routinely determined thanks to the grating spectrometer, specifically adapted to explore the mid-infrared region. First operating in a classical single-pass mode, the grating spectrometer will later be upgraded later in a double-pass mode including a narrow intermediate slit [Delbouille and Roland, 1963; Delbouille et al., 1973].

In 1974, the first FTS is installed at Jungfraujoch. Built in Liège, this spectrometer will record, in the forthcoming years, infrared observations, jointly with the grating spectrometer. In 1979, the FTS becomes more rapid (the observational mode moves from a step-by-step mode to a continuous mode), allowing to record FTIR spectra during both sunrises and sunsets, when the observational conditions change quickly. Fed by a 76 cm diameter telescope, its optimal spectral resolution reaches 0.0025 cm⁻¹. Regular observations with this instrument have started in the mid-eighties. To date, more than 10000 spectra have been recorded with the home-made instrument.

In 1990, the grating spectrometer is replaced by a commercial Bruker IFS-120HR FTS (Figure 2.4). Fed by an outdoor heliostat (top right inserted picture of Figure 2.4), this instrument is routinely in operation since 1992. The Bruker spectrometer can potentially record solar spectra with a maximum OPD of 500 cm (the corresponding spectral resolution being 0.001 cm⁻¹). However, the OPDs used in practice are optimized according to the line widths of the target gases and are therefore shorter: at highest resolution of 0.00285 cm⁻¹, the OPD is close to 175 cm. In addition, when the sun is low on the skyline, shorter OPDs are used in order to reduce acquisition time. Thus far, nearly 35000 spectra have been collected with the Bruker FTS.

Each FTIR spectrum recorded with the Bruker instrument generally corresponds to the average of three to five spectra, that are themselves the average of three to five scans. As a consequence, high signal-to-noise ratios are reached, in the order of several thousands. Both the home-made and the Bruker instruments have two detectors. The first one is a photoresistive detector made of HgCdTe, used for all recordings operated in the 5.6 to 14 μm region (mid-infrared). The second one is a photovoltaic cell made of InSb, sensitive in the region between 2 and 5.6 μm (near-infrared). Both detectors are cooled with liquid nitrogen, in order to increase their sensitivity.

Complete remote control of this spectrometer is possible since late 2008, thanks to the implementation over the last years of several mechanical and hydraulic systems in the heliostat and in the Bruker instrumentation. Furthermore, in addition to this task, a modernization procedure of the Bruker spectrometer, that mainly concerns the improvement of the acquisition chain, also currently takes place. Among others improvements, the record of FTIR spectra in "backward mode" (i.e. when the moving

mirror returns to its original position), the simultaneous usage of two detectors, better signal-to-noise as well as more precise knowledge of the ILS are still expected.

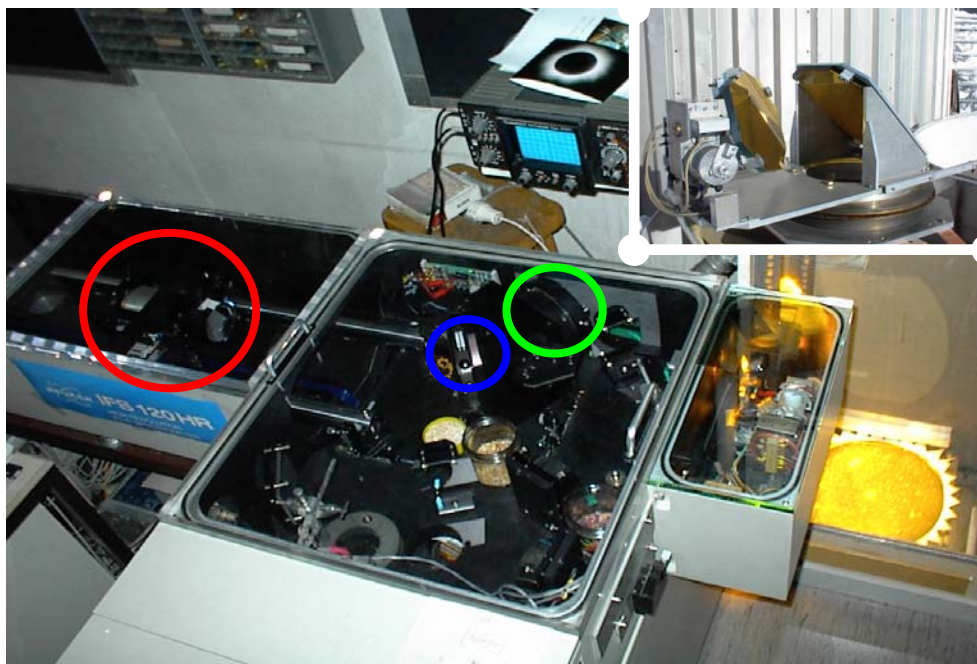


Fig. 2.4. The Bruker IFS-120HR Fourier transform spectrometer in operation at the International Scientific Station of the Jungfraujoch. The Solar and Atmospheric Physics Laboratory of the University of Liège currently gathers most of its observational data with this instrument. The moveable mirror, the beam-splitter and the fixed mirror are surrounded in red, blue and green, respectively. Top right inserted picture shows the outdoor heliostat that feeds the spectrometer.

Infrared spectral domains currently covered by both Jungfraujoch spectrometers (see Figure 2.5 and Table 2.1 on next page) allow the detection, as well as the short-, middle- and long-term study, of the evolution of more than two dozens atmospheric species, which is fundamental in the context of both the Montreal and the Kyoto Protocols. Among important gases whose vertical total abundances are routinely derived from FTIR spectra recorded at Jungfraujoch, one can cite: H_2O , CO_2 , CH_4 , O_3 , HCl , ClONO_2 , CFC-11, CFC-12, HCFC-22, HF , COF_2 and SF_6 . A more exhaustive list can be found for example in Zander et al. [2008].

The whole FTIR datasets gathered at Jungfraujoch by the two FTS since their respective commissioning already constitute a unique database worldwide, regarding its time range as well as its measurement density and quality. In addition, the possibility to compare FTIR data derived from two spectrometers simultaneously operated at the same location is a rare opportunity. During the formalization of the “Network for the Detection of Stratospheric Change” (NDSC) in 1989, in support of the 1985 Vienna Convention for the Protection of the Ozone Layer, it was thus without any surprise that the FTIR activities at the Jungfraujoch were readily selected to become the infrared component of the primary “NDSC Alpine Station” for monitoring the state of the stratosphere at northern mid-latitudes. The NDSC, renamed as “Network for the Detection of Atmospheric Composition Change” (NDACC; see <http://www.ndacc.org>) in 2005, will celebrate its 20th anniversary this year.

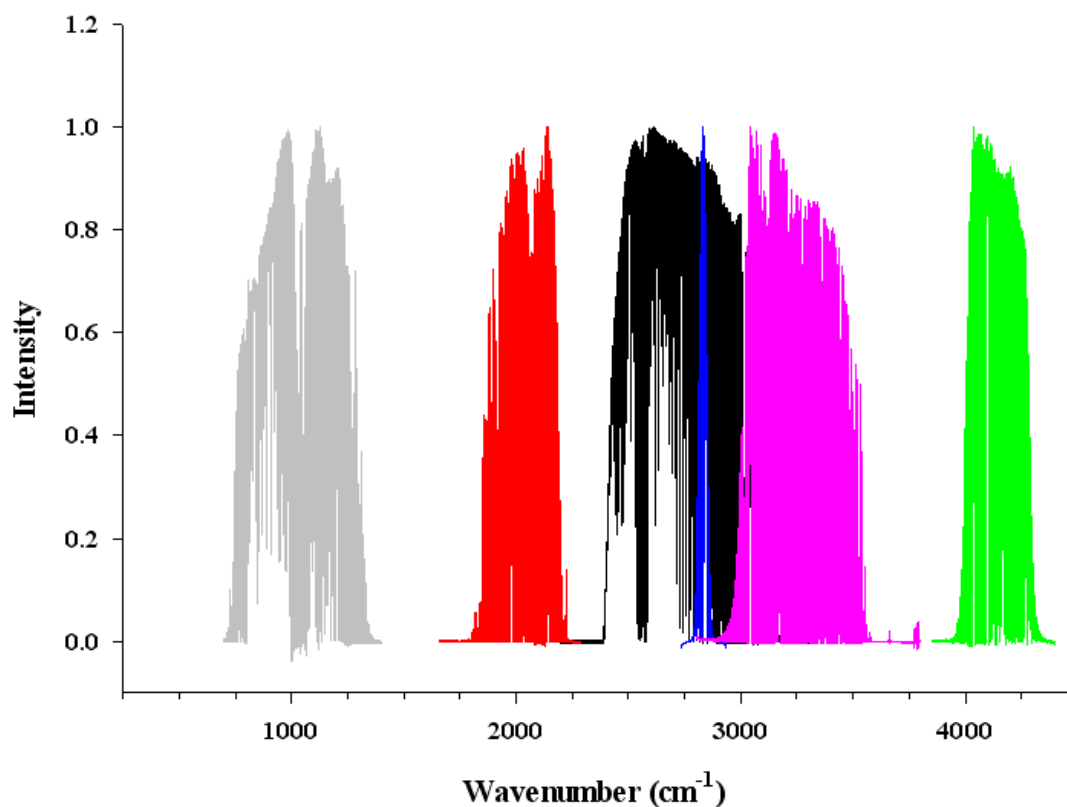


Fig. 2.5. Experimental Bruker 120HR spectrometer spectra recorded with the 6 most frequently used bandpass filters at Jungfraujoch (see Table 2.1 for precise wavenumber limits).

Filter Number	Wavenumber Range (cm ⁻¹)	Spec. Resolution (cm ⁻¹)	Main Target Species
1	350 – 1600	6.10 and 4.00	O ₃ , COF ₂ , CFC-11, CFC-12, HCFC-22
2	1800 – 2250	4.40 and 2.85	NO, COF ₂ , OCS, CO, O ₃
3	2200 – 3300	4.96 and 2.85	N ₂ , N ₂ O, CO ₂ , CH ₄ , HCl
4	2735 – 2935	5.03	H ₂ CO
5	2800 – 3800	4.00	HCN
6	3900 – 4350	4.40	HF

Table 2.1. Main characteristics of each bandpass filter illustrated (with the same color code) on Figure 2.5.

2.3. Inversion and characterization of FTIR products

Apart from direct *in situ* sounding from, for example, balloon or airplane flights, measurements of the Earth's atmosphere chemical composition generally use remote techniques. Remote instruments, such as ground-based FTIR spectrometers, record, in a given wavelengths domain, the intensity of an electromagnetic radiation (i.e. its luminance) after passing through the atmosphere. It does not consist in a direct measurement of the concentration of the atmospheric gases but in the direct impact of these latest ones on the electromagnetic radiation itself. With the FTIR technique, the problem we want to solve (often designated as the “inverse problem”) is thus the

following: to invert the vertical abundance and/or the vertical distribution of a given atmospheric gas from spectroscopic observations (i.e. FTIR spectra). While the atmospheric abundance of a given gas is directly linked to the area delimited by one of its absorption line, deriving information about its vertical distribution is also possible because of the pressure broadening of the lines that leads to an altitude dependence of the line shapes. While the line centers provide information about the higher altitudes of the vertical distribution, the wings of a line provide information about the lower altitudes (Figure 2.6). The atmospheric abundance of a gas derived from FTIR measurements is often expressed in terms of total (or partial) vertical columns, defined as the sum of all molecules of this gas contained in a squared-section column extending from the top of the atmosphere down to the measurement station, per unit area (units: molecules per centimeter square, i.e. molec./cm²). Vertical distributions are commonly given in VMR units (like ppmv, ppbv, pptv, etc).

However, remote measurements always bring, inherently, a limited information on the vertical distribution of a given atmospheric gas, due, for example, to technical aspects or to the noise contained in the measurement. As a direct consequence, it is thus impossible to invert a vertical profile with an infinite vertical resolution, but only a limited number of independent pieces of information. In other words, the inverse problem is an ill-posed and under-constrained mathematical problem: there are more unknowns than equations and there is no unique solution.

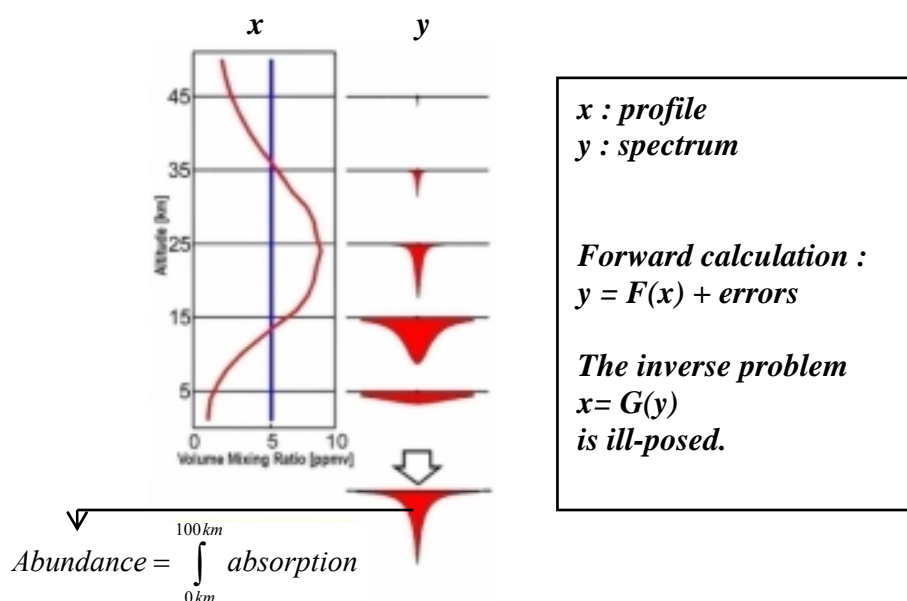


Fig. 2.6. Simplified representation of the inverse problem (source: <http://imk-ifu.fzk.de/295.php>)

As a consequence, to converge, inversion algorithms have thus to contain additional constraints, like, for example, a constraint on the vertical resolution of the inverted profile. Another type of constraint, often implemented in inversion algorithms, is the use of statistical data sets concerning the state of the atmosphere, like a climatology of a given gas that includes its spatial and temporal variability. Retrieved profiles are therefore not simple measurements of the real state of the atmosphere, but rather the best estimation of this state, knowing the measurement and the *a priori* state of the atmosphere as well as their respective uncertainties.

Among inversion methods, the most frequently used by the retrieval algorithms is the Optimal Estimation Method (OEM) [Rodgers, 1976]. Based on the Bayes' theorem, this statistical approach was initially developed for internal geophysics fields [Backus and Gilbert, 1968, 1970] and has been then transposed to process atmospheric remote measurements. In particular, the OEM matrix formalism developed by Rodgers [1990, 2000] allows to fully characterize the inversions, i.e. to quantify the information content associated to the measurement, to distinguish between the retrieved profile components coming from the measurement and from the *a priori* state, and to establish an error budget thanks to covariance matrices. In addition, this formalism is also applicable to other inversion methods, like the Tikhonov-Phillips regularization [Phillips, 1962; Tikhonov, 1963]. In the following pages, we give a brief summary of theoretical basics associated to the Rodgers formalism and implemented in the two retrieval algorithms used in this work (namely, SFIT-2 and PROFFIT). Sources used to write this part are principally Rodgers [2000], Steck [2002] and Ceccherini et al. [2005].

Let designate by \mathbf{y} the measurement vector. This vector contains, for example, the intensities measured at different wavelengths in a spectral region where the target gas presents absorption features. The state vector \mathbf{x} contains the finite number of unknown quantities to be determined during the retrieval process. For example, this could be the concentrations of a given gas at the different n altitude or pressure levels of the retrieval grid. The physics that gathers the \mathbf{x} and \mathbf{y} quantities is not perfectly known but can be estimated with a radiative transfert model (or forward model). The relationship between the state vector \mathbf{x} , the measurement vector \mathbf{y} and the forward model $\mathbf{F}(\mathbf{x})$ is given by:

$$y = F(x, b) + \varepsilon \quad (2.8)$$

where ε is the measurement noise vector. The forward model also depends on different parameters \mathbf{b} that are also not necessary perfectly known by the user, like spectroscopic parameters (e.g. absorption cross sections, line intensities, etc) or parameters that characterize the instrument. For example, with the SFIT-2 and PROFFIT codes, the forward model is a multi-layer multi-species line-by-line radiative transfert model. Instrumental parameters include, among others, a wavenumber scale multiplier (the wavenumber shift), background curve parameters (slope and curvature), the optical path difference and the field of view. Additional functions, such as apodization and phase error functions, are also included to account for deviations from a perfectly aligned FTS. Spectroscopic data necessary for the forward model are read from a spectroscopic line parameters database, such as HITRAN¹ (High-resolution TRANsmission molecular absorption database) or GEISA² (Gestion et Etude des Informations Spectroscopiques Atmosphériques).

¹ <http://www.hitran.com>

² <http://www.lmd.jussieu.fr/recherche/outils/bases-de-donnees/geisa>

The inverse problem thus consists in finding \hat{x} (the best estimator of the state vector \mathbf{x}) on basis of Eq. (2.8), knowing the measurement vector \mathbf{y} . For FTIR measurements, as the forward model is nonlinear, the optimal solution is iteratively reached by use of the Gauss-Newton method:

$$\mathbf{x}_{i+1} = \mathbf{x}_i + (\mathbf{K}_i^T \mathbf{S}_\varepsilon^{-1} \mathbf{K}_i + \mathbf{R})^{-1} \cdot [\mathbf{K}_i^T \mathbf{S}_\varepsilon^{-1} \cdot (\mathbf{y} - F(\mathbf{x}_i)) - \mathbf{R} \cdot (\mathbf{x}_i - \mathbf{x}_a)] \quad (2.9)$$

where \mathbf{K} is the Jacobian matrix of \mathbf{F} with respect to \mathbf{x} (the elements of \mathbf{K} are the partial derivatives of the measurement \mathbf{y} with respect to the retrieved parameters), \mathbf{S}_ε is the error covariance matrix, \mathbf{x}_a is the *a priori* state vector, the subscript i stands for the iteration index and the superscript T designates the transpose operation. During the iterative process, the forward model thus attempts to simulate the measurements at best, using the *a priori* state as a starting point. The measurement is fit to the calculated state, using a nonlinear least squares procedure (i.e. the Gauss-Newton method) during which the residuals (the differences between the measurement and the calculated state) are minimized through a series of iterations.

Equation (2.9) shows that the solution is the weighted mean of two terms. The first term between the square brackets corresponds to the contribution of the measurement to the retrieved solution. It measures how the forward model calculated in \mathbf{x} is able to reproduce the measurement, within the errors. The second term in the square brackets represents the contribution of the *a priori* state: it constraints the shape of the retrieved profile to follow that of \mathbf{x}_a . This constraint is applied through the regularization matrix \mathbf{R} . In the trivial case where \mathbf{R} is the identity matrix \mathbf{I} , the retrieved profile is obtained by applying a simple scaling operation to the *a priori* profile \mathbf{x}_a .

There are two principal different ways to incorporate constraints in atmospheric retrieval problems: climatological and smoothing constraints. With climatological constraints¹, the regularization matrix (square matrix of dimension $n \times n$) is the inverse of the *a priori* full covariance matrix \mathbf{S}_a , i.e. $\mathbf{R} = \mathbf{S}_a^{-1}$ in Eq. (2.9). Ideally, the *a priori* full covariance matrix \mathbf{S}_a should express the natural variability of the target gas: a large number of independent profiles from a climatological dataset is therefore required.

However, because of a lack of data, a full matrix is often not available and simplest matrices, such as pure diagonal or *ad hoc* matrices, are used. Extra-diagonal elements of an \mathbf{S}_a matrix expresses the fact that inter-layer correlation (ILC) exists between the concentrations of the target gas at different altitudes. For example, with the SFIT-2 algorithm, the user has the choice to introduce such extra-diagonal elements by defining a Gaussian or an exponential inter-correlation. In the first case (the most commonly used), the ILC at a given altitude z of the retrieval grid is simulated by the following function:

$$ILC(z) = \exp \left\{ - \left[\frac{a \cdot |z_i - z|}{l_c} \right]^2 \right\} \quad (2.10)$$

¹ When a climatological constraint is applied, the regularization method itself is often referenced as OEM, despite the fact that this constitutes an abuse of terminology.

in which a is a constant ($a = 0.832555$), z_i are the altitude levels of the retrieval grid and l_c is the inter-layer correlation length. For a given altitude z , this latter parameter physically corresponds to the distance beyond which VMR at other altitudes are no more in correlation with (i.e. no more influenced by) the VMR at the altitude z . A good approximation of l_c can be obtained from a 3D VMR-altitude correlation matrix \mathbf{C} , derived from climatological dataset (e.g. a set of m VMR profiles of the target gas, whose mean VMR is noted \overline{VMR}). Such \mathbf{C} matrix can be constructed according to the equation:

$$\mathbf{C} = \frac{1}{m} \mathbf{S} \mathbf{Y} \mathbf{Y}^T \mathbf{S}^T \quad (2.11)$$

The dimension of this square matrix is $n \times n$ and its c_{kl} element gives the correlation coefficient between the VMRs at altitude levels z_k and z_l .

The \mathbf{S} matrix is a $n \times n$ diagonal matrix whose diagonal elements are the inverse of the standard deviations computed, for each altitude level, over the whole VMR profiles considered, i.e.:

$$\mathbf{S} = \text{diag} \left(\frac{1}{s_1}, \dots, \frac{1}{s_n} \right) \quad (2.12)$$

with

$$s_i^2 = \frac{1}{m} \sum_{j=1}^m (VMR_{ij} - \overline{VMR}_i)^2 \quad (2.13)$$

for $i = 1, \dots, n$. The \mathbf{Y} matrix is a $m \times n$ matrix whose elements are given by:

$$y_{ij} = VMR_{ij} - \overline{VMR}_i \quad (2.14)$$

The determination of the optimal value for the ILC length l_c is performed by plotting columns of the \mathbf{C} matrix versus the altitude levels z_i . Grey curves of Figure 2.7 give an example of such plot for COF_2 and for all altitude levels between 24 and 40 km. The COF_2 VMR dataset used to derive the \mathbf{C} matrix envisaged here corresponds to all ACE-FTS satellite profiles recorded between February 2004 and September 2005 in the $41\text{-}51^\circ$ N latitude band (a contour plot of this \mathbf{C} matrix is provided on Figure 1 of Chapter 4). This represents more than 300 space occultations.

The three colored curves of Figure 2.7 represent the Gaussian approximations calculated by using Eq. (2.10) for the three altitude levels mentioned and for an ILC length of 2 km. The relative good agreement between these colored curves and their corresponding experimental curves let suggest that an ILC length of 2 km is a reasonable choice for stratospheric COF_2 amounts inversion. Unfortunately, the SFIT-2 code only allows to set the ILC length to a unique value for all altitudes. When the ILC length significantly varies with altitude, it is recommended to adopt the best compromise for l_c (e.g. its mean value or the value corresponding to the altitude

region where the sensitivity of the retrieval is maximum) or a full \mathbf{S}_a matrix if enough climatological data are available.

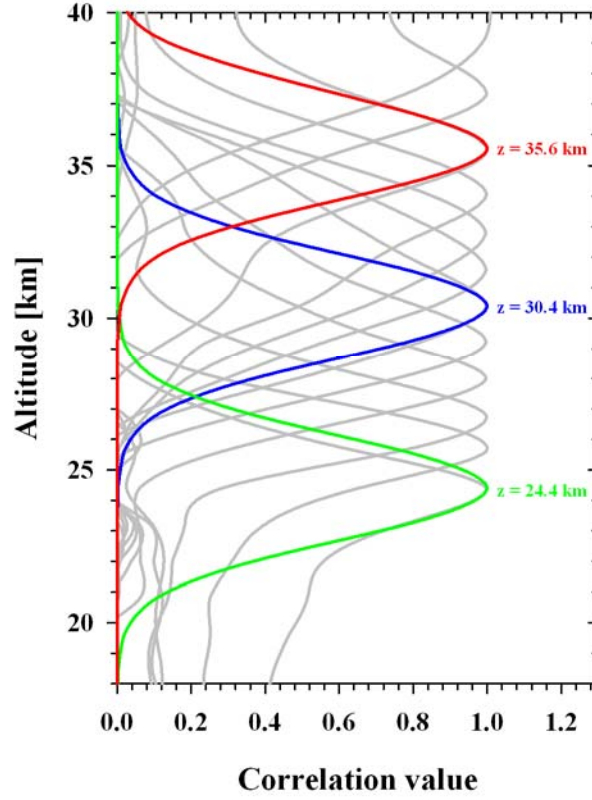


Fig. 2.7. Columns of the CO₂ VMR-altitude correlation matrix \mathbf{C} versus the altitude (grey curves), for all altitude levels comprises between 24 and 40 km. The three colored curves correspond to Gaussian approximations computed with an ILC length of 2 km, for the three discrete altitudes mentioned.

With smoothing constraints, the regularization matrix is set such as $R = \alpha L^T L$, where α is the strength of the constraint and \mathbf{L} is the constraint operator. The Tikhonov-Phillips regularization (or more simply, the Tikhonov regularization) is probably the *ad hoc* smoothing constraint the most commonly used in atmospheric retrieval problems. With the first-order Tikhonov regularization, the constraint operator \mathbf{L}_1 is defined by:

$$L_1 = \begin{pmatrix} -1 & 1 & 0 & \dots & 0 \\ 0 & -1 & 1 & \vdots & \vdots \\ \vdots & \ddots & \ddots & \ddots & 0 \\ 0 & \dots & 0 & -1 & 1 \end{pmatrix} \quad (2.15)$$

whose dimension is $(n-1) \times n$. Such operator constraints the shape of the retrieved profile, but not the absolute values. The determination of the absolute values is done through the information that is located in the measurement and not in the constraint. That is the fundamental difference between smoothing and climatological operators, as these latter inherently contain information on the absolute values, i.e. throughout

the information on the natural variability of the target gas contained in the S_a matrix. In practice, the lack of data to construct a reasonable *a priori* covariance matrix can also lead to the use of smoothing operators. Moreover, these operators often avoid the appearance of non-physical oscillations in the retrieved profiles, that could occur with climatological operators.

For regularization matrices of the type $R = \alpha L^T L$, different methods for determining the strength of the constraint α can be applied, depending on the available *a priori* knowledge of the problem and on the requirements defined by the user. The approach the most commonly used is based on the value of the degree of freedom for signal (DOFS), that quantitatively characterizes the information content of the retrieval (see description of Eq. 2.16). The idea is to tune the α parameter in order to reach a reasonable value for the DOFS. The dependence between α and the DOFS is such that when $\alpha \rightarrow 0$, the DOFS becomes close to n (the number of state parameters, i.e. the number of atmospheric layers in the forward model) and large oscillations in the retrieved profile occur, and when $\alpha \rightarrow +\infty$, the DOFS tends to zero and the retrieved profile merges with the *a priori* profile (see Figure 1 of Steck [2002]). In other words, the case $\alpha \rightarrow 0$ corresponds to a totally unconstrained profile retrieval while the case $\alpha \rightarrow +\infty$ is a simple profile scaling retrieval. This method (of tuning α aiming at a given DOFS) has been successfully used, for example, by Vigouroux et al. [2009] for their formaldehyde retrievals from FTIR measurements at Réunion Island. Additional approaches to determine the strength of the constraint, mainly based on error values, are discussed in Steck [2002]. For their FTIR water vapor retrievals at Zugspitze, Sussmann et al. [2009] also use the correlation between their FTIR measurements and coincident radio soundings to determine the optimal value of the α parameter.

As already evoked, the matrix formalism of Rodgers also allows the determination of the vertical sensitivity of the retrieved profile. This is done through the analysis of the so-called averaging kernels matrix \mathbf{A} , defined in Rodgers [2000] by:

$$A = (K^T S_e^{-1} K + S_a^{-1})^{-1} \cdot K^T S_e^{-1} K \quad (2.16)$$

The plot of the lines of the \mathbf{A} matrix versus the altitude provides bell-shaped curves, whose full widths at half maximum qualitatively describe the vertical resolution of the retrieval. The altitude range for which averaging kernels are close to the unity further indicates that the sensitivity is maximum. Outside the sensitivity range, the averaging kernels are close to zero and the retrieved profile merges with the *a priori* profile \mathbf{x}_a . The trace of the \mathbf{A} matrix provides the DOFS, i.e. the number of independent pieces of information that could be derived from the retrieval (mainly expressed in terms of partial columns). In addition, eigenvectors of \mathbf{A} (and their associated eigenvalues) allow to determine quantitatively which components of the inverted state are effectively coming from the measurements: while components with eigenvalues equal (or are close to) 1 are characterized by an information that is principally coming from the measurement, the components for which the eigenvalues are close to zero mainly reproduce the *a priori* state.

Averaging kernels are also useful in order to compare vertical profiles recorded by instruments characterized by different vertical resolutions. This difference has to be accounted for, if we want to perform a proper comparison. According to Connor et al.

[1994], one way to proceed is to consider the vertical profile characterized by the higher resolution, \mathbf{x}_h , as the reference, in order to obtain a smooth version \mathbf{x}_s of this latter profile:

$$x_s = x_a + A.(x_h - x_a) \quad (2.17)$$

in which the \mathbf{A} matrix is obviously the averaging kernels of the lower resolution instrument. In other words, the smooth profile \mathbf{x}_s is equivalent to the vertical profile that would be observed by the instrument with the higher resolution if this instrument was set in the same observational conditions as the lower resolution instrument.

Finally, the formalism of Rodgers [2000] allows to split the error in the retrieved profile in three different error sources: the smoothing error, the forward model parameters error and the retrieval noise. The smoothing error, that expresses the uncertainty linked to the limited vertical resolution of the retrieval, can be determined by its covariance matrix:

$$S_s = (A - I).S_{\text{var}}.(A - I)^T \quad (2.18)$$

where \mathbf{S}_{var} should represents the natural variability of the target gas, i.e. $\mathbf{S}_{\text{var}} = \mathbf{S}_a$. The covariance matrix associated to the forward model parameters error is given by:

$$S_f = (G_y K_b).S_b.(G_y K_b)^T \quad (2.19)$$

where \mathbf{G}_y is the gain matrix representing the sensitivity of the retrieved parameters to the measurement, \mathbf{K}_b is the sensitivity matrix of the measurement vector to the forward model parameters \mathbf{b} and \mathbf{S}_b is the covariance matrix associated to \mathbf{b} . The retrieval noise covariance matrix can be calculated from:

$$S_n = G_y S_\epsilon G_y^T \quad (2.20)$$

The total error covariance matrix is then simply given by:

$$S_{\text{tot}} = S_s + S_f + S_n \quad (2.21)$$

Errors on total column ϵ_{TC} can be easily derived from their corresponding covariance matrices \mathbf{S} by using:

$$\epsilon_{\text{TC}} = \mathbf{g}^T \mathbf{S} \mathbf{g} \quad (2.22)$$

in which \mathbf{g} is the operator that transforms the volume mixing ratio profile into total column amount. For the computation of errors on partial column ϵ_{PC} , the elements of \mathbf{g} in Eq. (2.22) are simply set to zero for all altitudes outside of the concerned partial column limits.

Practical applications of most of these concepts (i.e. information content analysis, smoothing operation and error budget estimation) to FTIR Jungfraujoeh measurements are proposed in Chapters 3 and 4.

2.4. The problematic of the instrumental line shape

The knowledge of the ILS that characterizes the FTIR spectrometer constitutes a major issue. Indeed, a misaligned spectrometer can see its ILS to be prone to distortions, leading to the retrieval of wrong gas concentrations from the atmospheric observations. In practical, some of these distortions can be taken into account by most of the inversion algorithms (like SFIT-2 or PROFFIT). These codes use effective apodization functions to simulate distortions generated by the rectangle function $D(x)$ that multiplies the interferogram $I(x)$ (see Eq. (2.7)).

Such effective apodization functions can be defined by the user as polynomial functions of degree N , Fourier series of order N or any other tabulated functions defined point by point. In any case, at ZPD, such functions equal 1. The effective apodization parameter (EAP) gives the value of the effective apodization function at the maximum OPD. During the atmospheric retrievals, when a first-order polynomial function is used as the effective apodization function (which is often the case in practice), an EAP value close to 1.0 is synonymous with a well-aligned instrument.

In principle, the ILS can be determined either with a single mode laser or with cell measurements. Cell measurements are however made quite easily, as it simply consists in placing a gas-contained cell in the optical pathway of the spectrometer. The light source used during such measurements is provided by a globar system. The analysis of cell spectra is performed, for example, through the LINEFIT code, developed by F. Hase and T. Blumenstock (KIT, Karlsruhe, Germany) and widely used within the NDACC infrared community [Hase et al., 1999]. Similar to the analysis of atmospheric spectra, cell spectra are analyzed by fitting synthetic spectra to measured ones. In the case of cell spectra, physical parameters that characterize the gas probed are well known (pressure, temperature, composition) and fitted parameters are ILS parameters. During the middle of the years 2000, the NDACC has provided to its primary stations HBr cells, in order to regularly check the good alignment of their FTIR spectrometers. The ILS of the Bruker IFS-120HR in station at the Jungfraujoch is thus frequently measured since more than 5 years.

Figure 2.8 reproduces the evolution with time of the EAP, for the Bruker instrument of the Jungfraujoch. Each data point of Figure 2.8 has been obtained from HBr cell measurements analyzed with the LINEFIT v.8 code and consists in the average of several cell observations performed during each campaign of cell measurements (error bars are $1-\sigma$ standard deviations). Except from some sparse episodes characterized by lower EAP values (i.e. at the end of the year 2001 and during the years 2005 and 2010), Figure 2.8 indicates that the alignment of the Bruker spectrometer is quite stable with time. The origin of these jumps is still under investigation but is possibly ascribable to cleaning operation of the mirrors located before the interferometric system.

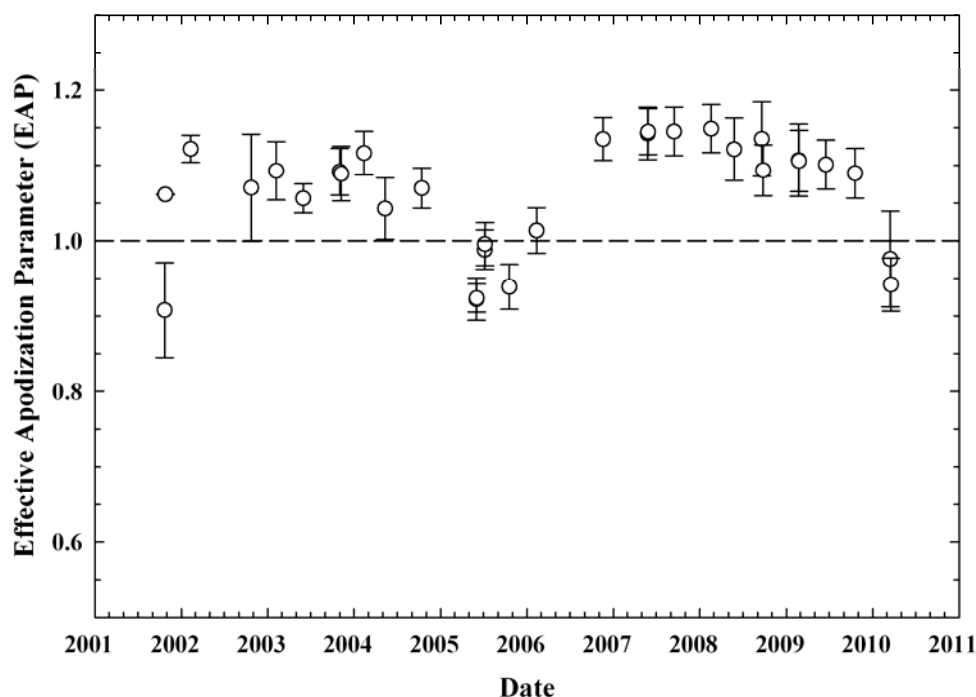


Fig. 2.8. Time evolution of the Effective Apodization Parameter characterizing the Bruker spectrometer in station at the Jungfraujoch, as deduced with the LINEFIT v.8 code.

The EAP values close to 1.0 observed for the 2002-2005 time period is the consequence of a realignment of the Bruker spectrometer operated by F. Hase in February 2002. Another realignment of the Bruker instrument has also taken place in June 1997, but no HBr cell spectra are available for that period. Retrievals of atmospheric measurements can fortunately be used to estimate the ILS of the spectrometer, when cell measurements are not available. This is performed by adjusting the EAP while fitting either N_2 or CO_2 . The choice of these two gases to invert EAP values from atmospheric lines principally lies in the fact that the vertical distributions of these species are very simple and well-known, since they are essentially constant throughout the atmosphere.

Here we have checked the possibility to derive EAP values from atmospheric ozone retrievals. Total vertical abundances of ozone above Jungfraujoch are notably retrieved from its absorption lines encompassed in the $3039.18 - 3040.05 \text{ cm}^{-1}$ microwindow. Inclusion of the inversion of EAP during the ozone retrieval procedure has been proposed by Barret et al. [2002]. These authors have indeed noticed that such EAP inversion allows correcting for distortions of the ILS while significantly improving the agreement between FTIR ozone retrieved products and correlative data (see Figures 6 and 7 of Barret et al., 2002). White dots on Figure 2.9 reproduce the deseasonalized EAP time series between 1994 and 2009, derived from ozone retrievals at Jungfraujoch. Red dots are the results of HBr cell measurements (i.e. the data points reproduced on Figure 2.8). However, in order to obtain a better agreement between both time series, “atmospheric measurements” have been scaled up by about 8%. The black trace on Figure 2.9 is a running mean computed over the “atmospheric observations”. The overall agreement obtained indicates that ozone retrievals near 3040 cm^{-1} constitute a good alternative to cell measurements in order to characterize the ILS of the Jungfraujoch Bruker spectrometer.

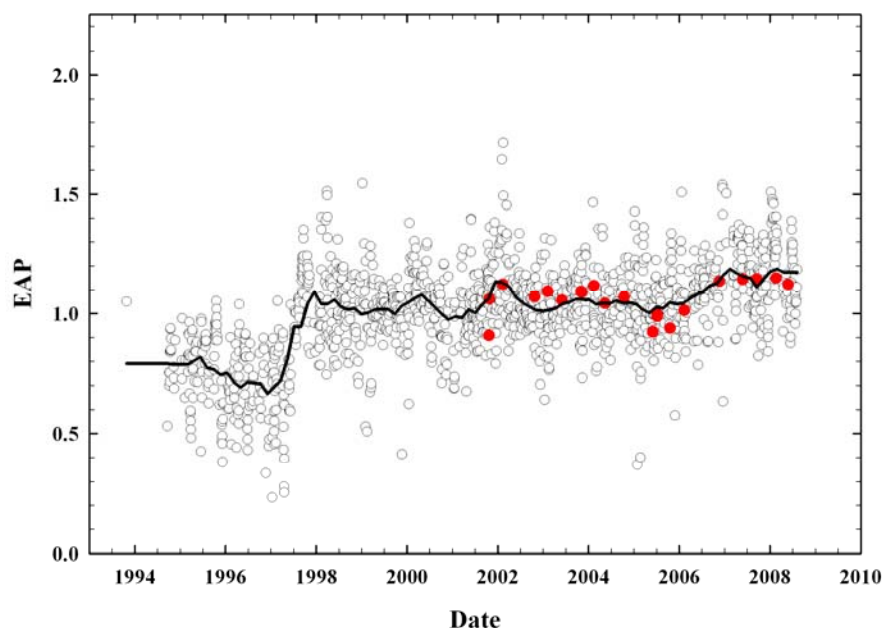


Fig. 2.9. 1994-2009 deseasonalized time series of EAP derived from atmospheric O_3 observations above Jungfraujoch. Red dots are HBr cell measurements of Figure 2.8.

It is important to account for the misalignment which has characterized the Bruker instrument before 1997. We have indeed noticed, before the realignment operated in June 1997, significantly lower or higher retrieved HF partial column amounts (whose corresponding time series are presented in Figure 3.5 of Chapter 3), as a direct consequence of well-marked non-geophysical oscillations in our retrieved HF profiles (see below). In order to correct our retrieved HF quantities, we have imposed, during the retrieval process of the FTIR observations recorded between 1994 and May 1997, fixed appropriate values to the EAP. Values adopted were deduced from a linear fit computed over the EAP time series plotted on Figure 2.9, for the corresponding problematic time period. Figure 2.10 illustrates an example of the impact on HF retrieved profiles when introducing such EAP correction in the retrieval procedure, for the May-June 1997 time period, i.e. before the realignment of the Bruker instrument.

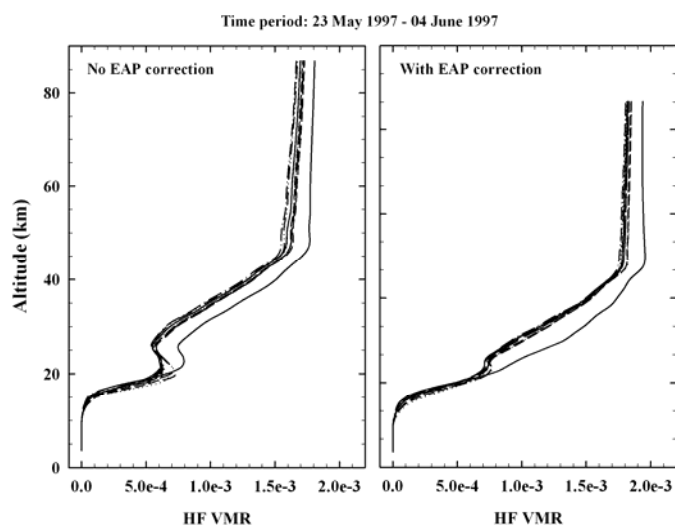


Fig. 2.10. Example of HF retrieved profiles with PROFFIT derived before the Bruker realignment. Left panel: when no correction on the EAP is applied (i.e. EAP is assumed to equal 1.0). Right panel: when the EAP value is derived from Figure 2.9, for the corresponding time period mentioned on top of this Figure.

Mainly, systematic oscillations observed in the lower stratosphere are significantly smoothed or totally removed. In addition, the two lower stratospheric HF partial columns (between 10 and 17 km, and between 17 and 25 km, respectively; see Chapter 3) see their values reduced (in average) by around 5% and 10%, respectively. The upper stratospheric HF partial columns (between 25 and 40 km, see Chapter 3) are the most impacted by the EAP correction, with average enhancement close to 20%. The impact on HF total columns is very limited, with average variations lower than 1%. Anyway, when an EAP correction is applied, the HF partial columns values are more consistent with the HF partial column time series starting after the Bruker realignment, for which we have assumed an EAP equal to 1.0, synonymous with a well aligned instrument. This constitutes a good approximation, as indicated by Figures 2.8 and 2.9.

References

- Backus, G. and F. Gilbert, The resolving power of gross Earth data, *Geophys. J. R. astr. Soc.*, 16, 169-205, 1968.
- Backus, G. and F. Gilbert, Uniqueness in the inversion of inaccurate gross Earth data, *Phil. Trans. R. Soc. London*, 266 (A1173), 123-192, 1970.
- Barret, B., M. De Mazière, and P. Demoulin, Retrieval and characterisation of ozone profiles from solar infrared spectra at the Jungfrauoch, *J. Geophys. Res.*, 107, NO. D24, 4788, 2002.
- Ceccherini, S., Analytical determination of the regularization parameter in the retrieval of atmospheric vertical profiles, *Opt. Lett.*, 30, 2554-2556, 2005.
- Connor, B. J., D. E. Siskind, J. J. Tsou, A. Parrish and E. E. Remsburg, Ground-based microwave observations of ozone in the upper stratosphere and mesosphere, *J. Geophys. Res.* 99, 16757-16770, 1994.
- Crutzen, P. J., The influence of nitrogen oxide on the atmospheric ozone content, *Quart. J. Roy. Met. Soc.* 96, 320, 1970.
- Delbouille, L. and G. Roland, Photometric atlas of the solar spectrum from λ 7498 to λ 12016, *Inst. d'Astrophysique et de Géophysique, Univ. de Liège*, 1963.
- Delbouille, L., L. Neven and G. Roland, Photometric atlas of the solar spectrum from λ 3000 to λ 10000, *Inst. d'Astrophysique et de Géophysique, Univ. de Liège*, 1973.
- Farman, J. C., B. G. Gardiner and J. D. Shanklin, Large losses of total ozone in Antarctic reveal seasonal ClO_x/NO_x interaction, *Nature* 315, 207, 1985.
- Hase, F., T. Blumenstock and C. Paton-Walsh, Analysis of instrumental line shape of high-resolution FTIR-spectrometers using gas cell measurements and a new retrieval software, *Appl. Opt.*, 3417-3422, 1999.

Johnston, H. S., Reduction of stratospheric ozone by nitrogen ozone catalysts from supersonic transport exhaust, *Science* 173, 517, 1971.

Migeotte, M. and L. Neven, Détection du monoxyde de carbone dans l'atmosphère terrestre à 3580 mètres d'altitude, *Physica* 16, 423-424, 1950.

Nielsen, A. H. and M. Migeotte, Abundance and verticale distribution of telluric methane from measurements at 3580 meters elevation, *Ann. Astrophys.* 15, 134-141, 1952.

Phillips, D. L., A technique for the numerical solution of certain integral equations of the first kind, *J. Assoc. Comput. Math.*, 9, 84-97, 1962.

Rodgers, C. D., Retrieval of atmospheric temperature and composition from remote measurement of thermal radiation, *Rev. Geophys. And Space Phys.*, 14, 609-624, 1976.

Rodgers, C. D., Characterization and error analysis of profiles retrieved from remote sounding measurements, *J. Geophys. Res.*, 95(D5), 5587-5595, 1990.

Rodgers, C. D., Inverse methods for atmospheric sounding, Series on atmospheric, oceanic and planetary physics, vol.2, World Scientific, Singapore, 2000.

Steck, T., Methods for determining regularization for atmospheric retrieval problems, *Appl. Opt.*, 41, 1788-1797, 2002.

Sussmann, R., T. Borsdorff, M. Rettinger, et al., Technical note: Harmonized retrieval of column-integrated atmospheric water vapor from the FTIR network – first example for long-term records and station trends, *Atmos. Chem. Phys.*, 9, 8987-8999, 2009.
Also available at <http://orbi.ulg.ac.be/handle/2268/34144>

Tikhonov, A., On the solution of incorrectly stated problems and a method of regularization, *Dokl. Akad. Nauk SSSR*, 151, 501-504, 1963.

Vigouroux, C., F. Hendrick, T. Stavrou, et al., Ground-based FTIR and MAX-DOAS observations of formaldehyde at Réunion Island and comparisons with satellite and model data, *Atmos. Chem. Phys.*, 9, 9523-9544, 2009.

Zander, R., Présence de HF dans la stratosphère supérieure, *C. R. Acad. Sci. Paris, Sér. B* 281, 213-214, 1975.

Zander, R., E. Mahieu, P. Demoulin, et al., Our changing atmosphere : Evidence based on long-term infrared solar observations at the Jungfraujoch since 1950, *Sci. Total Environ.*, 391, 184-195, 2008.
Also available at <http://orbi.ulg.ac.be/handle/2268/2421>

Chapter 3

Long-term FTIR time series of hydrogen fluoride

As described in Chapter 1, halogenated gases such as CFCs, Halons, HCFCs and HFCs are long to very long-lived species, as long as they stay in the troposphere. Once transported to the stratosphere, these gases are dissociated and release chlorine, bromine and fluorine atoms or radicals. While the two first aforementioned species significantly contribute to the destruction of stratospheric ozone through different catalytic cycles, fluorine radicals are quickly converted into hydrogen fluoride (HF), preventing fluorine to deplete the ozone layer [Stolarski and Rundel, 1975]. Moreover, its extreme stability makes HF the dominant fluorine reservoir in the middle and upper stratosphere, as well as the main contributor to the total inorganic fluorine burden. As a major consequence, measurements of the HF abundance provide a good idea on how much halogenated source gases are emitted from the surface and how much they are dissociated when they reach the stratosphere. Another interest to study HF lies in the fact that hydrogen fluoride constitutes an excellent dynamical tracer, which can then be used as a reference, for example to compare observations performed at different sites or to understand the variations of other species.

The main purpose of the present Chapter is to produce a long-term HF time series derived from FTIR observations performed at the Jungfraujoch station. Such time series are very useful since they allow, with the help of model simulations, to assess for the evolution of the release of anthropogenic source gases, whose emissions from the surface are continually evolving, in particular in response to international Protocols. In a first step, we deeply expose and characterize (on basis of the mathematical concepts evoked in Chapter 2) the retrieval strategy on which HF inversions from FTIR measurements at the Jungfraujoch are based. In particular, we critically discuss the impact of the choice of the line shape model adopted to simulate HF absorptions. Then, we perform comparisons of FTIR products with satellite and model data, to finally conclude with a study concerning the HF seasonal cycle. The appendix notably provides a complete information content analysis as well as a detailed error budget.

The following pages reproduce the full text of a scientific article accepted for publication in 2010 by *Journal of Geophysical Research*.

Hydrogen fluoride total and partial column time series above the Jungfraujoch from long-term FTIR measurements: Impact of the line-shape model, characterization of the error budget and seasonal cycle, and comparison with satellite and model data

P. Duchatelet¹, P. Demoulin¹, F. Hase², R. Ruhnke², W. Feng³, M.P. Chipperfield³, P.F. Bernath⁴, C.D. Boone⁵, K.A. Walker^{5,6} and E. Mahieu¹

¹ Institute of Astrophysics and Geophysics of the University of Liège, B-4000 Liège, Belgium

² Karlsruhe Institute of Technology, Institute for Meteorology and Climate Research (IMK-ASF), Karlsruhe, Germany

³ Institute for Climate and Atmospheric Science, School of Earth and Environment, University of Leeds, Leeds, UK

⁴ Department of Chemistry, University of York, Heslington, UK

⁵ Department of Chemistry, University of Waterloo, Waterloo, Canada

⁶ Department of Physics, University of Toronto, Toronto, Canada

Abstract

Time series of hydrogen fluoride (HF) total columns have been derived from ground-based Fourier transform infrared (FTIR) solar spectra recorded between March 1984 and December 2009 at the International Scientific Station of the Jungfraujoch (Swiss Alps, 46.5°N, 8.0°E, 3580 m asl) with two high resolution spectrometers (one home-made and one Bruker 120-HR). Solar spectra have been inverted with the PROFFIT 9.5 algorithm, using the optimal estimation method. An inter-comparison of HF total columns retrieved with PROFFIT and SFIT-2 – the other reference algorithm in the FTIR community - is performed for the first time. The effect of a Galatry line shape model on HF retrieved total columns and vertical profiles, on the residuals of the fits and on the error budget is also quantified. Information content analysis indicates that, in addition to HF total vertical abundance, three independent stratospheric HF partial columns can be derived from our Bruker spectra. A complete error budget has been established and indicates that the main source of systematic error is linked to HF spectroscopy and that the random error affecting our HF total columns does not exceed 2.5%. Ground-based middle and upper stratospheric HF amounts have been compared to satellite data collected by the HALOE or ACE-FTS instruments. Comparisons of our FTIR HF total and partial columns with runs performed by two 3D numerical models (SLIMCAT and KASIMA) are also included. Finally, FTIR and model HF total and partial columns time series have been analyzed to derive the main characteristics of their seasonal cycles.

3.1. Introduction

Fluorine enters the stratosphere mainly in the form of chlorofluorocarbons (CFCs) and hydrochlorofluorocarbons (HCFCs) which have been widely emitted at ground level by human activities over the past few decades. Among these man-made components, primary contributors to atmospheric fluorine are CFC-11 (CCl_3F) and CFC-12 (CCl_2F_2) [Zander et al., 1992; Montzka et al., 1999; Nassar et al., 2006] with more recent contributions from HCFC-22 (CHClF_2) [O'Doherty et al., 2004; Nassar et al., 2006], since CFC-11 and CFC-12 emissions from the ground have been progressively phased out by the Montreal Protocol and its subsequent Amendments. The long tropospheric lifetimes of these fluorine source compounds allow them to be transported into the lower stratosphere, where the photolysis of CFC-11 and CFC-12 leads to the formation of the two temporary reservoirs chlorofluoroformaldehyde (COCIF) and carbonyl fluoride (COF_2) which are characterized by lifetimes of the order of months in the lower stratosphere [Chipperfield et al., 1997]. Studies dealing with measurements of COF_2 or COCIF using ground-based, in situ or space-borne techniques include Wilson et al. [1989], Zander et al. [1994], Mélen et al. [1998], Nassar et al. [2006], Fu et al. [2009] and Duchatelet et al. [2009].

Subsequent photolysis of COF_2 and COCIF then releases F atoms, which can quickly react with CH_4 , H_2O or H_2 to form the extremely stable hydrogen fluoride (HF) gas, thus preventing a catalytic ozone destruction cycle involving fluorine [Stolarski and Rundel, 1975]. The formation of HF by these reactions is significant, as they make HF the largest fluorine reservoir in the middle and upper stratosphere. For example, near 40 km at midlatitudes, HF contributes almost 80% to the total inorganic budget F_y (see Figure 4a of Nassar et al., 2006). The extreme stability of HF also makes this gas an excellent tracer of air mass transport and subsidence in the lower stratosphere [Chipperfield et al., 1997]. The main sinks of stratospheric HF are its slow diffusion into the troposphere, with eventual rainout, and its upward transport into the mesosphere, where it is destroyed by photolysis.

Zander [1975] was the first to detect the presence of HF in the Earth's atmosphere. Since then, several studies dealing with HF total column amounts derived from ground-based infrared solar observations at several latitudes in both hemispheres have been published (e.g. Zander et al., 1987; Reisinger et al., 1994; Notholt et al., 1995; Rinsland et al., 2002). In addition, recent years have seen the emergence of more sophisticated retrieval algorithms allowing vertical distributions as well as partial column abundances to be determined from FTIR spectra recorded at ground-based stations affiliated with the Network for the Detection of Atmospheric Composition Change (NDACC; see <http://www.ndacc.org>). Illustration of such HF products can be found for example in Barret et al. [2005], Mahieu et al. [2008] and Senten et al. [2008].

Vertical distributions of hydrogen fluoride have also been measured by a large number of balloon, aircraft and space experiments (e.g. Coffey et al., 1989; Toon et al., 1992; Zander et al., 1992; Sen et al., 1996; Considine et al., 1999; Nassar et al., 2006). In particular, HF data gathered during four missions of the Atmospheric Trace Molecule Spectroscopy (ATMOS; Gunson et al., 1996) and by the Halogen Occultation Experiment (HALOE; Russell et al., 1993) from 1991 to 2005 have provided a significant set of global HF vertical distribution measurements. Since then,

the Atmospheric Chemistry Experiment Fourier Transform Spectrometer (ACE-FTS; Bernath et al., 2005) is the only space instrument currently monitoring most of major source and sink fluorine-containing gases (including HF) on a global scale. All of these ground-based or space observations have provided important information on the HF column amounts and vertical distributions, its seasonal and latitudinal dependence, its temporal trends and are of great interest for direct comparisons with numerical model calculations (see for example Rinsland et al., 1991; Chipperfield et al., 1997, Ruhnke et al., in preparation).

Despite the fact that fluorine does not directly participate in ozone depletion, measurements of the concentrations of individual F-containing species in different altitude ranges of the atmosphere are important as they reflect the amounts of anthropogenic gases - which often also contain ozone-depleting chlorine and/or bromine atom(s) - transported into the middle atmosphere. In addition, as anthropogenic surface emissions of F-containing species are continually evolving (e.g. see Table 1-7 of WMO, 2007), the study of long-term fluorine time series is mandatory as this helps in the assessment of the magnitude and development with time of their release to the atmosphere. The main purpose of this paper is to present a 26-year time series of HF total vertical abundances derived from FTIR ground-based solar observations performed at the high-altitude International Scientific Station of the Jungfraujoch (hereafter ISSJ; 46.5°N, 8.0°E, 3580 m asl), an Alpine station located in the Swiss Alps and affiliated with the NDACC since 1989.

In section 3.2, we first give a complete overview of the retrieval strategy adopted for our FTIR spectra inversion. In particular, we compare HF total vertical abundances derived from two different retrieval algorithms (namely, SFIT-2 and PROFFIT). We further quantify the impact of the line shape model adopted to simulate HF absorption lines (Voigt or Galatry line shape models) on HF retrieved total columns and vertical profiles as well as on fitting quality. This section also provides a typical HF error budget. In section 3.3, we compare our FTIR HF partial columns (and total columns, as far as possible) to corresponding products derived from satellite observations (namely, HALOE and ACE-FTS; see section 3.3.1) and from two three-dimensional (3-D) chemical transport model (CTM) simulations (SLIMCAT and KASIMA; see section 3.3.2). In addition, FTIR and CTMs time series are further analyzed in order to derive the main characteristics of the HF seasonal cycle at different altitudes. Comparisons with previous studies are also included. Section 3.3 closes with a correlation study between HF seasonal variation and the tropopause height cycle above Jungfraujoch.

3.2. HF observational database and retrieval strategy

All the results produced in this study have been derived from high resolution solar spectra recorded at ISSJ under clear-sky conditions with two FTIR spectrometers between March 1984 and December 2009. From 1984 onwards, observations were made with a home-made (HM) FTIR spectrometer, backed since 1990 by a commercial Bruker-120 HR instrument. The observational database analyzed here consists of a subset of all spectra recorded with solar zenith angles (SZA) up to 85° and that encompass the R(1) line (4038.965 cm^{-1}) of the fundamental 1-0 band of HF (see Table 3.1 for precise microwindow limits and interfering gases).

Range (cm ⁻¹)	Interfering species
4038.81 – 4039.07	H ₂ O, HDO, CH ₄

Table 3.1. HF microwindow used for our FTIR retrievals. Second column lists the interfering gases whose vertical distributions are adjusted during the retrieval process.

The HF line used here is probably the best transition for ground-based monitoring purposes as its spectroscopic parameters are well known [Pine et al., 1985], allowing HF column abundances to be accurately determined. This line is therefore commonly adopted for HF retrievals by FTIR ground-based stations (e.g. see Table 3 of Mahieu et al., 2008). Moreover, retrieval tests have also demonstrated that the adoption of additional HF microwindows (e.g. that encompass HF lines near 4000 or 4109 cm⁻¹) often provides a benefit for the information content, balanced however by a significant deterioration of the global fit residuals. Additional statistics concerning our FTIR database are provided in Section A1.

3.2.1. A priori information

The adopted a priori HF profile is a zonal mean (for the 41-51°N latitude band) of almost 800 occultations recorded by the ACE-FTS instrument between February 2004 and July 2008 (see left panel of Figure 3.1). These occultations are the version 2.2 of ACE-FTS products and corresponding HF measurements extend from about 14 km to 55 km. Above 55 km, the same a priori HF information used by ACE-FTS during its retrieval procedure has been adopted. For the lowest altitude levels (i.e. between the altitude site and 14 km), we have kept, for each individual profile, a constant value equal to the HF VMR value recorded by the ACE-FTS instrument at 14 km. Based on this climatological dataset, a full a priori covariance matrix S_a has been constructed. The (i,j) element of such covariance matrix is given, per definition, by:

$$S_a(i, j) = E[(VMR_i - \overline{VMR}_i) \times (VMR_j - \overline{VMR}_j)] \quad (3.1)$$

where VMR_k represents the kth element of a given VMR column vector, \overline{VMR}_k stands for the kth element of the mean VMR column matrix and E denotes the mathematical expectation, i.e. $E = \frac{1}{N} \cdot \sum_{i=1}^N y_i$, if we consider a set including N measurements vector

y_i . Since the covariance matrix we have obtained by using Eq. (3.1) with ACE-FTS climatological profiles was singular (non invertible), 20 % uncorrelated noise has been added to its diagonal elements. Right panel of Figure 3.1 illustrates the corresponding HF a priori variability profile, which corresponds to the diagonal elements of the S_a matrix.

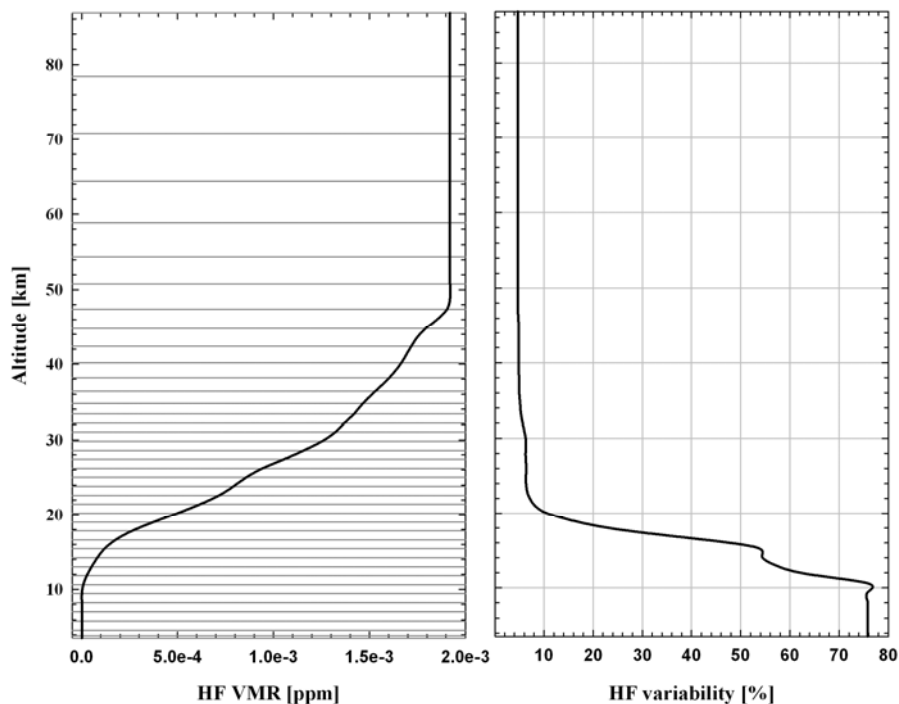


Fig. 3.1. A priori HF VMR profile (left) and corresponding variability profile (diagonal elements of S_a matrix; right panel) adopted for our FTIR HF retrievals. They are based on ACE-FTS measurements in the $[41-51]^\circ$ N latitude band. Background solid lines of left panel reproduce the 41 layer scheme adopted for the retrieval procedure.

3.2.2. Fitting algorithm

Our HF inversions have been performed with the PROFFIT v.9.5 algorithm, a code specifically developed at IMK-ASF, Karlsruhe, Germany, to derive total or partial columns and vertical profiles of atmospheric gases from high-resolution FTIR spectra [Hase et al., 2004]. With PROFFIT, the target gas as well as each interfering species can be fitted by applying, independently for each gas, one of the three following inversion techniques: (1) the optimal estimation method (OEM) [Rodgers, 2000]; (2) a Tikhonov-Phillips (TP) regularization [Tikhonov, 1963; Phillips, 1962]; (3) a scaling approach. In addition, when one of the two first regularization techniques is selected, the code can also perform inversions on a logarithmic vertical scale, in order to avoid non physical negative VMR values. The 9.5 version of PROFFIT also includes a module that allows a complete error budget to be established including contributions of the leading systematic or statistical (random) errors. A more detailed description of the PROFFIT code can be found in Hase et al. [2004].

Since the SFIT-2 algorithm [Rinsland et al., 1998] is the code most commonly used within the FTIR community to retrieve vertical abundances of atmospheric gases, we have found it useful to compare PROFFIT HF total column results with those generated by applying the SFIT-2 v3.91 algorithm. Such an intercomparison exercise has already been performed by Hase et al. [2004] for four atmospheric gases, including stratospheric (namely: ozone and HNO_3) and tropospheric (namely: HDO and N_2O) species, which are also characterized by different types of spectral signatures and by diverse spatial variability. Based on a typical set of three FTIR

spectra recorded at two high-latitude NDACC affiliated sites (Thule, 76.5°N, 68.7°W, 225 m asl and Kiruna, 67.8°N, 20.4°E, 420 m asl), Hase et al. [2004] have demonstrated the very good agreement found for retrieved total columns and retrieved vertical profiles of the four target gases, despite the fact that SFIT-2 and PROFFIT differ, notably in terms of ray tracing and radiative transfer algorithms. In particular, when similar regularization constraints are applied, the difference between total columns retrieved from both codes is within 1% for all gases under investigation.

For our own SFIT-PROFFIT intercomparison, we have adopted the following regularization parameters and ancillary inputs: (i) HF microwindow limits and interfering gases, as specified in Table 3.1: while an OEM procedure is applied for HF, VMR profiles of all interfering gases are simply scaled; (ii) a priori knowledge of HF (mean profile and covariance matrix) as described in section 3.2.1: similar a priori VMRs have also been adopted for the three interfering gases; (iii) the official HITRAN 2004 spectroscopic linelist [Rothman et al., 2005]; (iv) the pressure-temperature (p-T) profiles adopted during the retrievals are those provided by the National Centers for Environmental Prediction (NCEP, Washington, DC.; see <http://www.ncep.noaa.gov>), specifically computed for the ISSJ site on a daily basis; (v) all FTIR spectra recorded at ISSJ during 2005 and including the R(1) line of HF. The year 2005 has been selected because: (1) the large number of observations (~200) available that year; (2) the fact that special atmospheric events, like e.g. a polar vortex overpass, have occurred in 2005 above ISSJ.

Under these retrieval conditions, we have found a non significant mean relative difference in HF total columns (computed as $[(\text{SFIT-PROFFIT})/\text{PROFFIT}] \times 100$) equal to -0.99 ± 1.02 %, which is in excellent agreement with values reported by Hase et al. [2004]. The largest discrepancy (in absolute value) reaches 4.82 %. For the three observations recorded on 27 January (which corresponds to a vortex overpass above ISSJ - see Figure 4 of Duchatelet et al., 2009), the relative difference between both codes is close to 3 %, with PROFFIT HF total columns being higher than those retrieved with SFIT-2. Concerning interfering gases, it is important to mention that negative VMR values (mainly for HDO whose absorption in the HF microwindow at 4038 cm^{-1} is very weak at the high-altitude site of the Jungfraujoch) have been frequently derived with both codes. For example, for HF retrievals performed with SFIT-2, we have noticed negative HDO total columns in almost 20% of occurrences. For this reason we have decided to constrain all interfering gases with a TP first order smoothing regularization including a logarithmic vertical scale in our final HF PROFFIT retrieval strategy. For HF, we have kept the OEM approach including a priori information illustrated in Figure 3.1 but we have also worked on a logarithmic scale, for consistency.

3.2.3. Choice of line shape model

In the version 3.91 of SFIT-2, the direct model assumes a Voigt profile for the absorption line shape of each atmospheric gas. This profile takes simultaneously into account the perturbing influences of neighboring particles (pressure broadening effect) as well as the thermal translational motion of the target gas itself (Doppler broadening effect). The first effect leads to Lorentzian line shapes while the second one generates Gaussian line shapes. A Voigt profile is consequently given by the

convolution of a Lorentz function with a Gaussian one. However, as atmospheric molecules are also hindered in their free motion by collisions with the buffer gas, one can observe a narrowing of the Doppler component of the line shape. This collision-induced narrowing effect, most commonly known as the “Dicke effect” or “Dicke narrowing”, has been described for the first time by Dicke [1953] and by Wittke and Dicke [1956]. For most atmospheric molecules, this effect is weak, except for species with a free mean path greater than the wavelength of their transitions. According to Chou et al. [1999], this happens for HF when the pressure is less than 290 hPa (i.e. for altitudes approximately greater than 10 km).

Analytical models simultaneously including the Doppler broadening effect and the collision-induced narrowing effect exist and have been developed, for example, by Galatry [1961] (“soft” model) and by Rautian and Sobel’man [1967] (“hard” model). Barret et al. [2005] were the first to introduce such concepts in the direct model of an inversion algorithm of FTIR spectra (this code is called Atmosphit and has been developed at Université Libre de Bruxelles, Brussels, Belgium) to quantify the impact of the line narrowing effect on the retrievals of HCl and HF. It has been demonstrated by Barret et al. [2005] that, for HF inversions from its R(1) line performed with FTIR spectra recorded at Jungfraujoch, the introduction of the collisions-induced narrowing effect leads to smoother retrieved vertical profiles, mainly between 30 and 35 km. As a direct result, Barret et al. [2005] found that the agreement of such FTIR HF profiles with HALOE HF distributions improved and was more consistent with altitude, with a mean relative difference which does not exceed 10% between 15 and 50 km (see Figure 7 of Barret et al., 2005). In addition, Barret et al. [2005] also mention that this spectroscopic effect is almost without any consequence for HF retrieved total columns, with differences (relative to HF total columns obtained with a Voigt model) lower than 1%. In terms of spectral simulation quality, the differences they have obtained between synthetic spectra generated with the two line shape models are significant, especially in the center of the HF line. Barret et al. [2005] reports a relative difference between both models close to 3%, i.e. significantly larger than the spectral noise value (see also right panel of Figure 4 of Barret et al., 2005).

In addition to the Voigt model, the version 9.5 of PROFFIT is also able to perform retrievals including a Galatry “soft-collision” model. Even if these two line shape models are not “speed-dependent” models, which is not strictly valid, this is a minor issue for HF, as demonstrated by Pine and Ciurylo [2001]. Concerning our own HF retrievals, comparisons between both line shape models (Voigt and Galatry) have been performed with the same set of FTIR spectra used for the intercomparison of SFIT-2 with PROFFIT (see previous section). As in Barret et al. [2005], we have observed a significant smoothing of HF profiles when the Galatry model is used, mainly between 25 and 40 km (left panel of Figure 3.2). A small but significant relative difference (computed over the whole year 2005) between corresponding HF total columns of 1.18 ± 0.29 % was found (the error corresponds to 1- σ standard deviation), in good agreement with Barret et al. [2005]. Regarding fitting quality, a typical example of fit residuals is given in the top frame of the right part of Figure 3.2. A significant improvement is obtained when the Galatry model is adopted. In particular, systematic symmetric features observed in the center of the HF signature when the Voigt model is used are significantly reduced with the Galatry approach. The mean relative difference (for all FTIR observations of 2005) calculated as $[(\text{Voigt-Galatry})/\text{Galatry}] \times 100$ between fitting residuals obtained with both models is

18.97 ± 13.17 % ($\pm 1\text{-}\sigma$ standard deviation). This result highlights the fact that a Galatry line shape model definitely improves HF retrievals quality: it was consequently adopted in our final HF retrieval strategy with PROFFIT, whose main input parameters are summarized in Section A2.

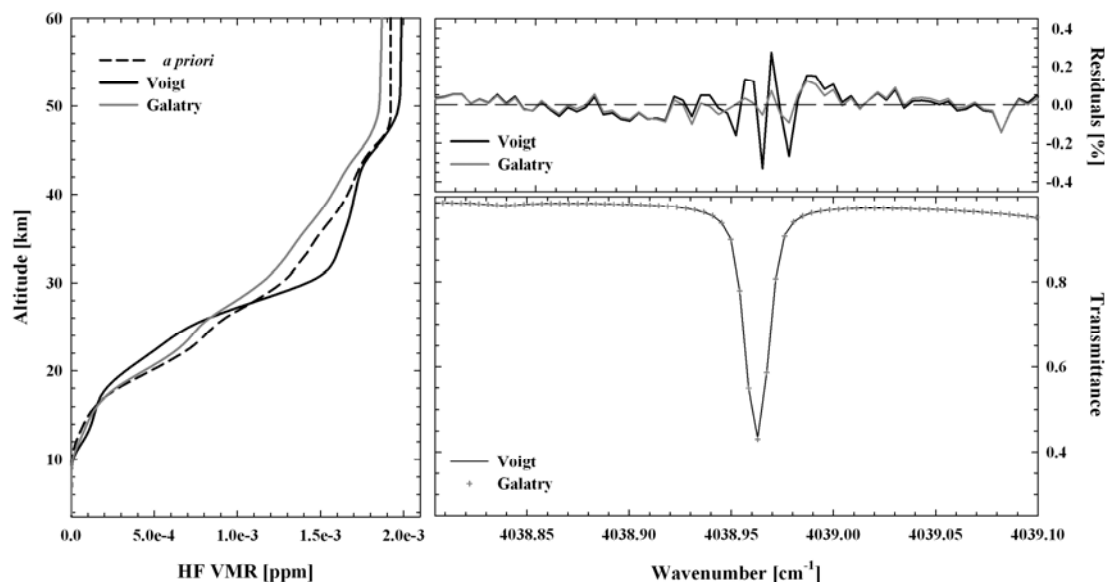


Fig. 3.2. Left panel: mean HF profiles (for the year 2005) retrieved with PROFFIT 9.5 and assuming Voigt line shape (black line) or Galatry line shape (grey line). The a priori profile adopted for the retrievals is reproduced with the dashed line. Right panel - bottom frame: typical example of synthetic spectra obtained for HF with a Voigt model (black line) and with a Galatry model (grey crosses). These two spectra were calculated during the fit with PROFFIT 9.5 of a FTIR observation (not shown here) recorded at ISSJ on January 8, 2005 at a solar zenith angle close to 73° (spectral resolution = 0.0044 cm^{-1}). For each case, corresponding residuals (measured minus simulated spectrum) are plotted on top frame.

3.2.4. Information content and error budget

Based on the information content analysis provided in Section A3, we have demonstrated that the DOFS characterizing our Bruker FTIR HF retrievals is around 3.0, which justifies the definition of three independent HF partial columns. As illustrated by AvK of Figure 3.8 (section A3), these three partial columns cover different regions of the stratosphere. The first one approximately extends from 10 to 17 km and covers the lowermost part of the stratosphere. Hereafter, we will refer to this partial column by using the acronym LMS (lowermost stratosphere). The second partial column roughly extends from 17 to 25 km and will be further denoted by MS (lower-middle stratosphere). Finally, the third partial column covers the middle-upper part of the stratosphere (approximately from 25 to 40 km) and will be reported as US (middle-upper stratosphere).

We have further deduced with PROFFIT 9.5 a typical HF error budget from 5 FTIR Bruker spectra whose main characteristics are summarized in Table 3.10 of Section A4. These spectra have been selected in order to cover a wide range of SZA and to include FTIR observations performed at different times of the year and recorded at various periods in our time series. The error module of PROFFIT 9.5 estimates

individual contributions associated with seven different error sources: the spectroscopy (including both half-width and line intensity errors), the temperature profile, solar parameters (including line intensity and spectral shift), the line of sight (LOS), the instrumental line shape (ILS, including both modulation and phase contributions), the baseline (including both offset and channeling contributions) and the spectral noise. For each error type (except for the spectral noise error, which is directly estimated from FTIR spectra during the retrieval process), Table 3.2 provides our estimates of input uncertainties (in percent, except for those labeled) which consist of reasonable error values assumed during the error estimation. Error quantities associated with spectroscopic uncertainties are in line with error indices referenced in the original HITRAN 2004 file for the R(1) HF line [Rothman et al., 2005]. For ILS error, error values are based on HBr cell spectra retrievals performed with the LINEFIT v.8.2 code [Hase et al., 1999]. In addition, since no channeling features were found in the HF region of our FTIR spectra, the corresponding error quantity has been set to zero. The two last columns of Table 3.2 also provide the weighting factors adopted in our error analysis in order to define systematic (SYS) and statistical (STA) contributions of each error type.

Error type	Error quantity [%]		SYS	STA
Spectroscopy ^a	5.0	2.0	1.0	0.0
Temperature profile ^b	1.0	2.0	5.0	0.3
Solar parameters ^c	1.0		10 ⁻⁴	0.2
LOS		1.0		0.1
ILS ^d		5.0		0.5
Baseline ^e	0.1		0.0	0.5
Spectral noise		-		0.0

^a First value is for line intensity. Second value is for line half-width

^b Error quantities are given in kelvin. First value is for altitudes below 10 km. Second value is for altitudes between 10 and 40 km. Third value is for altitudes above 40 km

^c First value is for line intensity. Second value is for spectral abscissa scale

^d Same values have been adopted for modulation and phase errors

^e First value is for offset error. Second value is for channeling error

Table 3.2. Error sources taken into account in our HF error budget with PROFFIT 9.5. Second column provides a priori error values assumed during the error estimation while two last columns give systematic (SYS) and statistical (STA) weights adopted for each error type.

Colored solid lines of Figure 3.3 reproduce the individual contributions to the error budget (in ppm) characterizing our HF retrievals below 60 km, for each error source reported in the legend (left panel is for systematic errors, right panel is for statistical errors). These error distributions correspond to mean profiles averaged over the 5 FTIR observations reported in Table 3.10 (see section A4) and have been obtained under the assumptions summarized in Table 3.2. To appreciate more easily the contribution of each error type, the HF a priori profile has also been plotted in both panels of Figure 3.3. While the error associated with HF spectroscopic parameters is the main source of systematic error in almost the entire altitude range, the spectral noise error dominates statistical errors below 25 km. Above 25 km, statistical errors due to spectral noise, ILS, LOS and temperature profile are about the same order of magnitude. For both systematic and statistical errors, the contribution of baseline and solar parameter errors remains smaller than other error sources, reflecting the very good definition of the zero absorption level of our FTIR spectra and the weak

interferences by solar lines in our HF microwindow, respectively. All details regarding the error budget characterizing our HF total and partial columns are provided in section A4.

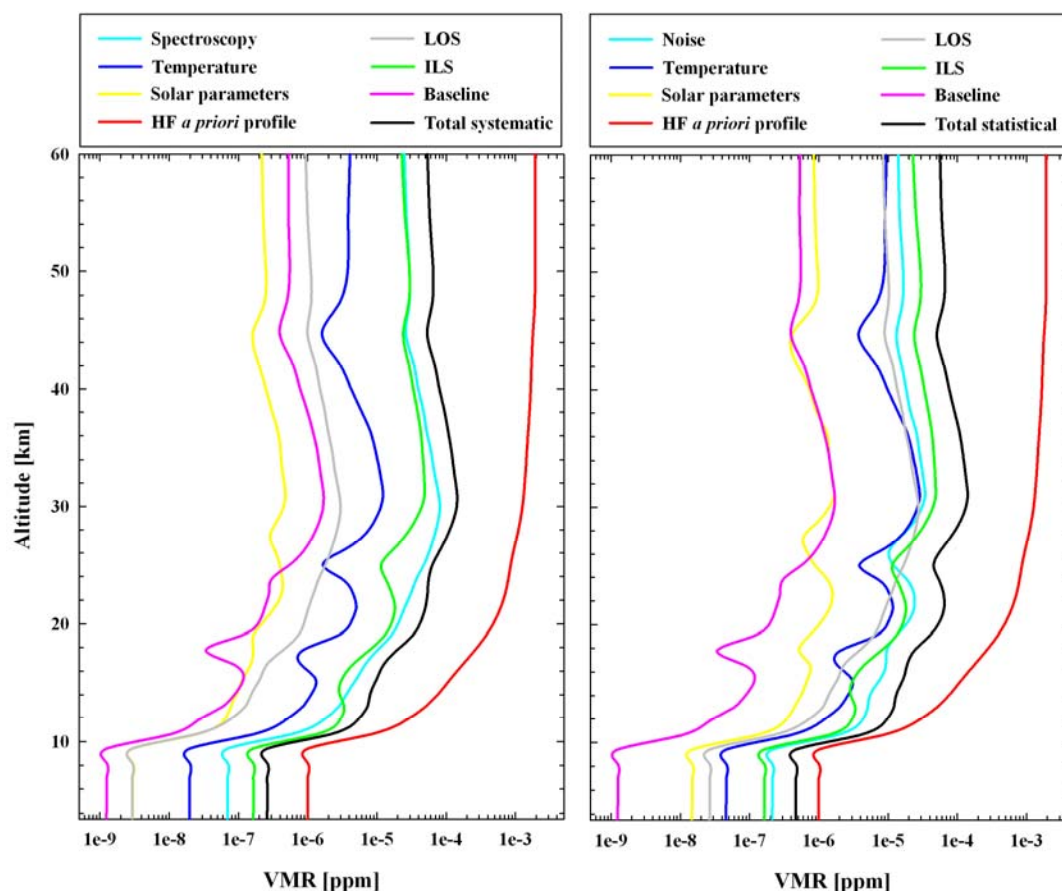


Fig. 3.3. HF error budget obtained with PROFFIT 9.5 below 60 km, for the different systematic (left panel) and statistical (right panel) error types reported in Table 3.2. To ease the evaluation of the contribution of each error source to the budget, the HF a priori profile has also been plotted in red in both panels. The error budget plotted here has been obtained by averaging individual error profiles derived from each FTIR spectra reported in Table 3.10 (section A4).

3.3. FTIR HF time series at Jungfraujoch and intercomparison

As the information content associated with our Bruker observations is greater than the one characterizing our home-made spectra (see section A3), we have selected the Bruker time series for studies dealing with partial columns and we have consequently adopted partial column limits obtained from the Bruker information content analysis (i.e. LMS, MS and US vertical abundances). The density measurements associated with our Bruker time series is also significantly greater (in particular, after 1996) and therefore more appropriate to such a comparison exercise. Home-made observations have however been kept when HF total columns are compared. It is thus crucial to first check the consistency between our two FTIR databases. For the 94 coincident measurement days available between January 1996 and January 2008, we have compared daily mean HF total columns derived from our two spectrometers and have found a mean relative difference ($\pm 1\text{-}\sigma$ standard deviation) computed as $[(\text{Bruker-HM})/\text{HM}] \times 100$ equals to $0.93 \pm 2.21 \%$. Considering this very good agreement, time

series derived from both instruments have been merged in further comparisons including HF total vertical abundances. For information, comparisons on partial columns have also been performed, with altitude ranges for partial columns computation being those derived from the HM information content analysis. Mean relative differences ($\pm 1\text{-}\sigma$ standard deviation) characterizing HF 10-20 km and 20-40 km partial columns are respectively equal to -11.49 ± 14.86 and 8.26 ± 9.71 and are consequently also not significant. Finally, additional tests have also been performed in order to check the consistency between HF quantities derived from HM spectra recorded with different optical filters. Coincident measurement days exist only for the two last HM filters described in Table 3.7 of section A1. For these 166 coincident days, relative differences in HF daily mean total and partial columns do not exceed 0.6 %.

3.3.1. FTIR versus space data

We have compared our PROFFIT daily means HF partial columns to coincident daily mean occultations performed in the 41-51°N latitude band by the two satellite instruments HALOE and ACE-FTS. The HF HALOE data are the v19 products and cover the 1991-2004 time period while the version 2.2 of ACE-FTS data between 2004 and 2009 have been used. For each instrument, both sunset and sunrise occultations have been retained. The good consistency between sunset and sunrise HF measurements has been previously demonstrated by Russell et al. [1996] for HALOE and by Mahieu et al. [2008] for ACE-FTS. Once daily mean profiles have been computed, the HALOE (resp. ACE-FTS) dataset includes almost 800 (resp. 160) mean profiles for which almost 100 (resp. 40) coincident FTIR measurements are available. It is worth mentioning that only MS and US abundances have been compared here, as HF vertical profiles recorded by HALOE (resp. ACE-FTS) typically cover the 15-60 km (resp. 14-55 km) altitude range and hence do not allow LMS or total column comparisons. As HALOE profiles are defined on a vertical pressure grid, corresponding MS and US partial columns have been calculated for pressure levels ranging from 85 to 25 hPa and from 25 to 2.5 hPa, respectively. Regarding ACE-FTS VMR profiles, they have been first interpolated on the same layering as used for our FTIR retrievals before being converted into partial columns. For both HALOE and ACE-FTS, the conversion from each individual VMR profile to partial column abundances has been performed by using corresponding pressure and temperature profiles simultaneously measured by these two instruments [Russell et al., 1993; Boone et al., 2005].

Figure 3.4 displays time series of daily mean HF MS (low panel) and US (top panel) vertical abundances deduced from our Bruker FTIR measurements (grey dots) as well as coincident daily means computed from HALOE (white triangles) and ACE-FTS (white diamonds) space occultations. As our FTIR a priori information is based on climatological data by ACE-FTS (see section 3.2.1), we have judged it necessary to also reproduce FTIR a priori partial columns (grey crossed-dots) for the comparison between our FTIR partial columns and those deduced from ACE-FTS. For both MS and US abundances, statistical results for comparisons between ground-based and space datasets are summarized in Table 3.3.

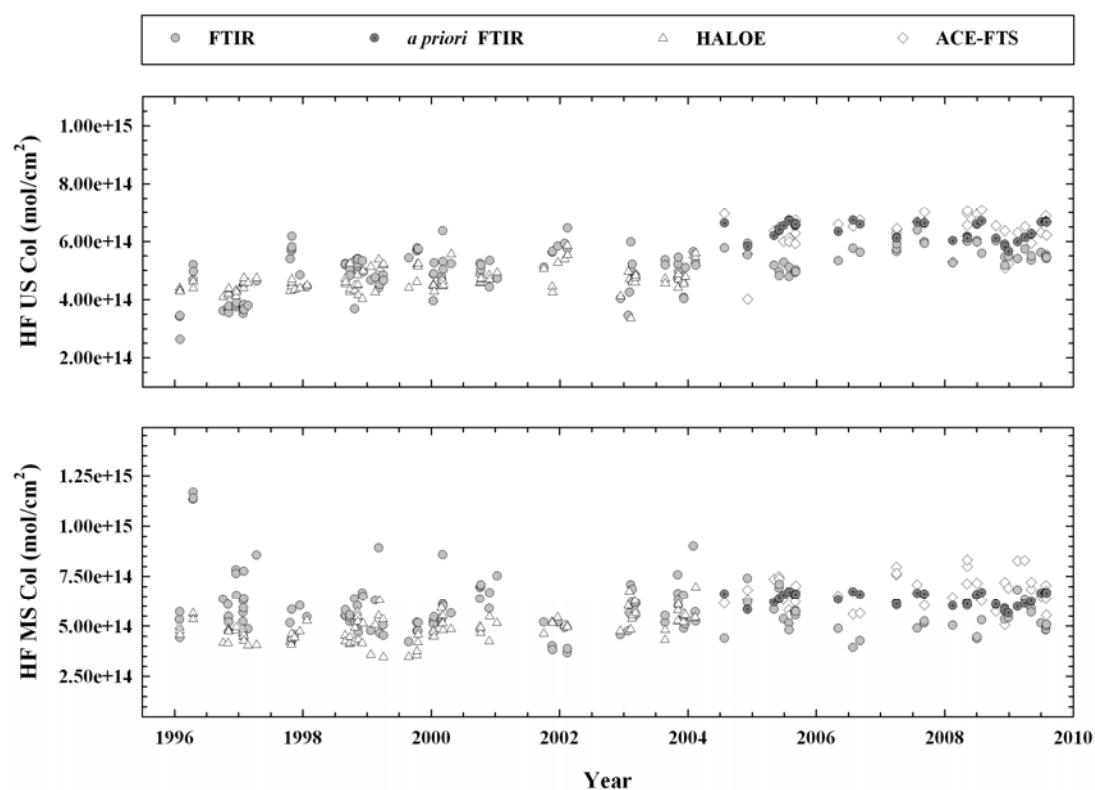


Fig. 3.4. Low-middle stratospheric (low panel) and middle-upper stratospheric (top panel) HF partial columns as observed at Jungfraujoch by FTIR technique (grey dots) and by space occultations (HALOE: white triangles; ACE-FTS: white diamonds). All data points correspond to daily mean values for coincident measurement days between groundbased and space observations. Grey crossed-dots reproduce initial guess values adopted during FTIR retrievals with the PROFFIT code.

Mean relative difference values (Δ) reported in Table 3.3 have been computed as $[(\text{FTIR-satellite})/\text{satellite}] \times 100$. These relative differences are also characterized by their standard deviations around the mean (σ). Table 3.3 shows that no significant bias exists between FTIR and HALOE observations, for both altitude ranges under consideration here. The larger values found from the ground-based data are also consistent with the ATMOS – HALOE comparison made by Russell et al. [1996] during the validation phase of this latter space instrument.

Satellite	Δ [%]	σ [%]	N
MS (17-25 km)			
HALOE v19	21.7	28.9	101
ACE-FTS v2.2	-17.5	11.2	42
US (25-40 km)			
HALOE v19	4.0	17.4	101
ACE-FTS v2.2	-12.0	11.8	42

Table 3.3. Statistical means (Δ) and standard deviations (σ) of the relative difference between the HF MS and US daily mean partial columns derived from our FTIR measurements with the PROFFIT code and coincident satellite observations. The number of comparisons involved in the statistics (N) is also given in last column.

Indeed, these authors mention that above 15 hPa (which corresponds to an altitude of around 30 km), HALOE HF VMR profiles are about 10% lower than those measured

by ATMOS. Below the 15 hPa level, the ATMOS - HALOE mean difference increases to reach a maximum value close to 35% in the lower stratosphere. The same conclusion can be drawn when Russell et al. [1996] compared HF HALOE VMRs with correlative HF vertical profiles recorded during balloon flights: the mean difference is lower than 7% from 5 hPa (~35 km) to 50 hPa (~20 km) and increases with increasing pressure. Nevertheless, as already mentioned in section 3.2.3, Barret et al. [2005] indicate that FTIR HF profiles above Jungfraujoch and correlative HF HALOE profiles (that have been smoothed with FTIR AvK) agree within 10% between 15 and 50 km, as a direct consequence of the introduction of a Galatry line shape model in the FTIR retrieval strategy.

Even if a Galatry model was adopted in our own retrieval procedure, we presently do not observe such good agreement between FTIR and HALOE partial amounts below 25 km. To try to explain this remaining difference, we have firstly restricted our spatial criterion adopted to select HALOE occultations, according to Barret et al. [2005]: only HALOE profiles measured in the [43.5-49.5]°N x [3-13]°E rectangle were retained. This new criterion assures that all HALOE occultations selected are located within 340 km (resp. 560 km) in latitude (resp. longitude) around the Jungfraujoch, i.e. within 655 km of the Jungfraujoch. Despite the fact that this criterion significantly reduces the number of coincident FTIR-HALOE measurements to 29 (the number of coincidences in Barret et al. [2005] reaches 21), it is in agreement with the last line of Table 4 of Mahieu et al. [2008] that indicates that a spatial criterion within 1000 km is still too large for that kind of comparison. Under these conditions, the mean FTIR-HALOE relative difference values reported in Table 3.3 becomes $18.4 \pm 18.2\%$ and $-2.3 \pm 12.7\%$, for MS and US regions, respectively. Finally, once these 29 HALOE profiles are smoothed with a typical FTIR averaging kernel matrix (the one for which partial column kernels are illustrated on Figure 3.8 of section A3), HF MS and US partial abundances are in very good agreement, with mean relative difference respectively equal to $0.8 \pm 19.4\%$ and $-4.0 \pm 11.9\%$. This agreement is twice as good as the one deduced by Barret et al. [2005] and highlights the fact that a smoothing operation is desirable for a proper comparison between data derived from two instruments characterized by different vertical resolutions.

In addition, comparisons made by Russell et al. [1996] with FTIR ground-based HF total columns above Jungfraujoch indicates that HALOE is able to clearly capture the HF annual cycle as well. That is also highlighted in both panels of Figure 3.4, despite the fact that the HALOE instrument does not seem able to detect large excursions that occur at times in the MS range, predominantly during one or two days from December to April (see for example 1996, 1997, 1999, 2000 and 2004). As indicated by potential vorticity maps over Europe (provided by the European Center for Medium-range Weather Forecasts – ECMWF, visit <http://www.ecmwf.int/>) at a potential temperature level of 475K (which corresponds to an altitude close to 20km), these large excursions are linked to HF-enriched air masses having moved above ISSJ from high northern latitudes.

It also appears from Figure 3.4 and statistics of Table 3.3 that, for both altitude regions, a small but significant bias exists between FTIR and ACE-FTS data, with satellite partial columns being higher than those deduced from ground-based observations. Mahieu et al. [2008] were the first to compare ground-based FTIR HF data recorded at various sites (including ISSJ) with ACE-FTS products. In this ACE-

FTS v2.2 measurements validation paper, these authors notably compare HF 12-27 km partial columns above Jungfraujoch with all coincident ACE-FTS occultations recorded between March 2004 and August 2007. Time and space criteria adopted for coincidence are ± 24 h and 1000 km, respectively. To take into account the difference in vertical resolutions between both instrumentations, ACE-FTS partial columns have also been smoothed with typical FTIR averaging kernels. For the 20 coincident measurements available in their study, Mahieu et al. [2008] found a bias close to 7% between FTIR and ACE-FTS data. Even if the bias observed in Mahieu et al. [2008] is not significant, the same tendency as in the present study is however observed, i.e. the fact that HF ACE-FTS products seem to be higher than those deduced from FTIR ground-based observations at Jungfraujoch.

In order to better compare our results with those published in Mahieu et al. [2008], we have also tightened our spatial criterion to $\pm 3^\circ$ latitude and $\pm 5^\circ$ longitude (i.e. the same criteria adopted in the second part of our FTIR-HALOE comparison). However, as this criterion reduces the number of coincidences between FTIR and ACE-FTS measurements to 5, we have kept the original 41-51°N latitude band and have relaxed the longitude criterion to $\pm 8^\circ$. The corresponding 16 coincidences, all approximately located within 1000 km of the Jungfraujoch, lead to mean relative differences of $-18.4 \pm 7.9\%$ and $-14.0 \pm 6.7\%$, for US and MS amounts, respectively. A smoothing operation applied to all coincident ACE-FTS profiles with a typical averaging kernel (the same adopted for the smoothing of HALOE profiles) transforms these two relative differences into $-15.4 \pm 6.1\%$ and $-15.8 \pm 5.1\%$, respectively. Similar significant biases are thus observed in both stratospheric regions (with ACE-FTS giving higher HF abundances), the tightened spatial criterion and smoothing operation reduces significantly the standard deviation of these mean values. The remaining difference with Mahieu et al. [2008] could perhaps be attributed to the difference in partial column limits used in the comparisons and to the absence of time criterion adopted in the present study. In addition, first comparison exercises involving ACE-FTS v3.0 products indicate a decrease of close to 5% in HF amounts (K. Walker, private communication, 2010), that will probably reduce the two present biases to values close to -10%.

3.3.2. FTIR versus model data

Our daily mean FTIR HF partial columns have also been compared with daily values specifically computed for the Jungfraujoch location using two different state-of-the-art 3-D numerical models, namely the KASIMA (Karlsruhe Simulation model of the Middle Atmosphere) and SLIMCAT CTMs. This time, the three HF partial columns (LMS, MS and US) are included in the comparison, as well as total vertical abundances. The KASIMA model used in this study is a global circulation model including stratospheric chemistry for the simulation of the behavior of physical and chemical processes in the middle atmosphere [Reddmann et al., 2001; Ruhnke et al., 1999]. The meteorological component is based on a spectral architecture with the

pressure altitude $z = -H \ln\left(\frac{p}{p_0}\right)$ as vertical coordinate where $H = 7$ km is a constant

atmospheric scale height, p is the pressure, and $p_0 = 1013.25$ hPa is a constant reference pressure. A horizontal resolution of T21 (about $5.6^\circ \times 5.6^\circ$) has been used. In the vertical regime, 63 levels between 10 and 120 km pressure altitude with a

0.75 km spacing from 10 up to 22 km and an exponential increase above were used. The meteorology module of the KASIMA model consists of three versions: the diagnostic model, the prognostic model and the nudged model which combines the prognostic and diagnostic model [Kouker et al., 1999]. In the version used here, the model is nudged towards the operational ECMWF analyses of temperature, vorticity and divergence between 18 and 48 km pressure altitude. Below 18 km, the meteorology is based on ECMWF analyses without nudging, above 48 km pressure altitude, the prognostic model is used. The rate constants of the gas phase and heterogeneous reactions are taken from Sander et al. [2003]. The photolysis rates are calculated online with the fast-j2 scheme of Bian and Prather [2002]. The distributions of the chemical species in this model run were initialized on 30 April 1972, with data from a long-term KASIMA run.

This study also uses results from the SLIMCAT 3D off-line CTM [Chipperfield, 2006]. The model is forced using winds and temperatures from meteorological analyses (e.g. ECMWF). The model uses a σ - θ vertical coordinate and in the stratosphere (θ level domain) vertical motion is diagnosed from calculated heating rates which gives a good representation of the slow stratospheric circulation (see Monge-Sanz et al., 2007). The model does not contain an explicit scheme for tropospheric convection and boundary layer mixing. Instead, the model assumes complete vertical mixing of species in the troposphere. The version used here is an updated version of the one used by Feng et al. [2007] to study long-term changes in ozone. The model was run at a resolution of $5.6^\circ \times 5.6^\circ$ and 32 levels from the surface to ~60km. The run extended from 1977 to 2010. From 1989 onwards, the period relevant for this study, the model was forced by ECMWF ERA-Interim reanalyses. The use of a continuous set of reanalysis data reduces the risk of spurious variations in the model tracer fields due to changes in meteorological input.

The model has a detailed description of stratospheric chemistry. During the last years, SLIMCAT has already been exploited to perform comparisons of fluorine species abundances with satellite and ground-based observations [Chipperfield et al., 1997]. More recently, it has also been used to derive long-term trends of atmospheric compounds [Feng et al., 2007] or for comparison with COF₂ measurements from ground-based FTIR [Duchatelet et al., 2009]. The run included 10 halogenated source gases including the following fluorinated species CFC-11, CFC-12, C₂Cl₂F₃ (CFC-113), HCFC-22. The surface mixing ratio of these compounds was specified following WMO [2007]. For inorganic fluorine (F_y) the model treats COClF, COF₂ and, the ultimate degradation product, HF. The sink of HF is transport to the troposphere and an imposed near-zero surface mixing ratio.

Figure 3.5 displays FTIR and CTMs HF daily mean data for all coincident days available between years 1984 and 2009. However, for partial column comparisons, the time period is limited to the Bruker measurements (1996-2009), for reasons discussed in section 3.3.1. For total column comparisons, Bruker and HM FTIR data have been averaged in order to cover the full 1984-2009 time period. Table 3.4 provides mean relative difference values (Δ) computed as $[(\text{FTIR}-\text{model})/\text{model}] \times 100$ for LMS, MS, US and total HF vertical abundances. Those relative differences are here again characterized by their standard deviations around the mean (σ). The last column of Table 3.4 provides the number of data points involved in each comparison.

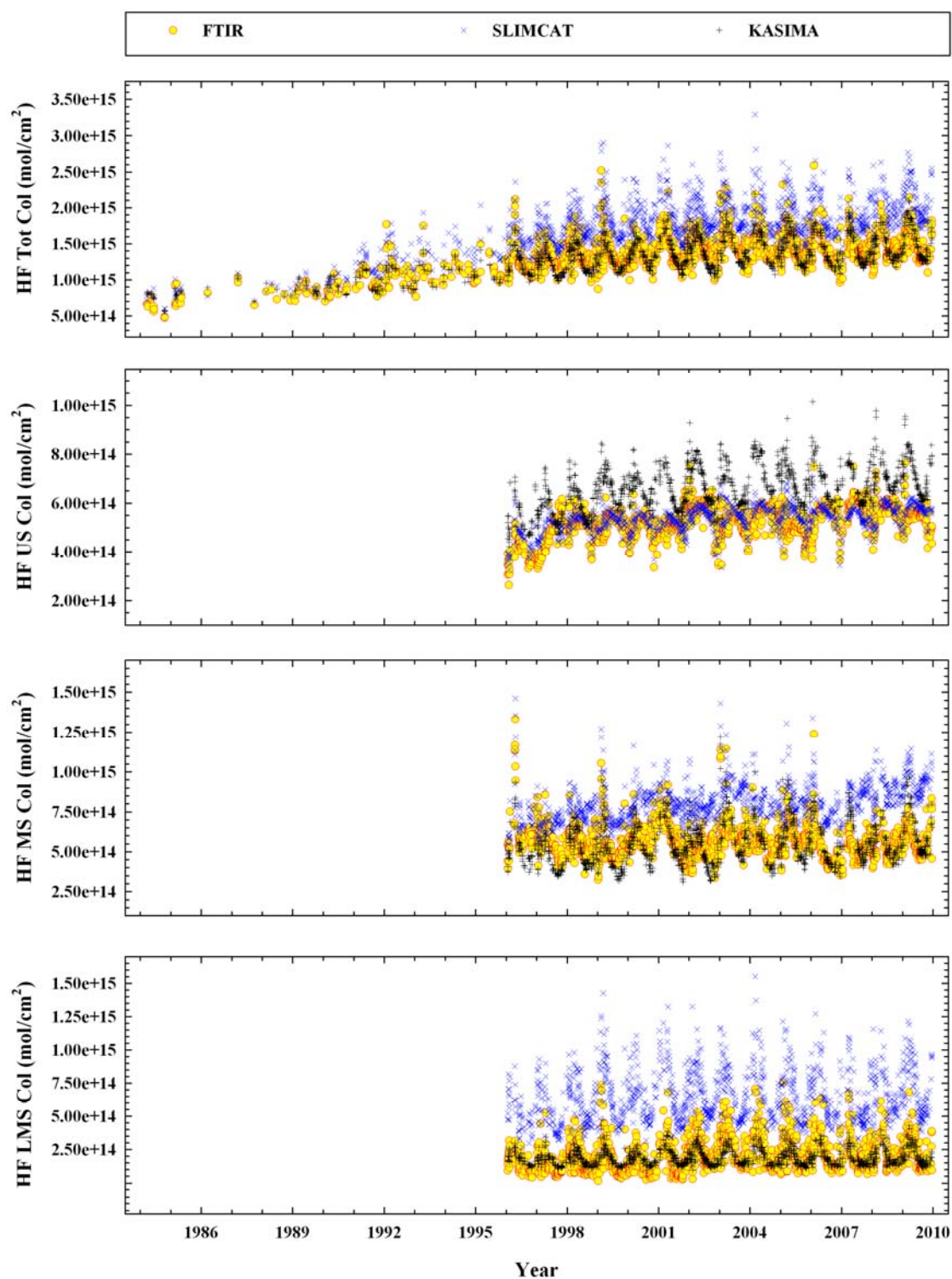


Fig. 3.5. From bottom to top panel: lowermost stratospheric, lower-middle stratospheric, middle-upper stratospheric and total HF abundance time series derived from FTIR measurements with the PROFFIT code (yellow dots) and from SLIMCAT (blue crosses) and KASIMA (black crosses) CTMs. FTIR data points correspond to daily means values for all coincident days with daily CTM data.

It is clear from Figure 3.5 and Table 3.4 that the agreement between FTIR and KASIMA time series is excellent below 25 km as well as for HF total columns. A significant bias close to 20% exists for the middle-upper stratosphere region, with KASIMA giving higher column values than FTIR measurements. Regarding the

FTIR-SLIMCAT comparisons, the contrary is observed, as the agreement is excellent for the 25-40 km partial columns and large significant biases exist for all other regions (including HF total columns which depend largely on the lower stratosphere). As the SLIMCAT model extends from the surface, the lower stratosphere is less constrained than the KASIMA model. Therefore problems in transport and chemistry in this region are more likely to manifest themselves.

Model	Δ [%]	σ [%]	N
LMS (10-17 km)			
SLIMCAT	-69.08	11.18	1335
KASIMA	3.41	38.48	1335
MS (17-25 km)			
SLIMCAT	-29.92	10.34	1335
KASIMA	7.01	18.94	1335
US (25-40 km)			
SLIMCAT	-1.78	8.93	1335
KASIMA	-19.64	11.35	1335
Total (3.58-86.8 km)			
SLIMCAT	-22.54	6.55	1542
KASIMA	3.02	9.58	1542

Table 3.4. Statistical means (Δ) and standard deviations (σ) of the relative difference between the HF LMS, MS, US and total daily mean abundances derived from our FTIR measurements with the PROFFIT code and coincident model calculations. The number of comparisons involved in the statistics (N) is also given in last column.

Each dataset appearing in Figure 3.5 has also been analyzed in order to derive seasonal cycles associated to HF LMS, MS, US and total columns time series. This analysis has been performed with a statistical tool developed at the National Physical Laboratory (Teddington, UK) and based on a bootstrap resampling method that allows both the long-term and intra-annual variability of a given dataset to be determined, including uncertainties affecting the trend value [Gardiner et al., 2008]. This tool was notably used for the 1995-2004 trend analysis of CH₄, C₂H₆, CO, HCFC-22, N₂O and O₃ time series derived from six affiliated-NDACC stations [Gardiner et al., 2008], as part of the European project “Time Series of Upper Free Troposphere Observations from a European Ground-based FTIR Network” (UFTIR – see www.nilu.no/uftir) [De Mazière et al., 2005]. It is worth mentioning that the HF trend analysis is not included in the present study but will be addressed in a separate publication dealing with the inorganic fluorine budget above ISSJ and its long-term evolution [Duchatelet et al., in preparation]. As given in Eq. (3) of Gardiner et al. [2008], the seasonal variability and the trend in an experimental time series are modeled by a function including both a linear component and a Fourier series. In the present study, a 3rd order Fourier series was used. Seasonal cycles deduced from total or partial HF time series of Figure 3.5 are illustrated in Figure 3.6. For each panel of Figure 3.6, grey dashed-dotted curves are derived from our FTIR ground-based observations while black dashed and black dashed-dotted curves reproduce seasonal cycles associated to SLIMCAT and KASIMA time series, respectively.

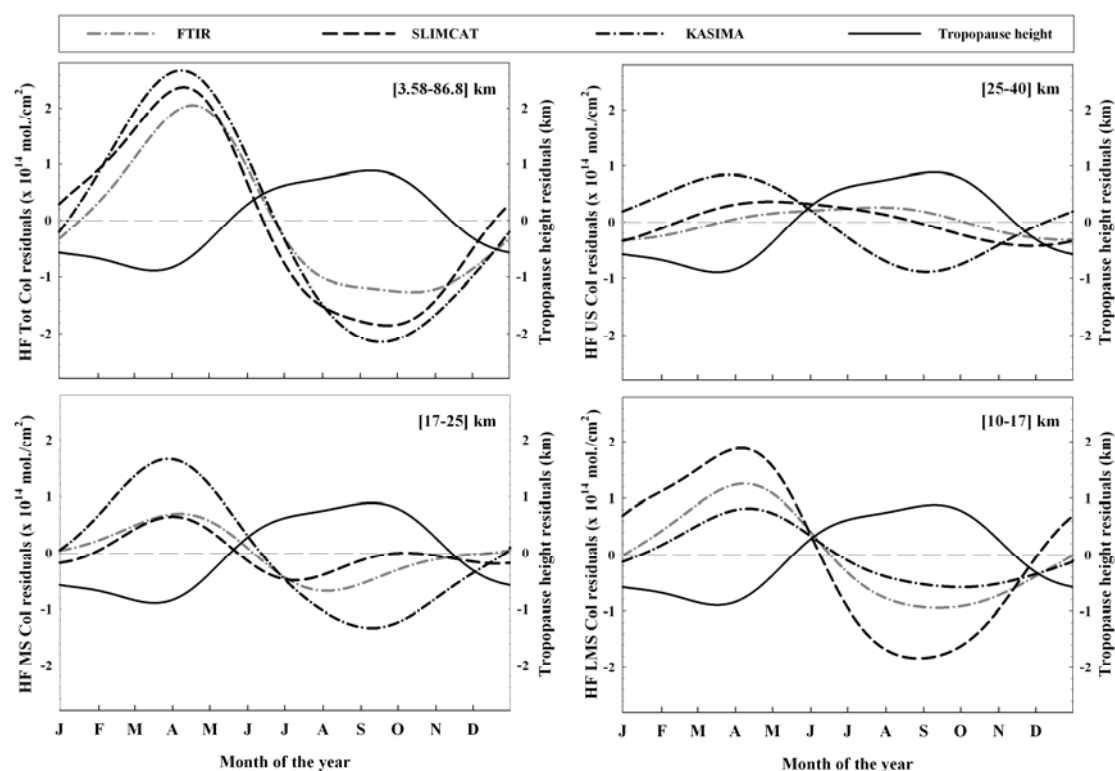


Fig. 3.6. Dashed lines: HF seasonal cycles derived from each time series in Figure 3.5. Solid line: tropopause height seasonal cycle as derived from NCEP p-T profiles computed for Jungfraujoch. The left vertical scale is valid for dashed lines. The right vertical scale is valid for the solid line.

Different panels of Figure 3.6 indicate that, except for the LMS region, the intra-annual variability deduced from the KASIMA model is the largest. In order to better compare the dashed curves of Figure 3.6, corresponding statistics are summarized in Table 3.5. For each altitude region and for each dataset involved in our comparison, the date for which HF maximum and minimum vertical abundances are observed are given in the two first columns. The third column of Table 3.5 provides peak-to-peak amplitudes of each seasonal cycle, expressed in vertical column abundance units. These amplitudes have also been converted to percent values (last column of Table 3.5) by applying the following approach: for each data set and each altitude range, HF yearly mean columns have been computed. For each year available for a given data set, the peak-to-peak amplitude (in column units) has then been simply expressed as a percentage of the corresponding HF yearly mean column. Values so deduced for each year have been finally averaged and appear in the last column of Table 3.5 ($\pm 1-\sigma$ standard deviation). Values between brackets correspond to two times the standard error on the mean.

Except for the US region, a very close agreement between the maximum of the seasonal cycles of all data sets is found, with higher HF columns always observed during spring time. Concerning the HF minimum, the best agreement is found for total column values. For other altitude ranges, results are more spread. In any case, all data sets capture lower HF columns during the second half of the year. These results are in reasonably good agreement with those published by Zander et al. [1987] and based on 3 years (years 1983 to 1985) of FTIR HF total columns above Jungfraujoch. These authors have also noticed a strong seasonal cycle with peak values in February-March and a minimum that occurs between September and November.

	Max	Min	Amplitude [$\times 10^{14}$ mol./cm ²]	Amplitude [%]
LMS (10-17 km)				
FTIR	08 April	13 September	2.20	113.26 \pm 27.96 [29.89]
SLIMCAT	06 April	28 August	3.72	59.59 \pm 5.76 [4.52]
KASIMA	11 April	01 October	1.39	74.19 \pm 5.00 [5.35]
MS (17-25 km)				
FTIR	07 April	04 August	1.37	24.37 \pm 1.64 [1.75]
SLIMCAT	01 April	09 July	1.13	14.16 \pm 1.24 [0.97]
KASIMA	28 March	10 September	2.99	55.39 \pm 5.11 [5.46]
US (25-40 km)				
FTIR	27 July	27 December	0.58	11.21 \pm 1.21 [1.29]
SLIMCAT	29 April	28 November	0.79	14.84 \pm 1.01 [0.79]
KASIMA	27 March	03 September	1.73	26.45 \pm 2.42 [2.59]
Total (3.58-86.8 km)				
FTIR	17 April	13 October	3.32	29.94 \pm 8.65 [6.79]
SLIMCAT	10 April	23 September	4.23	31.72 \pm 11.77 [9.24]
KASIMA	08 April	17 September	4.83	42.86 \pm 9.68 [7.59]

Table 3.5. HF main seasonal cycle characteristics associated to each panel of Figure 3.6. For both FTIR and model datasets, two first columns provide calendar dates for which HF maximum and minimum abundances occur. Third column lists peak-to-peak amplitudes in vertical column units. Corresponding values expressed in percents are provided in last column (see text for details). Values between brackets correspond to two times the standard error on the mean.

Regarding the amplitude of the seasonal cycle, no analysis is performed in Zander et al. [1987] but Figure 3 of this paper suggests a value that lies between 20 and 30%, in good agreement with the amplitudes reported in Table 3.5 for FTIR and SLIMCAT HF total columns. The value deduced from KASIMA runs is significantly higher. The same conclusion can be drawn when considering MS and US regions, with KASIMA amplitudes 2 to 4 times higher than those provided by SLIMCAT runs and FTIR measurements. Finally, both SLIMCAT and FTIR values indicate the same behavior in the stratosphere, i.e. that the amplitude of the HF seasonal cycle decreases with increasing altitude, suggesting that the HF variability is mainly controlled by dynamical effects that occur near the tropopause region. Among the few papers dealing with the HF seasonal cycle in the northern hemisphere, two separate studies by Rinsland et al. [1991, 2002] have exploited HF time series deduced from FTIR measurements performed at the US National Solar Observatory facility on Kitt Peak (31.9°N, 111.6°W, 2090 m asl) to characterize its seasonal variation. In both papers, the HF seasonal cycle is modeled with a function that includes a sinusoidal component. The HF total column time series spanning the 1977–1990 time period has allowed Rinsland et al. [1991] to obtain a seasonal cycle that is characterized by an amplitude of close to 13% and with maximum HF vertical abundances at the end of March. These values have also been compared with simulations performed by the AER 2D model [Ko et al., 1989] for 28.4°N latitude that provide an amplitude of 9% and maximum HF total columns around the beginning of July. In their subsequent paper, Rinsland et al. [2002] have performed a similar analysis of their HF stratospheric column amount time series (i.e. HF partial columns recovering the 14-50 km altitude range) above Kitt Peak between 1977 and 2001. Their investigations showed a seasonal amplitude of 10% and a maximum that occurs in mid March,

which is quite consistent with their previous results. The agreement between HF maxima found at Kitt Peak and at Jungfraujoch is good although the amplitude values differ substantially, probably as a direct consequence of the difference in latitude. This latter result is confirmed by examining an HF climatology at different latitudes, as exposed in Section A5.

Among factors that influence the amplitude of the HF seasonal cycle, the annual variation of pressure and temperature definitely plays a role. Based on tests performed on our HF a priori profile, we have quantified the impact of such p-T variations on HF seasonal variability. These tests have revealed that the annual cycle characterizing p-T profiles generates variations on HF LMS, MS, US and total vertical abundances that do not exceed 15%. Annual variations of pressure and temperature profiles above Jungfraujoch are consequently not able to fully explain the amplitude values reported in the last column of Table 3.5.

As HF is a very stable gas with VMRs essentially constant and weak throughout the troposphere, one can imagine that the tropopause altitude could also influence both HF vertical amounts and its seasonal cycle, mainly in the altitude levels located near the tropopause (the tropopause altitude definition adopted here is the thermal definition provided by WMO [1957], i.e. the altitude above which a temperature gradient lower than 2 °C/km is maintained for at least 2 km and located above the 500 hPa level). We have checked the validity of this hypothesis on the basis of tropopause heights deduced from NCEP temperature profiles computed for ISSJ. The use of NCEP data is justified by Bizzarri et al. [2006] who have demonstrated the good agreement that exists, for northern mid-latitudes, between tropopause heights deduced from NCEP data and from satellite measurements. In addition, the comparison between NCEP and ECMWF temperature profiles above Bremen, Germany (located within 800 km of ISSJ) shows an agreement within 2K below 40 km (C. Vigouroux, private communication, 2010). It is consequently reasonable to think that differences on tropopause heights derived from either of these data sets would be limited.

The 1999-2009 tropopause height time series above ISSJ has been analyzed with the NPL statistical tool in order to derive its seasonal cycle. To make comparisons with FTIR and model data easier, the tropopause altitude seasonal cycle above Jungfraujoch has been reproduced with a black solid line on each panel of Figure 3.6. For this latter curve, we have computed a peak-to-peak amplitude that is equal to 1.78 km or, based on annual mean values, around 16%. One can also observe that the tropopause height peaks at its maximum (resp. minimum) in March (resp. September), so that HF and tropopause height seasonal cycles are out of phase for all altitude ranges, except for the US region (HF cycle as derived from KASIMA data is however out of phase with the tropopause height cycle for all regions). For these 3 regions, an anti-correlation between the tropopause height and HF amounts should exist, i.e. that high (resp. low) tropopause heights should lead to low (resp. high) HF VMR and vertical abundances. This is well illustrated in Figure 3.7 that reproduces HF profiles retrieved from 2 distinct FTIR spectra recorded at Jungfraujoch during February and October 1999, respectively. Corresponding tropopause heights are 8.7 km and 13.8 km (for comparison, the 1999-2009 mean tropopause altitude above Jungfraujoch is close to 11.3 km; see below) and are well representative of low and high tropopause height conditions (see next paragraph). The HF a priori profile used during our inversions and based on ACE-FTS measurements (see section 3.2.1) is also

reproduced with a dashed line. For both retrieved profiles, corresponding HF LMS, MS, US and total columns are given in the legend. As expected, the influence of the tropopause altitude both on retrieved HF profiles and vertical abundances is clear. Based on partial column values reported in boxes, the impact of the tropopause height on HF abundances seems however to be limited above 25 km.

We have precisely quantified the impact of a change of tropopause height on HF partial and total vertical abundances. The mean tropopause height (for the 1999-2009 time period) above Jungfraujoch is close to 11.3 km (the corresponding 1- σ standard deviation equals 1.3 km). We have then selected all FTIR observations for which the corresponding tropopause height falls between 13.4 and 14.4 km (resp. 8.3 and 9.3 km), i.e. in an interval of 1 km width centered on the mean tropopause height value plus (resp. minus) 2- σ standard deviations. The first (resp. second) subset of FTIR data is consequently well representative of high (resp. low) tropopause height conditions and will be denoted hereafter by HTC (resp. LTC). These two subsets contain 166 (HTC) and 53 (LTC) individual FTIR spectra, respectively. A third subset, that contains all FTIR data for which the tropopause height lies between 10.8 and 11.8 km (i.e. in an interval of 1 km width, centered on the mean tropopause height value above Jungfraujoch) has been used as the reference (REF). This latter subset contains 738 individual FTIR observations.

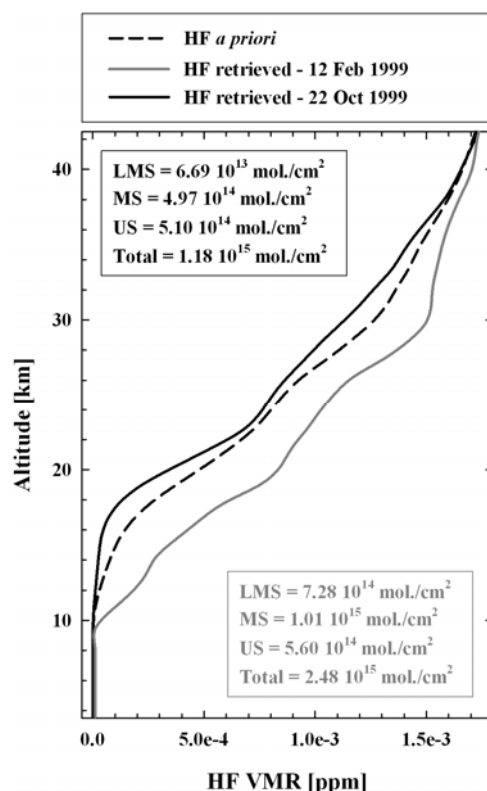


Fig. 3.7. Typical example of individual HF retrieved profiles with PROFFIT 9.5 (black and grey solid lines) from 2 FTIR measurements at Jungfraujoch when different tropopause heights are observed (here, the tropopause height equals 8.7 km on 12 February 1999 and 13.8 km on 22 October 1999). The HF a priori profile used for our inversion is reproduced with the dashed line. For each retrieved profile, corresponding total and partial columns are given in separate boxes.

For each subset, we have computed mean HF LMS, MS, US and total columns. Comparison of mean HF column values obtained from HTC and REF subsets leads to

the following relative differences (computed with respect to the REF subset, values are in percent) for LMS, MS, US and total columns, respectively: -55.2, -14.3, 3.0 and -13.3%. The same comparison performed for the LTC and REF subsets provides the following relative differences (for LMS, MS, US and total columns, respectively): 100.8, 5.5, 2.7 and 21.4 %. It thus appears that high tropopause heights significantly reduce HF amounts (almost all relative differences reported are negative), in particular in the LMS region. A slight increase is however observed for the US region. Moreover, low tropopause height conditions significantly increase HF abundances, in particular LMS and total amounts. In both tropopause height conditions, MS and US abundances are less affected. The impact observed on HF total columns is mainly ascribable to the variations observed in the LMS region.

Finally, to quantify the strength of the link that exists between HF partial or total column values and the tropopause height, we have evaluated correlation coefficients ρ between these parameters, by using the estimator:

$$\rho = \frac{\sum (X_i - X_{mean}) \cdot (Y_i - Y_{mean})}{\sqrt{\sum (X_i - X_{mean})^2} \cdot \sqrt{\sum (Y_i - Y_{mean})^2}} \quad (3.2)$$

Coefficient values obtained when considering FTIR or model HF data are reported in Table 3.6. As expected, the strongest and most significant anti-correlations are observed in the LMS range, which is the closest region to the tropopause and consequently, the most influenced by dynamical effects that alter the tropopause height. Except for the KASIMA data set, correlation coefficients are significantly reduced when moving from LMS to upper regions. Moreover, quite low variations observed for KASIMA correlation coefficients are in direct agreement with the permanent phase difference observed between KASIMA and tropopause height curves throughout each panel of Figure 3.6. Such behavior is probably ascribable to a slightly too strong Brewer-Dobson circulation in KASIMA simulations. That is further confirmed by Figure 11 of Stiller et al. [2008] that compares mean age of stratospheric air derived from KASIMA runs with those deduced from measurements of the Michelson Interferometer for Passive Atmospheric Sounding (MIPAS; Fischer et al., 2007). In particular, this Figure shows that, at mid-latitudes, KASIMA gives slightly younger mean age of air in the lowermost and lower-middle parts of the stratosphere. Finally, comparison between correlation coefficient values found for HF LMS and total columns also seem to indicate that the seasonal cycle characterizing HF total column time series is mainly ascribable to seasonal variations affecting HF abundances in the lowermost part of the stratosphere.

	ρ_{FTIR}	ρ_{SLIMCAT}	ρ_{KASIMA}
LMS (10-17 km)	-0.57	-0.60	-0.50
MS (17-25 km)	-0.25	-0.13	-0.41
US (25-40 km)	0.10	0.02	-0.33
Total (3.58-86.8 km)	-0.44	-0.54	-0.43

Table 3.6. Correlation coefficients between HF partial/total columns derived from FTIR measurements or model runs and corresponding tropopause heights. The number N of data couples used in each computation is 1330.

3.4. Summary and conclusions

This paper describes the updated retrieval strategy adopted to derive HF abundances and vertical profiles from solar spectra recorded at the northern mid-latitude ground-based station of the Jungfraujoch with two FTIR spectrometers (one home-made and one commercial Bruker 120 HR) between March 1984 and December 2009. Inversions are based on the HF R(1) absorption line and are performed with the PROFFIT 9.5 algorithm. As the SFIT 2 code is widely used within the FTIR community to retrieve vertical abundances of atmospheric gases, we have performed for the first time, a comparison between HF total columns retrieved with PROFFIT with those derived with SFIT 2. This comparison was based on one year of HF observations at Jungfraujoch (which corresponds to about 200 FTIR spectra) and indicates a non significant mean relative difference of less than 1%, in good agreement with previous studies by Hase et al. [2004] performed on other atmospheric species. As frequent negative retrieved VMRs profiles have been observed for interfering gases with both codes, our inversions are performed on a logarithmic vertical scale. In addition, the impact of the choice of the line shape model (Voigt or Galatry) adopted to simulate HF absorption lines for HF retrieved total columns and vertical profiles, on fitting quality and on error budget has also been quantified. While a small but significant difference close to 1% is observed for total columns, HF retrieved profiles are significantly smoother, mainly between 25 and 40 km, when a Galatry line shape model is adopted. Fitting residuals are also smaller with the Galatry model, with the mean relative difference between the approaches reaching almost 20%. Based on this, we have decided to include the Galatry line shape model in our retrieval approach.

The vertical information content analysis has also indicated that, in addition to its total column, three independent HF partial columns could be derived from our Bruker spectra. They cover the lowermost part of the stratosphere (10-17 km, LMS), the lower-middle stratosphere (17-25 km, MS) and the middle-upper stratosphere (25-40 km, US). Due to poorer spectral resolution and signal-to-noise ratio, it is only possible to derive two HF partial columns (approximately extending between 10 and 20 km, and between 20 and 40 km) from our home-made observations. Our HF error budget estimates the contribution of seven different systematic or statistical error sources and clearly confirms that, with a contribution ranging from 5 to 6.5% depending on the altitude region under investigation, the main component of the total systematic error is the spectroscopy. The total systematic error characterizing our Bruker HF total columns equals 6%. The corresponding statistical error is close to 2%. For other altitude ranges, the total statistical error varies between 4.5 and 11.5%, and decreases with increasing altitude. The impact of the line shape model (Voigt or Galatry) on the error budget remains globally limited, the main issue being that the use of the Voigt model allows to significantly reduce by a few percent the total systematic error in the lower stratosphere. This benefit is however small compared to major improvements obtained (i.e. on global fit residuals and on HF vertical retrieved profiles) when a Galatry model is adopted and consequently, does not justify by itself the adoption of the Voigt model in our final retrieval strategy.

We have also compared our Bruker HF MS and US vertical abundances with those derived from two satellite instruments (HALOE and ACE-FTS). For the two altitude ranges under consideration, no significant difference has been observed between

FTIR and HALOE measurements. The agreement is better in the US region than in the MS range, in line with previous comparisons involving HALOE HF products. Moreover, we have noticed a small but significant bias between FTIR and ACE-FTS HF partial columns, with satellite measurements being higher than those deduced from our ground-based observations. However, this bias should be reduced in the forthcoming comparisons involving ACE-FTS version 3.0 products.

Our daily mean FTIR HF total and partial columns have also been compared with those computed for Jungfraujoch by two numerical models (SLIMCAT and KASIMA). Comparisons for total columns cover the historical 1984-2009 time period and the 1996-2009 time period for the three partial columns. The agreement between FTIR and KASIMA data is excellent below 25 km and for total columns while a significant bias close to 20 % is observed in the US region. The contrary is observed when considering FTIR and SLIMCAT time series, as SLIMCAT runs seem to systematically overestimate total column HF abundances and the lower stratospheric contribution. For each of these data sets and for each altitude ranges, an analysis of the HF seasonal cycle has also been performed using a statistical tool based on a bootstrap resampling method. Except for the US region, we have found a strong seasonal variation, with the maximum observed in spring and the minimum in the second half of the year (between July and December). Peak-to-peak amplitudes characterizing FTIR and model HF total column seasonal cycles range from 30 to 40%. Comparison between HF abundances and tropopause height seasonal cycles indicates a strong phase difference. As expected, correlation coefficients computation between those two parameters suggests a good anti-correlation between HF LMS amounts and the tropopause height. Comparison between correlation coefficient found for HF total and LMS partial columns also suggests that the HF total column seasonal cycle is mainly ascribable to seasonal variations that occur in the lower stratosphere.

Appendix A

A1. Additional FTIR database statistics

For the Bruker (resp. home-made) spectrometer, our database includes 2471 (resp. 1092) FTIR spectra recorded over 1335 (resp. 301) sunny days. The spectral resolution (defined as the reciprocal of twice the maximum optical path difference) is equal to $4 \cdot 10^{-3} \text{ cm}^{-1}$ for the Bruker spectrometer. For the home-made instrument, three different optical filters have been used, leading to different spectral resolutions. More details regarding the investigated time periods, corresponding spectral resolutions as well as additional statistics are given in Table 3.7, for both instruments.

Spectrometer	Investigated time period	Filter range [cm^{-1}]	Resolution [10^{-3} cm^{-1}]	N
Home-made	March 1984 – May 1984	2850 – 5350	12.74	9
Home-made	May 1984 – January 2008	3900 – 5150	8.01	676
Home-made	June 1984 – January 2008	2380 – 4400	9.69	407
Bruker-120 HR	January 1996 - December 2009	3900 – 4350	4.00	2471

Table 3.7. Main characteristics of FTIR spectra analyzed in the present study. Last column provides number of FTIR spectra that has been fitted in each wavenumber range.

A2. Retrieval input parameters

Table 3.8 provides an overview of main retrieval input parameters adopted during our final HF retrieval strategy with the PROFFIT 9.5 algorithm.

Parameter	Adopted settings or inputs
Microwindow limits	4038.81- 4039.07 cm ⁻¹ (see Table 3.1)
Target gas	HF (VMR profile is fitted by OEM)
Interfering species	H ₂ O, HDO, CH ₄ (VMR profiles are fitted with a TP regularization)
a priori HF VMR	Mean of all ACE-FTS v2.2 records in [41-51] ^o N between 2004 and 2008 (see left panel of Figure 3.1)
a priori HF S _a	Based on all ACE-FTS v2.2 records in [41-51] ^o N between 2004 and 2008 (see section 3.2.1)
HF spectroscopy	HITRAN 2004, Galatry line shape model assumed
p-T profiles	NCEP daily profiles specifically computed for ISSJ
Layering	41 layers (see background on left panel of Figure 3.1)

Table 3.8. Main regularization parameters and ancillary inputs adopted for our final HF inversions with PROFFIT 9.5.

A3. HF information content analysis

The vertical information contained in the FTIR spectra can be fully characterized by the averaging kernel matrix **A**, which can be calculated via the following expression [Rodgers, 2000]:

$$A = \left(K^T S_e^{-1} K + S_a^{-1} \right)^{-1} K^T S_e^{-1} K \quad (3.3)$$

where **S_a** is the a priori covariance matrix (see section 3.2.1) and **S_e** the measurement error covariance matrix. The **K** matrix is the Jacobian of the forward model and indicates how much the FTIR measurements are sensitive to the parameters of the forward model adopted for the retrieval [Rodgers, 2000]. The averaging kernel matrix **A** depends on various experimental and retrieval parameters involved, such as the SZA, the spectral resolution, the spectral signal-to-noise ratio of the observation, the choice of microwindows, etc. Rows of **A** are the so-called averaging kernels (AvK) and characterize the vertical range as well as the altitude resolution of the retrievals. Indeed, at a given altitude, full width at half maximum (FWHM) of AvK provides a measure of the vertical resolution of the retrieval. Thin grey curves in left panel of Figure 3.8 reproduce typical (i.e. for a FTIR spectrum whose SZA is close to 55°, which corresponds to the mean SZA value found for our whole Bruker HF database) individual AvK for HF retrievals at ISSJ, i.e. AvK relative to each of the 41 atmospheric layers used in our forward model scheme. These curves indicate that our retrievals are most sensitive to HF between 10 and 40 km.

The vertical information content of the retrieved target gas can also be quantified by the number of degrees of freedom for signal (DOFS), which is the sum of the appropriate trace section of the **A** matrix. The DOFS indicates the number of

independent pieces of information that can be retrieved from the measurement. In our case, the mean DOFS ($\pm 1\text{-}\sigma$ standard deviation) computed over the whole Bruker time series equals 2.94 ± 0.24 , meaning that three independent HF partial columns can be derived from our Bruker FTIR measurements. Hereafter, we will discuss the HF partial column amounts, defined in three independent atmospheric layers. The layer limits are chosen such that the DOFS reaches at least 1.0 inside the associated partial column. Following this approach, additional black curves in the left frame of Figure 3.8 reproduce merged AvK for the three atmospheric layers obtained and for which limits are defined in the legend (the black solid curve reproduces the AvK corresponding to the HF total column). One can see that these three layers are effectively independent, as their AvK peaks are centered fairly closely on the middle of their corresponding layer limits. Based on the FWHM of AvK, the vertical resolution characterizing our HF retrieved profiles is close to 10 km. Due to poorer spectral resolution, the information content associated with our home-made spectra is lower and equals 2.40 ± 0.38 (mean DOFS value $\pm 1\text{-}\sigma$ standard deviation computed over our entire home-made database), indicating that only two HF partial columns can be derived from our home-made FTIR spectra. Corresponding averaging kernel analysis has demonstrated that these two partial columns approximately extend between 10 and 20 km and between 20 and 40 km, respectively.

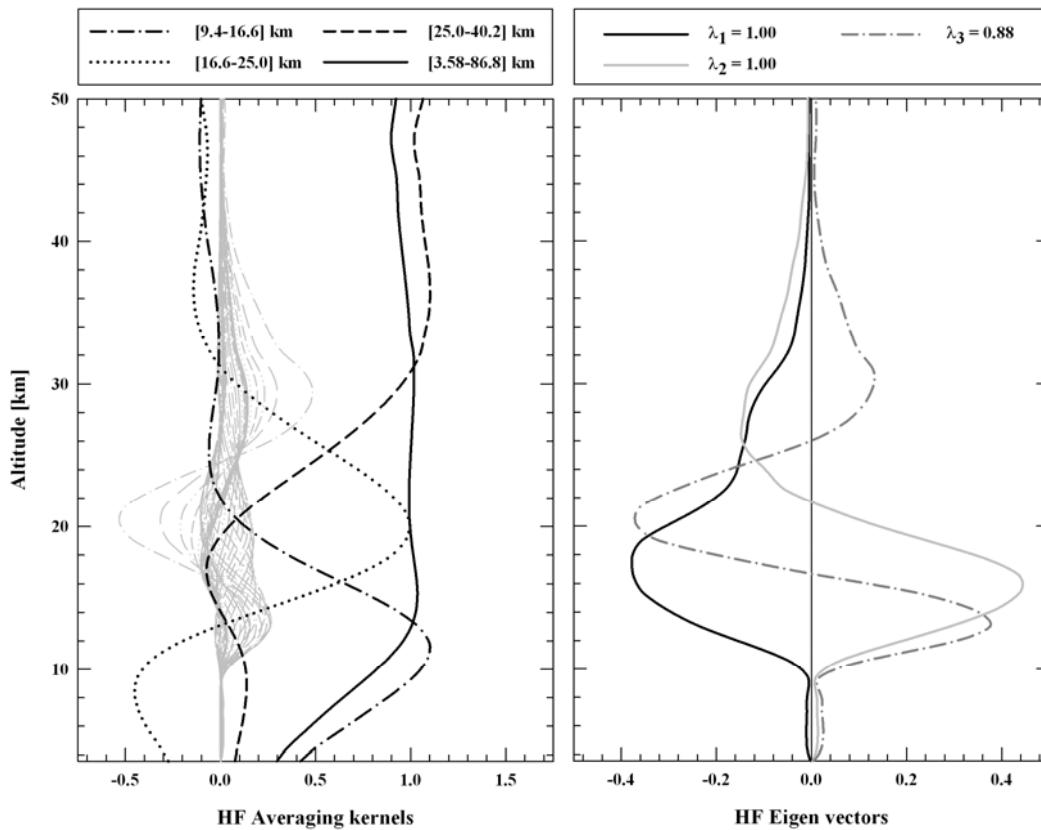


Fig. 3.8. Left panel: typical individual (thin grey curves) and merged (black curves) HF averaging kernels. For merged-layer kernels, corresponding atmospheric layers are specified in the legend box. Right panel: corresponding three first eigenvectors. Associated eigenvalues are given in the legend.

To examine and quantify the influence of the a priori state on the retrieval, eigenvectors (and associated eigenvalues) of the \mathbf{A} matrix can also be used [Rodgers, 1990, 2000]. Explicitly, while eigenvectors of \mathbf{A} provide an indication concerning the

sensitivity range, the associated eigenvalues give the fraction of information effectively coming from the measurement (the remaining information coming from the a priori). In other words, eigenvalues close to 1.0 represent components of the true profile which are well measured, while eigenvalues close to zero correspond to components which depend on the a priori state. The right part of Figure 3.8 illustrates the three first eigenvectors of the \mathbf{A} matrix for which A_{vk} are illustrated in the left part. Associated eigenvalues (λ_i) are given in the legend. In particular, this plot shows that eigenvectors with a vertical structure broader (resp. narrower) than the vertical resolution have less (resp. more) dependence on the a priori. The sensitivity range deduced from this eigenvector plot is also in good agreement with the thin grey curves reproduced in the left part of Figure 3.8. In addition, the third eigenvalue indicates that for the three HF partial columns defined, the fraction of information coming from the a priori is limited to around 10%.

A4. HF total and partial columns error budget

Systematic and statistical errors characterizing our HF total, LMS, MS and US columns have also been computed and are listed in Table 3.9 (in percent). These error values ΔC have been extracted from their associated VMR error covariance matrix \mathbf{S} using to the relation:

$$\Delta C = \sqrt{\left(\frac{\partial C}{\partial VMR}\right)^T \mathbf{S} \left(\frac{\partial C}{\partial VMR}\right)} \quad (3.4)$$

where the derivative $\frac{\partial C}{\partial VMR}$ is the operator that transforms volume mixing ratio profiles into partial column quantities. For a given partial column, it is a vector whose elements are set to zero outside the altitude range of the concerned column.

In order to estimate the impact of the line shape profile on our HF error budget, Table 3.9 provides error values for both Galatry (normal font) and Voigt (bold font) line shape models. Again, error values provided in Table 3.9 are mean errors averaged over the 5 FTIR observations reported in Table 3.10. As we have used 5 FTIR spectra to compute the mean errors, we have decided to derive uncertainties characterizing these means by taking two times the standard error on the mean ($2 \times \text{STE} = 2 \times \sigma / \sqrt{N}$, where σ is the standard deviation around the mean and N the number of FTIR spectra involved, i.e. $N=5$), in order to estimate the 95% confidence level.

Apart from errors due to spectroscopy, spectral noise, temperature profile and ILS, it is clear from Table 3.9 that for all other error sources and for all altitude ranges reported, the choice of line shape model has very limited impact. For the errors due to spectroscopy, spectral noise and ILS, the main difference between both line shape models is observed in the lowermost stratosphere (LMS), where the Voigt model gives lower error values. These differences are however not significant, based on the uncertainties characterizing these errors. The spectroscopy remains the main source of systematic error. For all altitude ranges, we found values in the range 5 to 6.5%, which seems to be in good agreement with the 5% spectroscopic uncertainty value reported by Rinsland et al. [2002] for their stratospheric HF columns. The error

estimation made by Rinsland et al. [2002] is however based on a 4% error for the HF lines intensity, instead of a 5% value assumed in the present study.

	Total column [3.58-86.8] km	LMS [10-17] km	MS [17-25] km	US [25-40] km
Systematic errors				
Spectroscopy	4.95±0.02 4.96±0.01	6.49±0.39 5.97±0.25	5.50±0.20 5.32±0.24	6.56±0.11 6.46±0.05
Temperature profile	0.20±0.01 0.20±0.01	<u>1.57±0.27</u> 1.06±0.10	0.67±0.22 0.82±0.21	<u>0.68±0.08</u> 0.55±0.04
Solar parameters	0.02±0.01 0.02±0.01	0.24±0.16 0.17±0.12	0.03±0.02 0.04±0.03	0.02±0.01 0.01±0.01
LOS	0.20±0.15 0.20±0.15	0.22±0.18 0.22±0.18	0.23±0.17 0.22±0.17	0.26±0.20 0.26±0.22
ILS	0.59±0.16 0.58±0.11	5.08±1.31 2.96±0.86	3.00±0.58 3.22±0.48	2.89±0.35 2.25±0.33
Baseline	0.06±0.01 0.06±0.01	0.11±0.05 0.09±0.02	0.03±0.01 0.03±0.01	0.12±0.05 0.11±0.04
<i>TOTAL</i>	6.03±0.32 6.03±0.26	<u>13.71±1.54</u> 10.47±1.09	9.47±0.58 9.65±0.35	10.54±0.59 9.64±0.49
Statistical errors				
Noise	0.47±0.13 0.59±0.14	8.76±3.63 6.73±2.41	2.97±0.67 3.90±0.51	1.62±0.45 1.31±0.41
Temperature profile	0.46±0.03 0.47±0.02	<u>3.66±0.63</u> 2.47±0.22	1.57±0.52 1.91±0.49	<u>1.59±0.18</u> 1.29±0.08
Solar parameters	0.07±0.03 0.07±0.03	0.98±0.64 0.70±0.50	0.13±0.07 0.16±0.11	0.06±0.05 0.04±0.04
LOS	1.84±1.39 1.72±1.50	1.94±1.59 1.88±1.67	2.00±1.49 1.85±1.64	2.34±1.80 2.19±1.89
ILS	0.59±0.16 0.58±0.11	5.08±1.31 2.96±0.86	3.00±0.58 3.22±0.48	2.89±0.35 2.25±0.33
Baseline	0.06±0.01 0.06±0.01	0.11±0.05 0.09±0.02	0.03±0.01 0.03±0.01	0.12±0.05 0.11±0.04
<i>TOTAL</i>	2.14±1.26 2.13±1.27	<u>11.43±3.21</u> 8.37±1.93	5.21±0.71 5.98±0.59	4.58±1.28 3.92±1.32

Table 3.9. Main systematic and statistical errors (in percent) for HF total and partial columns at Jungfraujoch (values in normal font are for a Galatry line shape model, bold values are for a Voigt model). Errors given here are mean values computed over a sample of 5 FTIR spectra (see Table 3.10). Associated uncertainties are two times the standard error on the mean. Underlined values appear when a significant difference occurs between the line shape models.

The only significant difference between both the Galatry and Voigt models (at 95% confidence level) is observed for the systematic and statistical contributions associated to temperature profile error in the LMS and US regions, where the Voigt model reduces corresponding errors.

Spectra name	Date	SZA [deg]	SNR ^a
124159SA	13 Apr 1997	40.52	2853
121437SA	02 Aug 1999	29.92	3925
092943SA	30 Sep 2002	54.81	3143
115420SA	15 Dec 2005	70.16	3303
144815SA	15 Jan 2009	80.04	2084

^a Signal-to-noise ratio

Table 3.10. Main characteristics of the FTIR spectra selected for our HF error budget evaluation. The name of each spectrum refers to the time (in UT hours, minutes and seconds) of recording (two last characters denote the optical filter).

These differences are probably ascribable to different dependences on temperature of the Voigt and Galatry models. As a consequence of the general improvement by the Voigt model in the LMS region, the total systematic error is significantly reduced by a few percent when adopting this line shape model. However, this benefit is small compared to the significant improvement observed in the fitting quality (close to 20%, see section 3.2.3) as well as other considerations based on Jungfraujoch spectra published by Barret et al. [2005] (i.e. smoother HF retrieved vertical profiles and better agreement with HALOE data), which altogether justify the adoption of the Galatry line shape model in our final HF retrieval strategy.

Finally, the error budget computation from 5 typical home-made spectra has allowed us to check the good consistency that exists between systematic and statistical total errors affecting HF total columns derived from our two instruments. Indeed, these errors are in close agreement, within their respective uncertainties, with total error values reported in Table 3.9. Regarding systematic and statistical total errors affecting HF partial columns we could extract from our home-made spectra, they respectively equal $9.91 \pm 1.61\%$ and $6.10 \pm 1.68\%$ for the 10-20 km altitude range, and $8.24 \pm 0.57\%$ and $2.76 \pm 0.62\%$ for the 20-40 km region. After comparison with Bruker error values obtained for the two same altitude ranges, it appears that our home-made total errors are higher than our Bruker total errors by a factor ranging from 0.5 to 2.5%, typically. This can be explained by the fact that our Bruker spectra are characterized by higher spectral resolution and signal-to-noise ratio, as well as by a better zero absorption level.

A5. Latitudinal effect on the HF seasonal cycle based on HALOE climatology

In a recent publication, Gross and Russell [2005] present the stratospheric climatology of six atmospheric gases (including HF) based on HALOE v19 measurements between 1991 and 2002, and compiled for 5° equivalent latitude belts from 82.5°N to 82.5°S . Our Figure 3.9 is based on the corresponding HF climatology (available as a supplement at <http://www.atmos-chem-phys.org/acp/5/2797/acp-5-2797-sp.tar>) and presents HF VMR monthly averages (and corresponding $1-\sigma$ standard deviations) for three selected equivalent latitude zones (respectively labeled with red, green and blue dots). The two first equivalent latitude regions (32.5°N and 47.5°N) are those that approximately correspond to Kitt Peak and Jungfraujoch locations, respectively. Results for a third equivalent latitude region (67.5°N) have also been plotted in Figure 3.9, in order to show the influence of increasing latitude on HF seasonal variation. In addition, each panel of Figure 3.9 corresponds to different pressure levels (corresponding approximate altitudes are given between parentheses, for information).

These levels have been selected such that they fall in the middle of our three FTIR sensitivity regions (i.e. LMS, MS and US regions). The lower panel of Figure 3.9 clearly highlights the strong influence of increasing latitude on the HF seasonal cycle amplitude, in good agreement with the Jungfraujoch – Kitt Peak comparison performed in the present study. For northern mid-latitudes (green dots on Figure 3.9), the HALOE experiment has also observed HF maximum (resp. minimum) abundances between March and May (resp. between September and November), in very good agreement with values reported in Table 3.5 for the LMS region.

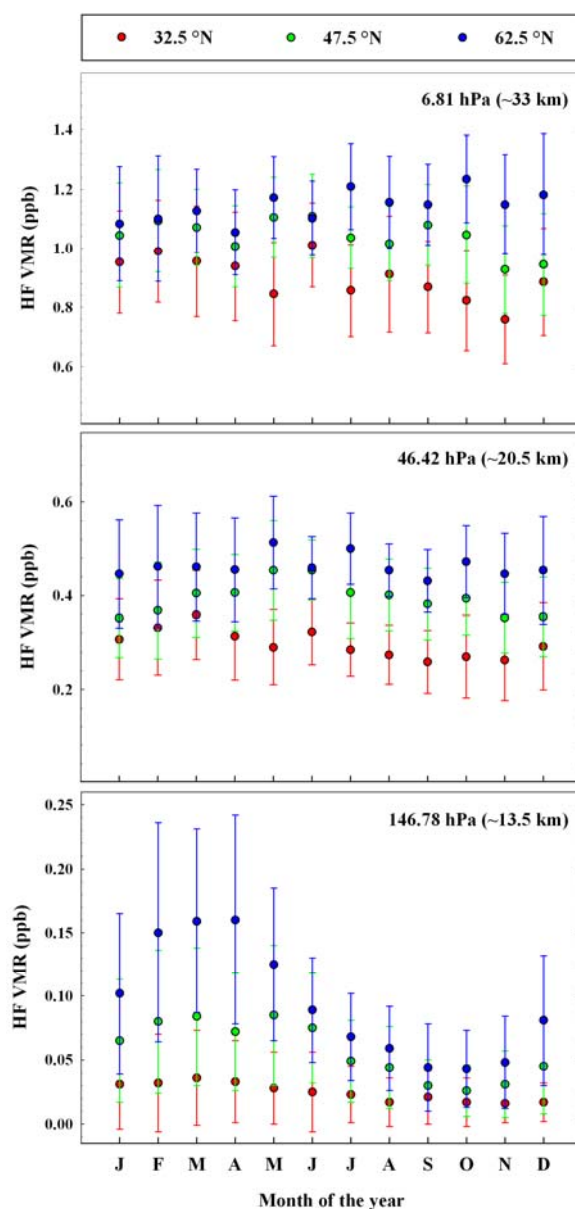


Fig. 3.9. HF monthly mean concentrations derived from the HALOE climatology between years 1991 and 2002 at three different equivalent latitudes (see legend on top of Figure) and for three pressure levels (corresponding approximate altitudes are given between parentheses). Error bars are 1- σ standard deviation around the mean. Data are available as a supplement to Gross and Russell [2005].

In addition, middle and top frames of Figure 3.9 indicate that, for all latitudes, the amplitude of the HF seasonal cycle is significantly reduced for higher altitude levels, although HALOE does not see a seasonal signal above 30 km. This is reasonably in

line with results derived from our FTIR and SLIMCAT time series (see gray dash-dotted and black dashed curves on Figure 3.6 and amplitude values reported in Table 3.5), even if FTIR and SLIMCAT data still display an amplitude of between 10 and 15% in the US region.

Acknowledgements

We would like to thank the International Foundation High Altitude Research Stations Jungfraujoch and Gornergrat (HFSJG, Bern) and the University of Liège for supporting the facilities needed to perform the observations and their analyses. University of Liège work is supported primarily by the Belgian Federal Science Policy Office (PRODEX projects ACE and SECPEA). Additional support by the EC-GEOMON project is further acknowledged. Thanks are also extended to two members of our research group (O. Flock and C. Servais) for crucial developing work of FTIR instrumentation at Jungfraujoch and to all collaborators (including colleagues from the Royal Observatory of Belgium and from the Belgian Institute for Space Aeronomy) having contributed to FTIR data acquisition. The Atmospheric Chemistry Experiment (ACE), also known as SCISAT, is a Canadian-led mission mainly supported by the Canadian Space Agency and the Natural Sciences and Engineering Research Council of Canada. We also thank the ECMWF for making their PV maps used in this work available. We are grateful to M. Schneider of IMK-ASF, Karlsruhe, Germany, for strong support during our learning phase with the PROFFIT code. Finally, we thank R. Zander of University of Liège, Belgium, for all fruitful discussions and for his permanent interest in this work.

References

Barret, B., D. Hurtmans, M. R. Carleer, et al. (2005), Line narrowing effect on the retrieval of HF and HCl vertical profiles from ground-based FTIR measurements, *J. Quant. Spec. and Rad. Transf.*, 95, 499-519.

Also available at <http://orbi.ulg.ac.be/handle/2268/2395>

Bernath, P. F., C. T. McElroy, M. C. Abrams, et al. (2005), Atmospheric Chemistry Experiment (ACE): mission overview, *Geophys. Res. Lett.*, 32, doi: 10.1029/2005GL022386.

Also available at <http://orbi.ulg.ac.be/handle/2268/2388>

Bian, H., and M. J. Prather (2002), Fast-J2: Accurate simulation of stratospheric photolysis in global chemical models, *J. Atmos. Chem.*, 41, 281-296.

Bizzarri, B., I. Bordi, A. Dell'Aquila, et al. (2006), Analysis of seasonal and daily mid-latitude tropopause pressure using GPS radio occultation data and NCEP-NCAR reanalyses, in *Atmosphere and climate studies by occultation methods*, edited by U. Foelsche et al., 253-263, Springer, Berlin.

Boone, C. D., R. Nassar, K. A. Walker, et al. (2005), Retrievals for the atmospheric chemistry experiment Fourier-transform spectrometer, *Appl. Opt.*, 44, 7218-7231.

Chipperfield, M. P., M. Burton, W. Bell, et al. (1997), On the use of HF as a reference for the comparison of stratospheric observations and models, *J. Geophys. Res.*, 102, 12901-12919.

Also available at <http://orbi.ulg.ac.be/handle/2268/14547>

Chipperfield, M. P. (2006), New version of the TOMCAT/SLIMCAT off-line Chemical Transport Model: intercomparison of stratospheric tracer experiments, *Q. J. R. Meteorol. Soc.*, 132, 1179-1203, doi:10.1256/qj.05.51.

Chou, S.-I., D. S. Baer, and R. K. Hanson (1999), Diode laser measurements of He-, Ar-, and N₂-broadened HF lineshapes in the first overtone band, *J. Mol. Spectrosc.*, 196, 70-76.

Coffey, M.T., W. G. Mankin, and A. Goldman (1989), Airborne measurements of stratospheric constituents over Antarctica in the austral spring, 1987 2. Halogen and nitrogen trace gases, *J. Geophys. Res.*, 94, 16597-16613.

Considine, G.D., L. E. Daver, E. E. Remsberg, and J. M. Russell III (1999), Analysis of near-global trends and variability in Halogen Occultation Experiment HF and HCl data in the middle atmosphere, *J. Geophys. Res.*, 104, 24297-24308.

De Mazière, M., C. Vigouroux, T. Gardiner, et al. (2005), The exploitation of ground-based Fourier transform infrared observations for the evaluation of tropospheric trends of greenhouse gases over Europe, *Environ. Sci.*, 2, 283-293.

Also available at <http://orbi.ulg.ac.be/handle/2268/2809>

Dicke, R. (1953), The effect of collision upon the Doppler width of spectral lines, *Phys. Rev.*, 89, 472-473.

Duchatelet, P., E. Mahieu, R. Ruhnke, et al. (2009), An approach to retrieve information on the carbonyl fluoride (COF₂) vertical distribution above Jungfraujoch by FTIR multi-spectrum multi-window fitting, *Atmos. Chem. Phys.*, 9, 9027-9042.

Also available at <http://orbi.ulg.ac.be/handle/2268/34266>

Duchatelet, P., et al. (in preparation), Long-term evolution of inorganic fluorine budget above Jungfraujoch derived from FTIR measurements.

Feng, W., M. P. Chipperfield, M. Dorf, et al. (2007), Mid-latitude ozone changes: studies with a 3-D CTM forced by ERA-40 analyses, *Atmos. Chem. Phys.*, 7, 2357-2369.

Fischer, H., M. Birk, C. Blom, et al. (2007), MIPAS: an instrument for atmospheric and climate research, *Atmos. Chem. Phys.*, 7, 8795-8893.

Fu, D., C. D. Boone, P. F. Bernath, et al. (2009), First global observations of atmospheric COClF from the Atmospheric Chemistry Experiment mission, *J. Quant. Spec. and Rad. Transf.*, 110, 974-985.

Galatry, L. (1961), Simultaneous effect of Doppler and foreign gas broadening on spectral lines, *Phys. Rev.*, 122, 1218-1223.

Gardiner, T., A. Forbes, M. De Mazière, et al. (2008), Trend analysis of greenhouse gases over Europe measured by a network of ground-based remote FTIR instruments, *Atmos. Chem. Phys.*, 8, 6719-6727.

Also available at <http://orbi.ulg.ac.be/handle/2268/2545>

Gross, J.-U., and J. M. Russell (2005), Technical note: A stratospheric climatology for O₃, H₂O, CH₄, NO_x, HCl and HF derived from HALOE measurements, *Atmos. Chem. Phys.*, 5, 2797-2807.

Gunson, M. R., M. M. Abbas, M. C. Abrams, et al. (1996), The atmospheric trace molecule spectroscopy (ATMOS) experiment: Deployment on the ATLAS Space Shuttle missions, *Geophys. Res. Lett.*, 23, 2333-2336.

Also available at <http://orbi.ulg.ac.be/handle/2268/14561>

Hase, F., T. Blumenstock, and C. Paton-Walsh (1999), Analysis of instrumental line shape of high-resolution FTIR-spectrometers using gas cell measurements and a new retrieval software, *Appl. Opt.*, 3417-3422.

Hase, F., J. W. Hannigan, M. T. Coffey, et al. (2004), Intercomparison of retrieval codes used for the analysis of high-resolution, ground-based FTIR measurements, *J. Quant. Spec. and Rad. Transf.*, 87, 25-52.

Ko, M. K. W., N. D. Sze, and D. K. Weisenstein (1989), The role of dynamical and chemical processes in determining the stratospheric concentrations of ozone in one-dimensional and two-dimensional models, *J. Geophys. Res.*, 94, 9889-9896.

Kouker, W., I. Langbein, T. Reddmann, and R. Ruhnke (1999), The Karlsruhe Simulation Model of the Middle Atmosphere (KASIMA), Version 2, FZK Report 6278, Forschungszentrum Karlsruhe, Germany.

Mahieu, E., P. Duchatelet, P. Demoulin, et al. (2008), Validation of ACE-FTS v2.2 measurements of HCl, HF, CCl₃F and CCl₂F₂ using space-, balloon- and ground-based instrument observations, *Atmos. Chem. Phys.*, 8, 6199-6221.

Also available at <http://orbi.ulg.ac.be/handle/2268/2344>

Mélen, F., E. Mahieu, R. Zander, et al. (1998), Vertical column abundances of COF₂ above the Jungfraujoch Station, derived from ground-based infrared solar observations, *J. Atmos. Chem.*, 29, 119-134.

Also available at <http://orbi.ulg.ac.be/handle/2268/14540>

Monge-Sanz, B., M. P. Chipperfield, A. Simmons and S. Uppala (2007), Mean age of air transport in a CTM: Comparison of different ECMWF analyses, *Geophys. Res. Lett.*, 34, L04801, doi:10.1029/2006GL028515.

Montzka, S. A., J. H. Butler, J. W. Elkins, et al. (1999), Present and future trends in the atmospheric burden of ozone-depleting halogens, *Nature*, 398, 690-694.

Nassar, R., P. F. Bernath, C. D. Boone, et al. (2006), A global inventory of stratospheric fluorine in 2004 on Atmospheric Chemistry Experiment Fourier transform spectrometer (ACE-FTS) measurements, *J. Geophys. Res.*, 111, D22313, doi: 10.1029/2006JD007395.

Also available at <http://orbi.ulg.ac.be/handle/2268/4285>

Notholt, J., A. Meier, and S. Peil (1995), Total column densities of tropospheric and stratospheric trace gases in the undisturbed arctic summer atmosphere, *J. Atmos. Chem.*, 20, 311-332.

O'Doherty, S., D. M. Cunnold, A. Manning, et al. (2004), Rapid growth of HFC-134a, HCFC-141b, HCFC-142b and HCFC-22 from AGAGE observations at Cape Grim, Tasmania and Mace Head, Ireland, *J. Geophys. Res.*, 109, doi:10.1029/2003JD004277.

Phillips, D. (1962), A technique for the numerical solution of certain integral equations of the first kind, *J. Assoc. Comput. Math.*, 9, 84-97.

Pine, A.S., A. Freid, and J. W. Elkins (1985), Spectral intensities in the fundamental bands of HF and HCl, *J. Molec. Spectrosc.*, 109, 30-45.

Pine, A. S. and R. Ciurylo (2001), Multispectrum fits of Ar-broadened HF with a generalized asymmetric lineshape: effects of correlation, hardness, speed dependence, and collision duration, *J. Mol. Spectrosc.*, 208, 180-187.

Rautian, S.G. and I. I. Sobel'man (1967), The effect of collisions on the Doppler broadening of spectral lines, *Sov. Phys. Usp.*, 9, 701-716.

Reddmann, T., R. Ruhnke, and W. Kouker (2001), Three-dimensional model simulations of SF₆ with mesospheric chemistry, *J. Geophys. Res.*, 106, 14 525-14 537.

Reisinger, A.R., N. B. Jones, W. A. Matthews, and C. P. Rinsland (1994), Southern hemisphere ground based measurements of carbonyl fluoride (COF₂) and hydrogen fluoride (HF): partitioning between fluoride reservoir species, *Geophys. Res. Lett.*, 21, 797-800.

Rinsland, C.P., J. S. Levine, A. Goldman, et al. (1991), Infrared measurements of HF and HCl total column abundances above Kitt Peak, 1997-1990: seasonal cycles, long-term increases and comparisons with model calculations, *J. Geophys. Res.*, 96, 15523-15540.

Rinsland, C. P., N. B. Jones, B. J. Connor, et al. (1998), Northern and southern hemisphere ground-based infrared measurements of tropospheric carbon monoxide and ethane, *J. Geophys. Res.*, 103, 28197-28218.

Also available at <http://orbi.ulg.ac.be/handle/2268/14545>

Rinsland, C.P., R. Zander, E. Mahieu, et al. (2002), Stratospheric HF column abundances above Kitt Peak (31.9°N latitude): trends from 1977 to 2001 and correlations with stratospheric HCl columns, *J. Quant. Spec. and Rad. Transf.*, 74, 205-216.

Also available at <http://orbi.ulg.ac.be/handle/2268/2384>

Rodgers, C.D. (1990), Characterization and error analysis of profiles retrieved from remote sounding instruments, *J. Geophys. Res.*, 95, 5587-5595.

Rodgers, C. D. (2000), Inverse methods for atmospheric sounding: Theory and Practice, Volume 2 of Series on Atmospheric, Oceanic and Planetary Physics, World Scientific.

Rothman, L. S., D. Jacquemart, A. Barbe, et al. (2005), The HITRAN 2004 molecular spectroscopic database, *J. Quant. Spec. and Rad. Transf.*, 96, 139-204.

Ruhnke, R., W. Kouker, and T. Reddmann (1999), The influence of the OH + NO₂ + M reaction on the NO_y partitioning in the late Arctic winter 1992/1993 as studied with KASIMA, *J. Geophys. Res.*, 104, 3755–3772.

Ruhnke, R., M. P. Chipperfield, M. De Mazière, et al. (in preparation), Measured and simulated time evolution of HCl, ClONO₂, and HF total columns.

Russell, J. M., L. L. Gordley, J. H. Park, et al. (1993), The Halogen Occultation Experiment, *J. Geophys. Res.*, 98, 10777-10797.

Russell, J. M., L. E. Deaver, M. Luo, et al. (1996), Validation of hydrogen fluoride measurements made by the HALOE experiment from the UARS platform, *J. Geophys. Res.*, 101, 10163-10174.

Sander, S. P., R. R. Friedl, A. R. Ravishankara, et al. (2003), Chemical kinetics and photochemical data for use in atmospheric studies, Evaluation Number 14, JPL Publication 02-25.

Sen, B., G. C. Toon, J.-F. Blavier, et al. (1996), Balloon-borne observations of midlatitude fluorine abundance, *J. Geophys. Res.*, 101, 9045-9054.

Senten, C., M. De Mazière, B. Dils, et al. (2008), Technical Note: New ground-based FTIR measurements at Ile de La Réunion: observations, error analysis, and comparisons with independent data, *Atmos. Chem. Phys.*, 8, 3483-3508.

Also available at <http://orbi.ulg.ac.be/handle/2268/2660>

Stiller, G. P., T. von Clarmann, M. Höpfner, et al. (2008), Global distribution of mean age of stratospheric air from MIPAS SF₆ measurements, *Atmos. Chem. Phys.*, 8, 677-695.

Stolarski, R.S. and R. D. Rundel (1975), Fluorine photochemistry in the stratosphere, *Geophys. Res. Lett.*, 22, 385-388.

Tikhonov, A. (1963), On the solution of incorrectly stated problems and a method of regularization, Dokl. Acad. Nauk. SSSR, 151, 501.

Toon, G.C., C. B. Farmer, P. W. Schaper, et al. (1992), Composition measurements of the 1989 Arctic winter stratosphere by airborne infrared solar absorption spectroscopy, J. Geophys. Res., 97, 7939-7961.

Wilson, S. R., G. Schuster, and G. Helas (1989), Measurements of COFCl and CCl₂O near the tropopause, in R.D. Bojkov and P. Fabian (eds), Ozone in the Atmosphere, A. Deepak Publisher, 302-305.

Wittke, J. and R. Dicke (1956), Redetermination of the hyperfine splitting in the ground state of atomic hydrogen, Phys. Rev., 103, 620-631.

World Meteorological Organization (1957), Definition of the tropopause, WMO Bull., 6, 136.

World Meteorological Organization (2007), WMO Report No. 50: Scientific Assessment of Ozone Depletion: 2006, P.O. Box 2300, Geneva 2, CH 1211, Switzerland.

Zander, R. (1975), Présence de HF dans la stratosphère supérieure, C.R. Acad. Sci. Paris. Sér. B., 281, 213-214.

Zander, R., G. Roland, L. Delbouille, et al. (1987), Monitoring of the integrated column of hydrogen fluoride above the Jungfraujoch Station since 1977: the HF/HCl column ratio, J. Atmos. Chem., 5, 385-394.

Zander, R., M. R. Gunson, C. B. Farmer, et al. (1992), The 1985 chlorine and fluorine inventories in the stratosphere based on ATMOS observations at 30° North latitude, J. Atmos. Chem., 15, 171-186.

Also available at <http://orbi.ulg.ac.be/handle/2268/2690>

Zander, R., C. P. Rinsland, E. Mahieu, et al. (1994), Increase of carbonyl fluoride (COF₂) in the stratosphere and its contribution to the 1992 budget of inorganic fluorine in the upper stratosphere, J. Geophys. Res., 99, 16737-16743.

Also available at <http://orbi.ulg.ac.be/handle/2268/14537>

Chapter 4

FTIR multi-spectrum multi-window fitting of carbonyl fluoride

As already evoked in Chapter 1, carbonyl fluoride (COF_2) is the second most important stratospheric fluorine reservoir. To gather experimental, high-quality, mid- or long-term COF_2 time series is therefore of great scientific interest. Several COF_2 infrared absorption lines, located either in the so-called InSb (1-5 μm) and MCT (2-16 μm) spectral ranges, can be used to determine its total column from ground-based high-resolution FTIR observations. In this context, several studies concerning the evolution of COF_2 total column above various ground-based stations in both hemispheres were published during the nineties (see the references at the end of this chapter). However, at this time, no study concerning the inversion of COF_2 vertical distributions from ground-based FTIR spectra has been published. This chapter deals with the feasibility of such inversions, using for the first time the multi-spectrum multi-window fitting procedure available in the SFIT-2 v3.91 algorithm.

The multi-spectrum approach consists in combining several FTIR observations, recorded during the same day and with the same spectral resolution, to increase the information content. In the following pages, this multi-spectrum multi-window approach is fully characterized in terms of fitting strategy, information content and error budget. Some examples of COF_2 vertical profiles inversions are also presented. The resulting COF_2 FTIR time series is finally compared with corresponding vertical abundances derived from two state-of-the-art numerical models, for the 2000-2008 time period. It is shown that the multi-spectrum approach is an interesting appropriate alternative to retrieve vertical abundances of atmospheric gases characterized by weak spectral signatures and relatively low intra-day variability.

The following pages reproduce the complete text of a scientific article accepted for publication in 2009 by *Atmospheric Chemistry and Physics*. The resulting COF_2 time series has been archived at the NDACC database. It has further been included as a reference data set in the WMO 2010 report (see Figure 1-23, corresponding caption and section).

An approach to retrieve information on the carbonyl fluoride (COF₂) vertical distributions above Jungfraujoch by FTIR multi-spectrum multi-window fitting

P. Duchatelet¹, E. Mahieu¹, R. Ruhnke², W. Feng³, M. Chipperfield³, P. Demoulin¹, P. Bernath^{4, 5}, C. D. Boone⁵, K. A. Walker^{5, 6}, C. Servais¹ and O. Flock¹

¹ Institute of Astrophysics and Geophysics of the University of Liège, B-4000 Liège, Belgium

² Forschungszentrum Karlsruhe, IMK, Karlsruhe, Germany

³ Institute for Climate and Atmospheric Science, School of Earth and Environment, University of Leeds, Leeds, UK

⁴ Department of Chemistry, University of York, Heslington, UK

⁵ Department of Chemistry, University of Waterloo, Waterloo, Canada

⁶ Department of Physics, University of Toronto, Toronto, Canada

Abstract

We present an original multi-spectrum fitting procedure to retrieve volume mixing ratio (VMR) profiles of carbonyl fluoride (COF₂) from ground-based high resolution Fourier transform infrared (FTIR) solar spectra. The multi-spectrum approach consists of simultaneously combining, during the retrievals, all spectra recorded consecutively during the same day and with the same resolution. Solar observations analyzed in this study with the SFIT-2 v3.91 fitting algorithm correspond to more than 2900 spectra recorded between January 2000 and December 2007 at high zenith angles, with a Fourier Transform Spectrometer operated at the high-altitude International Scientific Station of the Jungfraujoch (ISSJ, 46.5°N latitude, 8.0°E longitude, 3580 m altitude), Switzerland. The goal of the retrieval strategy described here is to provide information about the vertical distribution of carbonyl fluoride. The microwindows used are located in the ν_1 or in the ν_4 COF₂ infrared (IR) absorption bands. Averaging kernel and eigenvector analysis indicates that our FTIR retrieval is sensitive to COF₂ inversion between 17 and 30 km, with the major contribution to the retrieved information always coming from the measurement. Moreover, there was no significant bias between COF₂ partial columns, total columns or VMR profiles retrieved from the two bands. For each wavenumber region, a complete error budget including all identified sources has been carefully established. In addition, comparisons of FTIR COF₂ 17-30 km partial columns with KASIMA and SLIMCAT 3-D CTMs are also presented. If we do not notice any significant bias between FTIR and SLIMCAT time series, KASIMA COF₂ 17-30 km partial columns are lower of around 25%, probably due to incorrect lower boundary conditions. For each times series, linear trend estimation for the 2000-2007 time period as well as a seasonal variation study are also performed and critically discussed. For FTIR and KASIMA time series, very low COF₂ growth rates (0.4 ± 0.2 %/year and 0.3 ± 0.2 %/year, respectively) have been derived. However, the SLIMCAT data set gives a slight negative trend (-0.5 ± 0.2 %/year), probably ascribable to discontinuities in the meteorological data used by this model. We further demonstrate that all time series

are able to reproduce the COF₂ seasonal cycle, which main seasonal characteristics deduced from each data set agree quite well.

4.1. Introduction

Over the past few decades, the major sources of fluorine in the stratosphere are the man-made chlorofluorocarbons CFC-12 (CCl₂F₂) and CFC-11 (CCl₃F), which have been widely emitted at ground level by human activities. Photolysis of these compounds leads to release of chlorine atoms, while the fluorine is, for the first steps, present in the form of carbonyl compounds like carbonyl chlorofluoride (COCIF) and carbonyl fluoride (COF₂). These two species are long-lived enough to be detectable from the ground (Mélen *et al.*, 1998) or by *in situ* techniques (Wilson *et al.*, 1989) and their photolysis further liberates fluorine atoms, which are quickly converted to HF. Its extreme stability makes HF the largest fluorine reservoir in the stratosphere, but COF₂ also makes a large contribution to the inorganic fluorine budget F_y, because of its slow photolysis (Sen *et al.*, 1996): the COF₂ molecule has been shown to be the second most abundant stratospheric fluorine reservoir (Kaye *et al.*, 1991). The maximum contribution of COF₂ to F_y is in the tropics, where it accounts for about 32% at its peak altitude near 40 km (Nassar *et al.*, 2006). At midlatitudes, the COF₂ vertical distribution has a maximum around 30 km where it contributes to almost 25% to F_y (Nassar *et al.*, 2006). Despite the fact that fluorine does not directly participate in ozone depletion, measurement of the concentrations of individual fluorine-bearing species in different altitude ranges of the atmosphere is important: (1) to quantify the strengths of the various sources and to compare with emission inventories, (2) to assess their partitioning during the transformation from sources to sink species.

Measurements of COF₂ are however still sparse. Rinsland *et al.* (1986) were the first to detect COF₂ in the Earth's stratosphere and to produce a carbonyl fluoride vertical profile obtained from ATMOS/Spacelab 3 space observations using line parameters derived from laboratory spectra. These observations were in good agreement with model predictions published by Kaye *et al.* (1991). In addition, a comparison between mean COF₂ vertical distributions for different latitudinal regions recorded in 1985 and 1992 during the ATMOS/Spacelab 3 and ATMOS/Atlas 1 space missions, respectively, has been discussed by Zander *et al.* (1994). The Atmospheric Chemistry Experiment Fourier transform spectrometer (ACE-FTS), onboard the SCISAT-1 satellite, is the first instrument since the last ATMOS flight in 1994 to obtain COF₂ vertical profiles from space (Bernath *et al.*, 2005). Launched in August 2003, the ACE-FTS has been regularly taking COF₂ measurements with global coverage since early 2004. A paper by Walker *et al.* (in preparation) will exploit the v.3 of the ACE-FTS data to study the global distribution of carbonyl fluoride.

Several COF₂ IR absorption lines can also be used to determine its total column from ground-based Fourier transform infrared (FTIR) observations. In this context, different studies concerning the measurement of the COF₂ total column above various sites were published during the nineties: Rinsland *et al.* (1991) were the first to report a mean COF₂ total column measured above Kitt Peak (31.9°N latitude, 111.6°W longitude, 2090 m altitude) and to confront their results with calculations made by the two dimensional Atmospheric and Environmental Research (AER) model (Ko *et al.*, 1989). A subsequent paper by Reisinger *et al.* (1994) proposed innovative COF₂ measurements using the ν₄ absorption features at 1234 cm⁻¹. Independently Notholt *et*

al. (1995) have exploited a pair of COF₂ microwindows located either in the ν_1 (1935 and 1950 cm⁻¹ regions) or the ν_4 (1235 cm⁻¹ region) band to publish total column values measured at high northern latitude during summer 1993 and 1994. No significant bias between the two time series was found. The first contribution dealing with the full characterization of the seasonal variability and the global trend of carbonyl fluoride is a paper by Mélen *et al.* (1998). These authors have exploited two microwindows located in the ν_1 band to produce a time series covering the 1985-1995 time period from solar spectra recorded at the Jungfraujoch. One year later, Mélen *et al.* (1999) compared COF₂ total columns above Jungfraujoch derived from the ν_1 and the ν_4 bands and found a bias of 6%, with the ν_4 band results being lower than those derived from the ν_1 band. In addition, no information on the COF₂ vertical distribution could be retrieved following any of the studies described above.

To our knowledge, no study about the inversion of COF₂ vertical distributions from ground-based FTIR spectra has been published to date. This study deals with the possibility of such inversions using, simultaneously, a multi-microwindow and a multi-spectrum fitting procedure. A selection of microwindows in the so-called InSb (2-5.5 μm , including the ν_1 COF₂ band) and MCT (7-14 μm , including the ν_4 COF₂ band) spectral ranges, a complete discussion of the data characterization (e.g. information content and error budget) and typical examples of COF₂ retrieved products from ground-based FTIR spectra are presented here. Comparisons with KASIMA and SLIMCAT model data are also included.

4.2. Retrieval strategy

All the results produced in this study have been derived from high resolution solar spectra recorded at the International Scientific Station of the Jungfraujoch (ISSJ, Swiss Alps; 46.5°N latitude, 8.0°E longitude, 3580 m altitude) under clear-sky conditions with a commercial Bruker IFS 120HR spectrometer between January 2000 and December 2007. For the present work, two sets of spectral microwindows have been defined and selected in the ν_1 and the ν_4 COF₂ absorption bands. Table 4.1 summarizes the main characteristics of each set. Since COF₂ absorption lines are quite weak, only spectra with solar zenith angles greater than 70° and up to 90° have been analyzed. Spectral resolutions, defined as the inverse of twice the maximum optical path difference, are 2.85 and 4.40 millicm⁻¹ for the InSb set, and 4.00 and 6.10 millicm⁻¹ for the MCT microwindows. For each detector band, two different spectral resolutions are used, pending of the time of measurements (low or high sun in the sky) and weather conditions (clear or partly cloudy conditions).

The COF₂ column retrievals and profile inversions have been performed using the SFIT-2 v3.91 fitting algorithm. This retrieval code has been specifically developed to derive volume mixing ratio (VMR) profiles of atmospheric species from ground-based FTIR spectra. Inversion of vertical distributions from infrared measurements is often an ill-conditioned problem. Regularization methods are therefore frequently used to improve the conditioning of the solution (Ceccherini, 2005). The SFIT-2 algorithm employs a semi-empirical implementation of the Optimal Estimation Method (OEM) developed by Rodgers (2000), as well as error evaluation as discussed in Connor *et al.* (1995). The OEM is a regularization method that retrieves VMR profiles from a statistical weighting of *a priori* information and the measurements.

The weighting matrix (called the averaging kernel, AvK) produced during the iterative process can be further used to characterize the information content of the retrievals. A more complete description of the SFIT-2 code can be found, for example, in Pougatchev and Rinsland (1995), Pougatchev *et al.* (1995) and Rinsland *et al.* (1998).

Range (cm ⁻¹)	Interfering species
InSb range (2-5.5 μm)	
1936.15 - 1936.34	O ₃ , CO ₂ , H ₂ O, solar lines
1951.89 - 1952.05	O ₃ , H ₂ O, solar lines
1952.62 - 1952.78	O ₃ , CO ₂ , solar lines
MCT range (7-14 μm)	
1230.75 - 1231.20	CH ₄ , O ₃ , CO ₂ , H ₂ O ₂ , N ₂ O
1233.90 - 1234.20	CH ₄ , O ₃ , CO ₂ , H ₂ O ₂ , N ₂ O, solar lines
1234.35 - 1234.63	CH ₄ , O ₃ , CO ₂ , H ₂ O ₂ , N ₂ O, CH ₃ D

Table 4.1. Microwindows selected (in InSb and MCT ranges) for CO₂ profile inversions. Second column lists the interfering gases adjusted during the retrieval process. For each microwindow, examples of simulated spectra (for a solar angle close to 80°) with the contribution of CO₂ are reproduced on Figure 4.3.

During our retrievals, only the CO₂ vertical distribution has been fitted, while the *a priori* VMR profiles corresponding to interfering species were simply scaled. The synthetic spectra were calculated with the spectroscopic line parameters available in the latest 2004 version of the HITRAN compilation (Rothman *et al.*, 2005). During the retrievals, all microwindows of each set were fitted simultaneously. In addition, we have also performed multi-spectrum retrievals during which several FTIR spectra, recorded during the same day at identical resolutions and similar solar zenith angles, are fitted together to increase the information content (see section 4.3). However, for the InSb set, spectra recorded during the morning and during the afternoon have to be retrieved separately, due to the high variability of water vapor, a significant interference in the 1936 cm⁻¹ microwindow. During this multi-spectrum multi-window fitting procedure, individual airmass files are also computed for each spectrum.

Between 15 and 37 km, the adopted *a priori* CO₂ profile is a zonal mean (for the 41-51°N latitude band) of more than 300 occultations recorded by the ACE-FTS instrument between February 2004 and September 2005. The ACE-FTS CO₂ profiles used in this study consist in a research version of ACE-FTS v.2.2 products. They differ from the standard 2.2 version by higher retrieval heights for CO₂. Below 15 km, ACE-FTS VMR values have been smoothly connected to reach VMR values of about 1.5×10^{-13} at the altitude of the site (3.58 km), which corresponds to the CO₂ ground value used by Mélen *et al.* (1998). Above 37 km (this altitude corresponds to the highest ACE-FTS analyzed measurement), the *a priori* CO₂ profile used by ACE-FTS is scaled during its retrieval procedure. These scaled profiles (once again, for all ACE-FTS occultations located in the 41-51°N latitude band) have then been averaged in order to construct our own *a priori* CO₂ profile above 37 km. The *a priori* covariance matrix S_a has been derived from the same set of ACE-FTS measurements used for the construction of the *a priori* CO₂ profile. Each diagonal element of the S_a matrix has also been weighted by the square root of the

corresponding atmospheric layer thickness, to account for variable layer thicknesses. A Gaussian inter-layer correlation of 2 km has further been implemented, estimated from the 3D VMR-altitude correlation matrix, as calculated from the ACE-FTS observations. Top panel of Figure 4.1 illustrates the CO₂ *a priori* VMR and variability profiles (this latter one corresponding to diagonal elements of the S_a matrix) used for our retrievals. Background horizontal lines reproduce the 41 atmospheric layer scheme used during the retrieval procedure. The CO₂ VMR-altitude correlation matrix as seen by the ACE-FTS instrument and from which the correlation length parameter has been deduced is illustrated on the bottom panel of Figure 4.1. The adopted pressure-temperature (p-T) profiles were those provided by the National Centers for Environmental Prediction (NCEP, Washington, DC.; see <http://www.ncep.noaa.gov>), specifically computed for the Jungfraujoch site on a daily basis. The signal-to-noise ratio used during the retrievals and allowing to define diagonal elements of the diagonal measurement covariance matrix S_e was fixed to 250, following the L-curve method (for example, Steck (2002); Ceccherini (2005)).

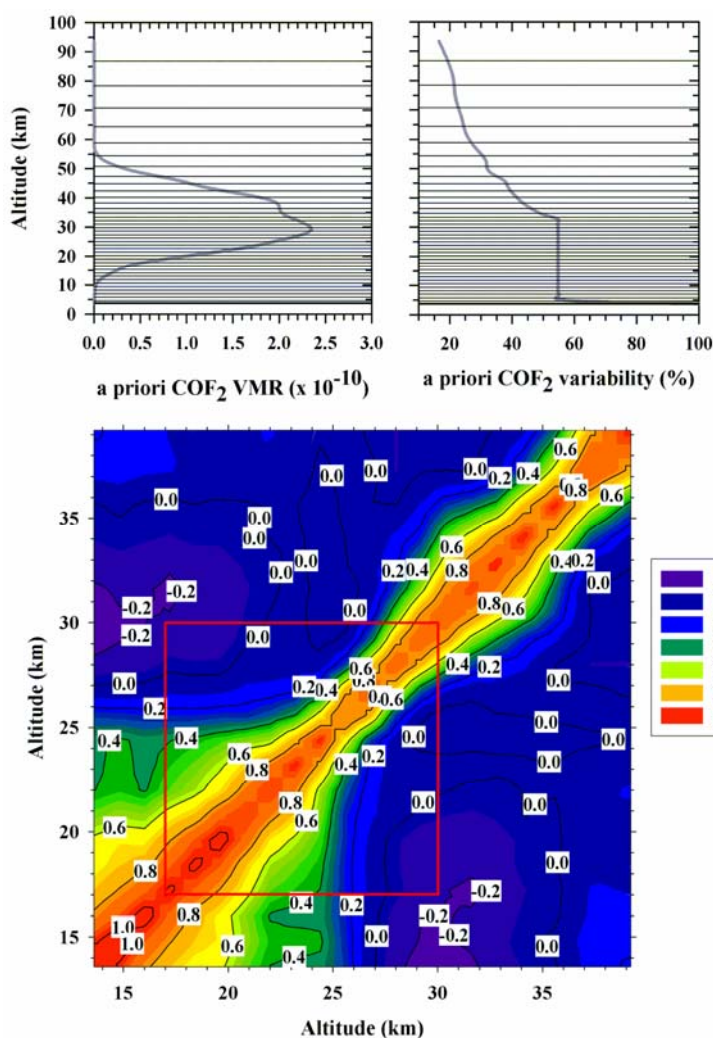


Fig. 4.1. Top panel: *a priori* VMR (left) and variability (right) profiles used for our CO₂ profile inversions. Horizontal lines reproduce the 41 atmospheric layers used during the retrieval procedure. Bottom panel: CO₂ VMR – altitude correlation matrix as deduced from ACE-FTS satellite mid-latitude observations (41–51°N). The red square indicates the altitude range where FTIR retrievals are sensitive to CO₂ inversion. Outside these ranges, the CO₂ variability mainly results from the ACE-FTS *a priori* information.

4.3. Information content and error budget

Under the input and observational conditions described here above, each microwindow set has been completely characterized in terms of information content. Table 4.2 objectively demonstrates the benefits of using, simultaneously, a multi-microwindow (MW) and a multi-spectrum (MS) approach for COF₂ retrievals. The last column of Table 4.2 provides, for each selected microwindow, typical values for the degrees of freedom for signal (DOFS) when the retrieval is done using this single microwindow alone: this parameter indicates how many independent pieces of information of the target gas distribution (computed here for partial columns) may be derived. Values between brackets (λ_1) correspond to the first eigenvalue of the corresponding AvK matrix and indicate the fraction of the information coming from the measurement.

Range (cm ⁻¹)	DOFS (λ_1)
InSb range (2-5.5 μ m)	
1936.15 - 1936.34	0.53 (0.49)
1951.89 - 1952.05	0.58 (0.53)
1952.62 - 1952.78	0.60 (0.54)
3MW	0.94 (0.53)
3MW + MS _[3 obs]	1.24 (0.92)
MCT range (7-14 μ m)	
1230.75 - 1231.20	0.37 (0.35)
1233.90 - 1234.20	0.35 (0.33)
1234.35 - 1234.63	0.35 (0.33)
3MW	0.68 (0.63)
3MW + MS _[3 obs]	0.95 (0.81)

Table 4.2. Typical information content of microwindows sets selected for COF₂ profile inversions. Second column gives the degrees of freedom for signal (DOFS) and the fraction of information coming from the measurement (λ_1) when each interval is fitted separately. Lines “3MW” and “3MW+MS_[3 obs]” indicate the DOFS and λ_1 when a multi-microwindow (including the 3 microwindows of the previous lines) and a multi-microwindow multi-spectrum (including 3 FTIR observations) fitting procedure is adopted, respectively. Solar zenith angles of the spectra used for these simulations are close to 78°.

The line “3MW” gives the DOFS and λ_1 resulting when all microwindows are fitted simultaneously. In the InSb case, a multi-microwindow fit provides a significant increase in the DOFS, but has a minor impact on the first eigenvalue. Only a multi-spectrum fitting procedure allows a larger fraction of the information to come from the measurement (see line “3MW+MS_[3 obs]” in Table 4.2; values reported are from the inclusion of 3 spectra). For the MCT range, a multi-microwindow fit doubles the DOFS and the λ_1 value compared to the single MW fits and an even larger improvement is obtained by applying the multi-spectrum approach. It is therefore possible to compute one COF₂ partial column (DOFS greater or close to 1) when such a multi-spectrum procedure is adopted, with very limited impact from the adopted *a priori*.

More complete statistics have been established by analyzing FTIR spectra recorded at the Jungfraujoch during the January 2000 – December 2007 time period. For the solar zenith angle range adopted here, our database contains 884 spectra recorded over 252

days for the InSb domain, and 2062 FTIR observations recorded over 439 days for the MCT range. Corresponding mean DOFS values are 1.23 ± 0.17 and 1.16 ± 0.30 for the InSb and MCT regions, respectively. For the InSb range, the minimum value of 0.88 for the DOFS is observed when combining 2 spectra and the maximum value of 2.07 is obtained by fitting 8 spectra simultaneously. Corresponding λ_1 are 0.76 and 0.99, respectively. For the MCT case, the minimum value of the DOFS is 0.60 for 2 FTIR spectra fitted simultaneously, while the maximum value peaks at 1.95 for the combination of 15 spectra in the retrievals. Corresponding λ_1 values are 0.56 and 0.99, respectively. It thus clearly appears that, for the same number of FTIR spectra combined during the retrieval procedure, the CO₂ lines selected in the ν_1 band provide more information than the CO₂ absorptions selected in the ν_4 region.

Among the factors explaining why the InSb microwindows bring higher information content, are: (1) the weakness of CO₂ absorption lines in the MCT region as compared to the lines selected in the InSb range (InSb CO₂ lines are stronger by almost a factor 2) and, (2) the higher spectral resolution of the ISSJ observations performed in the InSb region (as already mentioned in section 4.2). For the time period under investigation here, three spectra can be combined in almost 80% of cases for the InSb region, and in 48% of cases for the MCT range. In both spectral domains, the fraction of occurrences for which spectra are combined only in pairs never exceeds 12%.

For typical VMR averaging kernels, the first eigenvector of the AvK matrix and partial error budgets are plotted in the top panel of Figure 4.2 for the InSb range, in its lower panel for the MCT region. All these curves have been simulated by using 3 FTIR spectra in the multi-microwindow multi-spectra fitting procedure, as defined in Table 4.2. The observational conditions (including the resolutions) used for the simulation are indicated above each panel. Averaging kernels have been calculated for the altitude ranges defined in the legend. They indicate a good sensitivity of the ground-based FTIR observations for CO₂ retrievals between 17 and 50 km. Outside of this altitude range, the sensitivity to the measurement is quite poor. However, the half-width at half-maximum of the first eigenvector curve (middle frame) suggests that FTIR measurements are mostly sensitive between 17 and 30 km, with the maximum sensitivity observed around 25 km.

Corresponding first eigenvalues indicate that in both spectral ranges, the largest fraction of the information is coming from the measurement (contributions of 92% and 85% for the InSb and MCT domains, respectively). The value of the DOFS obtained in each case (1.24 and 1.00, as mentioned in the legend of Figure 4.2) indicates that one partial column can be extracted from CO₂ FTIR measurements, when performing a retrieval using the multi-microwindow multi-spectrum approach. The altitude limits of such a partial column could be, for example, the ones we have chosen to plot the non zero averaging kernels illustrated on the left part of Figure 4.2, i.e., 17-30 km.

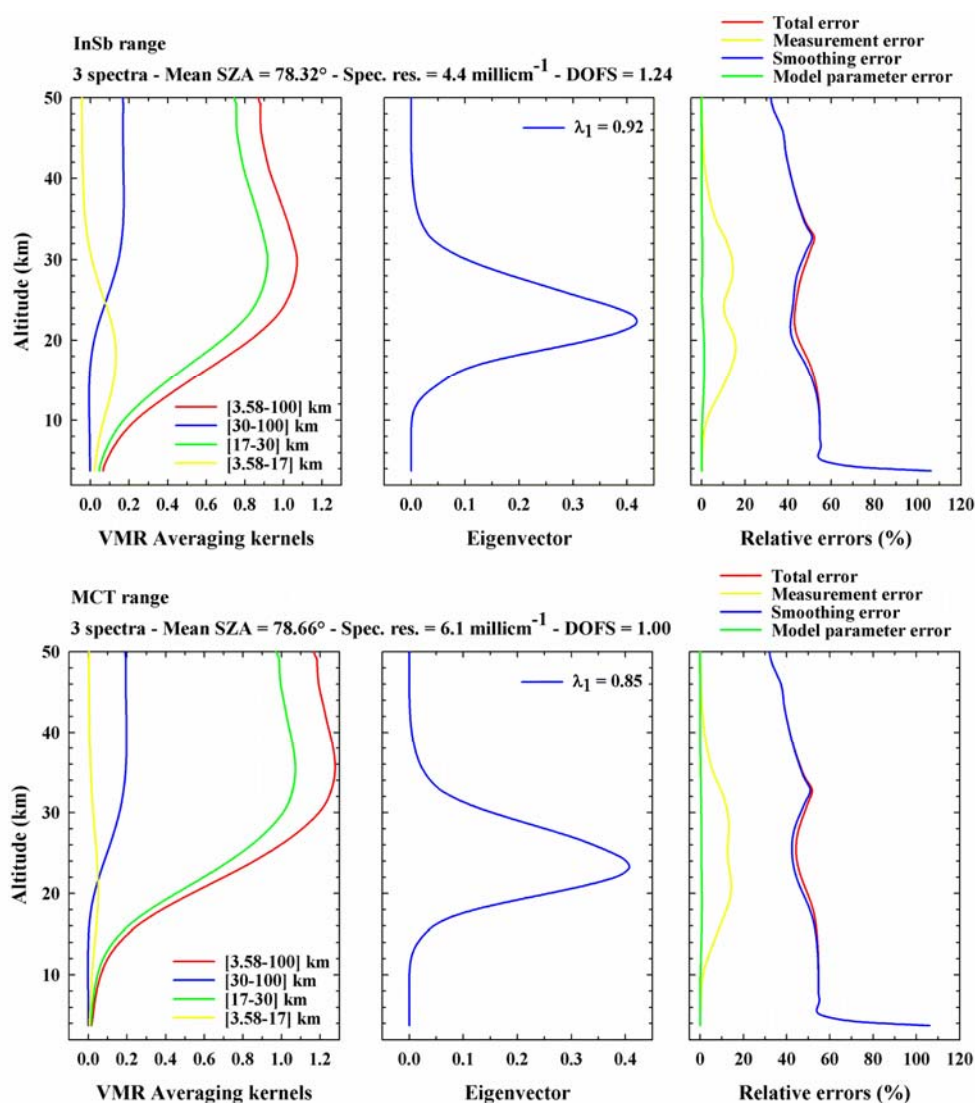


Fig. 4.2. Typical information content for CO₂ retrievals from ISSJ spectra using the InSb (top panel) and the MCT (lower panel) regions. For each spectral range, these curves have been calculated by applying simultaneously the multi-microwindow and multi-spectra fitting procedure on 3 FTIR spectra recorded at high and similar mean solar zenith angles, on 30 January 2006 for the InSb range, on 8 March 2002 for the MCT range.

Another way to highlight the altitude sensitivity range of our set of CO₂ absorption lines is to plot the \mathbf{K} matrix weighting function characterizing our CO₂ vertical profile inversions. A typical example of a \mathbf{K} matrix for the CO₂ retrieval using the multi-microwindow multi-spectrum approach is reproduced on the background colored plots of Figure 4.3. For each microwindow of our set (left column: InSb range; right column: MCT range) black and red traces (slightly vertically scaled, for clarity) reproduce all gases and CO₂ absorption contributions, respectively. These traces correspond to simulated spectra performed for a solar zenith angle close to 80°. Significant interference gases for which VMR profiles are scaled during the retrieval procedure are also labeled with black arrows. It clearly appears from Figure 4.3 that our FTIR measurements using the multi-microwindow multi-spectrum approach are most sensitive to CO₂ inversions between 17 and 30 km.

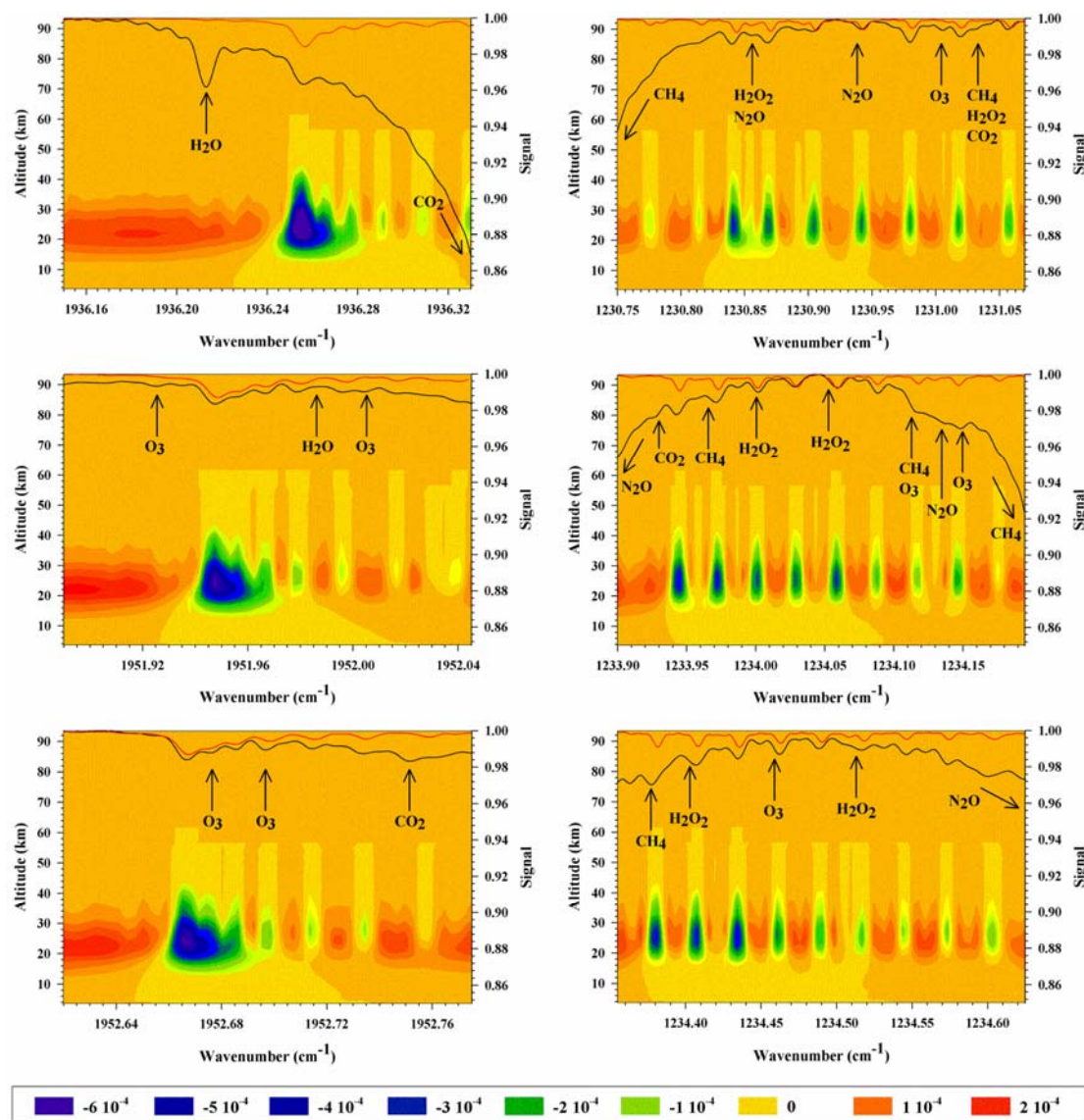


Fig. 4.3. Selection of microwindows in InSb (left column) and MCT (right column) ranges for COF₂ profile inversions. For each microwindow, black and red traces (slightly vertically scaled, for clarity) reproduce all gases and COF₂ absorptions, respectively (simulated spectra performed for a solar zenith angle of 80°). All atmospheric interference gases for which VMR profiles are scaled during the retrieval procedure are indicated with black arrows (minor interferences due to solar lines are not represented for clarity). Background colored plots reproduce, for each microwindow, corresponding typical **K** matrix weighting functions and highlight the altitude sensitivity range of each COF₂ absorption line.

Finally, a typical example of the error budget for the retrieved COF₂ VMR profiles is given in the right frames of Figure 4.2. Only contributions to the total error of the three most common random error components (namely, smoothing error, measurement error and forward model parameter error) are plotted; for the InSb range, these together correspond typically to 8% and 11% of the COF₂ total and 17-30 km partial columns, respectively. Due to lower information content and spectral resolution, the corresponding errors for the MCT range are a little higher, with typical values for total error of 11% and 15%, respectively. The **S_a** matrix used for the estimation of smoothing error is the variability matrix deduced from ACE-FTS satellite data (see end of Sect. 4.2). The forward model parameter error includes errors induced by retrieval parameters (like, e.g., the wavenumber shift, the background

slope, the background curvature, etc) which can improve fitting quality when they are adjusted during the retrieval procedure. In our case, only the wavenumber shift and the background slope are adjusted during the retrieval procedure, for each microwindow of both spectral regions (InSb and MCT). An independent wavenumber shift for each microwindow is also applied. When a microwindow contains solar absorption lines, the error induces by the solar line shift is also included in the forward model parameter error.

Three additional random error sources, namely errors associated with the temperature profiles used in the physical model adopted for the retrievals, with the instrument line shape (ILS) and with the solar zenith angle (SZA), have also been evaluated by using a perturbation method. To quantify the effect of temperature profile errors on CO₂ total and partial columns, we have included the temperature uncertainties provided by the NCEP in our retrieval procedure. The ILS error has been evaluated by assuming an effective apodization error of $\pm 10\%$, compared to a perfectly aligned instrument. For the time period studied here, this $\pm 10\%$ value is consistent with the analysis of HBr cell spectra made with the LINEFIT v.8.2 algorithm (Hase *et al.*, 1999). These cell spectra were recorded to characterize the instrumental line shape of the Jungfraujoch Bruker FTS. The SZA error impact on CO₂ retrievals has been deduced by assuming an accuracy of $\pm 0.2^\circ$ for zenith angles associated with each FTIR spectrum. This accuracy is compatible with the experimental observation conditions.

To complete our error budget, the impact of two systematic error sources has also been evaluated: the shape of the CO₂ *a priori* vertical distribution and the uncertainty affecting the CO₂ line intensities. Their magnitudes have also been estimated through sensitivity tests. To quantify the impact of the CO₂ *a priori* VMR profile on CO₂ retrieved products we have used the same CO₂ *a priori* distribution derived by Mélen *et al.* (1998) from the ATMOS/SL3 1985 experiment instead of the mean CO₂ VMR profile derived from ACE-FTS measurements that we have adopted in our FTIR analysis (described in the previous section). The shapes of these two profiles are slightly different. In particular, the CO₂ profile derived from ATMOS measurements peaks at higher altitude (close to 35 km). In practice, this 20-year old profile has also been horizontally scaled in order to obtain a more realistic CO₂ total column, close to the value deduced from the ACE-FTS profile.

To quantify the impact of the uncertainty in the CO₂ line intensities on our retrievals, we have modified the HITRAN 2004 spectroscopic line list in accordance with the intensity uncertainty indices reported in Table 5 of Rothman *et al.* (2005). For all CO₂ lines included in our InSb microwindows, these authors quote uncertainties on the line intensities of greater than 20%. For all CO₂ lines included in our MCT microwindows, the corresponding HITRAN 2004 indices indicate that intensity uncertainties are between 10 and 20%. We have thus included line intensities in our retrievals modified by 25% for the InSb domain, and by 15% for the MCT range.

For each spectral range, Table 4.3 provides contributions from each random or systematic error, listed above, on CO₂ total and 17-30 km partial columns. For each wavenumber region, these error values have been obtained by using representative subsets of FTIR spectra covering various observational and fitting conditions (SZA range, spectral resolution, period of the year, time of the day, number of spectra

combined during the multi-spectrum fit approach). When taking into account the six error sources presented in Table 4.3, the total random error affecting our COF₂ retrieved total columns is close to 10% for both spectral ranges. For the COF₂ 17-30 km partial columns, the total random error is a little higher, with values around 12% and 15% for InSb and MCT regions, respectively.

Error source	Error on COF ₂ total column (%)		Error on COF ₂ [17-30] km partial column (%)	
	InSb	MCT	InSb	MCT
Random errors				
	InSb	MCT	InSb	MCT
Smoothing error	4.8	8.5	7.9	11.1
Measurement error	6.4	7.5	8.1	9.6
Model parameter error	0.5	0.5	0.5	0.5
NCEP T profiles	0.4	2.5	0.8	2.2
ILS	1.3	2.4	1.5	2.8
SZA	1.2	1.8	1.5	2.1
TOTAL	8.2	12.0	11.5	15.3
Systematic errors				
	InSb	MCT	InSb	MCT
COF ₂ <i>a priori</i> VMR profile	0.8	1.9	5.2	7.0
COF ₂ line parameter uncertainties	27.9	12.9	34.4	15.8
TOTAL	28.7	14.8	39.6	22.8

Table 4.3. Major random and systematic error sources and resulting relative uncertainties (%) affecting COF₂ total and [17-30] km partial columns derived from InSb and MCT spectral ranges. For both domains, these values have been obtained by using the multi-microwindow multi-spectrum approach running with a representative subset of the whole FTIR database analyzed in this study (see text for details).

Considering the very weak absorptions of COF₂ in our selected microwindows, the precision obtained for carbonyl fluoride column values with the multi-spectrum approach is very good: for comparison, the retrieval approach used by Mélen *et al.* (1998) reported a total random error of 23% in the COF₂ total columns. The situation is not so good for systematic errors: the high error values observed are mainly due to large uncertainties of up to 30% in the COF₂ lines intensities in the InSb range. Mélen *et al.* (1998) reports a total systematic error affecting their COF₂ total column of 18%, with a spectroscopic uncertainty of only 10%. However, this value seems a rather optimistic, since no major updates for COF₂ lines intensities (and their corresponding uncertainties) in the ν_1 band have occurred between the 1996 and 2004 versions of HITRAN line list (see also the end of the next section). Finally, for each random or systematic error source discussed, corresponding vertical distributions are very similar in both spectral domains, with peak values always observed within the FTIR sensitivity range.

4.4. Discussion of line parameters and retrieval approach

We have shown in the previous section that the multi-spectrum retrieval approach is the most sensitive to COF₂ between 17 and 30 km, with the largest fraction of the

retrieved information always coming from the measurement. Using a simple example, we will further demonstrate that this sensitivity is also sufficient to distinguish between different air mass types, such as polar and midlatitude air masses. The top panel of Figure 4.4 shows the evolution of the polar vortex for the last seven days of January 2005 over Western Europe. The Jungfraujoch station is identified by a white circle on each map. Potential vorticity (PV) maps over Europe used here are provided by the European Center for Medium range Weather Forecasting (ECMWF; see <http://www.ecmwf.int/>). The potential temperature level of these maps (475 K, which corresponds to an altitude of about 20 km) is the level generally used to follow polar air masses. As the edge of the vortex (characterized by higher PV values – see colored legend of PV maps on the right part of Figure 4.4) passes over the Jungfraujoch site on January 27th, enhancement in stratospheric CO₂ VMR is observed in the corresponding carbonyl fluoride profile retrieved from ISSJ spectra by using both sets of microwindows and the multi-spectrum approach (lower panel of Figure 4.4: left: InSb range; right: MCT range).

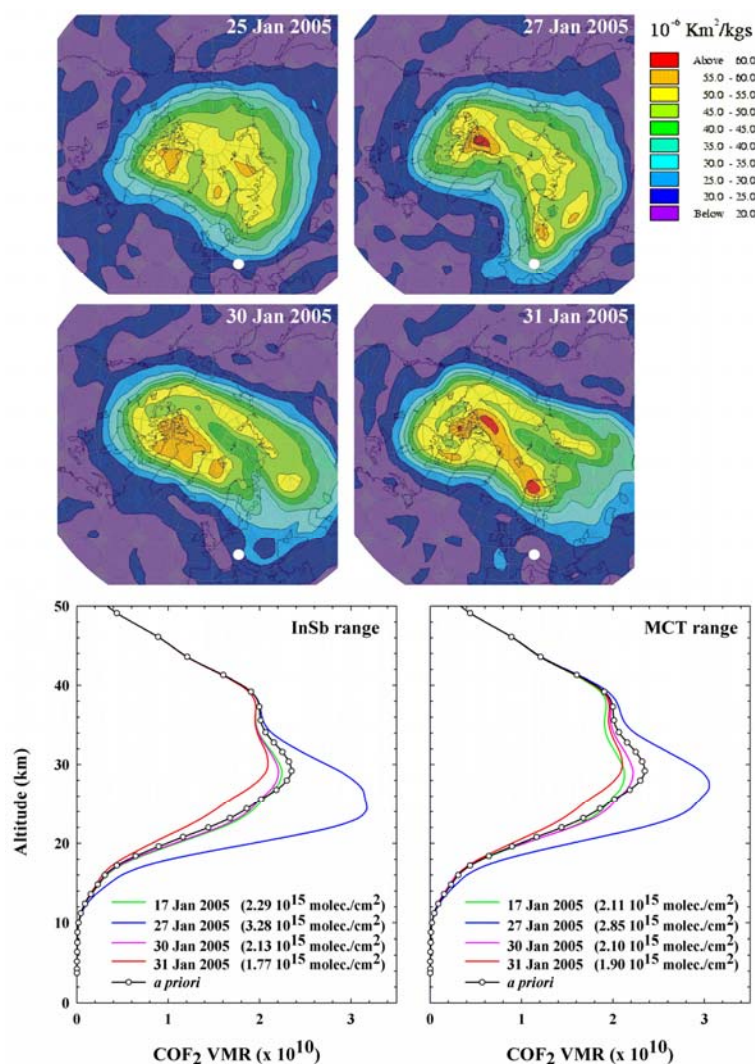


Fig. 4.4. Example of CO₂ vertical profiles derived by applying the multi-spectrum approach to FTIR ground-based observations performed at ISSJ during January 2005 (lower panel). The overpass, above the Jungfraujoch (white circle on ECMWF PV maps at 475 K level on top panel), of the edge of the vortex on January 27th is well captured by the FTIR measurements (low panel: left: CO₂ profiles derived from the InSb set of microwindows; right: CO₂ profiles derived from the MCT set of microwindows).

As these polar airmasses, enriched in fluorine compounds, leave the Jungfraujoch region, the CO₂ VMR decreases to values more in line with typical values observed during this period of the year (for each daily CO₂ VMR profile presented on Figure 4.4, corresponding 17-30 km partial column is also noted in the legend). Information content obtained from the multi-spectrum approach is sufficient to catch such special atmospheric events. We also see from Figure 4.4 that the consistency (e.g. in terms of profile shape) between the CO₂ vertical profiles retrieved from both wavenumber regions is very good.

We have mentioned previously (section 4.1) that a systematic bias of 6% was observed by Mélen *et al.* (1998) between CO₂ total columns independently derived from InSb and MCT regions. However, this bias was not found by Notholt *et al.* (1995). In order to compare the behavior of our time series with these previous results, we have computed the relative differences between CO₂ profiles retrieved from InSb and MCT microwindows for the 215 common measurement days in each time series over the period studied. The result corresponding to the sensitivity range (from 17 to 30 km) is plotted in red in frame (A) of Figure 4.5. Error bars correspond to a 1- σ standard deviation on the mean. Throughout the entire altitude range, we do not find any significant bias between the two data sets. In the sensitivity range, the relative mean difference has a maximum of around 12% in the lower stratosphere.

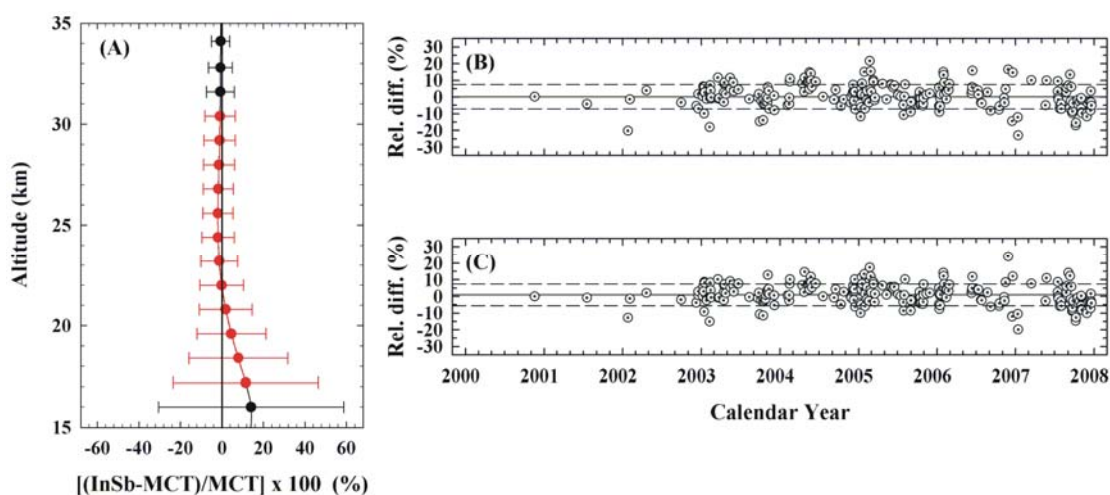


Fig. 4.5. Frame (A): relative mean differences (calculated as $[(\text{InSb-MCT})/\text{MCT}] \times 100$) between CO₂ vertical profiles retrieved from InSb and MCT spectral ranges using simultaneously a multi-microwindow and a multi-spectrum approach. The sensitivity range of the retrievals is plotted in red. Error bars indicate 1- σ standard deviation around the mean; frame (B): relative mean differences between CO₂ [17-30] km partial columns derived from both spectral ranges for the 215 common measurement days of the January 2000 – December 2007 time period; frame (C): relative mean differences between CO₂ total columns derived from both spectral ranges for the 215 common measurement days of the January 2000 – December 2007 time period. In frames (B) and (C), solid and dashed lines represent the mean value and 1 σ standard deviation around the mean, respectively.

A similar agreement is found when comparing total and partial columns derived from both spectral ranges for the same set of all common days between January 2000 and December 2007. Relative mean differences computed as $[(\text{InSb-MCT})/\text{MCT}] \times 100$ for CO₂ 17-30 km partial columns (see frame (B) of Figure 4.5) and for CO₂ total columns (see frame (C) of Figure 4.5) are $0.3 \pm 7.3\%$ and $1.0 \pm 6.5\%$, respectively. In frames (B) and (C) of Figure 4.5, the solid and dotted lines represent the mean value and 1- σ standard deviation on the mean, respectively. For the time period studied

here, no significant bias has thus been observed between the COF₂ total columns derived from the InSb (ν_1) and the MCT (ν_4) bands, in agreement with Notholt *et al.* (1995), but contrary to Mélen *et al.* (1999). The COF₂ spectroscopic parameters used by Mélen *et al.* (1999) were from the 1996 version of the HITRAN line list (Rothman *et al.*, 1998). In the present study, we have used the HITRAN 2004 edition, as mentioned in section 4.2.

Table 4.4 compares the number of COF₂ lines available in the 1996 and 2004 versions of HITRAN, in the wavenumber limits of each set of microwindow used for our retrievals. The last column provides relative mean differences and 1- σ standard deviations observed for the COF₂ lines intensities, calculated as [(HIT04-HIT96)/HIT96]*100 (%). The number N of lines common to both compilations and used to compute relative mean differences is given in parentheses.

Microwindow limits (cm ⁻¹)	# COF ₂ lines (HIT-1996)	# COF ₂ lines (HIT-2004)	Intensity relative differences (N)
InSb range			
1936.15 – 1936.34	52	80	2.80±0.02 (52)
1951.89 – 1952.05	23	42	2.80±0.02 (23)
1952.62 – 1952.78	23	42	2.80±0.02 (23)
MCT range			
1230.75 – 1231.20	136	136	0.00±0.00 (136)
1233.90 – 1234.20	96	96	0.00±0.00 (96)
1234.35 – 1234.63	86	86	0.00±0.00 (86)

Table 4.4. Number of COF₂ lines in each InSb and MCT microwindow, as listed in the HITRAN 1996 (second column) and HITRAN 2004 (third column) spectroscopic line lists. The 2004 version has been used in this study while the work by Mélen *et al.* (1999) was based on the 1996 compilation. The last column provides mean relative differences and 1- σ standard deviations observed on the line intensities (calculated as [(HIT04-HIT96)/HIT96]*100). The number N of lines common to both compilations and used to compute relative mean differences is given in parentheses. No updates have been observed for COF₂ lines located in the MCT range.

For the InSb region, line width parameters for COF₂ are the same in the 1996 and 2004 versions of HITRAN. However, a major update occurred with the number of COF₂ lines increasing by almost a factor 2. Corresponding line intensities have also been revised by almost 3%. For all microwindows in the MCT range, the 1996 and 2004 versions of HITRAN are identical. However, these spectroscopic differences are not sufficient to completely explain the 6% bias observed by Mélen *et al.* (1999) between COF₂ total columns derived from the ν_1 and the ν_4 bands. For one year of observations at ISSJ (namely, 2005 for which the available number of suitable spectra is a maximum), we have compared COF₂ columns retrieved by using the two spectroscopic parameters sets: the change in spectroscopic parameters causes mean differences of only $1.4 \pm 3.0\%$ for COF₂ total columns, and of only $0.9 \pm 4.1\%$ for COF₂ 17-30 km partial columns. We may thus suppose that, in addition to the spectroscopic updates (for COF₂ and interfering gas lines in our microwindows), it is the retrieval procedure and the use of different input parameters (*i.e.*, *a priori* COF₂ VMR profile and the sets and limits of microwindows selected for the retrievals) that is responsible of the better agreement between COF₂ abundances retrieved in the two spectral ranges.

4.5. Comparisons with model data

Our daily mean FTIR COF₂ 17-30 km partial columns have also been confronted with daily values specifically computed for the Jungfraujoch location using the KASIMA (Karlsruhe Simulation model of the Middle Atmosphere) and SLIMCAT models. The KASIMA model used in this study is a global circulation model including stratospheric chemistry for the simulation of the behavior of physical and chemical processes in the middle atmosphere (Reddmann *et al.*, 2001; Ruhnke *et al.*, 1999). The meteorological component is based on a spectral architecture with the pressure

altitude $z = -H \ln\left(\frac{p}{p_0}\right)$ as vertical coordinate where $H = 7$ km is a constant

atmospheric scale height, p is the pressure, and $p_0 = 1013.25$ hPa is a constant reference pressure. A horizontal resolution of T21 (about 5.6×5.6 degrees) has been used. In the vertical regime, 63 levels between 10 and 120 km pressure altitude and a 0.75 km spacing from 10 up to 22 km with an exponential increase above were used. The meteorology module of the KASIMA model consists of three versions: the diagnostic model, the prognostic model and the nudged model which combines the prognostic and diagnostic model (Kouker *et al.*, 1999). In the version used here, the model is nudged towards the operational ECMWF analyses of temperature, vorticity and divergence between 18 and 48 km pressure altitude. Below 18 km, the meteorology is based on ECMWF analyses without nudging, above 48 km pressure altitude, the prognostic model has been used. The rate constants of the gas phase and heterogeneous reactions are taken from Sander *et al.* (2003). The photolysis rates are calculated online with the fast-j2 scheme of Bian and Prather (2002). The distributions of the chemical species in this model run were initialized on April 30, 1972, with data from a long-term KASIMA run.

The 3-D SLIMCAT CTM uses various data (including meteorological data such as winds and temperature, emission scenario of the source gases, chemistry schemes, etc.) to derive the atmospheric transport and to calculate abundances of tropospheric and stratospheric gases. The first description of SLIMCAT appears in Chipperfield *et al.* (1993). During the last years, the SLIMCAT runs have already been exploited to perform comparisons of fluorine species abundances with satellite and ground-based observations (Chipperfield *et al.*, 1997). More recently, it has also been used to derive long-term trends of atmospheric compounds (Feng *et al.*, 2007). All information concerning the SLIMCAT model version used in this work can be found in Chipperfield (2006) or on the SLIMCAT website (see <http://www.env.leeds.ac.uk/slimcat>).

As we have shown in the previous section that there is no significant difference between InSb and MCT retrieved COF₂ partial columns, the InSb and MCT datasets have been merged to obtain a denser FTIR time series, more appropriate for trend studies and for comparisons with model or experimental datasets. So, between January 2000 and December 2007, there are 475 days available for direct comparisons with daily KASIMA and SLIMCAT simulations. As KASIMA and SLIMCAT models use ECMWF analyses to force their meteorology, their COF₂ VMR profiles have been converted into partial columns using pressure and temperature profiles from ECMWF operational analyses.

Figure 4.6 plots the merged FTIR time series with coincident KASIMA and SLIMCAT data. For the Jungfraujoch time series, error bars reproduce one mean standard deviation; FTIR data points without error bars correspond to days with only one measurement. It clearly appears from Figure 4.6 that a significant perturbation affects the middle of the SLIMCAT time series. This could be explained by the fact that the ECMWF meteorological analyses used by the SLIMCAT model are not an homogeneous set, as ECMWF has changed their vertical resolution several times. These changes cover three time periods, namely January 2000 – December 2001, January 2002 – January 2006 and February 2006 – onwards and cause a decrease in the SLIMCAT CO₂ columns from 2002 to 2006. However, the KASIMA time series is not affected by these changes in ECMWF vertical resolution as the calculation of the vertical velocities is different compared to SLIMCAT and as the ECMWF data are nudged to the KASIMA model environment in order to yield a realistic age of air (Reddmann et al., 2001). Furthermore, although the KASIMA time series seems to be able to reproduce special events (linked for example to particular air mass conditions), one can see in Figure 4.6 that the KASIMA variability is significantly less than in the other two time series.

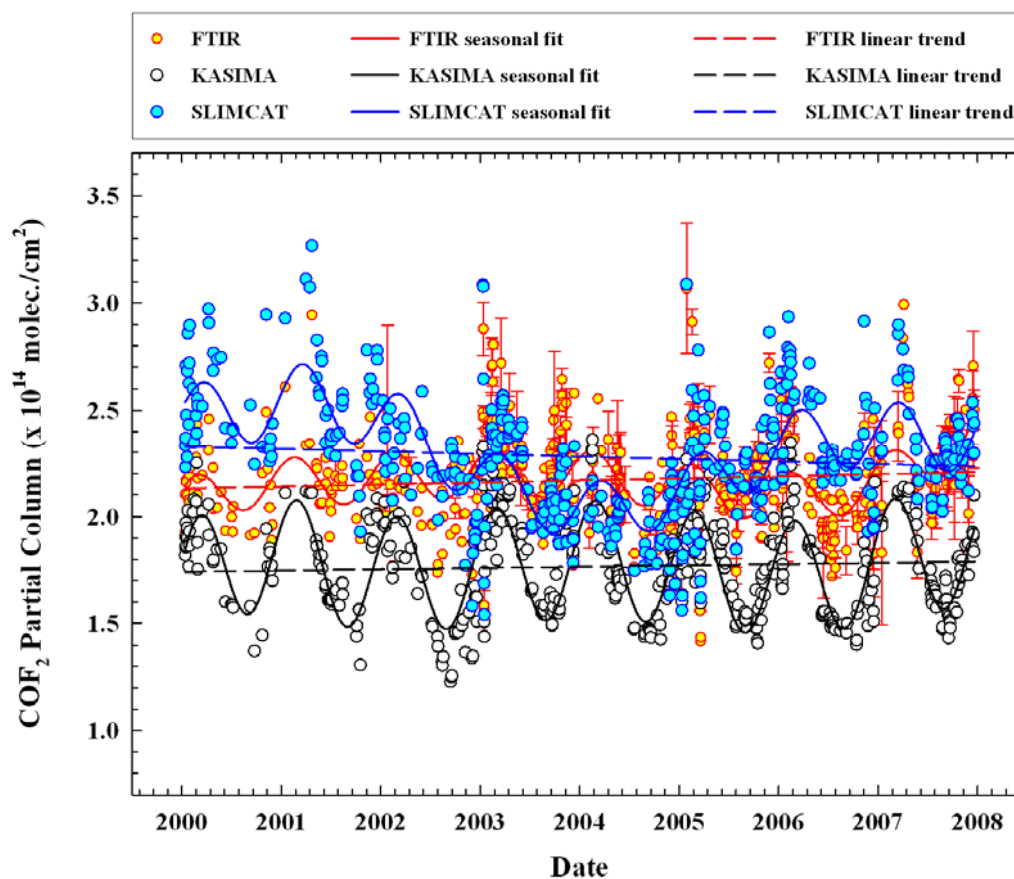


Fig. 4.6. CO₂ 17-30 km partial column time series as observed by the FTIR instrument operated at the Jungfraujoch station (yellow dots) and as computed by the KASIMA and SLIMCAT 3-D CTM models (white and blue dots, respectively). Solid lines reproduce seasonal variations adjusted for each data set while dashed lines correspond to a linear trend for the de-seasonalized time series.

Seasonal variations and trends in each data set have been fitted with a function $C(t)$ that combines a polynomial of degree n $C_n(t)$ and a cosine term, $C_{\cos}(t)$:

$$C_n(t) = c_0 + c_1 (t-t_0) + c_2 (t-t_0)^2 + \dots + c_n (t-t_0)^n \quad (4.1)$$

$$C_{\cos}(t) = A \cos(2\pi (t-t_0)-t_1) \quad (4.2)$$

$$C(t) = C_n(t) [1+C_{\cos}(t)] \quad (4.3)$$

where c_0 is the COF₂ partial column at an arbitrary reference time t_0 (taken as 2000, the beginning of the time period studied). A is the relative amplitude of the seasonal variation and t_1 is the fraction of the calendar year corresponding to the seasonal maximum.

Results of such fits are represented by solid lines in Figure 4.6. For each time series, the best agreements are obtained (on the basis of correlation coefficient values) when using a polynomial function of order 6 in Eq. (4.1). Seasonal variations are well captured in each case. Table 4.5 summarizes the fitted values of the main parameters appearing in Eq. (4.2), that characterize the seasonal variations of each time series. With a value close to 15%, the relative amplitude of the seasonal variation in the KASIMA data set is more than twice the values obtained from the other two time series (5 and 6%, for FTIR and SLIMCAT, respectively). We have compared these values to the one published by Mélen *et al.* (1998). The fitting approach used by Mélen *et al.* (1998) is based on two microwindows located in the ν_1 band and fitted separately during the retrieval procedure. For the 10-year time period (1985-1995) covered in that paper, Mélen *et al.* found a mean amplitude of about 9% for the seasonal cycle, i.e. just in the middle of the amplitude ranges deduced from the present study. For the phase of the seasonal cycle, the FTIR and KASIMA data give COF₂ maximum values between mid- and end of February while the SLIMCAT model predicts maximum values in the second part of March (Table 4.5). From these results, it can be seen that the maximum COF₂ abundances occur during or at the end of winter, when photodissociation process are at their minimum, while the minimum COF₂ concentrations occur in late summer. Mélen *et al.* (1998) have deduced a seasonal maximum value equal to 0.17 (in fractional calendar year units), which corresponds to the 3 March.

Data set	A (%)	t_1	t_1
FTIR	5.30	0.13	16 February
KASIMA	15.42	0.16	27 February
SLIMCAT	6.62	0.21	18 March

Table 4.5. Main seasonal characteristics of the time series fits presented in Figure 4.6. For each data set, second column (A) provides relative amplitude of the seasonal variation while third column (t_1) gives the time (expressed in fractional calendar year units) when the cosine component of each fit reaches its maximum value. This time is converted into calendar days in the last column.

To estimate linear trends (reproduced with dashed lines in Figure 4.6), the seasonal variations of each time series have been removed. Linear trends for the time period 2000-2007 are 3.5 ± 1.8 % and 2.7 ± 1.5 % for the FTIR and KASIMA time series, respectively. This corresponds to linear COF₂ increases of 0.4 ± 0.2 %/year and 0.3 ± 0.2 %/year, for FTIR and KASIMA data sets, respectively. A negative trend of

$-4.0 \pm 1.9 \%$ (or $-0.5 \pm 0.2 \%$ /year) is found from the SLIMCAT time series. This is probably a consequence of the discontinuity in the meteorological data used by the SLIMCAT model, as already described above.

Linear COF₂ trends deduced from the present study are considerably lower than the value found by Mélen *et al.* (1998) 10 years ago, who observed an average COF₂ linear trend equal to $4.0 \pm 0.5 \%$ /year for the 1985-1995 time period. This slowing down of this COF₂ linear trend, between 1985-1995 and 2000-2007, results from the phase out of its principal source gases (CFC-12 and CFC-113). Figure 1-1 of the WMO report (2007) shows the trends for these two species during the 1980-2005 time period. Data reproduced in that Figure are those provided by the Advanced Global Atmospheric Gases Experiment (AGAGE) network (Prinn *et al.*, 2000), as well as by the National Oceanic and Atmospheric Administration/Earth System Research Laboratory (NOAA/ESRL – Montzka *et al.*, 1999; Thompson *et al.*, 2004) and the University of California at Irvine (UCI – D.R. Blake *et al.*, 1996; N.J. Blake *et al.*, 2001). A small but obvious decrease in the abundance of CFC-113 is observed since the middle of the nineties, and the rate of growth of CFC-12 has slowed down since the end of the nineties. Table 1-2 of WMO (2007) also reports a grow rate of the CFC-113 mole fraction (expressed in ppt) of around -1.1% /year, for the 2003-2004 time period; the corresponding values published for CFC-12 are inconsistent: while AGAGE measurements give a slight decrease of 0.1% /year, an increase of 0.3% /year results from UCI analysis. No trend is observed from NOAA data. In addition, the annual changes in the CFC-12 vertical abundance above central Europe and from 1987 to 2005 can be also found in Zander *et al.* (2005); these authors report a decrease of 0.16% /year in the CFC-12 vertical total column (in molec./cm²) for the 2003-2004 time period. Whatever the CFC-12 trend value, a stabilization of the CFC-12 mole fraction at around 540 ppt between 2003 and 2005 is clearly visible in Figure 1-1 of WMO (2007). Until now, the decrease or the stabilization observed for these two major fluorine-containing source gases (CFC-12 and CFC-113) has only been partially compensated for by increases in CFC substitutes (such as HCFC-22 and HFC-134a), so that a slowdown of the increase in total inorganic fluorine F_y is observed (Figure 1-19 of WMO, 2007). Decreases observed in the COF₂ rates derived from FTIR and KASIMA time series presented in this study are a direct consequence of these changes.

While FTIR and SLIMCAT data sets do not show significant relative differences (mean relative difference computed over 17-30 km partial columns as $[(\text{FTIR}-\text{SLIMCAT})/\text{SLIMCAT}] \times 100$ is $-3.5 \pm 10.6\%$), it is obvious from Figure 4.6 that a large bias (around 25%) exists between the FTIR and KASIMA. Two main possibilities could explain this KASIMA underestimation. The first one is that KASIMA uses the wrong COF₂ VMR values at its lowest altitude level (i.e. 7 km). This could cause biased COF₂ abundances in the upper troposphere / lower stratosphere (UTLS). The second possibility is that the KASIMA partitioning between fluorine species (i.e. HF, COF₂ and COCIF) could be erroneous. As we have shown previously (section 4.3) that FTIR retrievals have no sensitivity to COF₂ below 17km, it is not possible to directly compare FTIR and KASIMA COF₂ UTLS partial columns, to check the validity of the first hypothesis. However, as previous comparisons have demonstrated the good agreement between FTIR and KASIMA abundances for HF (Ruhnke *et al.*, 2007), we thus have compared COCIF partial columns computed by the KASIMA model with ACE-FTS satellite data in order to

check on the validity of the second hypothesis (Figure 4.7). Satellite data are well suited for this exercise (Rinsland *et al.*, 2007; Fu *et al.*, 2008) as water vapor interferences make the detection of COCIF from FTIR ground-based spectra difficult. Only ACE-FTS occultations located in the 40-50°N latitude band have been compared with KASIMA data, which represents a set of 64 coincident points. Partial column limits (15-25 km) used are representative of the altitude range where the ACE-FTS instrument is able to record COCIF vertical profiles. The top panel of Figure 4.7 plots relative differences for the two time series. The mean relative difference value ($6.9 \pm 15.2\%$) indicates that there is no significant bias between the data sets and thus suggests that the second hypothesis mentioned above should be rejected. Moreover, very recent redesign of the KASIMA chemistry module has indicated that the lower boundary value of COF₂ within the troposphere indeed significantly affects KASIMA COF₂ total columns. For the 64 coincident days evoked above, corresponding COCIF partial columns computed by the SLIMCAT model are also reproduced on Figure 4.7 (light blue dots). As for the KASIMA time series, no significant bias with respect to the ACE-FTS data is observed, confirming the good agreement existing for COCIF between model calculations and satellite measurements.

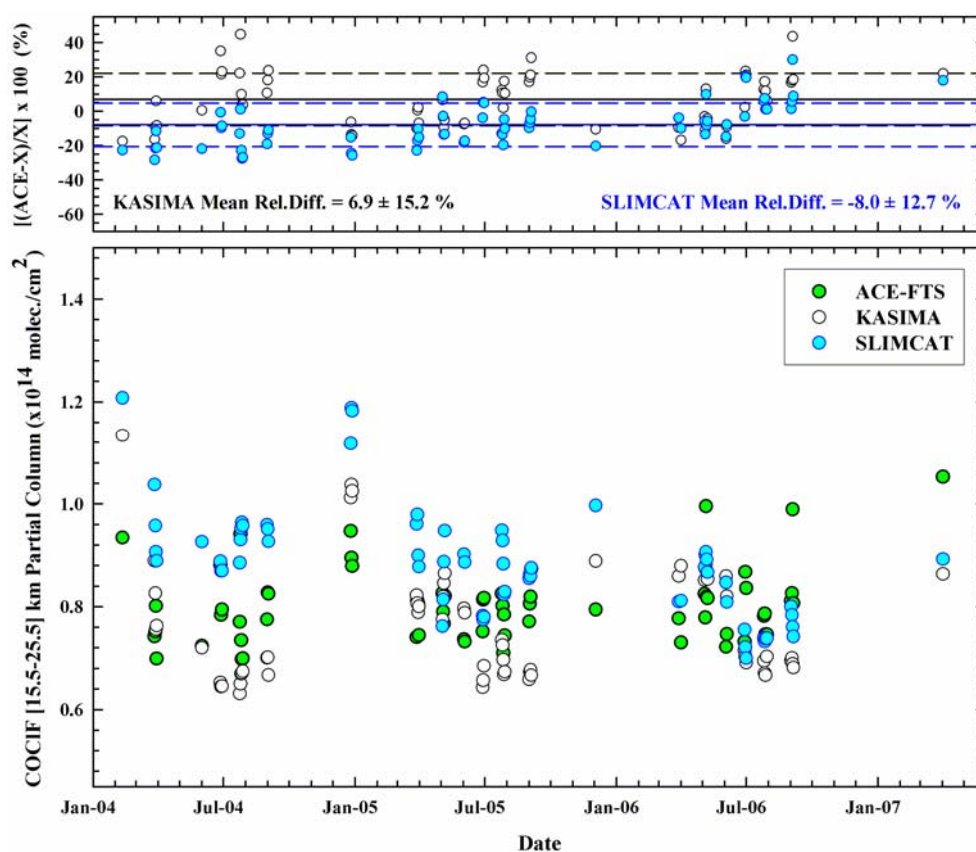


Fig. 4.7. COCIF [15.5-25.5] km partial columns time series as observed by the ACE-FTS space instrument (green dots) and as computed by the KASIMA and SLIMCAT 3-D CTM models (white and light blue dots, respectively). Top panel reproduces relative differences between ACE-FTS data and model data (solid line: mean relative difference; dotted lines: 1σ standard deviation on the mean).

4.6. Conclusions and perspectives

This paper describes the advantages of using a new approach to invert CO₂ vertical distributions from ground-based FTIR solar spectra. The idea is to combine data from several spectral microwindows and all available spectra, recorded at the same resolution during the same day, in the retrievals in order to increase the information content. We have selected two sets of three microwindows, located either in the ν_1 or in the ν_4 CO₂ absorption bands, and have demonstrated that there is a gain in information content in this multi-microwindows multi-spectrum fitting strategy. In each case, a significant improvement in DOFS and first eigenvalues is obtained, allowing us to derive one CO₂ partial column between 17 and 30 km. Mean DOFS values computed for the January 2000 – December 2007 time period are 1.23 ± 0.17 and 1.16 ± 0.30 for InSb (2-5.5 μm) and MCT (7-14 μm) regions, respectively. In all cases, the largest fraction of the information comes from the measurement rather than the *a priori*. We have also shown that the information content in the multi-spectrum approach is sufficient to observe special atmospheric events, such as polar vortex overpasses. In the ν_4 region, total random errors affecting CO₂ 17-30 km partial columns and CO₂ total columns are close to 12% and 8%, respectively. In the ν_1 region, the corresponding values are 15% and 12%. For both spectral ranges, the highest systematic total errors have been observed (ranging from 15% to 40%), mainly due to high uncertainties characterizing CO₂ lines intensities reported in the HITRAN 2004 database. Comparisons of CO₂ vertical profiles retrieved between 17 and 30 km as well as corresponding partial columns derived from both spectral ranges do not show any significant bias. The same conclusion can be made for total columns. This latter result is in agreement with results from Notholt *et al.* (1995) but is not consistent with the systematic 6% mean bias observed between CO₂ total columns derived from the ν_1 and the ν_4 absorption bands by Mélen *et al.* (1999). This difference in behavior between our results and those obtained by Mélen *et al.* (1999) cannot be attributed totally to the difference in spectroscopic parameters used for the retrievals. It seems that a different choice of input parameters and the multi-microwindow multi-spectrum procedure leads to a better agreement between CO₂ columns derived from the ν_1 and the ν_4 absorption bands.

Comparisons of the merged FTIR data set (i.e. obtained by averaging CO₂ data coming from ν_1 and ν_4 bands) with CO₂ 17-30 km partial columns generated by the KASIMA and SLIMCAT 3-D CTMs has also been presented. We did not notice any significant bias between the FTIR and SLIMCAT time series. However, a significant bias of about 25% has been observed between the FTIR and KASIMA data sets, with KASIMA giving lower CO₂ 17-30 km partial columns. It seems that this bias could be attributed to incorrect lower boundary conditions used in the KASIMA model. Linear trends over the 2000-2007 time period as well as the main seasonal variation parameters have also been derived for each time series. Except for the SLIMCAT time series, very low CO₂ growth rates have been derived from FTIR and KASIMA time series (0.4 ± 0.2 %/year and 0.3 ± 0.2 %/year, respectively). A negative trend (-0.5 ± 0.0 %/year) has been obtained from the SLIMCAT data set. However, this is probably due to discontinuities in the ECMWF data, which significantly decreases CO₂ SLIMCAT columns from 2002 to 2006. Decreases in the CO₂ growth rate can be mainly attributed to the stabilization of the CFC-12 tropospheric concentration and to the recent decrease observed in the CFC-113 atmospheric abundance.

Finally, the three time series all display the CO₂ seasonal cycle. The relative amplitudes range from 5 to 15%, with a seasonal maximum between mid-February and the end of March. These seasonal cycle results agree quite reasonably with the previous study by Mélen *et al.* (1998). However, it should be kept in mind that the time periods under investigations are not the same. In the future, it would be interesting to use the multi-microwindow multi-spectrum approach at other ground-based FTIR stations. This will serve to demonstrate the effectiveness of this fitting procedure and to increase the coverage of ground-based CO₂ measurements. This could be used to extend this study of CO₂ seasonal and latitudinal variability as well as the long-term trend at different sites. In addition, the use of a multi-microwindow multi-spectrum fitting procedure could increase the vertical information content for other atmospheric gases that have weak signatures in FTIR solar spectra.

Acknowledgements

We would like to thank the International Foundation High Altitude Research Stations Jungfrauoch and Gornergrat (HFSJG, Bern) and the University of Liège for supporting the facilities needed to perform the observations and their analyses. University of Liège work is supported primarily by the Belgian Federal Science Policy Office. Financial support by projects Prodex-ACE and SECPEA as well as GEOMON is further acknowledged. Thanks are also extended to all collaborators having contributed to the observations at the Jungfrauoch. The Atmospheric Chemistry Experiment (ACE), also known as SCISAT, is a Canadian-led mission mainly supported by the Canadian Space Agency and the Natural Sciences and Engineering Research Council of Canada. The authors also thank the ECMWF for providing the PV maps used in this work.

References

- Bernath, P. F., et al.: Atmospheric Chemistry Experiment (ACE): mission overview, *Geophys. Res. Lett.*, 32, doi: 10.1029//2005GL022386, 2005.
Also available at <http://orbi.ulg.ac.be/handle/2268/2388>
- Bian, H., and Prather, M. J.: Fast-J2: Accurate simulation of stratospheric photolysis in global chemical models, *J. Atmos. Chem.*, 41, 281-296, 2002.
- Blake, D. R., Chen, T.-Y., Smith, Jr., T. W., Wang, C. J.-L., Wingenter, O. W., Blake, N. J., Rowland, F. S., and Mayer, E. W.: Three-dimensional distribution of non-methane hydrocarbons and halocarbons over the northwest Pacific during the 1991 Pacific Exploratory Mission (PEM-West A), *J. Geophys. Res.*, 101, 1763-1778, 1996.
- Blake, N. J., Blake, D. R., Simpson, I. J., Lopez, J. P., Johnston, N. A. C., Swanson, A. L., Katzenstein, A. S., Meinardi, S., Sive, B. C., Colman, J. J., Atlas, E., Flocke, F., Vay, S. A., Avery, M. A., and Rowland, F. S.: Large-scale latitudinal and vertical distributions of NMHCs and selected halocarbons in the troposphere over the Pacific Ocean during the March-April 1999 Pacific Exploratory Mission (PEM-Tropics B), *J. Geophys. Res.*, 106, 32 627-32 644, 2001.
- Ceccherini, S.: Analytical determination of the regularization parameter in the retrieval of atmospheric vertical profiles, *Opt. Lett.*, 30, 2554-2556, 2005.

Connor, B. J., Parrish, A., Tsou, J.-J., and McCormick, P.: Error analysis of the ground-based microwave ozone measurements during STOIC, *J. Geophys. Res.*, 100, 9283-9291, 1995.

Chipperfield, M. P., Cariolle, D., Simon, P., Ramaroson, R., and Lary, D. J.: A 3-dimensional modeling study of trace species in the Arctic lower stratosphere during winter 1989-1990, *J. Geophys. Res.*, 98, 7199-7218, 1993.

Chipperfield, M. P., Burton, M., Bell, W., Paton Walsh, C., Blumenstock, T., Coffey, M. T., Hannigan, J. W., Mankin, W. G., Galle, B., Mellqvist, J., Mahieu, E., Zander, R., Notholt, J., Sen B., and Toon, G. C.: On the use of HF as a reference for the comparison of stratospheric observations and models, *J. Geophys. Res.*, 102, 12901-12919, 1997.

Also available at <http://orbi.ulg.ac.be/handle/2268/14547>

Chipperfield, M. P.: New version of the TOMCAT/SLIMCAT off-line Chemical Transport Model: intercomparison of stratospheric tracer experiments, *Q. J. R. Meteorol. Soc.*, 132, 1179-1203, doi:10.1256/qj.05.51, 2006.

Feng, W., Chipperfield, M. P., Dorf, M., Pfeilsticker, K., and Ricaud, P.: Mid-latitude ozone changes: studies with a 3-D CTM forced by ERA-40 analyses, *Atmos. Chem. Phys.*, 7, 2357-2369, 2007.

Fu, D., Boone, C. D., Bernath, P.F., Weisenstein, D. K., Rinsland, C. P., Manney G. L., and Walker, K. A.: First global observations of atmospheric COClF from the Atmospheric Chemistry Experiment mission, submitted to *J. Quant. Spec. and Rad. Transf.*, July 2008.

Hase, F., Blumenstock, T., and Paton-Walsh, C.: Analysis of instrumental line shape of high-resolution FTIR-spectrometers using gas cell measurements and a new retrieval software, *Appl. Opt.*, 3417-3422, 1999.

Kaye, J. A., Douglas, A. R., Jackman, C. H., Stolarski, R. S., Zander R., and Roland, G.: Two-dimensional model calculation of fluorine-containing reservoir species, *J. Geophys. Res.*, 96, 12865-12881, 1991.

Ko, M. K. W., Sze N. D., and Weisenstein, D. K.: The roles of dynamical and chemical processes in determining the stratospheric concentration of ozone in one-dimensional and two-dimensional models, *J. Geophys. Res.*, 94, 9889-9896, 1989.

Kouker, W., Langbein, I., Reddmann T., and Ruhnke, R.: The Karlsruhe Simulation Model of the Middle Atmosphere (KASIMA), Version 2, FZK Report 6278, Forschungszentrum Karlsruhe, Germany, 1999.

Mélen, F., Mahieu, E., Zander, R., Rinsland, C. P., Demoulin, P., Roland, G., Delbouille, L., and Servais, C.: Vertical column abundances of COF₂ above the Jungfraujoch Station, derived from ground-based infrared solar observations, *J. Atmos. Chem.*, 29, 119-134, 1998.

Also available at <http://orbi.ulg.ac.be/handle/2268/14540>

Mélen, F., Mahieu, E., Demoulin, P., Servais, C., and Zander, R.: Vertical column abundances of COF₂ above the Jungfraujoch Station: update and consolidation of the database with measurements in the ν_4 band region, in Proceedings of Atmospheric Spectroscopy Applications 1999, Reims, France, September 1-3 1999, 1999.

Montzka, S. A., Butler, J. H., Elkins, J. W., Thompson, T. M., Clarke, A. D., and Lock, L. T.: Present and future trends in the atmospheric burden of ozone-depleting halogens, *Nature*, 398, 690-694, 1999.

Nassar, R., Bernath, P. F., Boone, C. D., McLeod, S. D., Skelton, R., Walker, K. A., Rinsland, C. P., and Duchatelet, P.: A global inventory of stratospheric fluorine in 2004 on Atmospheric Chemistry Experiment Fourier transform spectrometer (ACE-FTS) measurements, *J. Geophys. Res.*, 111, D22313, doi: 10.1029/2006JD007395, 2006.

Also available at <http://orbi.ulg.ac.be/handle/2268/4285>

Notholt, J., Meier, A., and Peil, S.: Total column densities of tropospheric and stratospheric trace gases in the undisturbed arctic summer atmosphere, *J. Atmos. Chem.*, 20, 311-332, 1995.

Pougatchev, N. S., and Rinsland, C. P.: Spectroscopic study of the seasonal variation of carbon monoxide vertical distribution above Kitt Peak, *J. Geophys. Res.*, 100, 1409-1416, 1995.

Pougatchev, N. S., Connor, B. J., and Rinsland, C. P.: Infrared measurements of the ozone vertical distribution above Kitt Peak, *J. Geophys. Res.*, 100, 16689-16697, 1995.

Prinn, R. G., Weiss, R. F., Fraser, P. J., Simmonds, P. G., Cunnold, D. M., Alyea, F. N., O'Doherty, S., Salameh, P., Miller, B. R., Huang, J., Wang, R. H. J., Hartley, D.E., Harth, C., Steele, L. P., Sturrock, G., Midgley, P. M., and McCulloch, A.: A history of chemically and radiatively important gases in air deduced from ALE/GAGE/AGAGE, *J. Geophys. Res.*, 105, 17 751–17 792, 2000.

Reddmann, T., Ruhnke, R., and Kouker, W.: Three-dimensional model simulations of SF₆ with mesospheric chemistry, *J. Geophys. Res.*, 106, 14 525–14 537, 2001.

Reisinger, A. R., Jones, N. B., Matthews, W. A., and Rinsland, C. P.: Southern hemisphere ground based measurements of carbonyl fluoride (COF₂) and hydrogen fluoride (HF): partitioning between fluoride reservoir species, *Geophys. Res. Lett.*, 21, 797-800, 1994.

Rinsland, C. P., Zander, R., Brown, L. R., Farmer, C. B., Park, J. H., Norton, R. H., Russell, III, J. M., and Raper, O. F.: Detection of carbonyl fluoride in the stratosphere, *Geophys. Res. Lett.*, 13, 769-772, 1986.

Rinsland, C. P., Levine, J. S., Goldman, A., Sze, N. D., Ko, M. K. W., and Johnson, D. W.: Infrared measurements of HF and HCl total column abundances above Kitt Peak, 1997-1990: seasonal cycles, long-term increases and comparisons with model calculations, *J. Geophys. Res.*, 96, 15523-15540, 1991.

Rinsland, C. P., Jones, N. B., Connor, B. J., Logan, J. A., Pougatchev, N. S., Goldman, A., Murcray, F. J., Stephen, T.M., Pine, A. S., Zander, R., Mahieu E., and Demoulin, P.: Northern and southern hemisphere ground-based infrared measurements of tropospheric carbon monoxide and ethane, *J. Geophys. Res.*, 103, 28197-28218, 1998.

Also available at <http://orbi.ulg.ac.be/handle/2268/14545>

Rinsland, C. P., Nassar, R., Boone, C. D., Bernath, P., Chiou, L., Weisenstein, D. K., Mahieu, E., and Zander, R.: Spectroscopic detection of COClF in the tropical and mid-latitude lower stratosphere, *J. Quant. Spec. and Rad. Transf.*, 105, 467-475, 2007.

Also available at <http://orbi.ulg.ac.be/handle/2268/2413>

Rodgers, C. D.: Inverse methods for atmospheric sounding: Theory and Practice, Volume 2 of Series on Atmospheric, Oceanic and Planetary Physics, World Scientific Co. Pte. Ltd., 2000.

Rothman, L. S., Rinsland, C. P., Goldman, A., Massie, S. T., Edwards, D. P., Flaud, J.-M., Perrin, A., Camy-Peyret, C., Dana, V., Mandin, J.-Y., Schroeder, J., McCann, A., Gamache, R. R., Wattson, R. B., Yoshino, K., Chance, K. V., Jucks, K. W., Brown, L. R., Nemtchinov, V., and Varanasi, P.: The HITRAN molecular spectroscopic database and HAWKS (HITRAN Atmospheric Workstation): 1996 edition, *J. Quant. Spec. and Rad. Transf.*, 60, 665-710, 1998.

Rothman, L. S., Jacquemart, D., Barbe, A., Chris Benner, D., Birk, M., Brown, L. R., Carleer, M. R., Chackerian, Jr., C., Chance, K., Coudert, L. H., Dana, V., Devi, V. M., Flaud, J.-M., Gamache, R. R., Goldman, A., Hartmann, J.-M., Jucks, K. W., Maki, A. G., Mandin, J.-Y., Massie, S. T., Orphal, J., Perrin, A., Rinsland, C. P., Smith, M.A.H., Tennyson, J., Tolchenov, R. N., Toth, R. A., Vander Auwera, J., Varanasi, P., and Wagner, G.: The HITRAN 2004 molecular spectroscopic database, *J. Quant. Spec. and Rad. Transf.*, 96, 139-204, 2005.

Ruhnke, R., Kouker W., and Reddman, T.: The influence of the OH + NO₂ + M reaction on the NO_y partitioning in the late arctic winter 1992/1993 as studied with KASIMA, *J. Geophys. Res.*, 104, 3755–3772, 1999.

Ruhnke, R., Blumenstock, T., Duchatelet, P., Hamann, K., Hase, F., Kouker, W., Kramer, I., Mahieu, E., Mikuteit, S., Notholt, J., Reddman, T., Schneider, M., Sinnhuber, B.-M., Sussmann, R., Velazco, V., Warneke, T., and Wiehle, M.: Measured and modeled trends of stratospheric Cl_y and F_y column amounts in the northern hemisphere, *Geophysical Research Abstracts* 9, 07597, 2007.

Also available at <http://orbi.ulg.ac.be/handle/2268/4659>

Sander, S. P., Friedl, R. R., Ravishankara, A. R., Golden, D. M., Kolb, C. E., Kurylo, M. J., Huie, R. E., Orkin, V. L., Molina, M. J., Moortgat, G. K., and Finlayson-Pitts, B. J.: Chemical kinetics and photochemical data for use in atmospheric studies, Evaluation Number 14, JPL Publication 02-25, February 2003.

Sen, B., Toon, G. C., Blavier, J. -F., Fleming, E. L., and Jackman, C. H.: Balloon-borne observations of midlatitude fluorine abundance, *J. Geophys. Res.*, 101, 9045-9054, 1996.

Steck, T.: Methods for determining regularization for atmospheric retrieval problems, *Appl. Opt.*, 41, 1788-1797, 2002.

Thompson, T. M. (Ed.), Butler, J. H., Daube, B. C., Dutton, G. S., Elkins, J. W., Hall, B. D., Hurst, D. F., King, D. B., Kline, E. S., LaFleur, B. G., Lind, J., Lovitz, S., Mondeel, D. J., Montzka, S. A., Moore, F. L., Nance, J. D., Neu, J. L., Romashkin, P. A., Scheffer, A., and Snible, W. J.: Halocarbons and other atmospheric trace species, Section 5 in *Climate Monitoring and Diagnostics Laboratory: Summary Report No. 27, 2002-2003*, edited by R. Schnell, A.-M. Buggle and R. Rosson, 115-135, NOAA/Climate Monitoring and Diagnostics Laboratory, Boulder, Colo., 2004.

Walker, K. A., Cooper, M. D., Weigum, N., et al.: Global zonal mean distribution of carbonyl fluoride (COF₂), in preparation.

Wilson, S. R., Schuster, G., and Helas, G.: Measurements of COFCl and CCl₂O near the tropopause, in R.D. Bojkov and P. Fabian (eds), *Ozone in the Atmosphere*, A. Deepak Publisher, 302-305, 1989.

WMO Report No. 50: *Scientific Assessment of Ozone Depletion: 2006*, World Meteorological Organization, P.O. Box 2300, Geneva 2, CH 1211, Switzerland, 2007.

Zander, R., Rinsland, C. P., Mahieu, E., Gunson, M. R., Farmer, C. B., Abrams, M. C., and Ko, M. K. W.: Increase of carbonyl fluoride (COF₂) in the stratosphere and its contribution to the 1992 budget of inorganic fluorine in the upper stratosphere, *J. Geophys. Res.*, 99, 16737-16743, 1994.

Also available at <http://orbi.ulg.ac.be/handle/2268/14537>

Zander, R., Mahieu, E., Demoulin, P., Duchatelet, P., Servais, C., Roland, G., Delbouille, L., De Mazière, M., and Rinsland, C.P.: Evolution of a dozen non-CO₂ greenhouse gases above Central Europe since the mid-1980s, *Environmental Sciences* 2 (2-3), 295-303, June-September 2005.

Also available at <http://orbi.ulg.ac.be/handle/2268/2527>

Chapter 5

The inorganic fluorine budget above Jungfraujoch

As seen in Chapter 1, fluorine enters the stratosphere essentially in the form of the manmade CFCs (principally CFC-12 and CFC-11), HCFCs (mainly HCFC-22) and HFCs (mainly HFC-134a) which have been (or are still) widely emitted at surface level. We have further recalled that in the lower stratosphere, the photolysis of these halogenated source gases leads to the formation of the two temporary fluorine reservoirs COClF and COF₂, whose photolysis ultimately forms the extremely stable HF gas.

Despite the fact that fluorine does not directly participate in ozone destruction (see Chapter 1), there however exists several reasons to make an exhaustive inventory of atmospheric fluorine. Among the most important ones, one can cite: (1) the possibility to indirectly check the magnitude of CFCs, HCFCs and HFCs anthropogenic emissions from the surface and to compare them with emission inventories, (2) the necessity to assess the efficiency of important phase out calendars or emissions regulation schemes adopted by the Montreal and the Kyoto Protocols, that altogether control the consumptions or emissions of CFCs and of their substitute products, and (3) the opportunity to perform a supplemental check (proxy verification) of the build up of inorganic chlorinated and brominated compounds in the atmosphere (which are both contributors to stratospheric ozone losses), since most of halogenated source gases often contains fluorine and chlorine atoms in combination as well as bromine atoms in the case of halons. In addition, long-term monitoring of the fluorine budget informs on the partitioning between fluorine-containing reservoirs in the stratosphere, to verify its possible evolution with time in response to international Protocols.

The main objective of this Chapter is to produce a time series of the inorganic fluorine burden over the last twenty-five years, based essentially on HF and COF₂ datasets derived from long-term FTIR measurements at Jungfraujoch. A trend analysis of our time series is also performed and discussed in the context of past and current emissions of halogenated source gases. Comparisons with model and space data are also included.

All original results presented in this Chapter will be part of a scientific publication, once the hypotheses evoked in the last section will have been checked with the help of numerical simulations.

5.1. Overview of previous fluorine inventories

In this work, we define the total inorganic fluorine (F_y), the total organic fluorine (CF_y) and the total fluorine (F_{TOT}) burdens as follow:

$$F_y = [HF] + 2 \times [COF_2] + [COCIF] \quad (5.1)$$

$$CF_y = 2 \times [CCl_2F_2] + [CCl_3F] + 3 \times [CCl_2FCClF_2] + 2 \times [CHClF_2] \\ + \text{minor species} \quad (5.2)$$

$$F_{TOT} = F_y + CF_y + 6 \times [SF_6] \quad (5.3)$$

where the brackets designate the VMR (or the vertical abundance) of a given species and where each fluorine species is weighted by the number of its fluorine atoms. Due to its high chemical inertness in the stratosphere, sulfur hexafluoride (SF_6) essentially diffuses to the mesosphere and is generally not included in inorganic fluorine inventories, but rather in the total fluorine budget where it accounts for around 6 to 7 pptv [Krieg et al., 2005; Mahieu et al., 2010, 2011]. In the next sections, we will focus on the long-term evolution of the inorganic component of the atmospheric fluorine burden F_y , as defined in Eq. (5.1).

Space measurements are particularly well suited to establish fluorine inventories, as most of fluorinated sources and reservoirs are in general detectable by space instrumentation on a global scale. In that context, the occultation measurements of seven fluorine species (namely, HF, COF_2 , CF_4 , SF_6 , CFC-11, CFC-12 and HCFC-22) during the 1985 Atmospheric Trace Molecule Spectroscopy (ATMOS) space flight were exploited by Zander et al. [1992] to establish the first stratospheric fluorine budget at northern mid-latitudes. Comparison of ATMOS 1985 and 1992 measurements by Zander et al. [1994] has also allowed to assess the change in the F_y budget, controlled predominantly by anthropogenic source gases emissions from the surface. In parallel, experiments using balloon-borne instrumentation have also been exploited to provide information concerning major fluorinated sources and reservoirs (e.g. Sen et al., 1996). An interesting aspect of this work lies in the fact that, contrary to the above mentioned measurements of fluorinated gases from space, all of the eight gases included in this fluorine inventory (that altogether represent at least 94% of total atmospheric fluorine) have been simultaneously recorded in the same spectrum, reducing the uncertainties which arise when the different gases are successively measured with a suite of optical filters, at different locations.

Furthermore, HF data gathered, since the early nineties, by the Halogen Occultation Experiment (HALOE) space instrument at 55km were used as a proxy for F_{TOT} and compared to United Nations Environment Programme (UNEP) emission inventories and to other non-space experimental datasets in order to estimate the transport time necessary to tropospheric fluorine source gases to reach the stratosphere [Anderson et al., 2000]. In addition, HALOE HF measurements for several latitude bands (from 70°S to 70°N, in 10° increments) were also used to produce a near-globally total F_y time series which have been compared to UNEP emission scenarios, providing the opportunity to verify the impact of the Montreal Protocol and its subsequent Amendments and Adjustments [Anderson et al., 2000].

Since the end of operation of the ATMOS and HALOE instruments in 1994 and 2004, respectively, the Atmospheric Chemistry Experiment Fourier Transform Spectrometer (ACE-FTS) instrument, launched in August 2003 aboard the Canadian SCISAT satellite [Bernath et al., 2005], is the only instrument in orbit that currently monitors, on a global scale, most of the major fluorine source and reservoir species, including some replacements products which are now measurable from space (e.g. HFC-134a, HCFC-142b; see Nassar et al., 2006 and Dufour et al., 2005). Based on ACE-FTS v2.2 measurements recorded between February 2004 and January 2005, Nassar et al. [2006] have updated and described an inventory of global stratospheric fluorine including both CF_y and F_y species in five latitude zones (Figure 5.1).

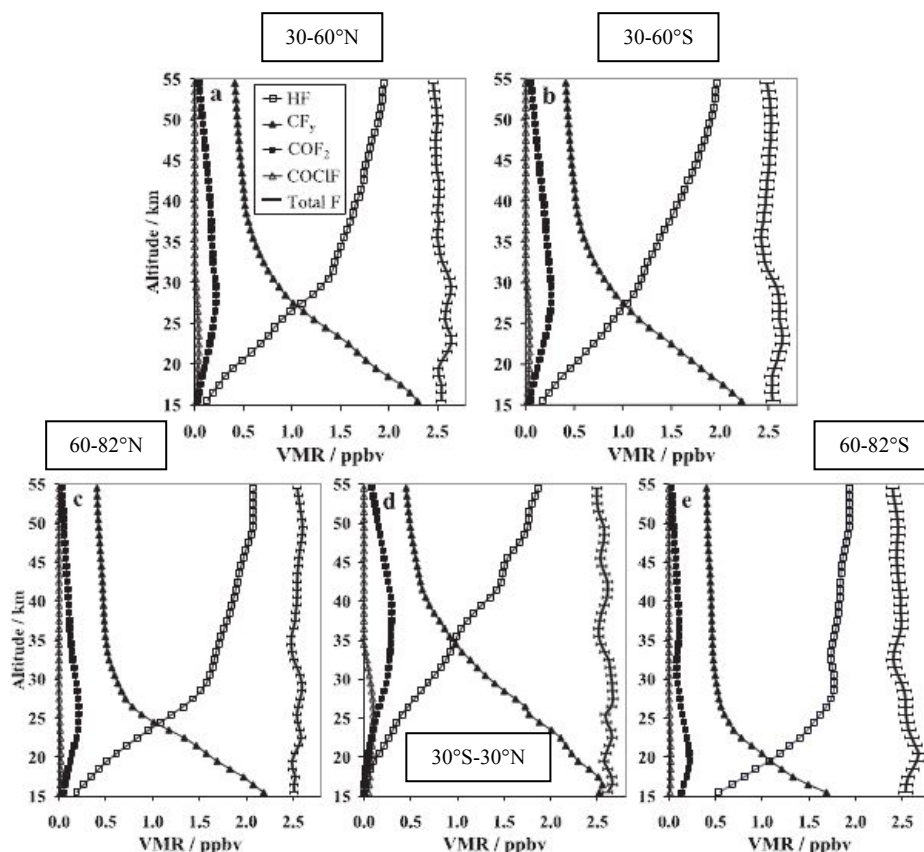


Fig. 5.1. Stratospheric fluorine inventories for the year 2004, derived from ACE-FTS space measurements in five different latitude belts. The error bars on the F_{TOT} profiles represent the 1- σ variability. From Nassar et al., 2006.

Figure 5.1 shows that while CF_y obviously dominates in the lower stratosphere, as the VMRs of halogenated source gases still present high values in this region of the atmosphere (see Figure 1.8), HF dominates the middle-upper stratosphere. The altitude at which the two corresponding curves cross is linked to the tropopause height, which decreases from the tropics towards the poles and which partially governs the shape of the vertical profiles of these fluorinated gases (see section 1.1.3). In all latitude zones under investigation by Nassar et al. [2006], stratospheric total fluorine nearly forms a straight line, indicating that the most significant species have been included in these fluorine budget evaluations. Small deviations from a perfect straight line may principally result from atmospheric variability, uncertainties the ACE-FTS data or from minor fluorine species that have not been included in the inventory (e.g. the short-lived gases COHF and CF_3OH).

For northern mid-latitudes, Nassar et al. [2006] computed, between 17.5 and 50.5 km, a mean total fluorine burden close to 2.55 ppbv. On basis of the corresponding F_{TOT} profiles provided in Table 3 of Nassar et al. [2006] and on basis of panel (a) of Figure 5.1, we have estimated that, at northern mid-latitudes, HF contributes to 70 to 90% of the total F_y burden between 30 and 50 km. Nassar et al. [2006] additionally mention that at 55 km almost all the inorganic fluorine F_y (around 98%) is present on the form of HF, with a contribution of 1.96 ppbv to an inorganic burden that equal 2 ppbv. This latter result is however around 10% higher than that based on HF HALOE measurements in 2004 [Anderson and Russell, 2004], but is commensurate with first comparisons between HALOE and ACE-FTS [McHugh et al., 2005]. Such a bias between HALOE and ACE-FTS was later confirmed by Mahieu et al. [2008]. According to Nassar et al. [2006], the COF_2 contribution to F_y is maximum near 30 km (around 20% of F_y), and only represents around half of this value at 50 km. Altogether, HF and COF_2 thus represent 80 to 95% of stratospheric inorganic fluorine between 30 and 50 km.

In the next section, we describe the approaches adopted to establish our own inorganic fluorine inventory, using measurements and model simulations relevant for the Jungfraujoch station. Corresponding time series, as well as their trend analysis, are presented and discussed in section 5.3.

5.2. Databases and method for determining inorganic fluorine above Jungfraujoch

For all datasets involved in our inventory (Table 5.1), the inorganic fluorine burden has been simply obtained by applying Eq. (5.1), with abundances expressed in terms of vertical columns. COCIF was however not included in our inventory. Indeed, the detection of COCIF from ground-based FTIR measurements at Jungfraujoch is problematic. This is obvious when looking at the ACE-FTS microwindows successively used by Rinsland et al. [2007] and by Fu et al. [2009] for their COCIF space-based retrievals.

Data set	Description	Location	Products ^a
FTIR	Ground-based solar IR absorption observations	Jungfraujoch station (46.5°N, 8°E, 3580m)	HF, COF_2
KASIMA	3-D Chemical Transport Model	Data simulated for the Jungfraujoch	HF, COF_2 , COCIF
SLIMCAT	3-D Chemical Transport Model	Data simulated for the Jungfraujoch	HF, COF_2 , COCIF
HALOE v19	Satellite observations by solar occultations	[41-51]°N latitude belt	HF [15-35]
ACE-FTS v3	Satellite observations by solar occultations	[41-51]°N latitude belt	HF [15-55], COF_2 [15-35], COCIF [17-25]

^a Provide the name of gases for which total columns are derived. For satellite data, only partial columns are available. The altitude ranges of these partial columns are specified in kilometers between the brackets, for each molecule.

Table 5.1. Some characteristics of the five datasets used in our inorganic fluorine inventory.

The black trace of Figure 5.2 reproduces a FTIR spectrum recorded at Jungfraujoch during June 2010, at a solar zenith angle close to 70° . The vertical red lines correspond to the centers of the eight COCIF microwindows reported in Table 1 of Rinsland et al. [2007]. Those labeled with a red star are also part of the selection by Fu et al. [2009] who have furthermore proposed three additional microwindows whose centers are reproduced on Figure 5.2 with vertical blue lines. More than half of them are strongly affected by intense water vapor absorptions centered around 1864 cm^{-1} and 1868 cm^{-1} and are consequently unusable to monitor COCIF from ground-based FTIR spectra. This remains true when dry observation conditions above Jungfraujoch are encountered, like in winter (see the grey trace of Figure 5.2 that corresponds to an FTIR spectrum recorded during January 2010, at similar solar zenith angle). The four remaining microwindows are less affected by water vapor isotopologues but the corresponding COCIF absorption features are very weak (typically, less than 0.5%) and numerous infrared spectral signatures of other solar or telluric gases likely limit the possibility to perform accurate retrievals of this fluorine reservoir.

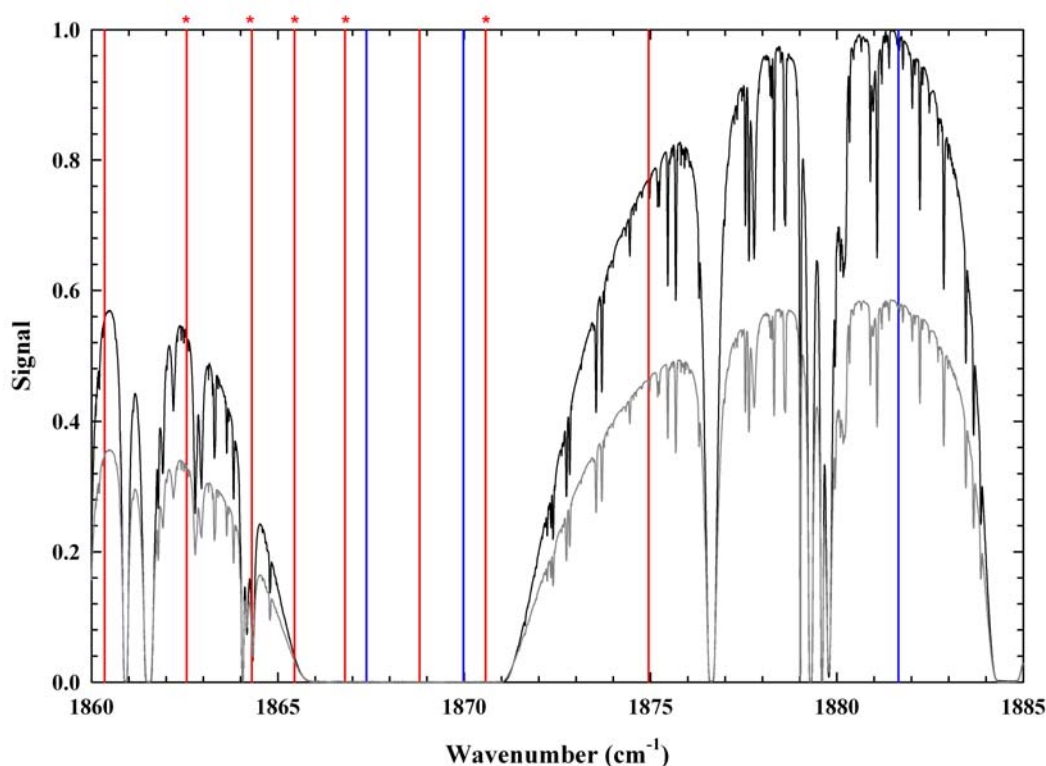


Fig. 5.2. Portion of two FTIR spectra recorded on 1st June 2010 (black trace) and on 12 January 2010 (grey trace) at Jungfraujoch at similar solar zenith angles close to 70° , encompassing COCIF absorptions. The vertical red lines denote the center of the eight microwindows used by Rinsland et al. [2007] for their COCIF retrievals from ACE-FTS satellite observations. The intense absorption lines centered around 1864 cm^{-1} and 1868 cm^{-1} are due to water vapor. Vertical lines labeled with a red star are also part of the selection by Fu et al. [2009]. The centers of additional COCIF microwindows used by Fu et al. [2009] are reproduced with vertical blue lines.

However, the exclusion of COCIF from our inorganic fluorine inventory does not constitute a critical issue since HF and COF_2 altogether represent the largest fraction of the stratospheric inorganic fluorine at northern mid-latitudes (see end of previous

section and end of section 5.3) and therefore, already constitute an excellent proxy for F_y (that will be designated hereafter by F_y^*). On the basis of COCIF data derived from satellite measurements or from model runs, we will further quantify the current contribution of this compound to F_y (see end of section 5.3).

Our inorganic fluorine budget F_y^* is based on Jungfraujoch FTIR observations. It therefore includes HF and COF₂ total vertical abundance time series from 1985 to 2010 produced and presented in Chapters 3 and 4 of our thesis. Coincident HF and twice COF₂ daily mean values have then been summed in order to produce the F_y^* time series.

We have further derived the fluorine inorganic burden F_y^* above ISSJ from daily HF and COF₂ total columns specifically computed, for the Jungfraujoch conditions, by two numerical 3-D model runs (namely, KASIMA and SLIMCAT; see Table 5.1). We refer the reader to Chapters 3 and 4 for a short description of the KASIMA and SLIMCAT models, as well as for additional references. For both HF and COF₂, we have considered modeled daily values for all coincident day with FTIR observations, between 1985 and 2010. However, while the KASIMA dataset covers the entire 1985-2010 time period, the SLIMCAT time series ends in July 2010, as some meteorological parameters were not yet available to extend the simulations. Despite the fact that both KASIMA and SLIMCAT are also able to simulate COCIF, we have not included this species in our inventory, for consistency with FTIR time series. However, the contribution of COCIF to the F_y budget will be discussed in section 5.3, notably on the basis of the modeled data.

For information, Table 5.2 and Table 5.3 summarize production and destruction reactions respectively adopted by KASIMA and SLIMCAT to simulate the abundance of the three main stratospheric fluorine reservoirs. Unlike KASIMA, the present SLIMCAT run does not include contributions from CFC-114 and -115, as well as from HCFC-141b and -142b. For both models, the relevant Sander et al. [2003] kinetics were adopted while the source gases scenario is taken from the CCMVal (Chemistry-Climate Model Validation Activity) webpages¹ (see Figure 1.13).

Satellite data have also been considered in our inorganic fluorine inventory (see Table 5.1), including HALOE, even if HF was the only fluorine target of that experiment. The last version (v19) of the HALOE products has been considered here. All individual HALOE solar occultations recorded in the [41-51]°N latitude belt have been selected and averaged to produce daily mean values. No time coincident criterion with FTIR data has been applied, in order to increase the number of HALOE data available for our analysis. The resulting HF HALOE time series extends from October 1991 to September 2004. We have checked that the HALOE sampling remains reasonably consistent over the 1991-2004 time period, in order to avoid any bias linked to seasonal effects in the trend computation.

Since VMR profiles occultation measurements do not extend down to the ground (due to loss of solar tracking around the tropopause), no HF total columns are available from HALOE.

¹ http://www.pa.op.dlr.de/CCMVal/Forcings/Halogens/CCMVal_halocarbons_REF2.txt

KASIMA	
Hydrogen fluoride (HF)	
Production	Destruction
$\text{COF}_2 + h\nu \rightarrow 2\text{HF} + \text{CO}_2$	no destruction reaction assumed
$\text{COCIF} + h\nu \rightarrow \text{Cl} + \text{HF} + \text{CO}_2$	
$\text{CFC-115} + h\nu \rightarrow \text{Cl} + \text{HF} + 2\text{COF}_2$	
$\text{H-1301} + h\nu \rightarrow \text{Br} + \text{HF} + \text{COF}_2$	
$\text{COCIF} + \text{O}(^1\text{D}) \rightarrow \text{ClO} + \text{HF} + \text{CO}_2$	
$\text{COF}_2 + \text{O}(^1\text{D}) \rightarrow 2\text{HF} + \text{CO}_2$	
$\text{CFC-115} + \text{O}(^1\text{D}) \rightarrow \text{ClO} + \text{HF} + 2\text{COF}_2$	
$\text{H-1301} + \text{O}(^1\text{D}) \rightarrow \text{BrO} + \text{HF} + \text{COF}_2$	
Carbonyl fluoride (COF₂)	
Production	Destruction
$\text{CFC-12} + h\nu \rightarrow 2\text{Cl} + \text{COF}_2$	$\text{COF}_2 + h\nu \rightarrow 2\text{HF} + \text{CO}_2$
$\text{HCFC-22} + h\nu \rightarrow \text{Cl} + \text{HO}_2 + \text{COF}_2$	$\text{COF}_2 + \text{O}(^1\text{D}) \rightarrow 2\text{HF} + \text{CO}_2$
$\text{CFC-113} + h\nu \rightarrow 2\text{Cl} + \text{COCIF} + \text{COF}_2$	
$\text{CFC-114} + h\nu \rightarrow 2\text{Cl} + 2\text{COF}_2$	
$\text{CFC-115} + h\nu \rightarrow \text{Cl} + \text{HF} + 2\text{COF}_2$	
$\text{HCFC-142b} + h\nu \rightarrow \text{Cl} + \text{CH}_3\text{O}_2 + \text{COF}_2$	
$\text{H-1211} + h\nu \rightarrow \text{Br} + \text{Cl} + \text{COF}_2$	
$\text{H-1301} + h\nu \rightarrow \text{Br} + \text{HF} + \text{COF}_2$	
$\text{CFC-12} + \text{O}(^1\text{D}) \rightarrow \text{ClO} + \text{Cl} + \text{COF}_2$	
$\text{CFC-114} + \text{O}(^1\text{D}) \rightarrow \text{ClO} + \text{Cl} + 2\text{COF}_2$	
$\text{CFC-115} + \text{O}(^1\text{D}) \rightarrow \text{ClO} + \text{HF} + 2\text{COF}_2$	
$\text{HCFC-142b} + \text{OH} \rightarrow \text{H}_2\text{O} + \text{Cl} + \text{CH}_2\text{O} + \text{COF}_2$	
$\text{HCFC-142b} + \text{O}(^1\text{D}) \rightarrow \text{OH} + \text{Cl} + \text{CH}_2\text{O} + \text{COF}_2$	
$\text{H-1211} + \text{O}(^1\text{D}) \rightarrow \text{BrO} + \text{Cl} + \text{COF}_2$	
$\text{H-1301} + \text{O}(^1\text{D}) \rightarrow \text{BrO} + \text{HF} + \text{COF}_2$	
Carbonyl chlorofluoride (COCIF)	
Production	Destruction
$\text{CFC-11} + h\nu \rightarrow 2\text{Cl} + \text{COCIF}$	$\text{COCIF} + h\nu \rightarrow \text{Cl} + \text{HF} + \text{CO}_2$
$\text{CFC-113} + h\nu \rightarrow 2\text{Cl} + \text{COCIF} + \text{COF}_2$	$\text{COCIF} + \text{O}(^1\text{D}) \rightarrow \text{ClO} + \text{HF} + \text{CO}_2$
$\text{HCFC-141b} + h\nu \rightarrow \text{Cl} + \text{CH}_3\text{O}_2 + \text{COCIF}$	
$\text{CFC-11} + \text{O}(^1\text{D}) \rightarrow \text{ClO} + \text{Cl} + \text{COCIF}$	
$\text{CFC-113} + \text{O}(^1\text{D}) \rightarrow \text{ClO} + \text{Cl} + \text{COCIF} + \text{COF}_2$	
$\text{HCFC-141b} + \text{OH} \rightarrow \text{H}_2\text{O} + \text{Cl} + \text{CH}_2\text{O} + \text{COCIF}$	
$\text{HCFC-141b} + \text{O}(^1\text{D}) \rightarrow \text{OH} + \text{Cl} + \text{CH}_2\text{O} + \text{COCIF}$	

Table 5.2. HF, COF₂ and COCIF production and destruction reactions assumed by the KASIMA model. For all these reactions, KASIMA adopts the kinetics given by Sander et al. [2003].

SLIMCAT	
Hydrogen fluoride (HF)	
Production	Destruction
$\text{COF}_2 + h\nu \rightarrow 2\text{HF} + \text{CO}_2$	no destruction reaction assumed
$\text{COCIF} + h\nu \rightarrow \text{Cl} + \text{HF} + \text{CO}_2$	
$\text{H-1301} + h\nu \rightarrow \text{Br} + \text{HF} + \text{COF}_2$	
$\text{COCIF} + \text{O}(^1\text{D}) \rightarrow \text{ClO} + \text{HF} + \text{CO}_2$	
$\text{COF}_2 + \text{O}(^1\text{D}) \rightarrow 2\text{HF} + \text{CO}_2$	
$\text{H-1301} + \text{O}(^1\text{D}) \rightarrow \text{BrO} + \text{HF} + \text{COF}_2$	
Carbonyl fluoride (COF₂)	
Production	Destruction
$\text{CFC-12} + h\nu \rightarrow 2\text{Cl} + \text{COF}_2$	$\text{COF}_2 + h\nu \rightarrow 2\text{HF} + \text{CO}_2$
$\text{HCFC-22} + h\nu \rightarrow \text{Cl} + \text{HO}_2 + \text{COF}_2$	$\text{COF}_2 + \text{O}(^1\text{D}) \rightarrow 2\text{HF} + \text{CO}_2$
$\text{CFC-113} + h\nu \rightarrow 2\text{Cl} + \text{COCIF} + \text{COF}_2$	
$\text{H-1211} + h\nu \rightarrow \text{Br} + \text{Cl} + \text{COF}_2$	
$\text{H-1301} + h\nu \rightarrow \text{Br} + \text{HF} + \text{COF}_2$	
$\text{CFC-12} + \text{O}(^1\text{D}) \rightarrow \text{ClO} + \text{Cl} + \text{COF}_2$	
$\text{HCFC-22} + \text{O}(^1\text{D}) \rightarrow \text{ClO} + \text{HO}_2 + \text{COF}_2$	
$\text{CFC-113} + \text{O}(^1\text{D}) \rightarrow \text{Cl} + \text{ClO} + \text{COCIF} + \text{COF}_2$	
$\text{H-1211} + \text{O}(^1\text{D}) \rightarrow \text{BrO} + \text{Cl} + \text{COF}_2$	
$\text{H-1301} + \text{O}(^1\text{D}) \rightarrow \text{BrO} + \text{HF} + \text{COF}_2$	
$\text{HCFC-22} + \text{OH} \rightarrow \text{ClO} + \text{H}_2\text{O} + \text{COF}_2$	
Carbonyl chlorofluoride (COCIF)	
Production	Destruction
$\text{CFC-11} + h\nu \rightarrow 2\text{Cl} + \text{COCIF}$	$\text{COCIF} + h\nu \rightarrow \text{Cl} + \text{HF} + \text{CO}_2$
$\text{CFC-113} + h\nu \rightarrow 2\text{Cl} + \text{COCIF} + \text{COF}_2$	$\text{COCIF} + \text{O}(^1\text{D}) \rightarrow \text{ClO} + \text{HF} + \text{CO}_2$
$\text{CFC-11} + \text{O}(^1\text{D}) \rightarrow \text{ClO} + \text{Cl} + \text{COCIF}$	
$\text{CFC-113} + \text{O}(^1\text{D}) \rightarrow \text{ClO} + \text{Cl} + \text{COCIF} + \text{COF}_2$	

Table 5.3. HF, COF₂ and COCIF production and destruction reactions assumed by the SLIMCAT model. For all these reactions, SLIMCAT adopts the kinetics given by Sander et al. [2003].

Indeed, HALOE vertical VMR distributions of HF typically extend between the 115mb and the 5mb pressure levels (i.e. between around 15 and 35km). But as vertical temperature versus pressure profiles are also retrieved during the HALOE data processing (by using the CO₂ transmittances; see Russell et al., 1993), the conversion of the HF VMRs between 15 and 35km into the corresponding partial column (PC) abundances can be performed, according to:

$$PC_i = \frac{100 p_i \Delta z_i N_a VMR_i}{R T_i} \quad (5.4)$$

where the subscript *i* designates the atmospheric layer index and where *p* is the pressure (in mb), Δz the atmospheric layer thickness (in km), N_a the Avogadro constant (i.e. $6.02205 \times 10^{23} \text{ mol}^{-1}$), *R* the ideal gas constant (i.e. 0.08205 L.atm/K.mol) and *T* the temperature (in K).

The partial column PC (in molec./cm²) between the altitude *n* and the altitude *m* is then given by the summation:

$$PC = \sum_{i=n}^m PC_i \quad (5.5)$$

As for HALOE, we have included the most recent ACE-FTS data available (v3) in our inorganic fluorine inventories. The same procedure as for HALOE (i.e. regarding the latitudinal criterion chosen as well as the production of daily mean partial column values) has been adopted for the HF, COF₂ and COCIF VMR profiles recorded by the ACE-FTS instrument.

The HF, COF₂ and COCIF time series derived from ACE-FTS measurements cover the March 2004–September 2010 time period. The altitude ranges adopted when ACE-FTS HF and COF₂ time series are considered separately (i.e. 15-55 km and 15-35 km, respectively) are specified in Table 5.1. Consequently, when HF and COF₂ data are combined to produce F_y^* amounts, only HF contributes above 35 km (i.e. above the peak value in COF₂ VMR profiles; see panel A of Figure 5.1). Concerning COCIF VMR profiles recorded by ACE-FTS, typical altitude range extends between 17 and 25km. According to Figure 5.1, this corresponds, for northern midlatitudes, to the region of the atmosphere where this gas is the most abundant.

5.3. Results and discussion

5.3.1. Inorganic fluorine trend analysis and partitioning

Figure 5.3 reproduces the $2 \times \text{COF}_2$ (black dots), HF (white dots) and their summation F_y^* (grey dots) monthly mean time series derived from FTIR long-term measurements above Jungfraujoch. Error bars are $1-\sigma$ standard deviations around the monthly mean values. It is also worth mentioning that only June to November data have been reproduced here, as they are less affected by the significant variability linked to transport and subsidence events that essentially occur during winter and spring times. Indeed, such sampling is appropriate to appraise the temporal evolution of these time series, on basis, for example, of non-parametric least squares fits (see the continuous black curves on Figure 5.3).

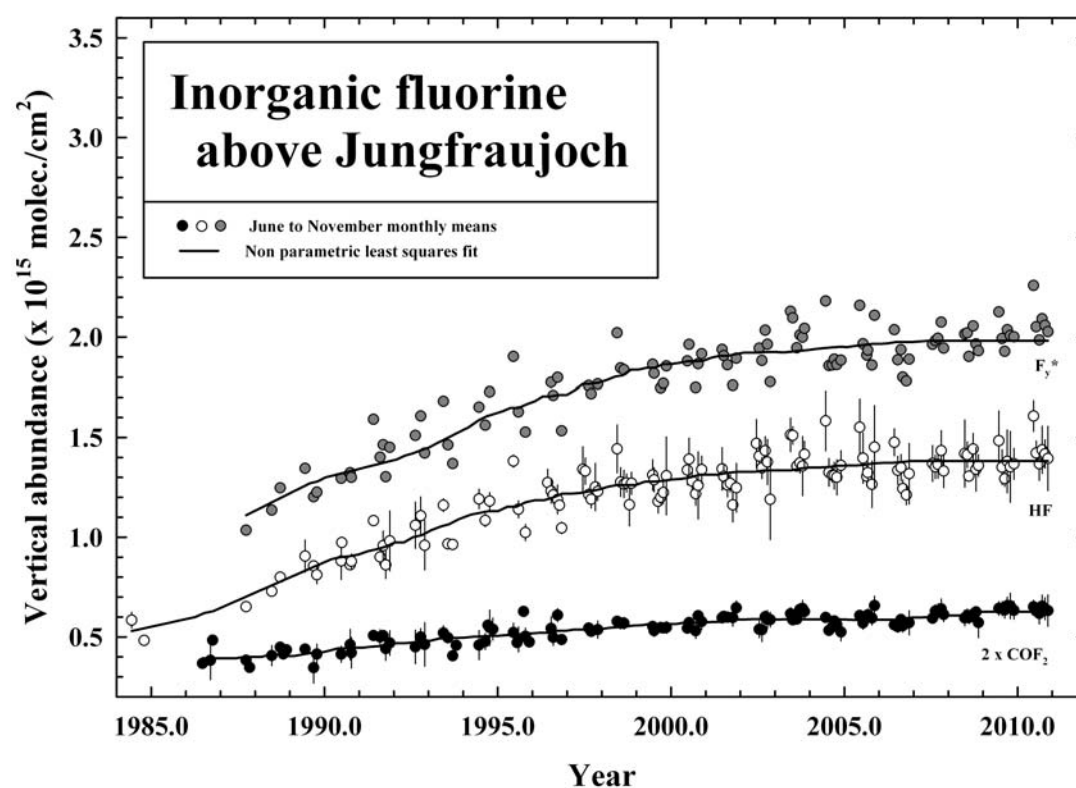


Fig. 5.3. Time series of monthly mean total vertical column abundances of $2 \times \text{COF}_2$ (black dots), HF (white dots) and their sum F_y^* (grey dots) derived from FTIR measurements at Jungfraujoch between 1984 and 2010. Only measurements from June to November are shown. The black lines through each time series represent non-parametric least squares fits, in order to better appraise their temporal evolutions. For the two lower time series, error bars are $1-\sigma$ standard deviation around monthly mean values.

In Figure 5.4 we have compared the FTIR time series with corresponding data set derived from numerical runs of the KASIMA (in red) and SLIMCAT (in green) 3-D CTMs.

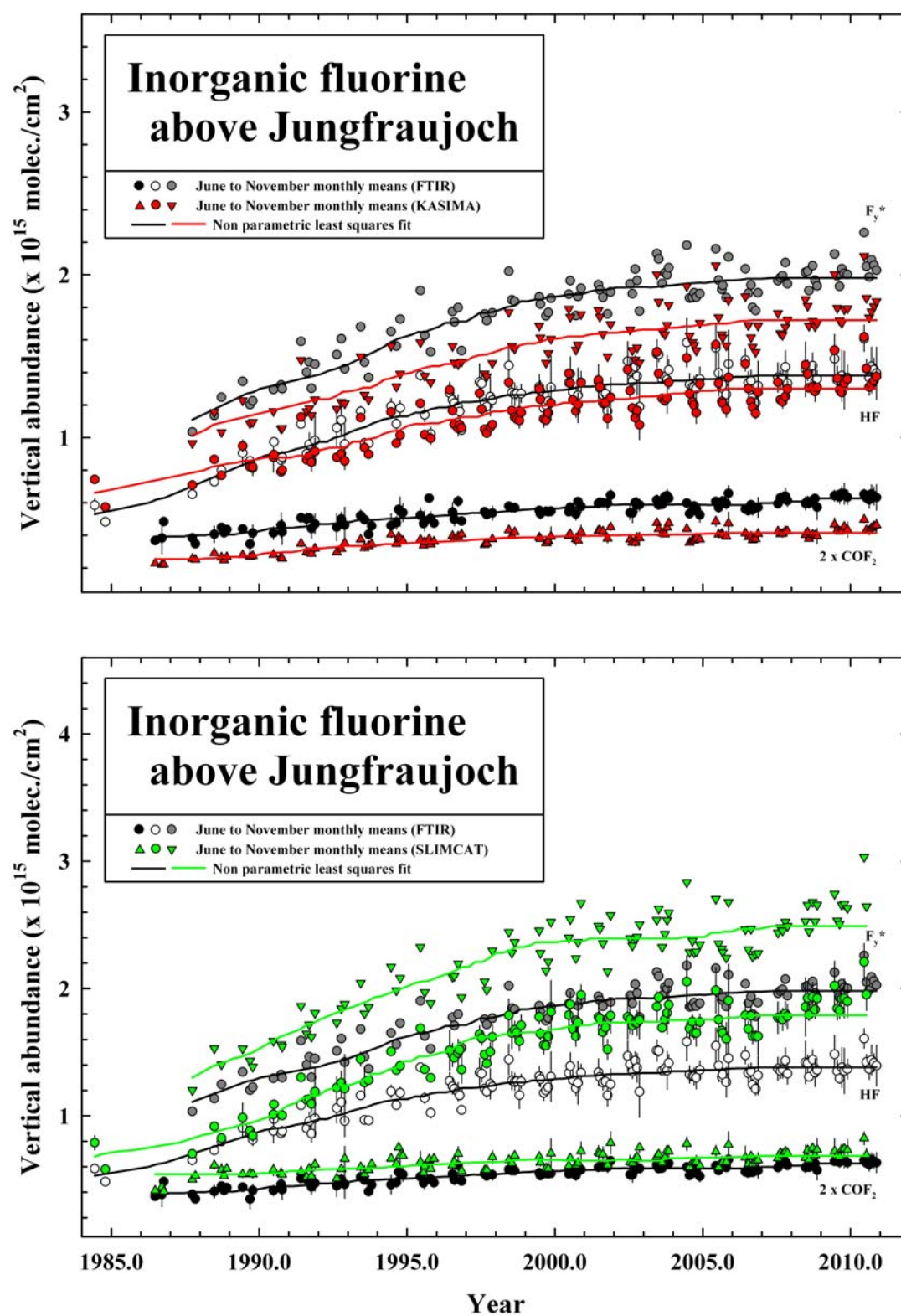


Fig. 5.4. Long-term time series of FTIR monthly mean total vertical column abundances of 2 x COF₂ (black dots), HF (white dots) and their sum F_y* (grey dots) compared with corresponding modeled data sets derived from KASIMA (red symbol on top panel) and SLIMCAT (green symbols on bottom panel) 3-D CTMs. COF₂, HF and F_y* model data are respectively reproduced with up triangles, circles and down triangles. Notice the different vertical scales adopted for the two panels.

The comparison between FTIR and KASIMA time series (top panel of Figure 5.4) points to a strong underestimation (about 45%) by the model of the COF₂ atmospheric loading, for reasons that have already been discussed in section 4.5. As a consequence, KASIMA also significantly underestimates by about 15% the inorganic fluorine loading F_y*. No significant bias is observed between the FTIR and KASIMA time series for HF (see Table 3.4).

Regarding the SLIMCAT time series, it is clear from bottom panel of Figure 5.4 that this model tends to significantly overestimate total column values for both HF and COF₂. For HF, this overestimation becomes important essentially after 1995 (about 20%; see also Table 3.4), leading to an overestimation of the same magnitude for F_y*. The significant reduction in the SLIMCAT F_y* values observed around 2005 results from decreases in the simulations of both COF₂ and HF. As evoked in section 4.5, these features are associated to inhomogeneity in the ECMWF meteorological data used by SLIMCAT for the early 2000's.

On both panels of Figure 5.4, black and colored solid lines correspond to running means computed for each monthly time series in order to depict the overall temporal evolution of each subset. However, in order to more precisely determine trend values, we have applied to the FTIR and model time series a bootstrap resampling approach by using the statistical tool developed by Gardiner *et al.* [2008] (see the Appendix A of the thesis for more information regarding this statistical method). To increase the statistics, these trends have been computed over daily mean time series (that have been produced following the method described in section 5.2), without discarding any specific period of the year. Four successive time periods have been considered, namely 1985-1995, 1995-2000, 2000-2005 and 2005-2010. We selected a 10-year length for the first time period in order to characterize at best the strong and regular increase that took place at that time for all data sets (see Figures 5.3 and 5.4).

For each time period, trends have been derived both in absolute and relative values (i.e. in molec./cm²/yr and in %/yr, respectively) and are reported in Table 5.4 (uncertainties represent the 95% confidence level). In all cases, trend values have been calculated with respect to a reference column which corresponds to the annual mean of the first year of the relevant time period. The N-values in Table 5.4 provide the number of coincident data involved in each trend computation. Since the SLIMCAT dataset does not cover the full year 2010, as specified above, less data are available for this model for the 2005-2010 trends computation.

To ease the comparison of the numerical data reported in Table 5.4, COF₂, HF and F_y* relative trend values (and their corresponding uncertainties) have been displayed on the different panels of Figure 5.5, with black, red and green rectangles for FTIR, KASIMA and SLIMCAT, respectively. When available, trends calculated from HALOE v19 and ACE-FTS v3 space measurements in the [41-51]°N latitude belt and summarized in Table 5.5 have also been plotted in Figure 5.5. These latter COF₂, HF and F_y* trend values are valid for the altitude ranges reported in Table 5.1, as explained at the end of section 5.2.

	FTIR	KASIMA	SLIMCAT
COF₂ linear trends			
Time period	x 10 ¹³ molec./cm ² /yr [%/yr]	x 10 ¹³ molec./cm ² /yr [%/yr]	x 10 ¹³ molec./cm ² /yr [%/yr]
1985-1995 N=283	0.71 ± 0.12 [3.25 ± 0.56]	0.84 ± 0.06 [6.39 ± 0.49]	0.89 ± 0.13 [4.00 ± 0.59]
1995-2000 N=271	0.53 ± 0.18 [2.04 ± 0.69]	0.33 ± 0.15 [1.66 ± 0.78]	0.45 ± 0.28 [1.37 ± 0.86]
2000-2005 N=348	-0.01 ± 0.16 [-0.04 ± 0.54]	0.05 ± 0.15 [0.23 ± 0.65]	-0.33 ± 0.27 [-0.90 ± 0.74]
2005-2010 N=445 ^a	0.69 ± 0.13 [2.29 ± 0.44]	0.51 ± 0.12 [2.27 ± 0.52]	1.28 ± 0.25 [3.64 ± 0.72]
HF linear trends			
Time period	x 10 ¹³ molec./cm ² /yr [%/yr]	x 10 ¹³ molec./cm ² /yr [%/yr]	x 10 ¹³ molec./cm ² /yr [%/yr]
1985-1995 N=161	5.66 ± 0.89 [7.55 ± 1.19]	4.58 ± 0.45 [5.61 ± 0.55]	8.81 ± 0.98 [10.37 ± 1.16]
1995-2000 N=483	2.53 ± 1.09 [2.21 ± 0.95]	3.95 ± 0.59 [3.61 ± 0.54]	7.48 ± 1.22 [5.15 ± 0.84]
2000-2005 N=609	2.38 ± 0.77 [1.78 ± 0.58]	1.70 ± 0.51 [1.26 ± 0.38]	0.65 ± 0.98 [0.35 ± 0.53]
2005-2010 N=598 ^b	2.19 ± 0.78 [1.50 ± 0.53]	3.35 ± 0.50 [2.35 ± 0.35]	7.52 ± 1.14 [4.04 ± 0.61]
F_y* linear trends			
Time period	x 10 ¹³ atom./cm ² /yr [%/yr]	x 10 ¹³ atom./cm ² /yr [%/yr]	x 10 ¹³ atom./cm ² /yr [%/yr]
1985-1995 N=94	5.95 ± 1.50 [4.63 ± 1.17]	5.97 ± 0.82 [5.49 ± 0.75]	10.50 ± 1.74 [7.96 ± 1.32]
1995-2000 N=192	3.18 ± 2.14 [1.96 ± 1.32]	4.46 ± 1.29 [3.07 ± 0.89]	8.28 ± 2.71 [4.05 ± 1.33]
2000-2005 N=317	2.26 ± 1.47 [1.19 ± 0.77]	1.78 ± 1.04 [0.98 ± 0.57]	-1.14 ± 1.97 [-0.44 ± 0.76]
2005-2010 N=414 ^c	3.61 ± 1.14 [1.77 ± 0.56]	4.42 ± 0.79 [2.37 ± 0.42]	10.50 ± 1.83 [4.14 ± 0.72]

^a For SLIMCAT, N=417

^b For SLIMCAT, N=563

^c For SLIMCAT, N=391

Table 5.4. COF₂, HF and F_y* linear trends (in molec.(atom.)/cm²/yr and in %/yr) calculated for the different time periods specified in the first column. These trends have been computed from the FTIR, KASIMA and SLIMCAT daily mean time series derived following the approach described in section 5.2. Uncertainties are the 95% confidence level. The N-values indicate the number of daily means involved in each trend computation.

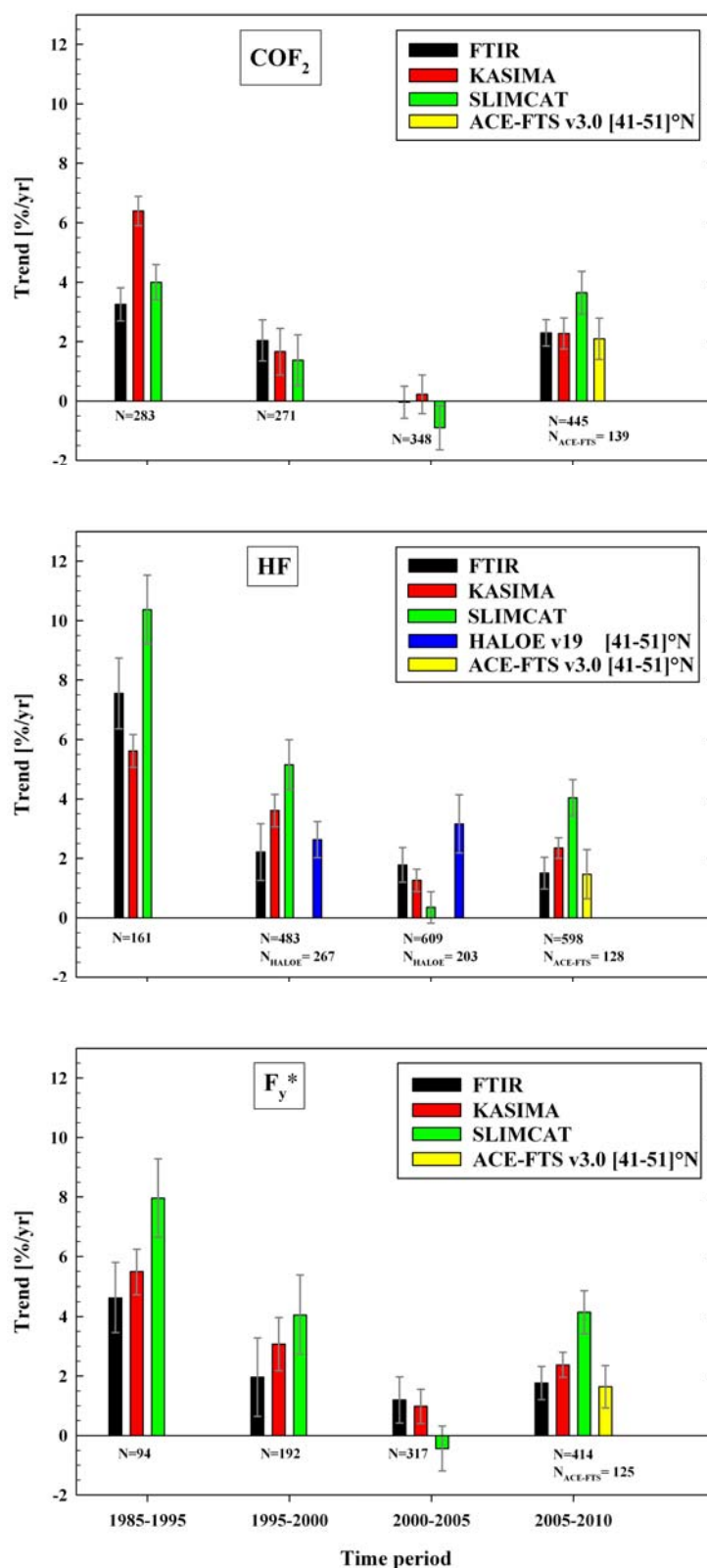


Fig. 5.5. Mean atmospheric COF₂, HF and F_y* growth rates (in %/yr) computed from FTIR, model and space data over four successive time periods (see text for details). Error bars depict the 95% confidence level. For FTIR and model data, trends and N-values are also reported in Table 5.4. For space data, N-values are specified separately. The second HF trend value derived from HALOE measurements has been computed over the 2000-2004 time period.

The FTIR trend values reproduced on the two top panels of Figure 5.5 indicate a significant slowing in the mean accumulation rates of both COF₂ and HF until 2005. For COF₂, this decrease is particularly obvious during the 2000-2005 time period. Over the last five years, our FTIR data further show a significant rise in the linear trend of this gas, at a mean rate close to the value that prevailed ten years before. The trend analysis of our FTIR data set further shows a stabilization in the HF growth rate during the last ten years.

Regarding the temporal development of the COF₂ trends, both KASIMA and SLIMCAT CTMs reveal the same tendency, consistent with the one shown by our FTIR data set. In particular, a nice agreement is found between FTIR and KASIMA COF₂ growth rates for the three last time periods. The significant negative trend obtained by SLIMCAT for the 2000-2005 time period as well as the significant higher trend value deduced for the 2005-2010 time interval are probably direct consequences of the significant – but questionable - drop in the COF₂ SLIMCAT total columns around the middle of the 2000-2010 decade (see Figure 4.6 and lower panel of Figure 5.4). Furthermore, this SLIMCAT feature seems to influence the trends of the adjacent time periods. It is however unlikely that the lack of SLIMCAT data after July 2010 is at the origin of the significant higher trend value deduced for the 2005-2010 time period. In addition, the overestimation by SLIMCAT of the COF₂ trend value for the 2005-2010 time period is supported by the excellent agreement between the 2005-2010 COF₂ growth rate deduced from ACE-FTS measurements (i.e. 2.09 ± 0.70 %/yr; see Table 5.5) and the corresponding FTIR and KASIMA trend values (i.e. 2.29 ± 0.44 %/yr and 2.27 ± 0.52 %/yr, respectively; see Table 5.4)

The slowing in the HF growth rate that occurred during the three first time periods under investigation here is especially well-marked from the SLIMCAT runs. The three corresponding trends deduced from KASIMA are more in line with FTIR trend values, in particular for the 2000-2005 time period for which a close agreement is found (see Table 5.4). However, unlike our FTIR data set, both models show a significant increase in the HF rate of growth after 2005, which is particularly well-pronounced for SLIMCAT. Again, for SLIMCAT, the strong contrast that exists between the HF trend values of the two last time periods is more likely ascribed to the non homogeneity in its meteorological data set. The very close agreement that exists for HF between 2005-2010 trends deduced from FTIR and ACE-FTS data (i.e. 1.50 ± 0.53 %/yr and 1.46 ± 0.83 %/yr, respectively; see Tables 5.4 and 5.5) however suggests that the HF build up has rather remained quite constant during the last ten years and thus, that the KASIMA model could foresee, perhaps owing to an inadequate CFCs, HCFCs and HFCs scenario emission, a potential future rise in the HF growth rate. Very recently, Kohlhepp *et al.* [2011] have similarly concluded to a stabilization of the atmospheric HF loading that occurs since around 2003. Their investigations are based on FTIR measurements above Kiruna (Northern Sweden, 67.8°N, 20.4°E, 419 m asl) and on KASIMA runs specifically computed for that site.

Regarding HF trend values deduced from HALOE measurements, the 1995-2000 trend agrees quite well with corresponding FTIR and KASIMA growth rates. For the 2000-2005 time period, the HALOE trend value looks high, even if this value is commensurate with the corresponding FTIR trend when considering their respective uncertainties. However, one should keep in mind that the HALOE trend is computed over a shorter time period (i.e. 2000-2004; see Table 5.5) since the corresponding

dataset ends in September 2004 (see section 5.2). When computed over the same time period, our FTIR trend for HF becomes 3.08 ± 0.78 %/yr, i.e. in better agreement with the corresponding value deduced from the HALOE measurements.

	HALOE v19	ACE-FTS v3
COF₂ linear trends		
Time period	$\times 10^{13}$ molec./cm ² /yr [%/yr]	$\times 10^{13}$ molec./cm ² /yr [%/yr]
2005-2010 N=139	- [-]	0.57 ± 0.19 [2.09 ± 0.70]
HF linear trends		
Time period	$\times 10^{13}$ molec./cm ² /yr [%/yr]	$\times 10^{13}$ molec./cm ² /yr [%/yr]
1995-2000 N=267	2.18 ± 0.51 [2.63 ± 0.61]	- [-]
2000-2004 N=203	3.02 ± 0.94 [3.16 ± 0.98]	- [-]
2005-2010 N=128	- [-]	1.76 ± 0.99 [1.46 ± 0.83]
F_y* linear trends		
Time period	$\times 10^{13}$ atom./cm ² [%]	$\times 10^{13}$ atom./cm ² [%]
2005-2010 N=125	- [-]	3.16 ± 1.37 [1.64 ± 0.71]

Table 5.5. COF₂, HF and F_y* linear trends (in molec.(atom.)/cm²/yr and in %/yr) calculated for the different time periods specified in the first column. These trends have been computed for the HALOE v19 and ACE-FTS v3 daily mean time series, using the same approach than in section 5.2. Uncertainties are the 95% confidence level. N-values indicate the number of data involved in each trend computation.

We can further compare our HF trend values to the findings of Rinsland *et al.* [2002] that have exploited long-term FTIR measurements performed at the US National Solar Observatory facility on Kitt Peak (Arizona, USA, 31.9°N, 111.6°W, 2090 m asl). For the 1977-2001 time period, these authors provide a linear trend for HF equal to 4.30 ± 0.15 %/yr. This value is slightly lower than HF trend values of 6.00 ± 0.47 and 5.28 ± 0.23 %/yr computed from FTIR and KASIMA time series, respectively, over the shorter 1985-2001 time period. Corresponding value for SLIMCAT amounts to 8.98 ± 0.47 %/yr and remains high with respect to the trend results by Rinsland *et al.* [2002]. However, the HF trend derived by SLIMCAT for the 1985-1995 time period shows the best agreement with the stratospheric 1985-1992 HF trend of 8.9 %/yr deduced by Zander *et al.* [1992] from ATMOS measurements at northern subtropical latitudes. The corresponding trend for COF₂ (9.2 %/yr) provided by these authors is also significantly higher than those deduced in the present study for the 1985-1995 time period. However, the limited duration in time of the ATMOS space-shuttle missions (typically, about ten days) inevitably affects the statistics derived by Zander *et al.* [1992] (e.g. during the 1992 ATMOS mission, this instrument has collected 94 space occultations, all latitudes) and can thus partially explain the observed biases.

Obviously, the combination of the evolutions with time of both HF and COF₂ trend values during the two last decades constrains the behavior of the corresponding trends that characterize the inorganic fluorine burden F_y^* (see bottom panel of Figure 5.5). Both FTIR and ACE-FTS measurements therefore agree to conclude that the significant rise observed in the COF₂ rate of growth during the last five years does not significantly impact the F_y^* trend that remains, like the growth rate of its main contributor HF, quite stable during the last ten years. Furthermore, both KASIMA and SLIMCAT models conclude to a significant increase in the F_y^* growth rate during the last five years, since they both show similar behaviors for HF and for COF₂ during the same time period, for reasons evoked above.

We close this section by considering how atmospheric fluorine has been distributed between the main stratospheric reservoirs HF, COF₂ and COCIF during the last twenty-five years. Table 5.6 lists partitioning values we have deduced from the different data sets (HALOE excepted) involved in our trend computations. These values express (in percents) the contribution of a given gas to the total inorganic fluorine loading F_y . As no COCIF total columns are available from FTIR measurements, we have alternatively used data derived from KASIMA and SLIMCAT runs for this gas in our FTIR partitioning evaluations. Values reported in Table 5.6 are averages computed over the specified time periods, while corresponding errors are 1- σ standard deviations. The lines 'Mean' provide the mean contributions calculated over the whole 1985-2010 time period. For ACE-FTS, the altitude ranges adopted for each fluorine reservoir are those specified in Table 5.1.

All data sets of Table 5.6 confirm the fact that HF represents the largest fraction of F_y at northern midlatitudes, with recent contributions ranging from 65 to 70%. However, the KASIMA model often systematically provides higher contributions by a few percents, the values deduced from FTIR, SLIMCAT and ACE-FTS being commensurate within their respective uncertainties for all time periods under investigation. When considering their respective uncertainties, these values additionally suggest that the HF contribution to F_y has remained unchanged during the last twenty-five years.

With recent contributions to inorganic fluorine close to 30%, carbonyl fluoride is the second most abundant fluorine reservoir. Contributions deduced for this compound from the two CTMs are however lower by a few percents, especially for KASIMA. The values deduced from FTIR and ACE-FTS for the last time period considered here are commensurate within their respective uncertainties. As for HF, no significant trend in the contribution of COF₂ to F_y can be deduced from the values reported in Table 5.6, except for SLIMCAT that indicates a regular decrease that finally significantly amounts to about 5%.

According all datasets of Table 5.6, the COCIF contribution to F_y remains limited to values generally close to 5%. However, ACE-FTS provides a 2005-2010 value that is almost two times lower than those deduced from model data. As a consequence of such a low contribution to F_y , the inclusion or exclusion of COCIF amounts into the trend computations performed for the inorganic fluorine burden have a limited impact. Indeed, we have checked from KASIMA and SLIMCAT data sets that trend values obtained for F_y when considering COCIF in our inorganic fluorine inventory differ of about 0.1 and 0.3%/yr, respectively (the values provided here are means of absolute

differences) from trend values reported in the two last columns of Table 5.4. For ACE-FTS, the corresponding difference is close to 0.1 %/yr.

	FTIR ^a	FTIR ^b	KASIMA	SLIMCAT	ACE-FTSv3
Contribution of HF to F_v (%)					
1985-1995	63.4 ± 3.0	61.1 ± 3.1	70.6 ± 1.8	61.9 ± 3.5	-
1995-2000	65.9 ± 2.9	64.0 ± 2.9	70.8 ± 2.3	66.7 ± 2.0	-
2000-2005	67.4 ± 2.7	65.7 ± 2.8	72.4 ± 2.0	68.6 ± 1.5	-
2005-2010	66.9 ± 2.7	65.5 ± 2.8	72.6 ± 1.8	68.9 ± 1.5	69.8 ± 1.4
Mean	66.5 ± 3.0	64.9 ± 3.1	72.0 ± 2.1	67.7 ± 2.9	69.8 ± 1.4
Contribution of 2 x COF₂ to F_v (%)					
1985-1995	31.5 ± 2.8	30.3 ± 2.6	23.8 ± 1.5	30.9 ± 2.6	-
1995-2000	29.1 ± 2.5	28.3 ± 2.4	23.8 ± 1.7	27.3 ± 1.5	-
2000-2005	28.3 ± 2.4	27.5 ± 2.3	22.8 ± 1.5	26.0 ± 1.1	-
2005-2010	28.9 ± 2.6	28.2 ± 2.6	22.7 ± 1.5	26.1 ± 1.1	27.5 ± 1.2
Mean	29.0 ± 2.7	28.2 ± 2.6	23.1 ± 1.6	26.8 ± 2.1	27.5 ± 1.2
Contribution of COClF to F_v (%)					
1985-1995	5.0 ± 0.6	8.5 ± 1.2	5.5 ± 0.6	7.2 ± 1.1	-
1995-2000	5.0 ± 0.8	7.6 ± 1.0	5.4 ± 0.7	6.0 ± 0.6	-
2000-2005	4.4 ± 0.6	6.8 ± 0.9	4.8 ± 0.6	5.4 ± 0.5	-
2005-2010	4.2 ± 0.5	6.3 ± 0.8	4.6 ± 0.5	5.0 ± 0.6	2.7 ± 0.4
Mean	4.5 ± 0.7	6.9 ± 1.2	4.9 ± 0.7	5.5 ± 1.0	2.7 ± 0.4

^a COClF data from KASIMA have been adopted.

^b COClF data from SLIMCAT have been adopted.

Table 5.6. Individual contributions (in %) of the three main stratospheric fluorine reservoirs to the total inorganic fluorine burden for the different time periods specified in the first column. The lines ‘Mean’ provide the mean contributions calculated over the entire 1985-2010 time period. FTIR values in italic remind that they are based on KASIMA or SLIMCAT model simulations.

Finally, it also appears from Table 5.6 that the SLIMCAT model reveals a more realistic partitioning scheme for the different inorganic fluorine reservoirs than KASIMA. Indeed, the agreement between the contributions deduced from SLIMCAT and the corresponding ACE-FTS or FTIR values (from both subsets) is generally better than for KASIMA. In addition, it is worth noting that FTIR and CTMs values reported in Table 5.6 can differ slightly from those obtained from the ACE-FTS v3 products or from those deduced from the study by Nassar *et al.* [2006] based on ACE-FTS v2.2 data (see end of section 5.1), since the altitude ranges covered by the various time series involved are sometimes different (i.e. between 30 and 50 km for Nassar *et al.* [2006] in comparison to values reported in Table 5.1).

However, all data reported in Table 5.6 remain consistent with values published in previous studies. For example, we deduce from Kaye *et al.* [1991] and from Mahieu and Zander [1999] the following ranges for the individual contributions to F_y: 50 to 70% for HF, 20 to 40% for COF₂ and 5 to 10% for COClF, these values depending on the latitude. Based on the fluorine inventory performed by Zander *et al.* [1992] from ATMOS measurements at northern midlatitudes in 1985 (see Table 2 of Zander *et al.*, 1992), we deduce the following individual contributions to F_y (mean values over the 15-52.5 km altitude range): 69.6% for HF and 30.4% for COF₂. These values are

consistent with our findings for the relevant time period, even if the contribution by COCIF has not been included in this estimation, as this gas was not measured by ATMOS. The same exercise performed from HF, COF₂ and COCIF balloon profiles at northern midlatitudes published in Table 2 of Sen *et al.* [1996] provides the following partitioning (individual contributions to F_y averaged over the 17-38 km altitude range): 60.3% for HF, 30.7% for COF₂ and 9.0% for COCIF. Again, these findings are commensurate with the results listed in Table 5.6.

5.3.2. Hypothesis for trends explanation

Here we review some tentative explanations for the observed changes in the COF₂ and HF trends deduced from our investigations. We mainly base the discussion developed in this section on halogenated source gases emissions during the time period under investigation (i.e. 1985-2010) as well as on the chemistry of atmospheric fluorine introduced in section 1.2.1. In the near future, our aim will be to confront these hypotheses to dedicated numerical model simulations which have still to be performed.

The top panel of Figure 5.6 reproduces the temporal evolution, from the early eighties till the middle of this century, of the most abundant long-lived fluorinated source gases, weighted by the number of F atoms in each species. Like for Figure 1.13, these curves are derived from the A1 emission scenario of WMO [2007]. The four successive time periods considered in the trend analysis of the previous section have been delimited with the black vertical solid lines. We have further distinguished between source gases which are precursors of COF₂ and COCIF by reproducing their temporal evolutions with solid grey curves and black dashed curves, respectively. As the dissociation of CFC-113 produces both COF₂ and COCIF, we show the evolution of this gas with a grey dashed curve.

To try to explain the trends that characterize the two most abundant inorganic fluorine reservoirs, it is also useful to combine the individual contributions of all source gases precursor of COF₂ or of COCIF. These combined contributions are reproduced in top panel of Figure 5.6 with the grey and black dotted curves, respectively. They are the sum of the relevant individual contributions displayed in top panel of Figure 5.6 but also include the weighted contributions of other minor source gases whose temporal evolutions have not been depicted, for clarity. Since the CFC-113 photolysis leads to both COF₂ and COCIF, we have – arbitrarily – split its contribution into two equal parts. The additional minor species included in the computation of the COF₂ (resp. COCIF) precursors curve are CFC-114, CFC-115, HCFC-142b, Halon-1211 and Halon-1301 (resp. HCFC-141b). Finally, the red solid curve reproduces the temporal evolution of the total organic fluorine burden CF_y, derived by using Eq. (5.2) where the minor species are those aforementioned.

In top panel of Figure 5.6, the dotted and red curves derived from the A1 emission scenario are also compared to global surface measurements performed within the AGAGE (Advanced Global Atmospheric Gases Experiment) network in 2004, 2007 and 2008 (see triangles on top panel of Figure 5.6). The AGAGE individual contributions used here are those published very recently in WMO [2010]. Except for the COCIF precursors curve, we notice small deviations between the simulated predictions and the AGAGE measurements from 2007-2008. This could notably result

from the fact that since 2008, the increase in the atmospheric burden of HCFC-22 is significantly more rapid than those foreseen in the A1 scenario (see Figure 1-1 of WMO, 2010).

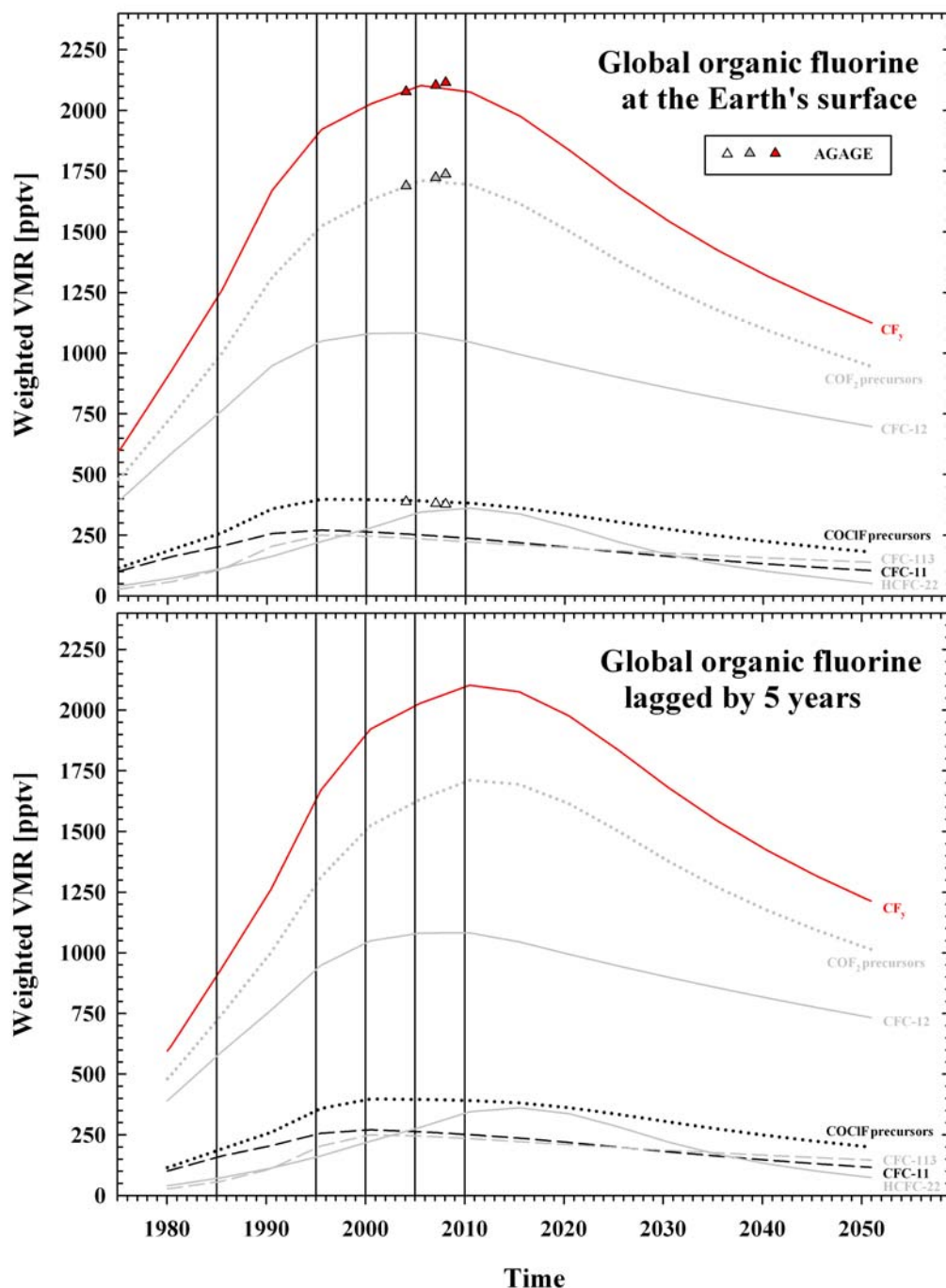


Fig. 5.6. Top panel: global temporal evolution of the most abundant halogenated source gases, weighted by the number of F atoms in each species, according to A1 emission scenario of WMO [2007]. The COF_2 and COClF precursors curves correspond to the sum of the relevant individual contributions (see text for details). The total organic fluorine CF_y includes the individual contributions of all F-containing source gases simulated by the A1 scenario. These three latter curves are compared to corresponding amounts derived from AGAGE surface measurements (colored triangles). Bottom panel: same curves as in the top panel, but lagged by 5 years to take into account the atmospheric transport. In both panels, the vertical black solid lines delimit the successive time periods considered in our trends computation.

As the inorganic fluorine reservoirs are essentially located in the stratosphere, it is also necessary to take into account the time needed for tropospheric source gases to propagate into the stratosphere. According to Anderson et al. [2000], the lag time for fluorine transport is close to 5 years. Considering this time delay, all curves displayed in the top panel of Figure 5.6 have been horizontally shifted to produce the bottom panel, on which the following discussion is based.

It appears from this latter panel that during the three first time periods under investigation, the stratospheric increase rate of the COF₂ precursors slows significantly, as a direct consequence of phase-out decisions adopted by the Montreal Protocol and its subsequent Amendments and Adjustments (see section 1.2.2). This is supported by the consideration of the individual temporal evolutions of CFC-12, CFC-11 and CFC-113 during the same time period. Such a behavior qualitatively explains the significant slowing observed in the rates of growth of COF₂ during the corresponding time period (see Table 5.4 and the top panel of Figure 5.5).

Between 2005 and 2010, the A1 emission scenario predicts a stratospheric increase for COF₂ precursors that remains almost unchanged with respect to the previous time period, probably because the stabilization or the decline of the most abundant CFCs is partially compensated by the increase of substitute products such as HCFC-22. This is however inconsistent with the significant rise observed in recent COF₂ trend values reported in Tables 5.4 - 5.5 and in the top panel of Figure 5.5 from FTIR and ACE-FTS measurements. This difference could perhaps partially result from the fact that recent HCFC-22 growth is effectively more rapid than the one assumed in the A1 emission scenario. One should also keep in mind that the A1 curves are global mean predictions (i.e. valid for all latitudes of both hemispheres) and that they could therefore significantly smooth atmospheric changes.

Considering the CF_y curve, we notice a similar behavior as for the COF₂ precursors curve, notably indicating that the total organic fluorine preferentially results from source gases that will be subsequently dissociated into COF₂, and then into HF. In particular, according to A1 curves, the almost unchanged growth rate in the stratospheric CF_y loading during the last ten years lets suggest a similar behavior for the total inorganic fluorine F_y – and also for HF, considering the dominant contribution of this fluorine reservoir to F_y (see Table 5.6) – as indeed observed from the recent FTIR and ACE-FTS trend values (see Tables 5.4 – 5.5 and the two lower panels of Figure 5.5).

At this stage, it is however difficult to explain why the rise observed in the COF₂ trend between 2005 and 2010 does not yet impact the corresponding HF trend, as observed by both FTIR and ACE-FTS data (see Figure 5.5 and Tables 5.4 and 5.5). Indeed, any changes in the COF₂ trend should result, within a few months (i.e. the typical lifetime of COF₂ in the lower stratosphere, according to Chipperfield et al., [1997]), in similar changes in the HF trends. Unfortunately, to our knowledge, no additional studies based on experimental data sets and dealing with the COF₂ atmospheric lifetime are available to date. Furthermore, it is also unlikely that trend values affecting COClF, the other intermediate fluorine reservoir species, could significantly influence the recent HF growth rates – like for F_y, see end of section 5.3.1 – as the relative abundance of COClF remains poor with respect to COF₂ (e.g. see Figures 1.8 and 5.1).

The temporary stabilization of COF₂ remains to be understood while its more recent re-increase will be verified by extending our time series. The evolution of HCFC-22, another target gas of the FTIR technique, will also be carefully monitored. Indeed, we think it will play a significant role in the timing and strength of the fluorine loading decrease which is expected to happen in the next 5 to 10 years, if we trust the A1 scenario.

References

Anderson, J., J. M. Russell III, S. Solomon and L. E. Deaver, Halogen Occultation Experiment confirmation of stratospheric chlorine decreases in accordance with the Montreal Protocol, *J. Geophys. Res.* 105, 4483-4490, 2000.

Anderson, J., and J. M. Russell III, Long term changes of HCl and HF as observed by HALOE, in *Ozone*, vol. II, Proceedings of the XX Quadrennial Ozone Symposium, Kos, Greece, 1– 8 June 2004, edited by C. S. Zerefos, pp. 223– 224, Univ. of Athens, Athens, 2004.

Bernath, P. F., C. T. McElroy, M. C. Abrams, et al., Atmospheric Chemistry Experiment (ACE): mission overview, *Geophys. Res. Lett.*, 32, doi: 10.1029/2005GL022386, 2005.

Also available at <http://orbi.ulg.ac.be/handle/2268/2388>

Dufour, G., C. D. Boone and P. F. Bernath, First measurements of CFC-113 and HCFC-142b from space using ACE-FTS infrared spectra, *Geophys. Res. Lett.*, 32, doi:10.1029/2005GL022422, 2005.

Fu, D., C. D. Boone, P. F. Bernath, et al., First global observations of atmospheric COClF from the Atmospheric Chemistry Experiment mission, *J. Quant. Spec. and Rad. Transf.* 110, 974-985, 2009.

Gardiner, T., A. Forbes, M. De Mazière, et al., Trend analysis of greenhouse gases over Europe measured by a network of ground-based remote FTIR instruments, *Atmos. Chem. Phys.*, 8, 6719-6727, 2008.

Also available at <http://orbi.ulg.ac.be/handle/2268/2545>

Kaye, J. A., A. R. Douglas, C. H. Jackman, et al., Two dimensional model calculations of fluorine containing reservoir species in the stratosphere, *J. Geophys. Res.*, 96, 12865-12881, 1991.

Kohlhepp, R., S. Barthlott, T. Blumenstock, et al., Trends of HCl, ClONO₂ and HF column abundances from ground-based FTIR measurements in Kiruna (Sweden) in comparison with KASIMA model calculations, *Atmos. Chem. Phys. Discuss.*, 11, 1489-1510, 2011.

Krieg, J., J. Notholt, E. Mahieu, et al., Sulphur hexafluoride (SF₆): comparison of FTIR-measurements at three sites and determination of its trend in the northern hemisphere, *J. Quant. Spec. and Rad. Transf.* 92, 383-392, 2005.

Also available at <http://orbi.ulg.ac.be/handle/2268/2398>

Mahieu, E., and R. Zander, Fifteen years-trend characteristics of key stratospheric constituents monitored by FTIR above the Jungfraujoch, in Proceedings of stratospheric ozone 1999, pp 99-182, Saint Jean de Luz, edited by N. R. P. Harris et al., Eur. Comm., 1999.

Mahieu, E., P. Duchatelet, P. Demoulin, et al., Validation of ACE-FTS v2.2 measurements of HCl, HF, CCl₃F and CCl₂F₂ using space-, balloon- and ground-based instrument observations, *Atmos. Chem. Phys.*, 8, 6199-6221, 2008.

Also available at <http://orbi.ulg.ac.be/handle/2268/2344>

Mahieu, E., C. P. Rinsland, T. Gardiner, et al., Recent trends of inorganic and halogenated source gases above the Jungfraujoch and Kitt Peak stations derived from high-resolution FTIR solar observations, poster presented at the EGU 2010 General Assembly, 2-7 May 2010, Vienna, Austria, 2010.

Also available at <http://orbi.ulg.ac.be/handle/2268/35065>

Mahieu, E., P. Duchatelet, R. Zander, et al., Trend and lifetime of sulfur hexafluoride (SF₆) at mid-latitudes deduced from ACE-FTS occultation measurements, poster presented at the “EGU 2011 General Assembly”, 3-8 April 2011, Vienna, Austria, 2011.

McHugh, M., B. Magill, K. A. Walker, et al., Comparison of atmospheric retrievals from ACE and HALOE, *Geophys. Res. Lett.*, 32, L15S10, doi:10.1029/2005GL022403, 2005.

Nassar, R., P. F. Bernath, C. D. Boone, et al., A global inventory of stratospheric fluorine in 2004 on Atmospheric Chemistry Experiment Fourier transform spectrometer (ACE-FTS) measurements, *J. Geophys. Res.*, 111, D22313, doi: 10.1029/2006JD007395, 2006.

Also available at <http://orbi.ulg.ac.be/handle/2268/4285>

Rinsland, C.P., R. Zander, E. Mahieu, et al., Stratospheric HF column abundances above Kitt Peak (31.9°N latitude): trends from 1977 to 2001 and correlations with stratospheric HCl columns, *J. Quant. Spec. and Rad. Transf.*, 74, 205-216, 2002.

Also available at <http://orbi.ulg.ac.be/handle/2268/2384>

Rinsland, C. P., R. Nassar, C. D. Boone, et al., Spectroscopic detection of COClF in the tropical and mid-latitude lower stratosphere, *J. Quant. Spec. and Rad. Transf.* 105, 467-475, 2007.

Also available at <http://orbi.ulg.ac.be/handle/2268/2413>

Russell, J. M., III, L. L. Gordley, J. H. Park, et al., The Halogen Occultation Experiment, *J. Geophys. Res.*, 98, 10,777–10,797, doi:10.1029/93JD00799, 2003.

Sander, S. P., R. R. Friedl, D. M. Golden, et al., Chemical kinetics and photochemical data for use in atmospheric studies: Evaluation number 14, JPL Publ., 02–25, 334 pp, 2003.

Sen, B., G. C. Toon, J.-F. Blavier, et al., Balloon-borne observations of midlatitude fluorine abundance, *J. Geophys. Res.* 101, 9045-9054, 1996.

World Meteorological Organization, WMO Report No. 50: Scientific Assessment of Ozone Depletion: 2006, P.O. Box 2300, Geneva 2, CH 1211, Switzerland, 2007.

World Meteorological Organization, WMO Report No. 52: Scientific Assessment of Ozone Depletion: 2010, P.O. Box 2300, Geneva 2, CH 1211, Switzerland, 2010.

Zander, R., M. R. Gunson, C. B. Farmer, et al., The 1985 chlorine and fluorine inventories in the stratosphere based on ATMOS observations at 30 north latitude, *Journal of Atmospheric Chemistry*, 15, 171-186, 1992.

Also available at <http://orbi.ulg.ac.be/handle/2268/2690>

Zander, R., C. P. Rinsland, E. Mahieu, et al., Increase of carbonyl fluoride (COF₂) in the stratosphere and its contribution to the 1992 budget of inorganic fluorine in the upper stratosphere, *J. Geophys. Res.* 99, 16737-16743, 1994.

Also available at <http://orbi.ulg.ac.be/handle/2268/14537>

Chapter 6

FTIR monitoring of carbon tetrafluoride

6.1. Introduction

Carbon tetrafluoride (CF₄ or PFC-14) is a potent greenhouse gas that is almost 10000 times more effective than CO₂ on a per molecule basis [WMO, 2007]. This high warming potential, combined with a very long atmospheric lifetime (CF₄ is one of the longest-lived atmospheric gas, with a lifetime exceeding 50000 years [i.e. Ravishankara et al., 1993; Mühle et al., 2010 and references therein]) led to the inclusion of CF₄ in the Kyoto Protocol's regulation scheme of anthropogenic emissions of various greenhouse gases. In the Northern Hemisphere, current atmospheric CF₄ concentrations are close to 78 pptv, with a significant fraction (between 35 and 40 pptv) coming from natural processes like lithospheric emissions [Harnisch et al. 1996, 2000; Harnisch and Eisenhauer, 1998; Mühle et al., 2010]. According to Harnisch et al. [1996, 2000] and to Harnisch and Eisenhauer [1998], lithospheric fluxes however remain about 10³ to 10⁵ lower than anthropogenic fluxes. Indeed, since the eighties, CF₄ has been used increasingly in electronic and semiconductors industry (e.g. cleaning operations, plasma etching, etc). This represents a contribution to the total atmospheric CF₄ burden close to 1 pptv [Khalil et al., 2003]. But with a current contribution close to 35 pptv [Khalil et al., 2003], the primary aluminum production processes have however been clearly identified as the most important anthropogenic source of CF₄ emissions (see Figure 6.1).

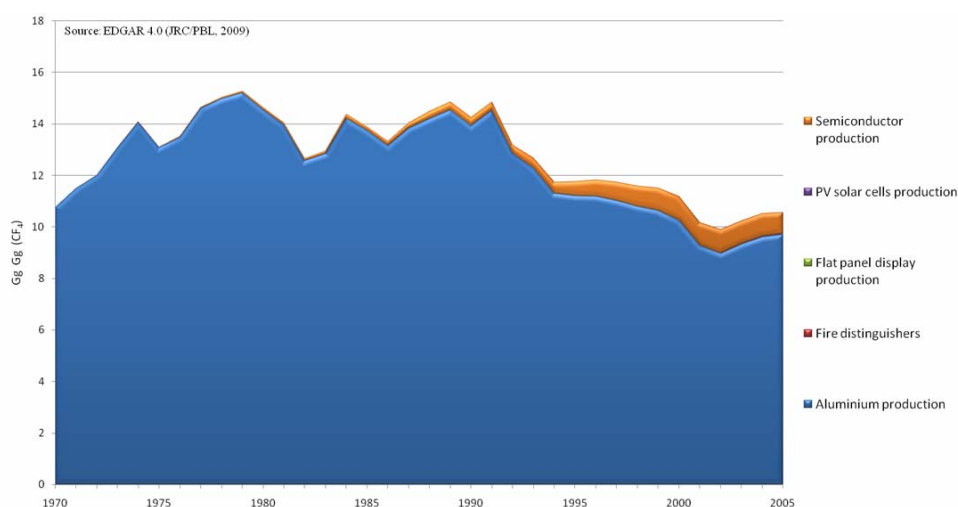


Fig. 6.1. CF₄ emissions (expressed in Gg) by major source categories in the EDGAR v4.0 datasets (source: the Emission Database for Global Atmospheric Research; see <http://edgar.jrc.ec.europa.eu>).

The primary aluminum production is a two-steps procedure. First, bauxite (the most important ore¹ of aluminum) is refined through the Bayer process to produce pure alumina (Al_2O_3). The largest amount of alumina so produced is then subsequently smelted using the Hall-Héroult process, in order to produce primary aluminum. The Hall-Héroult process is an electrolytic procedure where the smelting pot itself acts as the electrolysis cell (Figure 6.2). The alumina is dissolved in an electrolytic bath (mainly composed of molten cryolite, i.e. a sodium aluminum fluoride) between 950°C and 1000°C, following the reaction:

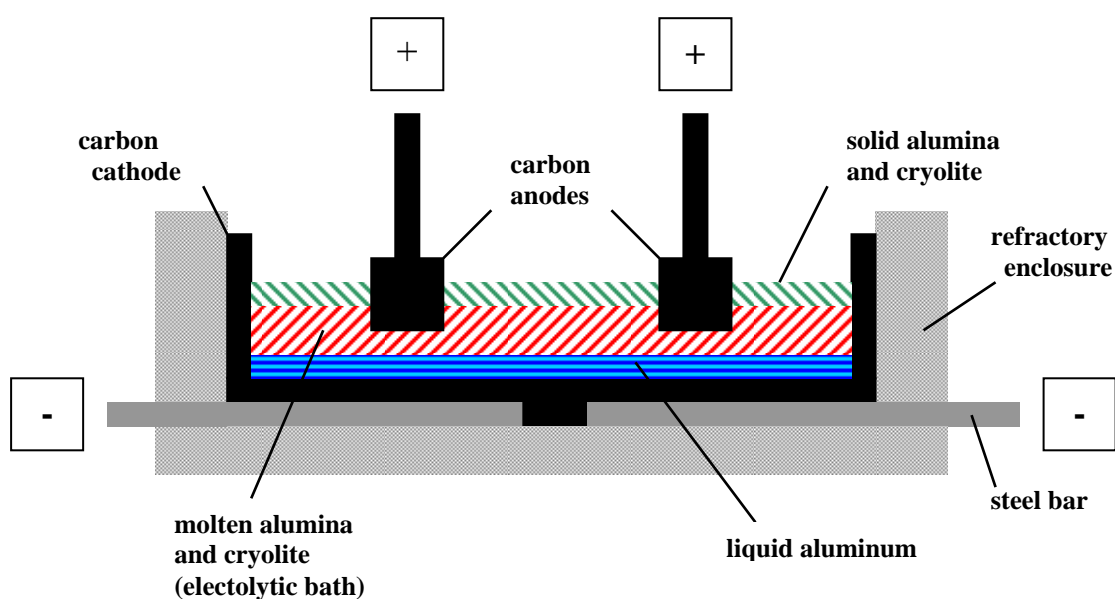


Fig. 6.2. Electrolytic bath used for the production of primary aluminum.

When a voltage is applied (5 volts, typically), an electric current circulates between the anode and two cathodes (both made of carbon). The aluminum is created at the cathodes, following the reaction:



As the aluminum's density (2.7) is higher than the density of the electrolytic bath (often close to 2.0), the liquid aluminum flows at the bottom of the cell, where it is collected by pumping. At the anode, a reaction leading to gaseous carbon dioxide occurs:



Carbon dioxide forms large bubbles that escape into the atmosphere.

¹ Type of rock that contains minerals with important elements including metals.

To keep a high level of efficiency, the alumina content in the electrolytic bath needs to be optimized and to be stable with time. In practice, this is however difficult to control and “anode effects” occur intermittently, when the alumina ore content of the electrolytic bath falls below critical levels required for electrolysis. During anode effects, rapid voltage increases (up to 25 volts to 50 volts) happen, accompanied by an overheating generated by Joule Effect. Anode effects form carbon from the anode and fluorine from the molten cryolite bath, both combine to produce PFCs, mainly tetrafluoride CF_4 (around 90% by mass) and hexafluoroethane C_2F_6 (around 10% by mass). The frequency and duration of anode effects depend primarily on the pot technology and operating procedures. Therefore, emissions of CF_4 and C_2F_6 vary significantly from one aluminum smelter to the next, depending on these parameters. The emission rate, and thus the PFCs concentrations, is highly variable during the anode effect: it rises during each anode effect episode and then rapidly falls to atmospheric background levels when the anode effect is extinguished.

According to the International Aluminum Institute¹, total emissions of CF_4 by the aluminum industry have been reduced by almost 60% between 1990 and 2009, despite the fact that the aluminum production has doubled over the same time period.

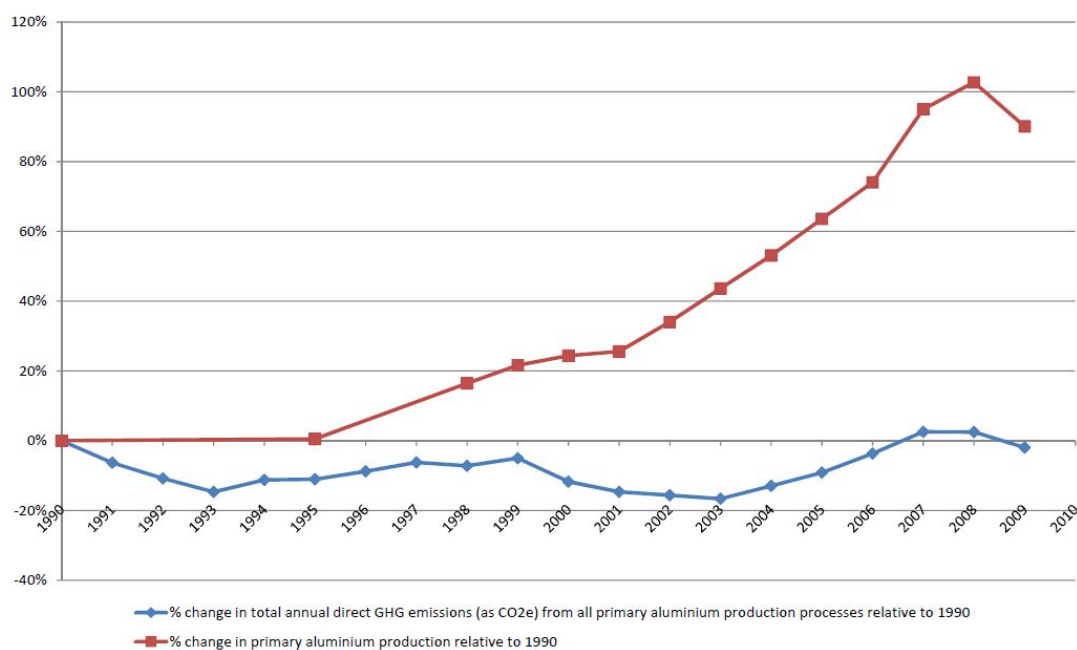


Fig. 6.3. Percentage change (relative to 1990) in primary aluminum production and total direct greenhouse gas emissions from all primary aluminum production processes for the 1990-2009 time period (Figure extracted from IAI, 2010¹).

This decrease results from the overall effort initiated some years ago by the global aluminum industry to reduce their PFCs emissions, with the voluntary objective of a 50% reduction by 2020, on a 2006 baseline. All in all, when considering total direct greenhouse gases (i.e. including mainly CO_2 and PFCs) emissions from all primary aluminum production processes (i.e. bauxite mining, alumina refining, anode production, aluminum smelting and casting), emissions remain within or close to their

¹ International Aluminum Institute, The International Aluminum Institute Report on the Aluminum Industry's Global Perfluorocarbon Gas Emissions Reduction Programme – Results of the 2009 Anode Effect Survey, International Aluminum Institute, London, 2010.

1990 level, despite the fact that the aluminum production has exploded during the last 15 years (Figure 6.3). This essentially stems from the reduction of PFCs emissions evoked above.

In order to dress their PFCs emission inventory, the International Aluminum Institute (IAI) collects anode effect data directly from primary aluminum producers. Participants to the IAI 2009 anode effect survey account for 60% of global primary metal production and for 51% of total industrial CF₄ emissions. The major concern regarding the participation rate is related to the low collaboration from important producers, like China for example (for the 2009 survey, the participation rate by production of China was 1.5%). With a primary aluminum production of 13 million tons in 2009 (i.e. around a third of the worldwide production), China is by far the single largest producing country (and also the largest consumer). To build reliable PFCs emission reports, a greater participation from Chinese facilities is therefore a crucial issue for the global aluminum industry, despite the fact that China has rapidly implemented modern technologies, synonymous with lower PFCs emissions during anode effect episodes.

This lack of information is clearly visible when comparing such kind of inventories with experimental time series, as illustrated on Figure 6.4. This Figure from Mühle et al. [2010] gathers CF₄ global emissions derived from experimental datasets, from numerical simulations or from data collected through inventories. We give below additional details about the origin of the ten different datasets reproduced on Figure 6.4, in the same order as specified in the inserted legend (from the top to the bottom):

- The AGAGE (Advanced Global Atmospheric Gases Experiment) time series results from inversion of AGAGE data with a 2-D box model. AGAGE data consist in ground-based air sample collected in both hemispheres.
- The Harnisch et al. results are CF₄ data derived from balloon measurements in the free troposphere or from surface samples.
- The Khalil et al. time series is derived from ground-based air samples collected in Oregon, Antarctica and Alaska.
- The Worton et al. results are CF₄ emissions reconstructed from firm air measurements performed in Greenland and Antarctica.
- The EDGAR time series results from model estimates based on scientific input data and guidelines on emission calculation methodologies (e.g. emission factors from the Intergovernmental Panel on Climate Change). This latter curve has also been split into two contributions: CF₄ emissions due to the metal industry (see penultimate curve) and CF₄ emissions ascribable to non-metal production (mainly electronic industry, see last curve).
- The UNFCCC results are CF₄ emission estimates based on PFCs emission data gathered by the United Nations Framework Convention on Climate Change process from Annex I reporting countries¹.
- The IAI emissions are CF₄ emissions collected by the International Aluminum Institute throughout their successive anode effect surveys.

¹ The complete list of concerned countries is available at the UNFCCC web pages (<http://unfccc.int>)

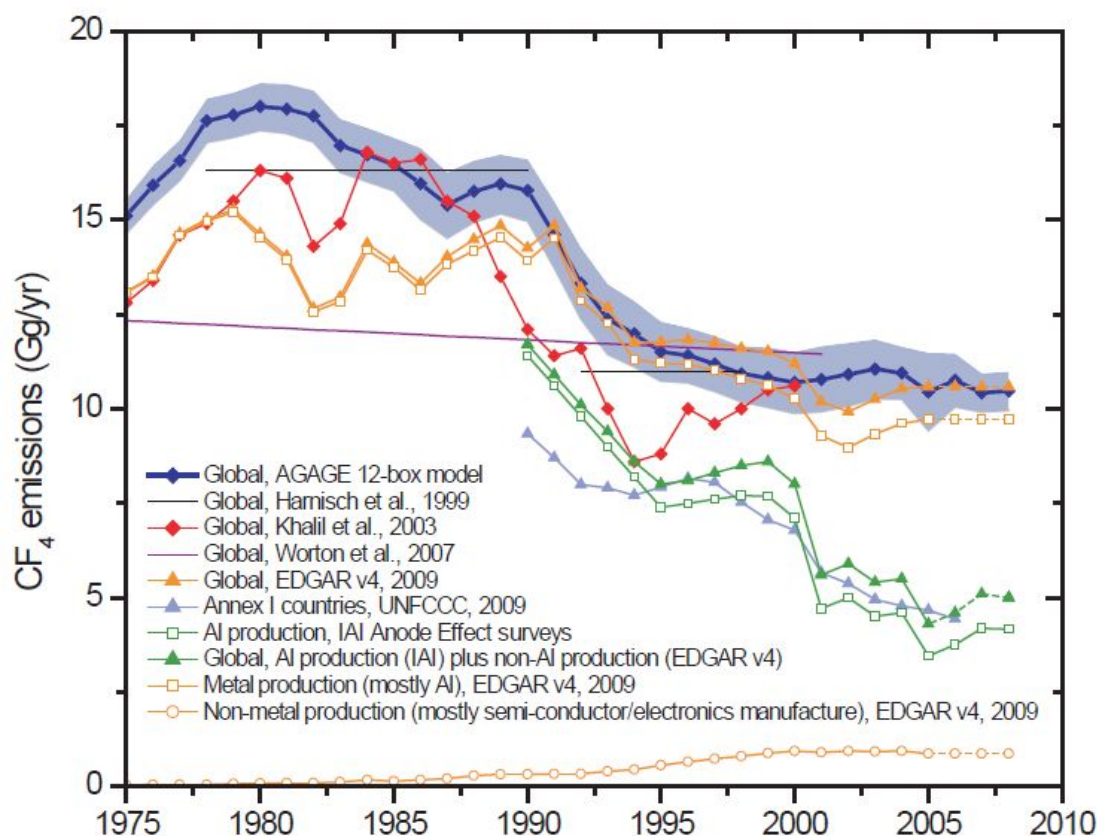


Fig. 6.4. Global CF_4 emissions (in Gg/yr) from several experimental datasets, numerical model inversions or estimates derived from surveys, as specified in the legend (Figure from Mühle et al., 2010).

- The green triangles curve corresponds to the sum of the previous curve (IAI emissions) and the non-metal contribution of the EDGAR estimates (see the last point below).
- The orange open squares curve reproduces the metal industry's contribution of the EDGAR estimates.
- The orange open circles curve reproduces the non-metal industry's contribution of the EDGAR estimates.

Figure 6.4 clearly highlights the breach that exists between experimental or model datasets and emission estimates derived from international inventories. The difference by a factor of two is justified, as already mentioned above, by the lack of data available for large CF_4 emitting countries. Among non-Annex I countries that emit PFCs from aluminum production and that are consequently not included in the UNFCCC emission estimates, one can cite China, Brazil, South Africa, India, United Arab Emirates and Bahrain. Altogether, these countries accounted for 50% of the global aluminum production in 2009¹. This justifies by itself the crucial need for CF_4 emissions reporting at a global scale or, at least, to pursue the collection of experimental CF_4 dataset in order to assess the reliability of the CF_4 emissions reported

¹ Source: the US Geological Survey – Mineral Yearbook. Data are available at the following URL: <http://minerals.usgs.gov/minerals/pubs/commodity/aluminum/mcs-2010-alumi.pdf>

by the industry and to estimate the future accumulation rate of this strong greenhouse gas in the atmosphere.

6.2. FTIR measurements of CF₄ at Jungfraujoch

As already mentioned in section 2.1, the FTIR spectroscopy is an appropriate technique to detect and derive total and partial vertical abundances of atmospheric gases characterized by well-isolated absorption features in the infrared. This is notably the case for CF₄ that presents several absorption lines in the mid-infrared (e.g. its ν_3 band near 1280 cm⁻¹). Retrievals are however challenging since the CF₄ absorption features do not exceed a few percents and are often perturbed by water vapor lines. As a consequence, the inversion of CF₄ abundances by FTIR technique requires high quality observations, in addition to atmospheric conditions as dry as possible. The Jungfraujoch site and observations match these criteria. Therefore, in this section, we set up for the first time and exploit a retrieval strategy allowing to derive CF₄ total vertical abundances from ground-based FTIR spectra.

The text contained in the following pages constitutes the draft version of a manuscript to be submitted this year for publication.

First retrievals of carbon tetrafluoride (CF₄) from ground-based FTIR solar observations: evidence of a relative emission decrease but absolute atmospheric loading increase based on the Jungfraujoch two-decades time series

P. Duchatelet¹, R. Zander¹, E. Mahieu¹, P. Demoulin¹, O. Flock¹, B. Lejeune¹, G. Roland¹, C. Servais¹, and J. Mühle²

¹ Institute of Astrophysics and Geophysics of the University of Liège, B-4000 Liège, Belgium

² Scripps Institution of Oceanography, University of California, San Diego, USA

Abstract

We report on the long-term evolution between 1990 and 2010 of carbon tetrafluoride (CF₄) above the high altitude Jungfraujoch station (Swiss Alps, 46.5°N, 8.0°E, 3580 m asl) derived from the spectrometric analysis of ground-based Fourier transform infrared (FTIR) solar observations. The investigation is based on three micro-windows, one encompassing absorption lines of the CF₄ ν₃ band at 1282 cm⁻¹ and two additional ones allowing to optimally account for two weak interfering gases (ClONO₂ and HNO₃). Our two decades-long time series reveals a steady accumulation of CF₄ above the Jungfraujoch amounting to about 11.5×10¹² molec./cm²/yr, which also corresponds to a mean linear growth close to 1.25%/yr. The corresponding global CF₄ emission required to sustain this increase is found equal to 13.2 Gg/yr. The findings reported here are discussed critically with related results found in the literature.

6.2.1. Introduction

Carbon tetrafluoride (CF₄) or tetrafluoromethane is a perfluorocarbon (PFC-14) increasingly released during the last decades of the previous century by ground level industrial activities [Mühle et al., 2010 and references therein]. Its main anthropogenic source is the primary aluminum (Al) production, during which CF₄ is released through “anode effect” episodes [Khalil et al., 2003]. Since the 1980s, however, CF₄ emissions have also increased due to semiconductor and other electronic devices manufacturing [Tsai et al., 2002]. The only known natural sources of CF₄ are lithospheric emissions [Harnisch et al., 1996, 2000; Harnisch and Eisenhauer, 1998], resulting in a cumulated background contribution to atmospheric carbon tetrafluoride that lies between around 35 and 45 pptv (see for example Table 2 of Mühle et al., 2010; 1 pptv = 10⁻¹² per unit volume).

PFCs are long-lived species with atmospheric lifetimes of many thousand years [i.e. Ravishankara et al., 1993; Mühle et al., 2010 and references therein]. With an atmospheric lifetime estimated to exceed 50000 yrs, CF₄ is among the longest-lived atmospheric gases. Combined with a high global warming potential of at least 7390 [100-yr horizon, WMO, 2007], this compound is a strong greenhouse gas whose emissions are deservedly regulated under the Kyoto Protocol [IPCC, 2001]. As a

result of its very long lifetime, CF₄ shows a nearly constant volume mixing ratio (VMR) profile, close to 75 pptv throughout the atmosphere (e.g. Figure 1 of Zander et al., 1996; Figure 1 of Nassar et al., 2006). According to Table 3 of Nassar et al. [2006], this represents a contribution to total atmospheric fluorine close to 3 %, between 15 and 50 km.

Recent in situ surface measurements of CF₄ in the northern hemisphere [Khalil et al., 2003; Mühle et al., 2010] or remotely from space [Rinsland et al., 2006] have indicated a significant slowdown in the increase rate of atmospheric CF₄, probably ascribable to lower frequency and duration of “anode effects”, given the implementation by the aluminum industry of procedures aiming at the reduction of related PFCs emissions [International (Primary) Aluminum Institute, 1996, 2009]. However, this is partially offset by the increasing aluminum and semiconductor production [Khalil et al., 2003; Worton et al., 2007]. According to AGAGE (Advanced Global Atmospheric Gases Experiment) inversion data with a 2-D box model (see Figure 4 of Mühle et al. [2010]), CF₄ emissions have reached their maximum during the early eighties (~18 Gg/yr), to progressively decline and stabilize at about 11 Gg/yr from 2000 to 2008.

This study reports on the determination of the long-term evolution (1990 - 2010) of the atmospheric carbon tetrafluoride vertical loading above the Jungfraujoch, derived from remote Fourier transform infrared (FTIR) solar observations. We further compare our findings with results available in the literature and with complementary data sets.

6.2.2. FTIR measurements and retrieval strategy

All results presented in this study are derived from the spectrometric analysis of solar spectra recorded under clear-sky conditions at the International Scientific Station of the Jungfraujoch (hereafter ISSJ; Swiss Alps, 46.5°N, 8.0°E, 3580 m asl) with two high resolution FTIR spectrometers between January 1990 and December 2010. Until March 1995, observations were predominantly made with a “home-made” instrument, baked onwards by a faster, more sensitive commercial Bruker-120 HR spectrometer [Delbouille and Roland, 1995].

The observational database analyzed here consists of a subset of all spectra that encompass the most intense infrared ν_3 band of CF₄ at 1282 cm⁻¹ [Goldman et al., 1979] recorded at solar zenith angles (SZA) smaller than 80°. The spectral resolution (defined as the reciprocal of twice the maximum optical path difference) of most observations is 6.1 x 10⁻³ cm⁻¹. Additional higher resolution spectra (4.0 x 10⁻³ cm⁻¹) are also recorded around midday with the fast Bruker instrument, when the sun is close to culmination and SZA variations are slow. Signal-to-noise (S/N) ratios vary between 300 (mainly for earlier home-made observations) up to more than 2500 (average spectra resulting from several successive individual Bruker scans).

The model atmosphere adopted above the 3.58 km altitude Jungfraujoch during the retrieval process consists in a 41 layers scheme: the two lower ones are respectively 0.32 and 0.70 km thick, followed by 24 layers equally spaced by 1.2 km, and by additional layers whose thicknesses progressively increase to reach the 100 km altitude limit. The pressure-temperature profiles adopted are those provided by the

National Centers for Environmental Prediction (NCEP, Washington, DC; see <http://www.ncep.noaa.gov>) and specifically computed for ISSJ on a daily basis. The a priori VMR profile adopted here for retrieving the CF₄ target gas is based on nearly 900 solar occultations performed between February 2004 and August 2009 in the 41-51°N latitude belt by the Atmospheric Chemistry Experiment Fourier Transform Spectrometer (ACE-FTS; Bernath et al., 2005) and is set constant at 72 pptv throughout our model atmosphere.

In this study, we have adopted the line parameters of the HITRAN 2004 spectroscopic dataset [Rothman et al., 2005]. However, as this compilation only contains cross-sections for CF₄, we have used the more recent HITRAN 2008 edition for this gas. According to Rothman et al. [2009], this is the first time that a reliable line list is produced and made available for CF₄. As reported in Rothman et al. [2009], the accuracy of the CF₄ line intensities in HITRAN 2008 remains low, namely about 20%. We have noticed that these more recent CF₄ parameters reduce the fitting residuals by about 3.5% and the retrieved CF₄ total columns by nearly 25%, when compared to the cross sections.

The analysis of the solar spectra retained here was performed with the SFIT-2 v3.91 algorithm, a code specifically developed to retrieve vertical column abundances and VMR profiles of atmospheric gases from FTIR observations [Rinsland et al., 1998]. However, considering the limited information content that characterizes the retrieved vertical distribution of CF₄, its a priori VMR profile was simply scaled during the fitting procedure. In addition, in order to properly account for weak interfering absorption features by ClONO₂ and HNO₃ occurring in the main micro-window selected to retrieve CF₄ vertical abundances (see Frame A of Figure 6.5), we have adopted a two-step retrieval approach, like in Zander et al. [2010]. During a first run, a priori VMR profiles of ClONO₂ and HNO₃ were adjusted from two distinct pre-selected micro-windows extending from 780.00 to 780.355 cm⁻¹ and from 868.00 to 868.68 cm⁻¹, respectively. These intervals are commensurate with those commonly adopted for ClONO₂ and HNO₃ retrievals by FTIR ground-based instruments operating within the frame of the Network for the Detection of Atmospheric Composition Change (NDACC; see <http://www.ndacc.org>; see also Table 2 of Wolff et al., 2008). The results from this first run were then used in a second fitting step that encompasses the 1284.73 – 1285.14 cm⁻¹ interval, in which the a priori VMR vertical distributions of CF₄, N₂O, ¹³CO₂, H₂O (including H₂¹⁶O, H₂¹⁷O and H₂¹⁸O and HDO isotopologues), H₂O₂ and HNO₃ were scaled. A S/N ratio of 500, commensurate with the noise level of most retained spectra, was adopted throughout the fitting process. The exo-atmospheric solar atlas of Farmer and Norton [1989] indicates that no solar absorption features occur in any of the three micro-windows used here.

Frame B of Figure 6.5 displays a sample spectrum observed at ISSJ on 14 February 2010 at a SZA of 65.07° (solid grey line), hence for a geometry corresponding to the simulation of frame A. Red crosses correspond to the synthetic spectrum calculated by the SFIT-2 code and adjusted to the observation during the retrieval process. Corresponding residuals (observed minus calculated signals) are plotted in Frame C. Frame A which reproduces individual contributions of all relevant gases encompassed in the CF₄ micro-window reveals strong interferences by the two most abundant water vapor isotopologues H₂¹⁶O and HDO. These absorptions strongly reduce the fitting quality for wet observational days. Consequently, we have decided to keep the driest

observations of our database. All observations leading to negative retrieved CF_4 VMR values as well as obvious abnormal high or low outliers were also discarded (see next section for details). Ultimately, our retained database upon which the following results and discussion are based, includes 2027 spectra encompassing 686 observational days.

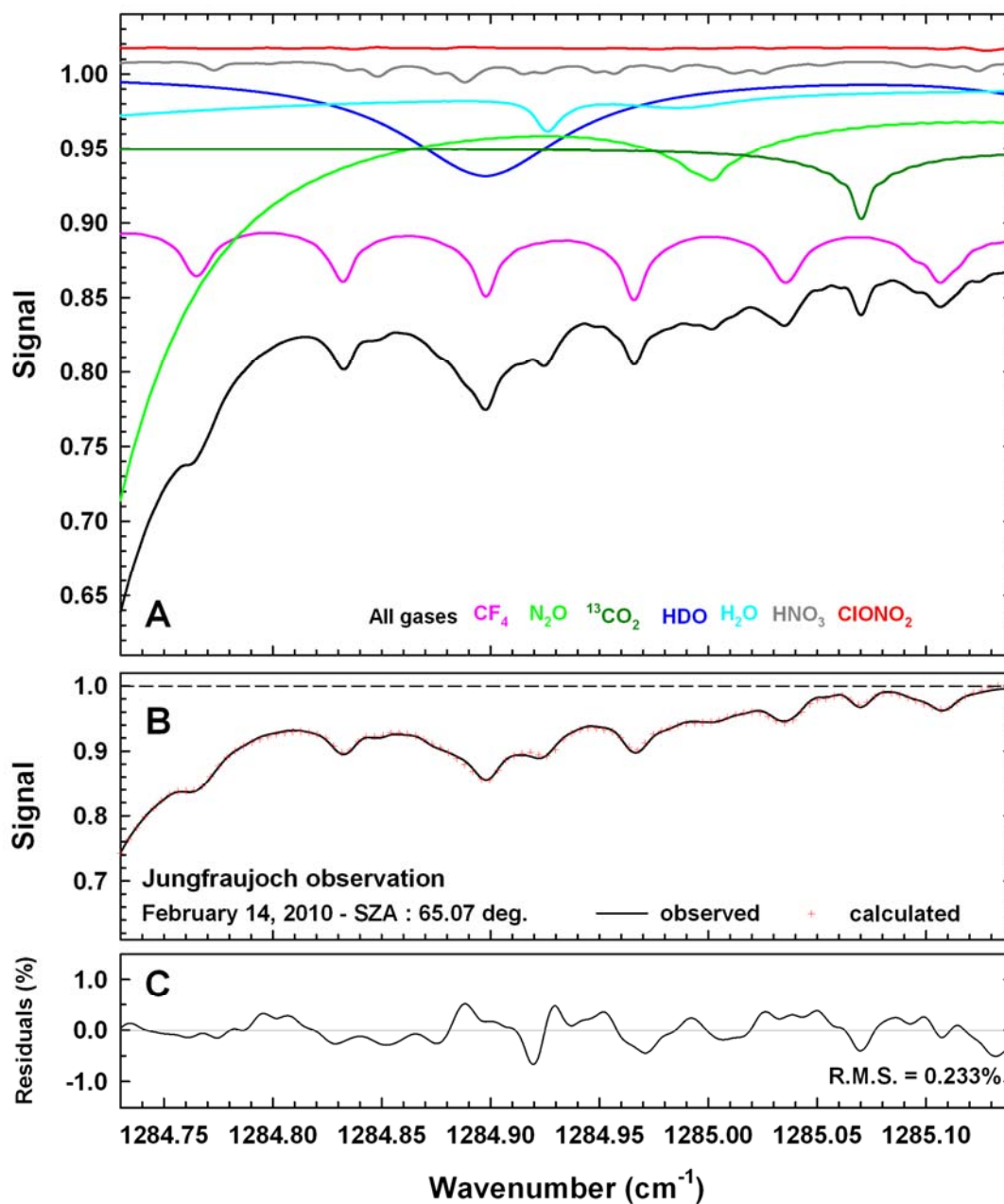


Fig. 6.5. Frame A: Individual absorptions of CF_4 and of the seven more significant interfering gases in the micro-window selected for our CF_4 retrievals (simulated spectrum calculated for a solar zenith angle of 65°). Individual contributions have been vertically scaled for clarity. The H_2O trace combines absorption features of the three isotopologues H_2^{16}O ($\sim 1284.93 \text{ cm}^{-1}$), H_2^{17}O ($\sim 1284.98 \text{ cm}^{-1}$) and H_2^{18}O ($\sim 1284.99 \text{ cm}^{-1}$). Frame B: Typical example of the adjustment with the SFIT-2 code (red crosses) of an FTIR spectrum recorded at the Jungfrauoch on February 2010 (solid black line). Corresponding residuals (observed minus calculated signals) are reproduced in Frame C.

Table 6.1 provides an error budget that characterizes typical individual FTIR CF₄ total column amounts above the Jungfraujoeh. These uncertainties were estimated by applying perturbations listed in the last column of Table 6.1 to a representative subset of dry-days spectra. The systematic error contributions result primarily from uncertainties on line intensities which, according to the uncertainty indices listed in HITRAN files, correspond to 20% and 10 % respectively for CF₄ and water vapor isotopologues.

Error source	Max. error value (%)	Comment
Random errors		
Spectra quality	6	Zero offset, S/N and instruments bias
CF ₄ a priori profile	<0.5	± 50% variability around a priori
H ₂ O a priori profile	1	Change by a factor 2 in a priori slope
HDO a priori profile	2	Change by a factor 2 in a priori slope
NCEP T profiles	<1	±4 K around T profiles
TOTAL	<7	
Systematic errors		
CF ₄ spectroscopy	20	According to HITRAN-08 uncertainties
H ₂ O spectroscopy	<0.5	Assuming the HITRAN-04 uncertainties (10%)
HDO spectroscopy	<0.5	Assuming the HITRAN-04 uncertainties (10%)
ILS and bias	5	± 10% misalignment assumed and instruments bias
TOTAL	<25	

Table 6.1. Impact of major sources of random and systematic errors on typical individual CF₄ total column retrievals above the Jungfraujoeh.

6.2.3. Results and discussion

Our objective selection has led to the CF₄ daily mean pressure-normalized total column time series reproduced in Figure 6.6, with the error bars representing the 1- σ standard deviations around the means. As we have not observed any significant relative difference (i.e. -1.12 ± 4.32 %) between coincident CF₄ total columns derived from the home-made and Bruker spectrometers, carbon tetrafluoride total abundances obtained from both instruments have been included and merged in the daily averages.

The long-term trend analysis of this time series was performed with a statistical tool developed by Gardiner et al. [2008] which is based on a bootstrap resampling method allowing both the long-term and intra-annual variability of a given dataset to be determined, including uncertainties affecting the trend value. This tool was used recently by Duchatelet et al. [2010] to characterize the HF seasonal cycle in three distinct regions of the stratosphere. As indicated in Eq. (3) of Gardiner et al. [2008], the seasonal variability and the trend in an experimental time series are modeled by a function including both a linear component and a Fourier series. In the present study,

a 3rd order Fourier series was used. The solid black line of Figure 6.6 reproduces the linear trend deduced from our complete 1990 – 2010 CF₄ total column time series. It is also worth noting that the amplitude of the CF₄ seasonal cycle deduced with the bootstrap resampling tool (close to 2%) is mostly ascribable (up to 95 %) to the seasonal variation affecting pressure and temperature profiles. All data points (19, not shown) outside the 2 black dotted lines of Figure 6.6, which correspond to the 1- σ standard deviation computed over our dataset, have been considered as outliers and removed from the trend calculations. Hereinafter, all trends have also been derived by systematically considering the central year of the time series as the reference. Unless otherwise specified, all uncertainties computed in this study correspond to the 95% confidence interval (i.e. 2- σ standard deviations).

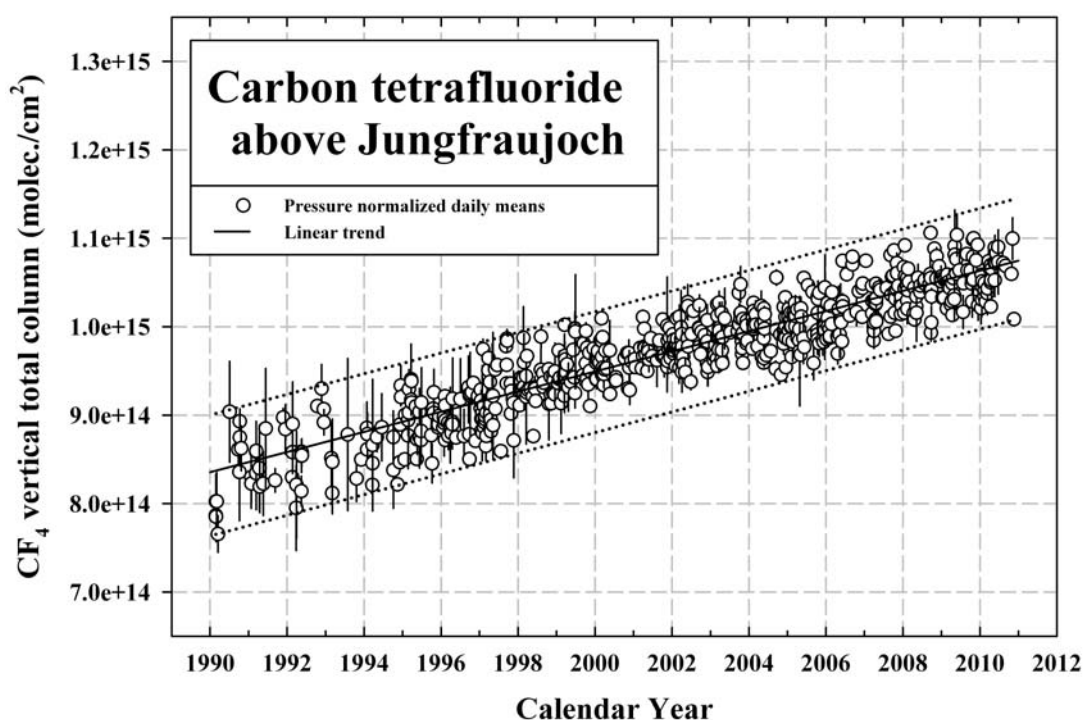


Fig. 6.6. FTIR time series of CF₄ vertical total abundance above the Jungfrauoch. Data points are daily mean values. Corresponding error bars are 1- σ standard deviations. The solid black line reproduces the linear fit through each data points. The 2 black dotted lines are the limits adopted to filter out our data set (see text for details).

The trend analysis of our CF₄ total column time series reproduced in Figure 6.6 provides a linear increase above the Jungfrauoch of $(1.14 \pm 0.04) \times 10^{13}$ molec./cm²/yr over the 1990-2010 time period. This growth rate is equivalent to a linear global accumulation above 3.58 km equal to 8.48 ± 0.26 Gg/yr. As about one third of the atmospheric mass is located below the Jungfrauoch altitude, this translates into a mean global accumulation rate of 13.2 ± 0.4 Gg/yr between 1990 and 2010. Global accumulation rates above Jungfrauoch of 15.4 ± 1.3 Gg/yr and 11.6 ± 0.8 Gg/yr have further been derived from the 1990-2000 and 2000-2010 FTIR CF₄ total column time series subsets, respectively, and are commensurate with the mean CF₄ emissions rates for the similar time periods deduced from Figure 4 of Mühle et al. [2010]. The comparison of these results with the mean increase rate of 18 Gg/yr derived by Zander et al. [1996] from stratospheric CF₄ measurements recorded in the northern hemisphere by the ATMOS (Atmospheric Trace MOlecule Spectroscopy) space

missions of 1985 and 1994 additionally confirms the significant slowing in the CF_4 emission rate that took place during the mid-nineties, as recently highlighted by Mühle et al. [2010, Figure 4].

Our CF_4 total columns have further been converted into VMR amounts in order to allow comparison with in situ and satellite measurements. Such a comparison is illustrated in Figure 6.7, where white dots correspond to the FTIR CF_4 monthly mean VMRs above Jungfraujoch. Due to the simple scaling of our a priori CF_4 vertical distribution during the retrieval procedure (see Section 6.2.2), our derived CF_4 VMR values remain the same at all altitude levels. Grey dots in Figure 6.7 correspond to simulated monthly CF_4 mixing ratios for the northern extra-tropics (i.e. 30-90°N) based on AGAGE air samples and in situ measurements performed at Mace Head (Ireland) and at Trinidad Head (California, USA) by using a lower tropospheric model box [Mühle et al., 2010]. The red up triangles correspond to the CF_4 mean stratospheric concentrations derived from the successive 1985, 1992, 1993 and 1994 ATMOS missions (version 3; Irion et al., 2002) and reported in Table 1 of Rinsland et al. [2006]. Similar stratospheric monthly mean CF_4 amounts derived from ACE-FTS satellite occultation observations (version 3 products) performed between 2004 and 2010 in the same latitude and altitude ranges as in Rinsland et al. [2006] have been reproduced in Figure 6.7 as red down triangles.

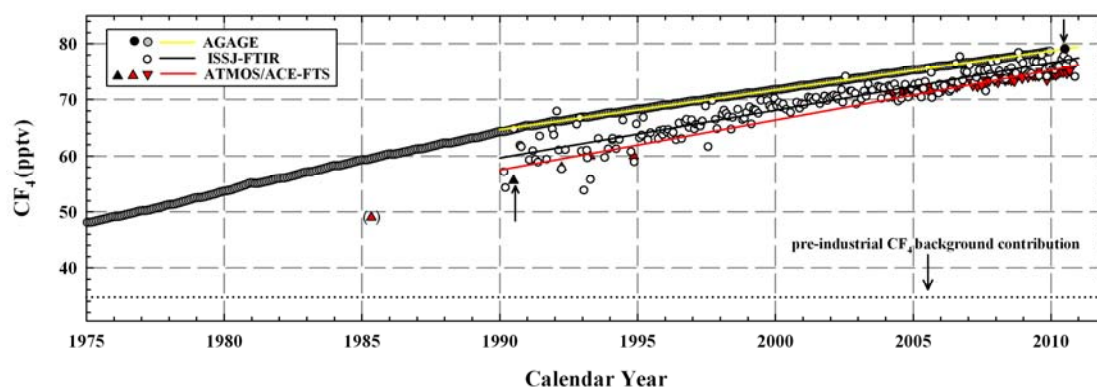


Fig. 6.7. FTIR (black circles), AGAGE (grey dots) and satellite (red up and down triangles) CF_4 monthly VMR time series. For each data set, solid lines reproduce the 1990-2010 linear trend fit. The black symbols identified with the black arrows are extrapolated values for mid-1990 and mid-2010, respectively, derived from the satellite and the AGAGE time series for the 1990-2010 trend calculation (see text for details). The isolated 1985 ATMOS data between parentheses has not been included in such trend computation. The horizontal black dotted line indicates the natural contribution to atmospheric CF_4 , estimated from AGAGE measurements (Mühle et al., 2010).

Using the same statistical tool than above, we have derived the 1990-2010 linear trend of each of these time series; they are reproduced in Figure 6.7 by the yellow, black and red solid lines for the AGAGE, FTIR and space data sets, respectively. However, in order to produce data sets which are consistent with time, we have first completed the ATMOS/ACE-FTS and the AGAGE time series with interpolated CF_4 mean VMR values (see black symbols labeled with black arrows in Figure 6.7). While a CF_4 VMR value for mid-1990 has been derived from the regression line computed over the four ATMOS mean VMRs of 1985, 1992, 1993 and 1994, a CF_4 tropospheric concentration for mid-2010 has been extrapolated from the 1990-2009 AGAGE data set. It is worth noting that for the satellite data set, the 1985 ATMOS value between

parentheses in Figure 6.7 has obviously not been included in our subsequent 1990-2010 trend computation. The horizontal black dotted line in Figure 6.7, which represents the natural contribution of atmospheric CF_4 (34.7 pptv) estimated from AGAGE measurements (see Table 2 of Mühle et al., 2010), has been drawn to better appraise the anthropogenic contribution to the total CF_4 atmospheric burden.

Linear growth rates for the 1990-2010 time period corresponding to the trend fits plotted in Figure 6.7 are expressed in pptv/yr and in %/yr in the two last columns of Table 6.2. With CF_4 growth rates close to 0.85 pptv/yr (i.e. ~ 1.25 %/yr), Table 6.2 indicates that a good agreement is found between FTIR and satellite measurements, while the linear increase deduced from AGAGE is lower, at around 0.70 pptv/yr (i.e. 0.97%/yr). The higher CF_4 growth rate of 1.6 ± 0.6 %/yr derived by Zander et al. [1996] from the 1985 and 1994 ATMOS missions supports the current observed slowing in the rate of atmospheric CF_4 accumulation as already noticed above on the basis of CF_4 emission rates. Such slowing, initiated during the nineties, is also evident from the work by Mühle et al. [2010], that reports CF_4 rise rates close to 1.07 pptv/yr before 1991 and close to 0.7 pptv/yr since 1993. Trend values deduced from our 1990-2000 and 2000-2010 FTIR time series amount to 0.94 ± 0.15 pptv/yr (i.e. 1.46 ± 0.23 %/yr) and to 0.73 ± 0.07 pptv/yr (i.e. 1.01 ± 0.10 %/yr), respectively.

Time series	Mean 1990-2010 growth rate (pptv/yr)	Mean 1990-2010 growth rate (%/yr)
AGAGE	0.700 ± 0.002	0.971 ± 0.003
ISSJ-FTIR	0.85 ± 0.04 [0.21]	1.23 ± 0.06
ATMOS/ACE-FTS	0.89 ± 0.05 [0.14]	1.33 ± 0.07

Table 6.2. CF_4 linear growth rates for the 1990-2010 time period deduced from each time series of Figure 6.7 at the 95% precision level. For FTIR and space measurements, values between brackets specify errors on the trends when the accuracy of the spectroscopic parameters adopted for CF_4 is considered (see text for details).

The time-related spacing between the different data sets displayed in Figure 6.7 are obviously linked, at least partially, to atmospheric transport, provided that the instruments involved sound different regions of the atmosphere, namely the boundary layer for AGAGE, the free troposphere and stratosphere for our FTIR observations, and the stratosphere only for the satellite data. Consequently, changes in the emissions of a long-lived gas at the ground will propagate in the global troposphere within one to two years, and in the stratosphere within 4 to 6 years. Examples of such time delays have been reported by Mühle et al. [2010] for CF_4 in the boundary layer of the northern and southern hemispheres and by Anderson et al. [2000] who found that the inorganic chlorine and fluorine loadings in the stratosphere lag the related organic loading at the ground by 4.5 to 5.5 years. Based on Figure 6.7, the mean time delays for concentrations measured by AGAGE (yellow line) to be observed by FTIR (black line) and by ATMOS/ACE-FTS (red line) are close to 5 and 7 years, respectively, thus commensurate with expectations. With the help of AGAGE CF_4 amounts modeled at higher altitudes, we further plan to quantify more precisely the time necessary for CF_4 to reach the middle stratosphere.

Finally, one should also keep in mind that the significant bias between concentrations presented here can also be ascribable to the inaccuracy affecting the CF_4 spectroscopic parameters. While this uncertainty reaches 20% for the FTIR dataset

(see Table 6.1), CF₄ VMR values derived from ATMOS and ACE-FTS experiments have an estimated spectroscopic accuracy of 10% [Brown et al., 1996; Rinsland et al., 2006]. The values between brackets of Table 6.2 specify errors on the CF₄ 1990-2010 absolute growth rates for both FTIR and space time series when their respective spectroscopic uncertainties are taken into account. These errors have been obtained by considering in our trend analysis the up- and down-scaled FTIR and space time series by 20 and 10%, respectively, and still correspond to the 95% confidence interval. Considering these error values, the differences between FTIR and AGAGE grow rates become non-significant, which is not the case when the AGAGE and ATMOS/ACE-FTS linear trends are compared.

6.2.4. Summary and conclusions

The analysis of solar spectra recorded at the high altitude Jungfraujoch station from 1990 to 2010 has allowed to derive, for the first time, the long term evolution of carbon tetrafluoride (CF₄) column abundance from ground-based remote FTIR measurements. In order to retrieve total vertical abundances of CF₄, we have adopted a two steps retrieval procedure involving three distinct micro-windows allowing to optimally account for critical interferences by the ClONO₂ and HNO₃ gases. The main micro-window encompasses CF₄ absorption features of the ν_3 band around 1285 cm⁻¹. Strong interferences by H₂¹⁶O and HDO, that degrade the fitting quality for wet observational days, have lead us to limit our database to the driest observations, i.e. 2007 individual FTIR spectra recorded over 686 days. The trend analysis of this monthly mean data set reveals a CF₄ mean linear increase equal to 0.85 ± 0.04 pptv/yr (or 1.23 ± 0.06 %/yr) between 1990 and 2010. The corresponding global linear increase of 0.89 ± 0.05 pptv/yr (or 1.33 ± 0.07 %/yr) derived from combined ATMOS and ACE-FTS satellite observations is in good agreement with our findings. Slightly but significantly lower values have been derived from simulations of tropospheric CF₄ concentrations based on ground-based air samples and in situ measurements within the AGAGE network in the northern hemisphere. This discrepancy in the concentrations is partially ascribable to the fact that the three measurements approaches involved in this study sound different regions of the atmosphere, which is confirmed by the better agreement obtained when the AGAGE time series is lagged horizontally. Our trend analysis further confirms the slowdown in the CF₄ growth rate, as a direct consequence of PFCs emission reductions by the aluminum industry, even if the atmospheric CF₄ burden of anthropogenic origin is still increasing since the last twenty years. Our FTIR measurements return CF₄ atmospheric loadings above the Jungfraujoch which increased from about 0.84 to 1.05×10^{15} molec./cm² between 1990 and 2010, which corresponds to a mean anthropogenic emission rate of 13.2 Gg/yr. Because of its extremely long life time and high warming potential, the ongoing increase of the CF₄ atmospheric loading is an important issue in the context of the Earth's global warming. Additional reductions in anthropogenic CF₄ emissions are therefore crucial. The overall consistency that exists between results derived from our FTIR CF₄ time series and other coincident data sets highlights the fact that FTIR measurements appear to be an appropriate technique for long-term monitoring of the CF₄ atmospheric content and its secular evolution. However, in order to significantly reduce the uncertainty levels of the FTIR data presented here, laboratory works dedicated to a more precise determination of CF₄ spectroscopic line parameters definitely remain highly desirable.

Acknowledgments

The present work at University of Liège was primarily supported by the Belgian Federal Science Policy Office, through the A3C and AGACC-II projects. We further acknowledge the support of the GAW-CH program. We thank the International Foundation High Altitude Research Stations Jungfraujoch and Gönnergrat (HFSJG, Bern) and the University of Liège for supporting the facilities needed to perform the observations and their analyses. Thanks are also extended to all members of our research group for regular instrumental development at Jungfraujoch, and for FTIR data acquisition. We further acknowledge observational support by colleagues from the Royal Observatory of Belgium and from the Belgian Institute for Space Aeronomy, Brussels. The Atmospheric Chemistry Experiment (ACE), also known as SCISAT, is a Canadian-led mission mainly supported by the Canadian Space Agency and the Natural Sciences and Engineering Research Council of Canada.

References

Anderson, J., J. M. Russell, S. Solomon, and L. E. Deaver (2000), Halogen Occultation Experiment confirmation of stratospheric chlorine decreases in accordance with the Montreal Protocol, *J. Geophys. Res.*, 105, 4483-4490.

Bernath, P. F., C. T. McElroy, M. C. Abrams, et al. (2005), Atmospheric Chemistry Experiment (ACE): mission overview, *Geophys. Res. Lett.*, 32, doi: 10.1029/2005GL022386.

Also available at <http://orbi.ulg.ac.be/handle/2268/2388>

Brown, L. R., M. R. Gunson, R. A. Toth, et al. (1996), 1995 Atmospheric Trace Molecule Spectroscopy (ATMOS) linelist, *Appl. Opt.*, 35, 2828-2848.

Delbouille, L., and G. Roland (1995), High resolution solar and atmospheric spectroscopy from the Jungfraujoch high-altitude station, *Opt. Eng.*, 34(9), 2736-2739.

Duchatelet, P., P. Demoulin, F. Hase, et al. (2010), Hydrogen fluoride total and partial column time series above the Jungfraujoch from long-term FTIR measurements: Impact of the line-shape model, characterization of the error budget and seasonal cycle, and comparison with satellite and model data, *J. Geophys. Res.*, 115, doi:10.1029/2010JD014677.

Also available at <http://orbi.ulg.ac.be/handle/2268/78827>

Farmer, C. B. and R. H. Norton (1989), A high-resolution atlas of the infrared spectrum of the sun and the earth atmosphere from space, Vol. I The Sun, NASA Reference Publication 1224.

Gardiner, T., A. Forbes, M. De Mazière, et al. (2008), Trend analysis of greenhouse gases over Europe measured by a network of ground-based remote FTIR instruments, *Atmos. Chem. Phys.*, 8, 6719-6727.

Also available at <http://orbi.ulg.ac.be/handle/2268/2545>

Goldman, A., et al. (1979), Identification of the ν_3 vibration-rotation band in infrared balloon-borne solar spectra, *Geophys. Res. Lett.*, 6, 609-612.

Harnisch, J., R. Borchers, P. Fabian, et al. (1996), Effect of natural tetrafluoromethane, *Nature*, 384, p.32.

Harnisch, J. and A. Eisenhauer (1998), Natural CF_4 and SF_6 on Earth, *Geophys. Res. Lett.*, 25, 2401-2404.

Harnisch, J. (2000), Atmospheric perfluorocarbons: sources and concentrations, in *Non- CO_2 greenhouse gases: scientific understanding, control and implementation*, edited by J. Van Ham et al., Kluwer Academic Publishers, Netherlands, 205-210.

Intergovernmental Panel on Climate Change (2001), in *Climate Change 2001: The scientific basis*, edited by J. T. Houghton et al., Univ. of Cambridge Press, New York.

International Aluminum Institute (2009), *The International Aluminum Institute Report on the Aluminum Industry's Global Perfluorocarbon Gas Emissions Reduction Programme – Results of the 2007 Anode Effect Survey*, International Aluminum Institute, London.

International Primary Aluminum Institute (1996), *Anode effect and PFC emission survey 1990-1993*, International Aluminum Institute, London.

Irion, F. W., M. R. Gunson, G. C. Toon, et al. (2002), The Atmospheric Trace Molecule Spectroscopy (ATMOS) experiment version 3 data retrievals, *Appl. Opt.*, 41, 6968-6979.

Also available at <http://orbi.ulg.ac.be/handle/2268/27967>

Khalil, M. A. K., R. A. Rasmussen, J. A. Culbertson, et al. (2003), Atmospheric perfluorocarbons, *Environ. Sci. Technol.*, 37, 4358-4361.

Mühle, J., A. L. Ganesan, B. R. Miller, et al. (2010), Perfluorocarbons in the global atmosphere: tetrafluoromethane, hexafluoromethane, and octafluoropropane, *Atmos. Chem. Phys.*, 10, 5145-5164.

Nassar, R., P. F. Bernath, C. D. Boone, et al. (2006), A global inventory of stratospheric fluorine in 2004 on Atmospheric Chemistry Experiment Fourier transform spectrometer (ACE-FTS) measurements, *J. Geophys. Res.*, 111, D22313, doi: 10.1029/2006JD007395.

Also available at <http://orbi.ulg.ac.be/handle/2268/4285>

Ravishankara, A. R., S. Solomon, A. A. Turnispeed and R. F. Warren (1993), Atmospheric lifetimes of long-lived halogenated species, *Science*, 259, 194-199.

Rinsland, C. P., N. B. Jones, B. J. Connor, et al. (1998), Northern and southern hemisphere ground-based infrared measurements of tropospheric carbon monoxide and ethane, *J. Geophys. Res.*, 103, 28197-28218.

Also available at <http://orbi.ulg.ac.be/handle/2268/14545>

Rinsland, C. P., E. Mahieu, R. Zander, et al. (2006), Long-term stratospheric carbon tetrafluoride (CF₄) increase inferred from 1985-2004 space-based solar occultation measurements, *Geophys. Res. Lett.*, 33, L02808, doi:10.1029/2005GL024709.

Also available at <http://orbi.ulg.ac.be/handle/2268/2410>

Rothman, L. S., D. Jacquemart, A. Barbe, et al. (2005), The HITRAN 2004 molecular spectroscopic database, *J. Quant. Spec. and Rad. Transf.*, 96, 139-204.

Rothman, L. S., I. E. Gordon, A. Barbe, et al. (2009), The HITRAN 2008 molecular spectroscopic database, *J. Quant. Spec. and Rad. Transf.*, 110, 533-572.

Tsai, W.-T., H.-P. Chen and W.-Y. Hsien (2002), A review of uses, environmental hazards and recovery/recycle technologies of perfluorocarbons (PFCs) emissions from the semiconductor manufacturing processes, *J. Loss Prev. Process Ind.*, 15, 65-75.

Wolff, M. A., T. Kerzenmacher, K. Strong, et al. (2008), Validation of HNO₃, ClONO₂, and N₂O₅ from the Atmospheric Chemistry Experiment Fourier Transform Spectrometer (ACE-FTS), *Atmos. Chem. Phys.*, 8, 3529-3562.

Also available at <http://orbi.ulg.ac.be/handle/2268/2667>

World Meteorological Organization (2007), WMO Report No. 50: Scientific Assessment of Ozone Depletion: 2006, P.O. Box 2300, Geneva 2, CH 1211, Switzerland.

Worton, D. R., W. T. Sturges, L. K. Gohar, et al. (2007), Atmospheric trends and radiative forcings of CF₄ and C₂F₆ inferred from firm air, *Environ. Sci. Technol.*, 41, 2184–2189, doi:2110.1021/es061710t.

Zander, R., S. Solomon, E. Mahieu, et al. (1996), Increase of stratospheric carbon tetrafluoride (CF₄) based on ATMOS observations from space, *Geophys. Res. Lett.*, 23, 2353-2356.

Also available at <http://orbi.ulg.ac.be/handle/2268/14567>

Zander, R., P. Duchatelet, E. Mahieu, et al. (2010), Formic acid above the Jungfrauoch during 1985-2007: observed variability, seasonality, but no long-term background evolution, *Atmos. Chem. Phys.*, 10, 10047-10065.

Also available at <http://orbi.ulg.ac.be/handle/2268/80089>

General conclusions and perspectives

The main objective of the present work was to study the long-term evolution of hydrogen fluoride (HF), of carbonyl fluoride (COF₂) and of the total inorganic fluorine loading (F_y) based on historical times series gathered with two high-resolution FTIR spectrometers operated at the International Scientific Station of the Jungfraujoch, one of the primary component of the NDACC for northern midlatitudes. In order to derive total or partial abundance as well as vertical distribution of both HF and COF₂ from FTIR spectra, we have used two different algorithms (SFIT-2 and PROFFIT) which implement the Optimal Estimation Method (OEM). This statistical approach combines the information contained in the FTIR spectra with the best a priori knowledge of the problem. The matrix formalism of the OEM additionally allows to fully characterize the FTIR inversions both in terms of information content and of error budget (see Chapter 2). Throughout this work, our retrieved FTIR products have been compared to satellite data (ATMOS, HALOE and ACE-FTS), to ground-based in situ measurements (AGAGE network) and to numerical runs simulated by two state-of-the-art 3-D models (KASIMA and SLIMCAT).

The retrieval strategy adopted to derive our HF abundances has been described in Chapter 3. Inversions are based on the HF R(1) absorption line and are performed with the PROFFIT 9.5 algorithm. A comparison between HF total columns retrieved with PROFFIT with those derived with the SFIT-2 code has been performed for the first time and indicates no significant bias. The effect of the choice of the line shape model (Voigt or Galatry) adopted to simulate HF absorption lines on HF retrieved total columns and vertical profiles, on fitting quality and on error budget has also been quantified. While the impact on error values remains globally limited, the adoption of a Galatry line shape model during the HF retrievals definitely improves the fitting quality. The error budget shows that the main component of the total systematic error is ascribed to the spectroscopy.

The vertical information content analysis has further indicated that, in addition to its total column, three independent stratospheric HF partial columns (whose altitude limits are 10-17 km, 17-25 km and 25-40 km, respectively) can be derived. For the two upper partial columns, our FTIR HF abundances compare well with those derived from HALOE. The corresponding amounts deduced from ACE-FTS v2.2 measurements are significantly slightly higher than our FTIR products. In addition, the agreement between FTIR data and KASIMA runs is excellent below 25 km and for total columns. The contrary is observed when considering FTIR time series and runs performed by the SLIMCAT model. Based on both FTIR and model total and

partial column time series, we have performed a deep analysis of the HF seasonal cycle that indicates a strong peak-to-peak amplitude ranging from 30 to 40% for HF total columns. The correlational study between HF abundances and tropopause height seasonal cycles further indicates that the HF total column seasonal variability is mainly ascribed to seasonal variations that occur in the lower stratosphere. Our work on HF has been part of a scientific publication and our FTIR HF time series should be archived at the NDACC database very soon.

We have described in Chapter 4 the advantages of using, with SFIT-2, a new retrieval approach based on a multi-spectrum multi-window strategy in order to invert COF₂ amounts from ground-based FTIR solar spectra. While all FTIR spectra recorded during the same day at the same resolution are combined, the retained COF₂ microwindows consist in two sets of three windows located in two distinct spectral regions (ν_1 and ν_4 bands). We have indeed shown that such retrieval procedure significantly increases the information content. In particular, we have demonstrated that our FTIR retrievals are the most sensitive to COF₂ inversion between 17 and 35 km, further allowing special atmospheric events such as polar vortex overpasses to be detected.

The comparison of our FTIR COF₂ partial column time series with the corresponding SLIMCAT data set has indicated no significant bias. However, KASIMA underestimates by about 25% the COF₂ 17-30 km partial columns, probably due to incorrect lower boundary conditions used in this model. All of the three time series also properly reproduce COF₂ seasonal cycle, with relative amplitudes ranging from 5 to 15%. The description and the characterization of the multi-spectrum multi-window approach for COF₂ has been part of a scientific publication and the corresponding time series for Jungfraujoch is archived at the NDACC database.

The combination of the long-term HF and COF₂ data sets, resulting from the retrieval strategies described in Chapters 3 and 4, has led to an FTIR F_y time series spanning the last twenty five-years (Chapter 5). The trend analysis of each of these time series over four successive time periods (namely 1985-1995, 1995-2000, 2000-2005 and 2005-2010) has then been performed. It has so been deduced that after a fifteen-years time period of slowing, the HF growth rate is significantly unchanged since 2005, at about 1.6 %/yr. For COF₂, the slowing observed in its rate of growth before 2005 is more sustained than for HF, particularly for the 2000-2005 time period during which a stabilization in its atmospheric burden has been observed. This stabilization is however followed by a rapid re-increase at a mean rate close to the value that prevailed ten years before (i.e. 2.3 %/yr).

We have further noticed that the important changes observed in the COF₂ accumulation rate during the last ten years do not significantly impact the F_y trend, which remains quite constant since the beginning of this century, at about 1.5 %/yr. That is explained by the fact that the COF₂ contribution to total inorganic fluorine is low with respect to HF. Indeed, based on our FTIR datasets, we have deduced HF and COF₂ partitioning values close to 65% and 30%, respectively. According to KASIMA and SLIMCAT CTMs, the remaining 5% is ascribed to the third inorganic reservoir COCIF. This is about a factor of 2 higher than the COCIF contribution deduced from ACE-FTS occultations observations. Generally, individual contributions to F_y derived from SLIMCAT concur better with FTIR or ACE-FTS values than contributions from

KASIMA, suggesting a less realistic partitioning for this latter model. We have also noticed that all these partitioning values have remained rather unchanged during the last twenty-five years. In addition, the low partitioning for COCIF explains why the rates of growth of this species does not significantly impact the F_y trend values, that could consequently be well evaluated on basis of the combination of HF and COF₂ time series.

We have also proposed some tentative explanations for the observed changes in the COF₂, HF and F_y trends deduced from our FTIR observations, mainly on basis of halogenated source gases emission curves derived from the A1 scenario of WMO. The 5-years time period needed for the source gases to propagate into the stratosphere has also been taken into account in our discussion. Before 2005, the slowing in the stratospheric accumulation rate of the COF₂ precursors – which is a direct consequence of the phase out decisions of the Montreal Protocol – qualitatively explains the significant slowing observed in the rates of growth of COF₂ during the corresponding time period. However, after 2005, the A1 scenario predicts an almost unchanged stratospheric increase for COF₂ precursors that is inconsistent with both FTIR and ACE-FTS observations. Such different behaviors between simulated and experimental data could perhaps result from the fact that the A1 scenario assumed a too slow accumulation rate for HCFC-22 from 2007. The extension of our FTIR time series will allow checking if this COF₂ increase is the beginning of a future rise era associated to the rapid HCFC-22 growth rate. Moreover, the evolution between 1985 and 2010 of the stratospheric organic fluorine loading derived from the A1 scenario is consistent with both our FTIR HF and F_y trend values for the same time period.

We have closed this work by demonstrating, for the first time, the ability to successfully derive carbon tetrafluoride (CF₄) total abundances from ground-based FTIR measurements (Chapter 6). The exceptional observational conditions encountered at Jungfraujoch combined with the very high performances of the spectrometers operating at that site explain such an achievement. Our long-term CF₄ time series has been derived by applying, with the SFIT-2 code, a two steps retrieval procedure that involves three distinct micro-windows allowing to optimally account for critical interferences occurring in the main micro-window that encompasses CF₄ absorption features of its ν_3 band.

The trend analysis of our FTIR 1990-2010 time series confirms the slowdown in the CF₄ growth rate (from 15.4 Gg/yr for the 1990-2000 time period to 11.6 Gg/yr between 2000 and 2010), as a direct consequence of PFCs emission reductions by the aluminum industry, even if the atmospheric CF₄ burden of anthropogenic origin is still increasing since the last twenty years (linear increase close to 1.25 %/yr). This latter result is in good agreement with combined ATMOS and ACE-FTS observations but slightly and significantly lower than the trend deduced from the modeled tropospheric CF₄ AGAGE time series.

As mentioned throughout this work, it is clear that additional efforts in the field of atmospheric fluorine could definitely be led in the continuity of the present thesis. One major issue is related to the accuracy of the spectroscopic parameters, which is often at the basis of large systematic errors on time series and on related trends. That is especially the case for CF₄, for which laboratory works for improving its line parameters definitely remain highly desirable.

In the future, we also plan to check how accurate would be the lonely consideration of HF time series to deduce trends of total inorganic fluorine above Jungfraujoch, with respect to the method used in this work. This would notably allow to precisely quantify the contribution of COF₂ to the F_y trends. Considering the different – and still unexplained – behaviors observed in recent trends of HF and COF₂, the continuation of the long-term monitoring of the vertical abundances of these two species additionally remains mandatory. In the same context, it would be interesting to check if a multi-spectrum multi-window retrieval strategy would be appropriate for COClF retrievals from ground-based FTIR observations. If successful, long-term COClF time series could therefore be used for comparison with model runs, in order to help them to adopt a better partitioning between the three main inorganic fluorine reservoirs. In a more general way, deviations sometimes encountered in this thesis between experimental and simulated time series definitely highlight the crucial need of long-term observational data sets in order to improve the numerical models and emission scenarios.

Finally, simulations performed with numerical models would be also required in order to assess some hypothesis evoked in this work or to complete studies that have been performed here. We notably think to the quantification of the individual contributions of halogenated source gases to the recent changes observed in the fluorine reservoirs trend values. In particular, we believe that in the forthcoming years, a special attention should be devoted to HFC-134a since it could also significantly influence the atmospheric abundance of COF₂. Indeed, despite efforts during the last years to limit HFC-134a emissions through the Kyoto Protocol, this precursor of COF₂ is currently characterized by rates of growth similar to those of HCFC-22 and by an atmospheric content – when weighted by its number of fluorine atoms – larger than 120 pptv. With the help of simulated AGAGE CF₄ stratospheric amounts, we further plan to quantify more precisely the time necessary for CF₄ to reach the middle stratosphere.

Appendix A

This Appendix provides additional information concerning the bootstrap resampling approach that has been used for our trends estimation. This section is mainly based on the work by Gardiner *et al.* [2008].

Let consider an ensemble of m experimental data points recorded with respect to time t (e.g. a FTIR time series) and let designate it by \mathbf{M}_i ($i=1,\dots,m$). Since FTIR measurements very often show significant periodic intra-annual effects (i.e. the seasonal variability), it is commonly appropriate to model these effects by using a Fourier series \mathbf{V} :

$$\mathbf{V}(t, \mathbf{b}) = b_0 + b_1.\cos(2\pi t) + b_2.\sin(2\pi t) + b_3.\cos(4\pi t) + b_4.\sin(4\pi t) + \dots \quad (\text{A.1})$$

where the coefficients b_n are the parameters of the Fourier series contained in the vector \mathbf{b} . The seasonal variation and the linear trend of a FTIR time series could therefore be modeled by a function \mathbf{F} :

$$\mathbf{F}(t, a, \mathbf{b}) = at + \mathbf{V}(t, \mathbf{b}) \quad (\text{A.2})$$

where a is the annual trend in the data, if t is expressed in years. Since the function \mathbf{F} has a linear dependency with respect to the parameters a and \mathbf{b} , it could be fitted to the time series \mathbf{M}_i by using a standard linear least squares method that minimizes the quantity:

$$\sum_{i=1}^m [\mathbf{M}_i - \mathbf{F}(t_i, a, \mathbf{b})]^2 \quad (\text{A.3})$$

with respect to a and \mathbf{b} . Eq. (A.3) simply express the deviations that exist between the measurements and the model function. The estimates a_0 and \mathbf{b}_0 minimizing these deviations thus correspond to the linear trend and to the Fourier coefficients associated to the best function \mathbf{F} that fits the FTIR time series \mathbf{M}_i .

Due to random and significant atmospheric intra-annual variations occurring in FTIR time series (linked, for example, to polar vortex overpasses above the observing site) which are obviously not taken into account by the model function (A.2), the observed distribution of measurements is likely non-Gaussian (non-normal). However, in order to determine precisely the confidence interval associated to the best trend value a_0 , it is necessary to take into account the potential non-normal behavior of the distribution associated with the measurements.

The bootstrap resampling approach is a technique allowing non-normally distributed data to be treated robustly [Gatz and Smith, 1995]. The basic idea is that the distribution associated with the random effects occurring in a data set is best represented by the deviations (A.3).

In other words, once the initial fit is performed, the deviations $\mathbf{R}_{i,0}$ obtained by using the a_0 and \mathbf{b}_0 parameters, i.e.:

$$\mathbf{R}_{i,0} = \mathbf{M}_i - \mathbf{F}(t_i, a_0, \mathbf{b}_0) \quad (\text{A.4})$$

are considered as a discrete representation of the distribution associated with the random effects present in the data set. In the bootstrap resampling method, the deviations (A.4) are then added to the best fit in order to create a new synthetic data set. In practice, m deviations are randomly extracted (with replacement) from the $\mathbf{R}_{i,0}$ set.

If we designate the set of selected deviations by $\mathbf{R}_{i,q}$ ($i=1, \dots, m$), the new synthetic data set given by:

$$\mathbf{M}_{i,q} = \mathbf{F}(t_i, a_0, \mathbf{b}_0) + \mathbf{R}_{i,q} \quad (\text{A.5})$$

is fitted by using the model function (A.2) to provide new best parameters a_q and \mathbf{b}_q . This process is repeated a large number of times ($q=1, \dots, N$ with $N=5000$, typically) to produce a vector \mathbf{A} (of dimension $1 \times N$) which contains the a_q and a matrix \mathbf{B} (of dimension $n \times N$) which contains the \mathbf{b}_q . The 2.5 and 97.5 percentiles of the empirical distribution contained in the vector \mathbf{A} are then used to derive the 95% confidence level characterizing the best trend a_0 .

References

Gardiner, T., A. Forbes, M. De Mazière, et al., Trend analysis of greenhouse gases over Europe measured by a network of ground-based remote FTIR instruments, *Atmos. Chem. Phys.*, 8, 6719-6727, 2008.

Gatz, D. F., and L. Smith, The standard error of a weighted mean concentration – II. Estimating confidence intervals, *Atmos. Environ.*, 29, 1195-1200, 1995.

Appendix B

List of acronyms commonly used in this PhD thesis.

A	Averaging Kernel Matrix
ACE-FTS	Atmospheric Chemistry Experiment – Fourier Transform Spectrometer
AGAGE	Advanced Global Atmospheric Gases Experiment
ATMOS	Atmospheric Trace MOlecule Spectroscopy
CCM	Chemical Climate Model
CFC	ChloroFluoroCarbon
COCIF	Carbonyl ChloroFluoride
COF ₂	Carbonyl Fluoride
CTM	Chemical Transport Model
DOFS	Degree Of Freedom for Signal
EAP	Effective Apodization Parameter
ECMWF	European Center for Medium-range Weather Forecasts
FTIR	Fourier Transform InfraRed
FTS	Fourier Transform Spectrometer
F _y	Inorganic Fluorine
F _y *	Proxy for F _y
GWP	Global Warming Potential
HALOE	HALogen Occultation Experiment
HCFC	HydroChloroFluoroCarbon
HF	Hydrogen Fluoride
HFC	HydroFluoroCarbon
HITRAN	High-resolution TRANsmission molecular absorption database
ILC	Inter-Layer Correlation
ILS	Instrumental Line Shape
IPCC	Intergovernmental Panel on Climate Change
IR	InfraRed
ISSJ	International Scientific Station of the Jungfraujoch
K	Weighting Function Matrix
KASIMA	KARlsruhe SIMulation model of the Middle Atmosphere
NCEP	National Centers for Environmental Prediction
NDACC	Network for the Detection of Atmospheric Composition Change
NOAA/ESRL	National Oceanic and Atmospheric Administration/Earth System Research Laboratory
ODP	Ozone Depletion Potential
OEM	Optimal Estimation Method
OPD	Optical Path Difference
PFC	PerFluoroCarbon
ppbv	Parts Per Billion Volume
ppmv	Parts Per Million Volume
pptv	Parts Per Trillion Volume
PSC	Polar Stratospheric Cloud
PV	Potential Vorticity

SLIMCAT	Single Layer Isentropic Model of Chemistry And Transport
SZA	Solar Zenith Angle
S_a	A priori Covariance Matrix
TP	Tikhonov-Philips
UNEP	United Nations Environment Program
UNFCCC	United Nations Framework Convention on Climate Change
UV	Ultra Violet
VMR	Volume Mixing Ratio
WMO	World Meteorological Organization

Appendix C

This annex gives a list of the scientific publications or contributions to conferences published as part of this PhD thesis.

Peer-reviewed publications

As first author:

Duchatelet, P., E. Mahieu, R. Ruhnke, W. Feng, M. Chipperfield, P. Demoulin, P. Bernath, C. D. Boone, K. A. Walker, C. Servais, and O. Flock, An approach to retrieve information on the carbonyl fluoride (COF₂) vertical distributions above Jungfraujoch by FTIR multi-spectrum multi-window fitting, *Atmos. Chem. Phys.*, 9, 9027-9042, 2009.

Also available at <http://orbi.ulg.ac.be/handle/2268/34266>

Duchatelet P., P. Demoulin, F. Hase, R. Ruhnke, W. Feng, M. P. Chipperfield, P. F. Bernath, C. D. Boone, K. A. Walker, and E. Mahieu, Hydrogen fluoride total and partial column time series above the Jungfraujoch from long-term FTIR measurements: Impact of the line-shape model, characterization of the error budget and seasonal cycle, and comparison with satellite and model data, *J. Geophys. Res.*, 115, D22306, doi10.1029/2010JD014677, 2010.

Also available at <http://orbi.ulg.ac.be/handle/2268/78827>

As contributor:

Mahieu E., P. Duchatelet, P. Demoulin, K. A. Walker, et al., Validation of ACE-FTS v2.2 measurements of HCl, HF, CCl₃F and CCl₂F₂ using space-, balloon-, and ground-based instrument observations, *Atmos. Chem. Phys.*, 8, 6199-6221, 2008.

Also available at <http://orbi.ulg.ac.be/handle/2268/2344>

Montzka, S. A., S. Reimann, A. Engel, K. Kruger, et al., "Ozone-Depleting Substances (ODSs) and Related Chemicals" (Chapter 1) in World Meteorological Organization, WMO Report No. 51: Scientific Assessment of Ozone Depletion: 2010, P.O. Box 2300, Geneva 2, CH 1211, Switzerland, 2011.

Also available at <http://orbi.ulg.ac.be/handle/2268/83929>

Nassar, R., P. F. Bernath, C. D. Boone, S. D. McLeod, R. Skelton, K. A. Walker, C. P. Rinsland, and P. Duchatelet, A global inventory of stratospheric fluorine in 2004 on Atmospheric Chemistry Experiment Fourier transform spectrometer (ACE-FTS) measurements, *J. Geophys. Res.*, 111, D22313, doi: 10.1029/2006JD007395, 2006.

Also available at <http://orbi.ulg.ac.be/handle/2268/4285>

Contributions to conferences

Duchatelet, P., E. Mahieu, P. Demoulin, P. Bernath, C. Boone, K. Walker, S. Wood, and D. Smale, Determination of COF₂ vertical distributions above Jungfraujoch by FTIR and multi-spectra fitting, poster presented at the EGU 2007 General Assembly, 15-20 April 2007, Vienna, Austria, 2007.

Also available at <http://orbi.ulg.ac.be/handle/2268/6949>

Duchatelet, P., E. Mahieu, R. Ruhnke, P. Demoulin, P. Bernath, C. Boone, K. Walker, and S. Wood, Carbonyl fluoride (COF₂) vertical information above Jungfraujoch by FTIR and multi-spectra fitting: error budget and comparisons with KASIMA 3-D CTM model calculations, poster presented at the EGU 2008 General Assembly, 13-18 April 2008, Vienna, Austria, 2008.

Also available at <http://orbi.ulg.ac.be/handle/2268/6946>

Duchatelet, P., P. Demoulin, F. Hase, E. Mahieu, P. Bernath, C. Boone, and K. Walker, Updating hydrogen fluoride (HF) FTIR time series above Jungfraujoch: comparison of two retrieval algorithms and impact of line shape models, poster presented at the EGU 2010 General Assembly, 2-7 May 2010, Vienna, Austria, 2010.

Also available at <http://orbi.ulg.ac.be/handle/2268/65732>

Duchatelet, P., W. Feng, M. Chipperfield, R. Ruhnke, P. Bernath, C. Boone, K. Walker, P. Demoulin, and E. Mahieu, The evolution of the inorganic fluorine budget since the mid-1980s based on FTIR measurements at northern mid-latitudes, poster presented at the EGU 2011 General Assembly, 3-8 April 2011, Vienna, Austria, 2011.

Duchatelet, P., R. Zander, E. Mahieu, J. Mühle, P. Demoulin, B. Lejeune, G. Roland, C. Servais, and O. Flock, First retrievals of carbon tetrafluoride (CF₄) from ground-based FTIR measurements: production and analysis of the two-decadal time series above the Jungfraujoch, poster presented at the EGU 2011 General Assembly, 3-8 April 2011, Vienna, Austria, 2011.



Measurements of hydrogen cyanide (HCN) and acetylene (C₂H₂) from the Infrared Atmospheric Sounding Interferometer (IASI)

V. Duflot¹, D. Hurtmans¹, L. Clarisse¹, Y. R'honi¹, C. Vigouroux², M. De Mazière², E. Mahieu³, C. Servais³, C. Clerbaux^{1,4}, and P.-F. Coheur¹

¹Spectroscopie de l'Atmosphère, Service de Chimie Quantique et Photophysique, Université Libre de Bruxelles, 50 Av. F. D. Roosevelt, 1050, Brussels, Belgium

²Belgian Institute for Space Aeronomy (BIRA-IASB), 3, Av. Circulaire, 1180, Brussels, Belgium

³Institut d'Astrophysique et de Géophysique, Université de Liège, 17, Allée du 6 Août, 4000, Liège, Belgium

⁴Université Paris 06, Université Versailles-St. Quentin, CNRS/INSU, LATMOS-IPSL, Paris, France

Correspondence to: V. Duflot (valentin.duflot@ulb.ac.be)

Received: 5 October 2012 – Published in Atmos. Meas. Tech. Discuss.: 16 October 2012

Revised: 19 March 2013 – Accepted: 20 March 2013 – Published: 9 April 2013

Abstract. Hydrogen cyanide (HCN) and acetylene (C₂H₂) are ubiquitous atmospheric trace gases with medium lifetime, which are frequently used as indicators of combustion sources and as tracers for atmospheric transport and chemistry. Because of their weak infrared absorption, overlapped by the CO₂ Q branch near 720 cm⁻¹, nadir sounders have up to now failed to measure these gases routinely. Taking into account CO₂ line mixing, we provide for the first time extensive measurements of HCN and C₂H₂ total columns at Reunion Island (21° S, 55° E) and Jungfraujoch (46° N, 8° E) in 2009–2010 using observations from the Infrared Atmospheric Sounding Interferometer (IASI). A first order comparison with local ground-based Fourier transform infraRed (FTIR) measurements has been carried out allowing tests of seasonal consistency which is reasonably captured, except for HCN at Jungfraujoch. The IASI data shows a greater tendency to high C₂H₂ values. We also examine a nonspecific biomass burning plume over austral Africa and show that the emission ratios with respect to CO agree with previously reported values.

for HCN are attributed to biomass burning, other sources exist, including emissions by fossil fuel combustion and higher plants, bacteria and fungi. The primary sink of HCN is thought to be ocean uptake (Cicerone and Zellner, 1983; Li et al., 2000). However, the magnitudes of these sources and sinks remain uncertain (Li et al., 2009). For C₂H₂, Xiao et al. (2007) evaluated biofuel combustion to be the dominant source, followed by fossil fuel combustion and biomass burning. Reaction with hydroxyl radical (OH) is the main sink for C₂H₂, which may also act as a precursor of secondary organic aerosols (Volkamer et al., 2009).

Aside from their chemical properties, HCN and C₂H₂ are useful tracers of atmospheric transport. Indeed, with a lifetime of 2–4 weeks (C₂H₂) (Logan et al., 1981) to 2–4 months (HCN) (Li et al., 2000), they are effective indicators of how the large-scale distribution of atmospheric pollutants is influenced by long-range transport of biomass and fossil fuel burning. Moreover, the study of the ratio C₂H₂/CO (carbon monoxide) can also help estimate the age of combustion plumes (Xiao et al., 2007).

There are only a limited number of long-term local measurements of HCN and C₂H₂, mainly from ground-based FTIR at selected stations of the Network for the Detection of Atmospheric Composition Change (NDACC, <http://www.ndacc.org>), even if C₂H₂ is not a regular NDACC target species. Hence, strong uncertainties remain with regard to the magnitude of sources and sinks of HCN and C₂H₂, as well as to their spatial distribution and seasonality

1 Introduction

Biomass burning is a considerable source of atmospheric trace gases and aerosols at a global scale (Crutzen and Andreae, 1990). Examples include hydrogen cyanide (HCN) and acetylene (or ethyne, C₂H₂). While the primary sources

in the atmosphere (Li et al., 2009; Parker et al., 2011). Satellite sounders have provided considerable new information in the past years, with measurements from the Atmospheric Chemistry Experiment (ACE-FTS) (Lupu et al., 2009), the Michelson Interferometer for Passive Atmospheric Sounding (MIPAS) (Wiegele et al., 2012) and the Microwave Limb Sounder (MLS) (Pumphrey et al., 2011). These measurements were all made in limb geometry and consequently mostly in the upper troposphere or higher; also the spatial sampling from these instruments is limited. HCN and C₂H₂ have recently been observed using the IASI infrared nadir-looking hyperspectral sounder in a specific biomass burning plume (Clarisse et al., 2011a), as well as in an anthropogenic pollution plume uplifted in the free troposphere (Clarisse et al., 2011b). The purpose of this paper is to show that HCN and C₂H₂ columns can indeed be routinely retrieved from IASI spectra, even in absence of exceptional columns or uplift mechanisms. Having a twice daily global coverage and a 12 km diameter footprint at nadir, the IASI infrared sounder (Clerbaux et al., 2009) aboard the MetOp-A has an obvious potential for providing measurements of these two species globally, and with higher spatial resolution and temporal sampling than what has been obtained up to now. We describe time series and analyze the seasonality of the columns of these two species above two ground-based FTIR observation sites. We also look into the retrieval performances in a typical biomass burning plume.

2 Retrievals

HCN and C₂H₂ are retrieved from IASI radiance spectra with an optimal estimation method (Rodgers, 2000) implemented in the radiative transfer model *Atmosphit* (Coheur et al., 2005), using absorption bands centered at 713 (ν_2) and 729 (ν_5) cm⁻¹, respectively. Both bands are close to one *Q* branch of CO₂ centered near 720 cm⁻¹, affected by line mixing and hence hampering the retrievals of HCN and C₂H₂ when the CO₂ bands cannot be properly simulated. For instance, Clarisse et al. (2011a) had to remove the 715–725 cm⁻¹ spectral range from their fits for HCN and C₂H₂ as their forward model did not take into account CO₂ line mixing.

The line mixing effect is due to the increasing overlap of *Q* lines with increasing pressure, which is such that the contributions of the various transitions are no more additive and the spectrum cannot be simulated by simply summing up the individual line profiles. This is explained theoretically by the fact that intermolecular collisions induce transfer of absorption intensity among the internal levels defining the optical transitions, thus resulting in intensity exchanges between the various spectral components (Hartmann et al., 2008).

The CO₂ line mixing effects are now taken into account in *Atmosphit* up to 30 km for a wide range of atmospheres (i.e. for a wide range of pressure-temperature profiles up to

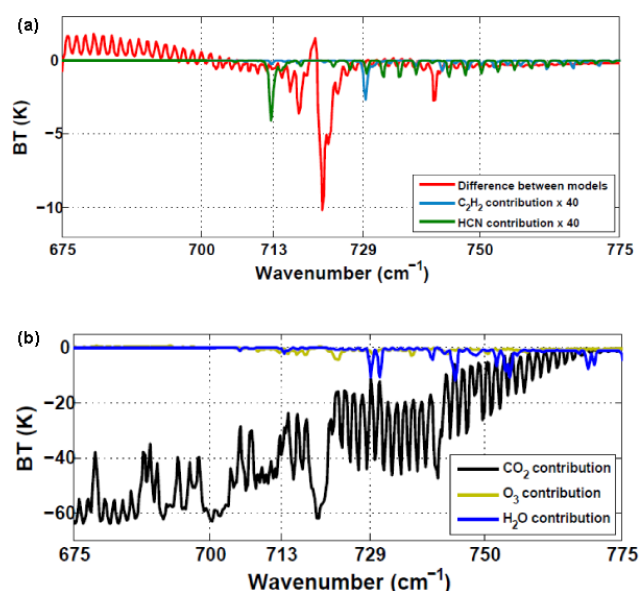


Fig. 1. (a) The red line shows the difference between the forward models with and without CO₂ line mixing considered. To make them visible, contributions of HCN (green line) and C₂H₂ (blue line) are shown for background concentrations multiplied by 40. (b) Contribution of CO₂ (black line), O₃ (ochre line) and H₂O (deep blue line) to a simulated spectrum for background concentrations in a standard atmosphere. Calculations have been made for the US Standard Atmosphere (US Government Printing Office, 1976) with CO₂ concentrations scaled to 390 ppmv.

30 km in order to cover all kind of atmospheres that can be encountered on earth) by calculating absorption cross sections of CO₂ following the method given in Gamache et al. (2012) and Lamouroux et al. (2012a, b). From 30 km to the top of the atmosphere, where collisions are less frequent, the individual line parameters from the HITRAN spectroscopic database (Rothman et al., 2009) are used. These are also used for all the other species in the line-by-line radiative transfer model.

Figure 1a (red line) shows the difference in the forward model between a spectrum simulated with and without line mixing, along with the spectral signature of HCN (ν_2) and C₂H₂(ν_5) (green and blue lines, respectively). It is clear from the residual spectrum that the spectral fits of HCN and C₂H₂ (and thus the retrievals of their abundance) are strongly dependent on the accuracy in the simulation of the CO₂ *Q* branch. For this study, line mixing is included throughout.

The inversion parameters detailed hereafter have been chosen to be the most general as possible. The purpose is to evaluate the capability of the retrieval strategy to detect HCN and C₂H₂ routinely, without any specific assumptions on the vertical distribution of the target and interfering species. The retrievals are performed over the 675 to 775 cm⁻¹ spectral range and CO₂, H₂O and O₃ are fitted simultaneously as interfering species. Figure 1b shows the contributions of each

of these interfering species assuming background concentrations. For HCN and C₂H₂, we use an ad hoc covariance matrix with a 100 % variability and we assume the correlation from layer to layer being a 7 km-length exponential decay. These admittedly over simplistic assumptions allow stabilizing the retrieval without too much influence from the a priori information. The a priori profiles used for the forward model and the retrievals with *Atmosphit* are from the US standard atmospheres when spectra are analyzed over temperate latitudes, and from the standard tropical modeled atmosphere (Anderson et al., 1986) when spectra are analyzed over subtropical latitudes. HCN and C₂H₂ are fitted as profiles, defined by 3 km thick layers from the ground up to 18 km, and by 7 km thick layers from 18 km up to 60 km. However, as the number of degrees of freedom for signal (DOFS) (Rodgers, 2000) is not larger than one for the two species, we analyze in the following only total columns.

3 Comparison with ground based FTIR measurements

We compare in this section HCN and C₂H₂ total columns retrieved from IASI spectra and from ground-based FTIR spectra for the years 2009 and 2010 for two selected NDACC observation sites: Reunion Island (21° S, 55° E) and Jungfraujoch (46° N, 8° E). Note that for both sites and both target species ground-based retrievals are performed in a spectral range between 3250 and 3332 cm⁻¹, which is outside the range covered by IASI. There, the main interfering species is H₂O and the CO₂ line mixing effects are less critical and are not accounted for. Total errors for ground-based measurements at Reunion Island are 17 % for both species and total errors for HCN and C₂H₂ ground-based measurements at Jungfraujoch are 5 and 7 %, respectively. Detailed description of ground-based FTIR data set, retrieval method and error budget can be found in Vigouroux et al. (2012) for Reunion Island and in Mahieu et al. (2008) and Li et al. (2009) for Jungfraujoch. Abundances retrieved from IASI spectra are calculated as columns above the altitude of the stations: 50 m and 3580 m a.m.s.l. (above mean sea level) for Reunion Island and Jungfraujoch, respectively. IASI cloudy spectra were removed from the data set using a 10 % contamination threshold on the cloud fraction in the pixel, and a posterior filter was also applied to remove poor fits, corresponding to a residual root mean square (RMS) greater than 4 × 10⁻⁶ Wm⁻² msr⁻¹. In all, 31 % of the total clear sky spectra fits were removed because of a high RMS fit error. The resulting mean total retrieval errors on the total columns for HCN and C₂H₂ are 53 and 47 % at Reunion Island, and 92 and 77 % at Jungfraujoch. The random (including smoothing) and systematic errors were taken into account. The smoothing error was found to be the most significant for HCN at Reunion Island and for C₂H₂ at Jungfraujoch (32 and 54 %, respectively), and the systematic error

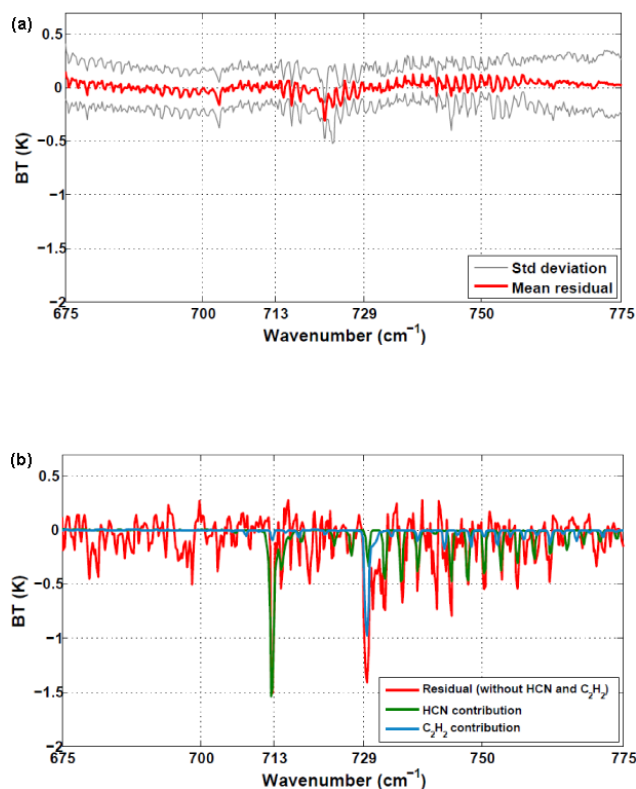


Fig. 2. (a) Residual averaged over the whole set of fits (red line) with its standard deviation (gray lines). (b) Difference (red line) between an observed spectrum on 10 October 2010 at 22.35° S and 33.63° E and the corresponding fitted spectrum when HCN and C₂H₂ have been excluded from the fit. The green and blue lines show the contributions at the top of the atmosphere of HCN and C₂H₂, respectively.

was found to be the major one for C₂H₂ at Reunion Island and for HCN at Jungfraujoch (42 and 75 %, respectively).

Figure 2a shows the residual averaged over the whole set of fits with its standard deviation. One can see that there is no noticeable residual bias except at ~ 720 cm⁻¹ where it reaches -0.3 K, which is close in absolute value to the instrumental noise of 0.2 K in this spectral region (Clerbaux et al., 2009).

Figure 3 shows the mean total column averaging kernels for IASI and for the ground-based FTIR at each of these sites, as well as the a priori profiles used in the retrievals (Fig. 3d). We find that the retrieved profiles from IASI spectra are mostly sensitive to the target species abundance in the mid-upper troposphere, with total column averaging kernels peaking at ~ 9 km for C₂H₂ for both sites, at ~ 10 km for HCN at Jungfraujoch and at ~ 14 km for HCN at Reunion Island. We also find that the retrieved profiles from IASI spectra are more sensitive to HCN abundance at Reunion Island than at Jungfraujoch, while the sensitivity to C₂H₂ abundance is quite similar at both sites. Note that both ground-based instruments have a good sensitivity to HCN

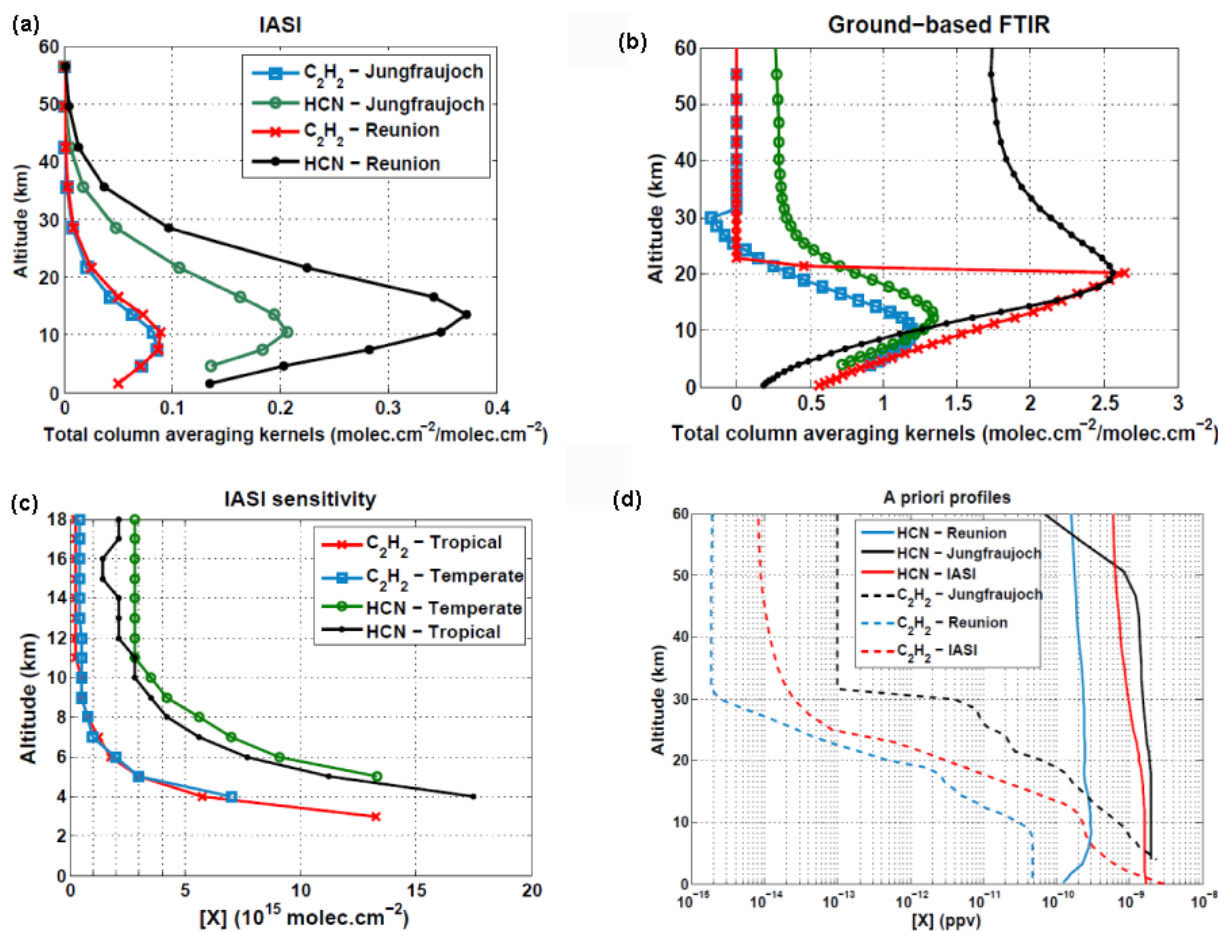


Fig. 3. (a) Total column averaging kernels of IASI and (b) ground-based FTIR in molecules cm⁻² for C₂H₂ at Jungfrauoch (blue squares and lines), HCN at Jungfrauoch (green circles and lines), C₂H₂ at Reunion and HCN at Reunion (black dots and lines). (c) Detectable concentrations by IASI as function of altitude for C₂H₂ in a temperate atmosphere (blue squares and line), C₂H₂ in a tropical atmosphere (red crosses and lines), HCN in a temperate atmosphere (green circles and lines) and HCN in a tropical atmosphere (black dots and line). (d) A priori profiles used in the retrievals for Reunion Island (blue lines), Jungfrauoch (black lines) and IASI (red lines) for HCN (solid lines) and C₂H₂ (dotted lines).

abundance in the stratosphere, while IASI total column averaging kernels decrease rapidly to zero above the tropopause.

To further analyze the sensitivity of IASI to the target species, we simulated spectra with various HCN and C₂H₂ concentrations for the standard temperate and tropical modeled atmospheres with CO₂ concentration scaled to a volume mixing ratio (vmr) of 390 ppmv. For this sensitivity analysis, HCN and C₂H₂ profiles have been constructed, with enhanced concentrations of the species located in a 1 km thick layer, whose altitude is varied from the ground up to 18 km (mean maximal tropical tropopause height). The simulated spectra were compared one by one to a standard spectrum (i.e. with background concentrations of the trace gases) and if the difference between the two spectra was higher than the instrumental spectral noise in this region (0.2 K), then the enhanced concentration was tagged as detectable. Figure 3c summarizes the results. We find that IASI is able to detect

HCN (C₂H₂) concentrations lower than 20×10^{15} mol cm⁻² above 4 km (3 km) for a tropical atmosphere, and above 5 km (4 km) for a temperate atmosphere. For the tropical atmosphere, the maximum sensitivity is reached for HCN (C₂H₂) at 15 km (11 km) with a detectable concentration of 1.4×10^{15} (0.25×10^{15}) mol cm⁻², while for the temperate atmosphere, the maximum sensitivity is reached for HCN (C₂H₂) at 11 km (13 km) with a detectable concentration of 2.8×10^{15} (0.4×10^{15}) mol cm⁻².

Figure 4 shows the comparison between the IASI and the ground-based measurements. IASI retrieved total columns were averaged on a daily basis and on a 1° × 1° area around the observation sites. The comparison of the space and ground-based retrievals was performed taking into account the differences in the a priori profiles and in the sensitivity of the instruments. This has been done following the method given in Rodgers and Connor (2003): the retrieval sets have

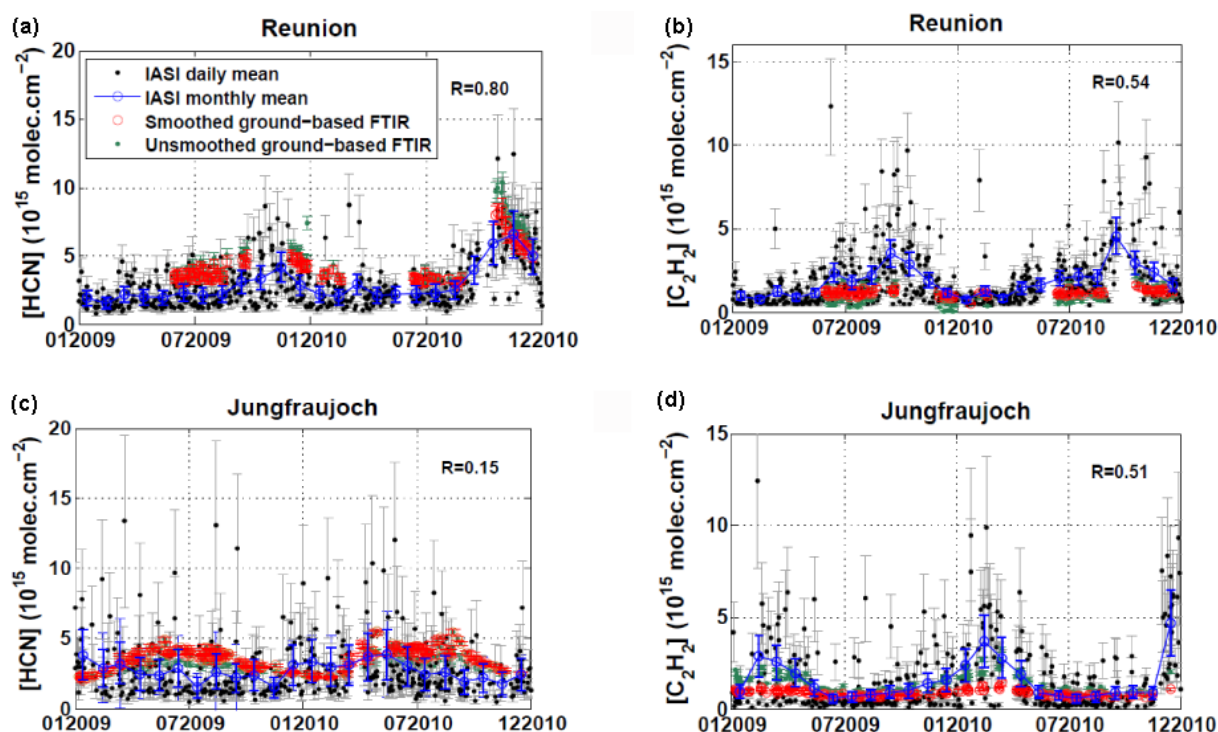


Fig. 4. Time series of HCN and C₂H₂ measurements for Reunion Island (a and b) and Jungfraujoch (c and d). IASI measurements are shown as daily and 1° × 1° means (black dots) with associated total retrieval error (gray lines), and as monthly and 1° × 1° means (blue circles and line) with associated total retrieval error (vertical blue lines). Ground-based FTIR measurements smoothed (unsmoothed) with respect to IASI averaging kernels are shown as daily means with associated total error by red circles and line (green dots and line). Correlation coefficients of daily means are given on each plot: (a) $R = 0.80$ (101 points), (b) $R = 0.54$ (101 points), (c) $R = 0.15$ (174 points), (d) $R = 0.51$ (174 points).

been expressed in terms of departure from the comparison ensemble mean (to take into account the a priori profiles differences), and the ground-based measurements have been smoothed with respect to IASI averaging kernels (to take into account the sensitivity differences). Note that the similarity of the averaging kernel shapes (Fig. 3) for both instruments allows comparisons of total columns to be performed with some confidence. Red circles show ground-based measurements smoothed with respect to IASI averaging kernels, while green dots show unsmoothed ground-based measurements. Note that green dots are not visible when overplotted by red circles.

One can see that there is an overall agreement between the IASI and the ground-based FTIR measurements considering the error bars. An important result from this study is that IASI seems to capture the seasonality in the two species in most of the cases. This is best seen by looking at the IASI monthly mean retrieved total columns (blue circles and line in Fig. 4).

Note that the a priori total columns for ground-based measurements at Reunion Island are 4.9 and 0.8 × 10¹⁵ mol cm⁻² for HCN and C₂H₂, respectively, for ground-based measurements at Jungfraujoch they are 2.8 and 1.3 × 10¹⁵ mol cm⁻² for HCN and C₂H₂, respectively, and for IASI a priori to-

tal columns are 3.4 and 1.2 × 10¹⁵ mol cm⁻² for HCN and C₂H₂, respectively. The retrieved low values for each of the target species, sites and instruments being lower than the a priori total columns, these low values can be considered as significant. The scattering and discrepancies of the IASI daily mean measurements (black dots) are due to the averaging on a 1° × 1° area around the observation sites, and possibly to improvable fits (Fig. 2a).

At Reunion Island the HCN and C₂H₂ peaks occur in October–November and are related to the Southern Hemisphere biomass burning season (Vigouroux et al., 2012). We find maxima of around 5 × 10¹⁵ molec cm⁻² for HCN and 3 × 10¹⁵ molec cm⁻² for C₂H₂, with somewhat larger values in 2010 in comparison to 2009. The seasonality and inter-annual variability matches very well that of the FTIR measurements for HCN (correlation coefficient of 0.80 for the entire daily mean data set) but with the IASI columns being biased low by 1.72 × 10¹⁵ molec cm⁻² when considering the smoothed ground-based measurements. The results are less satisfactory for C₂H₂ (correlation coefficient of 0.54 for the entire daily mean data set) due to a high bias of 0.67 × 10¹⁵ molec cm⁻² for IASI. When considering unsmoothed ground-based measurements and error bars, the

magnitudes of the annual cycles for C₂H₂ at Reunion Island captured by IASI and by ground-based FTIR are quite similar, except for two simultaneous measurements in September 2009. However, there is a lack of ground-based measurements during the biomass burning seasons (especially in October) to check the accordance between the IASI and ground-based measured amplitudes. Ground-based measurements performed in October 2004 and 2007 at Reunion Island show C₂H₂ total columns values up to $\sim 4.5 \times 10^{15}$ molec cm⁻² (Fig. 4 in Vigouroux et al., 2012), which agree with the IASI monthly mean measured columns in October 2009 and 2010. This gives some confidence in the monthly mean peak values observed by IASI. Comparison of additional simultaneous measurements during the biomass burning season is needed to further analyze this.

For the Jungfraujoch site, the agreement between IASI and the FTIR retrieved columns is acceptable for C₂H₂ ($R = 0.51$) and the seasonality is similar. The larger columns caused by the increased C₂H₂ lifetime in winter (Zander et al., 1991) are indeed retrieved in February by both instruments. Similarly to the measurements at Reunion Island, we note an apparent tendency of the ground-based FTIR towards lower columns of C₂H₂ than IASI in the season of peak values: we find a maximum of about 3×10^{15} molec cm⁻² for the IASI monthly mean and the unsmoothed ground-based measurements, and of about 1.8×10^{15} molec cm⁻² for the smoothed ground-based measurements. The most important disagreement is found for HCN at the Jungfraujoch site. The correlation coefficient is only 0.15 and the seasonality observed from the ground, showing higher values from spring to autumn due to northern African and boreal Asian biomass burning activity (Li et al., 2009), is not captured by IASI, which in fact does not seem to show any clear seasonal variation. This is likely to be due to the fact that in a temperate mid-latitude atmosphere, the IASI sensitivity to tropospheric HCN is lower than in a tropical atmosphere as shown in Fig. 3a and c. Moreover, stratospheric variations in HCN abundance, which are likely seen in the FTIR time series (Fig. 3b), are not captured by IASI.

To figure out the precision gained when including the CO₂ line mixing effects in the retrievals, we performed a set of retrievals without CO₂ line mixing on 500 randomly chosen spectra measured above the two sites. We found that including CO₂ line mixing effects in the retrievals decreases the residual of a factor three and increases the percentage of converging retrievals from 52 to 86 %. Moreover, note that if CO₂ line mixing effects are not considered in the IASI retrievals, retrieved total columns from IASI spectra do not agree any more with ground-based measurements: for both sites and both target species, IASI measurements become around one order of magnitude higher than the ground-based ones. This shows the importance of taking into account CO₂ line mixing effects in the forward and inverse models of the retrieval method when using absorption bands close to 720 cm⁻¹.

4 Case study: an austral African biomass burning plume

To further illustrate what can be achieved with the measurements of HCN and C₂H₂ total columns from IASI spectra, this section expounds the study of Clarisse et al. (2011a) for an exceptional fire event, to a regular biomass burning plume. We choose an event that took place over austral Africa and southern Mozambique Channel on 10 October 2010, which constitutes a typical biomass burning plume within the so-called “River of smoke” yearly exiting southern Africa toward the southern Indian Ocean during the Southern Hemisphere biomass burning season (Annegarn et al., 2002; Dufлот et al., 2010). To test the validity of the retrieval method for the widest range of situations, the retrievals were performed as exposed in Sect. 2, without any assumption on the altitude of the plume.

Figure 2b shows in red the difference between an observed spectrum on 10 October AM at 22.35° S and 33.63° E and the corresponding fitted spectrum with HCN and C₂H₂ excluded. A number of absorption features (most notably at 713 and 729 cm⁻¹) exceed the instrumental noise and can be attributed to HCN and C₂H₂ when compared to the top of the atmosphere contribution of these species (shown in green and blue for HCN and C₂H₂, respectively). In fact, the maximum radiance difference reaches 1.5 K for HCN and C₂H₂, which is an order of magnitude larger than the instrumental noise of 0.2 K in this region (Clerbaux et al., 2009).

Figure 5 shows the total columns (in molecules cm⁻²) of CO (retrieved in near-real-time from FORLI software (Hurtmans et al., 2012)), HCN and C₂H₂, respectively, on 10 October. Note that to produce the distributions, the cloudy spectra were removed from the data set and retrievals with errors greater than 100 % were also excluded. The resulting mean total retrieval errors for HCN and C₂H₂ total columns are 26 and 68 %. We see in Fig. 5 that the plume is similar in shape for the 3 species and extends from $\sim (15^\circ \text{S}, 20^\circ \text{E})$ to $\sim (35^\circ \text{S}, 45^\circ \text{E})$. The biomass burning spots detected by the Moderate Resolution Imaging Spectroradiometer (MODIS) in Zambia, Mozambique, Zimbabwe, Botswana and South Africa on 9 and 10 October are shown by black dots in these figures. Due to the closeness of the fires and the typical seasonality of such an event, the detected plume originates very likely from those fires. Maximum columns in the plume reach 5.9×10^{18} for CO, 4.8×10^{16} for HCN and 3.2×10^{16} molecules cm⁻² for C₂H₂.

Figure 6 shows the correlation plot between CO and HCN (black dots) and C₂H₂ (green circles) total columns. The correlation coefficients are 0.72 and 0.68 for HCN and C₂H₂, respectively, for a total of 1397 retrieval points. This high correlation between the three species, which share biomass burning as an important source, confirms the fire origin of the plume. Given the relatively long lifetimes of the species (several weeks to several months) and the vicinity of the fire sources, the slope of each correlation line gives the

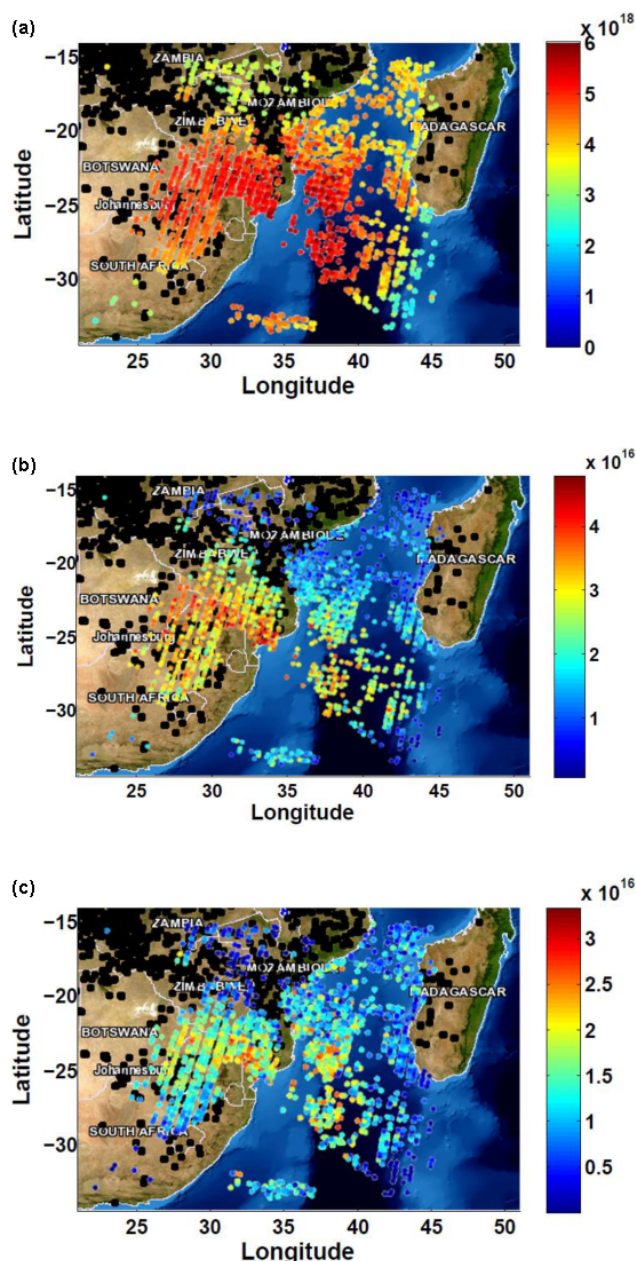


Fig. 5. Total columns of CO (a), HCN (b) and C₂H₂ (c) on 10 October 2010. Fires spots detected by MODIS on 9 and 10 October are shown by the black dots.

emission ratio of the corresponding species: 0.0092 ± 0.0016 and 0.0055 ± 0.0034 for HCN and C₂H₂, respectively. These values compare very well with the emission ratios with respect to CO derived by Sinha et al. (2003) from aircraft measurements over savanna fires in Southern Africa (0.0085 ± 0.0029 for HCN and 0.0043 ± 0.0013 for C₂H₂).

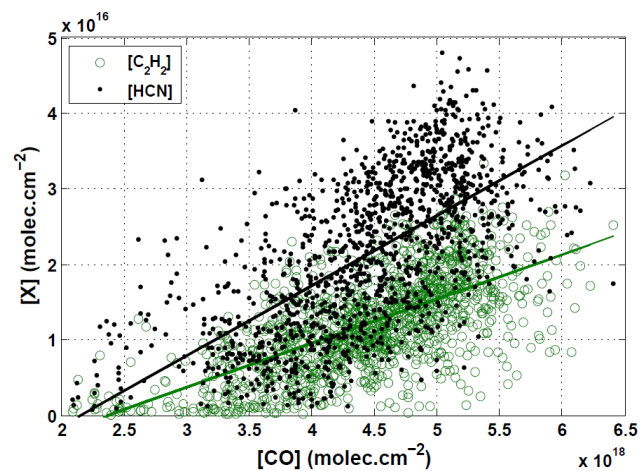


Fig. 6. Correlation plot between CO total columns and HCN (black dots) and C₂H₂ (green circles) total columns for the day and region shown on Fig. 5. The correlation coefficients are 0.72 (1397 points) and 0.68 (1397 points) for HCN and C₂H₂, respectively.

5 Conclusion and outlooks

We have demonstrated the possibility of retrieving HCN and C₂H₂ columns from IASI radiance spectra in the 720 cm⁻¹ region, by properly incorporating CO₂ line mixing in the radiative transfer model. This study shows that the sensitivity of IASI to the two species is mostly in the mid-upper troposphere above 6 km. Total columns have been retrieved for a two year period above Reunion Island and Jungfrau-joch, where routine FTIR measurements are available. The comparison between IASI and FTIR retrieved total columns demonstrates the capabilities of IASI to capture the seasonality in HCN and C₂H₂ in most cases (HCN and to lesser extent C₂H₂ at Reunion Island; and C₂H₂ at Jungfrau-joch). We also note a greater tendency of IASI data to high C₂H₂ values. The absence of seasonality of HCN at Jungfrau-joch could be rationalized by the low sensitivity of IASI to HCN abundance at mid-latitudes. The IASI total columns of HCN (C₂H₂) are shown in this preliminary comparison to be biased low (high) as compared to the smoothed ground-based measurements. A more complete validation study should be carried out to confirm this.

In addition, HCN and C₂H₂ total columns were retrieved within a biomass burning plume over austral Africa and emission ratios with respect to CO were derived from these measurements. The values of 0.0092 ± 0.0016 and 0.0055 ± 0.0034 for HCN and C₂H₂, respectively, agree with values reported in the literature for biomass burning plumes above austral Africa.

In summary, the results presented in this paper have shown for the first time that IASI spectra can be used to establish time series and trends of HCN columns at tropical latitudes and C₂H₂ columns at tropical and temperate latitudes, and both for background or highly concentrated (biomass

burning plume) environments. Due to a low sensitivity of IASI to HCN in a temperate atmosphere, this target specie cannot be considered as retrievable over mid-latitudes areas in background conditions. Work is ongoing to fully exploit the IASI spatial resolution and temporal sampling, to provide global distributions of these two species wherever its sensitivity to background conditions is sufficient.

Acknowledgements. IASI has been developed and built under the responsibility of the Centre National d'Etudes Spatiales (CNES, France). It is flown onboard the Met-Op satellites as part of the EUMETSAT Polar System. The IASI L1 data are received through the EUMETCast near real time data distribution service. Part of the research is supported by EUMETSAT through the O₃SAF project. P. F. C. and L. C. are, respectively, Scientific Research Worker and Research Associate at the F.R.S.-FNRS. The research in Belgium was funded by the F.R.S.-FNRS, the Belgian State Federal Office for Scientific, Technical and Cultural Affairs and the European Space Agency (ESA Prodex arrangements C4000103226 and the AGACC-II project). Financial support by the "Actions de Recherche Concertées" (Communauté Française de Belgique) is also acknowledged. The Liège team further acknowledges the Fédération Wallonie-Bruxelles for supporting travel costs to the Jungfraujoch station and wishes to thank the International Foundation High Altitude Research Stations Jungfraujoch and Gornergrat (HFSJG, Bern) for supporting the facilities needed to perform the observations.

Edited by: H. Worden

References

- Anderson, G. P., Clough, S. A., Kneizys, F. X., Chetwynd, J. H., and Shettle, E. P.: AFGL Atmospheric Constituent Profiles (0–120 km), Environmental Research Papers no. 954, Air Force Geophysics Laboratory, Hanscom AFB Massachusetts, AFGL-TR-86-0110, 1986.
- Annegarn, H. J., Otter, L., Swap, R. J., and Scholes, R. J.: Southern Africa's ecosystem in a test-tube: A perspective on the Southern African Regional Science Initiative (SAFARI 2000), *S. Afr. J. Sci.*, 98, 111–113, 2002.
- Cicerone, R. J. and Zellner, R.: The atmospheric chemistry of hydrogen cyanide (HCN), *J. Geophys. Res.*, 88, 10689–10696, 1983.
- Clarisse, L., R'Honi, Y., Coheur, P.-F., Hurtmans, D., and Clerbaux, C.: Thermal infrared nadir observations of 24 atmospheric gases, *Geophys. Res. Lett.*, 38, L10802, doi:10.1029/2011GL047271, 2011a.
- Clarisse, L., Fromm, M., Ngadi, Y., Emmons, L., Clerbaux, C., Hurtmans, D., and Coheur, P.-F.: Intercontinental transport of anthropogenic sulfur dioxide and other pollutants: An infrared remote sensing case study, *Geophys. Res. Lett.*, 38, L19806, doi:10.1029/2011GL048976, 2011b.
- Clerbaux, C., Boynard, A., Clarisse, L., George, M., Hadji-Lazaro, J., Herbin, H., Hurtmans, D., Pommier, M., Razavi, A., Turquety, S., Wespes, C., and Coheur, P.-F.: Monitoring of atmospheric composition using the thermal infrared IASI/MetOp sounder, *Atmos. Chem. Phys.*, 9, 6041–6054, doi:10.5194/acp-9-6041-2009, 2009.
- Coheur, P.-F., Barret, B., Turquety, S., Hurtmans, D., Hadji-Lazaro, J., and Clerbaux, C.: Retrieval and characterization of ozone vertical profiles from a thermal infrared nadir sounder, *J. Geophys. Res.*, 110, D24303, doi:10.1029/2005JD005845, 2005.
- Crutzen, P. J. and Andreae, M. O.: Biomass burning in the tropics: Impact on atmospheric chemistry and biogeochemical cycles, *Science*, 250, 1669–1678, 1990.
- Dufлот, V., Dils, B., Baray, J.-L., De Mazière, M., Atti, J.-L., Vanhaelewyn, G., Senten, C., Vigouroux, C., Clain, G., and Delmas, R.: Analysis of the origin of the distribution of CO in the subtropical southern Indian Ocean in 2007, *J. Geophys. Res.*, 115, D22106, doi:10.1029/2010JD013994, 2010.
- Gamache, R. R., Lamouroux, J., Laraia, A. L., Hartmann, J.-M., and Boulet, C.: Semiclassical calculations of half-widths and line shifts for transitions in the 30012←00001 and 30013←00001 bands of CO₂, I: Collisions with N₂, *J. Quant. Spectrosc. Ra.*, 113, 976–990, 2012.
- Hartmann, J.-M., Boulet, C., and Robert, D.: Collisional Effects on Molecular Spectra, Laboratory Experiments and Models, Consequences for Applications, Elsevier Edition, ISBN: 978-0-444-52017-3, 2008.
- Hurtmans, D., Coheur, P.-F., Wespes, C., Clarisse, L., Scharf, O., Clerbaux, C., Hadji-Lazaro, J., George, M., and Turquety, S.: FORLI radiative transfer and retrieval code for IASI, *J. Quant. Spectrosc. Ra.*, 113, 1391–1408, 2012.
- Lamouroux, J., Gamache, R. R., Laraia, A. L., Hartmann, J.-M., and Boulet, C.: Semiclassical calculations of half-widths and line shifts for transitions in the 30012←00001 and 30013←00001 bands of CO₂ II: Collisions with O₂ and air, *J. Quant. Spectrosc. Ra.*, 113, 991–1003, 2012a.
- Lamouroux, J., Gamache, R. R., Laraia, A. L., Hartmann, J.-M., and Boulet, C.: Semiclassical calculations of half-widths and line shifts for transitions in the 30012←00001 and 30013←00001 bands of CO₂. III: Self collisions, *J. Quant. Spectrosc. Ra.*, 113, 1536–1546, 2012b.
- Li, Q., Jacob, D., Bey, I., Yantosca, R., Zhao, Y., Kondo, Y., and Notholt, J.: Atmospheric hydrogen cyanide (HCN): Biomass burning source, ocean sink?, *Geophys. Res. Lett.*, 27, 357–360, 2000.
- Li, Q., Palmer, P. I., Pumphrey, H. C., Bernath, P., and Mahieu, E.: What drives the observed variability of HCN in the troposphere and lower stratosphere?, *Atmos. Chem. Phys.*, 9, 8531–8543, doi:10.5194/acp-9-8531-2009, 2009.
- Logan, J. A., Prather, M. J., Wofsy, S. C., and McElroy, M. B.: Tropospheric chemistry: A global perspective, *J. Geophys. Res.*, 86, 7210–7254, 1981.
- Lupu, A., Kaminski, J. W., Neary, L., McConnell, J. C., Toyota, K., Rinsland, C. P., Bernath, P. F., Walker, K. A., Boone, C. D., Nagahama, Y., and Suzuki, K.: Hydrogen cyanide in the upper troposphere: GEM-AQ simulation and comparison with ACE-FTS observations, *Atmos. Chem. Phys.*, 9, 4301–4313, doi:10.5194/acp-9-4301-2009, 2009.
- Mahieu, E., Duchatelet, P., Bernath, P. F., Boone, C. D., De Mazière, M., Demoulin, P., Rinsland, C. P., Servais, C., and Walker, K. A.: Retrievals of C₂H₂ from high-resolution FTIR solar spectra recorded at the Jungfraujoch station (46.5° N) and comparison with ACE-FTS observations, *Geophys. Res. Abstract*, 10,

- EGU2008-A-00000, 2008.
- Parker, R. J., Remedios, J. J., Moore, D. P., and Kanawade, V. P.: Acetylene C₂H₂ retrievals from MIPAS data and regions of enhanced upper tropospheric concentrations in August 2003, *Atmos. Chem. Phys.*, 11, 10243–10257, doi:10.5194/acp-11-10243-2011, 2011.
- Pumphrey, H. C., Santee, M. L., Livesey, N. J., Schwartz, M. J., and Read, W. G.: Microwave Limb Sounder observations of biomass-burning products from the Australian bush fires of February 2009, *Atmos. Chem. Phys.*, 11, 6285–6296, doi:10.5194/acp-11-6285-2011, 2011.
- Rodgers, C. D.: Inverse methods for atmospheric sounding: Theory and Practice, Series on Atmospheric, Oceanic and Planetary Physics – Vol. 2, World Scientific Publishing CO., Singapore, 2000.
- Rodgers, C. D. and Connor, B. J.: Intercomparison of remote sounding instruments, *J. Geophys. Res.*, 108, 4116, doi:10.1029/2002JD002299, 2003.
- Rothman, L. S., Gordon, I. E., Barbe, A., Chris Benner, D., Bernath, P. F., Birk, M., Boudon, V., Brown, L. R., Campargue, A., Champion, J.-P., Chance, K., Coudert, L. H., Dana, V., Devi, V. M., Fally, S., Flaud, J.-M., Gamache, R. R., Goldman, A., Jacquemart, D., Kleiner, I., Lacome, N., Lafferty, W. J., Mandin, J.-Y., Massie, S. T., Mikhailenko, S. N., Miller, C. E., Moazzen-Ahmadi, N., Naumenko, O. V., Nikitin, A. V., Orphal, J., Perevalov, V. I., Perrin, A., Predoi-Cross, A., Rinsland, C. P., Rotger, M., Simeckova, M., Smith, M. A. H., Sung, K., Tashkun, S. A., Tennyson, J., Toth, R. A., Vandaele, A. C., and Vander Auwera, J.: The HITRAN 2008 molecular spectroscopic database, *J. Quant. Spectrosc. Ra.*, 110, 533–572, 2009.
- Sinha, P., Hobbs, P. V., Yokelson, R. J., Bertschi, I. T., Blake, D. R., Simpson, I. J., Gao, S., Kirchstetter, T. W., and Novakov, T.: Emissions of trace gases and particles from savanna fires in southern Africa, *J. Geophys. Res.*, 108, 8487, doi:10.1029/2002JD002325, 2003.
- Standard Atmosphere 1976, National Atmospheric and Oceanic Administration S/T 76-1562, US Government Printing Office, Washington D.C., 1976.
- Vigouroux, C., Stavrakou, T., Whaley, C., Dils, B., Dufлот, V., Hermans, C., Kumps, N., Metzger, J.-M., Scolas, F., Vanhaelewyn, G., Müller, J.-F., Jones, D. B. A., Li, Q., and De Mazière, M.: FTIR time-series of biomass burning products (HCN, C₂H₆, C₂H₂, CH₃OH, and HCOOH) at Reunion Island (21° S, 55° E) and comparisons with model data, *Atmos. Chem. Phys.*, 12, 10367–10385, doi:10.5194/acp-12-10367-2012, 2012.
- Volkamer, R., Ziemann, P. J., and Molina, M. J.: Secondary Organic Aerosol Formation from Acetylene (C₂H₂), seed effect on SOA yields due to organic photochemistry in the aerosol aqueous phase, *Atmos. Chem. Phys.*, 9, 1907–1928, doi:10.5194/acp-9-1907-2009, 2009.
- Wiegele, A., Glatthor, N., Höpfner, M., Grabowski, U., Kellmann, S., Linden, A., Stiller, G., and von Clarmann, T.: Global distributions of C₂H₆, C₂H₂, HCN, and PAN retrieved from MIPAS reduced spectral resolution measurements, *Atmos. Meas. Tech.*, 5, 723–734, doi:10.5194/amt-5-723-2012, 2012.
- Xiao, Y., Jacob, D. J., and Turquety, S.: Atmospheric acetylene and its relationship with CO as an indicator of air mass age, *J. Geophys. Res.-Atmos.*, 112, D12305, doi:10.1029/2006JD008268, 2007.
- Zander, R., Rinsland, C. P., Ehhalt, D. H., Rudolph, J., and Demoulin, P. H.: Vertical column abundance and seasonal cycle of acetylene, C₂H₂, above the Jungfrauoch station, derived from IR solar observations (1991), *J. Atmos. Chem.*, 13, 389–372, 1991.



Acetylene (C₂H₂) and hydrogen cyanide (HCN) from IASI satellite observations: global distributions, validation, and comparison with model

V. Dufлот^{1,2}, C. Wespes¹, L. Clarisse¹, D. Hurtmans¹, Y. Ngadi¹, N. Jones³, C. Paton-Walsh³, J. Hadji-Lazarou⁴, C. Vigouroux⁵, M. De Mazière⁵, J.-M. Metzger⁶, E. Mahieu⁷, C. Servais⁷, F. Hase⁸, M. Schneider⁸, C. Clerbaux^{1,4}, and P.-F. Coheur¹

¹Spectroscopie de l'Atmosphère, Service de Chimie Quantique et Photophysique, Université Libre de Bruxelles (U.L.B.), 50 Av. F. D. Roosevelt, 1050, Brussels, Belgium

²Laboratoire de l'Atmosphère et des Cyclones (LACy), Université de la Réunion, UMR CNRS-Météo-France 8105, Saint-Denis de la Réunion, France

³School of Chemistry, University of Wollongong, Wollongong, New South Wales, Australia

⁴UPMC Université Paris 06, Université Versailles-St. Quentin, CNRS/INSU, LATMOS-IPSL, Paris, France

⁵Belgian Institute for Space Aeronomy (BIRA-IASB), 3, Av. Circulaire, 1180, Brussels, Belgium

⁶UMS3365 de l'OSU-Réunion, CNRS – Université de la Réunion, Saint Denis de la Réunion, France

⁷Institut d'Astrophysique et de Géophysique, Université de Liège, 17, Allée du 6 Août, B-4000, Liège, Belgium

⁸Institute for Meteorology and Climate Research (IMK-ASF), Karlsruhe Institute of Technology, Karlsruhe, Germany

Correspondence to: V. Dufлот (valentin.dufлот@univ-reunion.fr)

Received: 13 April 2015 – Published in Atmos. Chem. Phys. Discuss.: 21 May 2015

Revised: 23 August 2015 – Accepted: 4 September 2015 – Published: 24 September 2015

Abstract. We present global distributions of C₂H₂ and hydrogen cyanide (HCN) total columns derived from the Infrared Atmospheric Sounding Interferometer (IASI) for the years 2008–2010. These distributions are obtained with a fast method allowing to retrieve C₂H₂ abundance globally with a 5 % precision and HCN abundance in the tropical (sub-tropical) belt with a 10 % (25 %) precision. IASI data are compared for validation purposes with ground-based Fourier transform infrared (FTIR) spectrometer measurements at four selected stations. We show that there is an overall agreement between the ground-based and space measurements with correlation coefficients for daily mean measurements ranging from 0.28 to 0.81, depending on the site. Global C₂H₂ and subtropical HCN abundances retrieved from IASI spectra show the expected seasonality linked to variations in the anthropogenic emissions and seasonal biomass burning activity, as well as exceptional events, and are in good agreement with previous spaceborne studies. Total columns simulated by the Model for Ozone and Related Chemical Tracers, version 4 (MOZART-4) are compared to the ground-based

FTIR measurements at the four selected stations. The model is able to capture the seasonality in the two species in most of the cases, with correlation coefficients for daily mean measurements ranging from 0.50 to 0.86, depending on the site. IASI measurements are also compared to the distributions from MOZART-4. Seasonal cycles observed from satellite data are reasonably well reproduced by the model with correlation coefficients ranging from –0.31 to 0.93 for C₂H₂ daily means, and from 0.09 to 0.86 for HCN daily means, depending on the considered region. However, the anthropogenic (biomass burning) emissions used in the model seem to be overestimated (underestimated), and a negative global mean bias of 1 % (16 %) of the model relative to the satellite observations was found for C₂H₂ (HCN).

Table 1. Global HCN and C₂H₂ sources and sinks (Tg yr⁻¹).

	HCN	C ₂ H ₂
Sources		
Biomass burning	0.1–3.18	1.6
Biofuels	0.21	3.3
Fossil fuel	0.02–0.04	1.7
Residential coal	0.2	
Biogenic	0.2	
Total	0.47–3.22	6.6
Sinks		
Ocean uptake	1.1–2.6	
Reaction with OH	0.3	~ 6.6
Photolysis	0.2 × 10 ⁻²	
Reaction with O(¹ D)	0.3 × 10 ⁻³	
Total	1.4–2.9	~ 6.6

1 Introduction

Hydrogen cyanide (HCN) and acetylene (or ethyne; C₂H₂) are ubiquitous atmospheric trace gases with medium lifetime, which are frequently used as indicators of combustion sources and as tracers for atmospheric transport and chemistry. Typical abundances of C₂H₂ (HCN) range from 1 to 2 (2 to 5) × 10¹⁵ molec cm⁻² for background levels, and from 8 to 20 (30 to 40) × 10¹⁵ molec cm⁻² for biomass burning plume levels (Rinsland et al., 1999, 2001, 2002; Zander et al., 1991; Zhao et al., 2002; Clarisse et al., 2011a; Vigouroux et al., 2012; Dufлот et al., 2013). Table 1 summarizes the main sources and sinks for HCN and C₂H₂. For HCN, biomass burning is the primary source, followed by biofuel and fossil fuel combustions, and its primary sink is thought to be ocean uptake (Li et al., 2000, 2003). For C₂H₂, biofuel combustion is considered to be the dominant source, followed by fossil fuel combustion and biomass burning (Xiao et al., 2007). Reaction with hydroxyl radical (OH) is the main sink for C₂H₂, which may also act as a precursor of secondary organic aerosols (Volkamer et al., 2009).

With a tropospheric lifetime of 2–4 weeks for C₂H₂ (Logan et al., 1981) and 5–6 months for HCN (Li et al., 2000; Singh et al., 2003), these two species are interesting tracers for studying atmospheric transport. The study of the ratio C₂H₂/CO (carbon monoxide) can also help to estimate the age of emitted plumes (Xiao et al., 2007).

Long-term local measurements of HCN and C₂H₂ are sparse and mainly performed from ground-based Fourier transform infrared (FTIR) spectrometer at selected stations of the Network for the Detection of Atmospheric Composition Change (NDACC; <http://www.ndacc.org>) (Vigouroux et al., 2012, and references therein). Global distributions of HCN and C₂H₂ may thus help to reduce the uncertainties re-

maining with regard to the magnitude of their sources and sinks, as well as to their spatial distribution and seasonality in the atmosphere (Li et al., 2009; Parker et al., 2011).

Satellite sounders have provided considerable new information in the past years, with measurements from the Atmospheric Chemistry Experiment (ACE-FTIR) (Lupu et al., 2009; González Abad et al., 2011), the Michelson Interferometer for Passive Atmospheric Sounding (MIPAS) (Parker et al., 2011; Wiegeler et al., 2012; Glatthor et al., 2015) and the microwave limb sounder (MLS) (Pumphrey et al., 2011). These measurements were all made in limb geometry and consequently mostly in the upper troposphere or higher; also the spatial sampling from these instruments is limited, making it less well-suited when studying dynamical events on short timescales.

Having a twice daily global coverage and a 12 km diameter footprint at nadir, the Infrared Atmospheric Sounding Interferometer (IASI) infrared sounder (Clerbaux et al., 2009) aboard the MetOp-A satellite has the potential for providing measurements for these two species globally, and with higher spatial resolution and temporal sampling than what has been obtained up to now.

Previous studies have demonstrated that HCN and C₂H₂ can be observed with the IASI infrared nadir-looking hyperspectral sounder, e.g. in a specific biomass burning plume (Clarisse et al., 2011a), as well as in an anthropogenic pollution plume uplifted in the free troposphere (Clarisse et al., 2011b). More recently, Dufлот et al. (2013) have shown that HCN and C₂H₂ columns can be routinely retrieved from IASI spectra, even in the absence of exceptional columns or uplift mechanisms, when CO₂ line mixing is accounted for in the inversion scheme. These previous works were based on an optimal estimation method (OEM) developed and formalized by Rodgers (2000).

In this paper, we first present a fast scheme for the global detection and quantification of HCN and C₂H₂ total columns from IASI spectra. We describe 2008–2010 time series and analyze the seasonality of the columns of these two species above four NDACC sites in comparison with ground-based FTIR measurements. We finally present the global distributions for the years 2008 to 2010 that we compare with model outputs for these two species.

2 Instrument and method

2.1 IASI

IASI is on board the MetOp-A platform launched in a Sun-synchronous orbit around the Earth at the end of 2006. The overpass times are 09:30 and 21:30 MLT (mean local time). Combining the satellite track with a swath of 2200 km, IASI provides global coverage of the Earth twice a day with a footprint of 12 km at nadir. IASI is a Fourier transform spectrometer that measures the thermal infrared radi-

ation emitted by the Earth's surface and atmosphere in the 645–2760 cm⁻¹ spectral range with a spectral resolution of 0.5 cm⁻¹ apodized and a radiometric noise below 0.2 K between 645 and 950 cm⁻¹ at 280 K (Clerbaux et al., 2009). The IASI spectra used in this study are calibrated radiance spectra provided by EUMETCast near-real-time service.

2.2 Retrieval strategy

Up to now, 24 trace gases have been detected from IASI radiance spectra, including HCN and C₂H₂ (see Clarisse et al., 2011a, for the list of detected species), with an OEM (Rodgers, 2000) implemented in a line by line radiative transfer model called Atmosphit (Coheur et al., 2005). In the cases of HCN and C₂H₂, the accuracy of the retrievals has been recently improved by taking into consideration the CO₂ line mixing in the radiative transfer model (Duflot et al., 2013). This retrieval method, relying on spectral fitting, needs a high computational power and is time-consuming, especially when a large number of spectra has to be analyzed and fitted. This is therefore not suitable for providing global-scale concentration distributions of these trace gases in a reasonable time.

One of the commonly used methods for the fast detection of trace gases is the brightness temperature difference (BTD) between a small number of channels, some being sensitive to the target species, some being not. Such a method has been used from IASI spectra for sulfur dioxide (SO₂) (Clarisse et al., 2008) and ammonia (NH₃) (Clarisse et al., 2009). It is of particular interest in operational applications (quick alerts) or when large amounts of data need to be processed. However, relying on a cautious selection of channels to avoid the contamination with other trace gases, the BTD method does not fully exploit all the information contained in hyperspectral measurements. Especially, low concentrations of the target species may not be detected with such a method.

Walker et al. (2011) presented a fast and reliable method for the detection of atmospheric trace gases that fully exploits the spectral range and spectral resolution of hyperspectral instruments in a single retrieval step. They used it to retrieve SO₂ total column from a volcanic plume and NH₃ total column above India. More recently, Van Damme et al. (2014) presented a retrieval scheme to retrieve NH₃ from IASI spectra based on the work of Walker et al. (2011), and introduced a metric called hyperspectral range index (HRI). We use in the present study a similar approach.

2.2.1 Hyperspectral range index

The method used in this study is a non-iterative pseudo retrieval method of a single physical variable or target species x expressed following the formalism developed by Rodgers (2000):

$$\hat{x} = x_0 + (K^T S_\epsilon^{\text{tot}-1} K)^{-1} K^T S_\epsilon^{\text{tot}-1} (y - F(x_0)), \quad (1)$$

where y is the spectral measurements, x_0 is the linearization point, F is the forward model (FM), S_ϵ^{tot} is the covariance of the total error (random + systematic), and the Jacobian K is the derivative of the FM to the target species in a fixed atmosphere.

S_ϵ^{tot} can be estimated considering an appropriate ensemble of N measured spectra, which can be used to build up the total measurement error covariance S_y^{obs} :

$$S_\epsilon^{\text{tot}} \simeq \frac{1}{N-1} \sum_{j=1}^N (y_j - \bar{y})(y_j - \bar{y})^T = S_y^{\text{obs}}, \quad (2)$$

where \bar{y} is the calculated mean spectrum for the ensemble.

To generate S_y^{obs} , we randomly chose one million cloud free spectra observed by IASI all over the world, above both land and sea, during the year 2009. Then, we applied a BTD test to remove the spectra contaminated by the target species. For HCN (C₂H₂), the wave numbers 716.5 and 732 cm⁻¹ (712.25 and 737.75 cm⁻¹) were used as reference channels and 712.5 cm⁻¹ (730 cm⁻¹) was used as test channel (Fig. 1, middle panel). Given the medium lifetimes of the target species (few weeks for C₂H₂ to few months for HCN), and the limited accuracy of the BTD test due to the weak spectral signatures of the target species, it is likely that such randomly chosen and filtered spectra still contain a small amount of the target species whose signal may come out from the noise. This limitation decreases the sensitivity of the method, which is discussed in Sect. 2.2.3.

The spectral ranges considered to compute the S_y^{obs} matrices are 645–800 cm⁻¹ for HCN and 645–845 cm⁻¹ for C₂H₂ (Fig. 1, top panel). These ranges were chosen as they include parts of the spectrum which have a relatively strong signal from the target species but also from the main interfering species (CO₂, H₂O and O₃; Fig. 1, bottom panel) in order to maximize the contrast with the spectral background.

Having calculated S_y^{obs} and G , the HRI of a measured spectrum y can be defined as

$$\text{HRI} = G(y - \bar{y}) \quad (3)$$

with G the measurement contribution function

$$G = (K^T S_y^{\text{obs}-1} K)^{-1} K^T S_y^{\text{obs}-1} \quad (4)$$

The HRI is a dimensionless scalar similar, other than units, to the apparent column retrieved in Walker et al. (2011). Unlike the optimal estimation method, no information about the vertical sensitivity can be extracted. Note also that the use of a fixed Jacobian to calculate HRI does not allow for generating meaningful averaging kernels.

2.2.2 Conversion of HRI into total columns

Having calculated the matrices G for HCN and C₂H₂, each observed spectrum can be associated through Eq. (3) with

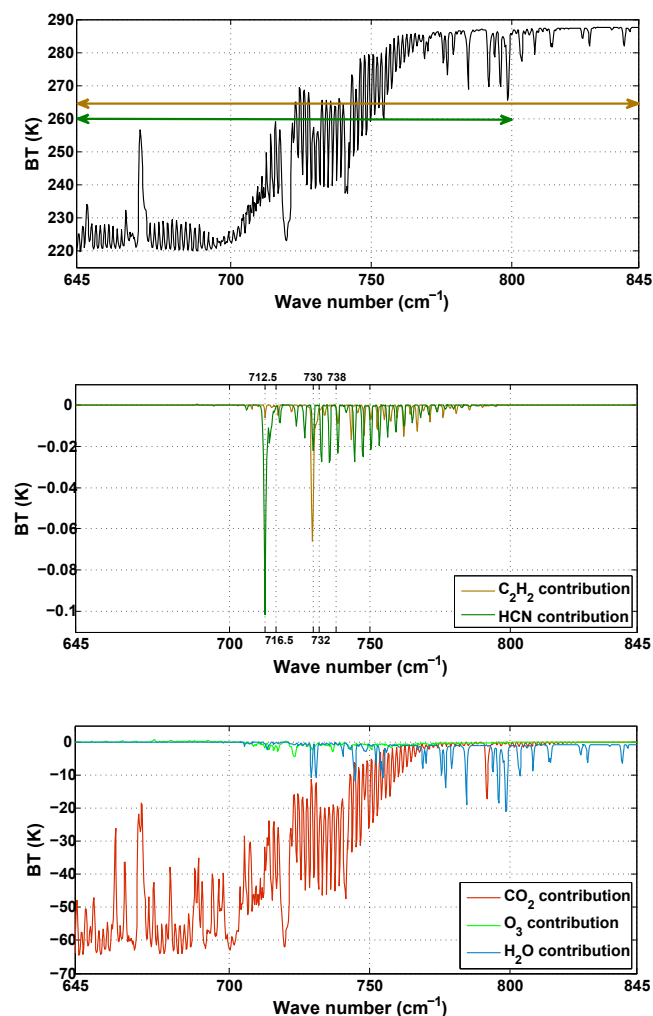


Figure 1. (Top) Simulated spectra in the region of the HCN ν_2 band and C₂H₂ ν_5 band. The green (brown) double sided arrow gives the spectral range used to compute the S_ϵ matrices for HCN (C₂H₂). (Middle) contributions of climatological background levels of HCN and C₂H₂. (Bottom) contribution of CO₂ (red line), O₃ (green line) and H₂O (blue line) to a simulated spectrum for background concentrations. Calculations have been made for the US standard atmosphere (Standard Atmosphere: National Atmospheric and Oceanic Administration, 1976) with CO₂ concentrations scaled to 390 ppmv.

a value of HRI for HCN (HRI_{HCN}) and C₂H₂ ($\text{HRI}_{\text{C}_2\text{H}_2}$). These HRIs are only metrics for determining whether levels of the gas are enhanced with respect to the climatological background over the vertical levels where the instrument is sensitive. For a given atmosphere (atm), the main challenge is then to link the HRI to a column amount of the target molecule, i.e. to find $B_{\text{HCN}_{\text{atm}}}$ and $B_{\text{C}_2\text{H}_2_{\text{atm}}}$ (in molec cm⁻²) such as

$$[X] = B_{X_{\text{atm}}} \text{HRI}_X, \quad (5)$$

[X] being the species abundance in molec cm⁻².

To determine these coefficients linking the HRIs to total column amounts, HCN and C₂H₂ profiles have been constructed, with enhanced concentrations of the species located in a 1 km thick layer, whose altitude is varied from the ground up to 30 km for HCN and up to 20 km for C₂H₂ (the choice of these maximum altitudes are made with respect to the Jacobians of the FM that are shown in Fig. 3 and commented on in Sect. 2.2.3). Each of the constructed profile has been associated with a spectrum through the FM of Atmosphit considering standard absorption profiles from modelled atmospheres for the other species. The associated values of HRI_{HCN} and $\text{HRI}_{\text{C}_2\text{H}_2}$ have then been computed for each of the simulated spectra. Figure 2 shows the look up tables (LUTs) of HRI_{HCN} (top) and $\text{HRI}_{\text{C}_2\text{H}_2}$ (bottom) as a function of the abundance of the target molecule and of the altitude of the polluted layer in a standard tropical modelled atmosphere (Anderson et al., 1986). Similar LUTs have been computed for standard temperate (US standard atmosphere) and polar (Anderson et al., 1986) atmospheres (data not shown). The satellite viewing angles were taken into account in the HRI calculation similarly to Van Damme et al. (2014). One can see that, for a given atmosphere and for a given altitude of the polluted layer, the abundances of both species linearly depend on the HRI value, which validates Eq. (5). For a given atm and a given species X, the different values of B with respect to the altitude z of the polluted layer will be noted $b_{X_{\text{atm}}}(z)$ and $k_{X_{\text{atm}}}(z)$ (in molec cm⁻²) in the following.

Figure 3 shows the normalized Jacobians of the FM for HCN and C₂H₂ averaged over the spectral ranges given in Sect. 2.2.1 (645–800 cm⁻¹ for HCN and 645–845 cm⁻¹ for C₂H₂) and for each of the three standard modelled atmospheres. These Jacobians express the sensitivity of the FM, i.e. both the radiative transfer model and IASI (through its instrumental function), to the target species abundance X in a fixed atm:

$$\begin{aligned} K_{X_{\text{atm}}} &= \left[\frac{\partial F_{\text{atm}}}{\partial X}(z_1) \dots \frac{\partial F_{\text{atm}}}{\partial X}(z_n) \right] \\ &= [k_{X_{\text{atm}}}(z_1) \dots k_{X_{\text{atm}}}(z_n)]. \end{aligned} \quad (6)$$

We then obtain the coefficients $B_{X_{\text{atm}}}$ by multiplying the $b_{X_{\text{atm}}}(z)$ by the value of the Jacobian at the altitude z:

$$\begin{aligned} B_{X_{\text{atm}}} &= \sum_{i=1}^n (b_{X_{\text{atm}}}(z_i) \times k_{X_{\text{atm}}}(z_i)) \\ \text{with } \sum_{i=1}^n k_{X_{\text{atm}}}(z_i) &= 1. \end{aligned} \quad (7)$$

Applying this method to the three standard modelled atmospheres (tropical, temperate and polar), we get a B_X value for each, which we have associated with the corresponding range of latitude ($[\pm 20^\circ]$, $[\pm 45^\circ : \pm 60^\circ]$, $[\pm 75^\circ : \pm 90^\circ]$, respectively), and linearly interpolated between. Figure 4 gives the resulting values of B_{HCN} (blue) and $B_{\text{C}_2\text{H}_2}$ (green) in a function of the latitude.

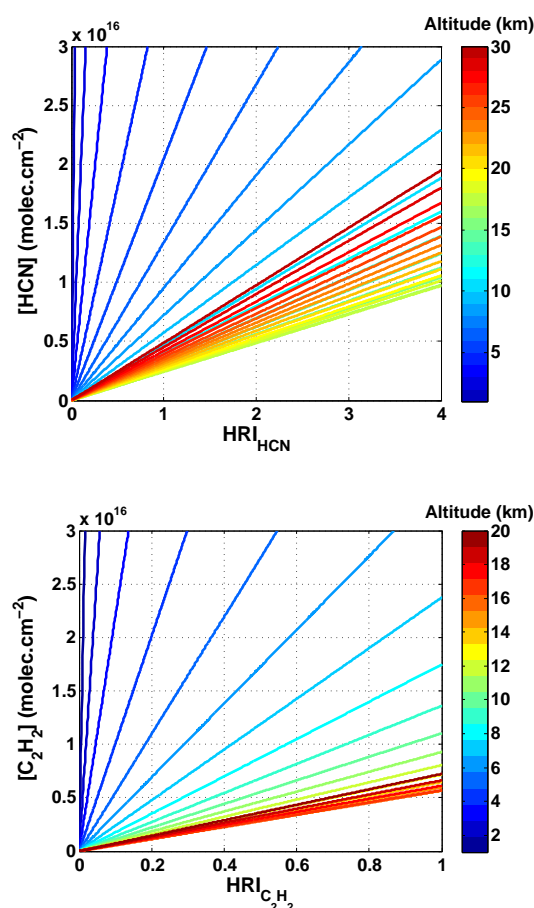


Figure 2. Variations of the HRI with HCN (top) and C₂H₂ (bottom) column (molec cm⁻²) integrated over the 1 km thick polluted layer in a standard modelled subtropical atmosphere from forward model simulations. The colour scale gives the altitude of the polluted layer.

2.2.3 Sensitivity and stability of the method

The sensitivity of the method can be assessed from the Jacobians presented in Fig. 3. For HCN, one can see that there is no sensitivity at the surface and above ~ 30 km, and the altitude of the sensitivity peak is located close to the tropopause at ~ 9 km, ~ 11 km and ~ 14 km for the polar, temperate and tropical atmospheres, respectively. For C₂H₂, there is no sensitivity above ~ 20 km, and the maximum sensitivity is reached at ~ 8, ~ 10 and ~ 11 km for the polar, temperate and tropical atmospheres, respectively. The vertical distribution in a standard temperate atmosphere (US standard atmosphere) is also shown for both species in Fig. 3. These standard distributions agree reasonably well (in shape and value) with observed profiles exhibited in previous studies (e.g. Li et al., 2003; Xiao et al., 2007). The C₂H₂ Jacobians match quite well with the standard distribution of the molecule (i.e. from the ground up to ~ 20 km), with somehow a lack of sensitivity close to the ground where C₂H₂ is the most abundant. For HCN, which shows a nearly “flat” vertical distribution up

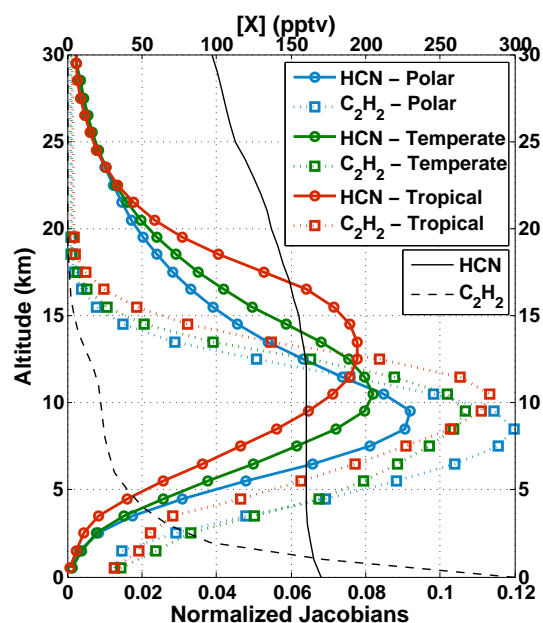


Figure 3. Normalized Jacobians of the forward model implemented in Atmosphit for HCN (solid lines) and C₂H₂ (dotted lines) and for the standard modelled polar (blue lines), temperate (green lines) and subtropical (red lines) atmospheres. These are averaged Jacobians over the spectral ranges 645–800 cm⁻¹ for HCN and 645–845 cm⁻¹ for C₂H₂. Are also plotted the HCN (black line) and C₂H₂ (black dashed line) vertical distributions in a standard temperate atmosphere.

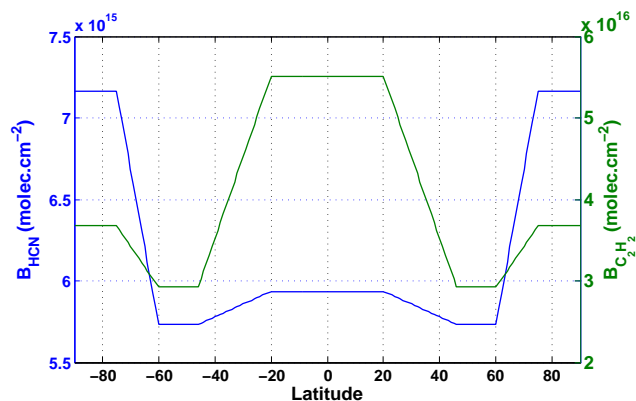


Figure 4. Values of B_{HCN} (blue) and $B_{\text{C}_2\text{H}_2}$ (green) as a function of the latitude.

to 30 km, the Jacobians show a lack of sensitivity close to the ground and above 30 km, where HCN is still present (HCN distribution decreases down to 60 pptv at 60 km – data not shown).

The HRIs presented here above are sensitive to the abundance of the target species – this is what they are made for – and to their vertical distribution. However, once cloudy spectra have been discarded, the measured column amount may also depend on (1) the proper suppression of the spectral

background, (2) the conditions of thermal contrast (TC) with the surface, and (3) the accuracy of the FM to simulate the spectra used to build up the LUTs. The latter was discussed already by Dufлот et al. (2013). In order to test the impact of the two first factors (spectral background suppression and TC) on the retrieved column amount, HCN and C₂H₂ profiles have been constructed with varying TC and concentrations of the interfering and target species. In general thermal contrast can be defined as the temperature difference between the surface and the air temperature at some altitude of interest. We consider here the same definition for the TC as in Van Damme et al. (2014): the TC is defined here as the difference between the skin (surface) temperature and that of the air at an altitude of 1.5 km. These variations in interfering species abundances and TC were considered to be independent and were taken within the range $\pm 2\%$ for CO₂ and $\pm 20\%$ for H₂O and O₃, and in the range ± 10 K for the TC. For a fixed column amount of the target species, the HRIs were compared one by one to a HRI corresponding to a standard spectrum (i.e. with background concentrations of the interfering species and a TC equal to zero) and if the difference between the two HRIs was lower than 10 %, then this fixed abundance of the target species was tagged as independently detectable from the listed parameters.

The TC was found to be the major source of HRI variation for both target species, and a serious cause of limitation only for HCN. Figure 5 shows the variation of HRI_{HCN} caused by a TC equal to ± 10 K. One can see that the HCN column amount can be detected with a variation due to the TC below 10 % when its abundance is higher than 0.28 , 1.2 and 1.6×10^{16} molec cm⁻² for the tropical, temperate and polar atmospheres, respectively. This gives the stability thresholds above which HCN column amount can be measured with a 10 % confidence in the independence of the retrieval method to the atmospheric parameters. Consequently, as the stability thresholds of the method for HCN in temperate and polar atmospheres are too high (1.2 and 1.6×10^{16} molec cm⁻², respectively) to allow for the detection of HCN background abundances as compared to usual background column of typically 0.35×10^{16} molec cm⁻² (Vigouroux et al., 2012; Dufлот et al., 2013), IASI HCN measurements have to be rejected in these two types of atmosphere, and considered in the tropical belt for values above 0.28×10^{16} molec cm⁻². In order to broaden the exploitable latitude range, we performed the same study for subtropical latitudes (considering a mix of tropical and temperate atmospheres), and we found a 25 % confidence in the independence of the retrieval method to the atmospheric parameters (data not shown). As a result, in the following, IASI HCN measurements are considered in the $\pm 35^\circ$ latitude band with a stability threshold of 0.28×10^{16} molec cm⁻², and confidence in the stability of the method is 10 % at tropical latitudes ($[\pm 20^\circ]$) and 25 % at subtropical latitudes ($[\pm 35^\circ : \pm 20^\circ]$). Oppositely to HCN, for C₂H₂, the variation of HRI_{C₂H₂} due to varying TC was found to be lower than 5 % for every C₂H₂ abundance (data

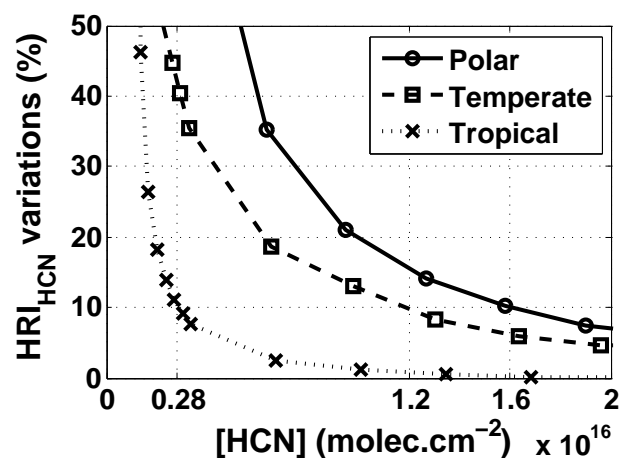


Figure 5. Variation of HRI_{HCN} caused by a TC equal to ± 10 K for the polar (solid line and circles), temperate (dashed line and squares) and tropical (dotted line and crosses) atmospheres.

not shown). Consequently, in the following no IASI C₂H₂ measurements are rejected.

3 Results

The goal of this section is to describe and evaluate the C₂H₂ and HCN total columns as measured by IASI. We first compare HCN and C₂H₂ total columns retrieved from IASI spectra and from ground-based FTIR spectra. We then depict the C₂H₂ and HCN total columns at global and regional scales. IASI global and regional distributions are finally compared with output from the Model for Ozone and Related Chemical Tracers, version 4 (MOZART-4) in order to evaluate the agreement between the model and the IASI distributions.

3.1 Comparison with ground-based observations

We compare in this section HCN and C₂H₂ total columns retrieved from IASI spectra and from ground-based FTIR spectra for the years 2008–2010 for four selected ground-based FTIR observation sites (i.e. wherever observations for these two species were available during the period of study): Wollongong (34° S; 151° E; 30 m above mean sea level, a.m.s.l.), Reunion Island (21° S; 55° E; 50 m a.m.s.l.), Izaña (28° N; 16° W; 2367 m a.m.s.l.) and Jungfraujoch (46° N; 8° E; 3580 m a.m.s.l.) (Fig. 6). IASI cloudy spectra were removed from the data set using a 10 % contamination threshold on the cloud fraction in the pixel. As exposed in Sect. 2.2.3, errors in retrieved species abundances from IASI spectra due to variations in atmospheric parameters are 10 % at tropical latitudes ($[\pm 20^\circ]$) and 25 % at subtropical latitudes ($[\pm 35^\circ : \pm 20^\circ]$) for HCN and 5 % for C₂H₂, and comparison with ground-based HCN measurements are only performed for tropical and subtropical sites (Reunion Island, Wollongong and Izaña).

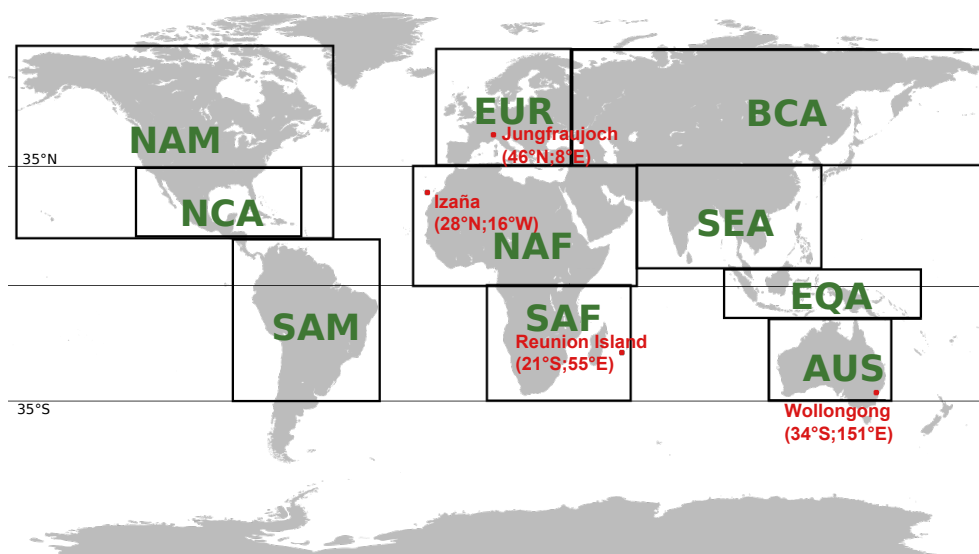


Figure 6. Locations of the four ground-based FTIR measurements sites (Jungfraujoch, Izaña, Reunion Island and Wollongong) and map of the 10 regions used in this study: NAM: northern America, NCA: north-central America, SAM: South America, EUR: Europe, NAF: northern Africa, SAF: southern Africa, BCA: boreal Central Asia, SEA: Southeast Asia, EQA: equatorial Asia, AUS: Australia.

The total error for ground-based measurements at Reunion Island is 17 % for both species, total error for HCN ground-based measurements at Wollongong is 15 %, total error for HCN ground-based measurements at Izaña is 10 %, and total error for C₂H₂ ground-based measurements at Jungfraujoch is 7 %. Detailed description of ground-based FTIR data set, retrieval method and error budget can be found in Vigouroux et al. (2012) for Reunion Island and in Mahieu et al. (2008) for Jungfraujoch. However, at Reunion Island, the retrieval strategies have been slightly improved from Vigouroux et al. (2012), mainly concerning the treatment of the interfering species, but the same spectral signatures are used. Izaña data set and error budget were obtained from the NDACC database (<ftp://ftp.cpc.ncep.noaa.gov/ndacc/station/izana/>). The Wollongong data set and error budget were calculated by N. Jones from the University of Wollongong, personal communication, 2014.

Figure 7 shows the mean total column averaging kernels for the ground-based FTIR at each of the four sites. Similar to IASI (Fig. 3), information content from ground-based instruments measurements is mostly in the middle-high troposphere for both species. The main difference can be observed for tropical C₂H₂: while IASI Jacobian peaks at 10 km for C₂H₂ in a tropical atmosphere, ground-based FTIR averaging kernel peaks at 15 km for C₂H₂ at Reunion Island.

Figure 8 shows the comparison between the IASI and the ground-based measurements. IASI retrieved total columns were averaged on a daily basis and on a 1° × 1° area around the observation sites. HCN retrieved abundances below 2.8 × 10¹⁵ molec cm⁻² have been removed from both ground-based and space measurements to allow for comparison of both data sets (cf. Sect. 2.2.3). One can see that there is

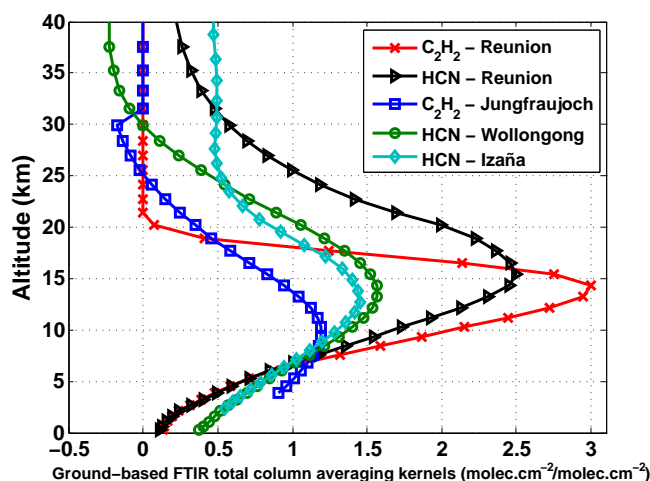


Figure 7. Total column averaging kernels of ground-based FTIR in molec cm⁻²/molec cm⁻² for C₂H₂ at Reunion Island (red stars and line), HCN at Reunion Island (black circles and line), HCN at Wollongong (green dots and line), HCN at Izaña (light blue diamonds and line) and C₂H₂ at Jungfraujoch (blue squares and line).

an overall agreement between the IASI and the ground-based FTIR measurements considering the error bars. An important result from this study is that IASI seems to capture the seasonality in the two species in most of the cases. This is best seen by looking at the IASI monthly mean retrieved total columns (black circles and lines in Fig. 8). The scatter of the IASI daily mean measurements (red dots) are due to the averaging on a 1° × 1° area around the observation sites.

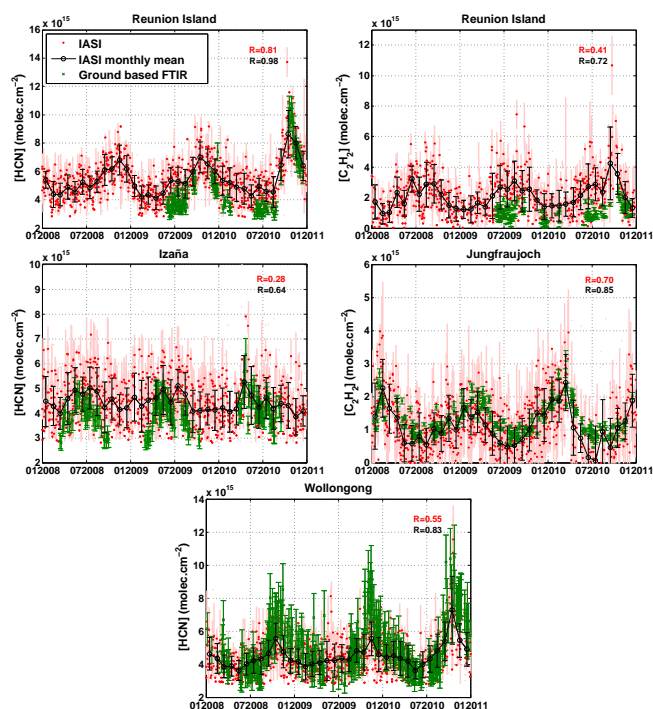


Figure 8. Time series of HCN (left panel) and C₂H₂ (right panel) measurements for Reunion Island (HCN and C₂H₂), Wollongong (HCN only), Izaña (HCN only), and Jungfraujoch (C₂H₂ only). IASI measurements are shown as daily and 1° × 1° means (red dots) with associated standard deviations (light red lines), and as monthly and 1° × 1° means (black circles and line) with associated standard deviation (vertical black lines). Ground-based FTIR measurements are shown as daily means with associated total error by green crosses and lines. Correlation coefficients are given on each plot for daily means in red and for monthly means in black.

At Reunion Island HCN and C₂H₂ peak in October–November and are related to the Southern Hemisphere biomass burning season (Vigouroux et al., 2012). IASI (ground-based FTIR) observed maxima are around 12 (10) × 10¹⁵ molec cm⁻² for HCN and 10 (3) × 10¹⁵ molec cm⁻² for C₂H₂. The seasonality and interannual variability matches very well with that of the ground-based FTIR measurements for HCN (correlation coefficient of 0.81 for the entire daily mean data set, and of 0.98 for the monthly mean data set) but with the IASI columns being biased high by 0.79 × 10¹⁵ molec cm⁻² (17%). For C₂H₂ at Reunion Island, the seasonality and interannual variability matches reasonably well that of the ground-based measurements (correlation coefficient of 0.40 for the entire daily mean data set, and of 0.72 for the monthly mean data set) but with the IASI columns being biased high by 1.10 × 10¹⁵ molec cm⁻² (107%). Such a high bias between the two data sets could be due to the difference between space and ground-based instruments sensitivity (Figs. 3 and 7). One can also notice that the C₂H₂ and HCN peaks are higher in 2010. As South American

biomass burning plumes are known to impact trace gases abundance above Reunion Island (Edwards et al., 2006a, b; Dufлот et al., 2010), these 2010 higher peaks are probably influenced by the 2010 great Amazonian fires (Lewis et al., 2011).

At Wollongong HCN peaks also in October–November due to the Southern Hemisphere biomass burning season (Paton-Walsh et al., 2010). We find maxima of around 11 × 10¹⁵ molec cm⁻² in October 2010 for both space and ground-based instruments, which is, similar to Reunion Island, very likely to be a signature of the great Amazonian fires as South American biomass burning plumes are known to impact trace gases abundance above Australia (Edwards et al., 2006a, b). The seasonality and interannual variability matches well with that of the ground-based FTIR measurements (correlation coefficient of 0.55 for the entire daily mean data set, and of 0.83 for the monthly mean data set), with the IASI columns being biased low by 0.48 × 10¹⁵ molec cm⁻² (10%).

At Izaña HCN peaks in May–July due to the biomass burning activity occurring in northern America and Europe (Sancho et al., 1992). We find maxima of around 8 (6) × 10¹⁵ molec cm⁻² in the IASI (ground-based FTIR) data set. The seasonality and interannual variability matches poorly with that of the ground-based FTIR measurements (correlation coefficient of 0.28 for the entire daily mean data set, and of 0.64 for the monthly mean data set), with the IASI columns being biased high by 0.45 × 10¹⁵ molec cm⁻² (11%). One can notice that HCN total columns as measured by ground-based FTIR are below the HCN stability threshold in boreal winter, which may result in erroneous IASI measurements (because unstable) and explain this poor match between the two data sets.

For C₂H₂ at the Jungfraujoch site, the agreement between IASI and the ground-based retrieved columns is good (correlation coefficient of 0.70 for the entire daily mean data set, and of 0.85 for the monthly mean data set), with the IASI columns being biased low by 0.15 × 10¹⁵ molec cm⁻² (12%), opposite to the observations at Reunion. The larger columns observed in late winter are caused by the increased C₂H₂ lifetime in that season (caused by the seasonal change in OH abundance) (Zander et al., 1991), and we find corresponding maxima of up to 4 (3) × 10¹⁵ molec cm⁻² in the IASI (ground-based FTIR) data set.

3.2 IASI Global distributions

We focus in this section on the description of the C₂H₂ and HCN distributions retrieved from IASI spectra. For practical reasons, the figures used in this section also show simulated distributions that will be analyzed afterwards.

The left panels of Figs. 9 and 10 provide the seasonal global and subtropical distributions of C₂H₂ and HCN total columns, respectively, as measured by IASI and averaged over the years 2008 to 2010.

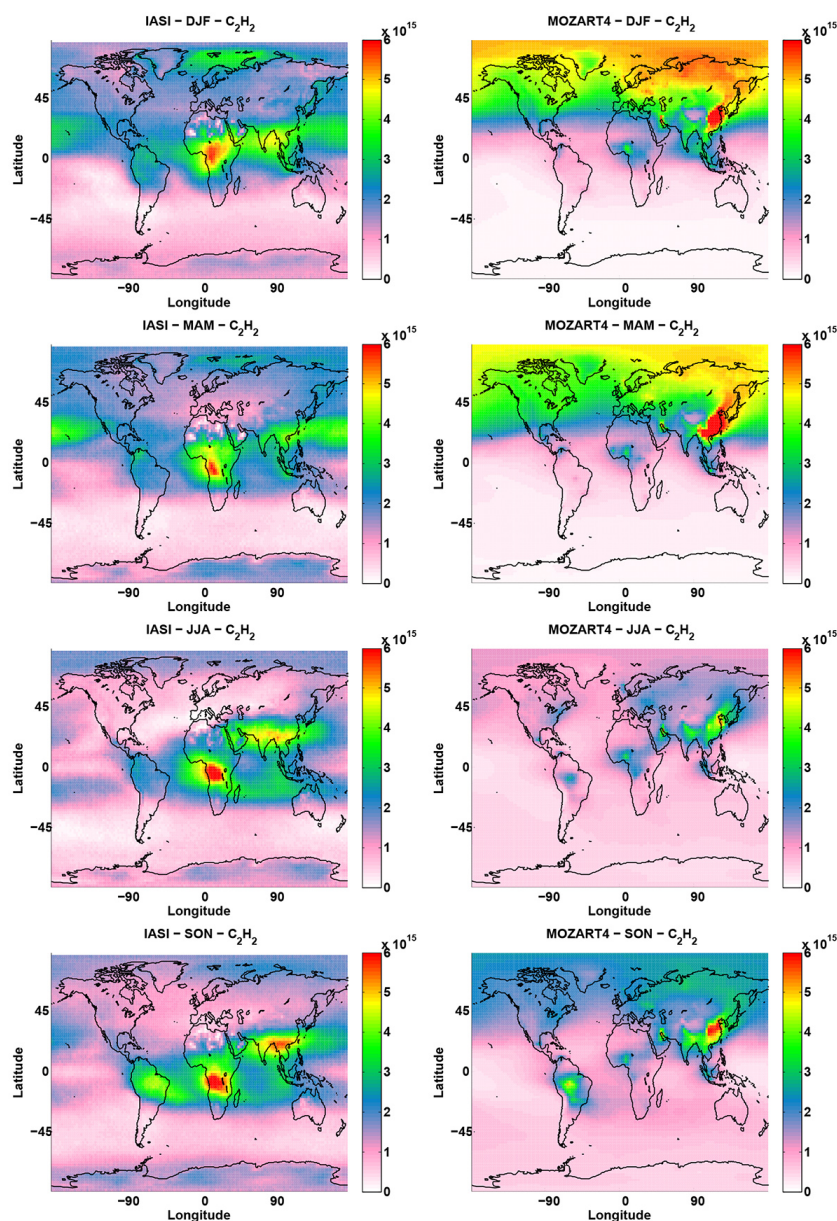


Figure 9. Seasonal distribution of the C₂H₂ total column (in molec cm⁻²) as measured by IASI (left panel) and simulated by MOZART-4 (right panel) averaged over the years 2008 to 2010. The IASI global distributions are given with the same horizontal resolution as MOZART-4 (1.875° latitude × 2.5° longitude). DJF represents December–January–February, MAM: March–April–May, JJA: June–July–August, and SON: September–October–November.

Looking at IASI measurements (Figs. 9 and 10 – left panels), one can notice the following main persisting features for both C₂H₂ and HCN:

- the hot spots mainly due to the biomass burning activity occurring in Africa and moving southward along the year (Sauvage et al., 2005; van der Werf et al., 2006);
- the hot spot located in Southeast Asia being likely a combination of biomass burning and anthropogenic activities;

- the transatlantic transport pathway linking the African west coast to the South American east coast and moving southward along the year (Edwards et al., 2003, 2006a, b; Glatthor et al., 2015).

The following seasonal features can also be observed:

- the transpacific transport pathway linking eastern Asia to western North America, especially in March–April–May (MAM) (Yienger et al., 2000);

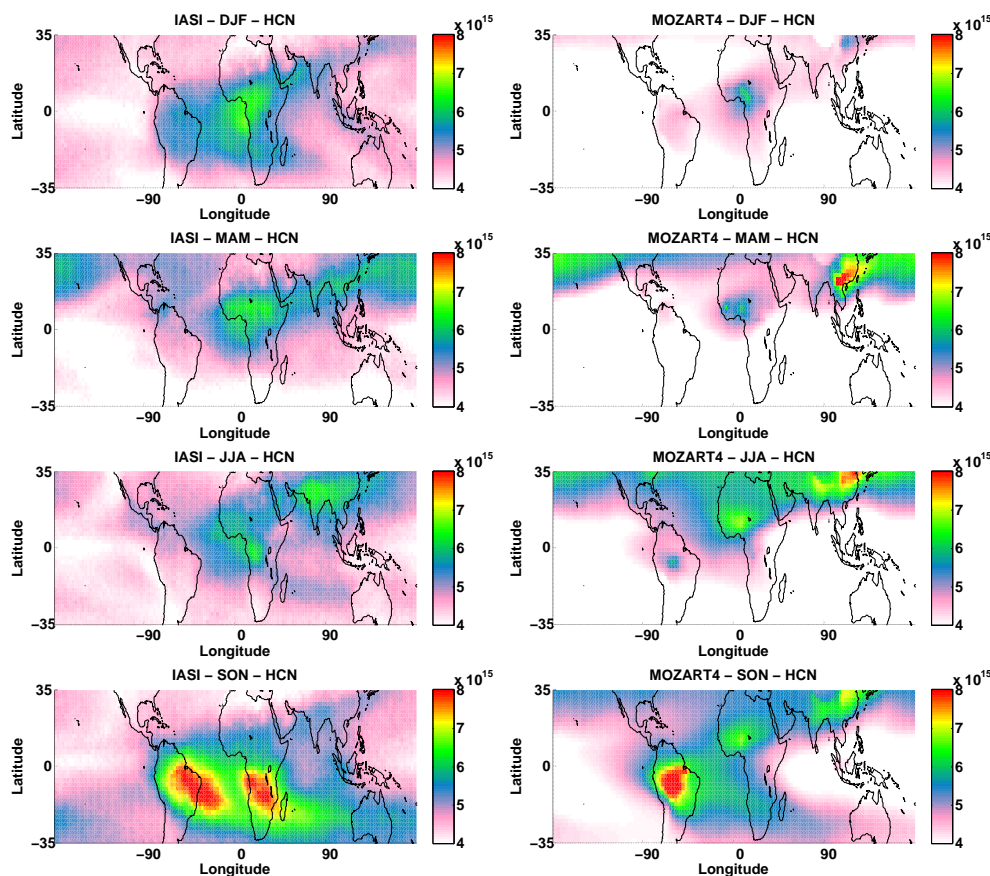


Figure 10. Same as Fig. 9 for HCN.

- the transport pathway from southern Africa to Australia in June–July–August (JJA) and September–October–November (SON) (Annegarn et al., 2002; Edwards et al., 2006a, b);
- the transport pathway linking South America (especially Amazonia) to southern Africa and Australia during the SON period (Edwards et al., 2006a, b; Glatthor et al., 2015);
- the transport of the northern African plume over southern Asia to as far as the eastern Pacific by the northern subtropical jet during the MAM period (Glatthor et al., 2015);
- the Asian monsoon anticyclone (AMA), which is the dominant circulation feature in the Indian–Asian upper troposphere–lower stratosphere (UTLS) region during the Asian summer monsoon, spanning Southeast Asia to the Middle East and flanked by the equatorial and subtropical jets (Hoskins and Rodwell, 1995). The AMA is a known region of persistent enhanced pollution in the upper troposphere, linked to rapid vertical transport of surface air from Asia, India, and Indonesia in deep convection, and confinement by the strong anticyclonic cir-

ulation (Randel et al., 2010). The enhanced abundance of C₂H₂ and HCN within the AMA in JJA observed by IASI is in accordance with previous studies (Park et al., 2008; Randel et al., 2010; Parker et al., 2011; Glatthor et al., 2015); however, one should keep in mind that this enhanced abundance measured by IASI is likely due to the combination of this pollution uplift and confinement with the higher sensitivity of the method in the upper troposphere (Fig. 2).

One can also notice the very good agreement between the seasonal HCN distributions shown in our Fig. 10 and the ones published recently in Glatthor et al. (2015, Fig. 3).

Figures 11 and 12 show the C₂H₂ and HCN total columns time series, respectively, as measured by IASI (red dots) with the associated standard deviation (light red lines) for each of the zones defined in Fig. 6.

In northern America, Europe and boreal Central Asia (Fig. 11 – zones NAM, EUR and BCA), C₂H₂ peaks in late boreal winter due to the increased C₂H₂ lifetime as already noticed over Jungfraujoch (Fig. 8). The boreal summer 2008 California wildfires event (Gyawali et al., 2009) is clearly visible in the NAM plot, as well as the August 2009 Russian

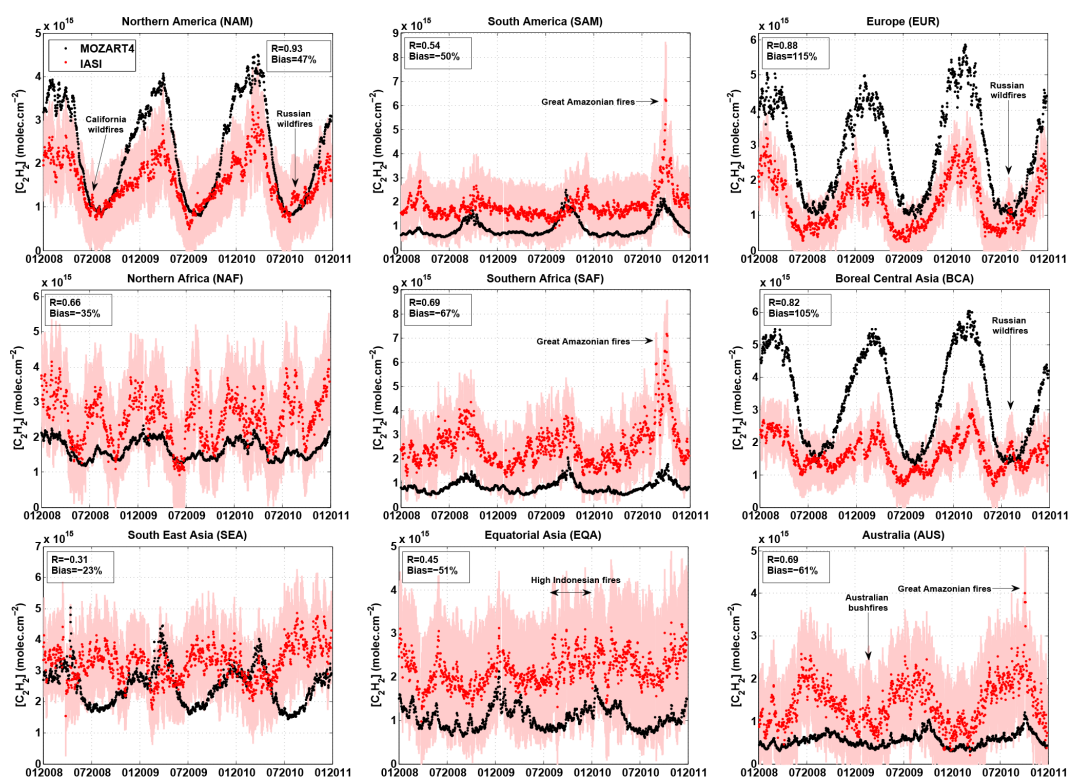


Figure 11. Evolution with time of the mean C₂H₂ total column (in molec cm⁻²) over the zones defined in Fig. 6 as measured by IASI (red dots) with associated standard deviation (light red lines), and as simulated by MOZART-4 (black dots). Correlation coefficients (*R*) and biases (*Bias*) between IASI and MOZART-4 are given on each plot for daily means.

wildfires in the NAM, EUR and BCA plots (Parrington et al., 2012; R'Honi et al., 2013).

In north-central America (Fig. 12 – zone NCA), the annual HCN peak in April–June is driven by local fire activity (van der Werf et al., 2010).

In South America, southern Africa and Australia (Figs. 11 and 12 – zones SAM, SAF and AUS), the Southern Hemisphere biomass burning season clearly drives the C₂H₂ and HCN peaks in September–November each year. The signature of the great 2010 Amazonian fires (Lewis et al., 2011) is visible on each of the these three zones, South American fire plumes being known to impact southern Africa and Australia (Edwards et al., 2003, 2006a, b). The February 2009 Australian bush fires (Glatthor et al., 2013) are also noticeable on zone AUS for both species.

In northern Africa (Figs. 11 and 12 – zone NAF), C₂H₂ and HCN peak in boreal winter because of the biomass burning activity occurring in the zone, and peak also in boreal summer because of the European and southern Mediterranean fires (van der Werf et al., 2010).

In Southeast Asia (Figs. 11 and 12 – zone SEA), the observed C₂H₂ and HCN peaks in July–September and January–March are due to local fire activity (Fortems-Cheiney et al., 2011; Magi et al., 2012). Additionally, the July–September peaks are also likely due to the combination

of the pollution uplift and confinement within the AMA with the higher sensitivity of the method in the upper troposphere.

In equatorial Asia (Figs. 11 and 12 – zone EQA), local fire activity is visible in July–October, as well as the Southeast Asian fire activity in January–March (Fortems-Cheiney et al., 2011; Magi et al., 2012). The high biomass burning activity occurring in Indonesia from July to December 2009 (Yulianti et al., 2013; Hyer et al., 2013) is also clearly noticeable.

C₂H₂ and HCN sharing important common sources (cf. Introduction), the same annual and seasonal features are observed for both species. However, biomass burning being the major source for HCN (while it is biofuel and fossil fuel combustions for C₂H₂), one can notice the especially high increase in HCN abundance (up to 13×10^{15} molec cm⁻²) in the Southern Hemisphere during the austral biomass burning season (September to November). These observations are in accordance with previous studies (Lupu et al., 2009; Glatthor et al., 2009; Wiegeler et al., 2012).

3.3 Comparison with model

In order to further evaluate the HCN and C₂H₂ distributions retrieved from IASI spectra, they are compared in this section to the output of MOZART-4 for the years 2008–2010. We first describe the simulation set-up before comparing simu-

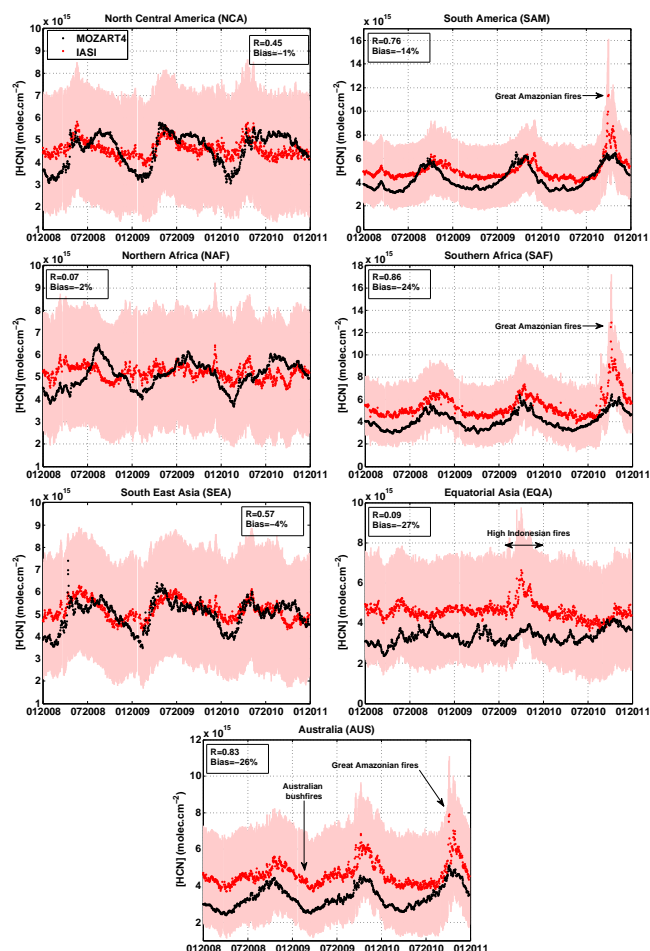


Figure 12. Same as Fig. 11 for HCN.

lated abundances with the ground-based observations at the four sites already studied in Sect. 3.1. We finally compare the simulated and observed global distributions.

3.3.1 MOZART-4 simulation set-up

The model simulations presented here are performed with the MOZART-4 global 3-D chemical transport model (Emmons et al., 2010a), which is driven by assimilated meteorological fields from the NASA Global Modeling and Assimilation Office (GMAO) Goddard Earth Observing System (GEOS). MOZART-4 was run with a horizontal resolution of 1.875° latitude × 2.5° longitude, with 56 levels in the vertical and with its standard chemical mechanism (see Emmons et al. (2010a) and Lamarque et al. (2012), for details). The model simulations have been initialized by simulations starting in July 2007 to avoid contamination by the spin-up in the model results. MOZART-4 simulations of numerous species (CO, O₃ and related tracers including C₂H₂ and HCN) have been previously compared to in situ and satellite observations and used to track the intercontinental transport of pol-

Table 2. Global C₂H₂ and HCN emission sources (Tg(species) yr⁻¹) during the period 2008–2010 from the data set used in MOZART-4.

	C ₂ H ₂			HCN		
Sources yr ⁻¹	2008	2009	2010	2008	2009	2010
Anthropogenic	3.37	3.37	3.37	1.67	1.67	1.67
Biomass burning	0.64	0.71	0.83	1.38	1.33	1.58
Total	4.01	4.07	4.20	3.05	3.00	3.25

lution (e.g. Emmons et al., 2010b; Pfister et al., 2006, 2008, 2011; Tilmes et al., 2011; Clarisse et al., 2011b; Wespes et al., 2012; Viatte et al., 2015).

The surface anthropogenic (including fossil fuel and bio-fuel) emissions used here were taken from the inventory provided by D. Streets and University of Iowa and created for the Arctic Research of the Composition of the Troposphere from Aircraft and Satellites (ARCTAS) campaign (see <http://bio.cgrrer.uiowa.edu/arctas/emission.html> for more information). This inventory was developed in the frame of the POLARCAT Model Intercomparison Program (POLMIP) and is a composite data set of regional emissions as representative of current emissions as possible; it is built upon the INTEX-B Asia inventory (Zhang et al., 2009) with the US NEI (National Emission Inventory) 2002 and CAC 2005 for North America and the EMEP (European Monitoring and Evaluation Programme) 2006 for Europe inventory to make up NH emissions (see Emmons et al. (2015) for an evaluation of POLMIP models). Emissions from EDGAR (Emissions Database for Global Atmospheric Research) were used for missing regions and species. Since only total volatile organic compounds (VOCs) were provided with this POLMIP inventory, the VOC speciation based on the RETRO emissions inventory as in Lamarque et al. (2010) was used. The anthropogenic emissions are constant in time with no monthly variations.

Daily biomass burning emissions were taken from the global Fire INventory from NCAR (FINN) version 1 (Wiedinmyer et al., 2011). The fire emissions for individual fires, based on daily MODIS fire counts, were calculated and then gridded to the simulation resolution (Wiedinmyer et al., 2006, 2011). The oceanic emissions are taken from the POET emissions data set (Granier et al., 2005) and the biogenic emissions from MEGANv2 (Model of Emissions of Gases and Aerosols from Nature) data set inventory (Guenther et al., 2006).

Model emissions for HCN and C₂H₂ used in this study are summarized in Table 2 and presented in Fig. 13. The majority of the emissions for both C₂H₂ and HCN are from anthropogenic source (about 80 and 55 % of the global source of C₂H₂ and HCN, respectively; see Table 2). Averaged over the period 2008–2010, the highest HCN and C₂H₂ anthropogenic surface emissions are observed over China, with elevated emissions over India, Europe and USA, due to in-

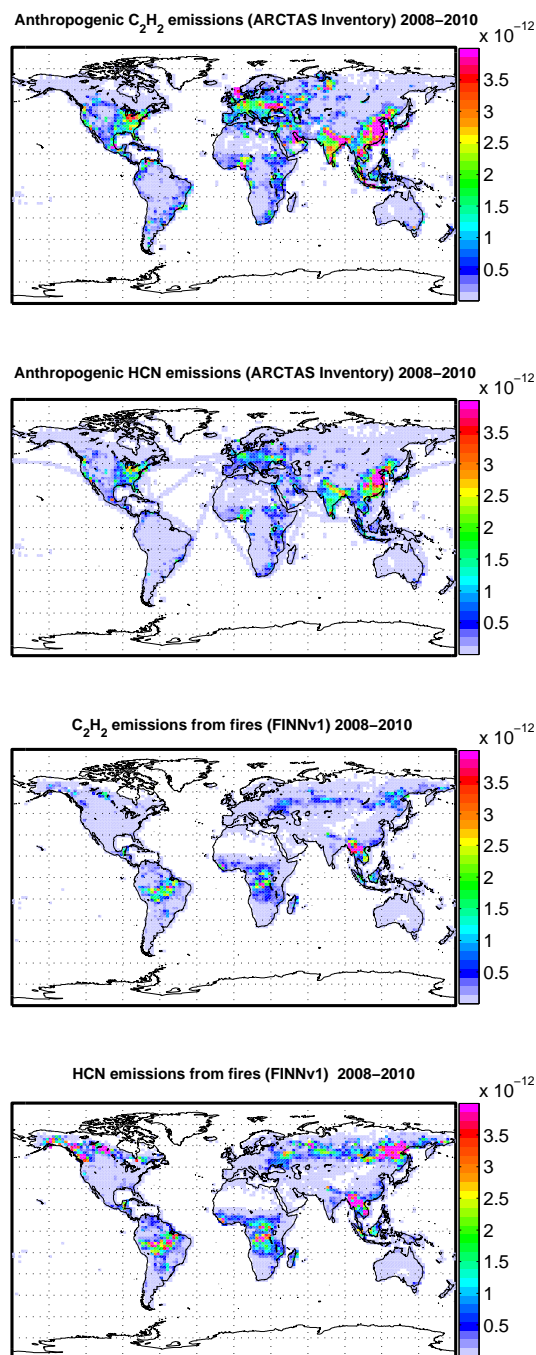


Figure 13. C₂H₂ and HCN surface emission fluxes ($\text{kg m}^{-2} \text{s}^{-1}$) averaged over the period 2008–2010 from the anthropogenic and fire emissions inventories used in MOZART-4.

tense industrialization, where values larger than $4 \times 10^{-12} \text{ kg(C}_2\text{H}_2) \text{ m}^{-2} \text{ s}^{-1}$ are entered in the model. The most intense HCN and C₂H₂ emissions due to biomass burning are observed over Southeast Asia, equatorial and southern Africa, South America, Siberia and Canada.

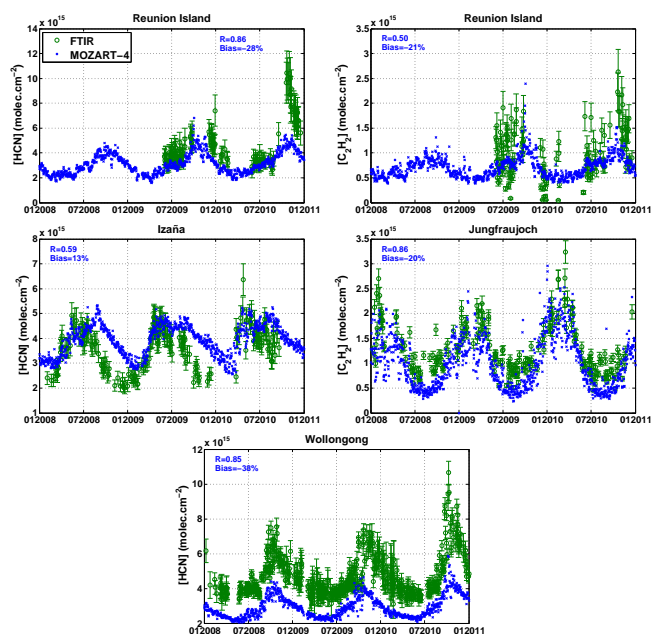


Figure 14. Time series of HCN (left panel) and C₂H₂ (right panel) measurements and simulations for Reunion Island (HCN and C₂H₂), Wollongong (HCN only), Izaña (HCN only), and Jungfraujoch (C₂H₂ only). MOZART-4 total columns are shown as daily and $1.875^\circ \times 2.5^\circ$ means (blue crosses). Ground-based FTIR measurements are shown as daily means with associated total error by green circles and lines. Correlation coefficient and bias are given on each plot for daily means.

3.3.2 Model vs. ground-based FTIR observations

MOZART-4 simulations can be first evaluated by comparing them to the ground-based measurements at the four sites studied previously (Sect. 3.1). To perform this comparison, we use the FTIR averaging kernels and a priori to degrade the model vertical profile to the FTIR vertical resolution, in order to obtain the model “smoothed” total column, which represents what the FTIR would measure if the model profile was the true state (see Eq. (25) of Rodgers and Connor (2003), and Vigouroux et al. (2012) for an example). Figure 14 shows the comparison between the simulated “smoothed” total columns and the ground-based measurements. Model outputs are given in a 1.875° latitude \times 2.5° longitude box (corresponding to the horizontal resolution of the model) over the ground-based measurement points. One can see that there is an overall agreement between the ground-based instruments and the model, the latter being obviously able to capture the seasonality in the two species in most of the cases.

For HCN, the model seasonality and interannual variability matches the ground-based FTIR measurements at Reunion Island very well (correlation coefficient of 0.86) and Wollongong (correlation coefficient of 0.85), and reasonably well at Izaña (correlation coefficient of 0.59). For this last site, one can see that the model correctly captures the abun-

dance peak occurring in May–July (cf. Sect. 3.1), but sets another peak around October. This second yearly peak for HCN at Izaña in the model simulations could be due to an overestimation of the southern African contribution to the northern African loading; this hypothesis will be analyzed in the next section. For HCN, the simulated total columns are biased low at Reunion Island by 1.29×10^{15} molec cm⁻² (28 %) and at Wollongong by 1.8×10^{15} molec cm⁻² (38 %). One can notice that the model does not capture the 2010 great Amazonian fires exceptional event visible on ground-based measurements at Reunion Island and Wollongong (cf. Sect. 3.1), which could explain the biases between the model and ground-based data sets at these two sites. At Izaña, the model is biased high by 0.46×10^{15} molec cm⁻² (13 %), which seems to be caused by the second yearly peak simulated by the model.

For C₂H₂, the model seasonality and interannual variability matches very well that of the ground-based FTIR measurements at Jungfrauoch (correlation coefficient of 0.86) and reasonably well at Reunion Island (correlation coefficient of 0.50). For this last site, one can see that the model captures correctly the yearly peak occurring in October–November (cf. Sect. 3.1), but struggles to simulate the large day-to-day variations observed by the ground-based FTIR. This is illustrated by the very good correlation coefficient between the two data sets when dealing with monthly mean observations: 0.87 (data not shown). For C₂H₂, the simulated total columns are biased low for every sites: 0.20×10^{15} molec cm⁻² (21 %) at Reunion Island, and 0.27×10^{15} molec cm⁻² (20 %) at Jungfrauoch. Similar to HCN, one can notice that the model does not capture the 2010 great Amazonian fires exceptional event visible on ground-based measurements at Reunion Island, which could explain the bias between the model and ground-based data sets at this site.

3.3.3 IASI vs. model global distributions

Figures 9 and 10 provide the seasonal global and subtropical distributions of C₂H₂ and HCN total columns, respectively, as measured by IASI and as simulated by MOZART-4 averaged over the years 2008 to 2010. For comparisons with IASI, the hourly output from MOZART-4 was interpolated to the overpass time of IASI. In addition, the high-resolution modelled layers were smoothed by applying each of the MOZART-4 simulated profiles, the Jacobians of the used forward model (cf. Sects. 2.2.3 and Fig. 3), to take into account the sensitivity of both the radiative transfer model and IASI. This has been done instead of applying the averaging kernels since our retrieval scheme does not provide such information. Note that here again HCN abundances below 2.8×10^{15} molec cm⁻² have been removed from both space measurements and simulated columns to allow for comparison of both data sets (cf. Sect. 2.2.3).

Table 3. Correlation coefficients (*R*) and biases (Bias) between IASI observations and MOZART-4 simulations for each of the zones defined in Fig. 6.

Zones	C ₂ H ₂		HCN	
	<i>R</i>	Bias (%)	<i>R</i>	Bias (%)
NAM	0.93	47		
NCA			0.44	-1
SAM	0.54	-50	0.76	-14
EUR	0.88	115		
NAF	0.66	-35	0.07	-2
SAF	0.69	-67	0.86	-28
BCA	0.82	105		
SEA	-0.31	-23	0.57	-4
EQA	0.45	-51	0.09	-27
AUS	0.65	-61	0.77	-26
Global	0.72	-1	0.69	-16

MOZART-4 simulations can be evaluated by looking at Figs. 9 and 11 for C₂H₂, and Figs. 10 and 12 for HCN. Figures 11 and 12 show the simulated C₂H₂ and HCN total columns time series, respectively, for each of the zones defined in Fig. 6 superimposed to IASI observations. Table 3 summarizes the biases and correlation coefficients resulting from the comparison between model and observations. Looking at these tables and figures, the following conclusions can be drawn:

- Seasonal cycles observed from satellite data are reasonably well reproduced by the model.
- The African, South American, Asian and Indonesian hot spots are clearly visible in the model.
- Exceptional events that are captured by IASI (cf. Sect. 3.2) are not simulated by MOZART-4.
- The model is more negatively biased in the Southern Hemisphere (bias = -61 % for C₂H₂ and bias = -25 % for HCN) than in the Northern Hemisphere (bias = 40 % for C₂H₂ and bias = -3 % for HCN), suggesting that anthropogenic (biomass burning) emissions are likely overestimated (underestimated) in the model. Note that in the MOZART-4 simulation presented here, the fire emissions are injected at the surface, which might result in an underestimation of concentrations at higher altitudes where IASI shows an increased sensitivity.
- The model reasonably reproduces the main transport pathways identified on IASI observations (cf. Sect. 3.2). However, the low background concentrations in the Southern Hemisphere as simulated by the model, especially for southern Africa and Australia (Figs. 11 and 12 – zones SAF and AUS and previous section at Reunion

Island and Wollongong), is possibly due to a mix of uncertainties introduced by the coarse grid of the model producing too much diffusion, problems in the transportation scheme for fine-scale plumes, the fire injection set at the surface and uncertainties in the emissions. The fact that only three representative Jacobians are used to perform the global comparison might also play a role.

In Table 3, for C₂H₂, the correlation coefficients are good (≥ 0.6) to very good (≥ 0.9) except for the zones SAM (South America), SEA (Southeast Asia) and EQA (equatorial Asia). For HCN, the correlation coefficients are good (≥ 0.6) except for the zones NCA (north-central America), NAF (northern Africa), SEA and EQA.

For South America (zone SAM), correlation coefficient is not as good for C₂H₂ ($R = 0.54$) due to a backward shift of the species abundance peaks in years 2008 and 2009: in the model, this increase occurs from July to October, while observations (and previous studies, e.g. van der Werf et al., 2010) show an increase from August to December. This backward shift is also visible for HCN (Fig. 12), but to a lesser extent.

For Southeast Asia and equatorial Asia (zones SEA and EQA), the low correlation coefficients (cf. Table 3) can be attributed to the difficulty of locating precisely with the model the intercontinental convergence zone (ITCZ) which drives the long-range transport of C₂H₂ and HCN-loaded plumes into the zone. Moreover, for Southeast Asia, the very low correlation coefficient for C₂H₂ (-0.31) may be caused by (i) the model setting the high abundance peaks in DJF and MAM (Fig. 9, especially visible over China coast, and Fig. 11), which may be due to an overestimation of the Asian anthropogenic emissions, and (ii) IASI observations exhibiting July–September peaks, which are likely due to the combination of the pollution uplift and confinement within the AMA with the higher sensitivity of the method in the upper troposphere. Additionally, for equatorial Asia, the too low fire emissions considered in the model for Indonesia from July to December 2009 may also be a cause for these low correlation coefficients.

For HCN in northern Africa (zone NAF), correlation coefficient is very low ($R = 0.07$) because the model sets the abundance peaks around August while observations show peaks occurring around December, which is in accordance with previous studies (van der Werf et al., 2010). This inadequate timing for HCN in the model simulations could be due to an overestimation of the southern African contribution to the northern African loading and is visible on Fig. 10 (JJA).

4 Conclusions

We have presented a fast method to retrieve HCN and C₂H₂ total columns from IASI spectra. The sensitivity of this method to the two species is mostly in the mid-upper troposphere. With this method, C₂H₂ total columns

can be retrieved globally with 5 % precision, while HCN abundances can be retrieved for abundances greater than 0.28×10^{16} molec cm⁻² with 10 % precision in the $\pm 20^\circ$ latitudinal band and with 25 % precision in the $[\pm 35^\circ : \pm 20^\circ]$ latitudinal band.

Total columns have been retrieved globally for a 3-year period and compared to routine FTIR measurements available at Reunion Island (HCN and C₂H₂), Wollongong (HCN), Jungfraujoch (C₂H₂), and Izaña (HCN). The comparison between IASI and FTIR retrieved total columns demonstrates the capabilities of IASI to capture the seasonality in HCN and C₂H₂ in most cases.

Global seasonal distributions, as well as regional time series of the total columns, have been shown for the two species. IASI is able to capture persisting, seasonal and exceptional features for both species, and the observed patterns are in a general good agreement with previous spaceborne studies (ACE-FTIR and MIPAS).

The comparison between MOZART-4 simulations and the ground-based FTIR measurements, together with the comparison between the IASI observations and MOZART-4 simulations leads to the following conclusions: (i) the model is able to capture most of the hot spots and seasonal cycles, but not the exceptional events; (ii) the anthropogenic (biomass burning) emissions used in the model seem to be overestimated (underestimated) for both species; (iii) discrepancies between simulations and observations are most probably due to the coarse grid of the model producing too much diffusion and problems in the transportation scheme for fine-scale plumes, as well as to the fire injection set at the surface.

Acknowledgements. IASI has been developed and built under the responsibility of the Centre National d'Etudes Spatiales (CNES, France). It is flown onboard the MetOp satellites as part of the EUMETSAT Polar System. The IASI L1 data are received through the EUMETCast near-real-time data distribution service. Part of the research is supported by EUMETSAT through the O3SAF project. P.-F. Coheur is Senior Research Associate and L. Clarisse is Research Associate at the F.R.S.-FNRS. The research in Belgium was funded by the F.R.S.-FNRS, the Belgian Science Policy Office, and the European Space Agency (ESA Prodex arrangements and the AGACC-II project). The Australian Research Council has provided financial support over the years for the NDACC site at Wollongong, most recently as part of project DP110101948. The Liège team further acknowledges the Fédération Wallonie-Bruxelles for supporting travel costs to the Jungfraujoch station and wishes to thank the International Foundation High Altitude Research Stations Jungfraujoch and Gornergrat (HFSJG, Bern) for supporting the facilities needed to perform the observations. Since 1999, the Izaña FTIR activities have been supported by different funding agencies: European Commission, European Research Council, European Space Agency, EUMETSAT, Deutsche Forschungsgemeinschaft, Deutsches Zentrum für Luft- und Raumfahrt, and the Ministerios de Ciencia e Innovación and Educación from Spain. The authors also wish to thank the French regional, national (INSU, CNRS), and international (NASA/GFSC) organizations for supporting the

OPAR (Observatoire de Physique de l'Atmosphère de la Réunion) station. The NDACC is also acknowledged for providing consistent and well-documented data sets.

Edited by: P. Monks

References

- Anderson, G. P., Clough, S. A., Kneizys, F. X., Chetwynd, J. H., and Shettle, E. P.: AFGL Atmospheric Constituent Profiles (0–120 km), Environmental Research Papers no. 954, Air Force Geophysics Laboratory, Hanscom AFB Massachusetts, AFGL TR-86-0110, 1986.
- Annegarn, H. J., Otter, L., Swap, R. J., and Scholes, R. J.: Southern Africa ecosystem in a test-tube-A perspective on the Southern African Regional Science Initiative (SAFARI 2000), *S. Afr. J. Sci.*, 98, 111–113, 2002.
- Clarisse, L., Coheur, P. F., Prata, A. J., Hurtmans, D., Razavi, A., Phulpin, T., Hadji-Lazaro, J., and Clerbaux, C.: Tracking and quantifying volcanic SO₂ with IASI, the September 2007 eruption at Jebel at Tair, *Atmos. Chem. Phys.*, 8, 7723–7734, doi:10.5194/acp-8-7723-2008, 2008.
- Clarisse L., Clerbaux C., Dentener F., Hurtmans D., and Coheur P.-F.: Global ammonia distribution derived from infrared satellite observations, *Nat. Geosci.*, 2, 479–483, doi:10.1038/NNGEO551, 2009.
- Clarisse, L., R'Honi, Y., Coheur, P.-F., Hurtmans, D., and Clerbaux, C.: Thermal infrared nadir observations of 24 atmospheric gases, *Geophys. Res. Lett.*, 38, L10802, doi:10.1029/2011GL047271, 2011a.
- Clarisse, L., Formm, M., Ngadi, Y., Emmons, L., Clerbaux, C., Hurtmans, D., and Coheur, P. F.: Intercontinental transport of anthropogenic sulfur dioxide and other pollutants: An infrared remote sensing case study, *Geophys. Res. Lett.*, 38, L19806, doi:10.1029/2011GL048976, 2011b.
- Clerbaux, C., Boynard, A., Clarisse, L., George, M., Hadji-Lazaro, J., Herbin, H., Hurtmans, D., Pommier, M., Razavi, A., Turquety, S., Wespes, C., and Coheur, P.-F.: Monitoring of atmospheric composition using the thermal infrared IASI/MetOp sounder, *Atmos. Chem. Phys.*, 9, 6041–6054, doi:10.5194/acp-9-6041-2009, 2009.
- Coheur, P.-F., Barret, B., Turquety, S., Hurtmans, D., Hadji-Lazaro, J., and Clerbaux, C.: Retrieval and characterization of ozone vertical profiles from a thermal infrared nadir sounder, *J. Geophys. Res.*, 110, D24303, doi:10.1029/2005JD005845, 2005.
- Dufлот, V., Dils, B., Baray, J. L., De Mazière, M., Attié, J. L., Vanhaelewyn, G., Senten, C., Vigouroux, C., Clain, G., and Delmas, R.: Analysis of the origin of the distribution of CO in the subtropical southern Indian Ocean in 2007, *J. Geophys. Res.*, 115, D22106, doi:10.1029/2010JD013994, 2010.
- Dufлот, V., Hurtmans, D., Clarisse, L., R'honi, Y., Vigouroux, C., De Mazière, M., Mahieu, E., Servais, C., Clerbaux, C., and Coheur, P.-F.: Measurements of hydrogen cyanide (HCN) and acetylene (C₂H₂) from the Infrared Atmospheric Sounding Interferometer (IASI), *Atmos. Meas. Tech.*, 6, 917–925, doi:10.5194/amt-6-917-2013, 2013.
- Edwards D. P., Lamarque, J.-F., Attié, J.-L., Emmons, L. K., Richter, A., Cammas, J.-P., Gille, J. C., Francis, G. L., Deeter, M. N., Warner, J., Ziskin, D. C., Lyjak, L. V., Drummond, J. R., and Burrows, J. P.: Tropospheric ozone over the tropical Atlantic: A satellite perspective, *J. Geophys. Res.*, 108, 4237, doi:10.1029/2002JD002927, 2003.
- Edwards, D. P., Emmons, L. K., Gille, J. C., Chu, A., Attié, J.-L., Giglio, L., Wood, S. W., Haywood, J., Deeter, M. N., Massie, S. T., Ziskin, D. C., and Drummond, J. R.: Satellite-observed pollution from Southern Hemisphere biomass burning, *J. Geophys. Res.*, 111, D14312, doi:10.1029/2005JD006655, 2006a.
- Edwards, D. P., Emmons, L. K., Gille, J. C., Chu, A., Attié, J.-L., Giglio, L., Wood, S. W., Haywood, J., Deeter, M. N., Massie, S. T., Ziskin, D. C., and Drummond J. R.: Satellite-observed pollution from Southern Hemisphere biomass burning, *J. Geophys. Res.*, 111, D14312, doi:10.1029/2005JD006655, 2006b.
- Emmons, L. K., Walters, S., Hess, P. G., Lamarque, J.-F., Pfister, G. G., Fillmore, D., Granier, C., Guenther, A., Kinnison, D., Laepple, T., Orlando, J., Tie, X., Tyndall, G., Wiedinmyer, C., Baughcum, S. L., and Kloster, S.: Description and evaluation of the Model for Ozone and Related chemical Tracers, version 4 (MOZART-4), *Geosci. Model Dev.*, 3, 43–67, doi:10.5194/gmd-3-43-2010, 2010a.
- Emmons, L. K., Apel, E. C., Lamarque, J.-F., Hess, P. G., Avery, M., Blake, D., Brune, W., Campos, T., Crawford, J., DeCarlo, P. F., Hall, S., Heikes, B., Holloway, J., Jimenez, J. L., Knapp, D. J., Kok, G., Mena-Carrasco, M., Olson, J., O'Sullivan, D., Sachse, G., Walega, J., Weibring, P., Weinheimer, A., and Wiedinmyer, C.: Impact of Mexico City emissions on regional air quality from MOZART-4 simulations, *Atmos. Chem. Phys.*, 10, 6195–6212, doi:10.5194/acp-10-6195-2010, 2010b.
- Emmons, L. K., Arnold, S. R., Monks, S. A., Huijnen, V., Tilmes, S., Law, K. S., Thomas, J. L., Raut, J.-C., Bouarar, I., Turquety, S., Long, Y., Duncan, B., Steenrod, S., Strode, S., Flemming, J., Mao, J., Langner, J., Thompson, A. M., Tarasick, D., Apel, E. C., Blake, D. R., Cohen, R. C., Dibb, J., Diskin, G. S., Fried, A., Hall, S. R., Huey, L. G., Weinheimer, A. J., Wisthaler, A., Mikoviny, T., Nowak, J., Peischl, J., Roberts, J. M., Ryerson, T., Warneke, C., and Helmig, D.: The POLARCAT Model Intercomparison Project (POLMIP): overview and evaluation with observations, *Atmos. Chem. Phys.*, 15, 6721–6744, doi:10.5194/acp-15-6721-2015, 2015.
- Fortems-Cheiney, A., Chevallier, F., Pison, I., Bousquet, P., Szopa, S., Deeter, M. N., and Clerbaux, C.: Ten years of CO emissions as seen from Measurements of Pollution in the Troposphere (MOPITT), *J. Geophys. Res.*, 116, D05304, doi:10.1029/2010JD014416, 2011.
- Glatthor, N., von Clarmann, T., Stiller, G. P., Funke, B., Koukouli, M. E., Fischer, H., Grabowski, U., Höpfner, M., Kellmann, S., and Linden, A.: Large-scale upper tropospheric pollution observed by MIPAS HCN and C₂H₆ global distributions, *Atmos. Chem. Phys.*, 9, 9619–9634, doi:10.5194/acp-9-9619-2009, 2009.
- Glatthor, N., Höpfner, M., Semeniuk, K., Lupu, A., Palmer, P. I., McConnell, J. C., Kaminski, J. W., von Clarmann, T., Stiller, G. P., Funke, B., Kellmann, S., Linden, A., and Wiegele, A.: The Australian bushfires of February 2009: MIPAS observations and GEM-AQ model results, *Atmos. Chem. Phys.*, 13, 1637–1658, doi:10.5194/acp-13-1637-2013, 2013.
- Glatthor, N., Höpfner, M., Stiller, G. P., von Clarmann, T., Funke, B., Lossow, S., Eckert, E., Grabowski, U., Kellmann, S., Linden,

- A., A. Walker, K., and Wiegeler, A.: Seasonal and interannual variations in HCN amounts in the upper troposphere and lower stratosphere observed by MIPAS, *Atmos. Chem. Phys.*, 15, 563–582, doi:10.5194/acp-15-563-2015, 2015.
- González Abad, G., Allen, N. D. C., Bernath, P. F., Boone, C. D., McLeod, S. D., Manney, G. L., Toon, G. C., Carouge, C., Wang, Y., Wu, S., Barkley, M. P., Palmer, P. I., Xiao, Y., and Fu, T. M.: Ethane, ethyne and carbon monoxide concentrations in the upper troposphere and lower stratosphere from ACE and GEOS-Chem: a comparison study, *Atmos. Chem. Phys.*, 11, 9927–9941, doi:10.5194/acp-11-9927-2011, 2011.
- Granier, C., Lamarque, J., Mieville, A., Müller, J., Olivier, J., Orlando, J., Peters, J., Petron, G., Tyndall, G., and Wallens, S.: POET, a database of surface emissions of ozone precursors, available at: <http://www.pole-ether.fr/eccad> (last access: 22 September 2015), 2005.
- Guenther, A., Karl, T., Harley, P., Wiedinmyer, C., Palmer, P. I., and Geron, C.: Estimates of global terrestrial isoprene emissions using MEGAN (Model of Emissions of Gases and Aerosols from Nature), *Atmos. Chem. Phys.*, 6, 3181–3210, doi:10.5194/acp-6-3181-2006, 2006.
- Gyawali, M., Arnott, W. P., Lewis, K., and Moosmüller, H.: In situ aerosol optics in Reno, NV, USA during and after the summer 2008 California wildfires and the influence of absorbing and non-absorbing organic coatings on spectral light absorption, *Atmos. Chem. Phys.*, 9, 8007–8015, doi:10.5194/acp-9-8007-2009, 2009.
- Hoskins, B. J. and M. J. Rodwell: A model of the Asian summer monsoon. Part I: the global scale, *J. Atmos. Sci.*, 52, 1329–1340, 1995.
- Hyer E. J., Reid, J. S., Prins, E. M., Hoffman, J. P., Schmidt, C. C., Miettinen, J. I., and Giglio, L.: Patterns of fire activity over Indonesia and Malaysia from polar and geostationary satellite observations, *Atmos. Res.*, 122, 504–519, 2013.
- Lamarque, J.-F., Bond, T. C., Eyring, V., Granier, C., Heil, A., Klimont, Z., Lee, D., Liou, S. C., Mieville, A., Owen, B., Schultz, M. G., Shindell, D., Smith, S. J., Stehfest, E., Van Aardenne, J., Cooper, O. R., Kainuma, M., Mahowald, N., McConnell, J. R., Naik, V., Riahi, K., and van Vuuren, D. P.: Historical (1850–2000) gridded anthropogenic and biomass burning emissions of reactive gases and aerosols: methodology and application, *Atmos. Chem. Phys.*, 10, 7017–7039, doi:10.5194/acp-10-7017-2010, 2010.
- Lamarque, J.-F., Emmons, L. K., Hess, P. G., Kinnison, D. E., Tilmes, S., Vitt, F., Heald, C. L., Holland, E. A., Lauritzen, P. H., Neu, J., Orlando, J. J., Rasch, P. J., and Tyndall, G. K.: CAM-chem: description and evaluation of interactive atmospheric chemistry in the Community Earth System Model, *Geosci. Model Dev.*, 5, 369–411, doi:10.5194/gmd-5-369-2012, 2012.
- Lewis S. L., Brando, P. M., Phillips, O. L., van der Heijden, G. M. F., and Nepstad, D.: The 2010 Amazon Drought, *Science*, 331, p. 554, doi:10.1126/science.1200807, 2011.
- Li, Q., Jacob, D., Bey, I., Yantosca, R., Zhao, Y., Kondo, Y., and Notholt, J.: Atmospheric hydrogen cyanide (HCN): Biomass burning source, ocean sink?, *Geophys. Res. Lett.*, 27, 357–360, 2000.
- Li, Q., Jacob, D. J., Yantosca, R. M., Heald, C. L., Singh, H. B., Koike, M., Zhao, Y., Sachse, G. W., and Streets, D. G.: A global three-dimensional model analysis of the atmospheric budgets of HCN and CH₃CN: Constraints from aircraft and ground measurements, *J. Geophys. Res.*, 108, 8827, doi:10.1029/2002JD003075, 2003.
- Li, Q., Palmer, P. I., Pumphrey, H. C., Bernath, P., and Mahieu, E.: What drives the observed variability of HCN in the troposphere and lower stratosphere?, *Atmos. Chem. Phys.*, 9, 8531–8543, doi:10.5194/acp-9-8531-2009, 2009.
- Logan, J. A., Prather, M. J., Wofsy, S. C., and McElroy, M. B.: Tropospheric chemistry: A global perspective, *J. Geophys. Res.*, 86, 7210–7254, 1981.
- Lupu, A., Kaminski, J. W., Neary, L., McConnell, J. C., Toyota, K., Rinsland, C. P., Bernath, P. F., Walker, K. A., Boone, C. D., Nagahama, Y., and Suzuki, K.: Hydrogen cyanide in the upper troposphere: GEM-AQ simulation and comparison with ACE-FTS observations, *Atmos. Chem. Phys.*, 9, 4301–4313, doi:10.5194/acp-9-4301-2009, 2009.
- Magi, B. I., Rabin, S., Shevliakova, E., and Pacala, S.: Separating agricultural and non-agricultural fire seasonality at regional scales, *Biogeosciences*, 9, 3003–3012, doi:10.5194/bg-9-3003-2012, 2012.
- Mahieu, E., Duchatelet, P., Bernath, P. F., Boone, C. D., De Mazière, M., Demoulin, P., Rinsland, C. P., Servais, C., and Walker, K. A.: Retrievals of C₂H₂ from high-resolution FTIR solar spectra recorded at the Jungfraujoch station (46.5° N) and comparison with ACE-FTS observations, *Geophys. Res. Abstract*, 10, <http://hdl.handle.net/2268/15191> (last access: 23 September 2015), 2008.
- Park, M., Randel, W. J., Emmons, L. K., Bernath, P. F., Walker, K. A., and Boone, C. D.: Chemical isolation in the Asian monsoon anticyclone observed in Atmospheric Chemistry Experiment (ACE-FTS) data, *Atmos. Chem. Phys.*, 8, 757–764, doi:10.5194/acp-8-757-2008, 2008.
- Parker, R. J., Remedios, J. J., Moore, D. P., and Kanawade, V. P.: Acetylene C₂H₂ retrievals from MIPAS data and regions of enhanced upper tropospheric concentrations in August 2003, *Atmos. Chem. Phys.*, 11, 10243–10257, doi:10.5194/acp-11-10243-2011, 2011.
- Parrington, M., Palmer, P. I., Henze, D. K., Tarasick, D. W., Hyer, E. J., Owen, R. C., Helmig, D., Clerbaux, C., Bowman, K. W., Deeter, M. N., Barratt, E. M., Coheur, P.-F., Hurtmans, D., Jiang, Z., George, M., and Worden, J. R.: The influence of boreal biomass burning emissions on the distribution of tropospheric ozone over North America and the North Atlantic during 2010, *Atmos. Chem. Phys.*, 12, 2077–2098, doi:10.5194/acp-12-2077-2012, 2012.
- Paton-Walsh, C., Deutscher, N. M., Griffith, D. W. T., Forgan, B. W., Wilson, S. R., Jones, N. B., and Edwards, D. P.: Trace gas emissions from savanna fires in northern Australia, *J. Geophys. Res.*, 115, D16314, doi:10.1029/2009JD013309, 2010.
- Pfister, G. G., Emmons, L. K., Hess, P. G., Honrath, R., Lamarque, J.-F., Val Martin, M., Owen, R. C., Avery, M. A., Browell, E. V., Holloway, J. S., Nédélec, P., Purvis, R., Ryerson, T. B., Sachse, G. W., and Schlager, H.: Ozone production from the 2004 North American boreal fires, *J. Geophys. Res.*, 111, D24S07, doi:10.1029/2006JD007695, 2006.
- Pfister, G. G., Emmons, L. K., Hess, P. G., Lamarque, J.-F., Thompson, A. M., and Yorks, J. E.: Analysis of the summer 2004 ozone budget over the United States using Inter-

- continental Transport Experiment Ozone-sonde Network Study (IONS) observations and Model of Ozone and Related Tracers (MOZART-4) simulations, *J. Geophys. Res.*, 113, D23306, doi:10.1029/2008JD010190, 2008.
- Pfister, G. G., Parrish, D. D., Worden, H., Emmons, L. K., Edwards, D. P., Wiedinmyer, C., Diskin, G. S., Huey, G., Oltmans, S. J., Thouret, V., Weinheimer, A., and Wisthaler, A.: Characterizing summertime chemical boundary conditions for air masses entering the US West Coast, *Atmos. Chem. Phys.*, 11, 1769–1790, doi:10.5194/acp-11-1769-2011, 2011.
- Pumphrey, H. C., Santee, M. L., Livesey, N. J., Schwartz, M. J., and Read, W. G.: Microwave Limb Sounder observations of biomass-burning products from the Australian bush fires of February 2009, *Atmos. Chem. Phys.*, 11, 6285–6296, doi:10.5194/acp-11-6285-2011, 2011.
- Randel W. J., Park, M., Emmons, L., Kinnison, D., Bernath, P., Walker, K. A., Boone, C., and Pumphrey, H.: Asian Monsoon Transport of Pollution to the Stratosphere, *Science*, 328, 611–613, 10.1126/science.1182274, 2010.
- R'Honi, Y., Clarisse, L., Clerbaux, C., Hurtmans, D., Dufлот, V., Turquety, S., Ngadi, Y., and Coheur, P.-F.: Exceptional emissions of NH₃ and HCOOH in the 2010 Russian wildfires, *Atmos. Chem. Phys.*, 13, 4171–4181, doi:10.5194/acp-13-4171-2013, 2013.
- Rinsland, C. P., Goldman, A., Murcray, F. J., Stephen, T. M., Pougatchev, N. S., Fishman, J., David, S. J., Blatherwick, R. D., Novelli, P. C., Jones, N. B., and Connor, B. J.: Infrared solar spectroscopic measurements of free tropospheric CO, C₂H₆, and HCN above Mauna Loa, Hawaii: Seasonal variations and evidence for enhanced emissions from the Southeast Asian tropical fires of 1997–1998, *J. Geophys. Res.*, 104, 18667–18680, 1999.
- Rinsland, C. P., Meier, A., Griffith, D. W. T., and Chiou, L. S.: Ground-based measurements of tropospheric CO, C₂H₆, and HCN from Australia at 34° S latitude during 1997–1998, *J. Geophys. Res.*, 106, 20913–20924, 2001.
- Rinsland C. P., Jones, N. B., Connor, B. J., Wood, S. W., Goldman, A., Stephen, T. M., Murcray, F. J., Chiou, L. S., Zander, R., and Mahieu, E.: Multiyear infrared solar spectroscopic measurements of HCN, CO, C₂H₆, and C₂H₂ tropospheric columns above Lauder, New Zealand (45° S latitude), *J. Geophys. Res.*, 107, 4185, doi:10.1029/2001JD001150, 2002.
- Rodgers, C. D.: Inverse methods for atmospheric sounding: Theory and Practice, Series on Atmospheric, Oceanic and Planetary Physics Vol. 2, World Scientific Publishing CO., Singapore, 2000.
- Rodgers, C. D. and Connor, B. J.: Intercomparison of remote sounding instruments, *J. Geophys. Res.*, 108, 4116–4129, 2003.
- Sancho, P., De La Cruz, J., Diaz, A., Martin, F., Hernandez, E., Valero, F., and Albarran, B.: A five-year climatology of back-trajectories from the Izaña baseline station, Tenerife, Canary Islands, *Atmos. Environ.*, 26, 1081–1096, 1992.
- Sauvage, B., Thouret, V., Cammas, J.-P., Gheusi, F., Athier, G., and Nédélec, P.: Tropospheric ozone over Equatorial Africa: regional aspects from the MOZAIC data, *Atmos. Chem. Phys.*, 5, 311–335, doi:10.5194/acp-5-311-2005, 2005.
- Singh, H. B., Salas, L., Herlth, D., Kolyer, R., Czech, E., Viezee, W., Li, Q., Jacob, D. J., Blake, D., Sachse, G., Harward, C. N., Fuelberg, H., Kiley, C. M., Zhao, Y., and Kondo, Y.: In situ measurements of HCN and CH₃CN over the Pacific Ocean: sources, sinks and budgets, *J. Geophys. Res.*, 108, 8795, doi:10.1029/2002JD003006, 2003.
- Standard Atmosphere: National Atmospheric and Oceanic Administration S/T 76–1562, US Government Printing Office, Washington DC, 1976.
- Tilmes, S., Emmons, L. K., Law, K. S., Ancellet, G., Schlager, H., Paris, J.-D., Fuelberg, H. E., Streets, D. G., Wiedinmyer, C., Diskin, G. S., Kondo, Y., Holloway, J., Schwarz, J. P., Spackman, J. R., Campos, T., Nédélec, P., and Panchenko, M. V.: Source contributions to Northern Hemisphere CO and black carbon during spring and summer 2008 from POLARCAT and START08/preHIPPO observations and MOZART-4, *Atmos. Chem. Phys. Discuss.*, 11, 5935–5983, doi:10.5194/acpd-11-5935-2011, 2011.
- Van Damme, M., Clarisse, L., Heald, C. L., Hurtmans, D., Ngadi, Y., Clerbaux, C., Dolman, A. J., Erisman, J. W., and Coheur, P. F.: Global distributions, time series and error characterization of atmospheric ammonia (NH₃) from IASI satellite observations, *Atmos. Chem. Phys.*, 14, 2905–2922, doi:10.5194/acp-14-2905-2014, 2014.
- van der Werf, G. R., Randerson, J. T., Giglio, L., Collatz, G. J., Kasibhatla, P. S., and Arellano Jr., A. F.: Interannual variability in global biomass burning emissions from 1997 to 2004, *Atmos. Chem. Phys.*, 6, 3423–3441, doi:10.5194/acp-6-3423-2006, 2006.
- van der Werf, G. R., Randerson, J. T., Giglio, L., Collatz, G. J., Mu, M., Kasibhatla, P. S., Morton, D. C., DeFries, R. S., Jin, Y., and van Leeuwen, T. T.: Global fire emissions and the contribution of deforestation, savanna, forest, agricultural, and peat fires (1997–2009), *Atmos. Chem. Phys.*, 10, 11707–11735, doi:10.5194/acp-10-11707-2010, 2010.
- Viatte, C., Strong, K., Hannigan, J., Nussbaumer, E., Emmons, L. K., Conway, S., Paton-Walsh, C., Hartley, J., Benmergui, J., and Lin, J.: Identifying fire plumes in the Arctic with tropospheric FTIR measurements and transport models, *Atmos. Chem. Phys.*, 15, 2227–2246, doi:10.5194/acp-15-2227-2015, 2015.
- Vigouroux, C., Stavrou, T., Whaley, C., Dils, B., Dufлот, V., Hermans, C., Kumps, N., Metzger, J.-M., Scolas, F., Vanhaelewyn, G., Müller, J.-F., Jones, D. B. A., Li, Q., and De Mazière, M.: FTIR time-series of biomass burning products (HCN, C₂H₆, C₂H₂, CH₃OH, and HCOOH) at Reunion Island (21° S, 55° E) and comparisons with model data, *Atmos. Chem. Phys.*, 12, 10367–10385, doi:10.5194/acp-12-10367-2012, 2012.
- Volkamer, R., Ziemann, P. J., and Molina, M. J.: Secondary Organic Aerosol Formation from Acetylene (C₂H₂): seed effect on SOA yields due to organic photochemistry in the aerosol aqueous phase, *Atmos. Chem. Phys.*, 9, 1907–1928, doi:10.5194/acp-9-1907-2009, 2009.
- Walker, J. C., Dudhia, A., and Carboni, E.: An effective method for the detection of trace species demonstrated using the MetOp Infrared Atmospheric Sounding Interferometer, *Atmos. Meas. Tech.*, 4, 1567–1580, doi:10.5194/amt-4-1567-2011, 2011.
- Wespes, C., Emmons, L., Edwards, D. P., Hannigan, J., Hurtmans, D., Saunio, M., Coheur, P.-F., Clerbaux, C., Coffey, M. T., Batchelor, R. L., Lindenmaier, R., Strong, K., Weinheimer, A. J., Nowak, J. B., Ryerson, T. B., Crounse, J. D., and Wennberg, P. O.: Analysis of ozone and nitric acid in spring and summer Arctic pollution using aircraft, ground-based, satellite observations and MOZART-4 model: source attribution and partitioning, *At-*

- mos. Chem. Phys., 12, 237–259, doi:10.5194/acp-12-237-2012, 2012.
- Wiedinmyer, C., Quayle, B., Geron, C., Belote, A., McKenzie, D., Zhang, X., O'Neill, S., and Wynne, K.: Estimating emissions from fires in North America for air quality modeling, *Atmos. Environ.*, 40, 3419–3432, 2006.
- Wiedinmyer, C., Akagi, S. K., Yokelson, R. J., Emmons, L. K., Al-Saadi, J. A., Orlando, J. J., and Soja, A. J.: The Fire INventory from NCAR (FINN): a high resolution global model to estimate the emissions from open burning, *Geosci. Model Dev.*, 4, 625–641, doi:10.5194/gmd-4-625-2011, 2011.
- Wiegele, A., Glatthor, N., Höpfner, M., Grabowski, U., Kellmann, S., Linden, A., Stiller, G., and von Clarmann, T.: Global distributions of C₂H₆, C₂H₂, HCN, and PAN retrieved from MIPAS reduced spectral resolution measurements, *Atmos. Meas. Tech.*, 5, 723–734, doi:10.5194/amt-5-723-2012, 2012.
- Xiao, Y., Jacob, D. J., and Turquety, S.: Atmospheric acetylene and its relationship with CO as an indicator of air mass age, *J. Geophys. Res.-Atmos.*, 112, D12305, doi:10.1029/2006JD008268, 2007.
- Yienger, J. J., Galanter, M., Holloway, T. A., Phadnis, M. J., Guttikunda, S. K., Carmichael, G. R., Moxim, W. J., and Levy II, H.: The episodic nature of air pollution transport from Asia to North America, *J. Geophys. Res.*, 105, 26931–26945, doi:10.1029/2000JD900309, 2000.
- Yulianti N. and Hayasaka, H.: Recent Active Fires under El Niño Conditions in Kalimantan, Indonesia, *American Journal of Plant Sciences*, 4, 685–696, 2013.
- Zander, R., Rinsland, C. P., Ehhalt, D. H., Rudolph, J., and Demoulin, P. H.: Vertical Column Abundances and Seasonal Cycle of Acetylene, C₂H₂, above the Jungfraujoch Station, Derived from IR Solar observations, *J. Atmos. Chem.*, 13, 359–372, 1991.
- Zhang, Q., Streets, D. G., Carmichael, G. R., He, K. B., Huo, H., Kannari, A., Klimont, Z., Park, I. S., Reddy, S., Fu, J. S., Chen, D., Duan, L., Lei, Y., Wang, L. T., and Yao, Z. L.: Asian emissions in 2006 for the NASA INTEX-B mission, *Atmos. Chem. Phys.*, 9, 5131–5153, doi:10.5194/acp-9-5131-2009, 2009.
- Zhao, Y., Strong, K., Kondo, Y., Koike, M., Matsumi, Y., Irie, H., Rinsland, C. P., Jones, N. B., Suzuki, K., Nakajima, H., Nakane, H., and Murata, I.: Spectroscopic measurements of tropospheric CO, C₂H₆, C₂H₂, and HCN in northern Japan, *J. Geophys. Res.*, 107, 4343, doi:10.1029/2001JD000748, 2002.